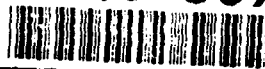


AD-A246 307



2



January 1991

DTIC
S D
FEB 19 1992

This document has been approved
for public release and sale; its
distribution is unlimited.

92 2 17 048

92-04024
■■■■■■■■■■



**Ocean Engineering
Studies**

Compiled 1991

**Volume X: External
Pressure Housings—
Concrete**

J. D. Stachiw

**PUBLISHED BY
NAVAL OCEAN SYSTEMS CENTER
SAN DIEGO, CALIFORNIA**

Foreword

Exploitation of the ocean floor for commercial or military use requires not only Remotely Operated Vehicles (ROVs), Autonomous Underwater Vehicles (AUVs), submersibles, and diving systems; it also requires 1-atmosphere enclosures permanently—or semipermanently—affixed to the ocean floor. These 1-atmosphere enclosures would serve as habitats for the crews, covers for mine shafts, and pressure-resistant buildings for ore or food-processing plants. Bottom-mounted pressure-resistant enclosures must be negatively buoyant, instead of positively buoyant (as they are with pressure hulls for submersibles). This allows them to be constructed from inexpensive materials with low specific compressive strength.

The primary choice for such applications is Portland cement concrete, since it is inexpensive, can be cast in situ, does not deteriorate under long-term immersion, and has a fair specific compressive strength. In fact, its specific compressive strength is high enough to qualify the material as a viable candidate for use in constructing large submarine oil tankers that require pressure hulls with only marginal positive buoyancy.

Since concrete has not previously been used for constructing pressure-resistant shells for ocean engineering structures, there was a total absence of engineering data on which to base the design of any pressure-resistant concrete housings for U.S. Navy applications. To make up for this deficiency, the U.S. Navy initiated a research program whose objective was to generate sufficient data to enable formulation of design criteria to construct concrete pressure housings. The principal investigators were Dr. Stachiw, and Messrs. Haynes, Albertsen, Kahn, Highberg, and Hoofnagle. The reports these investigators produced effectively summarize the scope and results of the research program.

The results of the program were sufficiently encouraging and comprehensive to allow formulation of design criteria for use by U.S. Navy engineers. The performance of model scale concrete housings employed in the research program provided the data to use for confidently designing full-scale pressure-resistant concrete enclosures with an infinite lifetime.

Volume IX is a compilation of reports that summarize the studies on 15-inch diameter spherical test specimens to experimentally evaluate the effect of wall thickness, impregnation, reinforcement techniques, and penetrations on critical pressure, creep, and permeability.

Volume X is a compilation of reports that summarize the studies on (1) 15-inch diameter cylinders and (2) 66-inch diameter spheres under short-term and long-term loading. This volume also contains the design criteria and recommendations formulated at the conclusion of the research program on concrete external-pressure housings.

Accession For	
NTIS CRA&I	<input checked="checked" type="checkbox"/>
DTIC TAB	<input type="checkbox"/>
Unannounced	<input type="checkbox"/>
Justification	
By	
Distribution	
Availability Codes	
Dist	Availability Codes
A-1	

J. D. Stachiw
Marine Materials Office
Ocean Engineering
Division

TABLE OF CONTENTS: VOLUME X

TR R790	Influence of Compressive Strength and Wall Thickness on Behavior of Concrete Cylindrical Hulls Under Hydrostatic Loading
TR R740	Influence of End-Closure Stiffness on Behavior of Concrete Cylindrical Hulls Subjected to Hydrostatic Loading
TR R735	Influence of Stiff Equatorial Rings on Concrete Spherical Hulls Subjected to Hydrostatic Loading
TR R679	Failure of Thick-Walled Concrete Spheres Subjected to Hydrostatic Loading
TR R774	Behavior of 66-Inch Concrete Spheres Under Short- and Long-Term Hydrostatic Loading
TR R805	Long-Term Deep-Ocean Test of Concrete Spherical Structures — Part I: Fabrication, Emplacement, and Initial Inspections
TR R869	Long-Term, Deep-Ocean Test of Concrete Spherical Structures — Results After 6 Years
TN 1760	Handbook for Design of Undersea, Pressure-Resistant Concrete Structures

Technical Report

R 790



Sponsored by

NAVAL FACILITIES ENGINEERING COMMAND

June 1973

NAVAL CIVIL ENGINEERING LABORATORY
Port Hueneme, California 93043



INFLUENCE OF
COMPRESSIVE STRENGTH
AND WALL THICKNESS
ON BEHAVIOR OF
CONCRETE CYLINDRICAL
HULLS UNDER
HYDROSTATIC LOADING

By

N. D. Albertsen

Approved for public release;
distribution unlimited.

INFLUENCE OF COMPRESSIVE STRENGTH AND WALL THICKNESS ON BEHAVIOR OF CONCRETE CYLINDRICAL HULLS UNDER HYDROSTATIC LOADING

Technical Report R-790

3.1610-1

by

N. D. Albertsen

ABSTRACT.

Sixteen unreinforced, cylindrical concrete hull models of 16-inch outside diameter were subjected to external hydrostatic loading to determine the effect of concrete strength and wall thickness on implosion and strain behavior. The test results showed that an increase in concrete strength of 70% produced an average increase in implosion pressure of 87%, while increases in hull wall thickness by factors of 2 and 6 produced increases in implosion pressure by factors of approximately 2 and 11, respectively. Changes in concrete strength had little effect on strain behavior; however, strain magnitudes generally increased with increasing wall thickness when comparisons were made at a constant percentage of P_{im} . Design recommendations are presented to aid in the design of cylindrical concrete hulls for underwater use.

Approved for public release; distribution unlimited.

Copies available at the National Technical Information Service (NTIS),
Sills Building, 5285 Port Royal Road, Springfield, Va. 22151

CONTENTS

	Page
INTRODUCTION	1
EXPERIMENTAL PROGRAM	1
Experiment Design	1
Fabrication of Specimens	2
Test Procedure	3
TEST RESULTS AND DISCUSSION	8
Mode of Failure	8
Implosion	10
Strain	13
DESIGN PROBLEM	19
FINDINGS	23
CONCLUSIONS	24
RECOMMENDATIONS	24
ACKNOWLEDGMENTS	24
APPENDIX — Control Cylinder Data	25
REFERENCES	26
LIST OF SYMBOLS	27

INTRODUCTION

Previous studies¹⁻⁸ conducted at the Naval Civil Engineering Laboratory (NCEL) have shown that concrete is an effective construction material for undersea pressure-resistant structures. Experiments on concrete cylindrical hulls^{5,7} with 16-inch outside diameters, 2-inch-thick walls, and 8- to 128-inch lengths have established the influence of the length-to-outside-diameter, L/D_o , ratio and the end-closure stiffness on implosion pressure, strain magnitude, and strain distribution. Figure 1 shows that the thick wall theory based on Lamé's equation conservatively predicts implosion pressure for cylindrical concrete hulls with a wall-thickness-to-outside-diameter, t/D_o , ratio of 0.125 and L/D_o ratios from 0 to 8. The strain and implosion data for these hulls indicate that the effects of hemispherical concrete end-closures are minimal at a distance ≥ 1 diameter from the edge of the cylinder, and, thus, cylinders with L/D_o ratios greater than 2 can be considered to be infinitely long. Variations in end-closure stiffness did not cause a reduction in the implosion pressure of cylindrical concrete hulls below values predicted by Lamé's equation; however, rigid end-closures produced high shear strains near the closure which would be undesirable for structures subjected to long-term submergence.

The objective of this study was to determine experimentally the relationship between implosion pressure, concrete strength, wall thickness, strain distribution, and strain magnitude in cylindrical concrete hulls subjected to external hydrostatic loading.

Data from this experimental study were used to develop design guidelines so that safe and economical pressure-resistant cylindrical concrete structures can be designed for underwater applications.

EXPERIMENTAL PROGRAM

Experiment Design

Sixteen concrete cylindrical hulls having four different wall thicknesses and two concrete strengths were tested to implosion under short-term hydrostatic loading. The hulls had wall thicknesses of 1/2, 1,

2, and 3 inches (Figure 2) which correspond to t/D_o ratios of 0.0312, 0.0625, 0.1250, and 0.1875. All cylinders were 16 inches in outside diameter and 64 inches long; each had hemispherical concrete end-closures of the same wall thickness as the cylinder. Two hulls of each wall thickness were made of concrete with a uniaxial compressive strength, f'_c , of approximately 6,000 psi and two of approximately 10,000 psi. One hull of each concrete strength and wall thickness was instrumented with electrical resistance strain gages. A summary of the design information for the cylindrical hulls is given in Table 1.

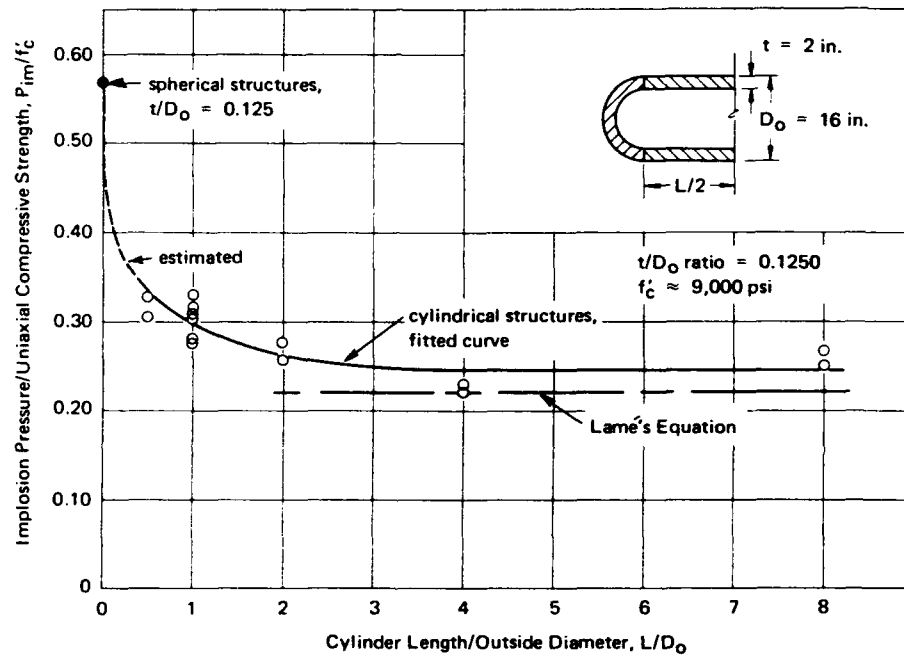


Figure 1. Analytical prediction of implosion pressure (after Reference 5).

Fabrication of Specimens

All cylinders and hemispherical end-closures were cast in rigid metal molds which had been machined to tolerances of $\pm 1/32$ inch. The cylinders and end-closures were made from a microconcrete mix consisting of type II portland cement, San Gabriel River Wash Aggregate, and freshwater. Concrete strengths of approximately 6,000 and 10,000 psi were produced by varying the water-to-cement ratio and the cure procedure. Table 2 gives the mix proportions and cure times, and Table 3 gives the aggregate proportions which remained the same for both mixes.

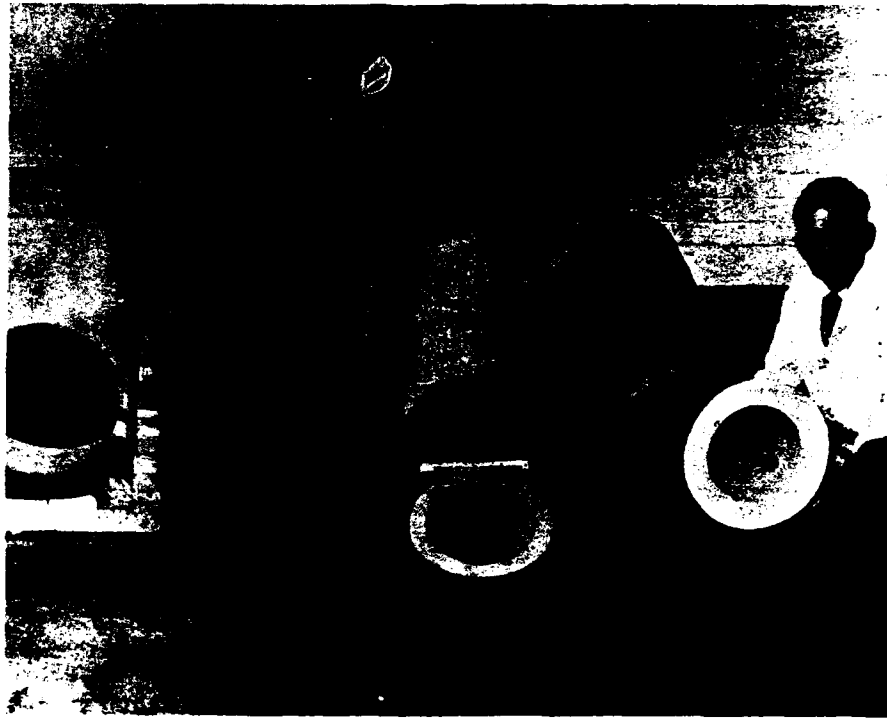


Figure 2. Cylindrical test specimens with wall thicknesses ranging from 1/2 inch to 3 inches.

After moist curing, the cylinders and end-closures were stored under room conditions while being prepared for test. Hull preparation began with a light sandblasting of surfaces to expose surface voids and to remove laitance. Small, shallow voids were filled with a cement-sand paste, while larger voids were filled with an epoxy adhesive. The mating surfaces of the cylinders and end-closures were ground flat by rotating them on a flat plate covered with No. 60 Silicon Carbide grit. Next the cylinders and hemispheres were water-proofed with a clear epoxy paint and bonded together with an epoxy adhesive. The final step in the specimen fabrication was to apply electrical resistance strain gages. Figure 3 shows a cross section of a fabricated cylindrical hull, and Figure 4 shows the strain gage layout for the hulls.

Test Procedure

The cylindrical hulls were tested in NCEL's 72-inch pressure vessel (Figure 5). The hulls were filled with water and vented to outside the pressure vessel. During a typical test, external pressure was applied to the hull at a

constant rate until implosion occurred. The pressurization rate was 20 psi/min for the 1/2-inch-thick hulls and 100 psi/min for the 1-, 2-, and 3-inch-thick hulls. At selected pressure intervals, the strain gages were interrogated and the change in volume of the specimen was recorded. Change in volume was measured by collecting the water displaced under load from the hull's interior.

Table 1. Description of Cylindrical Hulls

(All cylinders were 64 inches long and 16 inches in outside diameter.)

Cylinder Designation ^a	t/D _o Ratio	Wall Thickness (in.)	Nominal Uniaxial Compressive Strength of Concrete (psi)	Strain Gages on Hull ^b
1/2-10-G 1/2-10-N 1/2-6-G 1/2-6-N	0.0312	0.5	10,000 10,000 6,000 6,000	1 to 34 0 1 to 14 0
1-10-G 1-10-N 1-6-G 1-6-N	0.0625	1.0	10,000 10,000 6,000 6,000	1 to 34 0 1 to 14 0
2-10-G 2-10-N 2-6-G 2-6-N	0.1250	2.0	10,000 10,000 6,000 6,000	1 to 34 0 1 to 14 0
3-10-G 3-10-N 3-6-G 3-6-N	0.1875	3.0	10,000 10,000 6,000 6,000	1 to 34 0 1 to 14 0

^a Designation system is: Wall thickness (inches)—Nominal concrete strength (ksi)—Gaged or Not gaged hull.

^b See Figure 4 for location of gages.

Table 2. Mix Proportions and Cure Times

Approximate Uniaxial Compressive Strength of Mix (psi)	Water-to-Cement (by weight) Ratio	Aggregate-to-Cement (by weight) Ratio	Cure Time in 100% RH (days)	Approximate Age at Test (days)
10,000	0.56	3.30	90	120
6,000	0.65	3.30	7	28

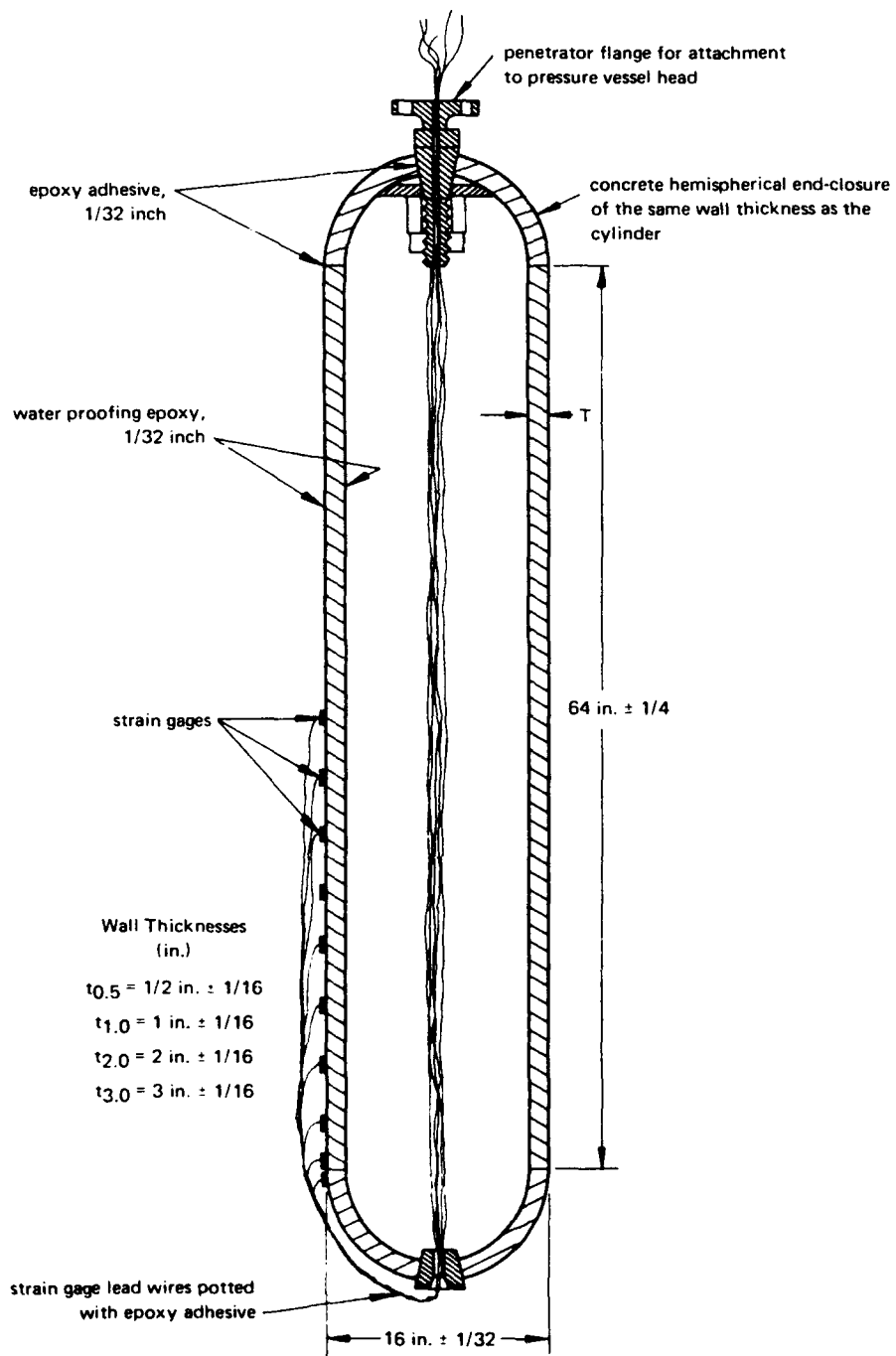
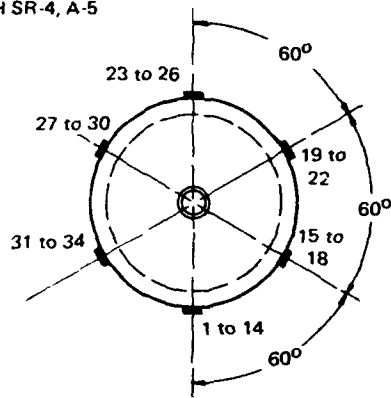


Figure 3. Cross-section of cylindrical hull with hemispherical end-closures.

Gage type: BLH SR-4, A-5



Cylinder Unfolded to Show Strain Gage Layout

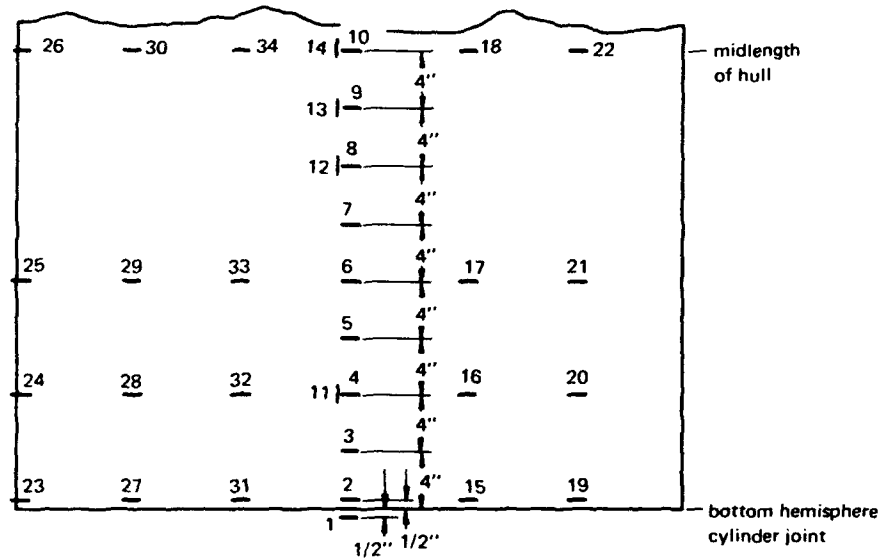


Figure 4. Strain gage layout for the cylindrical hulls.

Table 3. Aggregate Proportions

Sieve Size Designation		Percent Retained
Passing	Retained	
No. 4	No. 8	29.6
No. 8	No. 16	20.8
No. 16	No. 30	14.7
No. 30	No. 50	10.3
No. 50	No. 100	7.3
No. 100	pan	17.3

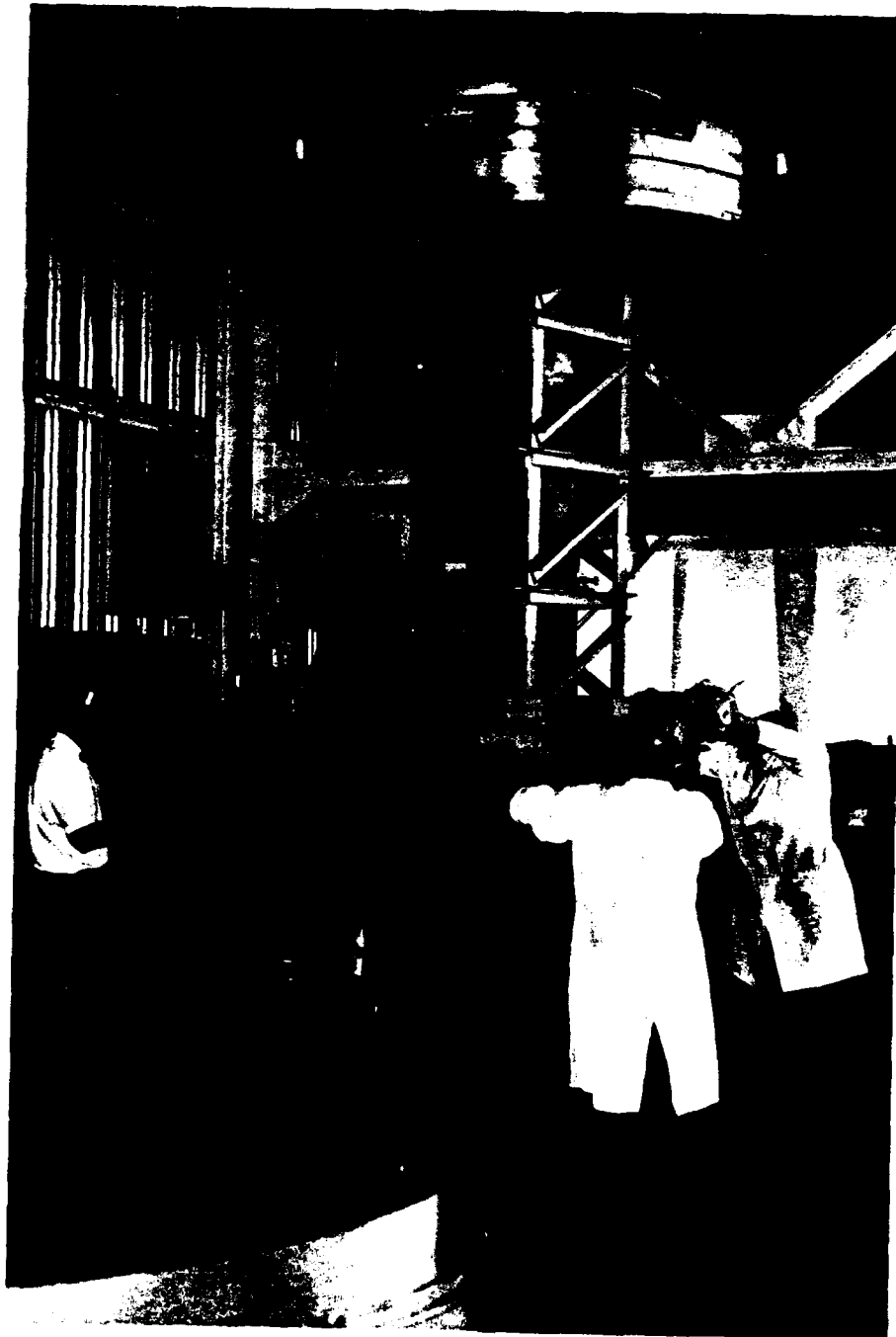


Figure 5. Cylindrical concrete hull prior to being lowered into the pressure vessel for test.

TEST RESULTS AND DISCUSSION

Mode of Failure

Inspection of the hulls after testing indicated that failure occurred, depending on wall thickness, either by compression-induced shear or by buckling. Hulls with 1-, 2-, or 3-inch-thick walls imploded when the concrete failed in the compressive-shear mode. The resulting shear plane could be easily identified by examining the specimens after test; a typical shear plane is shown in Figure 6. The shear planes were oriented parallel to the longitudinal axis of the cylinder and formed an angle of from 20 to 40 degrees with a tangent to the exterior surface. In most cases, the midlength of the shear plane was between 16 and 24 inches from the edge of the cylinder and coincided with the center of the implosion hole. This failure mode is representative of material failure.



Figure 6. Compressive-shear failure of specimen 3-10-N.

The shear planes that were evident in the thicker hulls were completely absent from the 1/2-inch-thick hulls. These hulls shattered into many pieces at failure (Figure 7), which made it impossible to locate the initial point of failure. The mode of failure for these thin specimens appeared to be by buckling, because at failure the maximum wall stresses ranged from 53 to 62 percent of the uniaxial compressive strength of the concrete (Table 4).



Figure 7. Fragments of specimen 1/2-10-G.

Table 4. Implosion Test Results

Specimen Number	Wall Thickness ^a (in.)	Compressive Strength of Concrete, f'_c (psi)	Implosion Pressure, P_{im} (psi)	$\frac{P_{im}}{f'_c}$	Calculated Interior Hoop Stress at Implosion, σ_{Hmax} (psi)	$\frac{\sigma_{Hmax}}{f'_c}$
1/2-10-N	1/2	10,700	376	0.035	6,210	0.58
1/2-10-G		10,900	349	0.032	5,765	0.53
1/2-6-N		5,420	203	0.037	3,355	0.62
1/2-6-G		5,760	214	0.037	3,535	0.61
1-10-N	1	10,700	1,110	0.104	9,470	0.88
1-10-G		10,480	1,103	0.105	9,410	0.90
1-6-G		6,620	547	0.083	4,665	0.70
1-6-N		5,920	530	0.090	4,520	0.76

continued

Table 4. Continued

Specimen Number	Wall Thickness ^a (in.)	Compressive Strength of Concrete, ^b f'_c (psi)	Implosion Pressure, P_{im} (psi)	$\frac{P_{im}}{f'_c}$	Calculated Interior Hoop Stress at Implosion, σ_{Hmax} (psi)	$\frac{\sigma_{Hmax}}{f'_c}$
2-10-G	2	9,840	2,335	0.237	10,670	1.08
2-10-N		9,950	2,455	0.247	11,220	1.13
2-6-N		6,080	1,387	0.228	6,340	1.04
2-6-G		6,060	1,447	0.238	6,615	1.09
3-10-G	3	10,350	3,755	0.363	12,315	1.19
3-10-N		10,800	4,107	0.380	13,470	1.25
3-6-N		7,000	2,405	0.344	7,890	1.13
3-6-G		6,200	1,980	0.319	6,495	1.05

^a Wall thicknesses of 1/2, 1, 2, and 3 inches correspond to t/D_o ratios of 0.0312, 0.0625, 0.1250, and 0.1875, respectively.

^b Average of six 3 x 6-inch control cylinders tested in uniaxial compression (see the Appendix).

No evidence was found in the debris from the tested specimens to indicate the presence of in-plane cracking. In-plane cracking is the development of cracks parallel to the maximum principal stresses (or in-the-plane of the wall) and has been found by other investigators working with concrete spherical⁴ and cylindrical^{5,11} hulls under biaxial stresses.

Implosion

Implosion performance was evaluated by comparing values for the ratio of implosion pressure to concrete strength, P_{im}/f'_c ; the implosion test results are presented in Table 4. This ratio accounts for small variations in concrete strength. Figure 8 shows the best fit relationship between P_{im}/f'_c and t/D_o for the test results. The empirical equation which defines the best fit curve is:

$$\frac{P_{im}}{f'_c} = 2.05 \frac{t}{D_o} - 0.028 \quad (1)$$

for $0.0312 \leq t/D_o \leq 0.1875$. Equation 1 can be used to predict the implosion pressure of cylindrical concrete hulls under hydrostatic loading.

The implosion pressure for concrete cylindrical hulls subjected to hydrostatic loading can be estimated by classical equations. Lamé's equation can be used to estimate the implosion pressure of cylindrical hulls which fail

in the compressive shear mode, if failure is assumed to occur when the maximum principal stress reaches the uniaxial compressive strength of the concrete.⁹ Lamé's equation is

$$P_{im} = f'_c \frac{r_o^2 - r_i^2}{2r_o^2} \quad (2)$$

where P_{im} = implosion pressure due to compressive shear failure (psi)

f'_c = uniaxial compressive strength of concrete (psi)

r_i = exterior radius of hull (in.)

r_o = interior radius of hull (in.)

The implosion pressure of cylindrical concrete hulls of finite length that fail by buckling can be estimated by Bresse's equation.¹⁰ The equation is:

$$P_{cr} = \frac{2E_s}{1 - \nu^2} \left(\frac{t}{D} \right)^3 \quad (3)$$

where P_{cr} = implosion pressure due to buckling (psi)

E_s = secant modulus of elasticity to $0.5 f'_c$ (psi)

ν = Poisson's ratio at $0.5 f'_c$

t = wall thickness of the hull (in.)

D = mean hull diameter (in.)

A graphical presentation of Equations 2 and 3 is also given in Figure 8.

Figure 8 shows that the 1/2- and 1-inch-thick hulls ($t/D_o = 0.0312$ and 0.0625) imploded at pressures lower than those predicted by Equation 2, while the 2- and 3-inch-thick hulls ($t/D_o = 0.1250$ and 0.1875) imploded at pressures higher than those predicted by Equation 2. For the thinner hulls, structural instability kept the concrete from developing its full compressive strength before buckling or premature compressive shear failure occurred. For the thicker hulls, the concrete in the walls was under a state of multi-axial stress which permitted the concrete to resist stresses greater than the uniaxial strength. At implosion, the 2- and 3-inch-thick hulls experienced stresses that *exceeded* f'_c by 4 to 25% (Table 4).

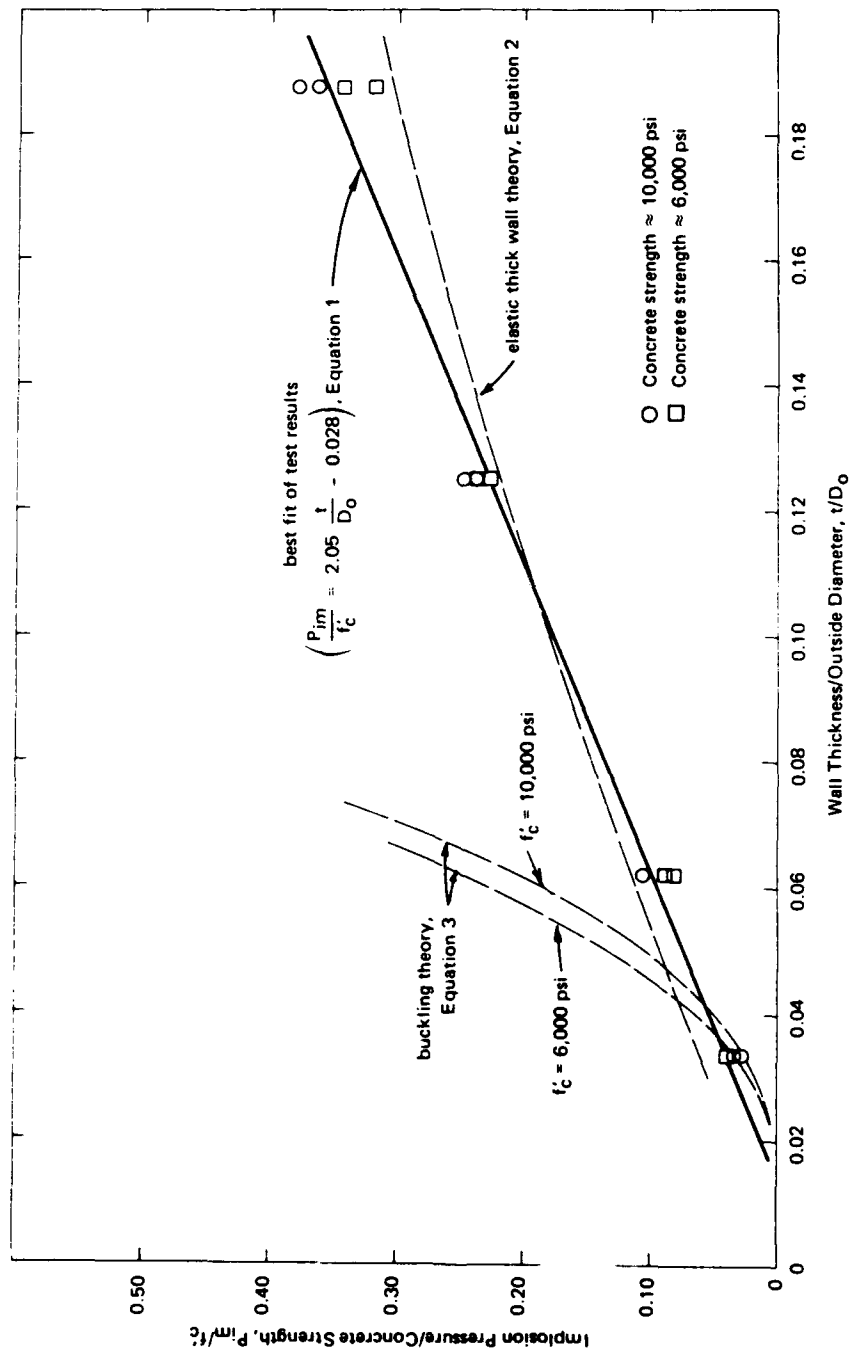


Figure 8. Comparison of implosion test results with elastic thick wall theory and buckling theory.

Strain

Figures 9 through 18 show the strain and radial displacement data for the instrumented hulls. These data helped to define the influence of wall thickness, concrete strength, and end-closure effects on the behavior of the hulls.

Figures 9 through 12 show the exterior hoop strain behavior for specimens of each wall thickness. These figures indicate that the hulls reacted to increasing hydrostatic pressure in approximately the same manner regardless of concrete strength. Within one outside diameter (16 inches) from the edge of the cylinder, large variations in strain magnitude were present; these variations in strain magnitude increased with increased pressure. Beyond 16 inches the strain magnitudes became somewhat uniform. This behavior was caused by the stiffness mismatch that existed between the stiff hemispherical end-closure and the more compliant cylinder; this is consistent with behavior observed in References 5 and 7.

The hoop strain data also show that as the hulls became thicker, the strain magnitude tended to become greater at a constant percentage of P_{im} . This behavior is reasonable because the concrete in the thicker walled hulls is subjected to higher triaxial loading conditions than the concrete in the thinner walled hulls. Table 5 shows that at $0.95 P_{im}$, the theoretical radial stress component on a midwall element increased from 3 to 26% of the hoop stress component and from 6 to 41% of the axial stress component when the wall thickness was increased from 1/2 to 3 inches. It is known that concrete under a high triaxial loading state can sustain higher stresses and strains than concrete under a low triaxial (or biaxial/uniaxial) loading state.

Table 5. Theoretical Midwall Stresses at $0.95 P_{im}$ ^a

(All stresses are compressive.)

Wall Thickness, t (in.)	Applied External Pressure, P (psi)	Radial Stress, σ_R (psi)	Hoop Stress, σ_H (psi)	Axial Stress, σ_A (psi)	$\frac{\sigma_R}{\sigma_H}$	$\frac{\sigma_R}{\sigma_A}$
1/2	345	170	5,460	2,820	0.03	0.06
1	1,050	580	8,380	4,480	0.07	0.13
2	2,280	1,380	9,020	5,210	0.15	0.25
3	3,740	2,520	9,720	6,130	0.26	0.41

^a P_{im} was 363, 1,105, 2,400, and 3,940 psi, respectively, for the 1/2-, 1-, 2-, and 3-inch-thick hulls.

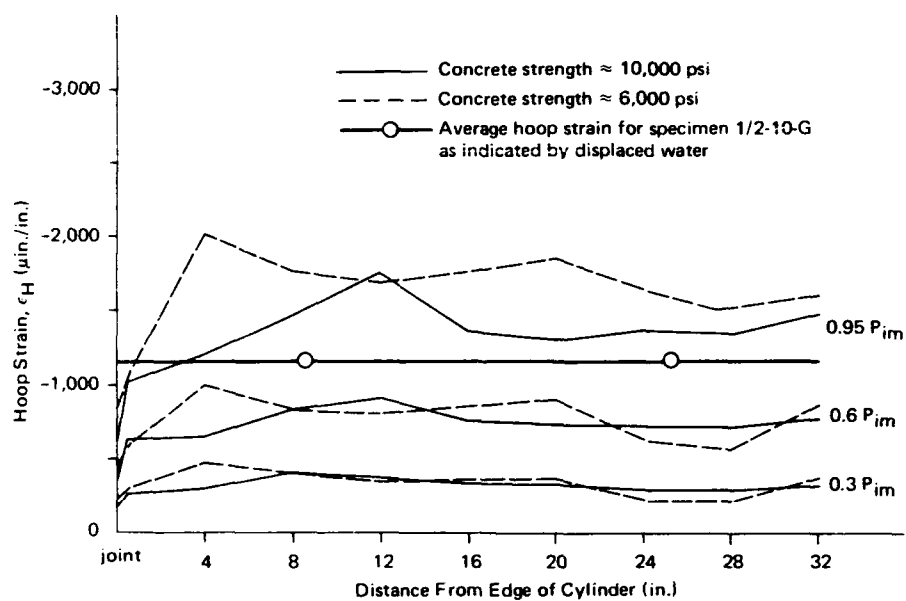


Figure 9. Exterior hoop strain for specimens 1/2-10-G and 1/2-6-G.

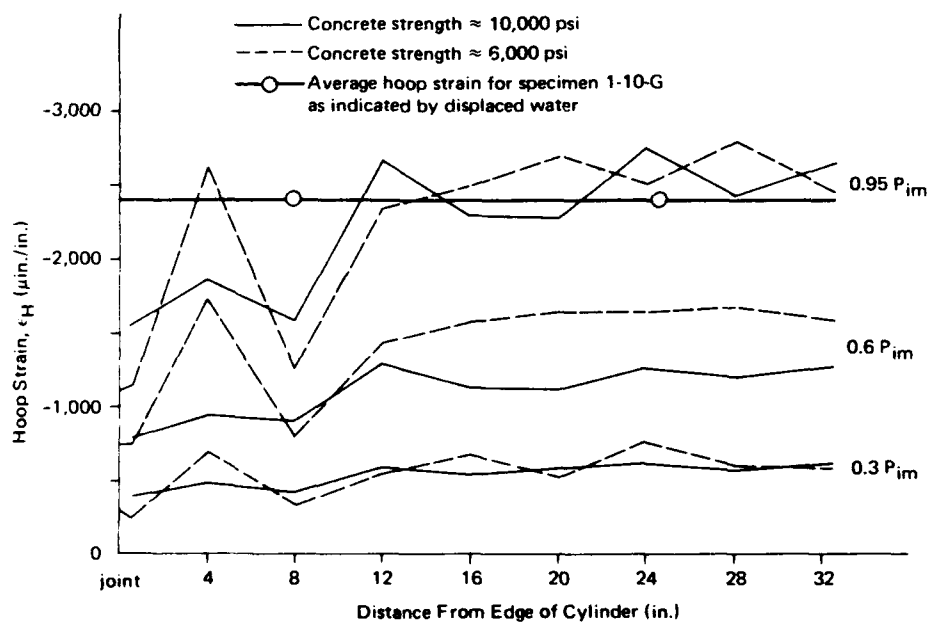


Figure 10. Exterior hoop strain for specimens 1-10-G and 1-6-G.

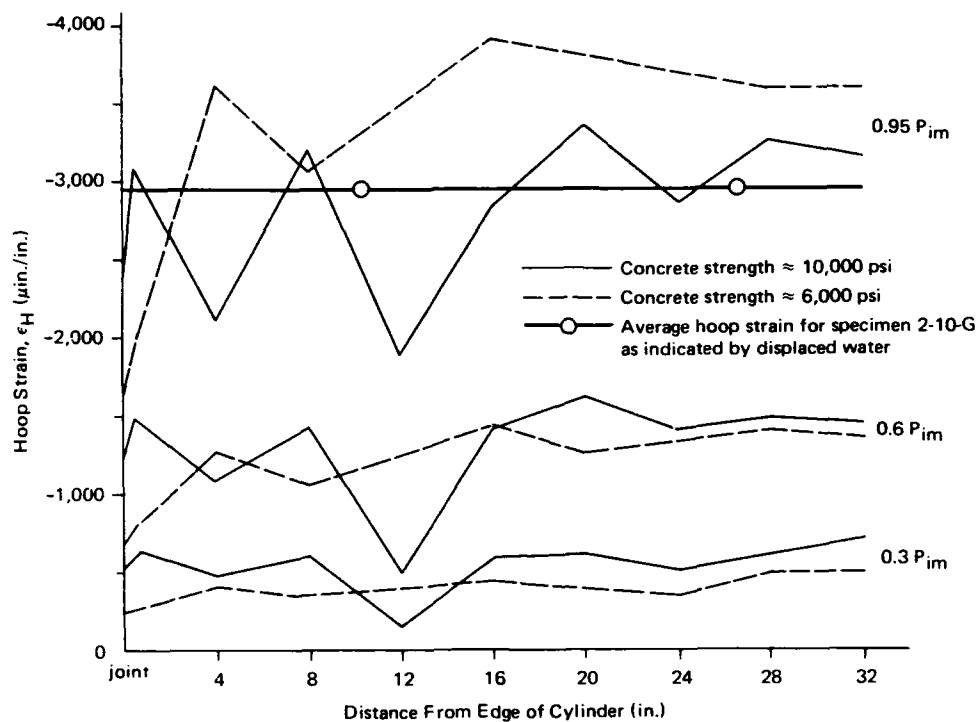


Figure 11. Exterior hoop strain for specimens 2-10-G and 2-6-G.

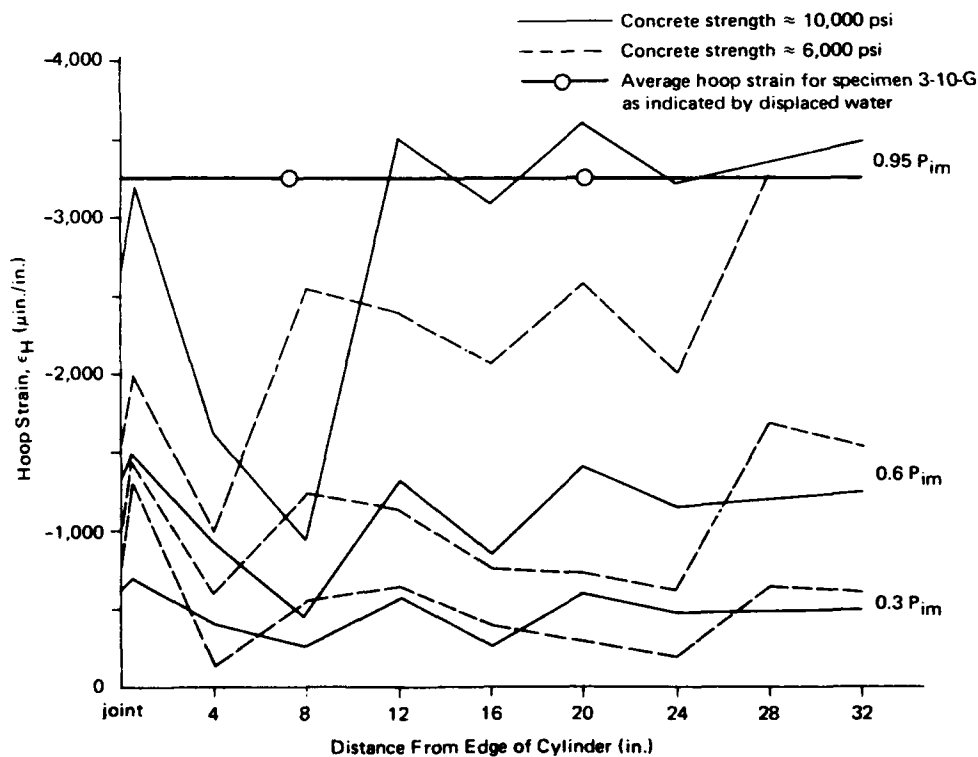


Figure 12. Exterior hoop strain for specimens 3-10-G and 3-6-G.

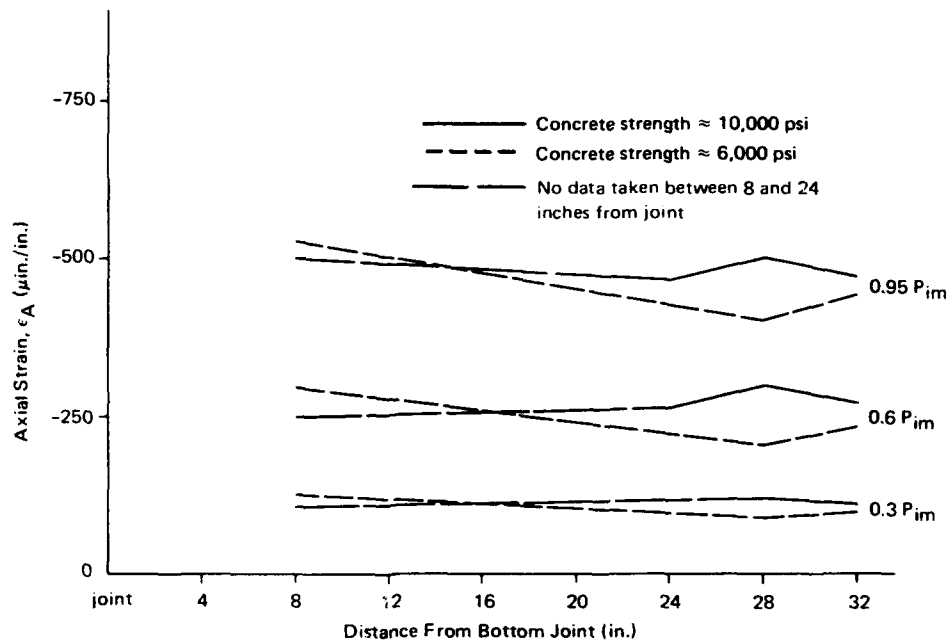


Figure 13. Exterior axial strain for specimens 1/2-10-G and 1/2-6-G.

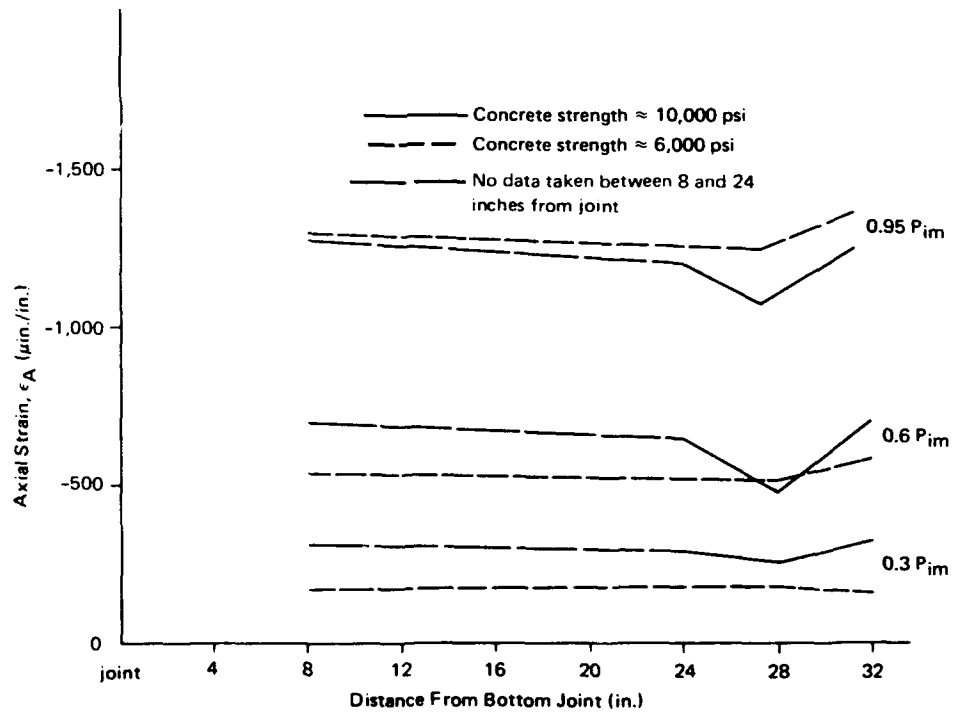


Figure 14. Exterior axial strain for specimens 2-10-G and 2-6-G.

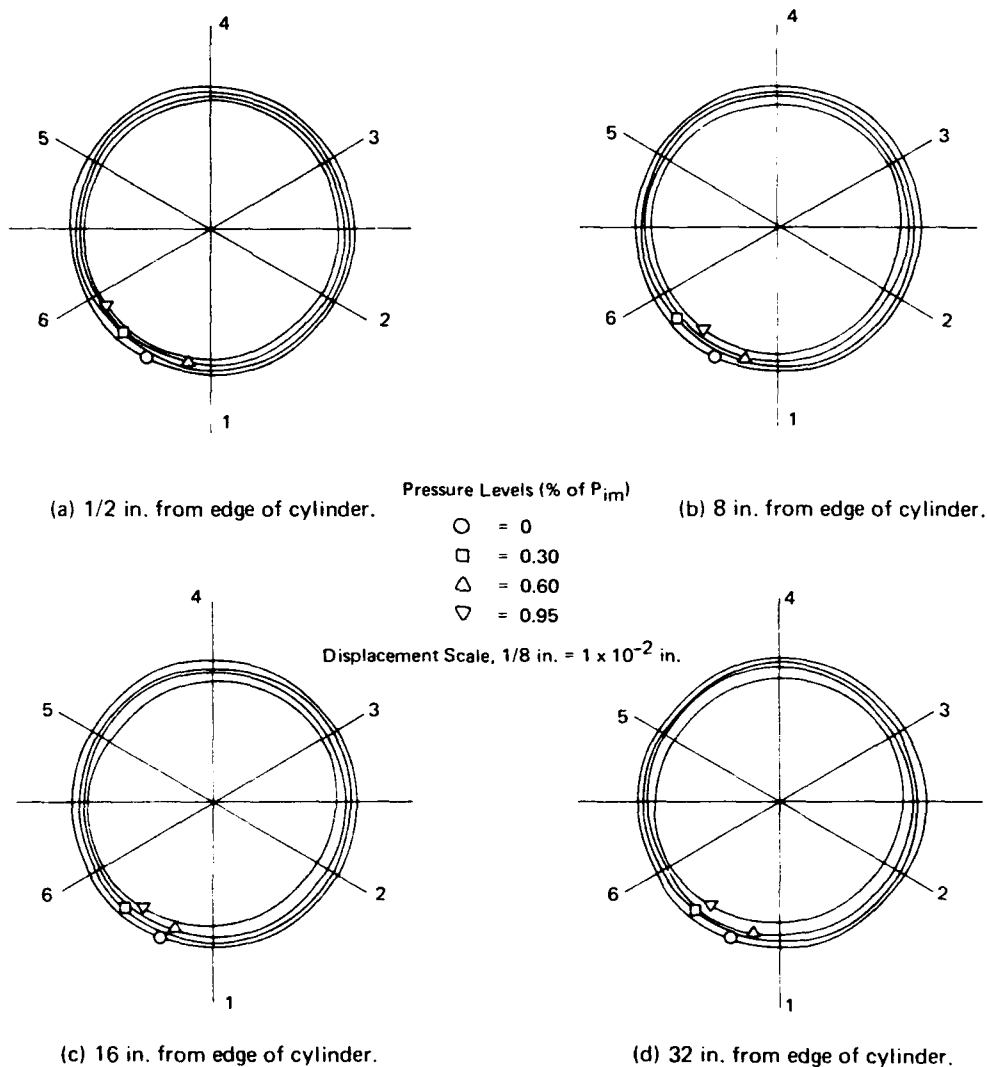


Figure 15. Radial displacement of the exterior surface of specimen 1/2-10-G.

The change-in-volume data were converted to average exterior hoop strain by the thick wall theory. These calculated average values for hoop strain are plotted in Figures 9 through 12 at $0.95 P_{im}$ and serve as a check on the strain gage data.

Figures 13 and 14 show the axial strain behavior of 1/2- and 2-inch-thick cylinders, respectively. These figures are typical for the behavior of all the instrumented cylinders. In general, the axial strain at 8 inches from the edge of the cylinder was the same as that near the cylinder's midlength. No distinct trends in axial strain behavior were found that could be attributed to variations in concrete strength.

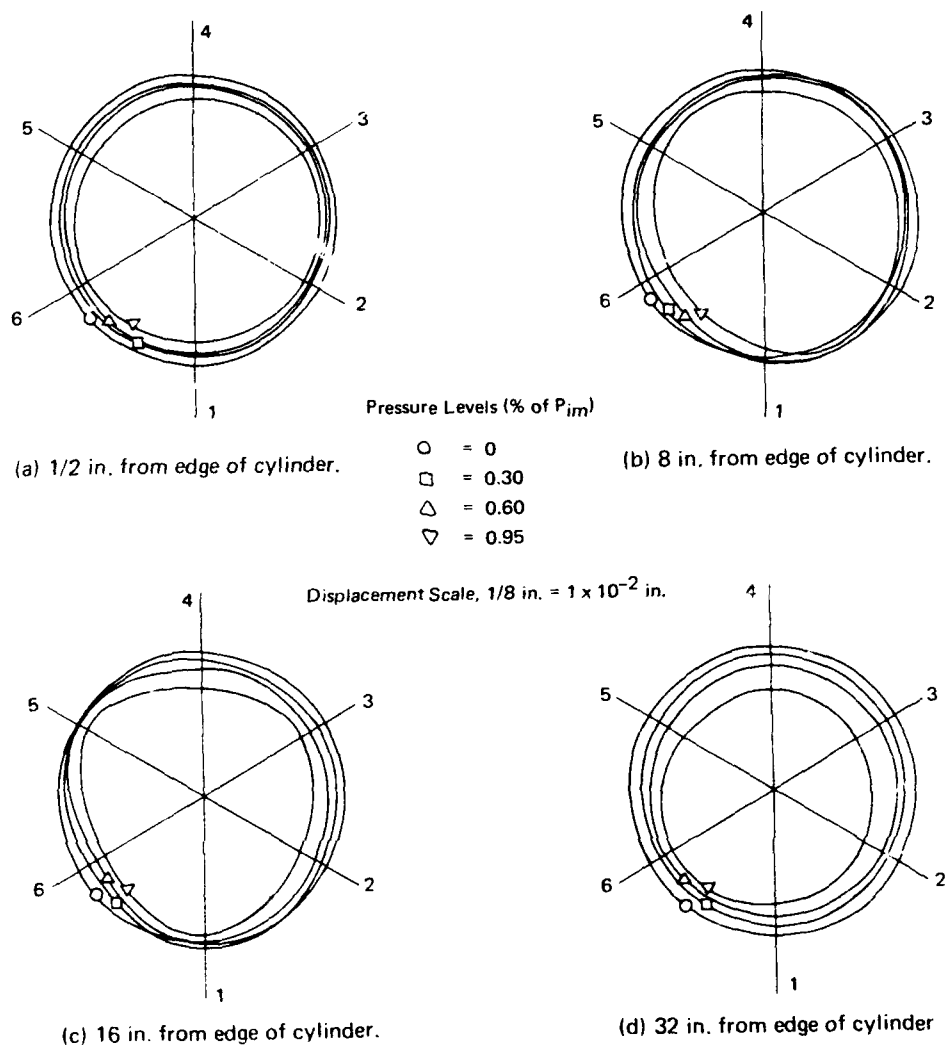


Figure 16. Radial displacement of the exterior surface of specimen 1-10-G.

Figures 15 through 18 show the radial displacement* of the exterior surface for the cylindrical hulls. These figures reveal some interesting patterns of behavior. At 1/2 and 32 inches from the edge of the cylinder, all specimens remained quite circular at all levels of pressure. At 8 and 16 inches from the edge, the 1- and 3-inch-thick specimens showed marked deviations from axial symmetry and large amounts of out-of-roundness under load. The probable cause for the deviations from symmetry and roundness is the presence of initial out-of-roundness in the specimens combined with the influence of the stiffness mismatch between the hemispherical end-closure and the cylinder.

* Radial displacement is the product of hoop strain and radius to the surface of interest.

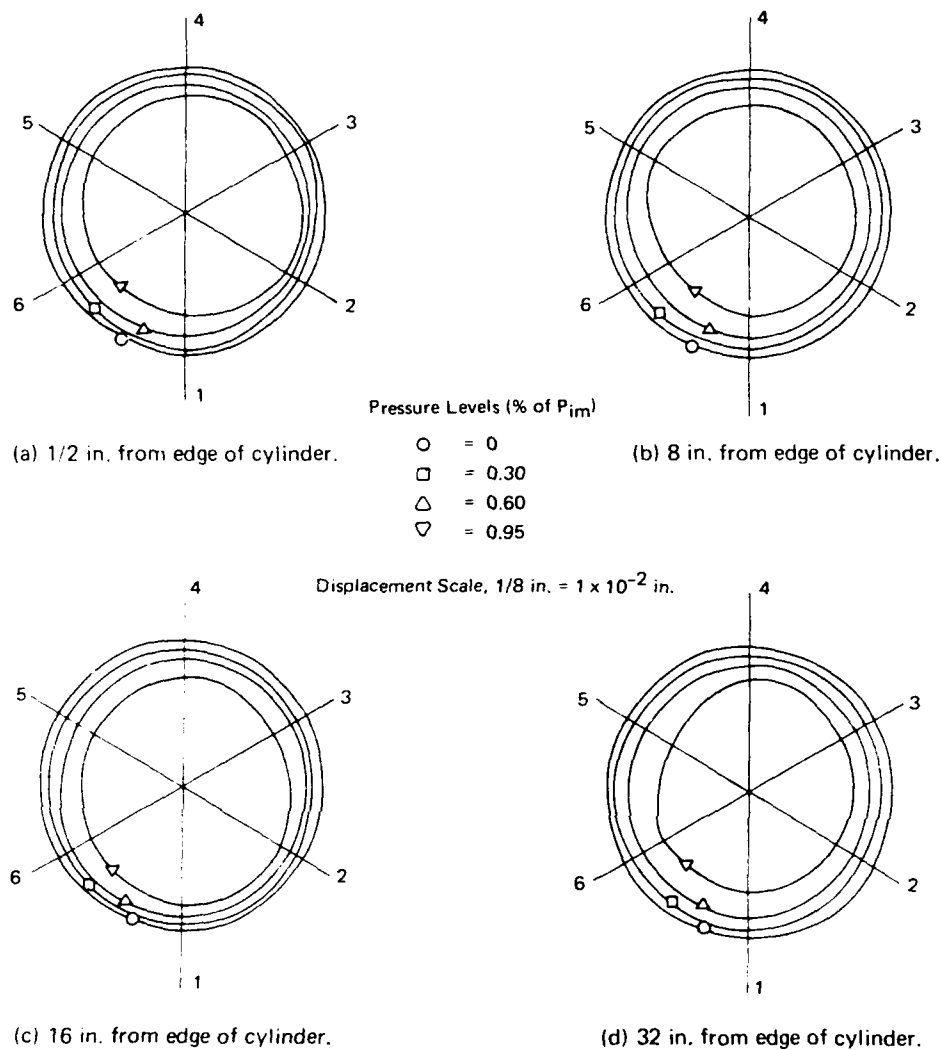


Figure 17. Radial displacement of the exterior surface of specimen 2-10-G.

DESIGN PROBLEM

Design a cylindrical concrete hull of 25-foot inside diameter, 100-foot length (cylinder portion only) and 100,000-pound positive buoyancy for long-term operation at a depth of 1,000 feet. Assume the use of hemispherical end-closures of the same wall thickness as the cylinder and concrete of 7,000-psi uniaxial compressive strength.

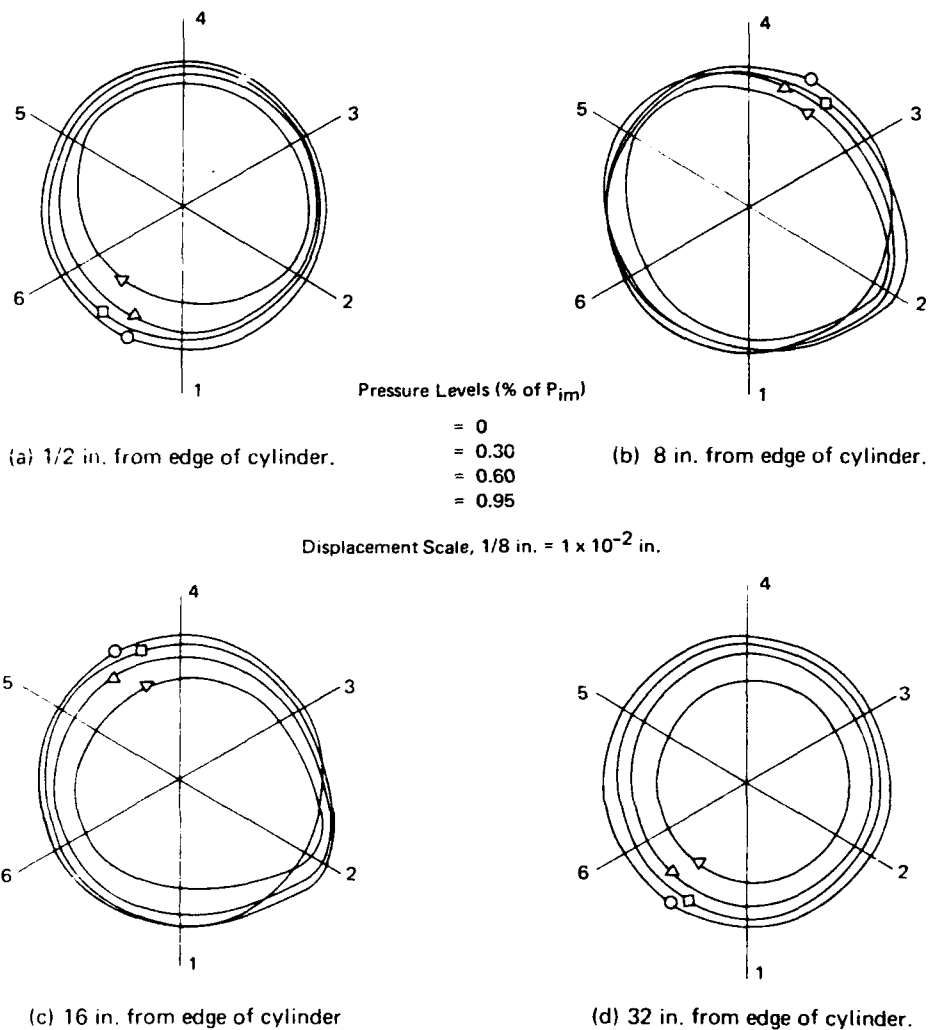


Figure 18. Radial displacement of the exterior surface of specimen 3-10-G.

Because a buoyancy requirement is part of the example problem, the first step is to determine *cylinder wall thickness* based on buoyancy.

$$\begin{aligned}
 \text{(a) Displacement of hull} &= 64 \left(\frac{\pi}{6} D_o^3 + \frac{100\pi}{4} D_o^2 \right) \\
 &= 33.51 D_o^3 + 5,027 D_o^2
 \end{aligned}$$

$$(b) \text{ Weight of hull} = 150 \left[\frac{\pi}{6} (D_o^3 - 25^3) + \frac{100\pi}{4} (D_o^2 - 25^2) \right]$$

$$= 78.54 D_o^3 + 11,780 D_o^2 - 8,590,000$$

(c) Displacement - Weight = Buoyancy

$$(1) (33.51 D_o^3 + 5,027 D_o^2) - (78.54 D_o^3 + 11,780 D_o^2 - 8,590,000)$$

$$= 100,000$$

$$(2) 45.03 D_o^3 + 6,753 D_o^2 = 8,490,000$$

$$(3) D_o = 32.17 \text{ ft}$$

$$(d) \text{ Wall thickness, } t = \frac{D_o - D_i}{2}$$

$$= \frac{32.17 - 25.00}{2}$$

$$= 3.58 \text{ ft}$$

Next, it is necessary to check the design to be sure that there is a *safety factor* of at least 3 on the structure as it may be manned and used for long-term operations.

$$(a) P_{im} = f'_c \left(2.05 \frac{t}{D_o} - 0.028 \right) \quad (1)$$

$$= 7 \times 10^3 \left(2.05 \frac{3.58}{32.17} - 0.028 \right)$$

$$= 1,397 \text{ psi}$$

(b) Convert 1,397 psi to depth of water in feet:

$$\text{Implosion Depth} = 1,397 \times 2.24$$

$$= 3,130 \text{ ft}$$

$$\begin{aligned}
 \text{(c) Safety Factor} &= \frac{\text{Implosion Depth}}{\text{Operating Depth}} \\
 &= 3,130/1,000 \\
 &= 3.13
 \end{aligned}$$

Since the safety factor is greater than 3.0, the wall thickness derived through buoyancy considerations is, therefore, satisfactory. If the safety factor had turned out to be less than 3.0, then a concrete mix with a compressive strength greater than the specified 7,000 psi would have been required.

If the structure's buoyancy is not of major concern, Figure 19 can be used to quickly determine the cylinder wall thickness needed for a given depth and factor of safety. To solve the example problem using Figure 19 as the design guide, the following steps are required.

(a) Convert operating depth to pressure in psi:

$$\text{Pressure, } P = 1,000 \text{ ft} \times 0.446 = 446 \text{ psi}$$

(b) Calculate P/f'_c :

$$P/f'_c = \frac{446}{1,000} = 0.064$$

(c) Enter Figure 19 at $P/f'_c = 0.064$ and read across until the 3.0 factor of safety curve is intersected. Read out $t/D_o = 0.108$

(d) Since $t = (D_o - D_i)/2$, $t = 0.108 D_o$, and $D_i = 25.00 \text{ ft}$, then

$$D_o = 31.89 \text{ ft}$$

$$t = 3.44 \text{ ft}$$

Note that the wall thickness obtained using Figure 19 is slightly less than that obtained using Equation 3 and buoyancy considerations. This is because depth controlled the design of Figure 19; the result is a structure that has approximately 150,000 pounds more buoyancy than the 100,000 pounds specified in the example problem.

The final design of cylindrical concrete hulls for use in the ocean would have to include steel reinforcement to resist handling loads; such design measures can be accomplished with conventional reinforced/prestressed design techniques and are not included herein.

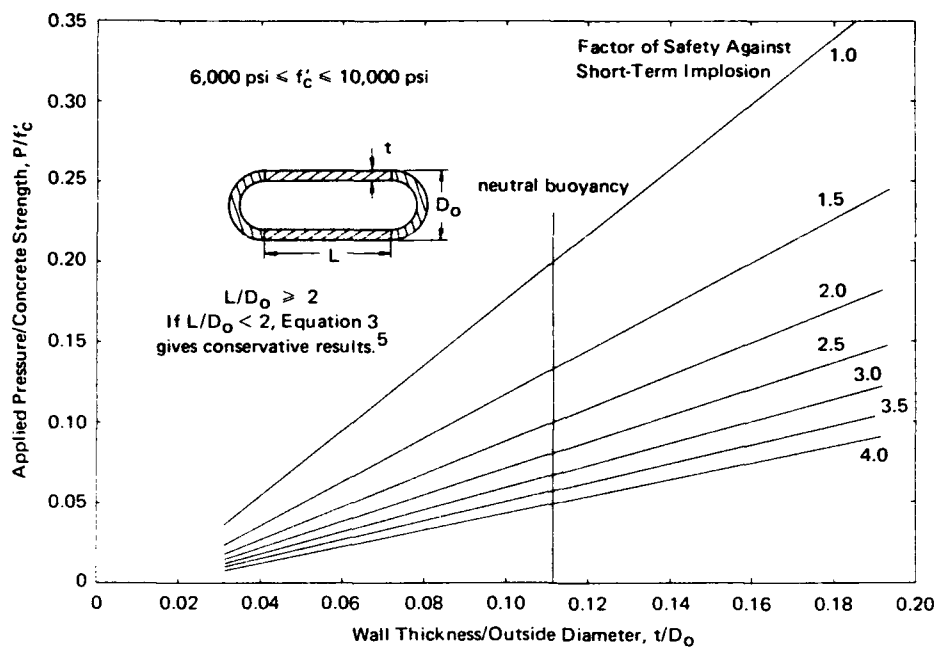


Figure 19. Design guideline for cylindrical concrete hulls with hemispherical end-closures (based on Equation 1).

FINDINGS

1. The implosion pressures for the concrete cylindrical hulls showed a direct relationship to increases in concrete strength from 6,000 to 10,000 psi and to increases in the ratio of wall thickness to outside diameter for values from 0.0312 to 0.1875. A linear empirical equation, Equation 1, was developed to predict the implosion pressures.
2. Implosion pressures ranged from 208 psi for the 1/2-inch-thick hulls of 6,000-psi concrete strength to 3,930 psi for the 3-inch-thick hulls of 10,000-psi concrete strength.
3. Two modes of failure for the hulls were observed: the 1/2-inch-thick hulls ($t/D_o = 0.0312$) failed by buckling, while the 1-, 2-, and 3-inch-thick hulls ($t/D_o = 0.0625, 0.1250$, and 0.1875) failed by compression shear type material failure.
4. Strain data showed that end-closure effects were minimal beyond one outside diameter from the end-closure-to-cylinder joint.

CONCLUSIONS

This study on the influence of concrete strength and wall thickness and previous studies on the influence of cylinder length and end-closure stiffness have demonstrated that concrete is a predictable material for pressure-resistant cylindrical structures. It is estimated that buoyant, cylindrical concrete structures will have applications to the ocean depth of 1,500 feet.

RECOMMENDATIONS

1. It is recommended that Equation 1 or Figure 19 be used as a guideline for the design of cylindrical concrete hulls for use under the sea.

$$P_{im} = f'_c \left(2.05 \frac{t}{D_o} - 0.028 \right) \quad (1)$$

where P_{im} = implosion pressure (psi)

f'_c = uniaxial compressive strength of concrete (psi)

t = wall thickness (ft)

D_o = outside diameter (ft)

2. It is recommended that the region between the end-closure-to-cylinder joint and one outside diameter from the joint not be used for penetrations in concrete cylindrical hulls if alternate locations are available. If this location is used for a penetration, then an appropriate increase in the factor of safety is recommended.*

ACKNOWLEDGMENTS

The author wishes to thank Mr. Harvey Haynes of the Ocean Structures Division for his constant interest, encouragement and many helpful suggestions. He also wishes to thank Mr. Philip Zubiarte whose special efforts in the fabrication of the test specimens allowed the timely completion of the work.

* The effect of penetrations in cylindrical hulls is under study.

Appendix

CONTROL CYLINDER DATA

The test results from the 3 x 6-inch control cylinders for the cylindrical hulls are presented in Table A-1. The nominal 10,000-psi concrete strength mix produced average values for f'_c , E_s , and ν of 10,460 psi, 3.56×10^6 psi, and 0.19, respectively; the nominal 6,000-psi concrete strength mix produced average values of 6,130 psi, 2.68×10^6 psi, and 0.16, respectively, for the same three parameters. All hemispherical end-closures were made from a high-strength mix which had average values of 8,840 psi, 3.18×10^6 psi, and 0.17, respectively.

Table A-1. Test Results for 3 x 6-Inch Control Cylinders

Specimen Designation	Compressive Strength of Concrete, f'_c (psi)	Secant Modulus of Elasticity, ^a E_s (psi x 10^6)	Poisson's Ratio, ^b ν	Age at Test (days)
1/2-10-N	10,700	3.47	0.18	101
1/2-10-G	10,900	3.85	0.18	124
1/2-6-N	5,420	2.58	0.18	16
1/2-6-G	5,760	2.29	0.16	32
1-10-N	10,700	3.72	0.20	117
1-10-G	10,480	3.55	0.20	118
1-6-G	6,620	2.67	0.16	28
1-6-N	5,920	2.70	0.17	27
2-10-G	9,840	3.58	0.18	118
2-10-N	9,950	3.36	0.19	124
2-6-N	6,080	2.91	0.15	23
2-6-G	6,060	2.87	0.12	24
3-10-G	10,350	3.59	0.22	119
3-10-N	10,800	3.40	0.14	119
3-6-N	7,000	2.80	0.15	27
3-6-G	6,200	2.66	0.21	27

^a Average of two 3 x 6-inch control cylinders to 0.5 f'_c .

^b Average of two 3 x 6-inch control cylinders.

REFERENCES

1. Naval Civil Engineering Laboratory. Technical Report R-517: Behavior of spherical concrete hulls under hydrostatic loading, pt. 1. Exploratory investigation, by J. D. Stachiw and K. O. Gray. Port Hueneme, Calif., Mar. 1967. (AD 649290)
2. _____. Technical Report R-547: Behavior of spherical concrete hulls under hydrostatic loading, pt. 2. Effect of penetrations, by J. D. Stachiw. Port Hueneme, Calif., Oct. 1967. (AD 661187)
3. _____. Technical Report R-588: Behavior of spherical concrete hulls under hydrostatic loading, pt. 3. Relationship between thickness-to-diameter ratio and critical pressures, strains and water penetration rates, by J. D. Stachiw and K. Mack. Port Hueneme, Calif., June 1968. (AD 835492L)
4. _____. Technical Report R-679: Failure of thick-walled concrete spheres subject to hydrostatic loading, by H. H. Haynes and R. A. Hoofnagle. Port Hueneme, Calif., May 1970. (AD 708011)
5. _____. Technical Report R-696: Influence of length-to-diameter ratio on behavior of concrete cylindrical hulls under hydrostatic loading, by H. H. Haynes and R. J. Ross. Port Hueneme, Calif., Sept. 1970. (AD 713088)
6. _____. Technical Report R-735: Influence of stiff equatorial rings on concrete spherical hulls subjected to hydrostatic loading, by L. F. Kahn and J. D. Stachiw. Port Hueneme, Calif., Aug. 1971. (AD 731352)
7. _____. Technical Report R-740: Influence of end-closure stiffness on behavior of concrete cylindrical hulls subjected to hydrostatic loading, by L. F. Kahn. Port Hueneme, Calif., Oct. 1971. (AD 732363)
8. _____. Technical Report R-774: Behavior of 66-inch concrete spheres under short and long term hydrostatic loading, by H. H. Haynes and L. F. Kahn. Port Hueneme, Calif., Sept. 1972. (AD 748584)
9. F. L. Singer. Strength of materials, 2nd ed. New York, Harper and Row, 1962, pp. 504-508.
10. S. Timoshenko. Theory of elastic stability, 2nd ed. New York, McGraw-Hill, 1961, pp. 289-293.
11. I. Rosenthal and J. Glucklich. "Strength of plain concrete under biaxial stress," American Concrete Institute, Journal, Proceedings, vol. 67, no. 11, Nov. 1970, pp. 903-914.

LIST OF SYMBOLS

D	Mean cylinder diameter (in.)
D_i	Inside diameter of cylinder (in.)
D_o	Outside diameter of cylinder (in.)
E_s	Secant modulus for the concrete to $0.5 f'_c$ (psi)
f'_c	Uniaxial compressive concrete strength (psi)
L	Length of cylinder (in.)
P	Applied pressure
P_{cr}	Implosion pressure due to buckling failure (psi)
P_{im}	Implosion pressure due to compressive shear failure (psi)
r_i	Interior radius of cylinder (in.)
r_o	Exterior radius of cylinder (in.)
t	Thickness of cylinder wall (in.)
ϵ_A	Axial strain (in./in.)
ϵ_H	Hoop strain (in./in.)
ν	Poisson's ratio
σ_A	Axial stress (psi)
σ_H	Hoop stress (psi)
σ_{Hmax}	Interior hoop stress at implosion
σ_R	Radial stress (psi)

DISTRIBUTION LIST

SNDL Code	No. of Activities	Total Copies	
—	1	12	Defense Documentation Center
FKAIC	1	10	Naval Facilities Engineering Command
FKNI	6	6	NAVFAC Engineering Field Divisions
FKN5	9	9	Public Works Centers
FA25	1	1	Public Works Center
—	9	9	RDT&E Liaison Officers at NAVFAC Engineering Field Divisions and Construction Battalion Centers
—	262	266	NCEL Special Distribution List No. 11 for persons and activities interested in reports on Ocean Engineering

<p>Naval Civil Engineering Laboratory</p> <p>INFLUENCE OF COMPRESSIVE STRENGTH AND WALL THICKNESS ON BEHAVIOR OF CONCRETE CYLINDRICAL HULLS UNDER HYDROSTATIC LOADING (Final), by N. D. Albersen</p> <p>TR-790 29 p. illus June 1973 Unclassified</p> <p>1. Concrete cylindrical hulls 2. Underwater application I. 3.1610-1</p> <p>Sixteen unreinforced, cylindrical concrete hull models of 16-inch outside diameter were subjected to external hydrostatic loading to determine the effect of concrete strength and wall thickness on implosion and strain behavior. The test results showed that an increase in concrete strength of 70% produced an average increase in implosion pressure of 87%, while increases in hull wall thickness by factors of 2 and 6 produced increases in implosion pressure by factors of approximately 2 and 11, respectively. Changes in concrete strength had little effect on strain behavior; however, strain magnitudes generally increased with increasing wall thickness when comparisons were made at a constant percentage of P_{im}. Design recommendations are presented to aid in the design of cylindrical concrete hulls for underwater use.</p>	<p>Naval Civil Engineering Laboratory</p> <p>INFLUENCE OF COMPRESSIVE STRENGTH AND WALL THICKNESS ON BEHAVIOR OF CONCRETE CYLINDRICAL HULLS UNDER HYDROSTATIC LOADING (Final), by N. D. Albersen</p> <p>TR-790 29 p. illus June 1973 Unclassified</p> <p>1. Concrete cylindrical hulls 2. Underwater application I. 3.1610-1</p> <p>Sixteen unreinforced, cylindrical concrete hull models of 16-inch outside diameter were subjected to external hydrostatic loading to determine the effect of concrete strength and wall thickness on implosion and strain behavior. The test results showed that an increase in concrete strength of 70% produced an average increase in implosion pressure of 87%, while increases in hull wall thickness by factors of 2 and 6 produced increases in implosion pressure by factors of approximately 2 and 11, respectively. Changes in concrete strength had little effect on strain behavior; however, strain magnitudes generally increased with increasing wall thickness when comparisons were made at a constant percentage of P_{im}. Design recommendations are presented to aid in the design of cylindrical concrete hulls for underwater use.</p>
<p>Naval Civil Engineering Laboratory</p> <p>INFLUENCE OF COMPRESSIVE STRENGTH AND WALL THICKNESS ON BEHAVIOR OF CONCRETE CYLINDRICAL HULLS UNDER HYDROSTATIC LOADING (Final), by N. D. Albersen</p> <p>TR-790 29 p. illus June 1973 Unclassified</p> <p>1. Concrete cylindrical hulls 2. Underwater application I. 3.1610-1</p> <p>Sixteen unreinforced, cylindrical concrete hull models of 16-inch outside diameter were subjected to external hydrostatic loading to determine the effect of concrete strength and wall thickness on implosion and strain behavior. The test results showed that an increase in concrete strength of 70% produced an average increase in implosion pressure of 87%, while increases in hull wall thickness by factors of 2 and 6 produced increases in implosion pressure by factors of approximately 2 and 11, respectively. Changes in concrete strength had little effect on strain behavior; however, strain magnitudes generally increased with increasing wall thickness when comparisons were made at a constant percentage of P_{im}. Design recommendations are presented to aid in the design of cylindrical concrete hulls for underwater use.</p>	<p>Naval Civil Engineering Laboratory</p> <p>INFLUENCE OF COMPRESSIVE STRENGTH AND WALL THICKNESS ON BEHAVIOR OF CONCRETE CYLINDRICAL HULLS UNDER HYDROSTATIC LOADING (Final), by N. D. Albersen</p> <p>TR-790 29 p. illus June 1973 Unclassified</p> <p>1. Concrete cylindrical hulls 2. Underwater application I. 3.1610-1</p> <p>Sixteen unreinforced, cylindrical concrete hull models of 16-inch outside diameter were subjected to external hydrostatic loading to determine the effect of concrete strength and wall thickness on implosion and strain behavior. The test results showed that an increase in concrete strength of 70% produced an average increase in implosion pressure of 87%, while increases in hull wall thickness by factors of 2 and 6 produced increases in implosion pressure by factors of approximately 2 and 11, respectively. Changes in concrete strength had little effect on strain behavior; however, strain magnitudes generally increased with increasing wall thickness when comparisons were made at a constant percentage of P_{im}. Design recommendations are presented to aid in the design of cylindrical concrete hulls for underwater use.</p>

Unclassified

Security Classification

DOCUMENT CONTROL DATA - R & D		
Security Classification of title, body of abstract and indexing annotation must be entered when the overall report is classified		
1. ORIGINATING ACTIVITY (Corporate author) Naval Civil Engineering Laboratory Port Hueneme, California 93043		2a. REPORT SECURITY CLASSIFICATION Unclassified
		2b. GROUP
3. REPORT TITLE INFLUENCE OF COMPRESSIVE STRENGTH AND WALL THICKNESS ON BEHAVIOR OF CONCRETE CYLINDRICAL HULLS UNDER HYDROSTATIC LOADING		
4. DESCRIPTIVE NOTES (Type of report and inclusive dates) Final; July 1970 - April 1972		
5. AUTHOR(S) (First name, middle initial, last name) N. D. Albertsen		
6. REPORT DATE June 1973	7a. TOTAL NO. OF PAGES 29	7b. NO. OF REFS 11
8a. CONTRACT OR GRANT NO. b. PROJECT NO 3.1610-1 c. d.	9a. ORIGINATOR'S REPORT NUMBER(S) TR-790	
9b. OTHER REPORT NO(S) (Any other numbers that may be assigned this report)		
10. DISTRIBUTION STATEMENT Approved for public release; distribution unlimited.		
11. SUPPLEMENTARY NOTES		12. SPONSORING MILITARY ACTIVITY Naval Facilities Engineering Command Alexandria, VA 22332
13. ABSTRACT Sixteen unreinforced, cylindrical concrete hull models of 16-inch outside diameter were subjected to external hydrostatic loading to determine the effect of concrete strength and wall thickness on implosion and strain behavior. The test results showed that an increase in concrete strength of 70% produced an average increase in implosion pressure of 87%, while increases in hull wall thickness by factors of 2 and 6 produced increases in implosion pressure by factors of approxi- mately 2 and 11, respectively. Changes in concrete strength had little effect on strain behavior; however, strain magnitudes generally increased with increasing wall thickness when comparisons were made at a constant percentage of P_{im} . Design recommendations are presented to aid in the design of cylindrical concrete hulls for underwater use.		

DD FORM 1473 (PAGE 1)

S/N 0101-807-6801

Unclassified

Security Classification

Unclassified

Security Classification

14 KEY WORDS	LINK A		LINK B		LINK C	
	ROLE	WT	ROLE	WT	ROLE	WT
Concrete cylindrical hulls						
Underwater applications						
Concrete strength						
Wall thickness						
Implosion behavior						
Strain behavior						
Hydrostatic loading						
Design guidelines						
Lame's equation						
Hemispherical end-closures						
Failure modes						
Compression-induced shear						
Buckling						
Bresse's equation						

Unclassified

Security Classification

R 740

Technical Report

**INFLUENCE OF END-CLOSURE STIFFNESS
ON BEHAVIOR OF CONCRETE CYLINDRICAL
HULLS SUBJECTED TO HYDROSTATIC
LOADING**

October 1971

Sponsored by

NAVAL FACILITIES ENGINEERING COMMAND



NAVAL CIVIL ENGINEERING LABORATORY

Port Hueneme, California 93043

Approved for public release; distribution unlimited.

INFLUENCE OF END-CLOSURE STIFFNESS ON BEHAVIOR OF CONCRETE CYLINDRICAL HULLS SUBJECTED TO HYDROSTATIC LOADING

Technical Report R-740

3.1610-1

by

L. F. Kahn

ABSTRACT

Twelve model concrete cylindrical hulls were subjected to hydrostatic loading to determine the influence of end-closure stiffness on implosion pressure and strain behavior of the cylinders. Results showed that variation of end-closure stiffness did not reduce the implosion pressure below that of a cylinder with a free end condition or below the implosion pressure predicted by elastic thick-wall theory. To vary the closure stiffness, concrete hemisphere and steel plate end closures were used to simulate free, pinned, beveled, and fixed end conditions. Strain variations along the length of the cylinders indicated that the influence of the closure was limited to a distance of one diameter from the closure. Recommendations are presented to aid in the design of concrete cylindrical hulls.

Approved for public release, distribution unlimited.

Copies available at the National Technical Information Service
(NTIS), Sills Building, 5285 Port Royal Road, Springfield, Va. 22151

CONTENTS

	page
INTRODUCTION	1
BACKGROUND	1
EXPERIMENTAL PROGRAM	2
Scope	2
Design of Specimens	3
Fabrication of Specimens	5
Instrumentation	11
Test Procedure	13
TEST RESULTS	13
Failed Specimens	13
Implosion Data	17
Strain Data	18
Linear Differential Transformer Data	26
Finite Element Analysis	26
DISCUSSION	27
Implosion Behavior	27
Strain Behavior	29
Comparison Between Experimental and Analytical Results	35
FINDINGS	36
SUMMARY	37
RECOMMENDATIONS	37

	page
ACKNOWLEDGMENT	38
APPENDIXES	
Appendix A – Concrete Proportions and Properties	39
Appendix B – Drawings of Cylinder End Closures	42
Appendix C – Discussion of Strain Behavior Along Cylinder Length	44
Appendix D – Discussion of Circumferential Strain	47
REFERENCES	49
LIST OF SYMBOLS	51

INTRODUCTION

The prospective use of concrete cylindrical hulls for undersea installations requires that some form of end closure be provided. The closure may be a shell or plate made of concrete or another material; or the closure may be another structure to which the cylindrical hull connects, such as a sphere. The difference in stiffness between the cylinder and the closure will affect the structural behavior of the cylindrical hull.

The primary objective of this investigation was to determine the effect of the end-closure stiffness on the structural behavior of thick-walled concrete cylindrical hulls subjected to hydrostatic loading. The effect of the end closure was studied by testing experimental models and by analyzing the models with a finite element technique. The secondary objective was to compare the experimental behavior with the analytical behavior to determine the accuracy of the analytical method.

The ultimate purpose of this research is to aid in developing design guidelines for the accurate and safe design of undersea concrete structures. Applications for such undersea structures include stations to monitor ocean activities, nuclear reactor containment structures, transportation tunnels, mineral refinement plants, and oil drilling enclosures.

BACKGROUND

Previous experimental research at the Naval Civil Engineering Laboratory (NCEL) on model cylindrical hulls determined the effect of the cylinder length-to-outside-diameter ratio (L/D_o)^{*} on the strain behavior and implosion pressure of the hulls and indicated the minimum length-to-diameter ratio which approximates a cylinder of "infinite"^{**} length.¹ Fourteen concrete cylindrical hulls were tested. These hulls had an outside diameter of 16 inches and a 2-inch wall thickness. End closures

^{*} A foldout list of symbols is included after References.

^{**} An "infinitely long" cylinder is one in which radial displacements are uniform along the length.

were concrete hemispheres with a 16-inch outside diameter and 2-inch wall thickness. The L/D_o ratio was varied from 0.5 to 8.0. Principal findings of the study were that:

1. A cylinder with an L/D_o ratio of 2.0 or greater can be considered infinitely long.
2. Exterior hoop strains were nearly uniform beyond a distance equal to or greater than one outside diameter from the cylinder end.
3. Cylinders with an L/D_o ratio greater than 2.0 imploded at a pressure loading of approximately 2,500 psi, which was conservatively predicted with Lamé's elastic thick-wall theory.
4. Hoop strains around the circumference of a cylinder at midlength were not uniform, apparently a flat spot developed which eventually resulted in the hull failure.

Along with the experimental investigation, the cylinders were analyzed with a finite element method developed by E. L. Wilson.² The finite element analysis indicated behavior similar to that determined in the experimental findings.

EXPERIMENTAL PROGRAM

Scope

This investigation was principally an experimental study of 12 model concrete cylindrical hulls with concrete hemisphere and steel plate end closures. The closures were used to create various amounts of fixity at the cylinder ends. The only intended variable in the experiment was the closure stiffness. The structural behavior of the cylinders was studied by measuring the exterior strain of the models as they were subjected to hydrostatic pressure loading. All cylinders were tested to implosion.

The experiments were designed to yield sufficient data to show the influence of end-closure stiffness on the structural behavior. These data were then compared with the results from a finite element analysis of the cylinder models to determine the difference between actual and theoretical behavior. The analytical and experimental findings were used to formulate the recommendations for design guidelines.

Design of Specimens

The 12 model concrete cylinders were similar to those fabricated in the previous research study,¹ with a length-to-diameter ratio (L/D_o) of 2.0 and thickness-to-diameter ratio (t/D_o) of 0.125. The cylinders had an outside diameter of 16 inches, wall thickness of 2 inches, and length of 32 inches.

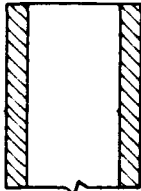
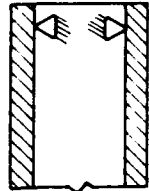
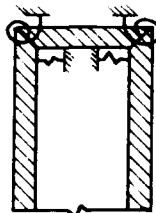
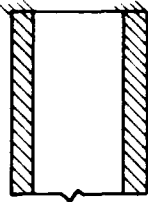
Four end-fixity conditions were used and ranged from approximately no end restraint to infinite restraint (Table 1). Two cylinders each were tested with free end and pinned end conditions, and four cylinders each were tested with beveled end and fixed end conditions.

To produce the least restraint, concrete hemispheres with a 16-inch outside diameter and 1-inch wall thickness were bonded with epoxy to each end of a cylinder (specimens 1 and 2). Elastic thick-wall theory predicted that the 1-inch-thick hemisphere would have a radial deflection 0.95 times the deflection of the 2-inch-thick cylinder; therefore, the hemispherical end closure was approximately 5% stiffer than the cylinder. Because of this small difference, the hemispherical closure would produce little end restraint, and the cylindrical hull would respond to hydrostatic loading in a manner similar to that of a portion of an infinitely long hull. Hence, hemispherical end closures having a wall thickness one-half that of the cylinder were considered as providing free end restraint conditions.

Specimens 3 through 8 had one end of the cylinder capped with a 16-inch-OD, 1-inch-thick concrete hemisphere and the other end with a steel plate closure. Specimens 9 through 12 had one end capped with a 16-inch-OD x 2-inch-thick concrete hemisphere and the other end with a steel plate closure. The 1-inch-thick hemisphere was used at one end so that any variation in the structural behavior along the length of the cylinder would be caused by the various plate closures and the cylinder would respond as a semi-infinitely long cylinder with one end restrained. Even though the 1-inch hemisphere would provide the desired free restraint conditions, it would produce an edge bearing effect which might influence the hull implosion behavior. The 2-inch hemispheres were used to avoid edge bearing effects, although the thicker hemispheres would somewhat restrain cylinder deflection.

A cylinder length-to-diameter ratio of 2.0 was chosen because, as determined by Haynes and Ross,¹ a cylinder with an L/D_o ratio of 2.0 or greater behaved as an infinitely long cylinder. Therefore, any variation in structural behavior caused by varying the end closures could be assumed to be the result of changing the restraint at one end of the cylinder and not of any influence at the other.

Table 1. End Closure Restraint Conditions

Specimen Nos.	Closure Systems	Radial Deflection	End Rotation	Diagram
1, 2	free end	unrestrained	unrestrained	
3, 4	pinned end	restrained	unrestrained	
5, 6, 9, 10	beveled end	partially restrained	partially restrained	
7, 8, 11, 12	fixed end	restrained	restrained	

The steel plate end closures are shown in Figure 1. Specimens 3 and 4 had a steel plate end closure which simulated a pinned end condition. The closure was designed to permit nearly free rotation while preventing radial displacement. As shown in Figure 2, a steel ring was grouted between the bearing edge of the closure and the concrete cylinder. This ring prevented excessively high bearing stresses. Because the ring was grooved and flexible, it did not restrain the cylinder rotation.

Specimens 5, 6, 9, and 10 had a beveled steel plate end closure (Figure 3). Both the plate and the cylinder were fabricated with a 45-degree beveled edge. This configuration was designed to partially restrain both the radial deflection and rotation of the cylinder. The beveled condition also represented a design which might be practical for movable closures.

The steel plate closure for specimens 7, 8, 11, and 12 was designed to ensure full fixity of the cylinder end by restraining radial deflection and rotation. The fixed end closure (Figure 4) fit around the cylinder end so that the cylinder penetrated the plate 3 inches.

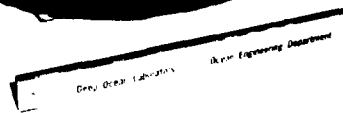
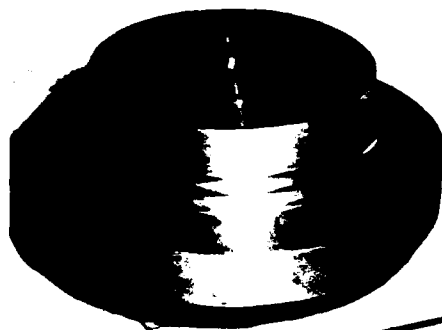
Fabrication of Specimens

The concrete (technically a microconcrete or mortar, because the largest aggregate passed a no. 4 sieve) used to cast both the cylinders and hemispheres had a compressive strength ranging from 5,910 to 10,640 psi and elastic moduli from 2.4×10^6 to 3.8×10^6 psi. Details of the mix design and physical properties of the concrete are presented in Appendix A.

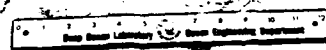
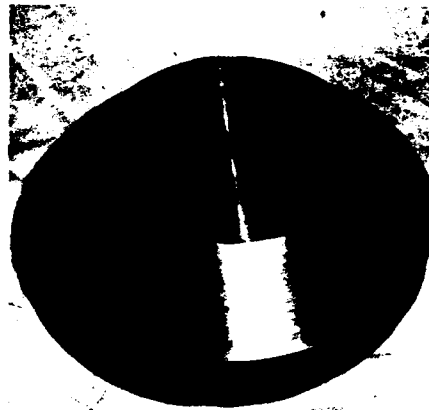
The cylinders were cast vertically in rigid steel molds (Figure 5). The molds were machined to diameter tolerances of $\pm 1/32$ inch, and could be separated into parts for easy removal from the cast cylinder.

The two cylinder sections which were to have the same type end closure were cast on the same day but from different batches of concrete. During casting, the concrete was vibrated both internally and externally to assure good compaction and homogeneity. The molds were removed one day after casting, and the sections were cured in a fog room at 100% RH and 73°F until the concrete aged 28 days. Upon removal from the fog room, the cylinders were stored at room conditions within a building while being instrumented and having the end closures attached.

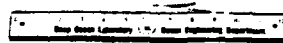
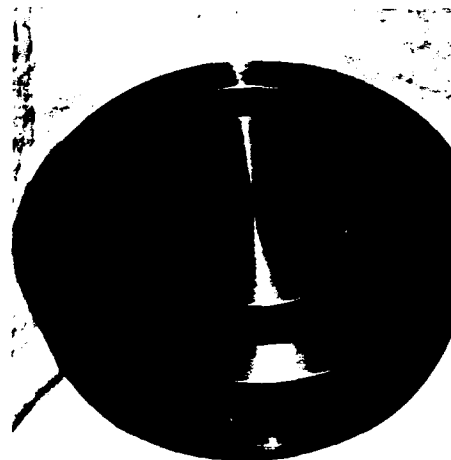
The concrete hemispheres were cast in rigid aluminum molds. External vibration was used during casting to ensure compaction. The hemispheres were cured under the same conditions as were the concrete cylinder sections. The flat edges on the cylinders and hemispheres were ground smooth and plane by rotating the sections on a sheet of plate glass covered with water and silicon carbide grit no. 60.



(a) Pinned.



(b) Beveled.



(c) Fixed.

Figure 1. Steel plate end closures.



Figure 2. Pinned end closure with bearing ring in cylinder.

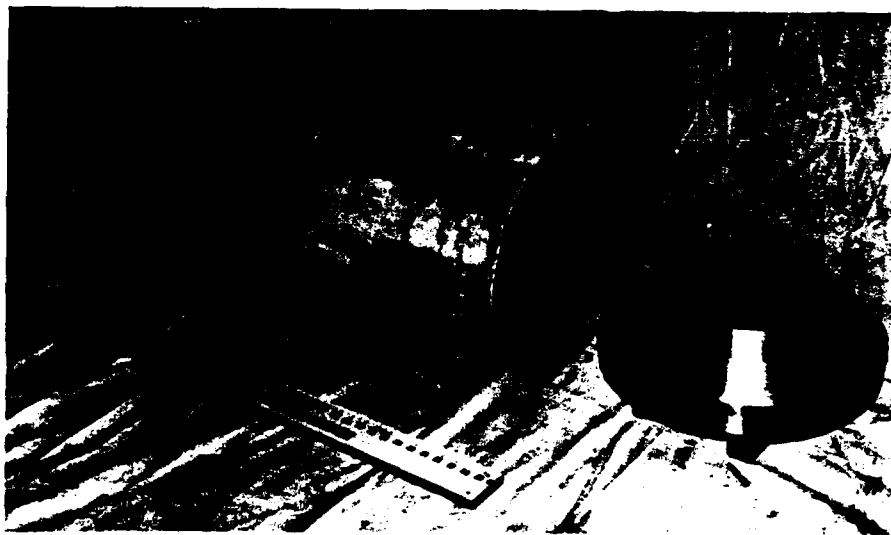


Figure 3. Beveled end closure with cylinder and hemispherical end.



Figure 4. Fixed end closure with cylinder and hemispherical end.

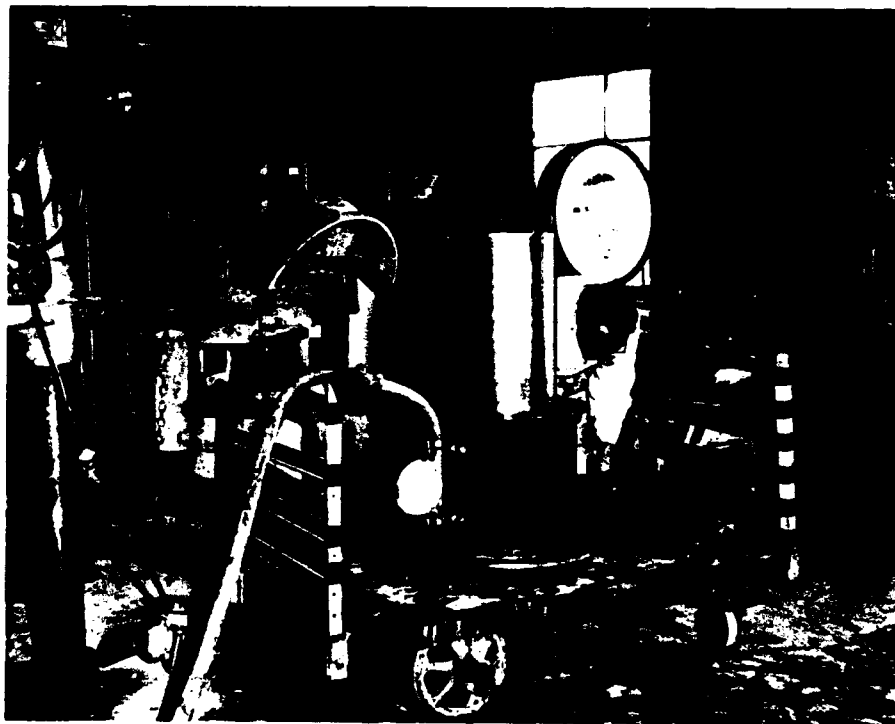


Figure 5. Rigid steel mold partially assembled for casting.

The steel end closures were machined from 6-inch-thick A36 steel plate. Dimensions were within a tolerance of ± 0.005 inch. Drawings of the plate closures are shown in Appendix B.

The end closures were epoxy-bonded to the cylinders while the cylinder was in a vertical position. The hemispherical closures were placed first (Figure 6), using a high-strength epoxy (Furane Plastics, Epocast 8288). After 1 week the cylinder was inverted, and the other closure was fitted in place. For specimens 1 and 2, the second hemisphere was epoxy-bonded to the edge of the cylinder. For specimens 3 and 4, steel bearing rings were grouted to the cylinder interior surface with a neat cement paste, then the pinned end closure was epoxy-bonded to the edge of the cylinder. The pinned end closure fit snugly into the bearing ring. The beveled end closure was epoxy-bonded to specimens having beveled edges (Figure 7) with a bond approximately 0.020 inch thick. To attach the fixed end closure, the deep groove of the closure was painted with a thick coat of a low-viscosity, steel-filled epoxy (Furane Plastics, Epibond 154) and the closure was lowered onto the cylinder. The epoxy flowed sufficiently to ensure that the bond between the closure and the cylinder was complete and that the closure was correctly seated.

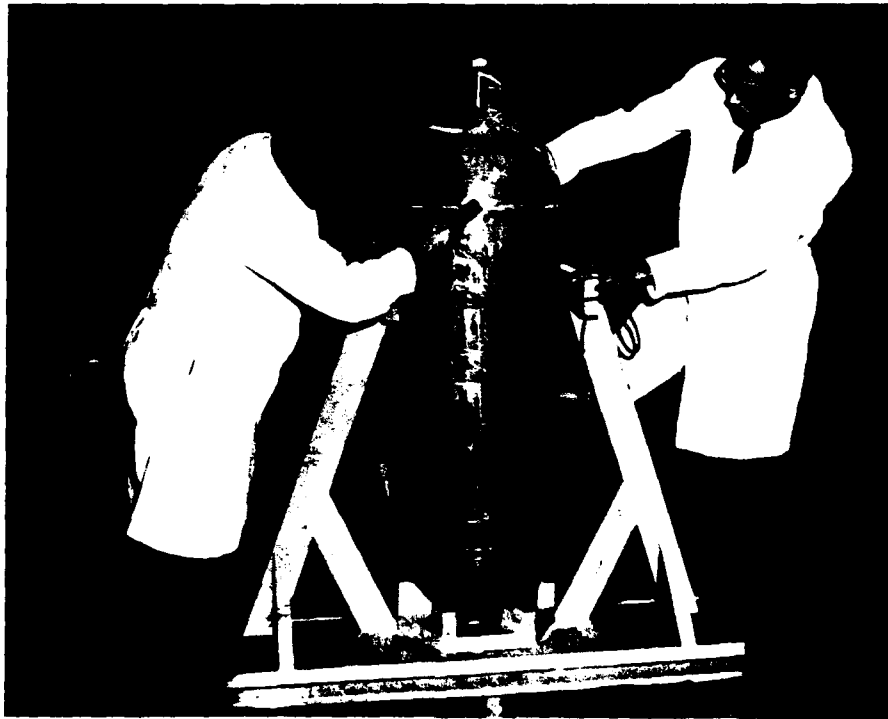


Figure 6. Hemispherical closure being epoxy-bonded to cylinder.



Figure 7. Beveled end closure with differential transformer ready for bonding.

After assembly, each specimen was coated with a waterproofing epoxy so that the concrete would remain dry during pressure testing.

Instrumentation

Specimens 1 through 8 were instrumented with electrical resistance strain gages (BLH A-5-1-S6) located on the exterior surface in the hoop direction only. Specimens 9 through 12 were not instrumented. Figures 8 through 11 show the gage layout for the free, pinned, beveled, and fixed end conditions, respectively. The gage layouts for the specimens were similar in that they measured the hoop strains along two radially opposite lines parallel to the cylinder axis. The strains along these lines, designated A and B, show the influence of the end closure on the radial displacement relative to the distance from the closure. Six gages were placed around the cylinder at locations 2, 8, and 16 inches from the edge of the closure. These strain measurements around the circumference show cylinder out-of-roundness and the development of flat spots.

The strain gages were attached to the cylinder with an epoxy (EPY 150) and were waterproofed with a microcrystalline wax.

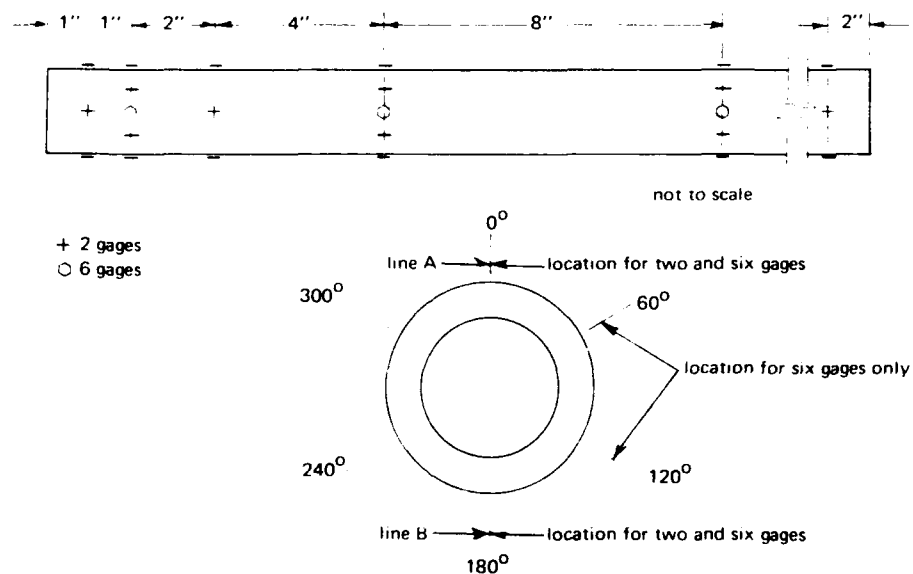


Figure 8. Strain gage layout, specimens 1 and 2 (free end closures).

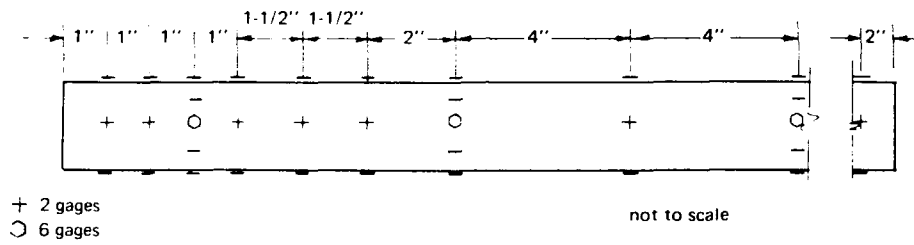


Figure 9. Strain gage layout, specimens 3 and 4 (pinned end closures).

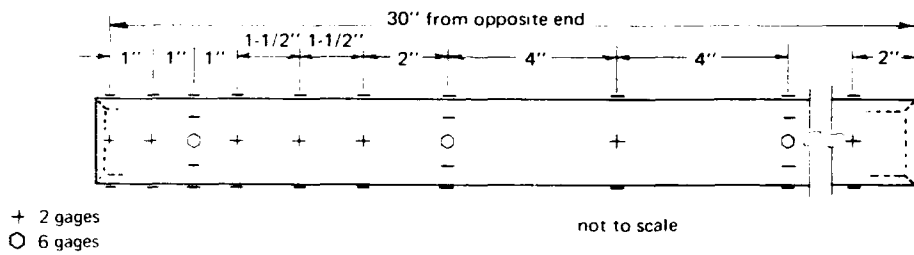


Figure 10. Strain gage layout, specimens 5 and 6 (beveled end closures).

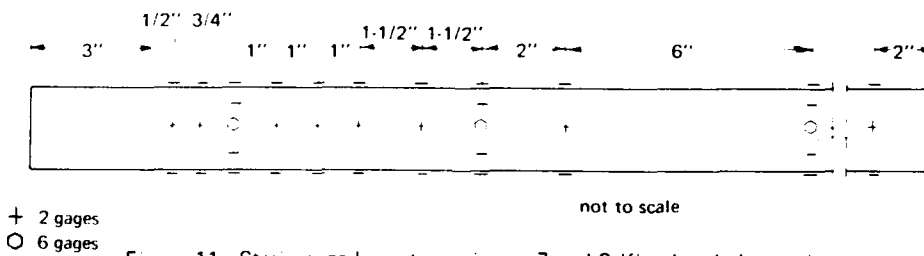


Figure 11. Strain gage layout, specimens 7 and 8 (fixed end closures).

A linear differential transformer was used on specimens 3 through 8 to measure the interior radial displacement of line A at a distance 1 to 3 inches from the closure. The transformer (pictured in Figure 7) was used principally to provide data for comparison with the exterior displacements measured by strain gages. The transformer was connected to a bracket having a highly magnetized base plate which rigidly adhered to the steel end closure.

During assembly of the specimens the strain gage lead wires were run down the exterior of the cylinder, through a penetration in the lower hemisphere to the interior, then out of the cylinder through the upper end closure. The lower penetration was potted with epoxy. The lead wire from the differential transformer was brought out of the cylinder through the upper end closure.

During the pressure test, strain gage readings were recorded on a Datran I Strain Indicator and Recorder System. The measurements were within an accuracy of $\pm 10 \mu\text{in./in.}$ The differential transformer was monitored with a N-type strain indicator previously used to calibrate the transformer.

Test Procedure

All specimens were tested in the 72-inch-ID x 160-inch-long hydrostatic pressure vessel at NCEL. After the specimen was attached to the head of the vessel (Figure 12), the cylinder was partially filled with water to reduce the violent forces created by implosion. The strain gage and differential transformer lead wires were brought out of the vessel through the connection in the vessel head.

The specimen was then loaded under hydrostatic pressure at a rate of 100 psi per minute between data recordings until implosion occurred. Strain and transformer readings were taken every 100 psi. The time required to record the data was approximately 30 seconds, during which the pressure loading was held constant.

After implosion the specimen was removed from the vessel and inspected.

TEST RESULTS

Failed Specimens

The failure mode of specimens 1, 2, 3, 4, 5, 6, and 8 was a bearing shear type failure at the joint between the concrete hemispherical end closure and the cylinder (Figure 13). The shear plane was at approximately

a 45-degree angle and ranged between one-sixth to one-half of the circumference at the joint. The failure plane was not limited to the cylinder section but ran continuously through the cylinder, epoxy joint, and hemisphere. In every case hemisphere fragments remained firmly bonded to the cylinder.

Implosion of specimen 7 was caused by a local failure of the concrete hemisphere (Figure 14). The sides of this local failure showed the typical concrete compression failure observed in previous studies of concrete spheres.^{3,4}

The failure mode of specimens 9, 10, 11, and 12 was a concrete compression type failure of the cylinder (Figures 15 and 16 show typical examples). The shear plane angle was between 30 and 45 degrees tangent to the exterior surface and ranged between the bottom and top of the hole (Figure 15). The failure plane was located between 4 and 12 inches from the edge of the steel plate end closures. This failure mode was identical to that observed by Haynes and Ross¹ on 2-inch-thick cylinders capped with 2-inch-thick hemispheres.

Forces created by implosion caused the bond to break between the cylinder and the pinned and beveled end closures. The fixed end closures remained attached to the cylinders. The steel plates showed no damage or dimensional change after the test.



Figure 12. Cylinder with fixed end closure being lowered into pressure vessel for hydrostatic test.



Figure 13. Bearing shear failure at cylinder edge for specimen 1.

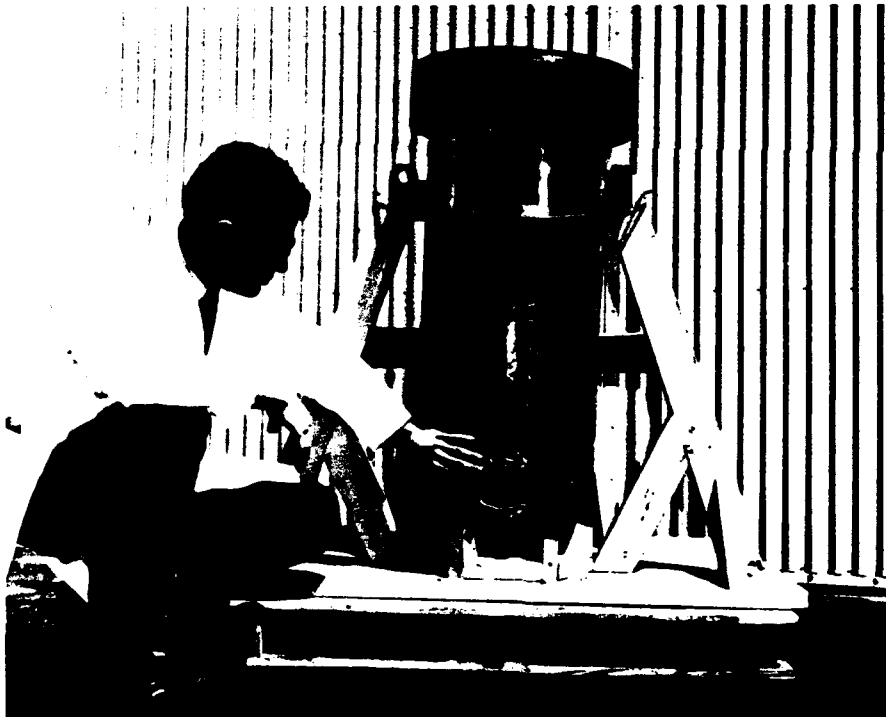


Figure 14. Local failure of hemispherical end on specimen 7.

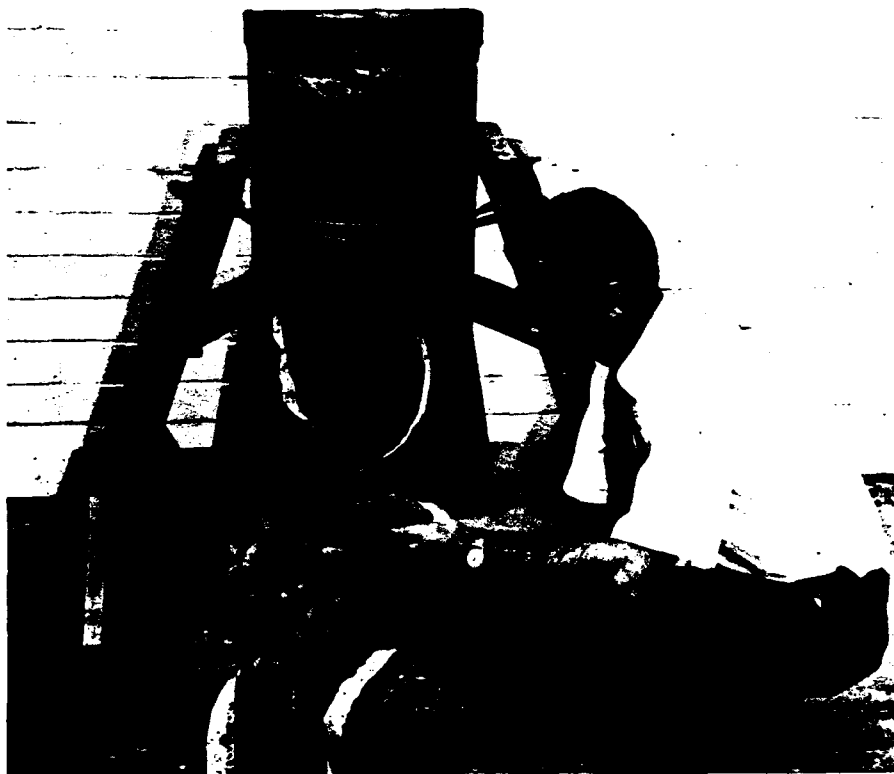


Figure 15. Failure of cylinder section for specimen 9.



Figure 16. Close up of failure plane of specimen 9.

Implosion Data

Implosion test results are presented in Table 2. The implosion behavior of the specimens was compared using the ratio of implosion pressure to concrete strength, P_{im}/f'_c . This ratio accounts for differences in implosion pressures caused by variation of concrete strength.

Table 2. Implosion Test Data

Specimen No.	End Condition	Implosion Pressure, P_{im} (psi)	Concrete Strength, f'_c	P_{im}/f'_c
1	free	1,800	7,860	0.229
2	free	2,195	9,800	0.224
3	pinned	2,300	9,420	0.244
4	pinned	2,355	9,270	0.254
5	beveled	1,145	5,940	0.193
6	beveled	1,350	5,910	0.229
7	fixed	2,275	9,100	0.250
8	fixed	2,190	9,260	0.236
9	beveled	2,655	10,480	0.253
10	beveled	2,480	10,640	0.233
11	fixed	2,835	8,700	0.326
12	fixed	2,435	9,580	0.254
5 ^b	2 in. thick hemisphere	2,600	10,120	0.257
6 ^b	2 in. thick hemisphere	2,800	10,120	0.277

^a The concrete strength is an average of six 3 x 6-inch control cylinders made from the same concrete used to cast the cylinder section.

^b Data from experiments by Haynes and Ross on concrete cylinders with $L/D_o = 2.0$ and with 16-inch OD x 2-inch-wall thickness hemispherical closures on each end.¹

Strain Data

Figures 17 through 24 present the exterior hoop strains of lines A and B versus the distance from the edge of the end closure for specimens 1 through 8, respectively. So that the various specimens could be easily compared, the strains were plotted at two pressure levels corresponding to two ratios of applied pressure to concrete strength of the cylinder section, $P/f'_c = 0.10$ and $P/f'_c = 0.20$. The measured "distance from edge of closure" for specimens 1 and 2 was the distance from the hemisphere—cylinder joint, for specimens 3 and 4 it was from the bearing point of the pinned end closure, for specimens 5 and 6 it was from the interior edge of the bevel of the cylinder section, and for specimens 7 and 8 it was from the edge of the interior face of the fixed end closure.

Figures 25 through 32 present the exterior hoop strains around the circumference at 2, 8, and 16 inches from the edge of the closure versus the degrees around the circumference for specimens 1 through 8, respectively. As before, the strains were plotted at two ratios of applied pressure to concrete strength. Line A was designated as the 0° point, and the angle around the circumference increased clockwise as one would view the cylinder from the end with the steel plate closure.

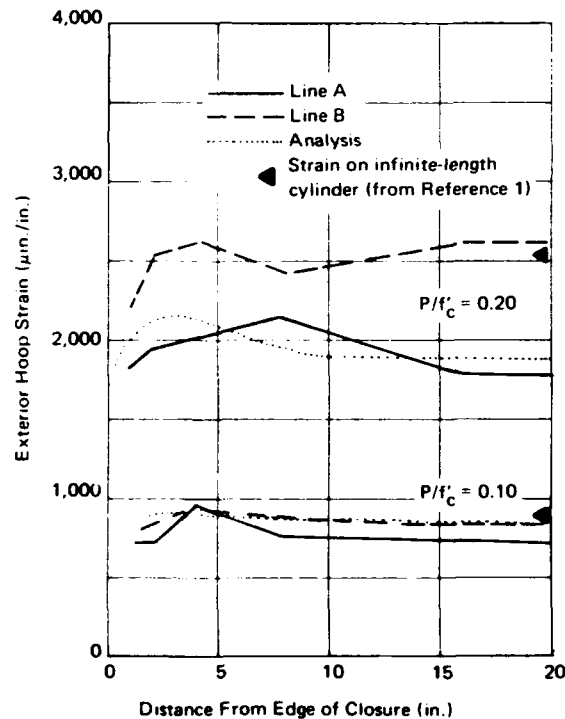


Figure 17. Strain along length of specimen 1.

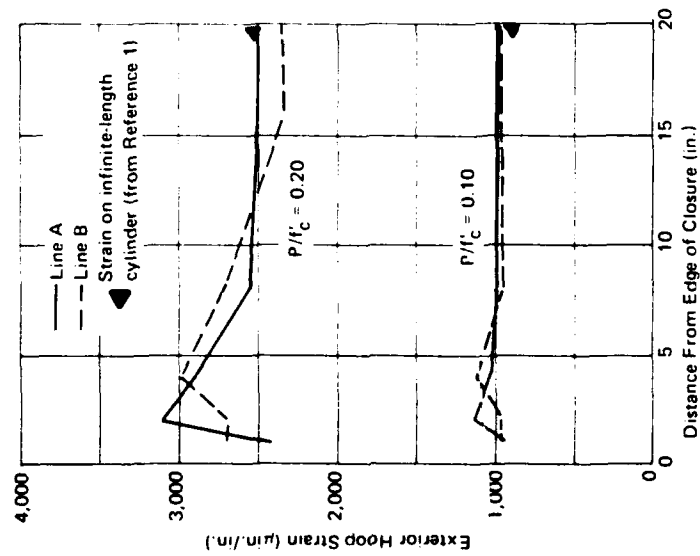


Figure 18. Strain along length of specimen 2.

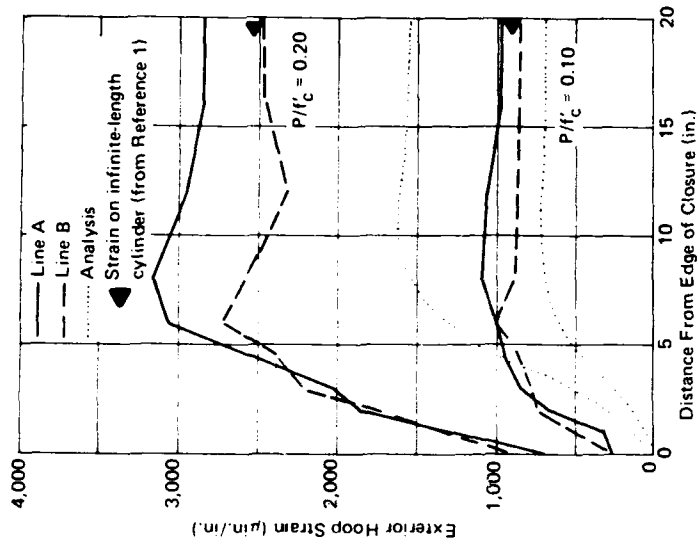


Figure 19. Strain along length of specimen 3.

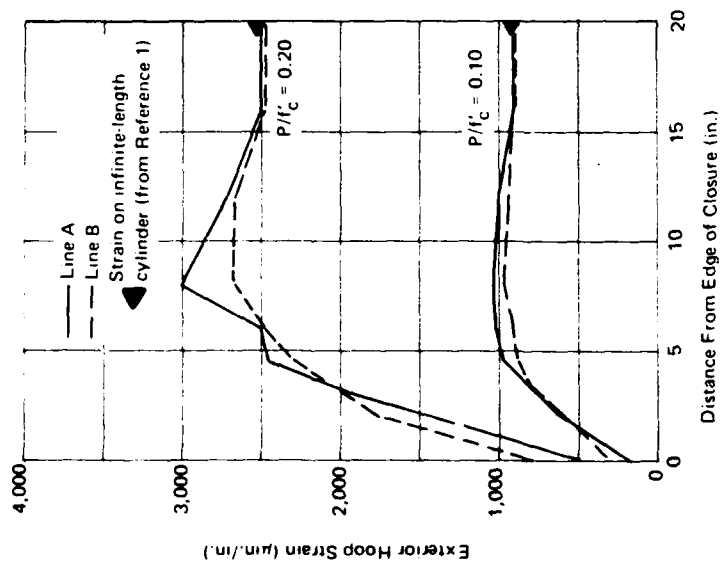


Figure 20. Strain along length of specimen 4.

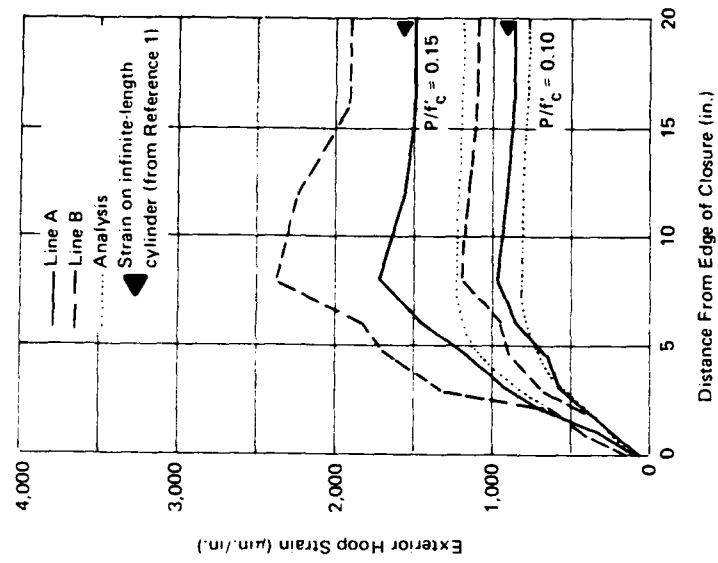


Figure 21. Strain along length of specimen 5.

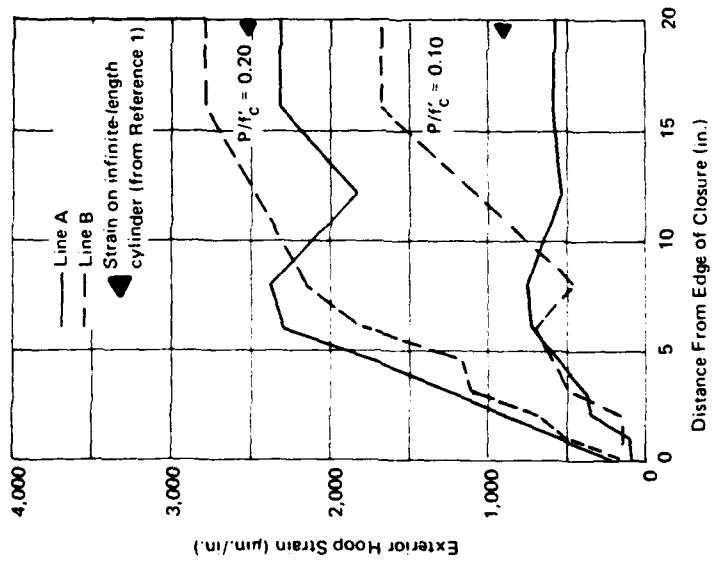


Figure 22. Strain along length of specimen 6.

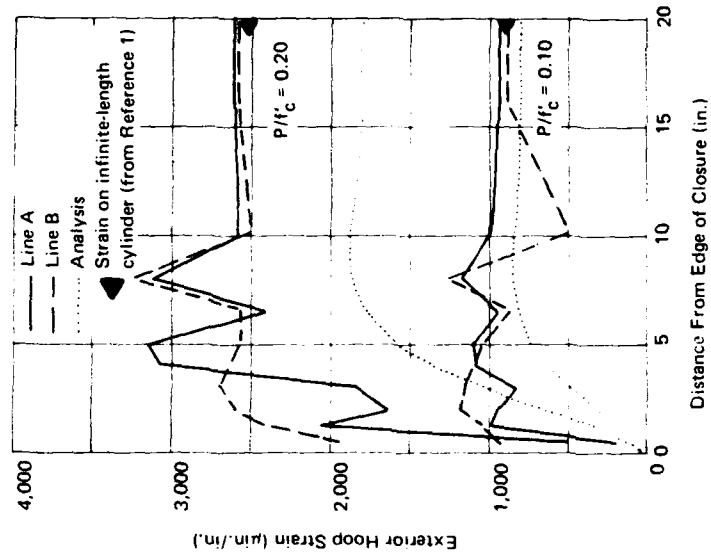


Figure 23. Strain along length of specimen 7.

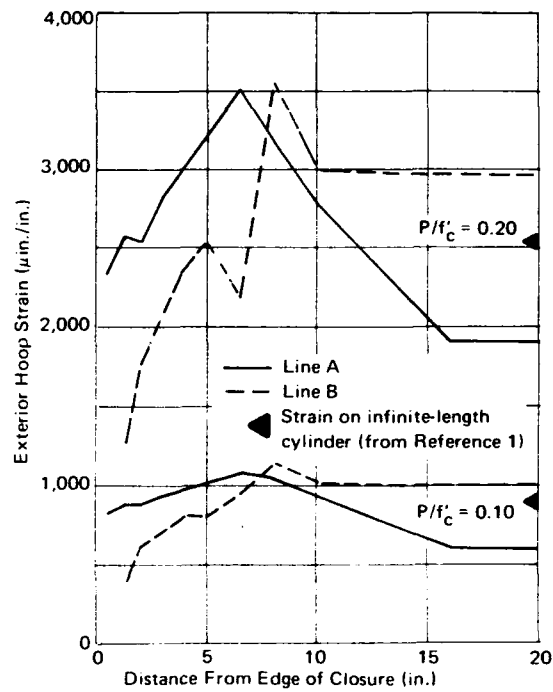


Figure 24. Strain along length of specimen 8.

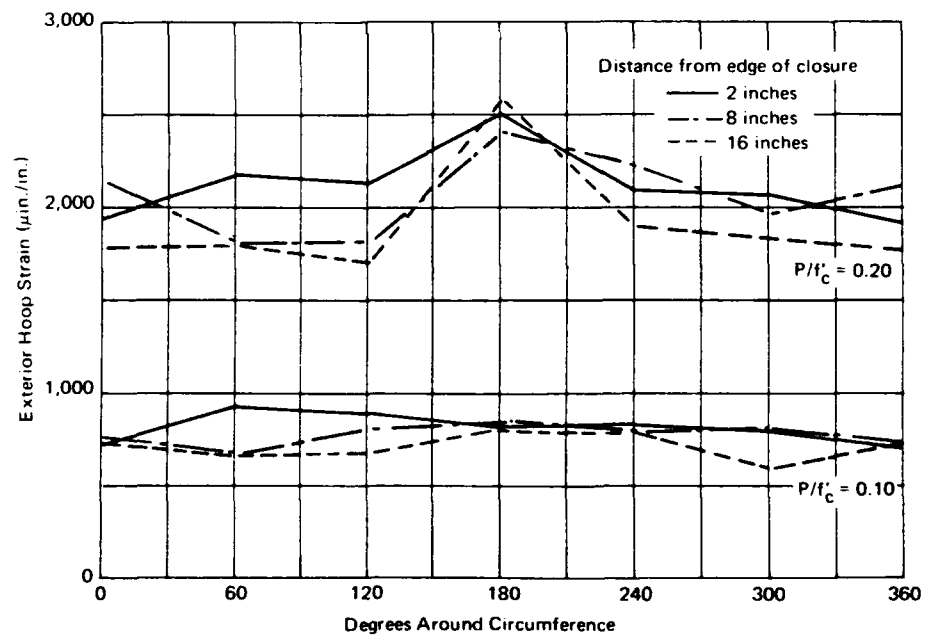


Figure 25. Circumferential strain, specimen 1.

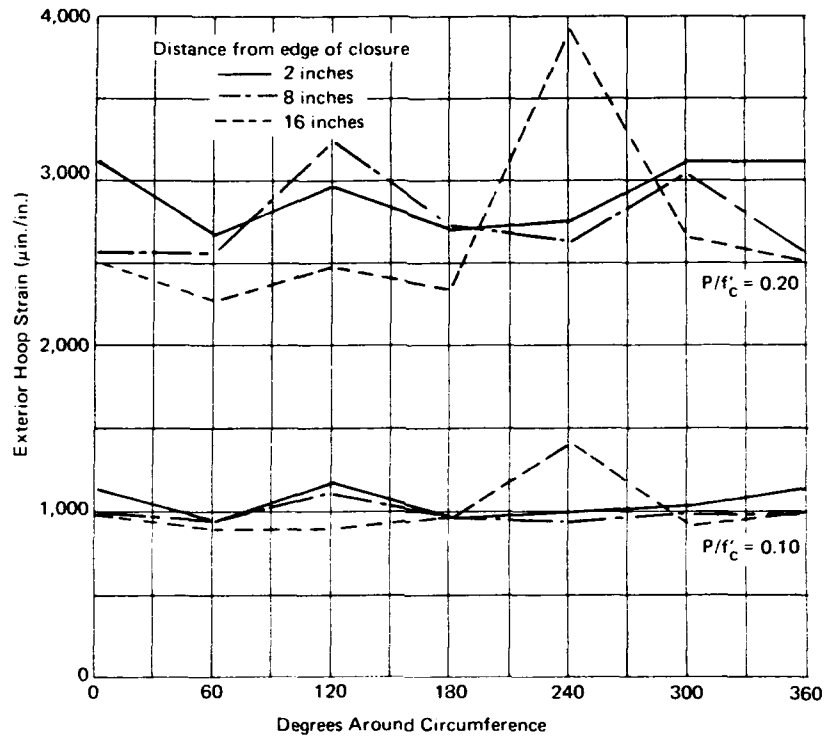


Figure 26. Circumferential strain, specimen 2.

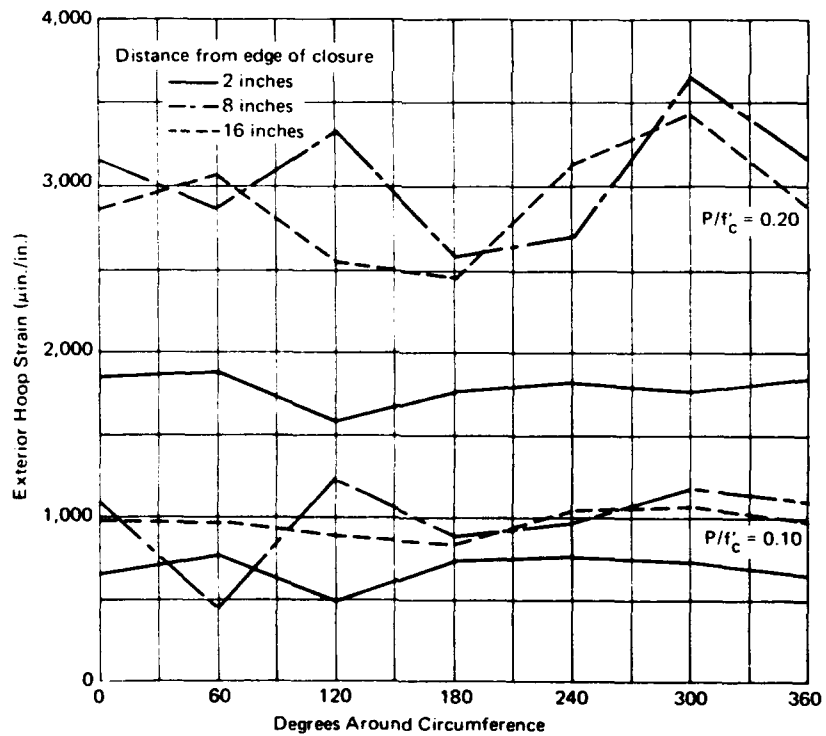


Figure 27. Circumferential strain, specimen 3.

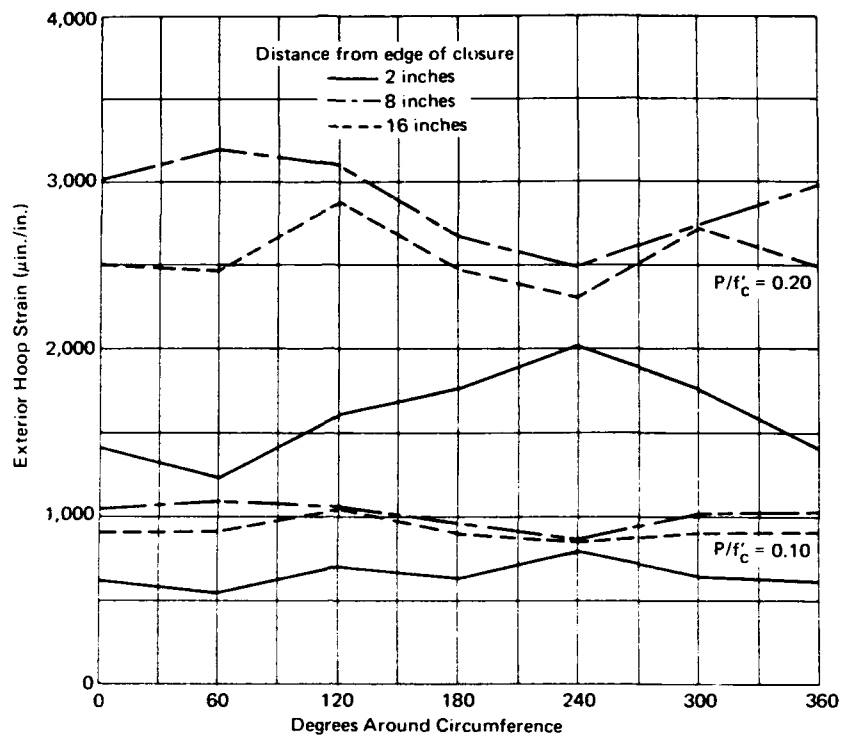


Figure 28. Circumferential strain, specimen 4.

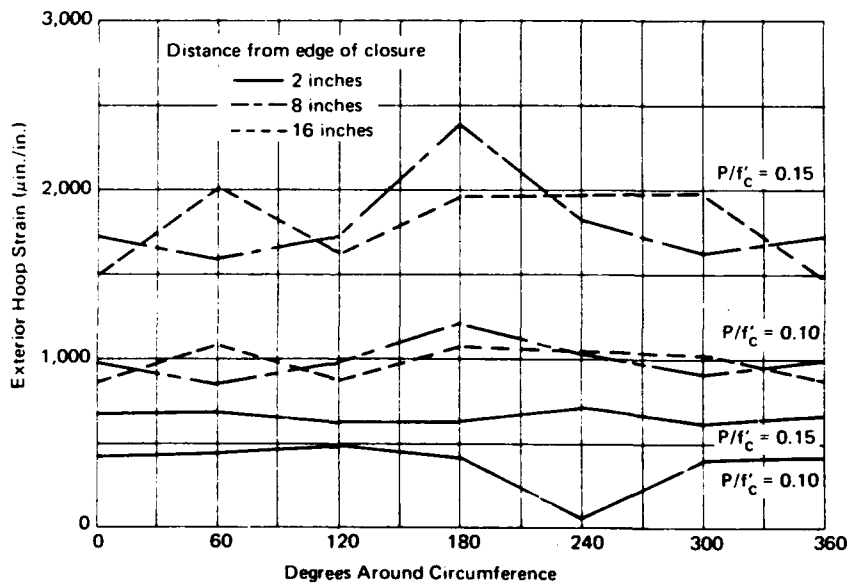


Figure 29. Circumferential strain, specimen 5.

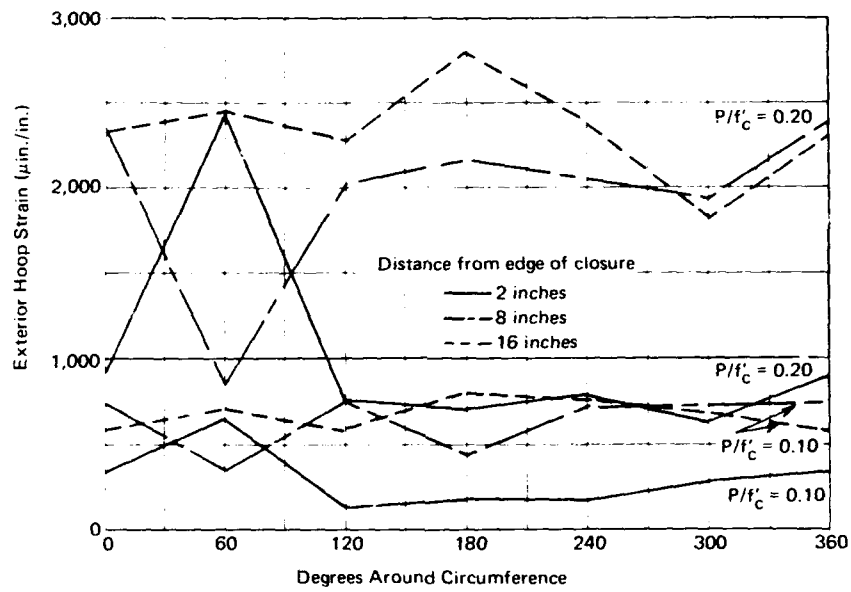


Figure 30. Circumferential strain, specimen 6.

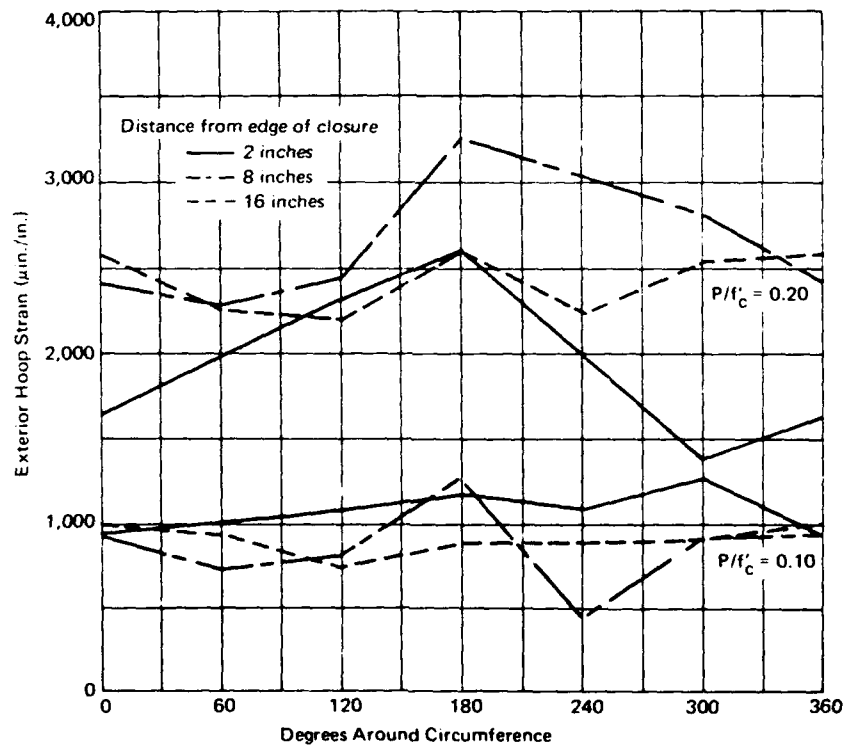


Figure 31. Circumferential strain, specimen 7.

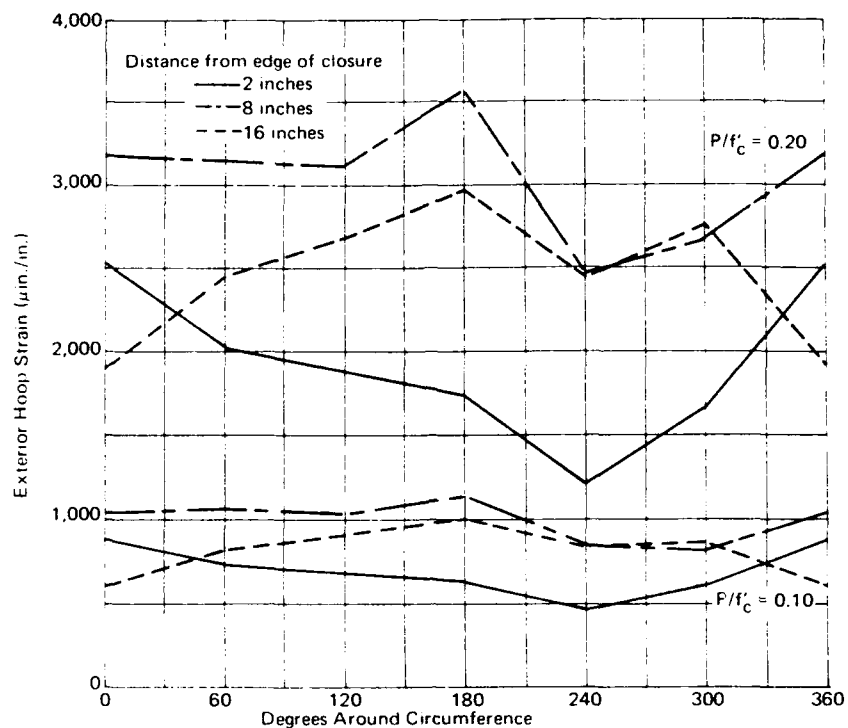


Figure 32. Circumferential strain, specimen 8.

Linear Differential Transformer Data

Differential transformers were not used on specimens 1 and 2. The transformers on specimens 5 and 7 were inoperable because when the closures were epoxied to the hulls some epoxy had flowed down the inner side of the hulls and bonded the rod to the coil. Figure 33 shows P/f'_c plotted versus the inside radial deflection and calculated interior hoop strain for specimens 3, 4, 6, and 8.

Finite Element Analysis

The finite element technique was used to analyze specimens 1, 3, 5, and 7. The concrete strengths of each cylinder and the bilinear stress-strain curves for the concretes were used in the analysis (the bilinear curve is discussed in Appendix A). The results of the analysis are plotted along with the experimental data on Figures 17, 19, 21, and 23 for the respective specimens. It was assumed that there was no initial out-of-roundness in any cylinder and therefore no development of a flat spot as load was applied. In the analysis, the mechanical properties of the cylinder also were used for

the hemisphere end. The connections between the cylinder sections and the steel plates were assumed to be "perfect" connections; that is, there was no discontinuity between the cylinder and the "pin" for specimen 3, the beveled plate was symmetric with a uniform epoxy joint for specimen 5, and full fixity occurred at the joint between the cylinder and the plate for specimen 7.

The exterior radial displacements were calculated for specimens 3, 5, and 7 at the positions where the differential transformers were located. These data are plotted in Figure 33 along with the experimental results.

DISCUSSION

Implosion Behavior

Lamé's elastic thick-wall theory was used to predict the implosion pressure of the cylindrical hulls by assuming that failure of the cylinder occurred when the interior hoop stress reached the ultimate concrete strength. The Lamé expression is

$$P_{im} = f'_c \left(\frac{r_o^2 - r_i^2}{2r_o^2} \right) \quad (1)$$

where P_{im} = implosion pressure (psi)

f'_c = ultimate uniaxial concrete strength (psi)

r_i = interior radius, which is the location under consideration (in.)

r_o = exterior radius (in.)

When the dimensions of the specimens are substituted in Equation 1, the resulting implosion pressure is

$$P_{im} = 0.219 f'_c \quad (2)$$

or the ratio of implosion pressure to concrete strength (P_{im}/f'_c) is 0.219.

All specimens except specimen 5 imploded at a pressure higher than that predicted by Lamé's equation. The P_{im}/f'_c ratio for specimen 5 was 12% lower than 0.219. The average P_{im}/f'_c ratio for specimens 1 through 8 was

0.232, for specimens 9 through 12 it was 0.266, and the average for all specimens was 0.244. Haynes and Ross¹ found that the P_{im}/f'_c ratio for cylinders with a L/D_o ratio greater than 2.0 ranged between 0.220 and 0.277 with an average of 0.250.

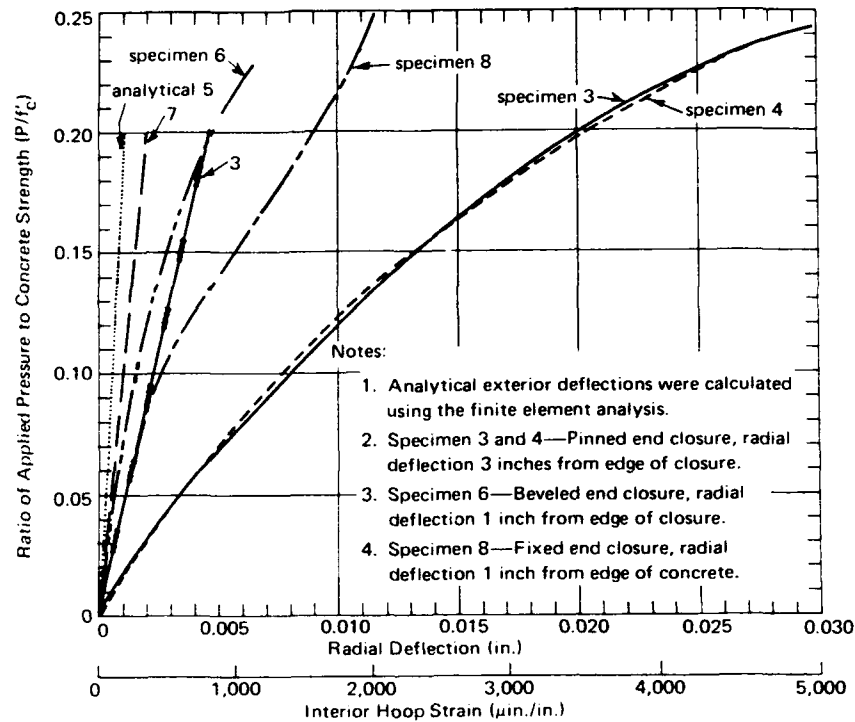


Figure 33. Linear differential transformer data: radial deflection and interior hoop strain near end closure on line A.

Therefore the specimens of this study generally failed at pressures between those which caused failure of "infinitely" long cylinders and those predicted by elastic theory.

The mode of failure observed by Haynes and Ross¹ was that a section of the cylinder imploded by forming a shear plane approximately parallel to the cylinder axis. An identical failure mode was observed in specimens 9 through 12. The shear plane in the latter specimens occurred near the hemispherical closure rather than near the plate closure. Although both closures induced a strain increase about 8 inches from the edge, the stiffer closure apparently restrained the cylinder more than did the hemisphere, allowing the concrete to collapse near the hemispherical closure. Except for sphere 7, specimens 1 through 8 failed by concrete shear created by high bearing stresses on the edge of the cylinders. This mode of failure caused

specimens 1 through 6 and specimen 8 to implode at pressures an average 15% lower than implosion pressures of specimens 9 through 12 and an average 8% lower than those recorded in the previous study. Table 3 lists the end bearing stresses produced by the hemispherical closure, the concrete strength of the cylinder section, and the percentage difference. The bearing stress at implosion was essentially equal to the concrete strength. This indicated that the specimens failed because the bearing stress reached the ultimate concrete strength.

Table 3. Bearing Stresses Produced by 1-Inch-Thick Hemispherical Closures

Specimen No.	Calculated Bearing Stress at Implosion	Concrete Strength of Cylinder Section, f'_c (psi)	Difference Between Bearing Stress and Concrete Strength ^a (%)
1	7,680	7,860	-2.3
2	9,380	9,800	-4.3
3	9,810	9,420	+4.1
4	10,050	9,270	+8.4
5	4,880	5,940	-17.8
6	5,760	5,910	-2.5
7	9,700	9,100	+6.6
8	9,350	9,260	+1.0

$$^a \text{ Difference} = \frac{\text{bearing stress} - f'_c}{f'_c} \times 100.$$

Strain Behavior

The strains observed in these experiments were exterior strains only. It is logical to assume that the locations of maximum exterior and interior hoop strains were the same and that the structural response at the exterior was similar to that at the interior. Elastic thick-wall theory predicted that the interior strain would be 33% greater than the exterior strain; Haynes and Ross found that the interior strains were between 33% and 50% greater.¹

Therefore, in reviewing the graphs of "strain versus distance from edge of closure" (Figures 17 through 24), the reader should recognize that the *maximum* strains were more than one-third greater than those recorded.

Strain Variation Along Cylinder Length. The influence of the end closure on the strain along the cylinder length is reviewed for each specimen in Appendix C. Generally, the pinned, beveled, and fixed closures produced similar cylinder behavior: nearly complete restraint against radial deflection at the cylinder end, a maximum deflection at a distance approximately 8 inches from the edge of the closure, and significant shear strain in the region between the end closure and the point of maximum deflection. The influence of all closures was limited to a distance of approximately 16 inches from the end.

This behavior was similar to that observed by Haynes and Ross.¹ Their results of "strain versus distance from edge of closures" are shown in Figure 34. On all the various length cylinders, the closures were 2-inch-thick hemispheres. Hoop strains were measured from the closure edge to the midlength of the cylinder. The response of cylinders with $L/D_o = 1$ and $L/D_o = 4$ was similar to that of specimens 3 through 8: restrained deflection near the closure, increased deflection between 4 and 8 inches from the edge, and more uniform deflection beyond 16 inches for the cylinder with $L/D_o = 4$.

The cylinder with $L/D_o = 8$ showed that beyond 16 inches from the edge the strains were relatively uniform. These strains are indicative of those of an infinitely long cylinder. The strain values between 16 inches and 64 inches from the edge were averaged at the two pressure levels ($P/f'_c = 0.10$ and 0.20) on the cylinder with $L/D_o = 8$. The averages represent a base line strain value for an infinitely long cylinder. These averages were plotted on Figures 17 through 24 as a comparison for the experimental strains found at 16 inches from the closure. In general these base line values were between the strains recorded on line A and line B at 16 inches from the edge or were nearly equal to one of those strain values. This agreement shows that the strains obtained at 16 inches from the closure on specimens 1 through 8 were representative of the strains of an infinitely long cylinder, and the agreement verifies that the influence of the closure is limited to a distance of one outside diameter from the edge of the closure.

The maximum radial deflection was a result of a longitudinal moment created by the bearing load of the end closure on the cylinder in conjunction with the uniform cylinder deflection. As pressure loading was applied and the concrete cylinder deflected radially, a moment arm was developed between the restrained end of the cylinder and portions farther from the end (Figure 35). The longitudinal moment thus created caused an increased radial deflection approximately 8 inches from the edge of the closure.

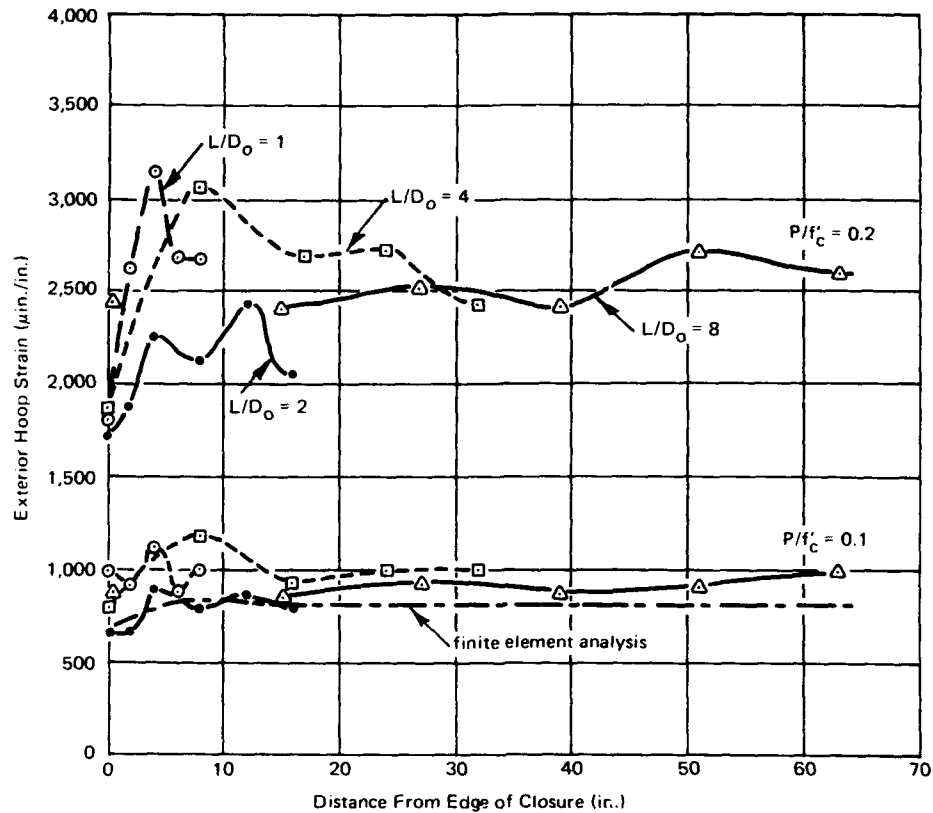


Figure 34. Comparison of exterior hoop strain behavior for cylinders of different lengths. (After Reference 1.)

A relative measure of this maximum deflection is the ratio of the maximum hoop strain and the strain at the midlength of the cylinder (16 inches from the edge). This ratio, termed strain magnification ratio, was calculated for the first eight specimens using strain values of both line A and line B, for the four models analyzed by the finite element method, and for the cylinder with $L/D_o = 4$ tested by Haynes and Ross.¹ The strain magnification ratios are listed in Table 4. A high ratio implies that the end-closure condition caused a larger strain (radial deflection) in the cylinder than that found on a cylinder of infinite length; a low value of the ratio means that the end-closure condition had little effect on the maximum strain behavior of the cylinder.

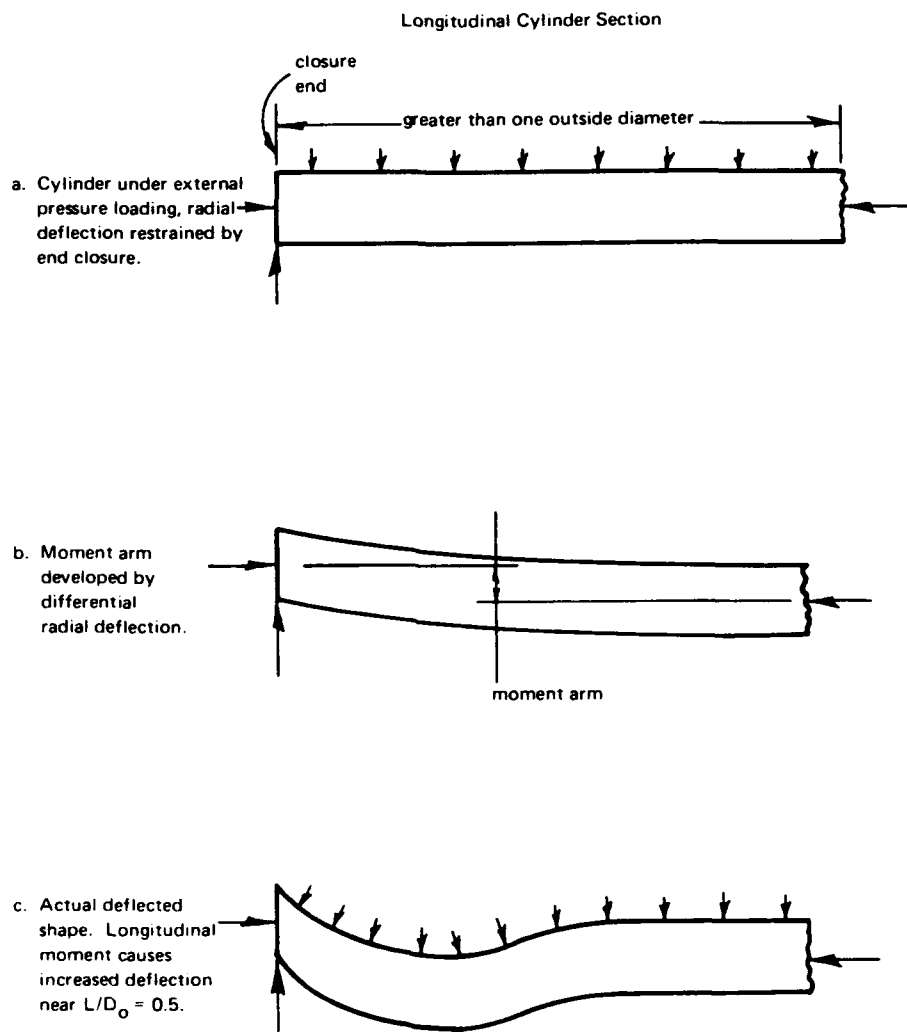


Figure 35. Schematic diagram of cylindrical hull deflection when radial deflection is restrained at one end.

Table 4. Strain Magnification Ratio at $P/f'_c = 0.10$ and 0.20^a

Specimen and Closure Type	Strain Magnification Ratio at—					
	$P/f'_c = 0.10$			$P/f'_c = 0.20$		
	Line A	Line B	Analysis	Line A	Line B	Analysis
1, free	0.24	0.12	0.10	0.19	0.00	0.14
2, free	0.14	0.17	—	0.24	0.27	—
3, pinned	0.11	0.16	0.03	0.12	0.11	0.03
4, pinned	0.14	0.07	—	0.20	0.08	—
5, beveled	0.13	0.08	0.04	0.15 ^b	0.24 ^b	0.04
6, beveled	0.27	0.00	—	0.03	0.00	—
7, fixed	0.24	0.40	0.02	0.21	0.25	0.03
8, fixed	0.75	0.12	—	0.32	0.21	—
Cylinder with $L/D_o = 4$ of Reference 1	0.24	—	—	0.14	—	—

^a Strain ratio = $\frac{\text{maximum strain} - \text{strain at 16 inches}}{\text{strain at 16 inches}}$.

^b Ratio at $P/f'_c = 0.15$.

The experiments showed that all cylinders had a magnification ratio greater than 10%, which indicated that all end closures produced a significant strain increase. Specimens 1 through 6 and the cylinder with $L/D_o = 4$ of Reference 1 had similar ratios, the free, pinned, beveled, and 2-inch-thick hemispherical closures caused approximately the same strain increase. Specimens 7 and 8, with the fixed end closure, had greater strain magnification ratios. It is believed that the moment induced by the fixed end closure in conjunction with the longitudinal moment created by the end bearing of the closure produced the larger maximum strain increase.

Strain Variation Around Cylinder Circumference. In general the differences in circumferential strains in a single specimen were as great as the strain differences caused by varying the end closures between specimens. Apparently the end closures did not prevent flat spot development near the cylinder ends; all sections of the cylinders developed similar out-of-round conditions.

The circumferential strains at 2, 8, and 16 inches from the closure showed the out-of-roundness and the unsymmetric response of the eight cylinders. The circumferential strain data in Figures 25 through 32 have been reduced to quantitative parameters at two pressure levels ($P/f'_c = 0.10$ and 0.20) and are listed in Table D-1 of Appendix D. A nondimensional "roundness ratio" was computed as the difference between the maximum and mean strains divided by the mean strain. This ratio was determined at locations 2, 8, and 16 inches away from the edge of the closure and at pressure levels $P/f'_c = 0.10$ and 0.20 . The roundness ratios are listed in Table 5.

Table 5. Roundness Ratio at $P/f'_c = 0.10$ and 0.20^a

Specimen No.	Roundness Ratio at —					
	$P/f'_c = 0.10$			$P/f'_c = 0.20$		
	2 Inches From Closure	8 Inches From Closure	16 Inches From Closure	2 Inches From Closure	8 Inches From Closure	16 Inches From Closure
1	0.7	0.09	0.16	0.16	0.16	0.33
2	0.13	0.13	0.38	0.08	0.16	0.44
3	0.12	0.27	0.07	0.04	0.20	0.18
4	0.22	0.08	0.04	0.25	0.11	0.12
5	0.35	0.22	0.09	0.09 ^b	0.27 ^b	0.15 ^b
6	1.27	0.21	0.08	1.36	0.27	0.20
7	0.17	0.47	0.11	0.32	0.20	0.09
8	0.31	0.16	0.19	0.38	0.18	0.17

^a Roundness ratio = $\frac{\text{maximum circumferential strain} - \text{mean circumferential strain}}{\text{mean circumferential strain}}$

^b Ratio at $P/f'_c = 0.15$.

A high roundness ratio indicated that the cylinder was deflecting considerably more in one area than in another, that the cylinder was out-of-round, and that a flat spot was developing. A lower ratio value showed that the cylinder was maintaining uniform curvature and equal deflection around the circumference.

The roundness ratios listed in Table 5 indicated that out-of-roundness was random. In general the cylinders were not restrained from developing a flat spot near the closure; out-of-roundness at the midlength was not significantly different from that near the closure.

A comparison between the nondimensional roundness ratios and strain magnification ratios showed that out-of-roundness produced as much strain deviation as that produced by the end-closure condition. The end closures induced higher absolute strain values near the cylinder end, but these strain increases did not appear to alter the flat spot development.

A further discussion of minor differences in circumferential strain is continued in Appendix D.

Comparison Between Experimental and Analytical Results

The finite element analysis predicted behavior similar to that observed, except that the calculated strains were between 0% and 130% less than those recorded. Figure 36 compares the experimental and analytical results by showing the maximum strain occurring between the closure and 16 inches from the closure and the strain at 16 inches from the closure (for the experimental results, the mean strain listed in Table D-1 is shown).

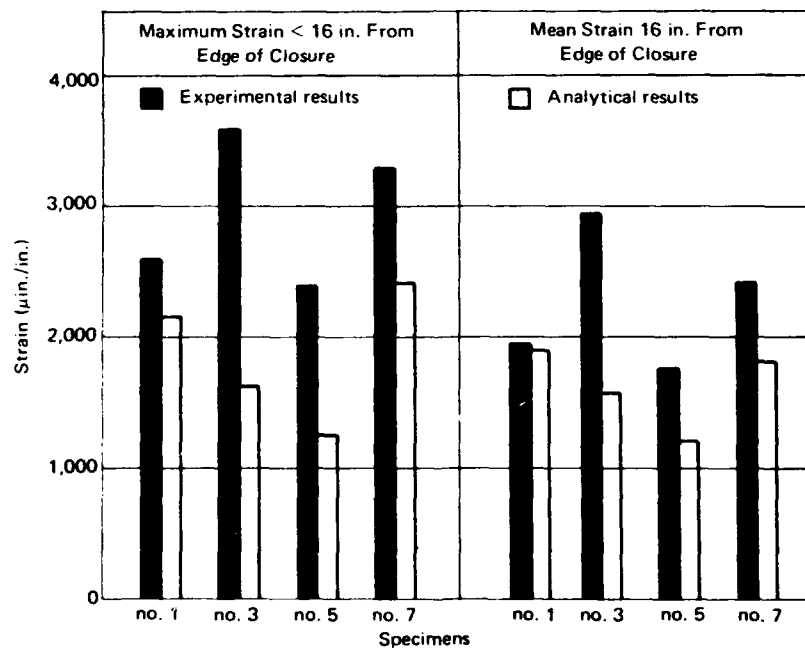


Figure 36. Comparison of experimental and analytical strain results at $P/f'_c = 0.20$.

The analysis was closest for the cylinder with the 1-inch-wall-thickness hemispherical closures at both ends, because no abrupt discontinuity in radial stiffness was introduced. Where more rigid end-closure restraints were introduced, the actual response of each finite element along the cylinder length was different from that of its neighboring element because of the nonlinearity of concrete and because of the influence of triaxial loading on the concrete properties. This difference in response was particularly important near the closure. The bilinear stress-strain curve used in the analysis did not accurately account for these real differences in response between the elements.

To analyze the structures more accurately, the real concrete stress-strain curve should be used in the computer program. Nevertheless, the linear analysis does show the areas of stress concentration, which may aid the designer in selecting the closure which induces the least stress conditions.

For cylinders with metal plate end closures, the maximum radial deflection was found both analytically and experimentally at a distance about one-half the outside diameter from the closure edge.

FINDINGS

1. Variations in the stiffness of cylinder end closures did not significantly alter the short-term implosion pressures of concrete cylindrical hulls from those pressures determined by Haynes and Ross.¹
2. By using the concrete strength (f'_c) as the failure stress, Lamé's elastic thick-wall theory predicted implosion pressures less than those of the models, which had a $t/D_o = 0.125$, by approximately 10%.
3. For specimens with a 1-inch-thick hemispherical end closure, implosion resulted from a high bearing stress produced at the joint between the 1-inch-thick hemisphere and the 2-inch-thick cylinder section.
4. For specimens with a 2-inch-thick hemispherical end closure, implosion resulted from a concrete compression failure in the cylinder at a distance approximately one-half the outside diameter from the hemispherical closure.
5. The pinned, beveled, and fixed end closures produced similar cylinder behavior. Maximum radial deflection occurred at a distance from the closure equal to about one-half the outside diameter, and a region of high shear strain existed between the end closure and the point of maximum deflection.
6. Cylinder out-of-roundness and flat spot development caused as much strain variation in a specimen as that produced by the different end-closure conditions.

7. The influence of the end closures was limited to a distance equal to one outside diameter from the edge of the closure.
8. A finite element analysis using a bilinear stress—strain curve for concrete predicted the general behavior of cylindrical hulls with various end closures, but the analysis yielded strain values less than the values observed.

SUMMARY

Variation of end-closure stiffness did not reduce the implosion pressure of cylindrical concrete hulls below the implosion pressure of a cylinder with a free end condition or below the implosion pressure predicted with Lamé's theory. However, rigid end closures produced a severe shear strain near the closure and a maximum radial deflection at a distance approximately one-half the outside diameter from the closure restraint. The influence of end-closure stiffness was limited to the region one outside diameter from the closure.

RECOMMENDATIONS

In designing cylinder end closures and cylindrical hulls, the following guidelines are recommended:

1. The bearing load of the end closure on the cylinder should be applied at the center of cylinder wall thickness.
2. The closure stiffness should be approximately the same as that of the cylinder to reduce the maximum strains and create a uniform strain condition along the length of the cylinder.
3. Penetrations in the cylindrical hull should not be placed in the high-shear area between the closure and one-half the diameter from the closure.
4. Lamé's equation for thick-walled cylinders (Equation 1) may be used for a conservative prediction of implosion pressure for cylinders with $t/D_o = 0.125$.
5. Long-term operating pressures for cylindrical hulls with end-closure restraints should be based upon the maximum strain occurring at one-half the diameter from the closure rather than on the uniform strain found at one diameter or more from the closure. The operating pressure based on maximum strain could be as much as 30% less than the pressure based on strain of an infinite-length cylinder.

ACKNOWLEDGMENT

Mr. John E. Crawford, Research Structural Engineer, NCEL, prepared the finite element analysis of the cylindrical hulls.

Appendix A

CONCRETE PROPORTIONS AND PROPERTIES

The concrete material constituents were portland type III high early strength cement, San Gabriel River Wash aggregate, and fresh water, proportioned as follows: aggregate-to-cement ratio was 3.30 by weight and water-to-cement ratio was 0.55 by weight.

The aggregate was supplied to NCEL kiln dried and bagged. The aggregate was proportioned as shown in Table A-1. All material passed the no. 4 size sieve; therefore, the mix was technically a mortar or microconcrete.

Table A-1. Aggregate Proportions

Sieve Size Designation		Percent Retained
Passing	Retained	
no. 4	no. 8	29.6
no. 8	no. 16	20.8
no. 16	no. 30	14.7
no. 30	no. 50	10.3
no. 50	no. 100	7.3
no. 100	pan	17.3

The concrete compressive strength, modulus of elasticity, and Poisson's ratio are presented in Table A-2. The results were obtained from 3 x 6-inch control cylinders tested under uniaxial compression the same day the cylindrical structure was tested. The concrete used in the hollow cylinder sections had an average compressive strength of approximately 8,830 psi and average secant modulus of elasticity of 3.37×10^6 psi.

Table A.2. Concrete Properties

Specimen No.	Cylinder Section						Hemispherical Caps	
	f'_c (psi)	E_s (psi $\times 10^6$)	E_e (psi $\times 10^6$)	E_p (psi $\times 10^6$)	ν	Age (days)	f'_c (psi)	Age (days)
1	7,860	2.72	2.93	1.37	0.180	127	10,000	147
2	9,800	3.40	3.63	1.91	0.154	130	8,980	144
3	9,420	3.47	3.51	2.31	0.150	239	9,620	129
4	9,270	3.75	4.18	2.08	0.155	134	9,270	130
5	5,940	2.40	2.44	1.17	0.125	139	9,190	209
6	5,910	3.07	3.25	1.82	0.150	264	9,870	138
7	9,100	3.45	3.55	2.39	0.172	252	8,620	135
8	9,260	3.36	3.51	1.98	0.167	140	9,600	251
9	10,480	3.51	3.68	2.17	0.170	53	9,640	253
10	10,640	3.69	3.79	2.06	0.174	60	9,790	133
11	8,700	3.82	3.82	2.86	0.120	202	9,820	1,127
12	9,580	3.80	3.85	2.79	0.190	211	9,950	1,132
							9,950	1,103
							9,560	1,237

Note: f'_c = ultimate uniaxial concrete strength.
 E_s = secant modulus to strain at $1/2 f'_c$.
 E_e = elastic modulus for bilinear stress-strain relationship.
 E_p = plastic modulus for bilinear stress-strain relationship.
 ν = Poisson's ratio of strain at $1/2 f'_c$.
Age = age of concrete at time of testing.

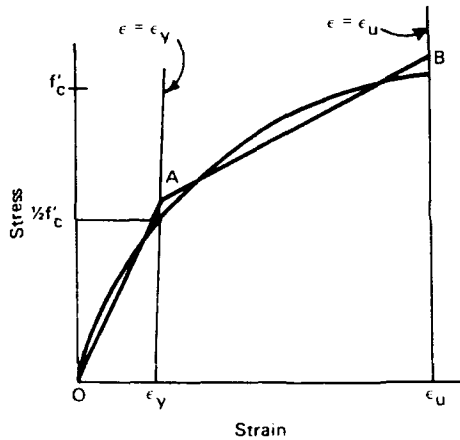


Figure A-1. Construction of bilinear stress-strain curve.

A bilinear stress-strain relation was determined for the concrete of each specimen. An elastic modulus (E_e) and a plastic modulus (E_p) were determined so that the area under the bilinear stress-strain curve was equal to the area beneath the actual curve. As shown in Figure A-1, E_e was found by (1) finding the strain (ϵ_y) at one-half the concrete strength ($1/2 f'_c$) and drawing a vertical line at ϵ_y ($\epsilon = \epsilon_y$), (2) drawing a straight line (OA) so that the area bounded by OA and line $\epsilon = \epsilon_y$ was equal to the area bounded by the real stress-strain curve and line $\epsilon = \epsilon_y$. The slope of line OA was the E_e . The plastic modulus was found by (1) drawing a vertical line through the ultimate strain ($\epsilon = \epsilon_u$), (2) drawing line AB so that the area bounded by $\epsilon = \epsilon_y$ and line $\epsilon = \epsilon_u$ was equal to the area bounded by the actual stress-strain curve and line $\epsilon = \epsilon_u$. The slope of line AB was E_p .

Appendix B
DRAWINGS OF CYLINDER END CLOSURES

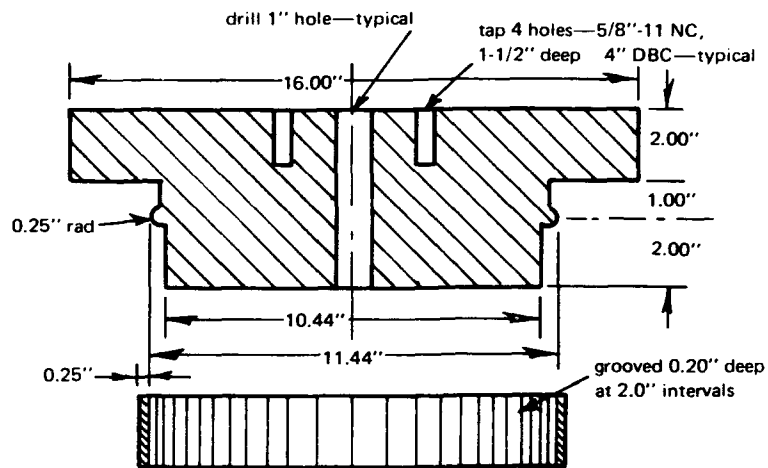


Figure B-1. Pinned end closure and bearing ring.

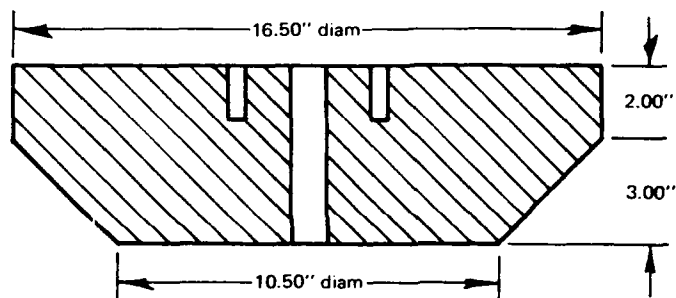


Figure B-2. Beveled end closure.

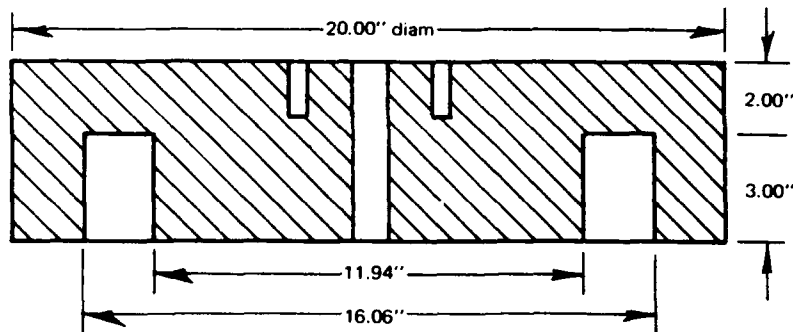


Figure B-3. Fixed end closure.

Appendix C

DISCUSSION OF STRAIN BEHAVIOR ALONG CYLINDER LENGTH

FREE END CLOSURE (SPECIMENS 1 AND 2)

Figures 17 and 18 show that the 1-inch hemispherical end closure affected the behavior of the cylinder. Though the hemisphere provided free end restraint, it induced edge bearing stresses in the cylinder, causing increased strain at a distance of 4 inches from the cylinder edge. Figure 17 shows that at the lower loads the corresponding strains on lines A and B of specimen 1 were the same but at higher loads line B had much higher strains. It is likely that such strain increases were due to nonsymmetry of the cylinder.

Figure 18 shows that the opposite sides of specimen 2 had similar behavior. It appears that the influence of the closure was within a distance of one-half the diameter from the end and that the strains at greater distances were nearly uniform.

The behavior of specimens 1 and 2 indicated that the hemisphere restrained the radial movement of the cylinder at the edge while producing an increased deflection between 2 and 4 inches from the closure. The bearing of the hemisphere on the outer edge of the cylinder produced a shear and moment which increased the radial deflection.

In future design of hemispherical ends, a lower shear distortion and moment would result from centering the bearing surface of the hemisphere on the cylinder wall.

PINNED END CLOSURE (SPECIMENS 3 AND 4)

Figures 19 and 20 show that the pinned end closures provided significant restraint to radial deflection at the cylinder edge. If the cylinders had been fully restrained at the interior, the exterior hoop strains would have been approximately $200 \mu\text{in./in.}$ at $P/f'_c = 0.20$ because of the radial compressibility of the concrete and the deflection of the steel plate. The actual strains at $P/f'_c = 0.20$ were between 500 and $900 \mu\text{in./in.}$ These higher strains indicated that the pinned end closure of the model cannot be considered an ideal pinned end but rather one that approximates the pin-type restraint.

At low loads the effect of the closure was limited to a short distance from the end. As the pressure was increased the effect became more pronounced at greater distances. The distance from the edge at which the maximum strain occurred increased as the pressure loading increased. The maximum strains of lines A and B were between 5 and 10 inches from the edge.

The strain gradient between the closure end and the point of maximum strain was nearly the same for both specimens. The gradient indicates a high-shear area between the end and the point of maximum deflection.

BEVELED END CLOSURE (SPECIMENS 5 AND 6)

Figures 21 and 22 show that the beveled end closure provided nearly complete restraint to the radial deflection of the cylindrical hulls. At $P/f_c = 0.20$, the exterior strains on specimens 5 and 6 at the closure were between 150 and 250 $\mu\text{in./in.}$ Since a 200- $\mu\text{in./in.}$ exterior strain implies zero interior strain, the beveled end closure permitted almost no radial deflection at the cylinder edge. This restraint shows that the closure fit snugly onto the ends, that the cylinders were symmetric at the beveled end, that the epoxy bond between the closure and the cylinder was good, and that little relative movement between the closure and cylinder occurred during test.

The closure affected the cylinder behavior within 16 inches from the edge. The highest strain value was recorded at a distance of one-half the diameter from the edge.

FIXED END CLOSURE (SPECIMENS 7 AND 8)

Figure 23 shows that specimen 7 was significantly restrained at the closure edge. On both lines A and B the strain gradient at the edge indicated a near-zero strain at the joint between the closure and the cylinder. The strain gradient near the edge was steep, with line B showing higher strain values than those of line A. As illustrated in Figure 31, line B had strains considerably greater than the average strain around the circumference of the cylinder.

Figure 24 shows that the response of specimen 8 was similar to that of specimen 7, except that lines A and B had different behavior. The strains on line B tend toward zero strain at the cylinder edge, while the strains on line A do not. This means that at line A the cylinder was not fixed to the end closure at the joint, but the cylinder may be considered fixed at some point within the closure.

On both cylinders the maximum strain occurred between 5 and 10 inches from the cylinder edge and its magnitude was over 4,000 $\mu\text{in./in.}$ Between 2 and 5 inches from the edge there was a strain decrease or a strain plateau. Such behavior was observed only with the fixed end closures and was apparently a result of a moment acting at the closure edge.

Appendix D

DISCUSSION OF CIRCUMFERENTIAL STRAIN

The very large strain difference on specimens 7 and 8 at a distance of 2 inches from the edge indicated that the specimens were out-of-round near the cylinder end and that the fixed end closure did not prevent the unsymmetric deflection of the cylinder near the closure. The fixed closure apparently restrained radial movement at some points and provided no restraint at others. For specimen 7, Figure 31 shows that at 0° (line A) more restraint was provided than at 180° (line B). This behavior corresponded to the difference in the strain along lines A and B given in Figure 23. Similarly the opposite behavior is shown in Figure 32 for specimen 8. On one side of each cylinder the closure acted to provide a fixity, while on the opposite side little restraint was provided. Therefore, the fixed end closure did not provide the total fixity desired.

On specimen 6 the strain difference at 2 inches from the edge was larger than at farther distances. The difference apparently was due to a localized strain increase rather than a general nonsymmetry. Such a sudden development of a high peak strain would not have resulted from a general out-of-round condition; this peak might have been caused by the development of a crack at that point.

Table D-1 summarizes the circumferential strain data by listing the strain difference and mean strain at locations 2, 8, and 16 inches from the edge of the closure and at pressure levels $P/f'_c = 0.10$ and 0.20 . In general, the data of Table D-1 show the following:

1. The mean strains indicate that the metal plate end closures restrained the radial deflection near the closure.
2. The similarity in mean strains at 16 inches implies that the effect of the end closures was negligible at a distance of one diameter from the cylinder edge.
3. Strain differences, therefore out-of-round differences, increased with increasing load.

Table D-1. Maximum Minus Minimum Circumferential Strain and Mean Circumferential Strain at $P/f'_c = 0.10$ and 0.20

Specimen No.	Maximum-Minimum Strain ($\mu\text{in./in.}$)			Mean Strain ($\mu\text{in./in.}$)		
	2 Inches From Closure	8 Inches From Closure	16 Inches From Closure	2 Inches From Closure	8 Inches From Closure	16 Inches From Closure
At $P/f'_c = 0.10$						
1	110	190	230	840	790	740
2	230	180	500	1,040	990	1,010
3	280	790	230	700	970	970
4	260	210	90	680	1,000	900
5	430	350	230	360	990	1,000
6	530	400	110	300	630	670
7	340	810	240	110	860	910
8	420	330	390	660	990	840
At $P/f'_c = 0.20$						
1	590	610	860	2,180	2,080	1,940
2	440	700	1,630	2,880	2,800	2,710
3	300	1,060	980	2,760	3,050	2,930
4	800	690	580	1,630	2,870	2,560
5	1,000 ^d	810 ^d	520 ^d	650 ^d	1,800 ^d	1,760 ^d
6	1,830	1,530	1,070	1,040	1,900	2,340
7	1,240	960	410	1,990	2,710	2,410
8	1,340	1,110	1,070	1,840	3,040	2,540

^d Strain at $P/f'_c = 0.15$.

REFERENCES

1. Naval Civil Engineering Laboratory. Technical Report R-696: Influence of length-to-diameter ratio on behavior of concrete cylindrical hulls under hydrostatic loading, by H. H. Haynes and R. J. Ross. Port Hueneme, Calif., Sept. 1970. (AD 713088)
2. E. L. Wilson. "Structural analysis of axisymmetric solids," American Institute of Aeronautics and Astronautics, Journal, vol. 3, no. 12, Dec. 1965, pp. 2269-2274.
3. Naval Civil Engineering Laboratory. Technical Report R-588: Behavior of spherical concrete hulls under hydrostatic loading, pt. III. Relationship between thickness-to-diameter ratio and critical pressures, strains, and water permeation rates, by J. D. Stachiw and K. Mack. Port Hueneme, Calif., June 1968. (AD 835492L)
4. ———. Technical Report R-679: Failure of thick-walled concrete spheres subjected to hydrostatic loading, by H. H. Haynes and R. A. Hoofnagle. Port Hueneme, Calif., May 1970. (AD 708011)

LIST OF SYMBOLS

D_o	Outside diameter of cylinder (in.)
E_e	Elastic modulus for bilinear stress—strain relationship (psi)
E_p	Plastic modulus for bilinear stress—strain relationship (psi)
E_s	Secant modulus (psi)
f'_c	Ultimate uniaxial compressive concrete strength (psi)
L	Length of cylinder (in.)
L/D_o	Ratio of cylinder length to outside diameter
P	Applied pressure (psi)
P/f'_c	Ratio of applied pressure to concrete strength
P_{im}	Implosion pressure (psi)
P_{im}/f'_c	Ratio of implosion pressure to concrete strength
r_i	Interior radius of cylinder (in.)
r_o	Exterior radius of cylinder (in.)
t	Thickness of cylinder wall (in.)
t/D_o	Ratio of cylinder wall thickness to outside diameter
ϵ	Strain (in./in.)
ϵ_u	Ultimate strain (in./in.)
ϵ_y	Yield strain (in./in.)
ν	Poisson's ratio

DISTRIBUTION LIST

SNDL Code	No. of Activities	Total Copies	
—	1	12	Defense Documentation Center
FKAIC	1	10	Naval Facilities Engineering Command
FKNI	6	6	NAVFAC Engineering Field Divisions
FKN5	9	9	Public Works Centers
FA25	1	1	Public Works Center
—	9	9	RDT&E Liaison Officers at NAVFAC Engineering Field Divisions and Construction Battalion Centers
—	355	355	NCEL Special Distribution List No. 9 for persons and activities interested in reports on Deep Ocean Studies

Naval Civil Engineering Laboratory

INFLUENCE OF END-CLOSURE STIFFNESS ON
BEHAVIOR OF CONCRETE CYLINDRICAL HULLS
SUBJECTED TO HYDROSTATIC LOADING, by L. F. Kahn
TR 740 53 p. illus October 1971 Unclassified

1. Concrete hulls

I. 3.1610-1

Twelve model concrete cylindrical hulls were subjected to hydrostatic loading to determine the influence of end-closure stiffness on implosion pressure and strain behavior of the cylinders. Results showed that variation of end-closure stiffness did not reduce the implosion pressure below that of a cylinder with a free end condition or below the implosion pressure predicted by elastic thick-wall theory. To vary the closure stiffness, concrete hemisphere and steel plate end closures were used to simulate free, pinned, beveled, and fixed end conditions. Strain variations along the length of the cylinders indicated that the influence of the closure was limited to a distance of one diameter from the closure. Recommendations are presented to aid in the design of concrete cylindrical hulls.

Naval Civil Engineering Laboratory

INFLUENCE OF END-CLOSURE STIFFNESS ON
BEHAVIOR OF CONCRETE CYLINDRICAL HULLS
SUBJECTED TO HYDROSTATIC LOADING, by L. F. Kahn
TR 740 53 p. illus October 1971 Unclassified

1. Concrete hulls

I. 3.1610-1

Twelve model concrete cylindrical hulls were subjected to hydrostatic loading to determine the influence of end-closure stiffness on implosion pressure and strain behavior of the cylinders. Results showed that variation of end-closure stiffness did not reduce the implosion pressure below that of a cylinder with a free end condition or below the implosion pressure predicted by elastic thick-wall theory. To vary the closure stiffness, concrete hemisphere and steel plate end closures were used to simulate free, pinned, beveled, and fixed end conditions. Strain variations along the length of the cylinders indicated that the influence of the closure was limited to a distance of one diameter from the closure. Recommendations are presented to aid in the design of concrete cylindrical hulls.

Naval Civil Engineering Laboratory

INFLUENCE OF END-CLOSURE STIFFNESS ON
BEHAVIOR OF CONCRETE CYLINDRICAL HULLS
SUBJECTED TO HYDROSTATIC LOADING, by L. F. Kahn
TR 740 53 p. illus October 1971 Unclassified

1. Concrete hulls

I. 3.1610-1

Twelve model concrete cylindrical hulls were subjected to hydrostatic loading to determine the influence of end-closure stiffness on implosion pressure and strain behavior of the cylinders. Results showed that variation of end-closure stiffness did not reduce the implosion pressure below that of a cylinder with a free end condition or below the implosion pressure predicted by elastic thick-wall theory. To vary the closure stiffness, concrete hemisphere and steel plate end closures were used to simulate free, pinned, beveled, and fixed end conditions. Strain variations along the length of the cylinders indicated that the influence of the closure was limited to a distance of one diameter from the closure. Recommendations are presented to aid in the design of concrete cylindrical hulls.

Naval Civil Engineering Laboratory

INFLUENCE OF END-CLOSURE STIFFNESS ON
BEHAVIOR OF CONCRETE CYLINDRICAL HULLS
SUBJECTED TO HYDROSTATIC LOADING, by L. F. Kahn
TR 740 53 p. illus October 1971 Unclassified

1. Concrete hulls

I. 3.1610-1

Twelve model concrete cylindrical hulls were subjected to hydrostatic loading to determine the influence of end-closure stiffness on implosion pressure and strain behavior of the cylinders. Results showed that variation of end-closure stiffness did not reduce the implosion pressure below that of a cylinder with a free end condition or below the implosion pressure predicted by elastic thick-wall theory. To vary the closure stiffness, concrete hemisphere and steel plate end closures were used to simulate free, pinned, beveled, and fixed end conditions. Strain variations along the length of the cylinders indicated that the influence of the closure was limited to a distance of one diameter from the closure. Recommendations are presented to aid in the design of concrete cylindrical hulls.

Unclassified

Security Classification

DOCUMENT CONTROL DATA - R & D		
<i>Security classification of title, body, and abstract and indexing annotation must be entered when the overall report is classified.</i>		
1. ORIGINATING ACTIVITY (Corporate author) Naval Civil Engineering Laboratory Port Hueneme, California 93013		2a. REPORT SECURITY CLASSIFICATION Unclassified
		2b. GROUP
3. REPORT TITLE INFLUENCE OF END-CLOSURE STIFFNESS ON BEHAVIOR OF CONCRETE CYLINDRICAL HULLS SUBJECTED TO HYDROSTATIC LOADING		
4. DESCRIPTIVE NOTES (Type of report and inclusive dates) Not final; July 1969-April 1971		
5. AUTHOR(S) (First name, middle initial, last name) L. F. Kahn		
6. REPORT DATE October 1971	7a. TOTAL NO. OF PAGES 53	7b. NO. OF REFS 4
8a. CONTRACT OR GRANT NO. b. PROJECT NO. 3.1610-1 c. d.		9a. ORIGINATOR'S REPORT NUMBER(S) TR-740 9b. OTHER REPORT NO(S) (Any other numbers that may be assigned this report)
10. DISTRIBUTION STATEMENT Approved for public release; distribution unlimited.		
11. SUPPLEMENTARY NOTES		12. SPONSORING MILITARY ACTIVITY Naval Facilities Engineering Command Washington, D. C. 20390
13. ABSTRACT Twelve model concrete cylindrical hulls were subjected to hydrostatic loading to determine the influence of end-closure stiffness on implosion pressure and strain behavior of the cylinders. Results showed that variation of end-closure stiffness did not reduce the implosion pressure below that of a cylinder with a free end condition or below the implosion pressure predicted by elastic thick-wall theory. To vary the closure stiffness, concrete hemisphere and steel plate end closures were used to simulate free, pinned, beveled, and fixed end conditions. Strain variations along the length of the cylinders indicated that the influence of the closure was limited to a distance of one diameter from the closure. Recommendations are presented to aid in the design of concrete cylindrical hulls.		

DD FORM 1473

(PAGE 1)

S/N 0101-807-6801

Unclassified

Security Classification

Unclassified

Security Classification

14 KEY WORDS	LINK A		LINK B		LINK C	
	ROLE	WT	ROLE	WT	ROLE	WT
Underwater construction						
Concrete cylindrical hulls						
Hydrostatic tests						
Implosion pressure						
End closures						
Model concrete cylinders						
Cylindrical hulls						
End-closure stiffness						
Pressure-resistant structures						
Concrete shells						
Thick-wall shells						

DD FORM 1473 (BACK)
1 NOV 66
(PAGE 2)

Unclassified
Security Classification

Technical Report

R 735

**INFLUENCE OF STIFF EQUATORIAL RINGS
ON CONCRETE SPHERICAL HULLS SUBJECTED
TO HYDROSTATIC LOADING**

August 1971

Sponsored by

NAVAL FACILITIES ENGINEERING COMMAND



NAVAL CIVIL ENGINEERING LABORATORY

Port Hueneme, California

Approved for public release; distribution unlimited.

INFLUENCE OF STIFF EQUATORIAL RINGS ON CONCRETE SPHERICAL HULLS SUBJECTED TO HYDROSTATIC LOADING

Technical Report R-735

3.1610-1

by

L. F. Kahn and J. D. Stachiw

ABSTRACT

Thirteen hollow concrete spheres of 16-inch outside diameter x 14-inch inside diameter and one sphere of 66-inch outside diameter x 57.75-inch inside diameter were assembled from hemispheres fastened together with equatorial joint rings of different stiffnesses. The joint rings were made from polycarbonate plastic, glass reinforced plastic laminate, aluminum, titanium, low carbon steel, and alloy steel. After instrumentation with electrical resistance strain gages, the spheres were tested to destruction under external hydrostatic loading. Equatorial joints that are either considerably stiffer or more compliant than concrete lower the short-term implosion pressure of the concrete spheres by as much as 27%; the glass reinforced plastic joint ring did not significantly reduce the implosion pressure. It is recommended that equatorial joint rings be designed to have a stiffness approximately equal to that of the concrete shell and be made of glass reinforced plastic. If stiffer joint rings are used, the operational pressure should be 30% lower than that of a sphere without a mechanical lock joint mechanism.

Approved for public release; distribution unlimited.

Copies available at the National Technical Information Service
(NTIS), Sillis Building, 5285 Port Royal Road, Springfield, Va. 22151

CONTENTS

	page
INTRODUCTION	1
Statement of Problem	1
Objective of Study	1
Background Information	2
Scope of Investigation	2
DESIGN OF EXPERIMENT	3
FABRICATION OF SPECIMENS	3
Hemispheres	5
Joint Rings	7
Spheres	7
INSTRUMENTATION	8
TEST PROCEDURE	10
TEST OBSERVATIONS	13
Implosion Failure	13
Strain Results	13
DISCUSSION OF RESULTS	20
Implosion Behavior	20
Strain Behavior	21
Bending Moment Response	23
FINDINGS	26
CONCLUSION	27

	page
RECOMMENDATIONS	27
APPENDIXES	
A – Operational Lock Joint	28
B – Material Properties	44
C – Strain Data	47
D – Longitudinal and Latitudinal Stress Data at $P/f'_c = 0.20$	54
REFERENCES	59
LIST OF SYMBOLS	61

INTRODUCTION

Statement of Problem

Undersea spherical capsules made of concrete to contain instruments or some other payload require that the interior be readily accessible for loading and unloading. Access to the interior may be through a hatch located in a penetration through the hull or by separation of the sphere at the equator. The latter is, in many cases, preferable, because it permits access to the whole interior of the capsule for rapid placement or removal of payload.

Exploratory research¹⁻³ on the incorporation of hatches into concrete spherical capsules has been conducted, and sufficient data are on hand to permit preliminary design of hatch penetrations in concrete spheres. However, no information is available on spheres with a mechanical joint at the equator. Because it is not known what effects a mechanical joint has on the magnitude and distribution of strains or on the strength of concrete spheres, the design of equatorial joints for concrete spheres is a matter of engineering judgment. Therefore, experimental data are needed on the relationship between joint stiffness and implosion pressure for spheres under hydrostatic loading.

Objective of Study

The objective of this study was to explore experimentally the relationship between the stiffness of equatorial joint rings and (1) the implosion pressure of the sphere assembly, (2) the distribution of strains, and (3) the magnitude of strains in the sphere.

The experimental data generated in this exploratory study serve two purposes. They permit a rational design of spherical concrete capsules with equatorial joints and serve as basis for future analytical studies attempting to correlate the stiffness mismatch between the concrete hull and equatorial joint ring with the magnitude of strains and implosion pressure of the spherical hulls.

Background Information

Four previous studies¹⁻⁴ have shown that concrete is an effective material for the construction of undersea pressure resistant structures. Experiments^{3,4} using concrete spheres with 16-inch OD (outside diameter) and different wall thicknesses have shown that the implosion pressure, P_{im} ,* is predictable if the ratio of thickness to outside diameter, t/D_o , and the concrete strength, f'_c , are known.

The objective of the first exploratory study¹ of concrete spherical hulls was to establish the basic performance parameters of unreinforced concrete spherical hulls. Model concrete spheres with 16-inch OD and 14-inch ID (inside diameter) were cast using the same mix design and were subjected to similar curing conditions. When they were tested to destruction, the average ratio of implosion pressure to concrete strength (P_{im}/f'_c) was found to be 0.293 with a standard deviation of only 0.008.

The second exploratory investigation² concentrated on the relationship between stiffness of a penetration insert and the implosion pressure of the concrete spherical hull. Figure 1 shows a typical specimen studied in this investigation. The preliminary design guide that resulted from the study indicates that for round penetrations with a spherical angle less than or equal to 32 degrees, the penetration insert should be of equal or greater stiffness than that of the replaced concrete in order not to decrease the implosion pressure of the spherical hull. A model of an ocean bottom habitat was built and tested to destruction to prove the applicability and validity of this finding. The results from that test verified this basic design guide.

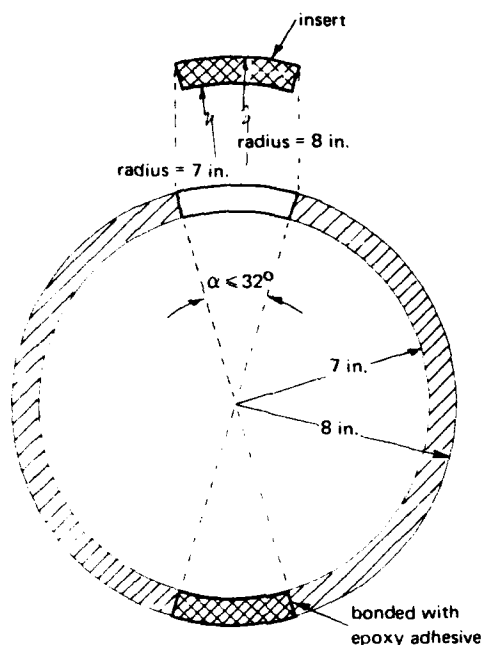
Scope of Investigation

The primary study was an experimental investigation of spherical concrete hulls with equatorial joint rings made of various materials. Eleven concrete spheres were tested to implosion under short-term hydrostatic loading. The 16-inch-OD x 14-inch-ID spheres were equipped with rings of different rigidities at the joint between the two hemispheres.

The experimental data recorded during these tests consisted of strains measured on the interior and exterior surfaces of the concrete hull, strains measured on the equatorial ring, the pressure at which the sphere imploded, and the fracture pattern after failure.

A secondary phase of the investigation was to design an operational equatorial joint for two 16-inch-OD x 14-inch-ID spheres and for a 66-inch-OD x 57 3/4-inch-ID sphere. These three specimens were also instrumented and pressurized to implosion. This second phase is described in Appendix A.

* A foldout list of symbols appears after References.



Insert materials investigated

Plastic (PVC)	— E = 0.35×10^6 psi
	$\sigma_{yp} = 4,000$ psi
Aluminum	— E = 10×10^6 psi
	$\sigma_{yp} = 60 \times 10^6$ psi
Steel	— E = 30×10^6 psi
	$\sigma_{yp} = 90,000$ psi

Figure 1. Concrete spherical specimen with penetration inserts previously investigated.

DESIGN OF EXPERIMENT

Joint ring rigidity was varied over as wide a range as possible to establish an empirical relationship between the rigidity of the ring and the behavior of the sphere under hydrostatic loading. The rings selected for this phase of the investigation merely simulated operational lock joints; operational ones would entail only additional expense without benefiting the test program.

The radial stiffness of the rings was varied by a factor of more than 100 by selecting materials with different elastic moduli and by changing the cross section of the ring. The various test assemblies are listed in Table 1.

FABRICATION OF SPECIMENS

The test specimens were formed from two 16-inch-OD x 14-inch-ID concrete hemispheres and a 17.40-inch-OD x 13.48-inch-ID x 0.50-inch-thick solid ring (Figure 2). The concrete hemispheres were formed so that when the hemispheres and ring were assembled the specimen would be a true sphere within tolerances of $\pm 1/32$ inch in the radial direction.

Table 1 Joint Assemblies^a
(Average joint modulus of elasticity, E_c , for concrete $\frac{3.5}{4} \times 10^6$ psi)

Sphere No.	Joint Ring Material	Joint Type (Figure 2)	Ring Properties		Relative Stiffness ^b
			Modulus of Elasticity, E_r (psi $\times 10^6$)	Stiffness, $E_r A_r$ (lb $\times 10^6$)	
1	polycarbonate plastic	A	0.3	0.33	0.18
2	glass fiber reinforced plastic	A	1.95	2.12	1.19
3	aluminum	A	10.5	11.42	6.40
4	aluminum	A	10.5	11.42	6.40
5	titanium	A	15.8	17.18	9.62
6	steel	A	30.0	32.60	18.26
7	steel	A	30.0	32.60	18.26
8	steel	B	30.0	39.90	22.35
9	steel	C	30.0	42.50	23.81
10	titanium	A	15.8	17.18	9.62
11	aluminum	D	10.5	17.65	9.89

^a All test assemblies are composed of two 16 inch OD \times 14 inch ID hemispheres bonded with epoxy adhesive to equatorial joint rings.

^b Relative stiffness = $E_r A_r / E_c A_c$, where A_c is area of concrete removed and replaced by joint ring

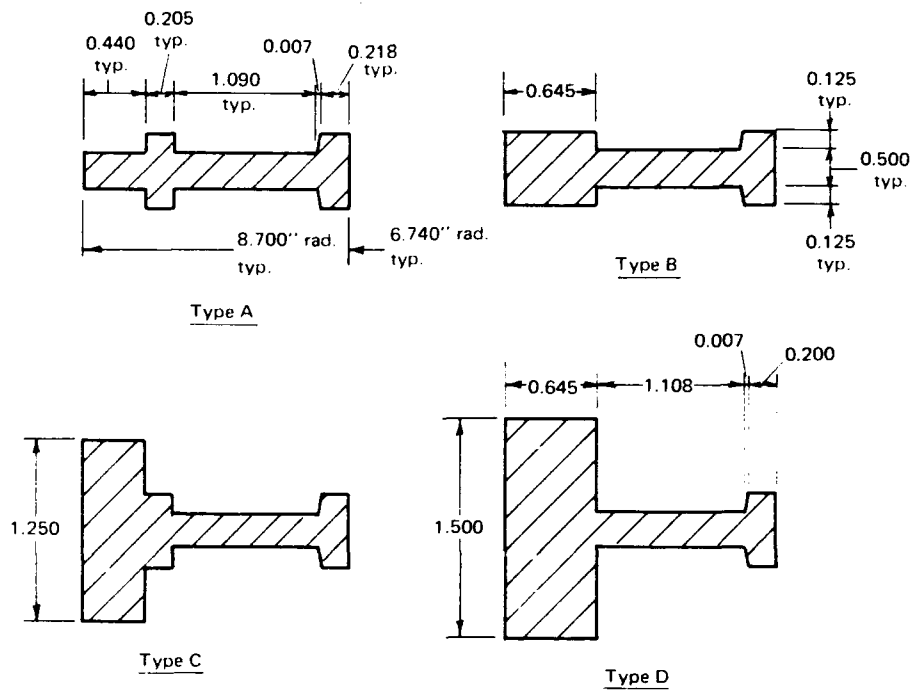


Figure 2. Dimensions of simulated equatorial lock joint assembly.

Hemispheres

The concrete constituents were portland type III cement, San Gabriel River Wash aggregate, and freshwater. The water-to-cement ratio was 0.55 by weight, and the aggregate-to-cement ratio was 3.30 by weight. Table 2 presents the proportions of the aggregate.

The concrete hemispheres were cast in a rigid male and female aluminum mold (Figure 3). The molds were prepared for casting by initially spraying the aluminum with clear enamel paint and then applying a coat of silica grease. An external form vibrator was attached to the underside of the mold and was in operation throughout the casting process. The concrete was mixed in a pan-type mixer for a total of 3 minutes and slowly placed into the mold, usually within the next 4 minutes. The concrete was then screeded to 1/4 inch below the top edge of the form.

Table 2. Proportions of Aggregate

Sieve Size Designation		Percent Retained
Passing	Retained	
No. 4	No. 8	29.6
No. 8	No. 16	20.8
No. 16	No. 30	14.7
No. 30	No. 50	10.3
No. 50	No. 100	7.3
No. 100	pan	17.3

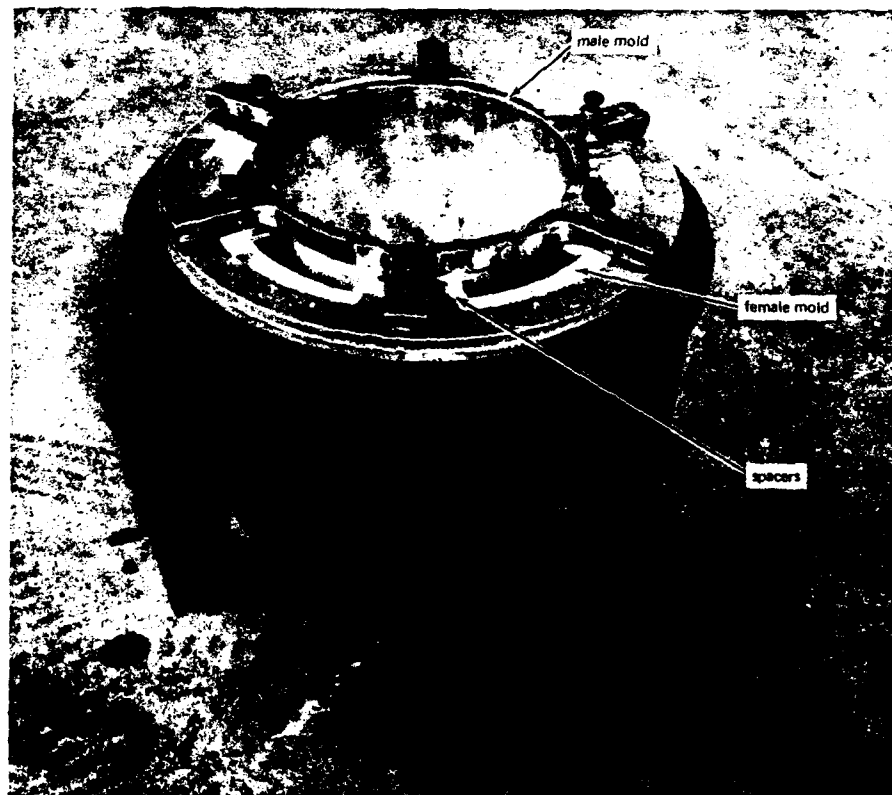


Figure 3. Mold used in casting concrete spheres of 16-inch external and 14-inch internal diameter.

The hemisphere was removed from the mold on the day after casting. The interior surface was usually pitted with some small air pockets; these were fully exposed by rubbing with steel wool. The voids were filled with a cement paste of type III portland cement and par-size aggregate in a ratio of 1:1 with only sufficient water to make a workable mix. The hemisphere was cured for 27 days in an environment of 100% relative humidity and 73°F. Thereafter the concrete was cured under room conditions (30 to 70% relative humidity and 45°F to 80°F) for approximately 100 days.

Six 3 x 6-inch control cylinders were cast with each hemisphere. These cylinders were used to determine the uniaxial compressive strength of the concrete. One of the six was instrumented with a 90-degree strain rosette of two BLH (Baldwin-Lima-Hamilton) A-5-S6 electrical resistance gages to obtain measurements of the modulus of elasticity and Poisson's ratio of the concrete. The compressive strength of concrete for all the spheres varied from 9,810 to 11,740 psi. The average secant modulus of elasticity for the concrete was determined to be 3.57×10^6 psi, and the average Poisson's ratio was 0.16; individual cylinder data are described in Appendix B.

Joint Rings

Various materials were used to make the rings: polycarbonate plastic, glass fiber reinforced plastic (GRP, fiberglass), aluminum, titanium, and low carbon and 4130 alloy steel. All rings were machined from flat, solid plates originally 19 inches in diameter and 3/4 to 1-1/2 inches thick, depending on the ring cross section (Figure 2). Machine tolerances were within ± 0.005 inch.

For each ring, four material control specimens were machined from the same plate used for machining the ring. The control specimens were cylinders 1/2 inch in diameter and 2 inches in length.

To measure the modulus of elasticity, all material cylinders were instrumented with two BLH FAE-25-12S6 electrical resistance strain gages on opposite sides of the specimen. To measure Poisson's ratio, a BLH FAE-12S-35S13 electrical resistance strain gage was oriented in the hoop direction at midlength of all cylinders. The compressive yield stress of the joint ring material varied from 8,320 to 140,800 psi, the modulus of elasticity from 0.39×10^6 to 30.0×10^6 , and the Poisson's ratio from 0.23 to 0.40, depending on the joint ring material (Appendix B).

Spheres

The spheres were fabricated by bonding a ring between two hemispheres; an epoxy bonding agent, Furane Plastics Epocast 8288, was used. The annular mating surface of each hemisphere section was ground smooth and level by

rotating the hemisphere on a sheet of plate glass covered with water and silica carbide grit no. 60. The concrete mating surface was then cleaned and etched with a 10% hydrochloric acid solution to ensure good bond between the epoxy and the concrete. All rings were cleaned with acetone to ensure a good bond with the epoxy adhesive. The titanium ring for sphere 10 was etched with a solution of one part hydrochloric acid, one part nitric acid, and two parts glycerin. The aluminum joints for spheres 4 and 11 were etched with a 10% phosphoric acid, 1% hydrofluoric acid solution. The other rings were not etched.

The adhesive was spread smooth in the groove of the ring, and one hemisphere was inverted and placed into the groove (Figure 4). The hemisphere was rotated to ensure bonding between it and the ring. After the adhesive had cured 1 day, the second hemisphere was bonded to the ring/hemisphere assembly (Figure 5).

Subsequently, a steel feedthrough was epoxy-bonded at the apex of the top hemisphere for attaching the sphere to the pressure vessel end closure and for passing the instrumentation wires from the interior of the sphere. Another feedthrough, in the bottom hemisphere, allowed strain gage lead wires attached to gages on the sphere exterior to be led into the interior. The bottom penetration was also bonded to the concrete with epoxy and was carefully potted with epoxy to ensure that no water leaked into the specimen along the wire insulation.

The completed sphere was painted with a thin coat of clear epoxy to prevent water permeation into the concrete.

INSTRUMENTATION

All specimens, except spheres 4, 10, and 11, were instrumented with electrical resistance strain gages applied to one of the concrete hemispheres and the joint ring. Three 3-gage, 45-degree rosettes and two 2-gage, 90-degree rosettes were used on both the interior and exterior surfaces of the hemisphere (Figures 6 and 7). The rosettes were fabricated from single BLH A-5-S6 resistance gages. The median of the joint ring was designated as the "equator." Five latitudes were chosen for strain gage locations: 7.5, 22.5, 37.5, 55.0, and 72.5 degrees from the equator.

Longitudinal (meridional) and latitudinal (hoop) gages were positioned at each latitude. At three levels of latitude, 7.5, 37.5, and 72.5 degrees, the angle between the meridian and latitude was bisected, forming a 45-degree line. A gage was positioned on each of these 45-degree lines. The interior and exterior gages were placed radially opposite each other.



Figure 4. Typical hemisphere assembly with simulated lock joint ring.

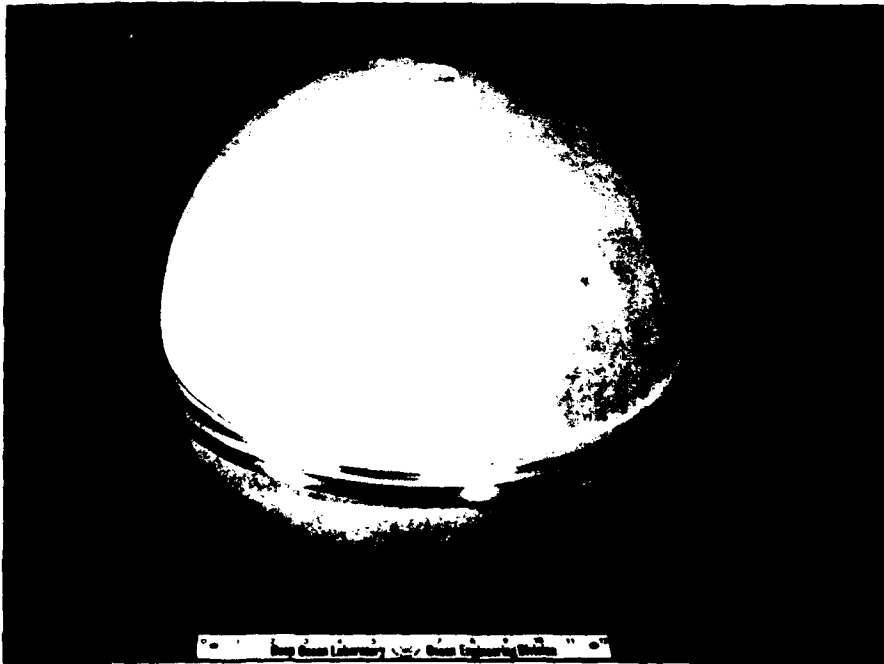


Figure 5. Typical assembled sphere with simulated lock joint ring prior to insertion of penetrators.

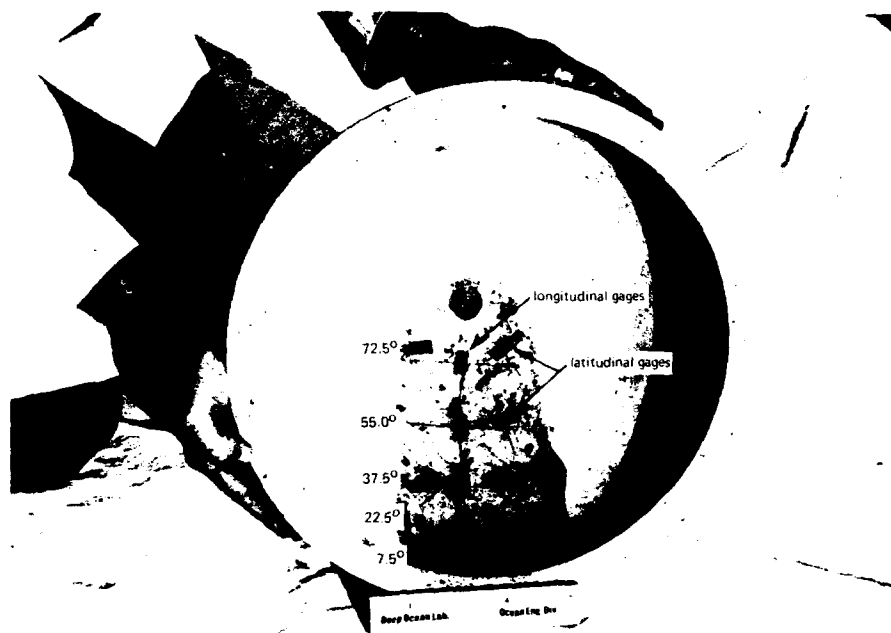


Figure 6. Location of strain gages on sphere's interior.

An interior and an exterior gage were placed on the ring at and parallel to the equator. Dentronic 204N-C6 electrical resistance strain gages were used on the rings.

After lead wires were soldered to each gage, the gages were covered with a microcrystalline wax waterproofing compound. The lead wires from the interior gages were led from the interior through the upper feedthrough. The exterior lead wires were run down along the sphere surface, through the bottom feedthrough, then up and out of the sphere through the upper feedthrough (Figure 8).

TEST PROCEDURE

The concrete spheres were tested under hydrostatic pressure in an 18-inch-ID pressure vessel. The upper feedthrough was securely fastened to the pressure vessel end closure (Figure 8), and the end closure was seated and locked in place. The lead wires were connected to the strain balancing and

recording unit (Budd System Datran Digital Strain Indicator and Printer Control Unit). A Bourdon-type pressure indicator, accurate to 5 psi, was connected to the vessel, and the vessel was filled with water.

The specimen was pressurized at a loading rate of 100 psi/min until implosion occurred. Strain readings were taken every 100 psi. After implosion, the concrete fragments and the ring were removed from the pressure vessel and inspected to determine where the fracture initiated and the quality of the bond between the concrete hemispheres and the ring.

Concurrently with the sphere test, the associated concrete cylinders were tested to destruction under uniaxial compression.

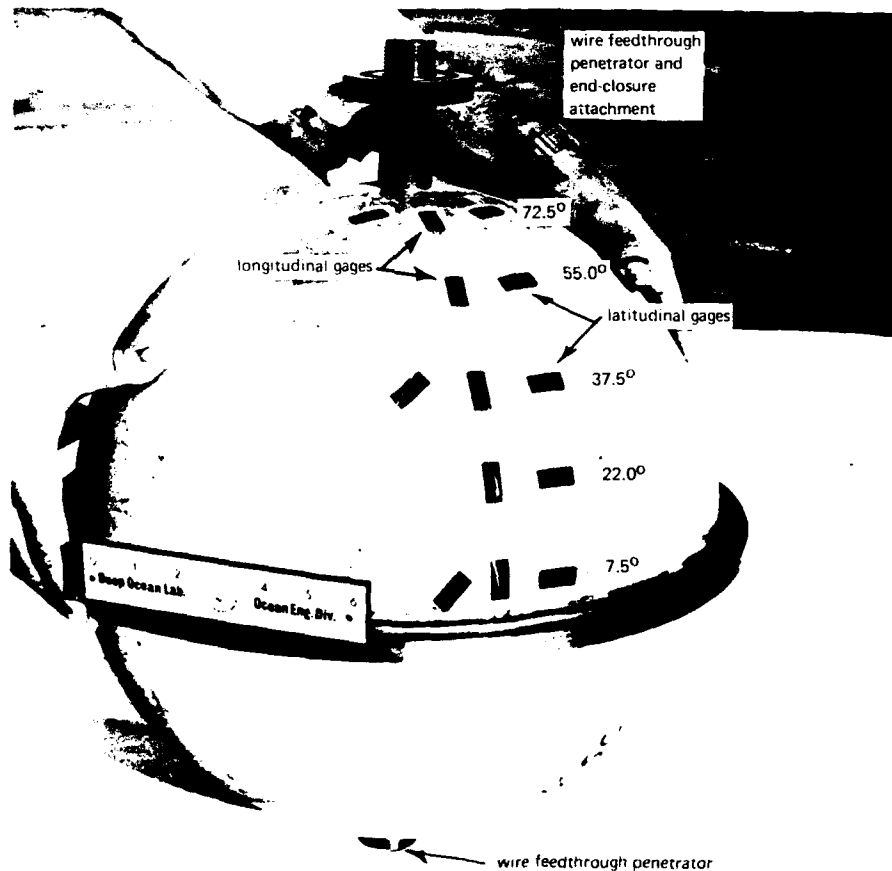


Figure 7. Location of strain gages on sphere's exterior.

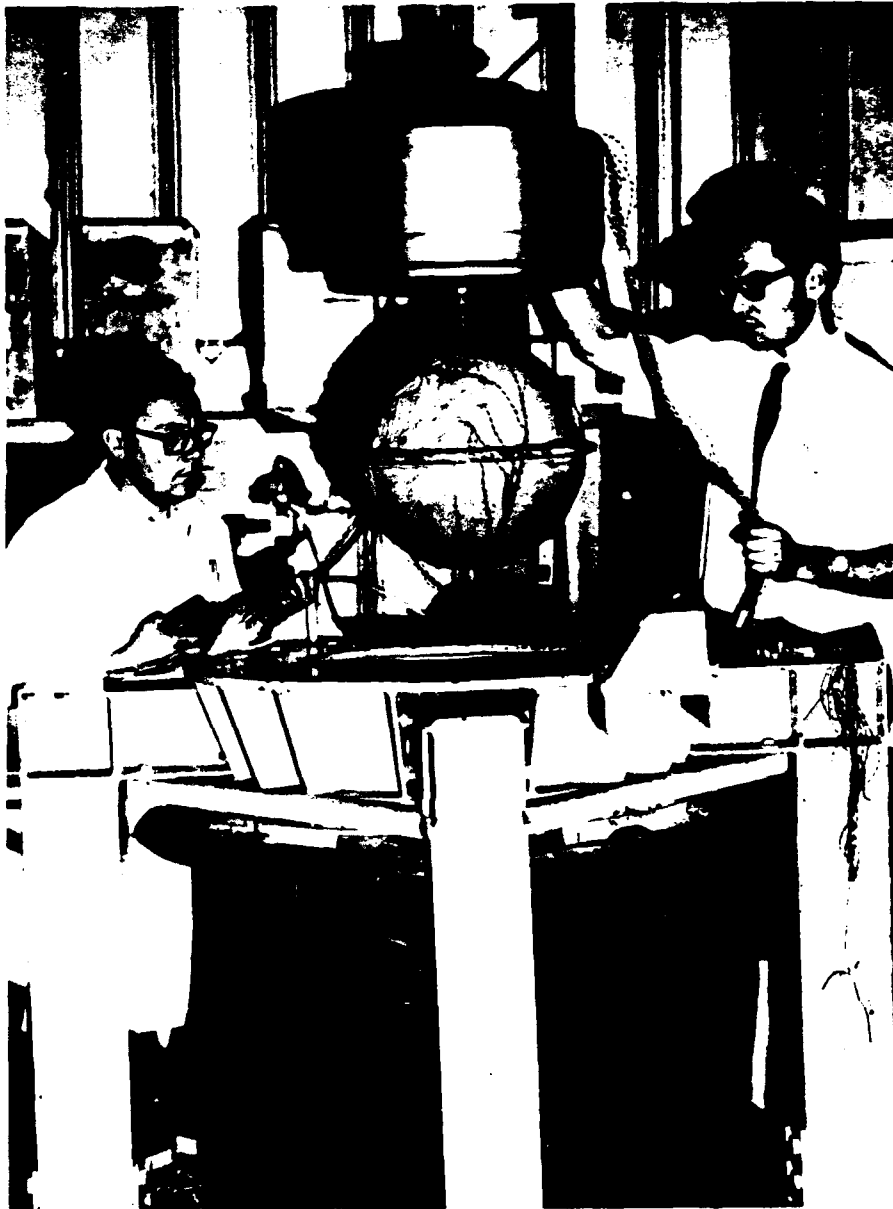


Figure 8. Sphere assembly attached to pressure vessel end closure being lowered into 18-inch-diameter vessel.

TEST OBSERVATIONS

Implosion Failure

All specimens failed by a violent, sudden implosion, which shattered the concrete into many fragments. Table 3 lists the implosion pressure, P_{im} , and the ratio of implosion pressure to concrete strength, P_{im}/f'_c , for each specimen. Also listed are the ring material strengths and the relative stiffnesses of the ring and sphere. For all specimens, the concrete strength listed in Table 3 is the lower strength of the two hemispheres. The ratio P_{im}/f'_c is used to account for any variation in concrete strength between specimens. As noted before, a previous study⁴ has shown a linear relation between implosion pressure and concrete strength; therefore, specimens of different strengths can be compared by using the parameter P_{im}/f'_c .

Inspection of the broken fragments of the concrete sphere and the joint ring showed the following:

1. The polycarbonate plastic ring of sphere 1 was the only ring fractured during the test (Figure 9).
2. For all spheres except spheres 3 and 5, the remnants of concrete were securely bonded to the ring as shown in Figures 10 and 11. On the aluminum ring of sphere 3 and the titanium ring of sphere 5, the concrete was completely stripped from the ring; yet the epoxy remained bonded to the fragments of the concrete. On spheres 4, 10, and 11, also made of titanium and aluminum, the bond was satisfactory.
3. On all spheres except spheres 3 and 5, a distinct cone-type concrete compression failure could be observed near the joint. Although some portions of the sphere remained attached to a section of each ring, the shear plane indicated that the concrete failure was initiated near the equatorial joint. The cone-type failure was a reasonable indication that the concrete failed because the compressive stresses exceeded the compressive strength of the concrete.

Strain Results

The general behavior of the concrete spheres under hydrostatic loading was observed by recording surface strains at various pressure levels and reducing them to principal strains along longitudinal and latitudinal directions.

All specimens imploded with a maximum recorded concrete strain greater than $3,500 \mu\text{in./in.}$ Except for spheres 1 and 2, the maximum strain was in the longitudinal direction at latitude 7.5 degrees; yet those maximum strains had a wide variation between $3,700 \mu\text{in./in.}$ and $9,000+ \mu\text{in./in.}$

Table 3. Test Results

Sphere No.	Concrete Strength, f'_c (psi) ^a	Joint Ring Material	Ring Yield Strength (psi)	Joint Type	Joint Ring Relative Stiffness ^b	Implosion Pressure, P_{im} (psi)	P_{im}/f'_c
1	10,100	polycarbonate	8,320	A	0.18	2,220	0.220
2	10,960	GRP	15,900	A	1.19	3,120	0.285
3	11,080	aluminum	75,600	A	6.40	2,450	0.221
4	10,620	aluminum	75,600	A	6.40	2,790	0.263
5	10,210	titanium	140,800	A	9.62	2,200	0.216
6	10,800	steel	41,200	A	18.26	2,730	0.253
7	11,030	steel	49,700	A	18.26	2,710	0.245
8	10,400	steel	54,200	B	22.35	2,470	0.237
9	11,110	steel	32,700	C	23.81	2,800	0.252
10	9,820	titanium	140,800	A	9.62	2,110	0.215
11	9,810	aluminum	75,600	D	9.89	2,840	0.290

^a Compressive strength of the weaker hemisphere.^b See "Discussion of Results."

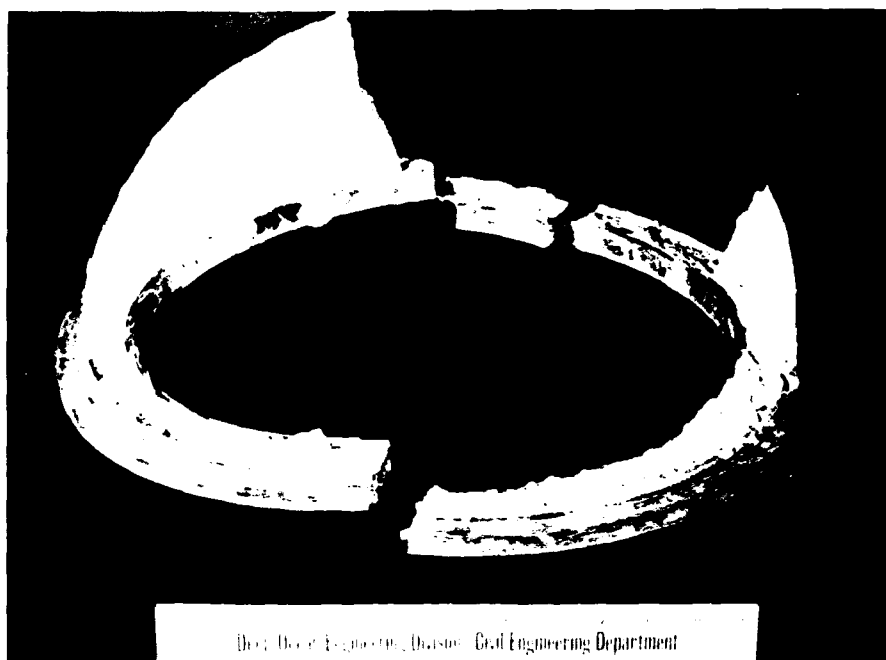


Figure 9. Fractured polycarbonate plastic joint ring after implosion testing of sphere assembly.



Figure 10. Steel ring with remnants of concrete securely attached. (View of sphere's interior.)



Figure 11. Steel ring with remnants of concrete securely attached. (View of sphere's exterior.)

Figures 12, 13, and 14 present the results of the longitudinal and latitudinal strain for the interior and exterior of spheres 1, 2, and 6, respectively. These results are typical of the strain patterns produced by an equatorial joint ring less stiff, slightly stiffer, and much stiffer than the concrete replaced by the ring. Appendix C presents the strain results for all spheres except spheres 4, 10, and 11, which were not instrumented. The abscissa of these graphs is the latitude in degrees (spherical angle) at which the strain was measured. The median of the joint ring was the equator (zero degrees). The ordinate is the strain in $\mu\text{in./in.}$ The strain values have been plotted for several pressure loading levels expressed as a nondimensional ratio of applied pressure to concrete strength, P/f'_c .

As a reference, the average strain magnitude for a sphere without a joint has also been plotted. These strain values were obtained in previous studies.¹⁻³

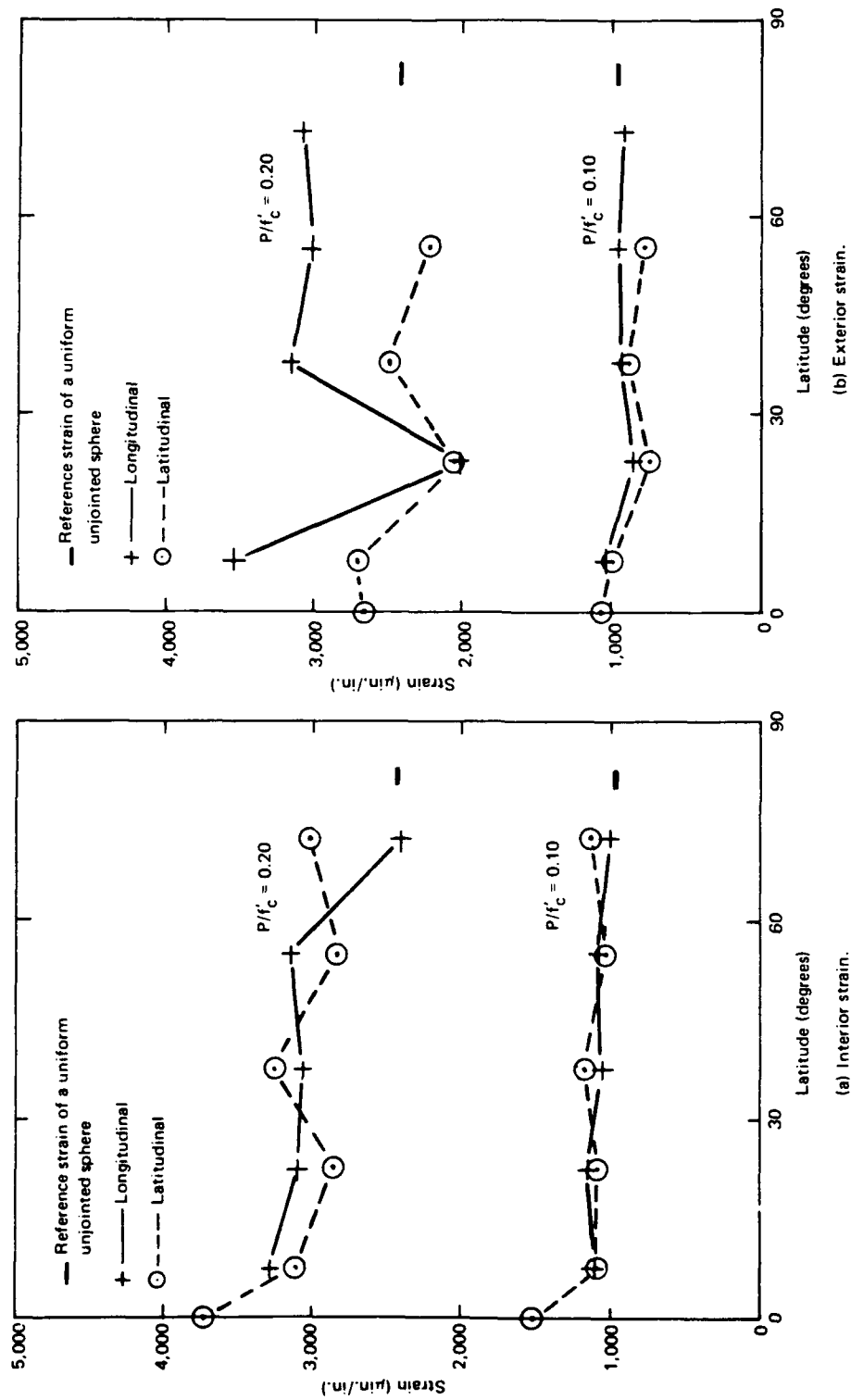


Figure 12. Interior and exterior strains for sphere 1 with joint ring stiffness less than concrete sphere stiffness.

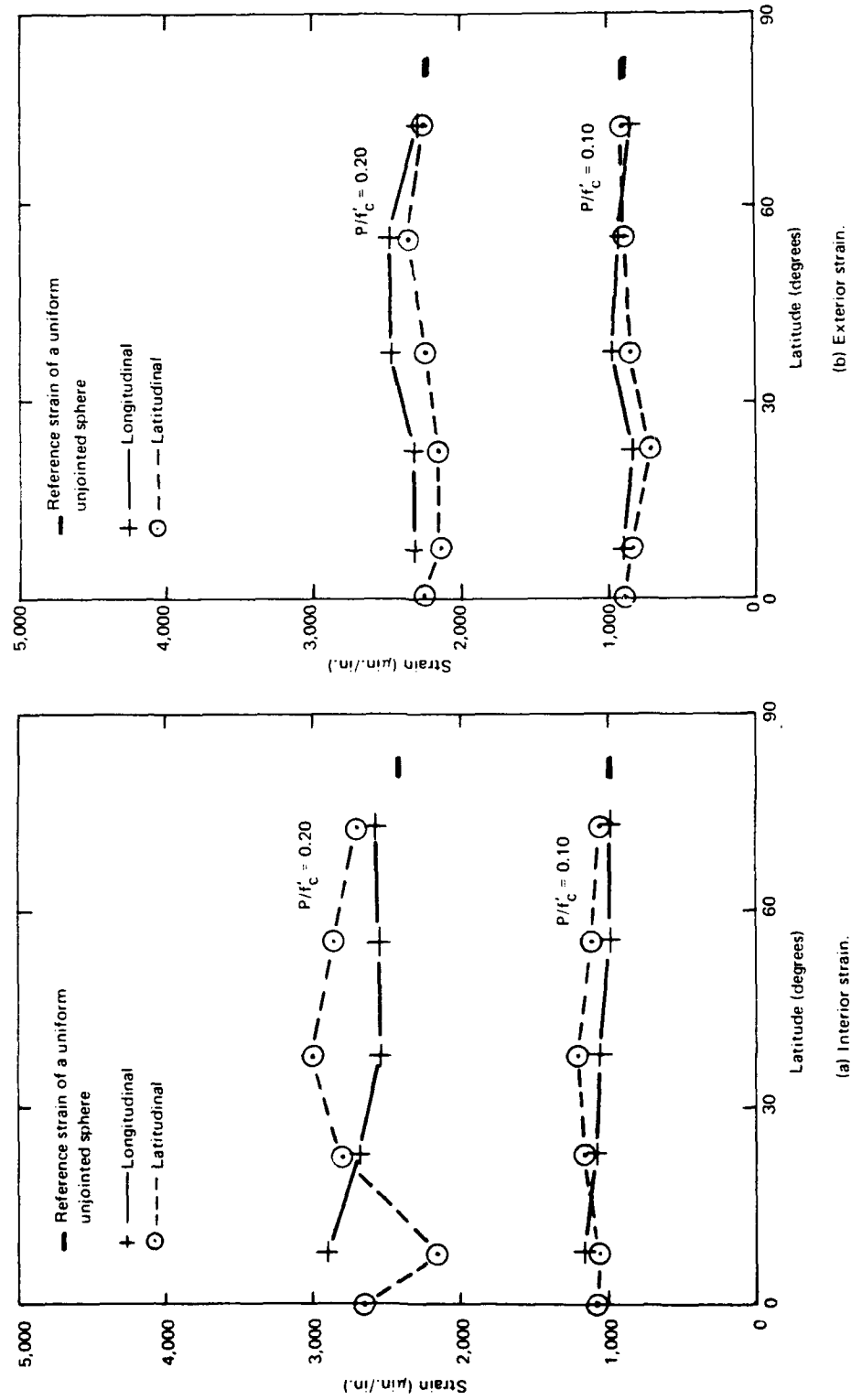


Figure 13. Interior and exterior strains for sphere 2 with joint ring stiffness slightly greater than concrete sphere stiffness.

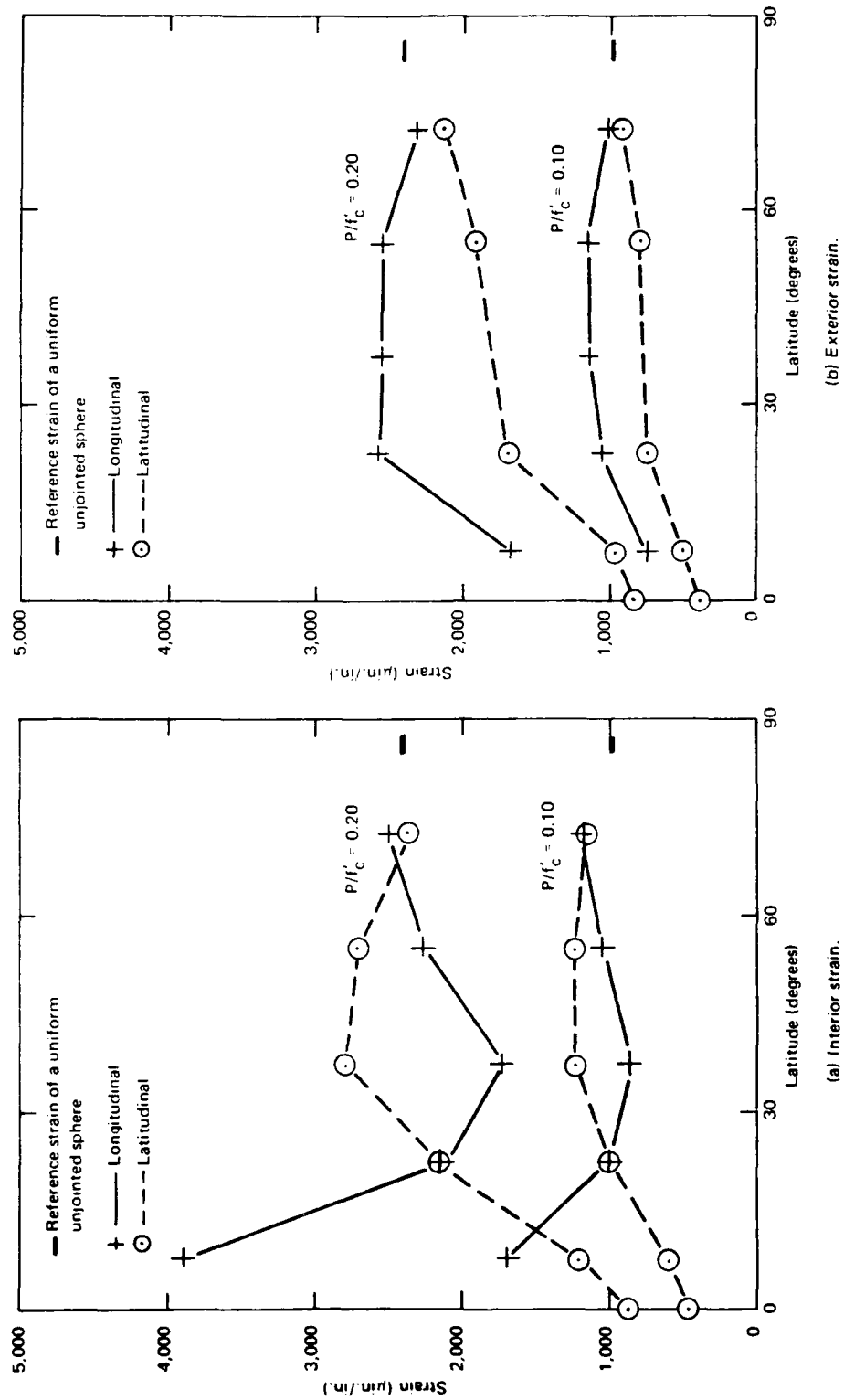


Figure 14. Interior and exterior strains for sphere 6 with joint ring stiffness much greater than concrete sphere stiffness.

DISCUSSION OF RESULTS

Implosion Behavior

An effective means of relating the behavior of the different joint rings in the concrete spheres was to calculate a *relative* stiffness for the rings. This relative stiffness is expressed as

$$R = \frac{E_r A_r}{E_c A_c}$$

where R = relative stiffness

E_r = modulus of elasticity of ring material

A_r = cross-sectional area of joint ring

E_c = secant modulus of elasticity of concrete

A_c = area of concrete removed and replaced by joint ring

Figure 15 is a graphical presentation of the P_{im}/f'_c relationship versus the relative stiffness of the 11 rings plus two operational specimens discussed in Appendix A. Where the relative stiffness equals unity, the plotted values of P_{im}/f'_c are for spheres which were tested in previous studies¹⁻³ and which did not include a joint ring at the equator.

Figure 15 illustrates the following:

1. A ring with a stiffness one-fifth that of the concrete caused implosion failure at a pressure 27% less than a sphere with no ring.
2. A ring with a stiffness greater than 15 times that of the concrete caused implosion about 18% lower.
3. A ring stiffness 1.2 times that of the concrete caused only a 5% reduction in implosion pressure. The latter difference is within the experimental variation for spheres without mechanical joints.

At a relative stiffness greater than 15, the P_{im}/f'_c ratio varied little. The variation of P_{im}/f'_c among specimens 6, 7, 8, and 9 (all with a steel joint) indicates that changes in the ring stiffness do not further influence the failure pressure of the concrete sphere. In effect a ring with a relative stiffness greater than 15 may be regarded as an "infinitely" stiff or "perfectly" rigid joint, because any increase in joint stiffness does not affect the structural behavior of the sphere.

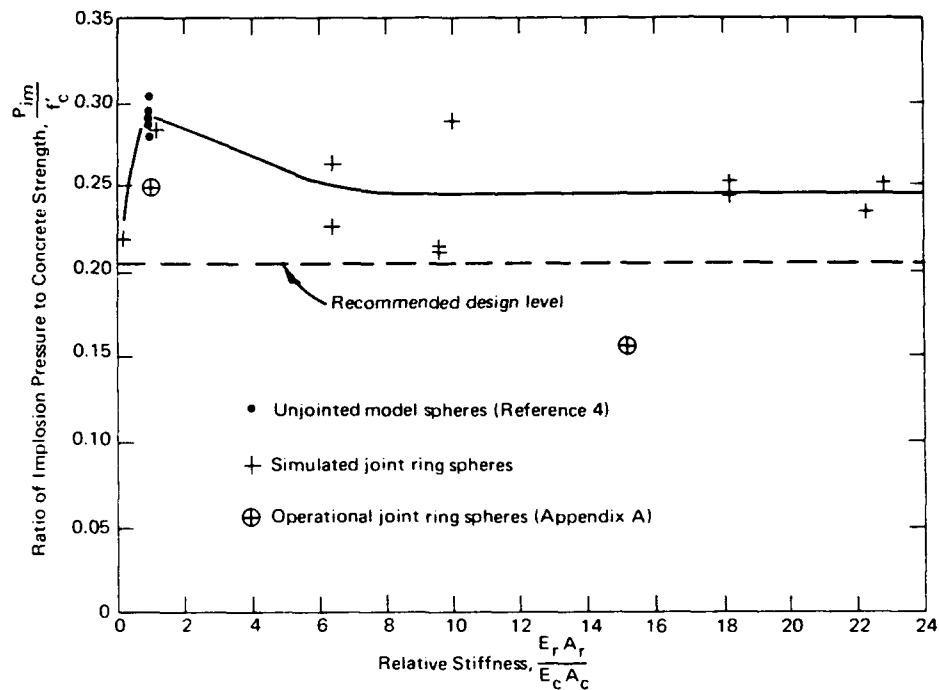


Figure 15. Effect of ring's relative stiffness on short-term strength of sphere under external hydrostatic loading.

At a relative stiffness less than unity, the P_{im}/f'_c appears to decrease rapidly. This agrees with results of Reference 2, where hull penetrations with a stiffness less than that of concrete caused a significant decrease in implosion pressure, while the stiffer penetrations did not.

This study has not clearly defined the relation between P_{im}/f'_c and relative stiffness in the 1 through 15 range. Structurally there is no apparent reason why a sphere with a ring of intermediate stiffness should fail at a pressure lower than spheres with an infinitely stiff ring. Therefore, the curve of Figure 15 has not been drawn through the points for specimens 3, 5, and 10.

Failure of both specimens with a titanium ring (specimens 5 and 10) at nearly the same P_{im}/f'_c ratio shows that both were fabricated in the same manner, but it does not necessarily mean that any sphere with that relative stiffness would fail at the lower pressure. Specimen 11, with an aluminum joint only slightly stiffer than the titanium ring, failed at nearly the same pressure as a sphere without a joint ring.

The lower implosion pressures of specimens 5 and 10 were probably due to poor fabrication of the jointed specimens. After sphere 5 failed and the poor bond between the ring and concrete was observed, it was believed that the poor bond caused the lower implosion pressure. Sphere 10 was then fabricated with measures taken to ensure that the titanium ring was carefully acid-etched to improve the bond. The test on sphere 10 showed that the bond

was adequate, yet the specimen failed at the same low pressure as sphere 5. It was then hypothesized that the ring was inducing an added stress raiser not present with the other rings. Because of the very close tolerance between the ring and the hemispheres, one section of a hemisphere of specimens 5 and 10 may have rested on the inner lip of the ring rather than on the bottom of the groove. This fabrication error was encountered in a later specimen, but the situation was corrected before the epoxy set up. Such incorrect seating would not have been detected by the limited strain gage layout. It appears from the test results that poor seating of the hemisphere did not occur in any other spheres whose ring had the same groove dimension as the titanium ring.

To check the hypothesis, the aluminum ring for specimen 11 was designed with a larger groove (the inner radius of the groove was reduced) and with a stiffness approximately that of the titanium ring. The larger groove ensured that the hemispheres of specimen 11 would seat properly. The epoxy, which filled the space between the hemispheres and the inner lip of the ring did restrain the radial movement of the hemisphere at the joint, but the restraint was not as much as if the hemisphere had been resting directly against the inner lip.

Pressure testing of sphere 11 showed that it imploded at a pressure significantly greater than that of spheres 5 and 10. Therefore, it was concluded that the lower implosion pressures of spheres 5 and 10 were due to poor fabrication of the specimens and were not the general structural response of spheres with a ring of a particular relative stiffness.

It is believed that drying shrinkage of the concrete hemispheres caused the dimensional change which resulted in the poor seating in spheres 5 and 10. Such shrinkage would also have been present in all other hemispheres. The magnitude of change was sufficiently large in spheres 5 and 10 to cause a difference in results.

The spread of P_{im}/f'_c values in Figure 15 was principally a result of variation of the ring stiffness; yet the quality of fabrication of the specimen (that is, how the hemispheres fit into the joint grooves) was an important factor in the implosion results.

The quality of attachment of the ring was difficult to control in the experimental study. Attaching operational mechanical joints to hemispheres would also be difficult in practice. Therefore, the lower implosion pressures should be used when considering the operational characteristics of a sphere with a metal joint ring. This would ensure a conservative, safe design.

Strain Behavior

Longitudinal Strain. For all spheres the equatorial joint ring induced a longitudinal strain on the interior surface adjacent to the joint greater than the strain on a uniform unjointed sphere at the same P/f'_c level.

The longitudinal strain behavior for the different spheres is characterized as follows:

1. Where the ring stiffness was less than the concrete stiffness, interior and exterior strains were nearly uniform but were greater than the strain of a uniform sphere.
2. Where the ring stiffness was slightly greater than the concrete stiffness, the interior and exterior strains were nearly uniform and were only slightly greater than the strain of a uniform sphere.
3. Where the ring stiffness was significantly greater than the concrete stiffness, the interior and exterior strains were very nonuniform. The difference in strain gradient between latitudes on the interior and exterior indicated high shearing strain, and the strain differences indicated increased curvature near the joint and the apex and decreased curvature in the midlatitudes. The maximum strain adjacent to the joint was much greater than the strain of a uniform sphere.

Latitudinal Strain. The latitudinal strain behavior of the spheres is characterized as follows:

1. Where the ring stiffness was less than the concrete stiffness, the interior and exterior strains were greater than those of a uniform sphere. The wide strain difference between surfaces shows that the ring significantly altered the normal behavior.
2. Where the ring stiffness was slightly greater than the concrete stiffness, the strains were nearly the same as those of a uniform sphere.
3. Where the ring stiffness was significantly greater than the concrete stiffness, the interior and exterior strains were the same or lower than the strain of a uniform sphere. The very low strain near the joint with increasing strain at greater latitudes indicates that the ring restrained the sphere deflection.

Bending Moment Response

The general behavior of the spheres can be more easily visualized in terms of the longitudinal bending moment induced in the jointed sphere. The interior and exterior longitudinal and latitudinal stresses were calculated at $P/f'_c = 0.20$. Graphs of stress versus latitude and the manner in which the stresses were computed are presented in Appendix D.

To calculate the longitudinal moment, it was first assumed that the stress distribution across the wall thickness was linear. In a simple analogy to concrete beam theory, this assumption would imply that the total compressive load, C , is carried in a trapezoidal stress block, higher stress at the

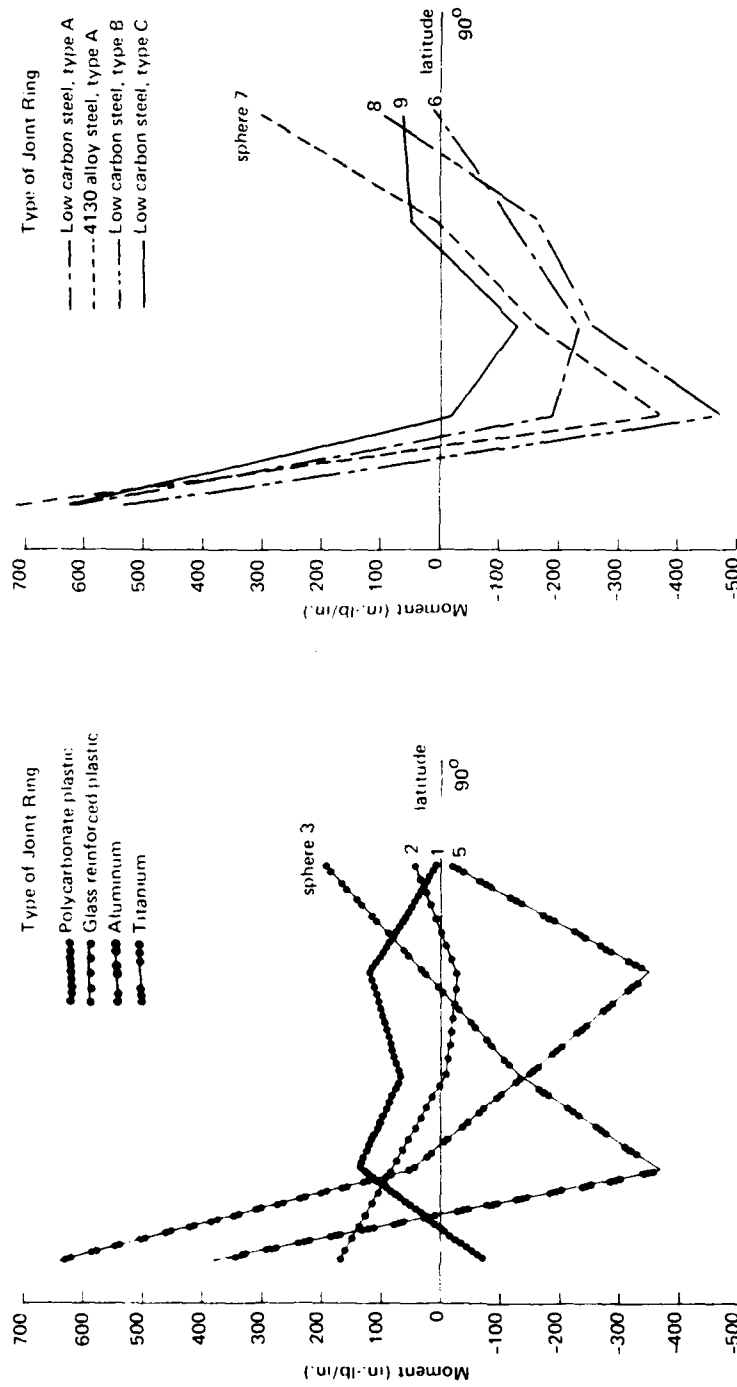
interior surface. In a sphere with no bending, the centroid of this stress block is located on the neutral plane; a force acting in this plane creates no bending. In this case, where there are bending stresses in the sphere, the loading is resolved into a concentrated load at the neutral plane and a couple. The following method was used for the moment calculation:

1. From jointless spheres tested in a previous study, the basic stress block was determined and the neutral plane was established at a distance of 0.493 inch from the interior surface of the sphere, or at a radius of 7.493 inches.
2. The previously calculated interior and exterior stresses were used to determine the stress block at each latitude for the eight specimens.
3. The basic stress block was then subtracted from the stress blocks of step 2 (above) at the many locations, resulting in a typical bending stress diagram for each latitude.
4. The areas of the bending stress diagrams were used to calculate the added load at the particular latitude, the eccentricity of that load, and the couple acting at that latitude.

These calculated moments are listed in Table 4 and are plotted against the degrees of latitude for each specimen in Figure 16. Positive moments are those which tend to increase the sphere curvature; negative moments are those which tend to decrease it.

It can be seen from Figure 16 that spheres with rings stiffer than concrete demonstrate a similar moment pattern: a high positive moment near the equator, a negative moment in the latitude range of 20 to 60 degrees, and a decrease to approximately zero or change to a somewhat positive moment near the apex. This moment pattern definitely indicates that the restraint imposed by the ring induces a significant bending behavior in the spheres. The magnitude of positive bending moment is particularly large in spheres with joint rings whose relative stiffness is more than twice that of the concrete replaced by the ring. This can be noted by comparing the magnitude of bending moment for sphere 2 with the GRP ring (1.19 times stiffer than concrete) and the bending moments of spheres with metallic rings (spheres 3, 5, 6, 7, 8, and 9).

The moment pattern of the sphere with the polycarbonate plastic ring (sphere 1) is the opposite of those of the other spheres: a negative moment near the joint, a positive moment in the latitude range of 10 to 60 degrees, and a negative moment near the apex. The reversal of moment pattern established for rings stiffer than concrete could be expected here because the polycarbonate plastic ring is less stiff than the concrete.



(a) Spheres 1, 2, 3, and 5.

(b) Spheres 6, 7, 8, and 9.

Figure 16. Longitudinal moment versus latitude.

Table 4. Calculated Longitudinal Moments

Latitude (deg)	Longitudinal Moment ^a (in.-lb/in.) for—							
	Sphere 1	Sphere 2	Sphere 3	Sphere 5	Sphere 6	Sphere 7	Sphere 8	Sphere 9
7.5	-67	+172	+637	+384	+617	+715	+537	+624
22.5	+139	+81	+50	-364	-189	-371	-468	-22
37.5	+68	-5	-129	-132	-232	-164	-257	-130
55.0	+120	-18	—	-350	-118	+10	-162	+51
72.5	+8	+47	+196	-16	+4	+307	+97	+63

^a Positive moment decreases radius of curvature; negative moment increases radius of curvature.

These moment patterns indicate the presence of shear loading on the hull. Where there is a rapid change in moment, there is a high shear condition. Thus, one may conclude that the rings produce a high shear near the equator and that the magnitude of shear stress is directly related to the mismatch between the stiffness of the ring and that of the concrete shell.

As noted before, all shell failures were initiated at or near the joint. On the spheres with the stiffer rings, the high positive moment near the joint plus the average compressive stress in the wall produced a high longitudinal *interior* strain which resulted in concrete failure. On sphere 1 with the ring less stiff than the concrete, the negative moment near the joint plus the average compressive stress in the wall produced a high longitudinal *exterior* strain which resulted in concrete failure.

FINDINGS

1. The implosion strength of hollow concrete spheres with equatorial joint rings varies with the magnitude of the relative stiffness of ring. Spheres with rings that are either stiffer or more compliant than concrete fail at pressures as much as 27% lower than do spheres without equatorial joint rings.
2. An equatorial joint ring in hollow concrete spheres introduces a strain raiser if the relative stiffness of the ring is significantly higher or lower than the stiffness of the concrete that the ring replaces. For joint rings stiffer

than concrete, maximum strains are typically found on the interior surface adjacent to the joint ring, while the minimum strains are typically found on the exterior surface also adjacent to the ring.

3. An equatorial ring with its stiffness different from the concrete stiffness produces bending moments in the concrete shell whose magnitudes are directly related to the mismatch in stiffness between the ring and the concrete shell.

CONCLUSION

Equatorial joint rings can be incorporated into hollow concrete spheres without significant reduction in strength, providing that the stiffness mismatch between the ring and the concrete it replaces is small. Glass fiber reinforced plastics appear to satisfy this requirement satisfactorily.

RECOMMENDATIONS

As a preliminary design guideline for mechanical joints in spheres, the authors recommend the following:

1. If possible, the designer should use a glass reinforced plastic material to make the mechanical joint ring and should dimension the joint to have a relative stiffness near one. The operational pressure should be 15% lower than that of uniform unjointed spheres.
2. If the mechanical joint is over 5 times stiffer than the concrete sphere, the operating pressure of the spherical capsule should be 30% lower than a uniform unjointed sphere.
3. A mechanical joint with a relative stiffness less than one should not be used.
4. Penetrations for windows and electrical entries should be located between 30 degrees and 60 degrees latitude or at an apex to avoid the high shear strain conditions in jointed spheres at latitudes near the equator and the apex.

Appendix A

OPERATIONAL LOCK JOINTS

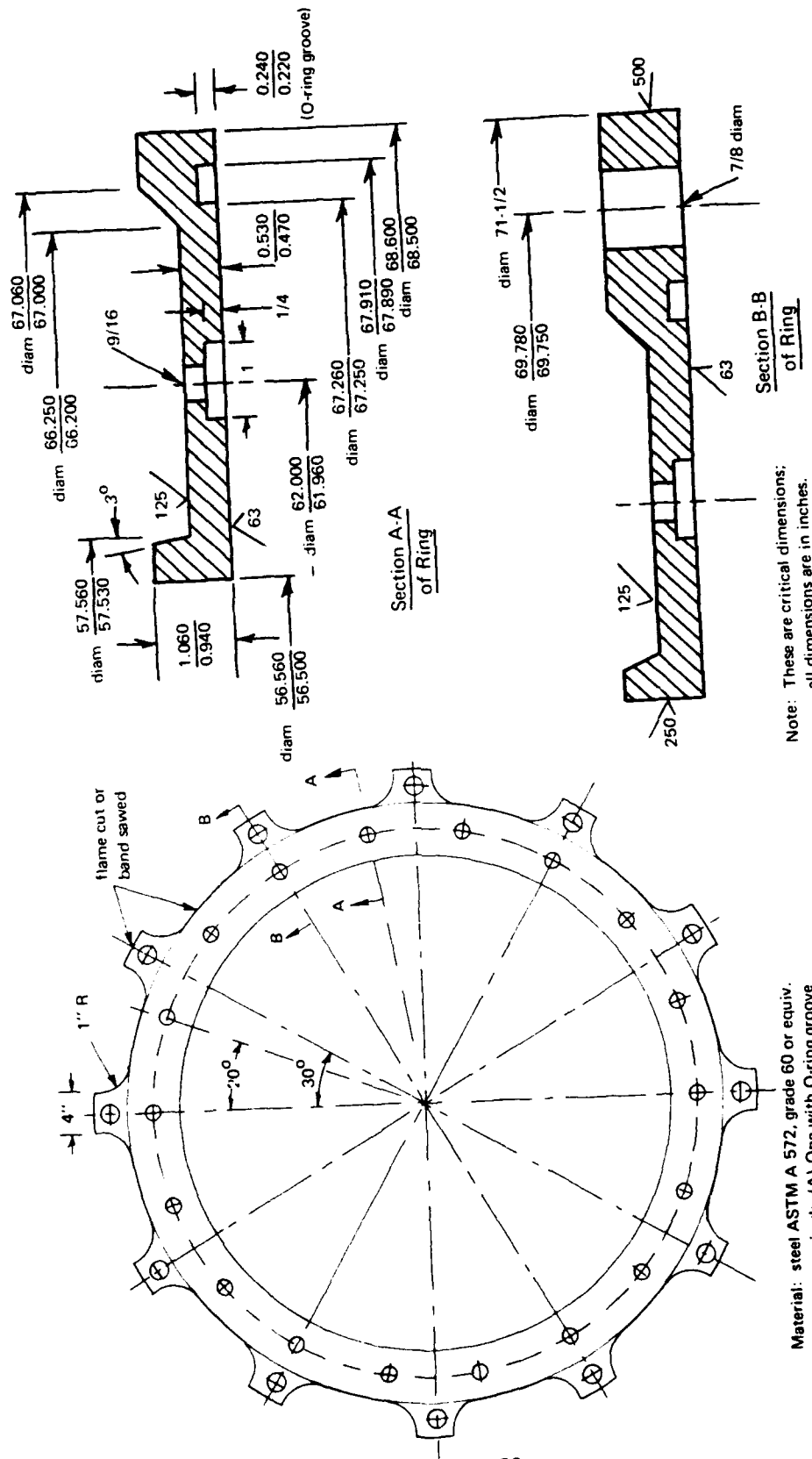
BACKGROUND

In the main study, the relationship between equatorial joint ring stiffness and concrete sphere behavior was investigated, but little consideration was given to the problems associated with operational lock joints. Thus, for example, no investigations were conducted into the problems of (1) securely attaching lock joint rings to hemispheres, (2) sealing the mating surface of lock joint rings, and (3) locking the joint rings together. No need existed to make provisions other than adhesive bonding for securely attaching the joint ring to concrete because the test spheres were exposed only to external hydrostatic pressure loading. The sphere assembly would not be exposed to forces tending to separate the hemispheres from the equatorial joint ring such as those present during a launching operation. Sealing was no problem; once bonded together, the hemispheres did not have to be separated. Locking arrangements also were not necessary, as the simulated lock joint ring was monolithic.

TEST SPECIMENS

Two materials were chosen for investigation of operational lock joints, glass fiber reinforced plastic (GRP) and steel. The GRP operational lock joint was to be incorporated only into the 16-inch-OD x 14-inch-ID sphere, while steel joints were to be incorporated into both the 16-inch-OD x 14-inch-ID and 66-inch-OD x 57.75-inch-ID concrete spheres. One concrete sphere assembly specimen was to be built with each type of joint and subsequently evaluated under hydrostatic loading.

The design chosen for the equatorial lock joints was simple (Figure A-1). It consisted of two mating equatorial rings to be securely attached to concrete hemispheres. The two ring-equipped hemispheres were to be later locked together with bolts located around the circumference of the joint assembly. An O-ring between the mating equatorial rings completed the operational joint assembly. Special features of the ring design for the 16-inch spheres were the following: (1) anchor pins were used to reinforce the adhesive bond between the joint ring and the concrete, (2) the cross-sectional area for the operational joint was approximately one-half that used in the simulated lock joint (although the relative stiffness was only slightly reduced), (3) the same size of concrete seating groove was used in the joint as in the simulated joints.



(b) For 66-inch-diameter concrete spheres.

Figure A-1. Dimensions of equatorial lock joints (continued).

FABRICATION

Concrete

The 16-inch hemispheres were cast identically to those described in the main body of the report. The 66-inch hemispheres were cast in a steel mold (Figure A-2), using the same concrete mix as for the casting of 16-inch hemispheres.⁵ A field-type curing technique was used for 66-inch hemispheres, producing shells somewhat lower in strength than the 16-inch hemispheres. The grinding of the equatorial edge for the small and the large sphere was performed in the same manner as described in the main body of the report.

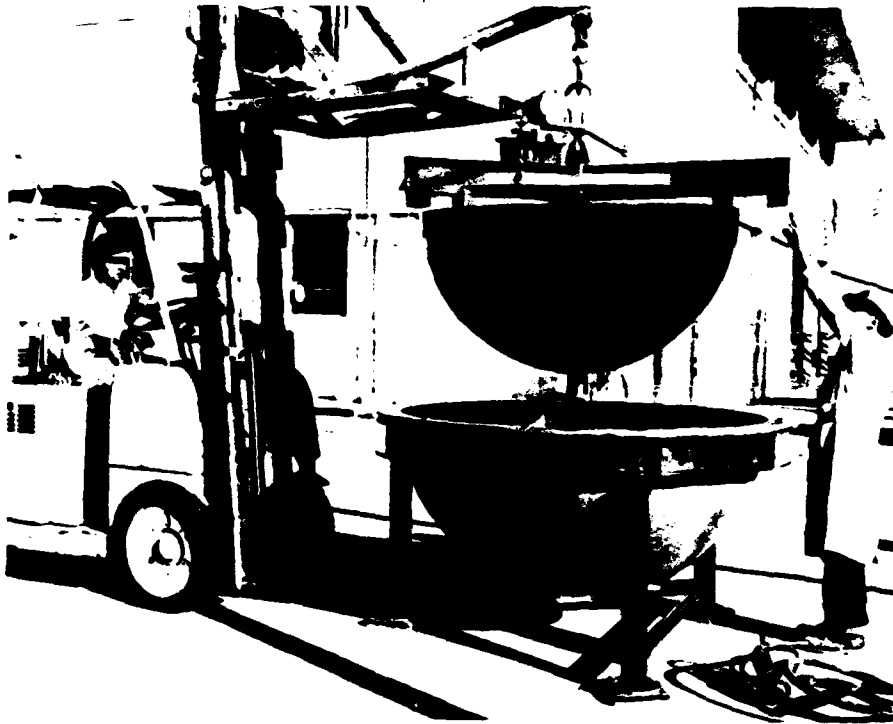


Figure A-2. Molds for casting 66-inch concrete hemispheres.

Joint Rings

The equatorial joint rings (Figure A-3) for both the small and large concrete hemispheres were machined from flat plate stock—the small ones in a horizontal lathe and the large one in a vertical mill. Difficulties arose in

maintaining flatness of the joint rings because the small rings were only 1/8 inch thick and the large rings were 1/2 inch thick. It was found, particularly for the steel joints, that upon removal from the machining fixture considerable twisting of the joint in the equatorial plane took place. The twisting created a very noticeable deviation from flatness. For the ring for the 66-inch-diameter capsule, this deviation was approximately 1/4 inch.

The problems encountered in fabricating a flat steel lock joint appeared to be a potential source of trouble for concrete sphere assemblies to be built for operational use. Therefore, the assembly technique for the test specimens was modified to permit fabrication of the 16-inch sphere with twisted joint rings. For the 66-inch sphere, special procedures were developed that resulted in a sphere assembly with parallel mating flat joint rings.

Assembly

The equatorial joint rings were attached to the concrete hemispheres by epoxy adhesive (Fisher Plastics Epocast 8288) and steel pins (Figures A-4 and A-5). The steel pins were set into mating holes drilled into the concrete. The steel joint ring bonded to the concrete shell served as the drilling template. For the 16-inch sphere assembly that was to operate with the twisted steel joint rings, each joint ring was placed separately on the adhesive-coated edges of the 16-inch concrete hemispheres. The thick layer of epoxy easily adjusted to the uneven surface of the joint, ensuring a watertight seal between the uneven ring and the flat equatorial plane of the shell. When the two hemispheres with twisted rings were mated, a gap of approximately 1/16 inch was found on the external edge of the lock joint assembly. The gap extended completely around the circumference of the joint. To seal the mating rings, RTV (Room Temperature Vulcanizing silicone rubber) was forced into the gap after the joint was bolted together.

To flatten out the steel rings for the 66-inch sphere, both rings were clamped together tightly with the joint retaining bolts. The clamping force exerted by the retaining bolts was sufficient to mate the two twisted rings of the lock joint assembly together so that a reliable watertight seal could be achieved by the O-ring. The clamped lock joint assembly was bonded to both hemispheres. When the adhesive had set, the lock joint assembly was unbolted and the individual joint rings inspected for flatness. It was found that this sphere assembly procedure resulted in a joint that deviated from true flatness less than 0.020 inch. The adhesive bond between the concrete and the rings prevented the steel rings from returning to the twisted shape.

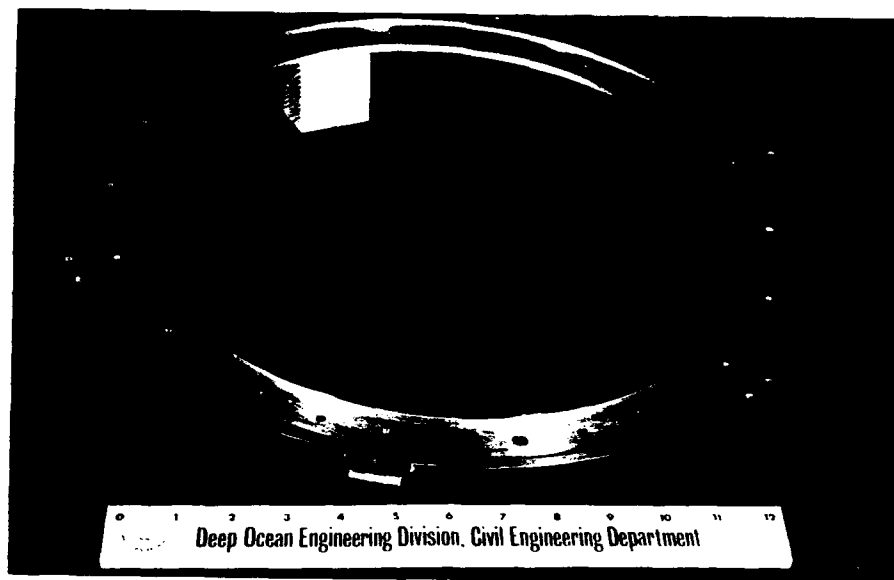


Figure A-3a. Lock joint ring for 16-inch sphere assembly. (View of surface in contact with concrete.)

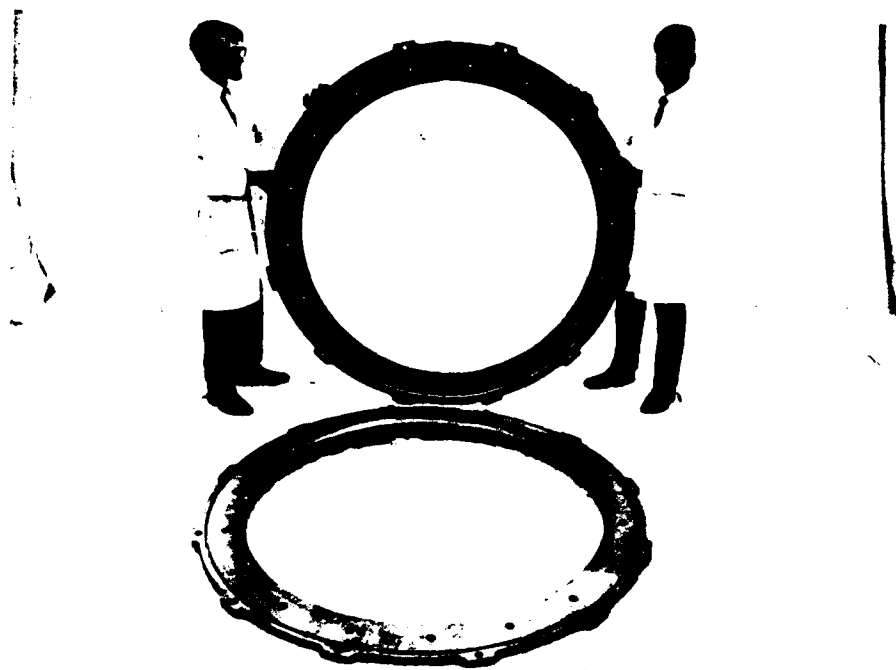
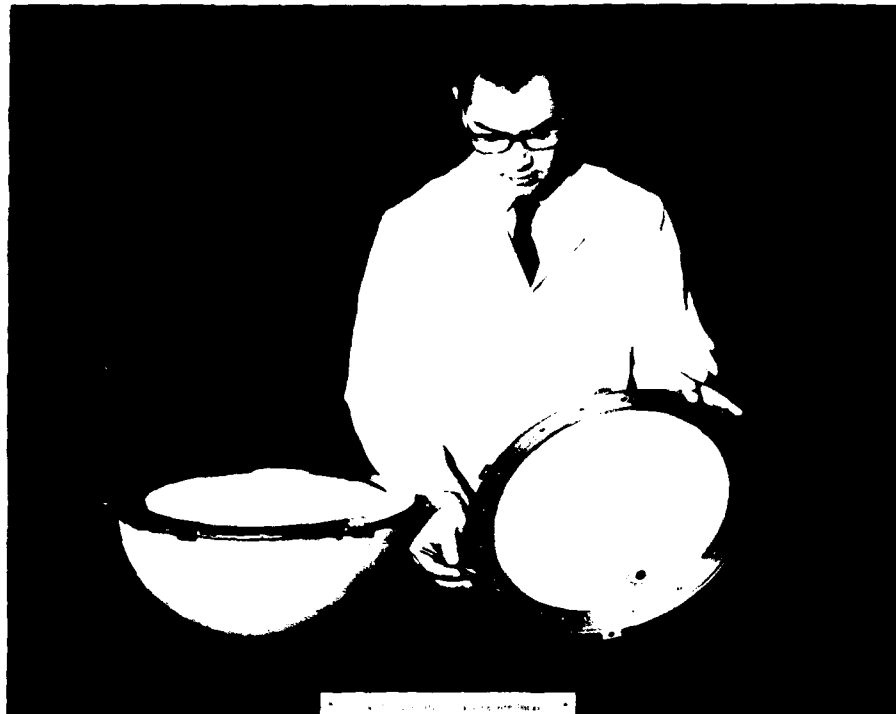
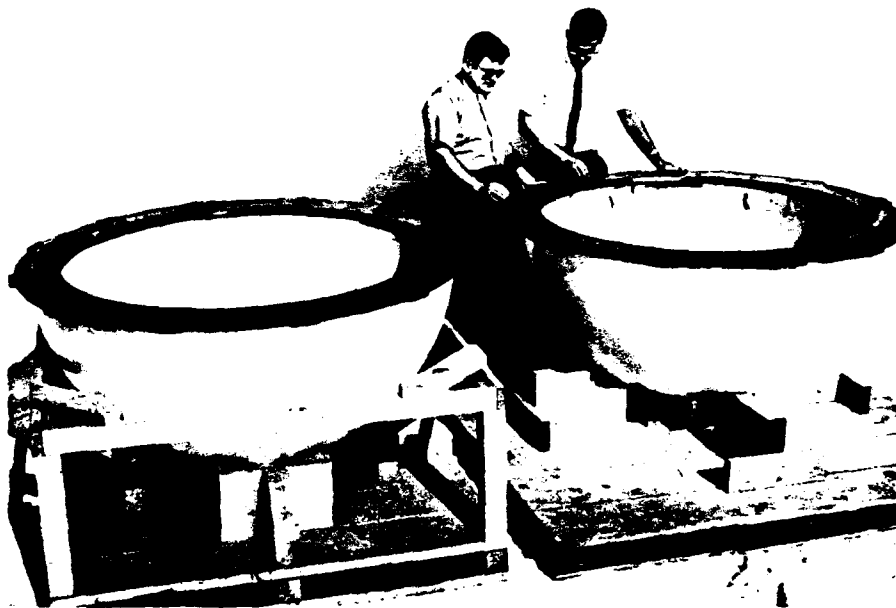


Figure A-3b. Lock joint rings for 66-inch sphere assembly. (View of interior and exterior surfaces of joint ring.)



(a) For 16-inch-diameter model.



(b) For 66-inch-diameter model.

Figure A-4. Lock joint rings bonded to hemispheres.

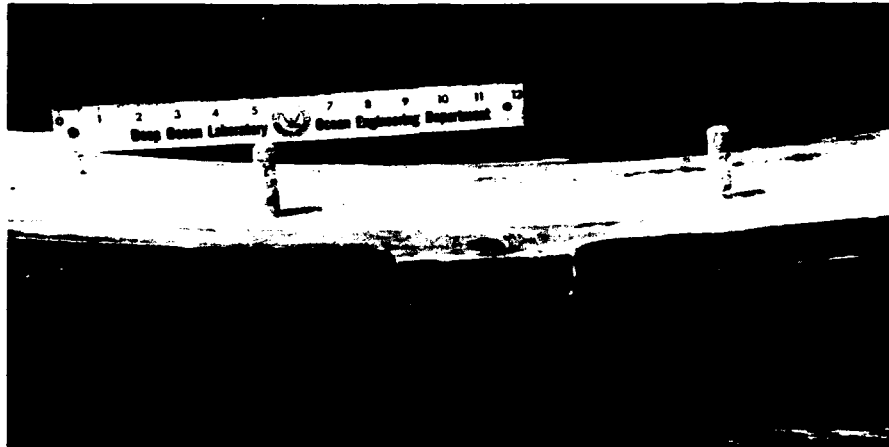


Figure A-5. Typical anchor pins for securing joint ring to 66-inch hemisphere.

Instrumentation

The 16-inch sphere assemblies with operational lock joints were instrumented for hydrostatic testing with electrical resistance strain gages at eight locations; four on the inside surface at 7.5- and 55-degree latitudes and four on the outside radially opposite the interior gages. The 66-inch sphere assembly was instrumented at the same latitudes but only on the sphere's interior surface.

TEST PROCEDURES

Both the small and large spheres with operational lock joints on the equator were rigidly attached to the vessel end closures by steel feedthroughs. The small spheres were tested in the same vessel as the spheres described in the main body of the report. The large sphere was tested in the 72-inch-diameter pressure vessel (Figure A-6).

The small sphere assemblies with operational lock joints were tested to destruction under short-term loading conditions. The hydrostatic pressure was raised at a rate of 100 psi/min to implosion. Strains were recorded at 100-psi pressure intervals.



Figure A-6. Test arrangement for 66-inch sphere assembly.

The 66-inch sphere assembly was subjected to a long-term loading test. It was pressurized at a 100-psi/min rate to 1,350 psi and was held at that pressure until implosion took place. The 1,350-psi pressure level chosen for sustained loading was equal to 83% of the expected short-term strength* for 66-inch spheres without joint rings. The reason for choosing the high sustained loading level was to measure the behavior of a sphere with joint rings under a sustained loading condition while ensuring a termination of the test (because of implosion) after only several hours. For actual operations in the ocean, where the sphere assembly would be equipped with a payload, the sustained loading level would be much lower—probably in the range of 20 to 30% of the short-term strength.

OBSERVATIONS AND DISCUSSION

Implosion Failure

Small sphere assemblies imploded violently. The sphere with the steel joint imploded at $P_{im}/f'_c = 0.157$ and the one with the GRP joint at $P_{im}/f'_c = 0.250$. The fracture pattern was similar to that of the spheres with simulated operational lock joints described in the main body of the report (Figure A-7). The implosion data are listed in Table A-1 and plotted in Figure 15.

The P_{im}/f'_c of 0.250 for the GRP operational joint was 13% lower than the P_{im}/f'_c of 0.286 for sphere 2 with the simulated GRP joint. The test indicated (1) that the short-term strengths of spheres with operational joint rings are somewhat lower than, though comparable with, strengths of spheres having joints of similar stiffness and (2) that an operational lock joint assembly made of two mating halves behaves in a manner like that of a simulated operational lock joint of similar stiffness but of monolithic construction.

The P_{im}/f'_c of 0.157 for the sphere with the steel operational lock joint was 36% lower than the average P_{im}/f'_c of 0.247 for spheres with a simulated lock joint of steel. The sphere's strength seems significantly affected by improper mating between lock joint rings; therefore, precautions must be taken to ensure that the mating halves of an operational lock joint mate evenly over the whole circumference of the joint.

The large sphere assembly failed under sustained 1,350-psi hydrostatic loading after 240 minutes. The failure was localized (Figure A-8). Such a local failure is generally triggered by some dimensional irregularity of the sphere, such

* The P_{im}/f'_c short-term strengths of three 66-inch spheres fabricated by the identical technique as the sphere equipped with the joint ring were 0.222, 0.216, and 0.195, with a calculated average of 0.211.⁵

as changes in radius of curvature or thinner cross section of the wall. In the sphere tested, the local implosion occurred in a location where the wall was approximately 3/16 inch thinner and the internal radius of curvature 1/16 inch longer than specified. The local wall thickness and sphericity deviation induce the material at that location to creep at a higher rate, causing the shell to form a local flat spot. Such a local flat spot induces great flexure stresses around the periphery of the flat spot as well as at its center. Ultimately the combined stress becomes so large that it exceeds the compressive strength of the material, causing the formation of a conical fracture plane. Close observation of the fracture pattern on the large sphere confirms this fracture mechanism, as the edges of the hole are beveled inward, forming the boundaries of a conical fracture plane typical of concrete compression failures.

The $P_{im}/f'_c = 0.175$ of the 66-inch sphere under sustained loading was found to be lower than the average $P_{im}/f'_c = 0.211$ established previously⁵ for identical large spheres without any joint rings. Using the 0.89 ratio between the P_{im}/f'_c of a 16-inch sphere with simulated steel lock joint (sphere 6) and the P_{im}/f'_c of a 16-inch sphere without joint rings as a guide, the ratio of short-term implosion pressure to concrete strength of the large spheres with a steel joint ring is extrapolated to be 0.187. When this extrapolated $P_{im}/f'_c = 0.187$ is compared with the experimentally obtained long-term strength of $P_{im}/f'_c = 0.175$, much better agreement is found. Because sustained hydrostatic loading invariably causes spheres of viscoelastic material to fail at lower pressures than those obtained under short-term loading conditions, it could be postulated that the short-term P_{im}/f'_c of the 66-inch sphere with the steel lock joint rings is at least equal to, and probably slightly higher than, the extrapolated $P_{im}/f'_c = 0.187$ value.

Table A-1. Results of Tests on Spheres With Operational Joints

Sphere	Outside Diameter (in.)	Joint Material	Relative Stiffness ^a of Joint Ring	P_{im} (psi)	f'_c (psi)	P_{im}/f'_c
12	16	GRP	0.99	2,650	10,600	0.250
13	16	steel	15.18	1,730	11,020	0.157
14	66	steel	15.09	1,350	7,720	0.187 ^b

$$^a \frac{E_r A_r}{E_c A_c}$$

^b See discussion in text.



(a) With operational steel lock joints.



(b) With operational GRP lock joints.

Figure A-7. Imploded 16-inch sphere assembly.



Figure A-8. Local implosion of 66-inch concrete sphere assembly.

It would thus appear that the operational lock joints of steel performed properly and did not lower the short-term strength of the concrete sphere below the strength level expected from spheres with simulated lock joints of equivalent stiffness. The acceptable performance of the large concrete sphere compared with the unacceptable performance of the small sphere with operational steel lock joints of identical stiffness reinforces the observation made previously that improper mating between individual rings significantly lowers the depth capability of a concrete sphere equipped with an equatorial lock joint.

Strain Behavior

Strain data are listed in Table A-2 for the three spheres with operational joints. In small sphere assemblies the magnitude and distribution of strains differed significantly between the steel and the GRP operational joints.

The sphere assembly with GRP operational joints registered strains which both in magnitude and distribution were similar* to those measured previously on sphere 2 with a monolithic GRP joint.

There was very little similarity between the strains measured on the 16-inch-OD sphere assembly with an operational steel joint and sphere 6 equipped with a monolithic steel joint. The pattern of longitudinal strains on the sphere with the operational steel joint was the opposite of that found on sphere 6. On sphere 6, the maximum longitudinal strain was measured on the interior of the sphere adjacent to the joint; whereas, on sphere 13 with the operational lock joint, it was found on the exterior adjacent to the joint. Such a dissimilarity in strain patterns between the small sphere with operational joints and sphere 6 was to be expected, because the uneven mating of the operational joint caused nonuniform stress concentrations.

That the dissimilarity in strains between operational and simulated steel lock joints is only a function of poor mating between the joint rings is further substantiated by the similarity of the strains measured on the 66-inch sphere with properly mating rings to the strains on sphere 6 with the simulated steel lock joint. The similarity between the small sphere assembly with the simulated steel lock joint and the large sphere with the operational steel lock joint also confirms the postulate that the strains measured on a small-scale assembly are applicable to design of large-scale concrete sphere assemblies, provided the relative stiffness ratio of the equatorial joint rings is about the same in both cases.

FINDINGS

1. Strains measured on concrete sphere assemblies with simulated equatorial lock joints can be used to predict strains in concrete sphere assemblies with operational lock joints if the relative stiffness ratio between the equatorial lock joint assembly and the concrete is similar.
2. Improper mating between the rings of the lock joint assembly is more detrimental to the implosion strength of the concrete sphere assembly than a change in the relative stiffness of the joint.
3. The operational equatorial lock joints fabricated from glass reinforced plastic provide the closest match to the properties of the concrete shells.

* When comparing the strains from assemblies with operational joints to those from assemblies with simulated joints, one must recall that in the former the gages were located at two different latitudes whereas in the latter they were located at five different latitudes.

Table A-2. Strain Data for Spheres With Operational Lock Joint Rings

Sphere	P/f'_c	Longitudinal Strain ($\mu\text{in./in.}$)				Latitudinal Strain ($\mu\text{in./in.}$)			
		Interior		Exterior		Interior		Exterior	
		7-1/2°	55°	7-1/2°	55°	7-1/2°	55°	7-1/2°	55°
12 (16" OD, GRP ring)	0.05	830	450	400	110	470	900	420	20
	0.10	1,770	1,000	920	110	960	1,750	730	300
	0.15	3,460	1,560	1,450	1,150	1,640	1,960	1,280	1,360
13 (16" OD, steel ring)	0.05	110	520	120	300	150	510	80	440
	0.10	450	1,110	1,070	650	450	1,080	1,000	920
	0.15	160	1,820	1,220	960	1,470	1,700	1,070	1,420
14 (66" OD, steel ring)	0.05	520	360	-	-	130	580	-	-
	0.10	1,320	830	-	-	530	1,140	-	-
	0.15	2,330	1,420	-	-	900	2,000	-	-

CONCLUSIONS

Concrete hollow spheres can be equipped at the equator with operational lock joints that will decrease the hydrostatic load carrying capability of a sphere without a joint ring by only 10 to 20%. Such operational joints should be made of glass fiber reinforced plastic. Joint rings made of steel will decrease the hydrostatic load carrying capability of a uniform unjointed sphere by up to 50% if the ring is not properly mated to the sphere.

Appendix B

MATERIAL PROPERTIES

The material properties of compressive strength, modulus of elasticity, and Poisson's ratio for the concrete and ring materials are presented in Table B-1.

Table B-1. Material Properties

Sphere	Hemisphere	Concrete Strength, f'_c (psi)	Joint Rings			
			Material	Yield Strength, f_y (psi)	Modulus of Elasticity, E (psi x 10 ⁶)	Poisson's Ratio
Simulated Lock Joints						
1	1-A	10,100	polycarbonate plastic	8,320	0.39	0.40
	1-B	12,110				
2	2-A	10,960	GRP	15,900	1.95	0.38
	2-B	11,760				
3	3-A	11,080	aluminum	75,600	11.0	0.32
	3-B	11,120				
4	4-A	10,900	aluminum	75,600	11.0	0.32
	4-B	10,620				
5	5-A	10,210	titanium	140,800	17.4	0.23
	5-B	10,500				
6	6-A	11,740	steel	41,200	30.0	0.27
	6-B	10,800				
7	7-A	11,040	steel	49,700	30.0	0.27
	7-B	11,030				
8	8-A	10,470	steel	54,200	30.0	0.27
	8-B	10,400				
9	9-A	11,160	steel	32,700	30.0	0.27
	9-B	11,110				
10	10-A	9,820	titanium	140,800	17.4	0.23
	10-B	9,870				
11	11-A	9,810	aluminum	75,600	10.5	0.32
	11-B	9,960				
Operational Lock Joints						
12	12-A	10,600	GRP	15,900	1.95	0.38
	12-B	—				
13 ^a	13-A	11,020	steel	49,700	30.0	0.27
	13-B	11,390				
14 ^b	14-A	7,740	steel	50,000	30.0	0.27
	14-B	7,780				

Note: Concrete modulus of elasticity averaged 3.57×10^6 psi, Poisson's ratio for concrete averaged 0.16.

^a 16-inch-OD sphere.

^b 66-inch-OD sphere.

The modulus of elasticity for concrete used to calculate the relative stiffness and the concrete stress was a secant modulus. The stress-strain relations obtained for each hemisphere by testing 3 x 6-inch control cylinders were averaged to give a mean stress-strain curve for the concrete. A secant line was drawn from the origin through a point on the curve at one-half the ultimate concrete strength ($1/2 f'_c$) as shown in Figure B-1. The slope of this straight line was the secant modulus and was equal to 3.57×10^6 psi. This secant modulus is less than the modulus calculated from the formula presented in the American Concrete Institute Building Code Requirements (ACI 318-63). The ACI formula, $E = W^{1.5} (33)\sqrt{f'_c}$, yields a modulus of 5.64×10^6 psi.

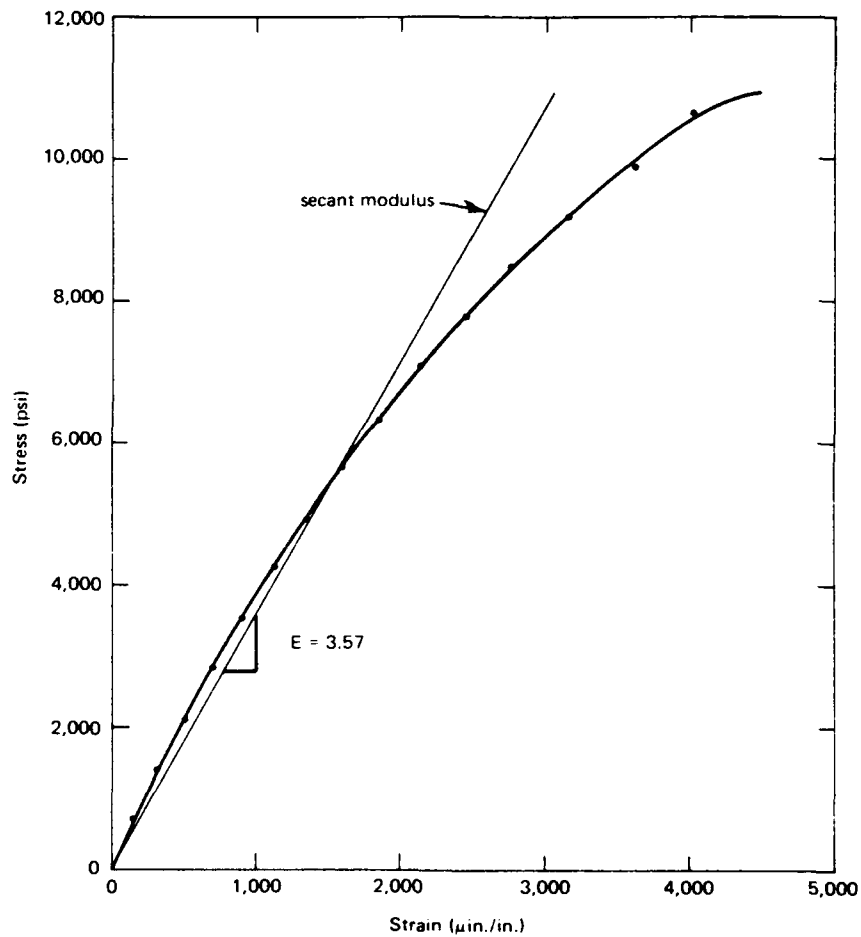


Figure B-1. Mean uniaxial concrete stress-strain behavior of 3 x 6-inch control cylinders.

The Poisson's ratio was determined using an average of the axial strain versus transverse strain relations obtained from the 3 x 6-inch control cylinders. A straight line was drawn through the mean axial strain versus transverse strain curve in such a manner as to average the variations. The slope of this line is the Poisson's ratio, as shown in Figure B-2.

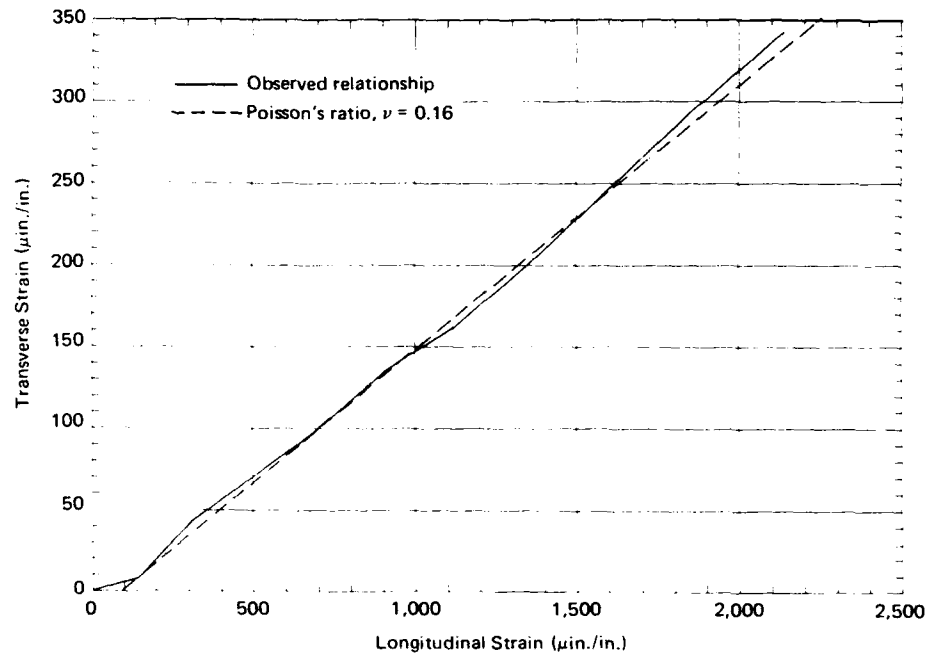


Figure B-2. Transverse strain versus longitudinal strain for control cylinders.

Appendix C

STRAIN DATA

Graphs of strain versus latitude for the eight instrumented specimens are presented in Figures C-1 through C-4.

LONGITUDINAL STRAINS

Figures C-1 and C-2 present the interior and exterior longitudinal strains measured at five latitudes and plotted at various P/f'_c loading ratios. The general observations of the *interior longitudinal strains* are as follows:

1. On the sphere with the polycarbonate plastic joint ring (sphere 1), the strains were nearly uniform at all latitudes under low loading levels, while at higher loading levels the strain near the apex was somewhat lower than at other latitudes. The magnitude of strains was approximately the same as in spheres without equatorial joint rings.
2. On the sphere with the GRP joint ring (sphere 2), strains showed only a minor increase near the joint compared with those at other latitudes. The magnitude of the increase appeared to be proportional to the magnitude of loading. In the 30- to 70-degree latitude range, the magnitude of measured strains was approximately the same as in spheres without equatorial joint rings.
3. All spheres with metal joint rings (spheres 3, 5, 6, 7, 8, and 9) showed similar strain behavior. In all cases the strain near the equatorial joint was considerably higher than at all other latitudes, the lowest strain occurred between 20 and 60 degrees of latitude, and strain near the apex was somewhat greater than the strain between 20 to 60 degrees of latitude but still less than the strain near the joint. Only the strains in the 30- to 40-degree range of latitude were approximately the same as in spheres without equatorial joint rings.

The general observations of the *exterior longitudinal strains* are as follows:

1. On the sphere with the polycarbonate plastic joint ring (sphere 1), the strains were nearly uniform at all latitudes under all pressure loadings except just prior to implosion. Under $P/f'_c = 0.22$ loading, the strain at 22.5-degrees latitude appeared to decrease significantly below strains at other latitudes. That anomaly probably was caused by the failure in the adhesive between the gage and the concrete at that loading level. The strains in the 20- to 70-degree latitude range were approximately equal to strains in spheres without equatorial joint rings.

2. On the sphere with the GRP joint ring (sphere 2), the strains were nearly uniform at all latitudes and approximately equal to those in spheres without joint rings.

3. All spheres with metallic joint rings (spheres 3, 5, 6, 7, 8, and 9) showed the same general strain characteristics. The greatest strain occurred between 20 and 60 degrees of latitude, the lowest strain was near the equator, and the strain near the apex was larger than that at the equator but less than that in the 20- to 60-degree latitude range. Only the strains near the apex were of the same magnitude as those in the sphere without equatorial joint rings.

LATITUDINAL STRAINS

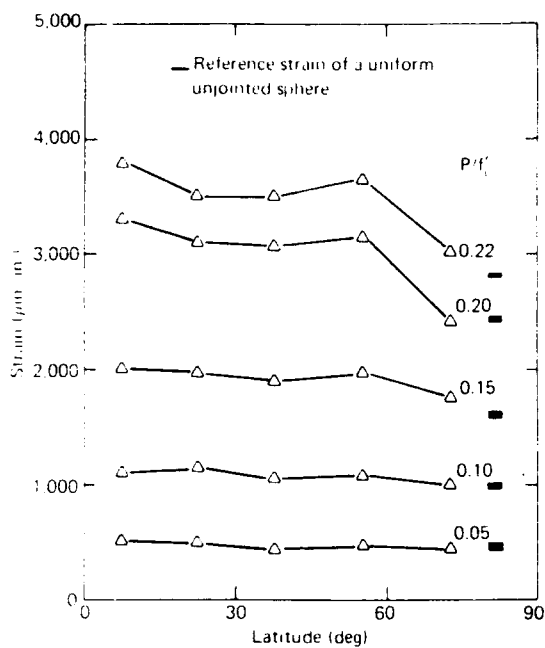
Figures C-3 and C-4 present the interior and exterior latitudinal strains measured at the five latitudes and plotted at various P/f'_c ratios. Also plotted are the strains at the equator for the interior and exterior of the sphere. These strains were calculated based on the measured strains on the interior and exterior of the ring joint. It was assumed that the strain gradient across the ring was linear. Interpolation between the strain at a radius equal to 6.74 inches (interior surface of the ring) and at 8.70 inches (exterior surface of the ring) gave the strains at radii of 7.00 inches and 8.00 inches, the interior and exterior of the spherical hull.

The 1/32-inch-thick epoxy layers between the concrete hemispheres and the joint ring permitted some differential movement, yet, because the inner lip of the ring fitted tightly against the inner surface of the concrete hemisphere, the differential movement was believed to be small. Therefore, the difference between the strain values plotted at 0 and 7.5 degrees is believed to be the actual strain difference with little influence from differential movement between the concrete hemisphere and the joint ring.

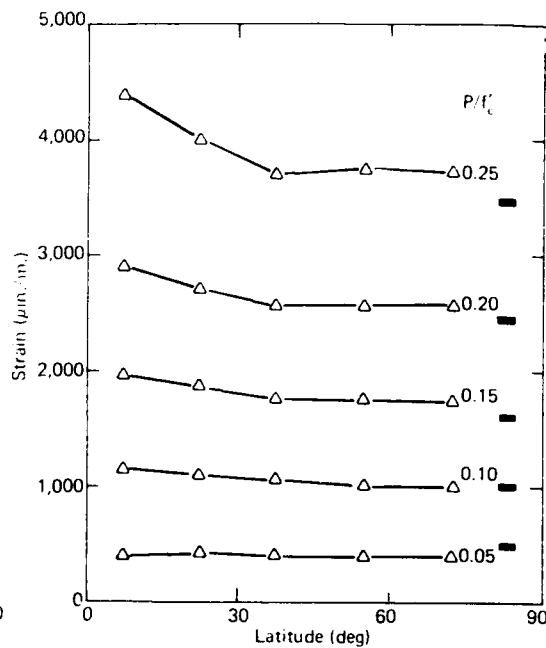
The general observations of the *interior latitudinal strains* are as follows:

1. On the sphere with the polycarbonate plastic joint ring (sphere 1), the strains measured at all latitudes on concrete were nearly uniform, while the strain on the polycarbonate plastic ring was considerably higher. The magnitude of strains in the concrete was approximately the same as in spheres without equatorial joint rings.

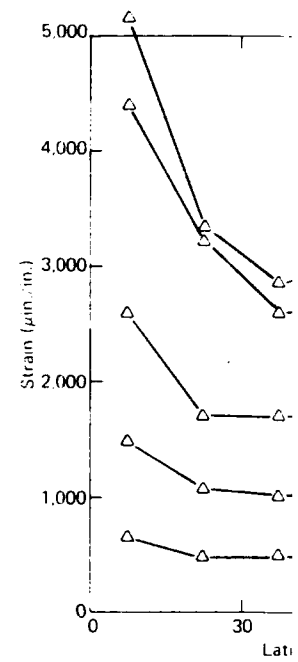
2. On the sphere with the GRP joint ring (sphere 2), the concrete strains and the strain of the joint ring were very similar, and the strain magnitude was approximately the same as that in spheres without equatorial joint rings.



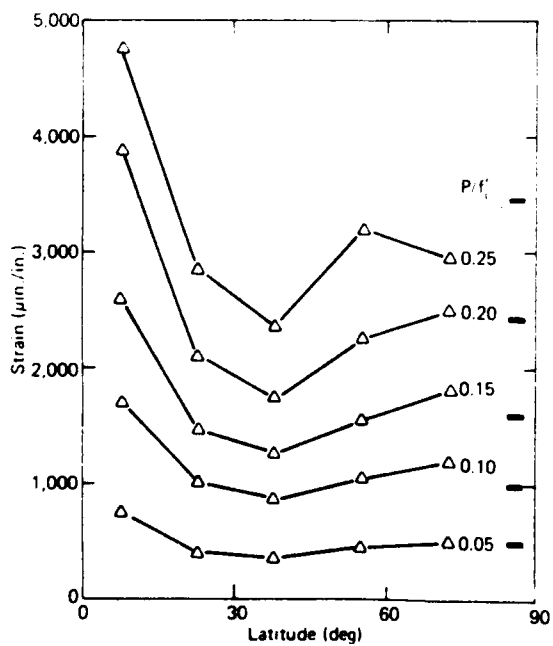
(a) For sphere 1.



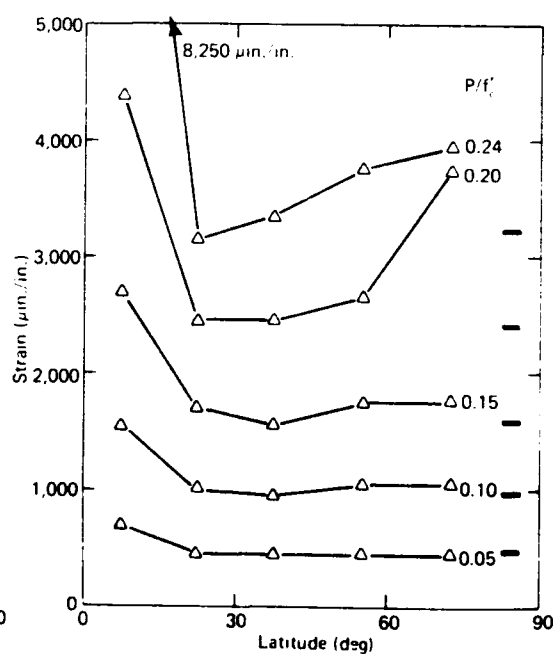
(b) For sphere 2.



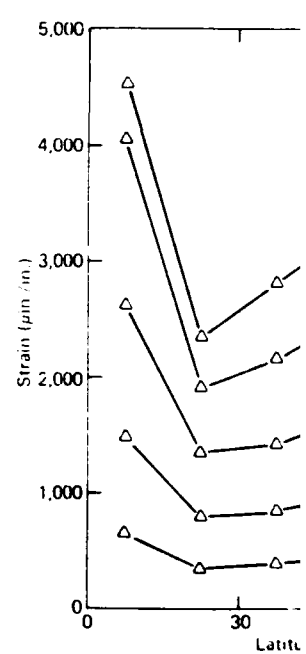
(c) For sphere 3.



(e) For sphere 6.



(f) For sphere 7.



(g) For sphere 8.

Figure C-1. Interior longitudinal strains.

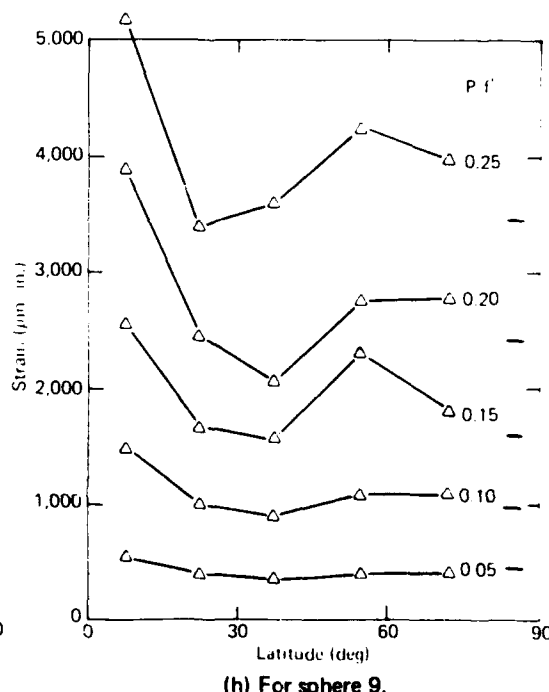
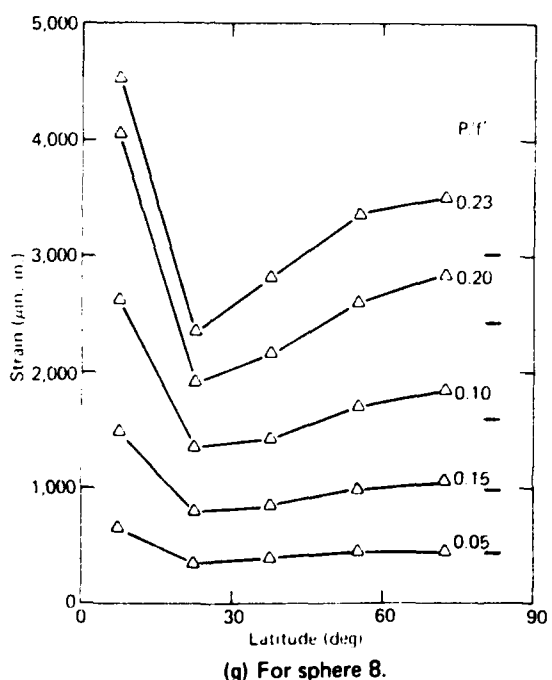
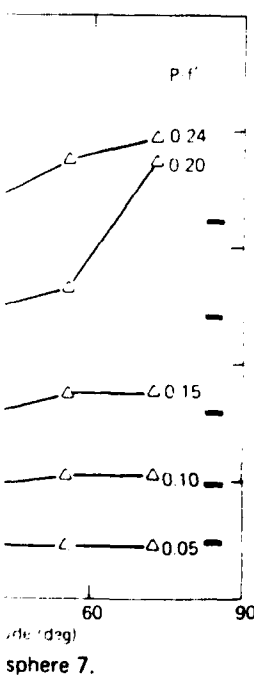
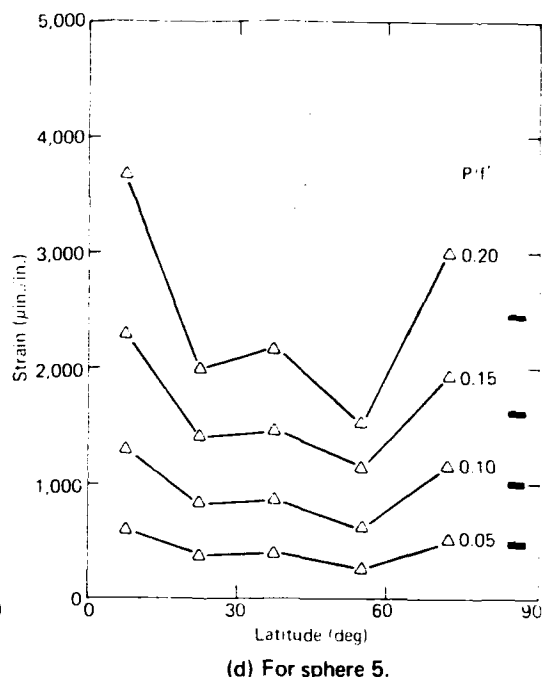
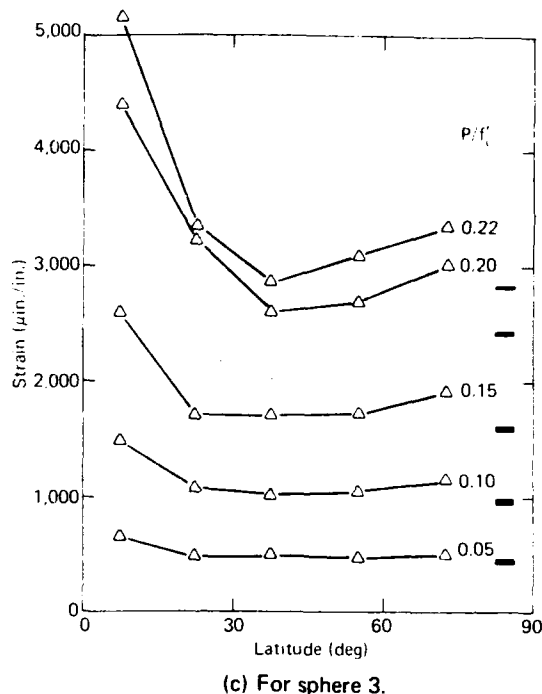
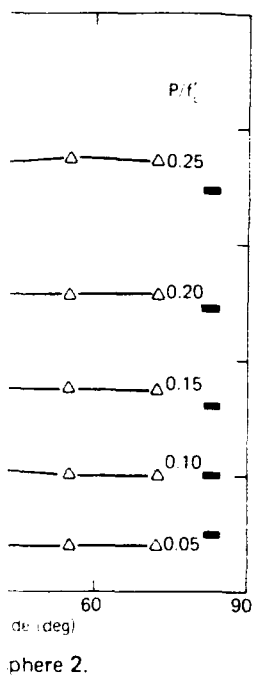
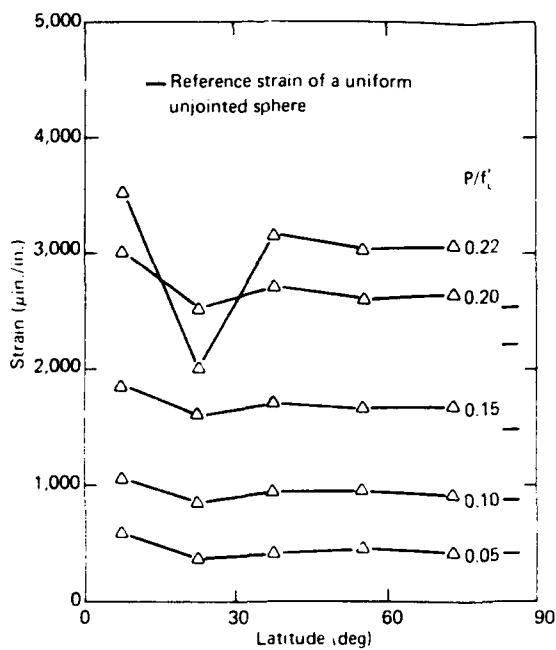
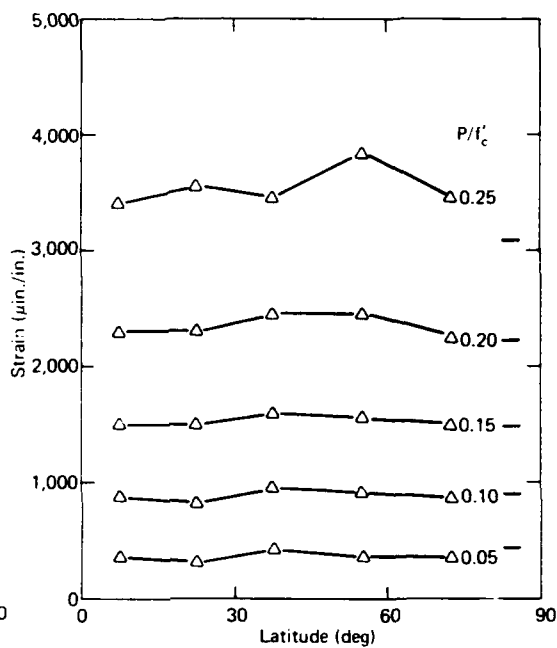


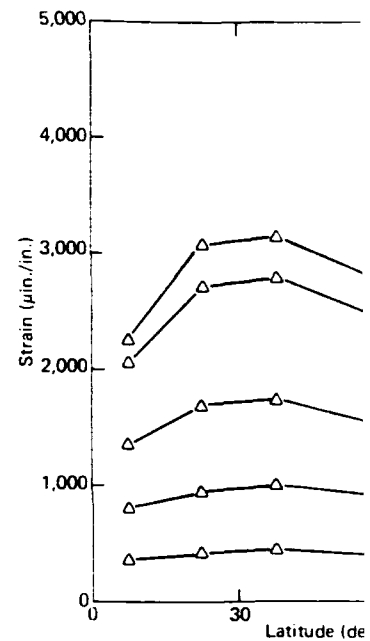
Figure C-1. Interior longitudinal strains.



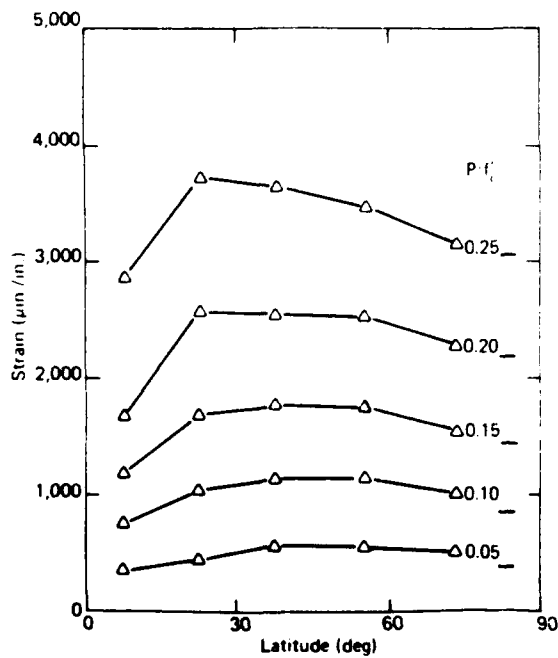
(a) For sphere 1.



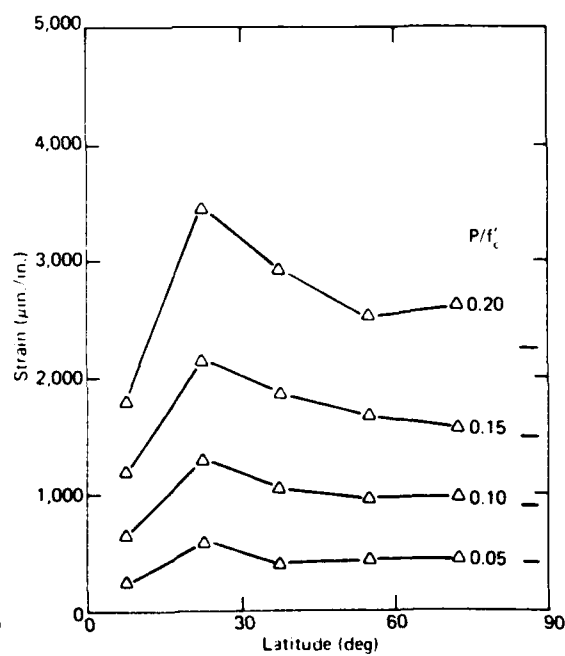
(b) For sphere 2.



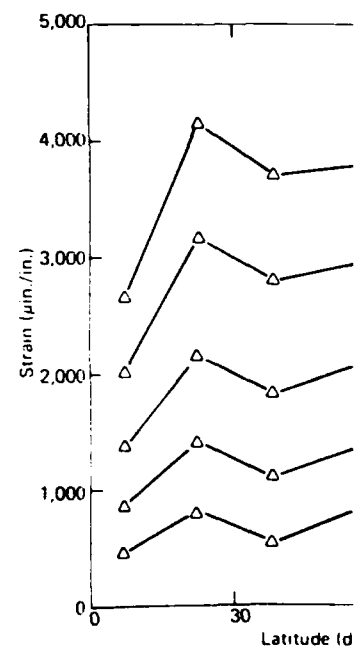
(c) For sphere 3.



(e) For sphere 6.

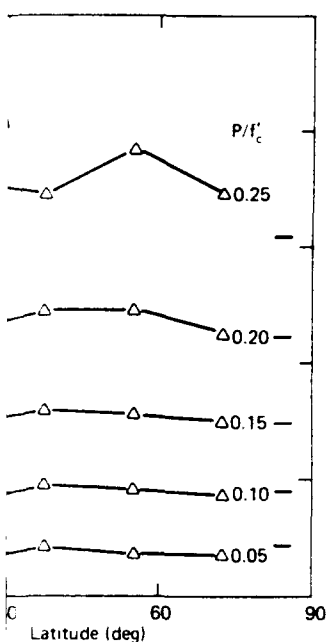


(f) For sphere 7.

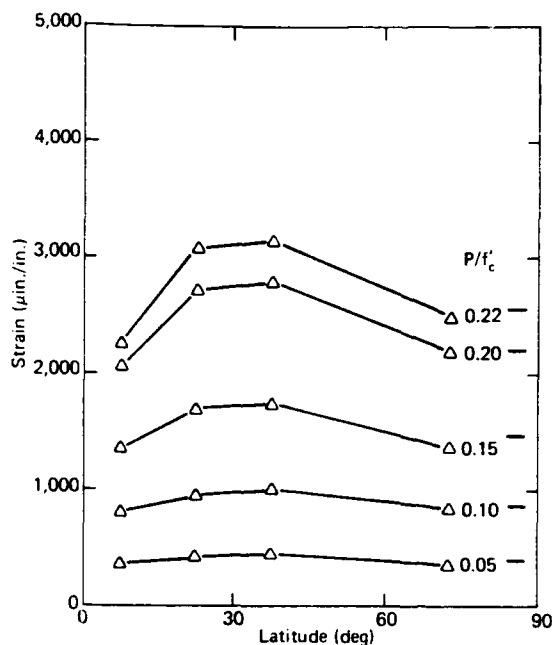


(g) For sphere 8.

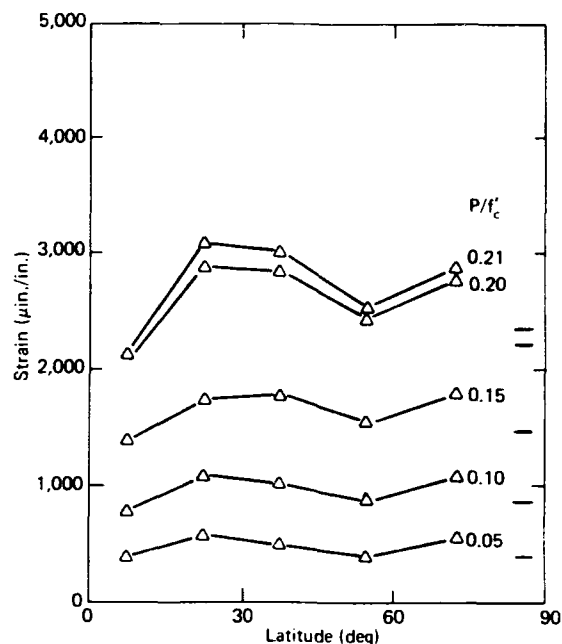
Figure C-2. Exterior longitudinal strains.



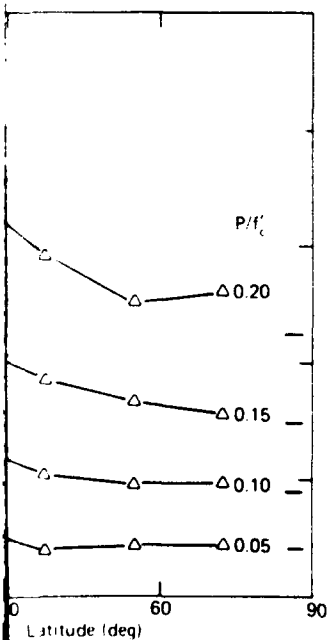
(b) For sphere 2.



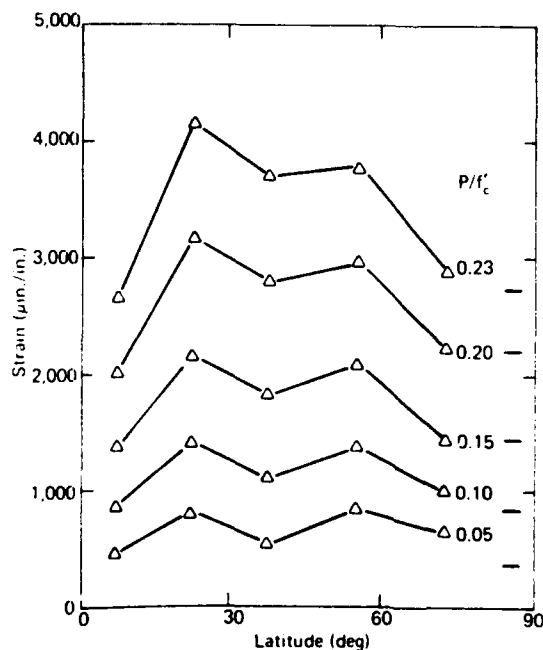
(c) For sphere 3.



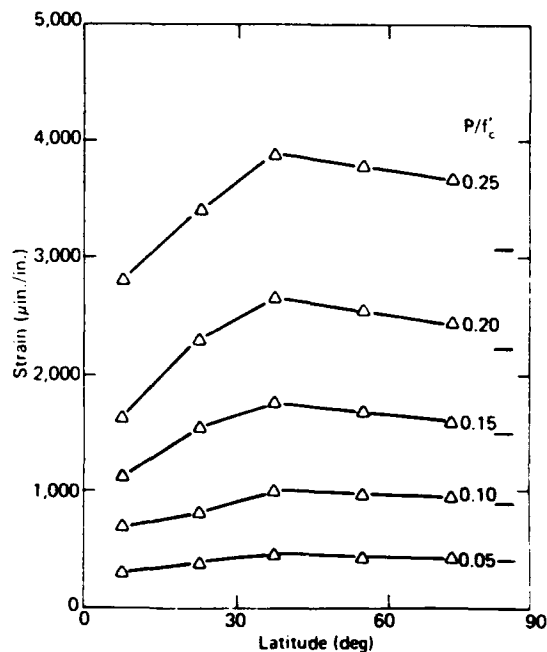
(d) For sphere 5.



(f) For sphere 7.

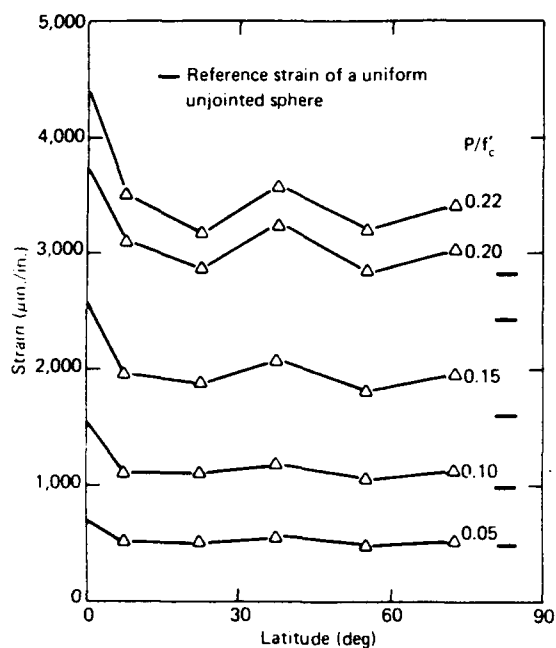


(g) For sphere 8.

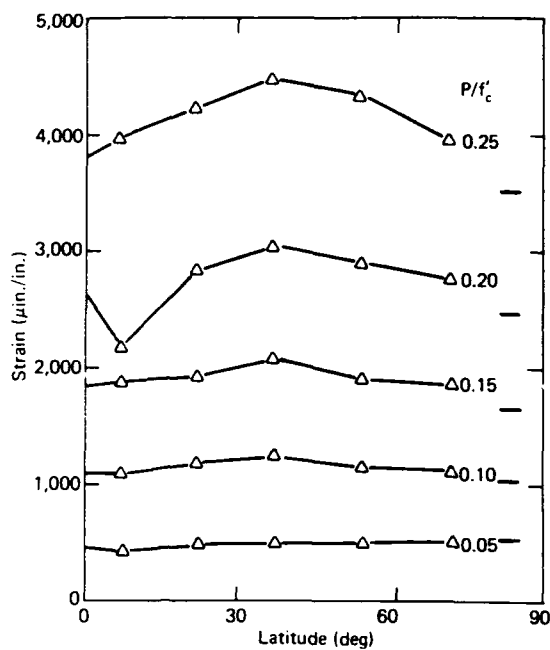


(h) For sphere 9.

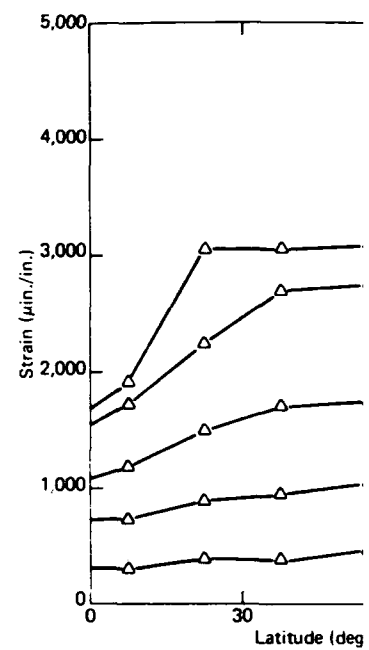
Figure C-2. Exterior longitudinal strains.



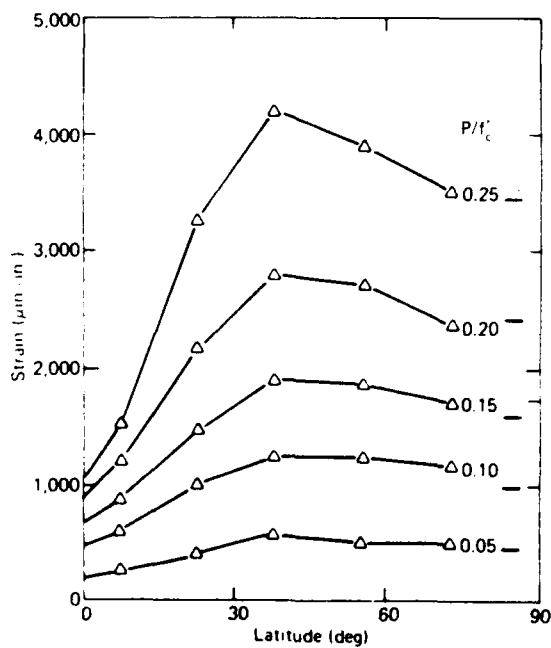
(a) For sphere 1.



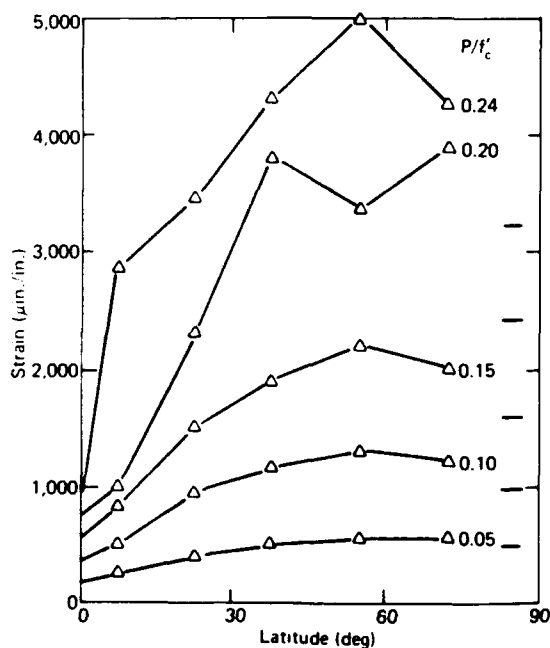
(b) For sphere 2.



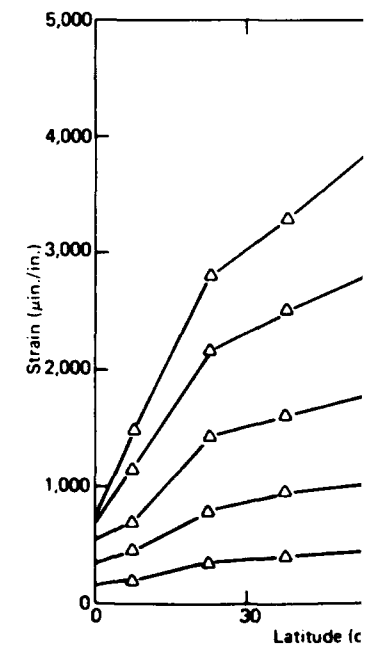
(c) For sphere 3.



(e) For sphere 6.



(f) For sphere 7.



(g) For sphere 8.

Figure C-3. Interior latitudinal strains.

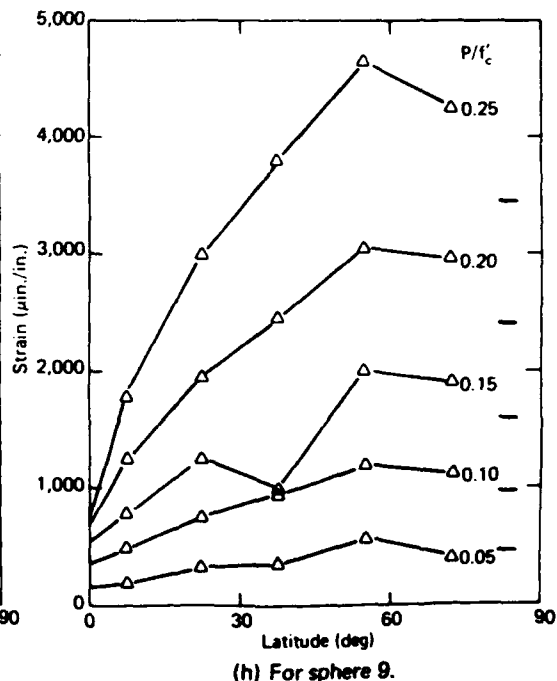
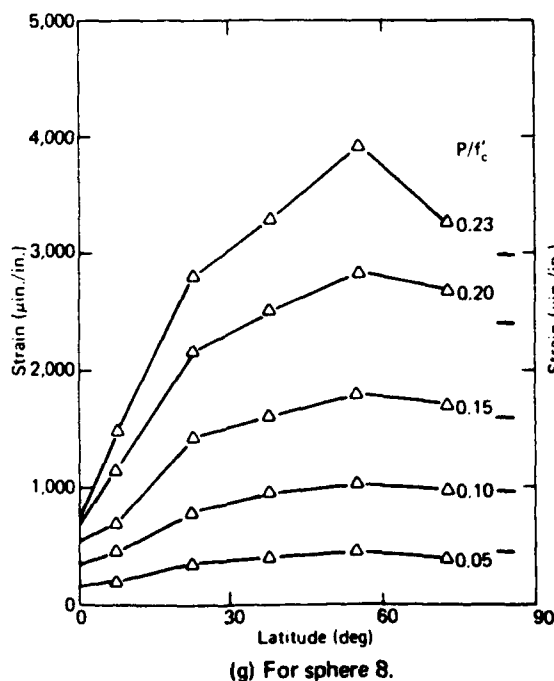
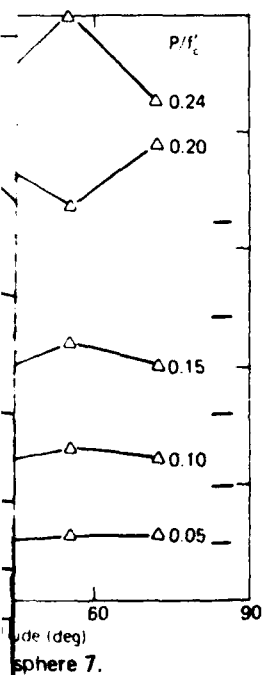
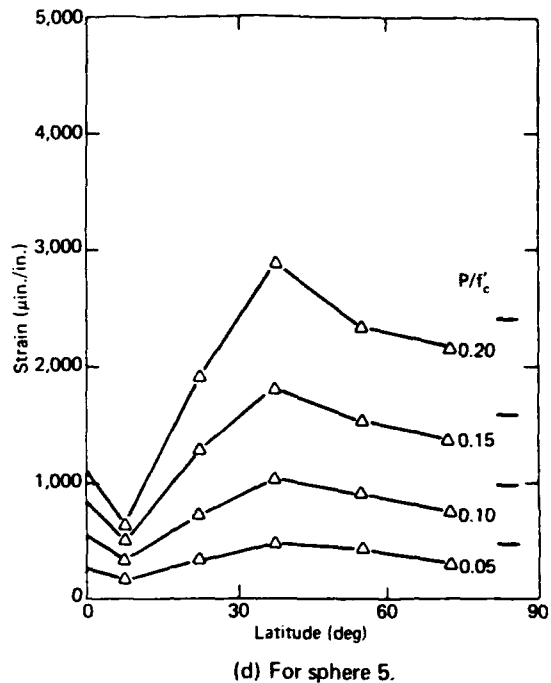
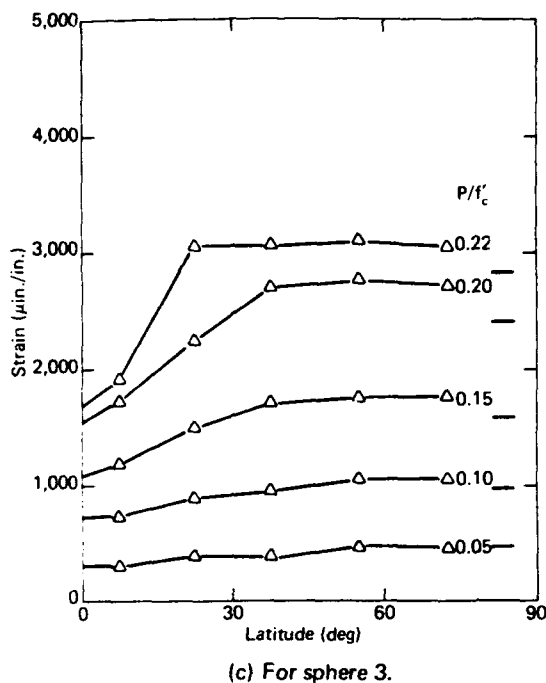
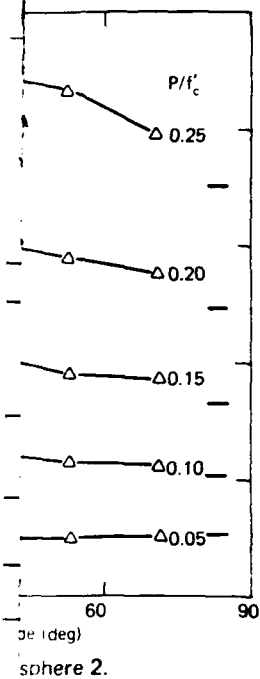
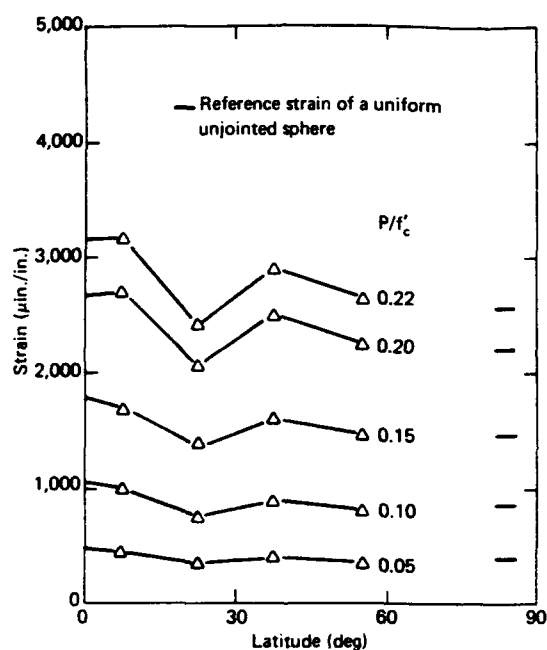
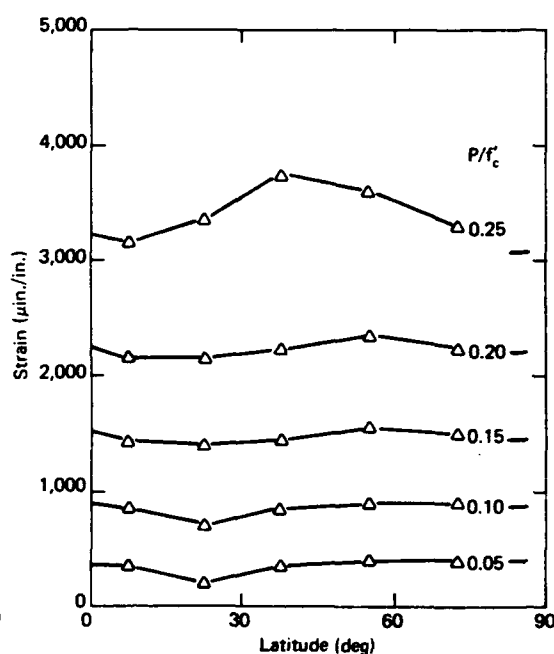


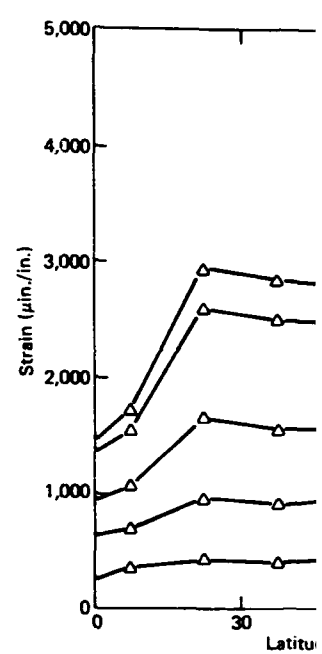
Figure C-3. Interior latitudinal strains.



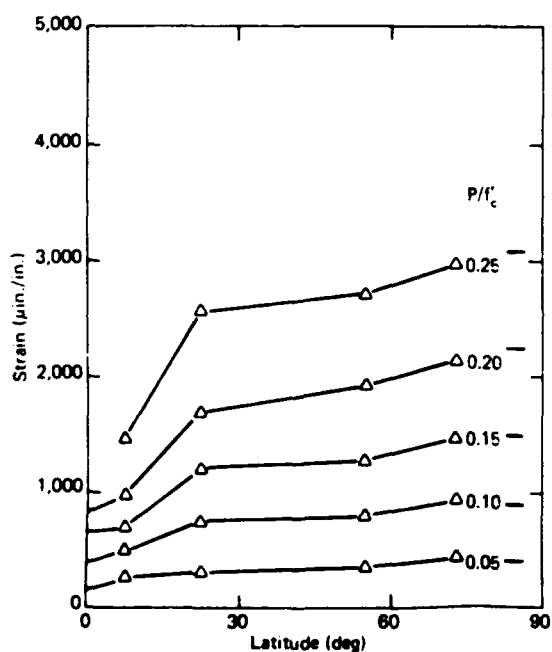
(a) For sphere 1.



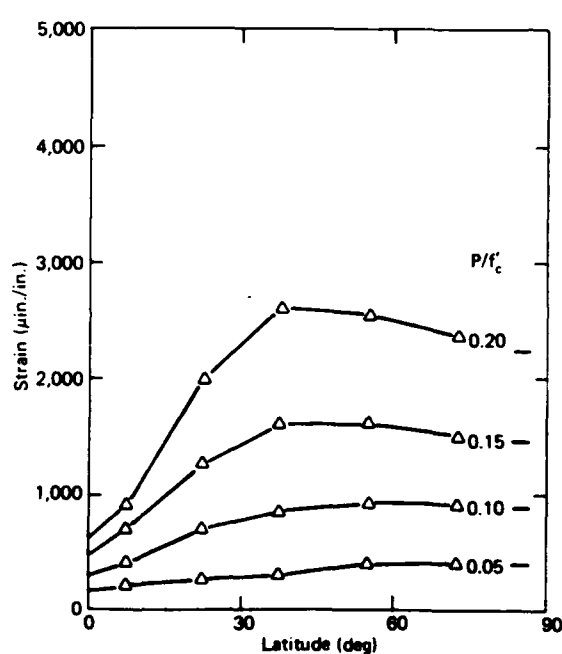
(b) For sphere 2.



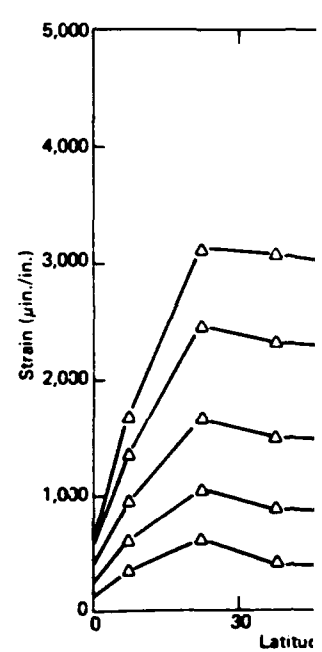
(c) For sphere 3.



(e) For sphere 6.



(f) For sphere 7.



(g) For sphere 8.

Figure C-4. Exterior latitudinal strains.

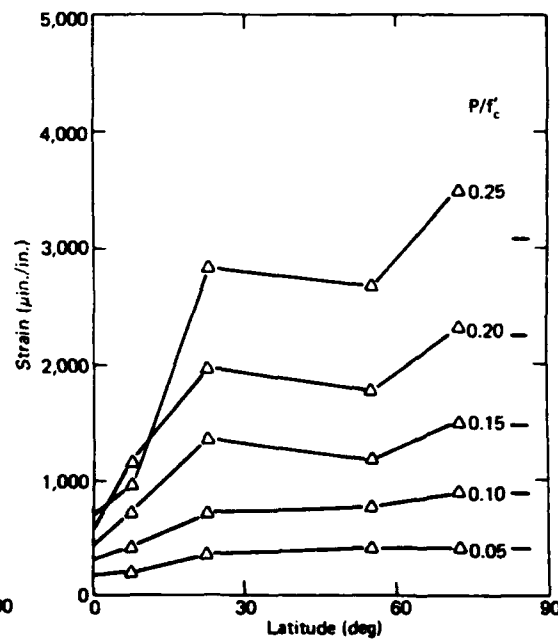
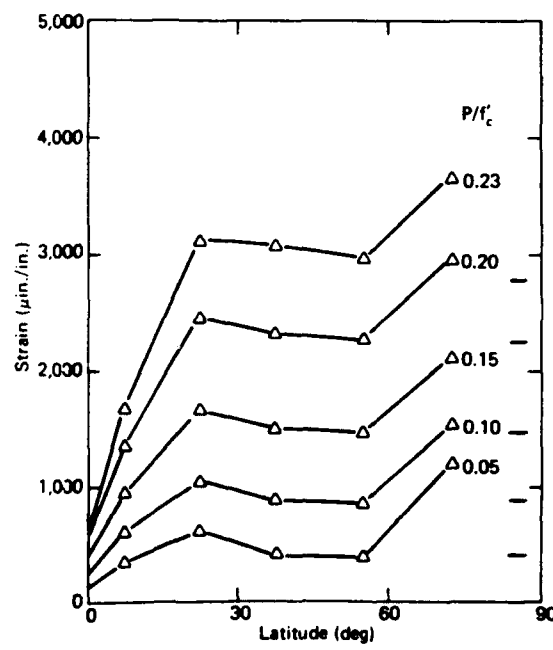
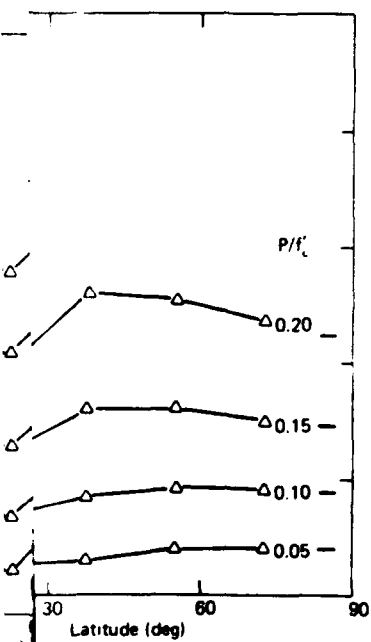
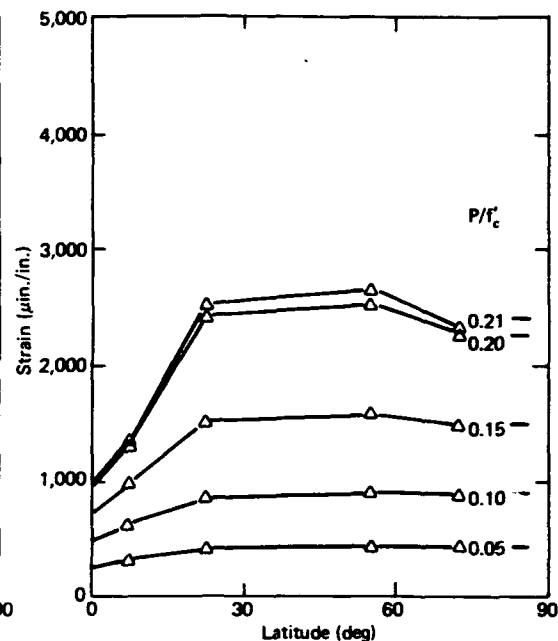
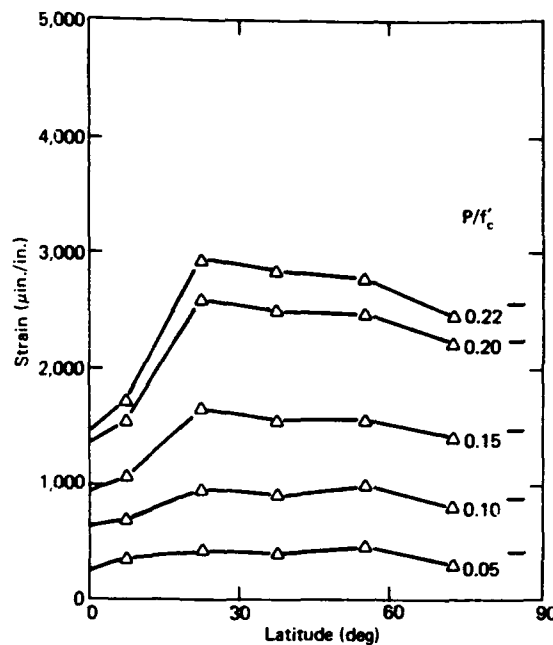
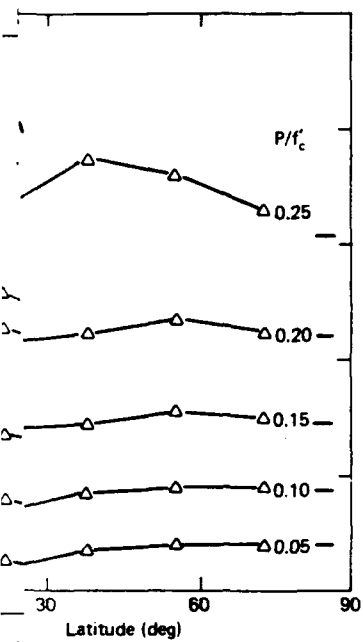


Figure C-4. Exterior latitudinal strains.

3. The strain behavior on all spheres with metal joint rings (spheres 3, 6, 7, 8, and 9) was similar except for sphere 5. Generally, the minimum strain occurred on the joint ring, with the lowest concrete strain being recorded near the joint. The maximum strain occurred in the 40- to 60-degree latitude range. The strains near the apex are approximately the same as in spheres without equatorial joint rings.

4. On sphere 5 the minimum strain occurred at 7.5 degrees latitude, with the strain of the titanium ring appearing as much as 70% greater. It is believed that this is the result of improper bonding between the gage and concrete.

The general observations of the *exterior latitudinal strains* are as follows:

1. On the sphere with the polycarbonate plastic joint ring (sphere 1), the strains were relatively uniform, with the largest strains occurring on the ring. Strains near the apex were approximately the same as in spheres without equatorial joint rings.

2. On the sphere with the GRP joint ring (sphere 2), the strain variation was the least for all the spheres with joint rings. The magnitude of strains at all latitudes and on the joint was approximately the same as in spheres without equatorial joint rings.

3. On all spheres with a metal joint ring (spheres 3, 5, 6, 7, 8, and 9), the smallest strain was on the joint, with the lowest concrete strain being recorded near the joint.

4. On spheres 3, 5, and 7, the maximum strain occurred between 20 and 60 degrees latitude.

5. On spheres 6, 8, and 9, the maximum strain was observed at 72.5 degrees latitude.

6. In all of the spheres except sphere 8, the strains near the apex were approximately the same as in spheres without joint rings.

Appendix D

LONGITUDINAL AND LATITUDINAL STRESS DATA AT $P/f'_c = 0.20$

For each specimen at a ratio of pressure loading to concrete strength (P/f'_c) of 0.20, the interior and exterior stresses were calculated using the following equations:

$$\sigma_{i, \text{long}} = \frac{E}{1 - \nu^2} (\epsilon_{i, \text{long}} + \nu \epsilon_{i, \text{lat}})$$

$$\sigma_{e, \text{long}} = \frac{E}{1 - \nu^2} (\epsilon_{e, \text{long}} + \nu \epsilon_{e, \text{lat}}) + \frac{\nu}{1 - \nu} P$$

$$\sigma_{i, \text{lat}} = \frac{E}{1 - \nu^2} (\epsilon_{i, \text{lat}} + \nu \epsilon_{i, \text{long}})$$

$$\sigma_{e, \text{lat}} = \frac{E}{1 - \nu^2} (\epsilon_{e, \text{lat}} + \nu \epsilon_{e, \text{long}}) + \frac{\nu}{1 - \nu} P$$

where

$\sigma_{i, \text{long}}$ = interior longitudinal stress (psi)

$\sigma_{e, \text{long}}$ = exterior longitudinal stress (psi)

$\sigma_{i, \text{lat}}$ = interior latitudinal stress (psi)

$\sigma_{e, \text{lat}}$ = exterior latitudinal stress (psi)

$\epsilon_{i, \text{long}}$ = interior longitudinal strain (in./in.)

$\epsilon_{i, \text{lat}}$ = interior latitudinal strain (in./in.)

$\epsilon_{e, \text{long}}$ = exterior longitudinal strain (in./in.)

$\epsilon_{e, \text{lat}}$ = exterior latitudinal strain (in./in.)

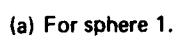
E = modulus of elasticity = 3.57×10^6 psi

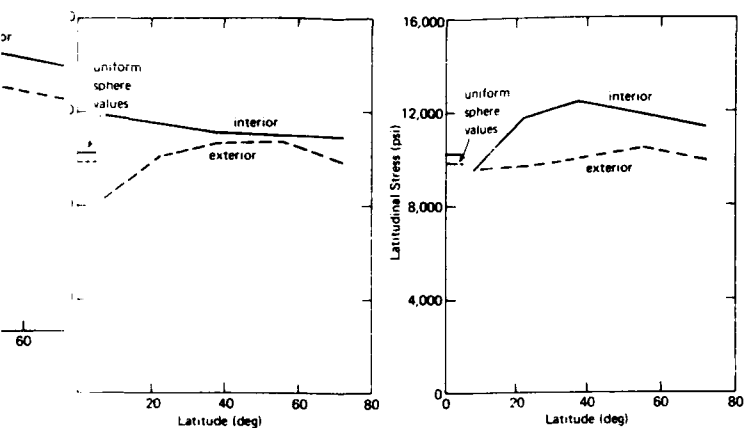
ν = Poisson's ratio = 0.16

P = external applied pressure (psi)

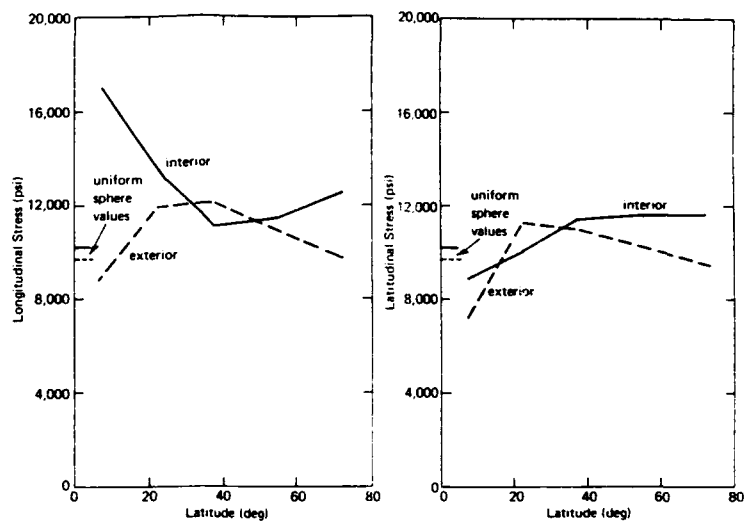
Aspects of the longitudinal behavior on all spheres with a metal joint ring (illustrated in Figure D-1) are:

1. The longitudinal stress on the exterior surface is greater than on the interior surface at the midlatitudes (Figures D-1c to D-1h).
2. Near the joint the interior stress is much greater than that of a uniform sphere while the exterior stress is less.
3. At the midlatitudes the interior stress is often less than that of a uniform sphere while the exterior stress is greater.

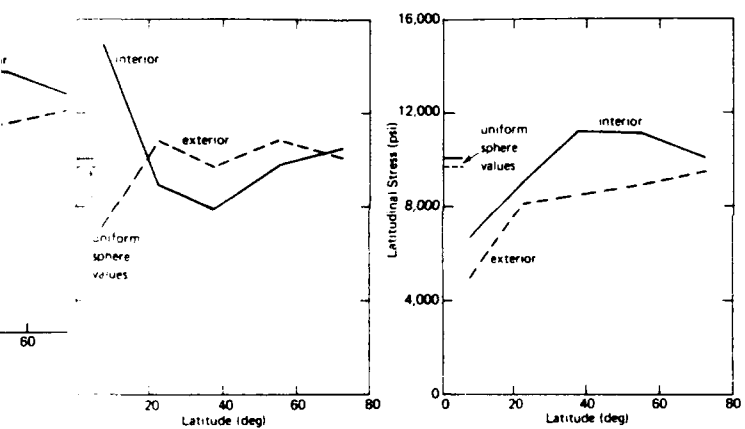




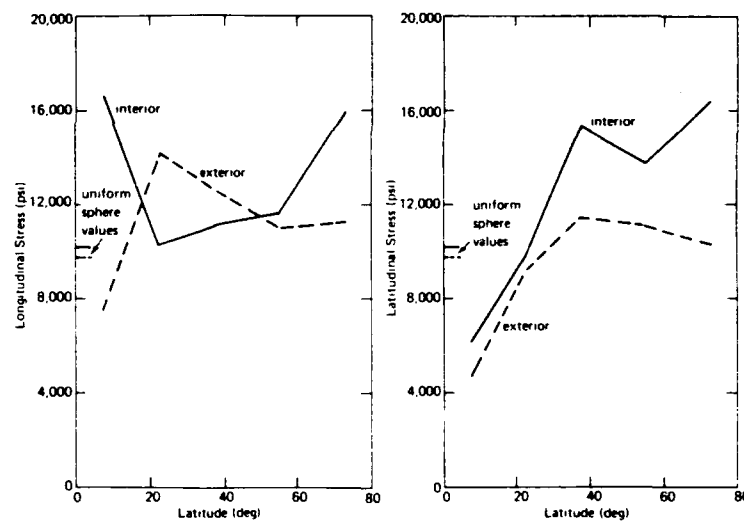
(b) For sphere 2.



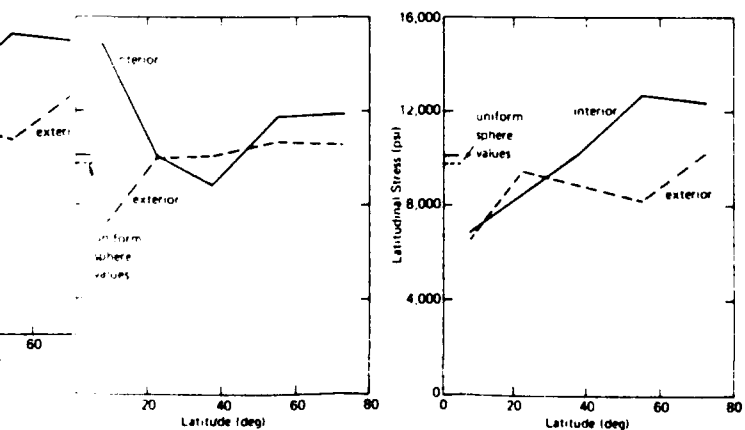
(c) For sphere 3.



(e) For sphere 6.



(f) For sphere 7.



(h) For sphere 9.

Figure D-1. Stress versus latitude at $P/f_c = 0.20$.

REFERENCES

1. Naval Civil Engineering Laboratory. Technical Report R-517: Behavior of spherical concrete hulls under hydrostatic loading, pt. 1. Exploratory investigation, by J. D. Stachiw and K. O. Gray. Port Hueneme, Calif., Mar. 1967. (AD 649290)
2. ———. Technical Report R-547: Behavior of spherical concrete hulls under hydrostatic loading, pt. 2. Effect of penetrations, by J. D. Stachiw. Port Hueneme, Calif., Oct. 1967. (AD 661187)
3. ———. Technical Report R-588: Behavior of spherical concrete hulls under hydrostatic loading, pt. 3. Relationship between thickness-to-diameter ratio and critical pressures, strains, and water permeation rates, by J. D. Stachiw and K. Mack. Port Hueneme, Calif., June 1968. (AD 835492L)
4. ———. Technical Report R-679: Failure of thick-walled concrete spheres subjected to hydrostatic loading, by H. H. Haynes and R. A. Hoofnagle. Port Hueneme, Calif., May 1970. (AD 708011)
5. ———. Technical Report R- : Behavior of 66-inch OD concrete spherical Hulls under Hydrostatic Loading, by H. H. Haynes and L. F. Kahn. Port Hueneme, Calif. (In preparation, 1971.)

LIST OF SYMBOLS

	Area of concrete removed and replaced by joint ring	$\sigma_{e, \text{long}}$	Exterior longitudinal stress (psi)
	Cross-sectional area of joint ring	$\sigma_{i, \text{lat}}$	Interior latitudinal stress (psi)
	Outside diameter of sphere (in.)	$\sigma_{i, \text{long}}$	Interior longitudinal stress (psi)
	Modulus of elasticity (psi)	σ_{yp}	0.2% offset yield point
	Secant modulus of elasticity of concrete (psi)		
	Modulus of elasticity of ring material (psi)		
	Ultimate uniaxial concrete strength (psi)		
	Applied pressure (psi)		
p_c	Ratio of applied pressure to concrete strength		
p_i	Implosion pressure (psi)		
p_i/f'_c	Ratio of implosion pressure to concrete strength		
	Relative stiffness		
	Wall thickness of sphere (in.)		
t_o	Ratio of wall thickness to outside diameter		
	Unit weight of concrete (pcf)		
	Spherical angle (deg)		
ϵ_{lat}	Exterior latitudinal strain (in./in.)		
ϵ_{long}	Exterior longitudinal strain (in./in.)		
ϵ_{lat}	Interior latitudinal strain (in./in.)		
ϵ_{long}	Interior longitudinal strain (in./in.)		
	Poisson's ratio		
σ_{lat}	Exterior latitudinal stress (psi)		

DISTRIBUTION LIST

SNDL Code	No. of Activities	Total Copies	
—	1	12	Defense Documentation Center
FKAIC	1	10	Naval Facilities Engineering Command
FKNI	6	6	NAVFAC Engineering Field Divisions
FKN5	9	9	Public Works Centers
FA25	1	1	Public Works Center
—	9	9	RDT&E Liaison Officers at NAVFAC Engineering Field Divisions and Construction Battalion Centers
—	353	353	NCEL Special Distribution List No. 9 for persons and activities interested in reports on Deep Ocean Studies

<p>Naval Civil Engineering Laboratory</p> <p>INFLUENCE OF STIFF EQUATORIAL RINGS ON CONCRETE SPHERICAL HULLS SUBJECTED TO HYDROSTATIC LOADING (Final), by L. F. Kahn and J. D. Stachiw</p> <p>TR-735 63 p. illus August 1971 Unclassified</p> <p>1. Undersea concrete spheres</p> <p>Thirteen hollow concrete spheres of 16-inch outside diameter x 14-inch inside diameter and one sphere of 66-inch outside diameter x 57.75-inch inside diameter were assembled from hemispheres fastened together with equatorial joint rings of different stiffnesses. The joint rings were made from polycarbonate plastic, glass reinforced plastic laminate, aluminum, titanium, low carbon steel, and alloy steel. After instrumentation with electrical resistance strain gages, the spheres were tested to destruction under external hydrostatic loading. Equatorial joints that are either considerably stiffer or more compliant than concrete lower the short-term implosion pressure of the concrete spheres by as much as 27%; the glass reinforced plastic joint ring did not significantly reduce the implosion pressure. It is recommended that equatorial joint rings be designed to have a stiffness approximately equal to that of the concrete shell and be made of glass reinforced plastic. If stiffer joint rings are used, the operational pressure should be 30% lower than that of a sphere without a mechanical lock joint mechanism.</p>	<p>Naval Civil Engineering Laboratory</p> <p>INFLUENCE OF STIFF EQUATORIAL RINGS ON CONCRETE SPHERICAL HULLS SUBJECTED TO HYDROSTATIC LOADING (Final), by L. F. Kahn and J. D. Stachiw</p> <p>TR-735 63 p. illus August 1971 Unclassified</p> <p>1. Undersea concrete spheres</p> <p>Thirteen hollow concrete spheres of 16-inch outside diameter x 14-inch inside diameter and one sphere of 66-inch outside diameter x 57.75-inch inside diameter were assembled from hemispheres fastened together with equatorial joint rings of different stiffnesses. The joint rings were made from polycarbonate plastic, glass reinforced plastic laminate, aluminum, titanium, low carbon steel, and alloy steel. After instrumentation with electrical resistance strain gages, the spheres were tested to destruction under external hydrostatic loading. Equatorial joints that are either considerably stiffer or more compliant than concrete lower the short-term implosion pressure of the concrete spheres by as much as 27%; the glass reinforced plastic joint ring did not significantly reduce the implosion pressure. It is recommended that equatorial joint rings be designed to have a stiffness approximately equal to that of the concrete shell and be made of glass reinforced plastic. If stiffer joint rings are used, the operational pressure should be 30% lower than that of a sphere without a mechanical lock joint mechanism.</p>
<p>Naval Civil Engineering Laboratory</p> <p>INFLUENCE OF STIFF EQUATORIAL RINGS ON CONCRETE SPHERICAL HULLS SUBJECTED TO HYDROSTATIC LOADING (Final), by L. F. Kahn and J. D. Stachiw</p> <p>TR-735 63 p. illus August 1971 Unclassified</p> <p>2. Equatorial joints</p> <p>1. 3.1610-1</p>	<p>Naval Civil Engineering Laboratory</p> <p>INFLUENCE OF STIFF EQUATORIAL RINGS ON CONCRETE SPHERICAL HULLS SUBJECTED TO HYDROSTATIC LOADING (Final), by L. F. Kahn and J. D. Stachiw</p> <p>TR-735 63 p. illus August 1971 Unclassified</p> <p>2. Equatorial joints</p> <p>1. 3.1610-1</p>

Unclassified

Security Classification

DOCUMENT CONTROL DATA - R & D		
<small>(Security classification of title, body of abstract and indexing annotation must be entered when the overall report is classified)</small>		
1. ORIGINATING ACTIVITY (Corporate author) Naval Civil Engineering Laboratory Port Hueneme, California 93043		2a. REPORT SECURITY CLASSIFICATION Unclassified
		2b. GROUP
3. REPORT TITLE INFLUENCE OF STIFF EQUATORIAL RINGS ON CONCRETE SPHERICAL HULLS SUBJECTED TO HYDROSTATIC LOADING		
4. DESCRIPTIVE NOTES (Type of report and inclusive dates) Final; July 1968-January 1971		
5. AUTHOR(S) (First name, middle initial, last name) L. F. Kahn and J. D. Stachiw		
6. REPORT DATE August 1971	7a. TOTAL NO. OF PAGES 63	7b. NO. OF REFS 5
8a. CONTRACT OR GRANT NO.	9a. ORIGINATOR'S REPORT NUMBER(S) TR-735	
b. PROJECT NO 3.1610-1		
c.	9b. OTHER REPORT NO(S) (Any other numbers that may be assigned this report)	
d.		
10. DISTRIBUTION STATEMENT Approved for public release; distribution unlimited.		
11. SUPPLEMENTARY NOTES		12. SPONSORING MILITARY ACTIVITY Naval Facilities Engineering Command Washington, D. C. 20390
13. ABSTRACT <p>Thirteen hollow concrete spheres of 16-inch outside diameter x 14-inch inside diameter and one sphere of 66-inch outside diameter x 57.75-inch inside diameter were assembled from hemispheres fastened together with equatorial joint rings of different stiffnesses. The joint rings were made from polycarbonate plastic, glass reinforced plastic laminate, aluminum, titanium, low carbon steel, and alloy steel. After instrumentation with electrical resistance strain gages, the spheres were tested to destruction under external hydrostatic loading. Equatorial joints that are either considerably stiffer or more compliant than concrete lower the short-term implosion pressure of the concrete spheres by as much as 27%; the glass reinforced plastic joint ring did not significantly reduce the implosion pressure. It is recommended that equatorial joint rings be designed to have a stiffness approximately equal to that of the concrete shell and be made of glass reinforced plastic. If stiffer joint rings are used, the operational pressure should be 30% lower than that of a sphere without a mechanical lock joint mechanism.</p>		

DD FORM 1473

5/N 0101-807-6801

(PAGE 1)

Unclassified

Security Classification

Unclassified
Security Classification

14 KEY WORDS	LINK A		LINK B		LINK C	
	ROLE	WT	ROLE	WT	ROLE	WT
Concrete shells						
Concrete hulls						
Spherical hulls						
Ocean bottom habitations						
Hydrostatic loading						
Joint rings						
Equatorial rings						
Implosion pressure						
Instrumentation capsules						
Domes						
Stiffening rings						

R 679

Technical Report

**FAILURE OF THICK-WALLED CONCRETE SPHERES
SUBJECTED TO HYDROSTATIC LOADING**

May 1970

Sponsored by

NAVAL FACILITIES ENGINEERING COMMAND



NAVAL CIVIL ENGINEERING LABORATORY

Port Hueneme, California

This document has been approved for public release and sale; its distribution is unlimited.

FAILURE OF THICK-WALLED CONCRETE SPHERES SUBJECTED TO HYDROSTATIC LOADING

Technical Report R-679

56-015

by

H. H. Haynes and R. A. Hoofnagle

ABSTRACT

Two modes of failure for hollow concrete spheres subjected to hydrostatic pressure loadings are discussed, and the experimental results are presented. The first mode of failure was crack development in the plane of the concrete wall, and the second mode was implosion. From experiments using 16-inch-OD spheres, the difference between the pressures at failure for the two modes ranged from 0 to 50%. Expressions to predict the pressures *at initiation of in-plane cracking of the concrete wall* and the pressures at implosion are presented.

This document has been approved for public release and sale; its distribution is unlimited.

Copies available at the Clearinghouse for Federal Scientific & Technical Information (CFSTI), Sills Building, 5285 Port Royal Road, Springfield, Va. 22151

CONTENTS

	page
OBJECTIVE	1
INTRODUCTION	1
BACKGROUND	2
TEST PROGRAM	4
Experiment Design	4
Test Results	5
DISCUSSION	8
Introduction	8
In Plane Cracking	8
Implosion Failure Mode	14
UNDERWATER CONCRETE STRUCTURAL APPLICATIONS . .	19
FINDINGS	21
CONCLUSIONS AND RECOMMENDATIONS	24
APPENDIX—Specimen Fabrication and Test Procedure	25
REFERENCES	31
LIST OF SYMBOLS	33

OBJECTIVE

The main objective was to develop preliminary expressions which would describe the failure behavior of concrete spheres under hydrostatic loading. The equations would be useful in predicting the range of depths in the ocean where concrete spheres could have application. A secondary objective was to determine the influence of concrete strength on the failure of thick-walled spheres under hydrostatic loading.

INTRODUCTION

In general, material development for underwater structures has been directed toward producing materials, namely steels and aluminums, with a high strength-to-weight ratio for use in movable structures. The high-strength material approach was necessary to advance state-of-the-art technology for military submarines and research submersibles. *For structures located permanently or semipermanently on the ocean floor, the functional requirements of the construction material are different from those of submersibles.* Permanent structures do not require positive buoyancy and, therefore, could be constructed from materials with a low strength-to-weight ratio. These weaker materials could prove to have a major economic advantage over high-strength materials. The United States Navy desired to develop various materials which would be suited for different operational requirements. Concrete is one material which appeared suited for permanent structures.

Concrete possesses the desirable features of low cost, good compressive behavior, and high resistance to deterioration in seawater.¹ The ability of the material to function in the ocean at depths to 130 feet has already been demonstrated; the Chesapeake Bay Bridge Tunnel in Virginia, the St. Lawrence River Tunnel at Montreal, and the Trans-Bay Tube at San Francisco are examples of transportation tunnels that were constructed from precast concrete sections joined together underwater. However, the maximum depth capability for underwater concrete structures has not been investigated. Therefore, this study was initiated to determine the range of depths within which concrete structures would have application.

The approach of the study toward fulfilling the objective was as follows. To permit the analytical prediction of the failure pressures of concrete spheres, an experimental program was performed to determine the influence of concrete strength on implosion pressure. By incorporating this data with results from previous studies,²⁻⁴ sufficient data was available to develop an empirical expression to predict implosion of spheres.

A study on the mechanics of failure of the spheres generated a concept of a different mode of failure. This failure mode considered the cracks which initiated in the concrete wall prior to implosion and which developed in a direction parallel to the maximum principal stresses. Previously conducted research was employed to validate a modified expression for elastic thick-walled spheres, which was developed to predict the pressure at the initiation of in-plane cracking.

BACKGROUND

Since 1966, the Naval Civil Engineering Laboratory has been involved in experimental studies on concrete hollow spheres subjected to simulated hydrospace loadings. The major objective of this research was to determine the practicability of employing concrete as a construction material for deep-ocean (below 600 feet) structures. The research programs²⁻⁴ were exploratory investigations into the behavior of concrete spheres under external hydrostatic loading; they were designed to define areas for future research.

The first investigation² on concrete pressure hulls showed that model spheres with 16-inch outside diameter (OD) and 1-inch wall thickness (t/D_o ratio of 0.0625) were capable of ultimate resistances equal to the pressure loading imposed at approximately 7,000 feet in the ocean. These buoyant hulls with a weight-to-displacement ratio of 0.725 imploded at hydrostatic pressures greater than predicted by elastic thick-walled theory. Thus, the pressure-resistant behavior of the concrete spheres showed the material had potential for use in deep-ocean structures.

The objective of the second investigation³ was to determine the effect of hull discontinuities, such as hatches, windows, or electrical penetrations, on the structural behavior of concrete spheres. It was reported that hull penetrations with a greater stiffness (modulus of elasticity) than concrete had no significant effect on the strain distribution or implosion pressure of concrete spheres.

The third study⁴ investigated the influence of the wall-thickness-to-outside-diameter ratio (t/D_o) on the behavior of concrete spheres. Four t/D_o ratios were investigated: 0.0625, 0.1250, 0.1875, and 0.2500. The wall

thickness varied from 1 to 4 inches in increments of 1 inch, while a constant outside diameter of 16 inches was maintained. The test results showed that implosion pressure was a quasilinear function of the t/D_o ratio. As is shown in Figure 1, this finding was anomalous to elastic thick-walled theory. Another test result observed by Stachiw⁴ but not predicted by elastic theory was the strain behavior on the interior surface of spheres with wall thicknesses of 2, 3, and 4 inches (t/D_o ratios of 0.1250, 0.1875, and 0.2500 respectively). The strains were congruent with elastic behavior until at some pressure loading they began to decrease in magnitude, while the spheres continued to sustain considerable increases in pressure loading. It was postulated that the interior concrete surface began to spall, which would have accounted for the relaxation in strains. This explanation does not appear to the authors as complete; with spalling, the wall thickness would become thinner which would tend to cause, not delay, implosion. Discussion of this strain behavior is presented in this report under "In-Plane Cracking."

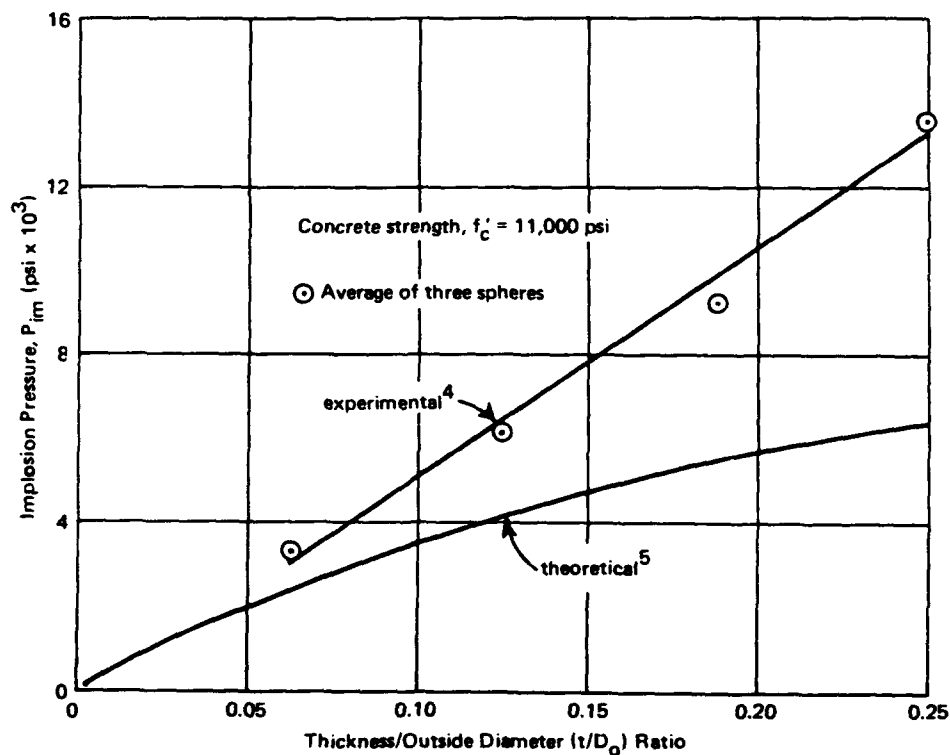


Figure 1. Comparison of experimental and theoretical implosion behavior.

An analytical method was proposed by Stachiw⁴ to predict strains on the interior and exterior surfaces of concrete spheres. The classical Lamé expressions for thick-walled elastic spheres were utilized and predicted strains with good agreement to experimental values, providing the instantaneous secant modulus of elasticity was used in the calculations instead of the initial modulus.

To minimize variables, all of Stachiw's work was performed on spheres constructed using the same concrete mix design; hence, the ultimate concrete strength of the sphere specimens remained essentially constant within a range of 9,000 to 11,000 psi. (The concrete strength was determined by uniaxial compression tests on 3 x 6-inch concrete control cylinders.) Concrete strength as an independent variable was not investigated.

The experimental program of the present study was designed to generate data from spheres constructed of a concrete with a strength different from that of previous studies²⁻⁴ so that a more general understanding of the failure modes of concrete spheres could be obtained.

TEST PROGRAM

Experiment Design

The objective of the test program was to generate experimental results so that the effect of concrete strength on the implosion pressures of spheres of various t/D_o ratios could be determined. The experimental program consisted of testing spheres with a lower strength concrete than that in previous tests while maintaining casting, fabricating, and testing procedures similar to those in past work.²⁻⁴ The concrete mix design used in Stachiw's work was altered to obtain a strength of 6,000 psi by increasing the water/cement ratio, decreasing the curing period, and changing the type of cement. However, when the altered mix was compared to the original mix design, they were, except for strength, essentially equivalent because the type of aggregate, aggregate proportions, and aggregate/cement ratio were identical.

Four 16-inch-OD model concrete spheres were constructed and tested in ocean simulation facilities. The spheres had wall thicknesses of 1, 2, 3, and 4 inches as shown in Figure 2, which correspond to t/D_o ratios of 0.0625, 0.1250, 0.1875, and 0.2500 respectively. Two hemisphere sections joined with an epoxy bonding agent formed the spherical hulls. Hydrostatic pressure testing of the hulls was performed in the NCEL pressure test facility; the general test setup is shown in Figure 3. The spheres were loaded at a constant pressurization rate of 100 psi/min until implosion. A detailed description of specimen fabrication and test procedure is presented in the Appendix.

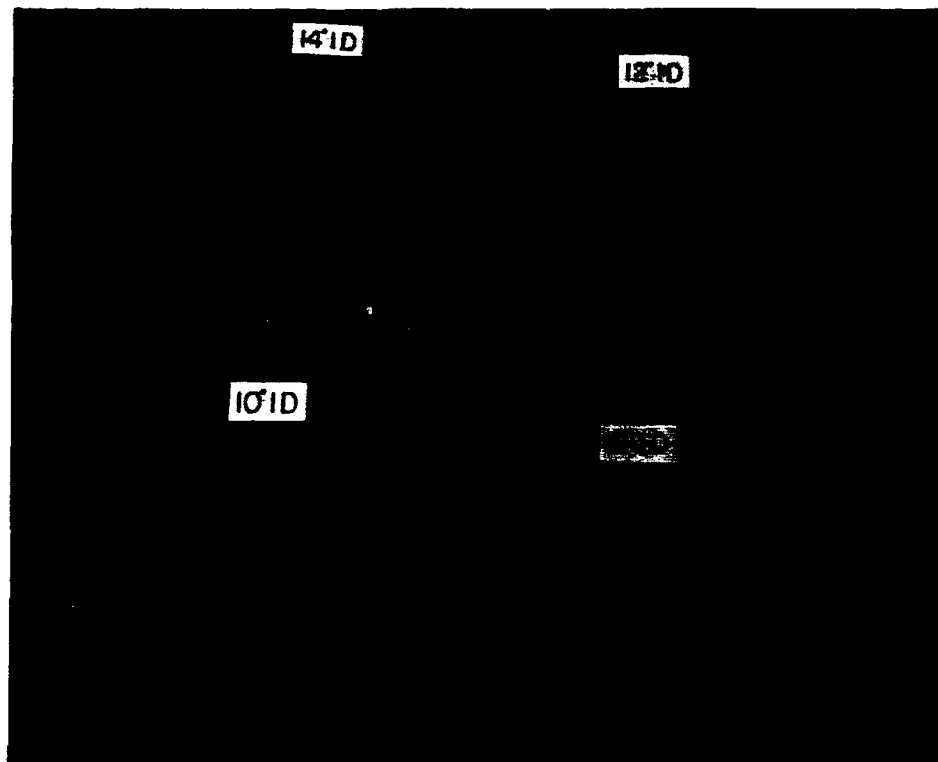


Figure 2. Concrete hemispheres of 16-inch outside diameter.

Test Results

Implosion pressures of spheres and corresponding concrete strengths are presented in Table 1. Figure 4 shows the relationship between wall-thickness-to-outside-diameter ratio (t/D_o) and implosion pressure (P_{im}). The relationship is closely approximated by a straight line. Stachiw⁴ reported a similar linear relationship for spheres with a concrete strength of 11,000 psi as shown in Figure 1.

Another finding, which coincided with earlier work,⁴ was evidence that the concrete had cracked in the plane of the wall. Figure 5 is a view of this in-plane cracking, which was visible in the wall of the sphere with a t/D_o ratio of 0.2500. The following section discusses the development and the influence of these cracks on the behavior of the spheres.

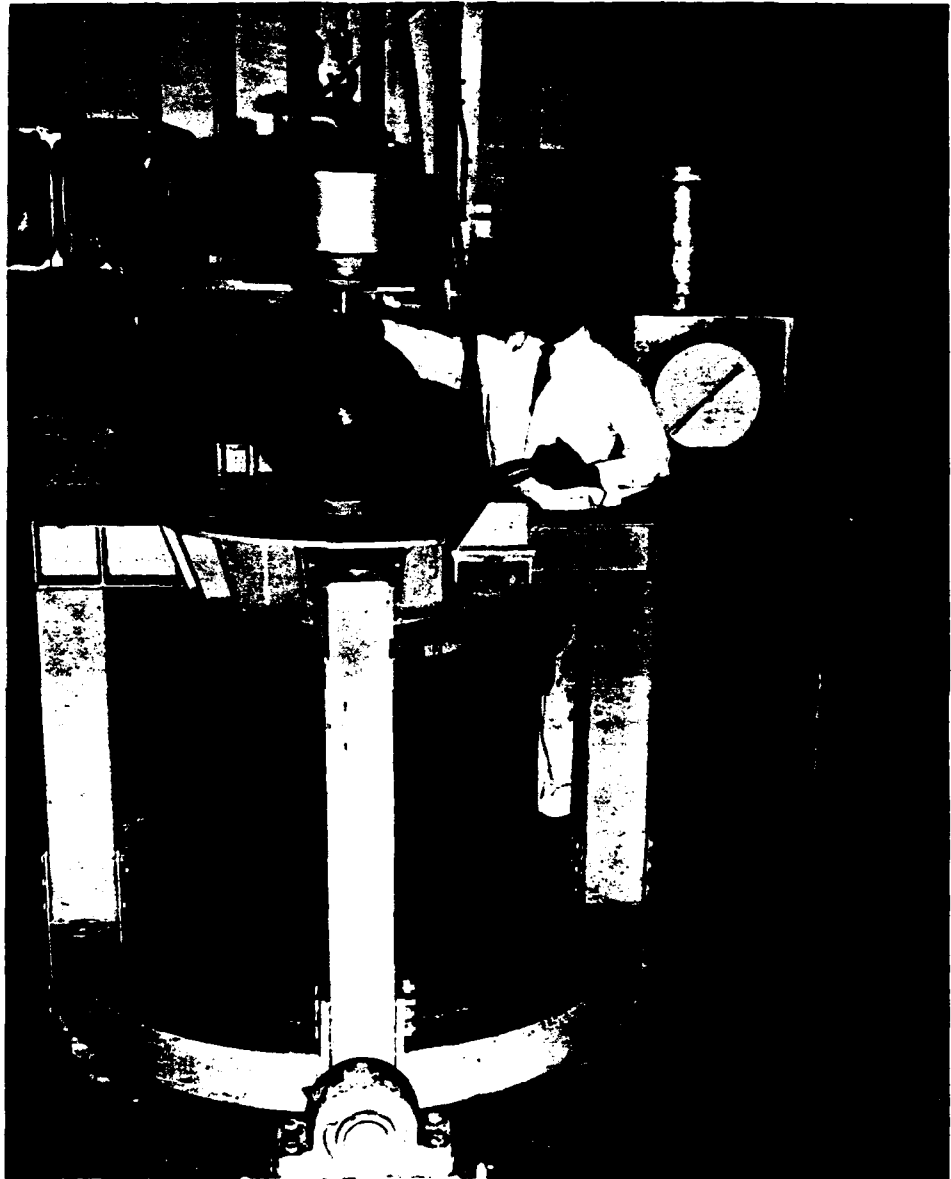


Figure 3. Concrete sphere prior to placement in pressure test facility.

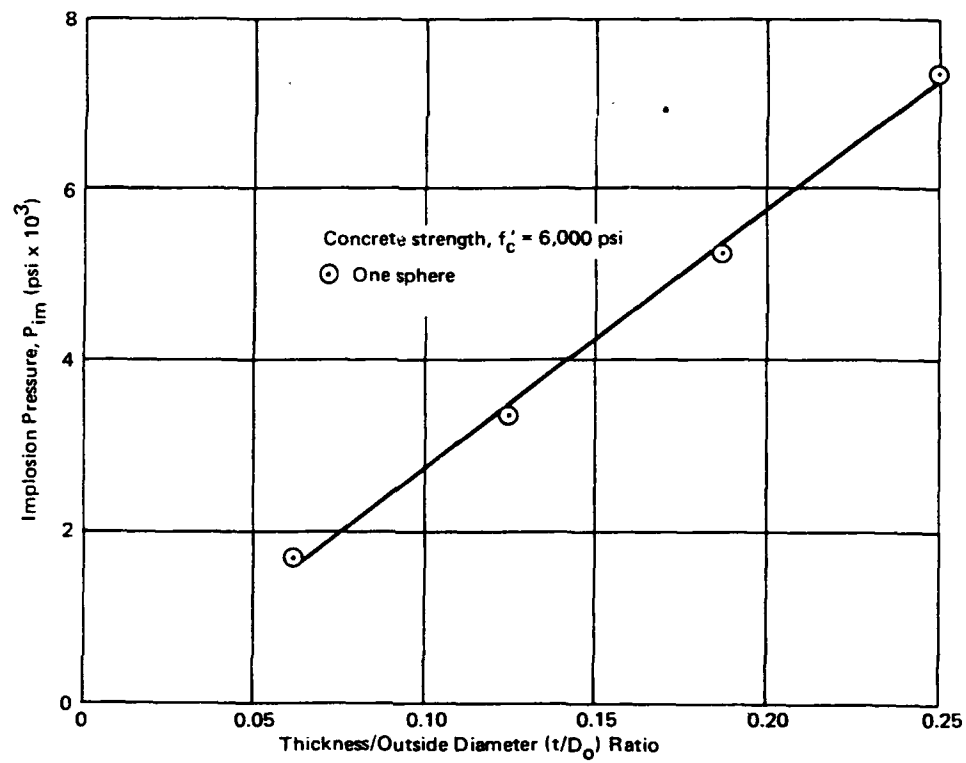


Figure 4. Experimental relationship between implosion pressure and t/D_o ratio for concrete spheres.



Figure 5. Evidence of in-plane cracking in sphere 38, t/D_o ratio 0.2500.

Table 1. Concrete Sphere Test Results

Sphere Number ^a	t/D _o Ratio	Implosion Pressure, P _{im} (psi)	Concrete Strength, ^b f' _c (psi)	P _{im} /f' _c Ratio
35	0.0625	1,710	6,090	0.281
36	0.1250	3,375	5,750	0.587
37	0.1875	5,280	5,990	0.882
38	0.2500	7,370	6,080	1.212

^a Numbering system is continued from Reference 4.

^b Average of six 3 x 6-inch control cylinders tested under uniaxial compression.

DISCUSSION

Introduction

The response of concrete spheres to short-term hydrostatic loading was sequentially: elastic behavior, crack development near the interior wall and, finally, implosion. The development of cracks within the concrete wall relieved strains and commenced a mode of behavior which had an overall effect of increasing the implosion pressures of concrete spheres beyond the limits predicted by elastic theory. Because the presence of such cracks would probably be detrimental to the structural behavior of spheres under cyclic or long-term loading, the initiation of cracking in the concrete wall was defined as a failure mode. In-plane cracking failure is discussed prior to implosion failure so that the effect of cracking on the mechanics of implosion may be better understood.

In-Plane Cracking

A combined stress state is induced in the wall of a thick-walled sphere which is subjected to hydrostatic pressure loading. Most of the wall cross section is under a triaxial stress state where tangential stresses at a defined radius are equal and where the radial stress varies from maximum at the exterior surface to zero at the interior surface. Thus, the interior surface is under biaxial stress. Figure 6 illustrates schematically the stresses that are imposed on elements of the wall at the interior and exterior surfaces. Because the maximum tangential stress exists at the interior surface and because concrete is weaker in biaxial than in triaxial compression, the interior surface is the critical location.

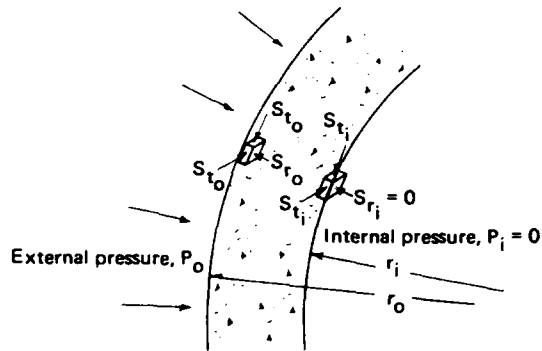


Figure 6. Stresses on elements located at exterior and interior wall surface of concrete sphere loaded under external hydrostatic pressure.

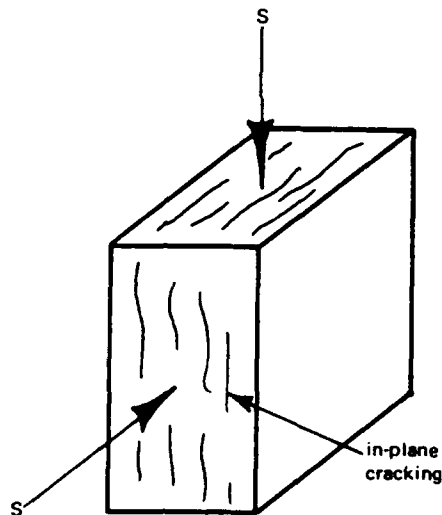


Figure 7. Crack development in concrete under biaxial loading.

The development of cracks in concrete subjected to compressive biaxial stress has been observed by Robinson⁶ to develop in the direction parallel to the maximum principal stresses. His experiments using biaxially loaded concrete slabs showed that cracking occurred in the plane of the slab, as seen in Figure 7, due to the Poisson effect in the unrestrained direction. Similar cracking would be expected to occur in the walls of concrete spheres because biaxial stresses existed at the interior wall and because within the wall the maximum principal stresses in the tangential direction were many times greater than the minimum principal stresses in the radial direction.

Stachiw⁴ reported a relaxation or decrease of strains as shown in Figure 8, while the spheres continually resisted increases in hydrostatic pressure loading. From fragments of imploded spheres, he also observed that cracks existed in the plane of the wall. In the present investigation, in-plane cracking was observed in the fragments of imploded spheres with t/D_o ratios of 0.1875 and 0.2500. Figure 5 shows distinctly a crack which runs in the plane of the wall approximately 1 inch from the exterior surface; this type of cracking on a more extensive basis probably occurred within the 1 inch of concrete missing on the interior surface.

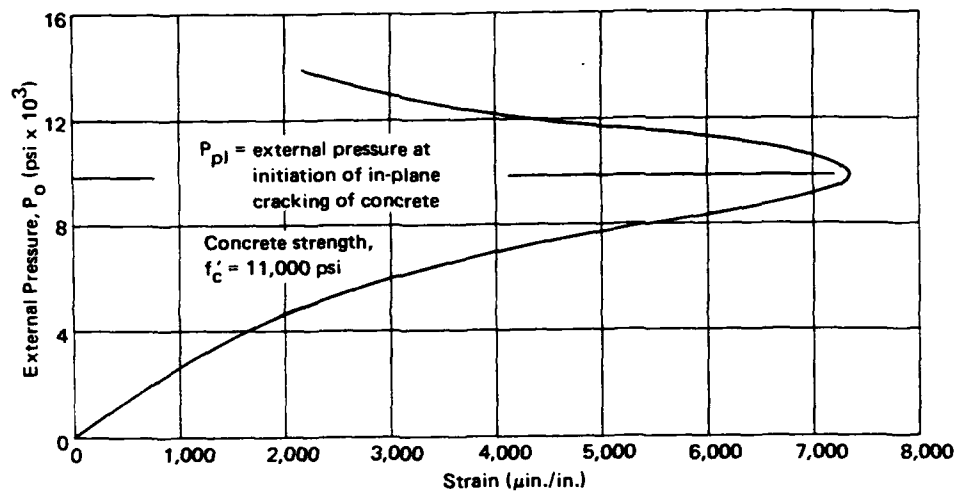


Figure 8. Typical strains on interior wall of sphere with $t/D_o = 0.2500$ (after Stachiw⁴).

From test results presented by Stachiw,⁴ the hydrostatic pressure at which in-plane cracking of concrete commenced, P_{pl} , can be determined and, as shown in Figure 8, was taken at the point where strains began to decrease. Table 2 presents experimental values of in-plane cracking taken from Stachiw's⁴ work, and Figure 9 shows the relation between the pressures at in-plane cracking and implosion. As the wall-thickness-to-outside-diameter ratio increased, the difference in pressures between the two modes of failure also increased.

Table 2. In-Plane Cracking Results

Sphere Number	t/D_o Ratio	Experimental ^a			Calculated ^b P_{pl}/f'_c	$\frac{\text{Exp } P_{pl}/f'_c}{\text{Calc } P_{pl}/f'_c}$
		P_{pl} (psi)	f'_c (psi)	P_{pl}/f'_c		
21	0.0625	3,240	11,240	0.288	0.297	0.97
25	0.1250	5,960	10,920	0.545	0.520	1.05
29	0.1875	7,220	11,530	0.626	0.680	0.92
33	0.2500	8,860	10,920	0.812	0.788	1.03

^a Data was obtained from experimental results after Stachiw.⁴

^b These values were calculated using Equation 5 of this report.

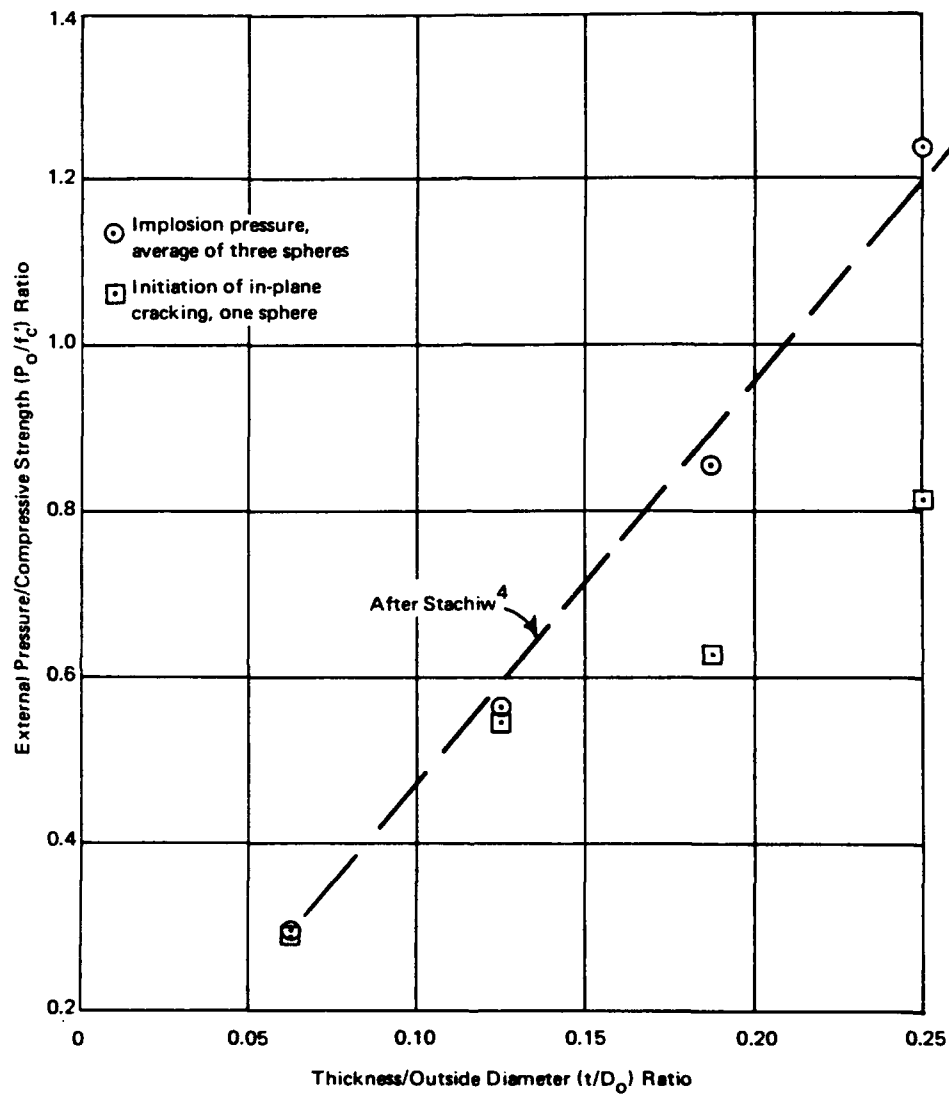


Figure 9. Initiation of in-plane cracking in relation to implosion pressure (after Stachiw⁴).

In order to predict the pressures at which in-plane cracking of concrete commenced, the Lamé classical expression to calculate the stress distribution within a sphere subjected to uniform external pressure was initially applied to the data and was then modified to account for the biaxial strength of concrete. The elastic thick-wall theory in its general form is expressed as follows:

$$S_t = \frac{P_o r_o^3}{2 r^3} \left(\frac{r_i^3 + 2 r^3}{r_o^3 - r_i^3} \right) \quad (1)$$

and

$$S_r = \frac{P_o r_o^3}{r^3} \left(\frac{r^3 - r_i^3}{r_o^3 - r_i^3} \right) \quad (2)$$

where S_t = wall stress in tangential direction (psi)

S_r = wall stress in radial direction (psi)

P_o = external pressure (psi)

r_o = exterior radius (inches)

r_i = interior radius (inches)

r = radius to location in wall under consideration (inches)

To find the stress at the critical location, $r = r_i$ was substituted into Equations 1 and 2. The equations reduced to the form

$$S_t = \frac{3}{2} P_o \left[\frac{1}{1 - \left(\frac{r_i}{r_o} \right)^3} \right] \quad (3)$$

and

$$S_r = 0$$

It was assumed that the pressure at initiation of in-plane cracking, P_{pi} , initiated when the maximum principal stresses equaled f'_c , the compressive strength of the control cylinders. Substituting f'_c for S_t and P_{pi} for P_o in Equation 3 yielded an expression for the pressure at initiation of in-plane cracking in terms of sphere geometry and concrete strength,

$$P_{pi} = \frac{2}{3} f'_c \left[1 - \left(\frac{r_i}{r_o} \right)^3 \right] \quad (4)$$

where P_{pl} = pressure at initiation of in-plane cracking (psi)

f'_c = compressive strength of concrete control cylinders (psi)

Equation 4 is based on elastic thick-wall theory. Figure 10 shows that Equation 4 predicted a lower in-plane cracking pressure than experimentally observed, probably because major cracking did not occur at a wall stress equal to the uniaxial compressive strength. Instead, the improved concrete strength under biaxial compression must have increased the pressure load required to begin in-plane cracking.

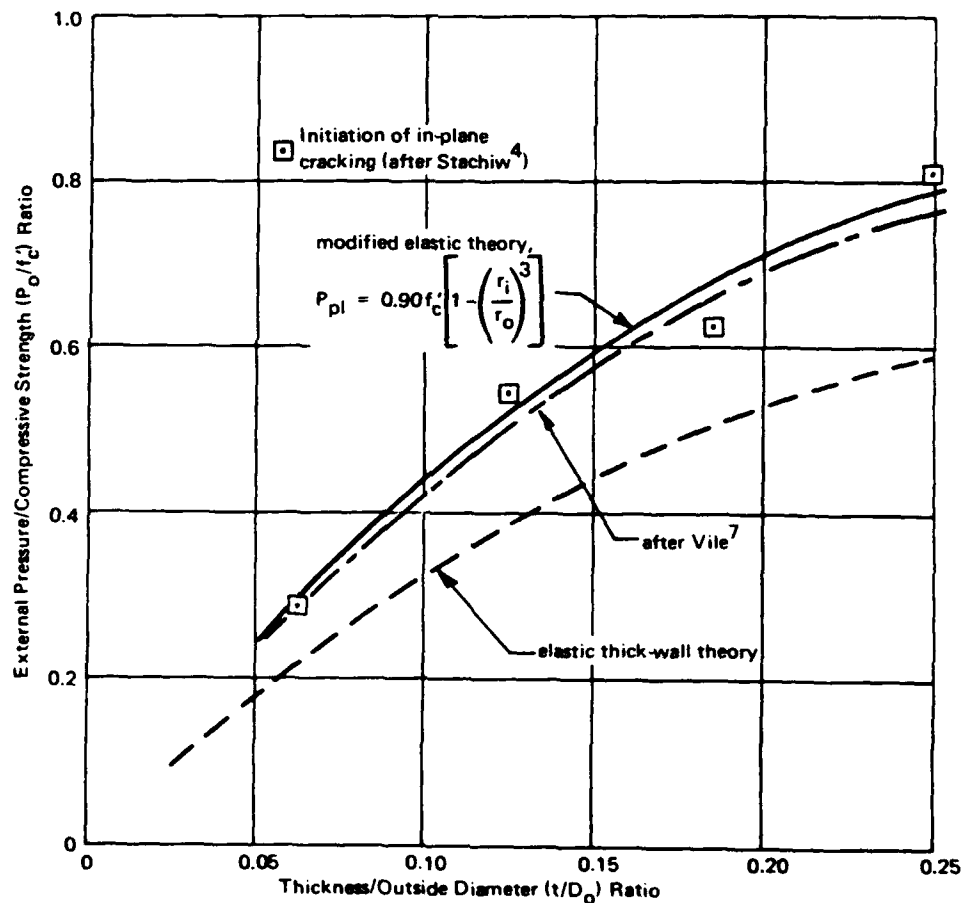


Figure 10. Prediction of in-plane cracking in concrete spheres with various t/D_o ratios.

Vile,⁷ in one of the most comprehensive publications on the strength of concrete and mortar under short-term biaxial loading, reported that the strength of mortar subjected to equal biaxial stresses increased by a factor of 1.30 over the uniaxial strength. (The concrete used in the spheres was technically a mortar.) Figure 10 shows the effect of increasing the concrete strength, f'_c , in Equation 4 by Vile's factor of 1.30. The function is in agreement with experimental data; however, the curve is still conservative which indicates that Vile's factor of 1.30 may possibly be low for the spheres. The biaxial strength factor could have been greater for the concrete in the spherical test specimens than in Vile's cube test specimens because in the sphere the curvature of the interior surface may have contributed a positive influence on strength due to geometry; also the triaxially stressed concrete adjacent to the interior surface may have had a small but positive effect on increasing the strength.

The actual biaxial strength of the concrete in the spheres was determined by assuming that for the spheres with a t/D_o ratio of 0.0625, in-plane crack initiation and implosion occurred simultaneously; the assumption appeared valid for the test results. Equation 3 yielded an ultimate biaxial stress of 15,300 psi. The uniaxial concrete strength from control cylinders was 11,340 psi; therefore, the uniaxial-to-biaxial strength increase was a factor of 1.35. Equation 4 was modified to account for this increase in uniaxial concrete strength as follows:

$$P_{pi} = \frac{2}{3} (1.35) f'_c \left[1 - \left(\frac{r_i}{r_o} \right)^3 \right]$$

or

$$P_{pi} = 0.90 f'_c \left[1 - \left(\frac{r_i}{r_o} \right)^3 \right] \quad (5)$$

Figure 10 shows that Equation 5, a modified elastic theory expression which accounted for the biaxial strength of concrete, predicted the pressure at initiation of in-plane cracking in good agreement with the experimental results. Table 2 presents the correlation between experimental and calculated values of in-plane cracking pressures.

Implosion Failure Mode

Including Stachiw's data,²⁻⁴ a total of 27 spheres have been tested to implosion under short-term loading conditions. Table 3 summarizes the test results for these specimens, and Figure 11 shows the influence of concrete strength on the implosion pressures of spheres of various t/D_o ratios. In general, an increase in concrete strength resulted in an increase in implosion

pressure. Figure 12 shows the relationship between two nondimensional parameters (a) implosion-pressure-to-concrete-strength ratio (P_{im}/f'_c) and (b) wall-thickness-to-outside-diameter ratio (t/D_o) as a straight-line function. A least squares analysis gave the following empirical relationship.

$$P_{im} = 4.8 f'_c \left(\frac{t}{D_o} \right) \quad 0.06 \leq t/D_o \leq 0.25 \quad (6)$$

where P_{im} = implosion pressure (psi)

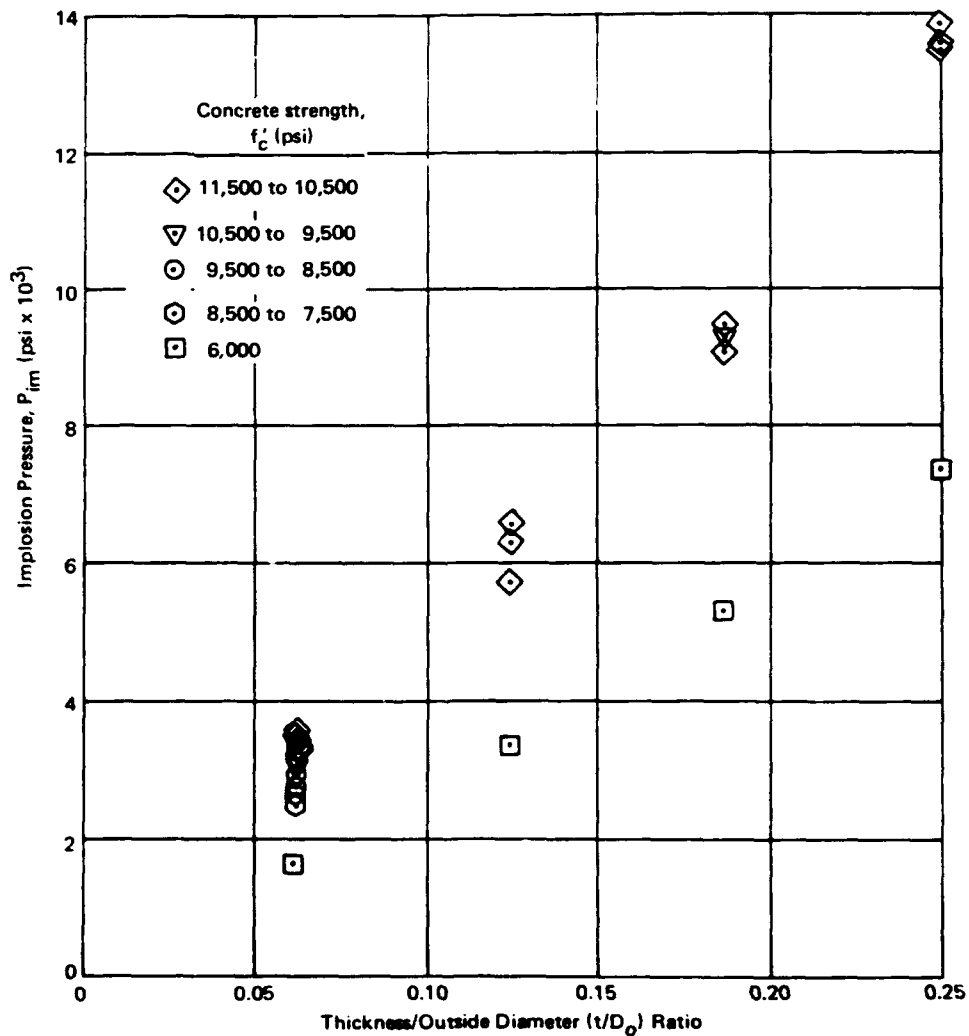


Figure 11. Implosion pressures of spheres of various concrete strengths.

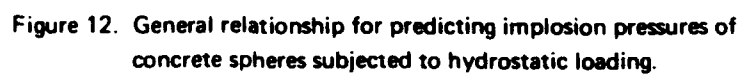


Table 3. Summary of Implosion Test Results^a

Sphere ^b	t/D _o Ratio	Implosion Pressure, P _{im} (psi)	Concrete Strength, f' _c (psi)	P _{im} /f' _c Ratio
1	0.0625	3,100	8,990	0.345
2	0.0625	3,050	9,750	0.313
3	0.0625	3,200	9,930	0.322
5	0.0625	2,850	8,160	0.349
6	0.0625	2,500	8,140	0.307
8	0.0625	3,600	11,200	0.322
12	0.0625	2,750	7,790	0.353
14	0.0625	3,300	9,640	0.343
15	0.0625	3,485	11,210	0.311
16	0.0625	3,400	11,170	0.304
18	0.0625	3,375	11,480	0.294
19	0.0625	3,450	11,270	0.306
20	0.0625	3,425	11,530	0.297
21	0.0625	3,240	11,240	0.288
23	0.1250	5,720	11,190	0.512
24	0.1250	6,330	11,040	0.573
25	0.1250	6,590	10,920	0.602
27	0.1875	9,250	10,370	0.892
28	0.1875	9,175	10,830	0.846
29	0.1875	9,500	11,530	0.823
31	0.2500	13,800	10,990	1.255
32	0.2500	13,575	11,180	1.215
33	0.2500	13,550	10,920	1.240
35	0.0625	1,710	6,090	0.281
36	0.1250	3,375	5,750	0.587
37	0.1875	5,280	5,990	0.882
38	0.2500	7,370	6,080	1.212

^a Sphere numbers 1-16 were subjected to various loading conditions. Spheres 18-38 were tested under identical loading conditions where pressurization rate was 100 psi/min.

^b Concrete spheres were all waterproofed except numbers 5, 6, and 12. Missing sphere numbers pertain to spheres that were used to study other variables.

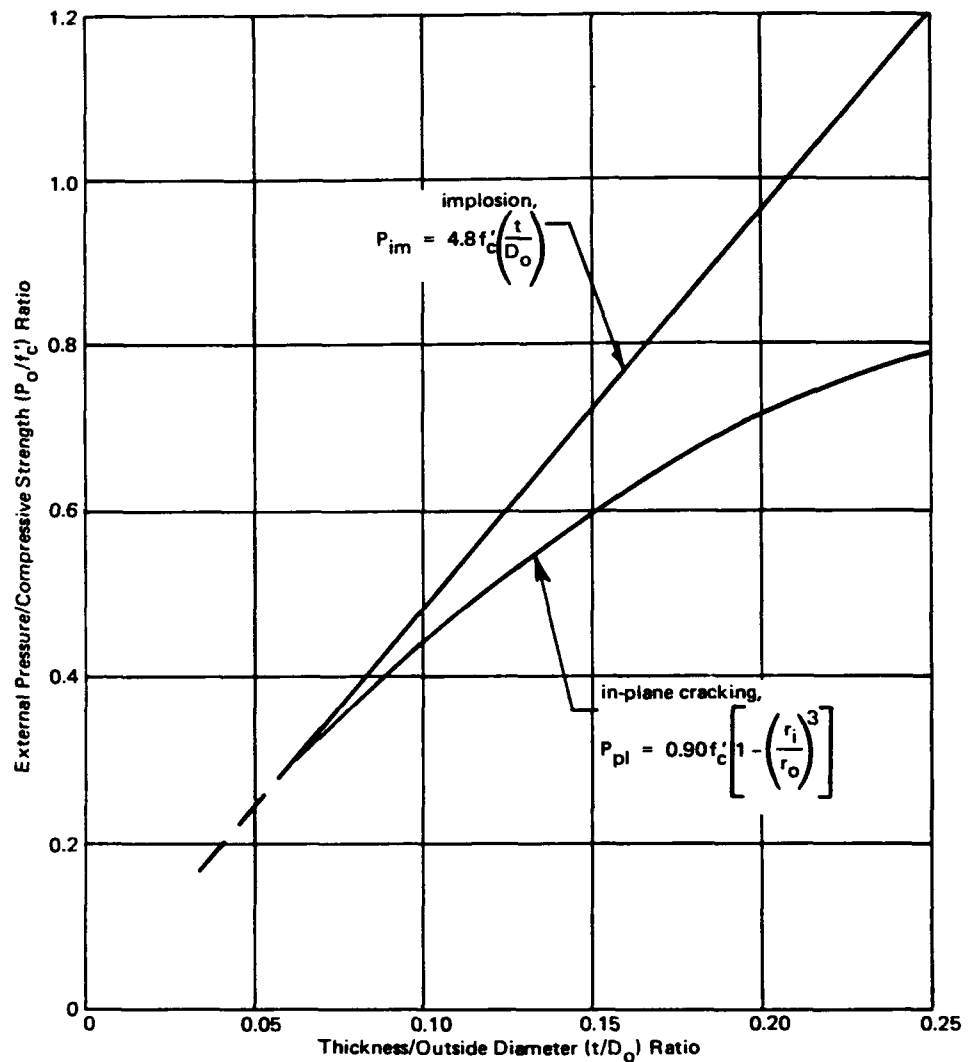


Figure 13. Comparison of failure modes for concrete spheres subjected to hydrostatic loading.

Figure 13 graphically compares the implosion and in-plane cracking modes of failure for hydrostatically loaded spheres. The deviation between the modes of failure resulted from in-plane cracks which caused a redistribution of stresses within the wall. With commencement of in-plane cracking, the highest stresses on the interior wall were relieved and the concrete nearer midthickness sustained increased load. Within the wall triaxial stress conditions existed so the concrete was capable of attaining considerably higher levels of stress than concrete subjected to uniaxial stresses. As the wall thickness became greater, two conditions aided in increasing the implosion failure pressure of the sphere beyond that predicted by elastic thick-wall theory. The first was that a greater percent area across the wall reached the ultimate concrete compressive

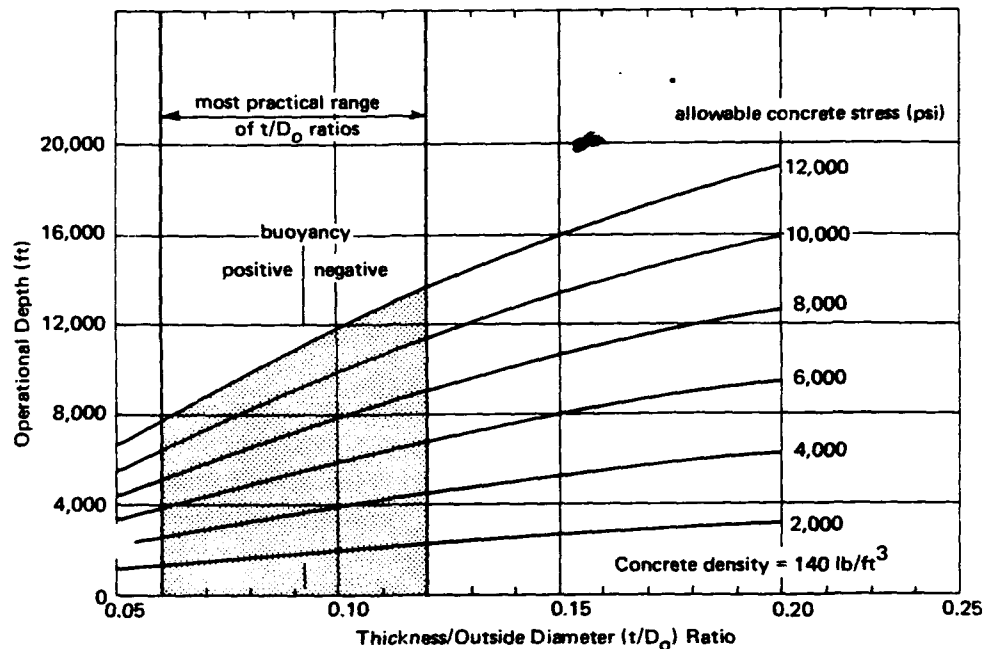


Figure 14. Tentative operational depth ranges of concrete spheres based on the failure mode of in-plane cracking.

strength resulting in a near uniform stress distribution across the wall. The second was that the greater wall thickness confined the concrete more effectively than in the thinner walls so that the actual ultimate compressive strength of the concrete was greater in the thicker walled spheres. Hence, as the wall thickness increased the concrete was capable of attaining a higher and more uniform stress state than that in the thinner walled spheres. This behavior would permit the possibility of attaining a straight-line relationship between P_{im}/f'_c and t/D_o .

UNDERWATER CONCRETE STRUCTURAL APPLICATIONS

The depth range for which concrete structures have application in the ocean can be forecast on the basis of the experimental information generated to date. It is important that a tentative ocean depth range for concrete be ascribed so that ocean structural engineers are cognizant of the potential of concrete for undersea construction. Figure 14 shows tentative operational depths for concrete spheres for a wide range of t/D_o ratios and allowable concrete strengths. The curves are based on initiation of in-plane cracking (Equation 5). A factor of safety can be applied to the curves by the individual

reader by assuming an *allowable* concrete stress (as opposed to the ultimate concrete strength). State-of-the-art concrete technology would permit the upper limit on *allowable* concrete strength to be approximately 4,000 psi; however, in the near future allowable strengths on the order of 10,000 psi may be feasible with the development of concrete-polymer materials.⁸

Buoyancy considerations constrain the practical range of t/D_o ratios for concrete spheres to between 0.06 and 0.12. Hence, at the present time, 3,000 feet in the ocean appears as the limiting operational depth for concrete spheres; however, this depth will become greater as concrete technology advances.

Another design constraint on underwater structures is the ratio of the hull weight to the weight of displaced seawater. (Positively buoyant structures have a weight/displacement ratio of less than 1.) Figure 15 shows the relationship between weight/displacement and t/D_o ratios for various densities of concrete. The figure portrays the design flexibility inherent in using concrete as a construction material for creating positively or negatively buoyant spheres.

The major advantage of utilizing concrete in pressure-resistant structures is that very large installations, 50 feet in diameter and greater, could be built economically. Spheres having a constant t/D_o ratio but an increase in outside diameter have an exponential weight increase; hence, for large diameter spheres, small changes in the weight/displacement ratio represent significant changes in actual pounds of buoyancy. Therefore, a requirement of large facilities is to have a weight/displacement ratio that is in the approximate range of 0.90 to 1.10; because outside this range the actual buoyancy, either positive or negative, becomes excessive. Figures 16 and 17 show actual buoyancy values for various t/D_o ratios; note in Figure 16 that a sphere 50 feet in outside diameter with a t/D_o ratio of 0.08 (or a 4.0-foot wall thickness) would have a positive buoyancy of 400,000 pounds, but by increasing the t/D_o ratio to 0.09 (a 4.5-foot wall thickness) the buoyancy would be reduced to 100,000 pounds.

Permanent facilities located on or under the ocean floor will eventually represent a large portion of all underwater structures, although at present, no such facilities exist which are not land connected. However, with the advent of new generation submersibles capable of carrying high payloads, men and equipment will be easily transferred to and from permanent structures. Concrete as a material will someday be as important for underwater construction as it is on land today.

Applications for permanent facilities are numerous. Some examples are concrete containment vessels for undersea nuclear reactors; facilities to function as undersea garages for the repair of submarines; stations to monitor all sea-going vessels; and enclosures to process minerals, pump oil, or farm sea life.

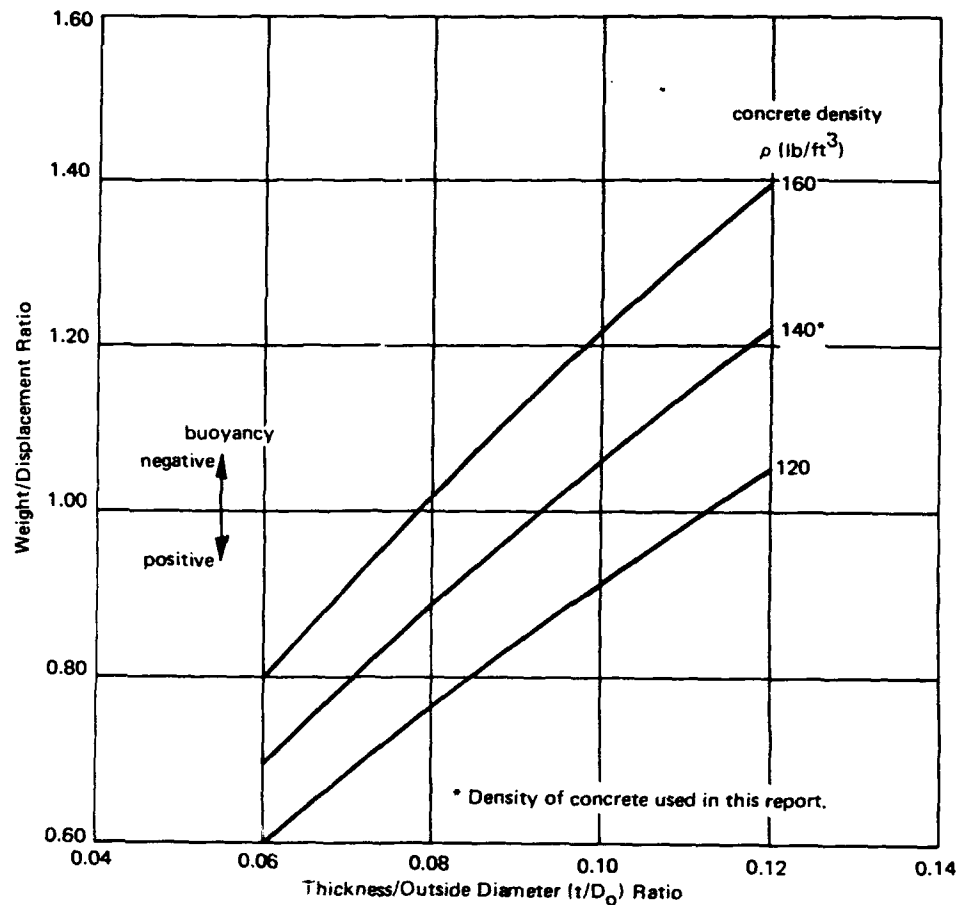


Figure 15. Weight/displacement values for concrete spheres of various t/D_o ratios.

FINDINGS

1. A straight-line relationship between implosion pressure and wall-thickness-to-outside-diameter ratio was established for a given concrete strength; the slope of the straight-line relationship increased for increases in concrete strength.
2. Two modes of failure, in-plane cracking and implosion, existed for thick-walled concrete spheres having a t/D_o ratio greater than 0.0625, while spheres having a t/D_o ratio of 0.0625 appeared to experience implosion failure only.
3. A modified elastic theory expression, (Equation 5) which accounted for the strength of concrete under combined stresses was developed to predict the pressure at initiation of in-plane cracking in concrete spheres.
4. A linear, empirical expression, (Equation 6) was developed to predict the implosion pressures of small concrete spheres.

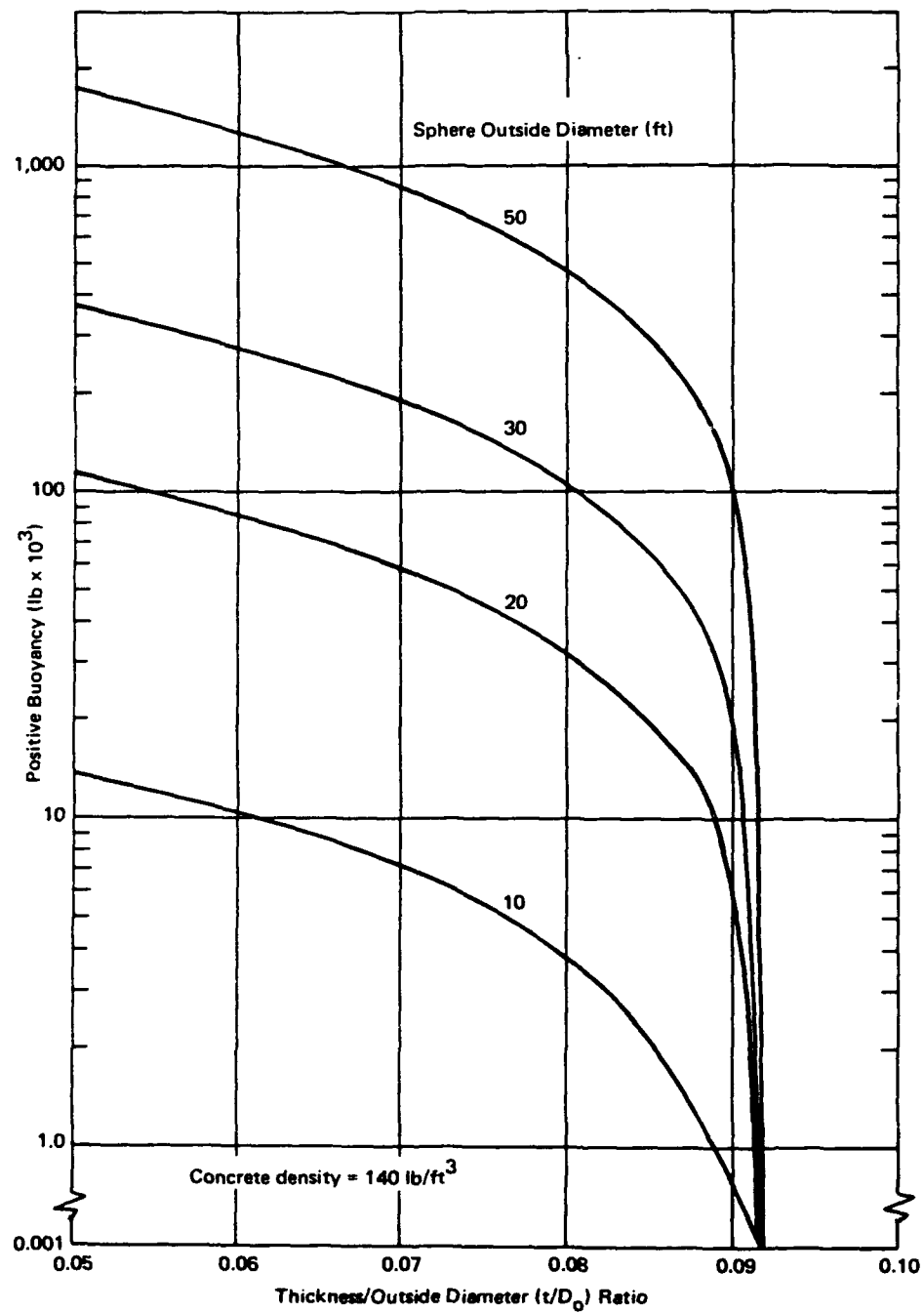


Figure 16. Positive buoyancy values for concrete spheres.

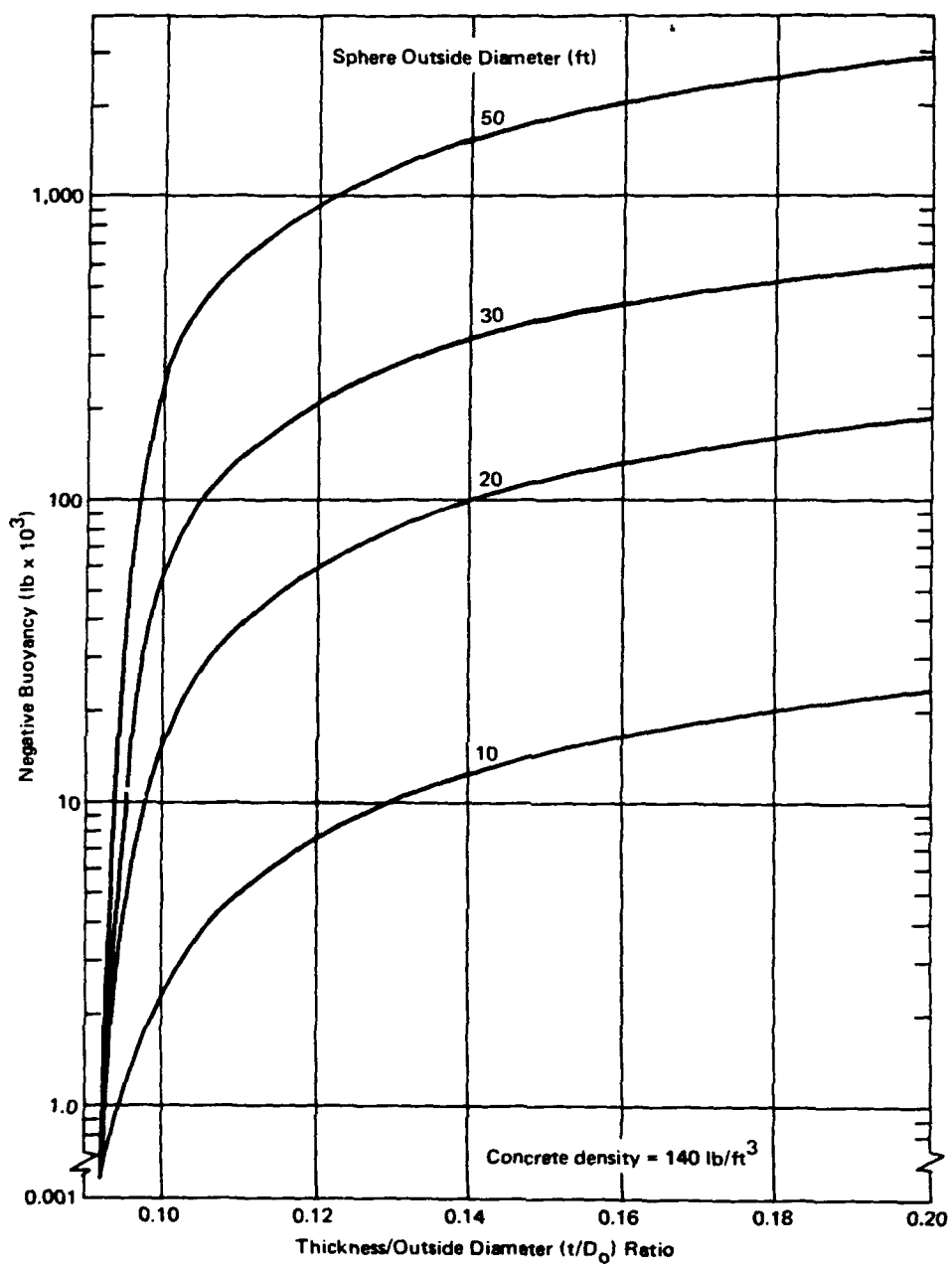


Figure 17. Negative buoyancy values for concrete spheres.

CONCLUSIONS AND RECOMMENDATIONS

It appears that small concrete spheres subjected to short-term hydrostatic loading implode at pressures which are linearly related to the wall-thickness-to-outside-diameter ratio in the range 0.0625 through 0.2500.

Caution must be exercised in applying the results presented on in-plane cracking. The expression to predict this failure mode (Equation 5) was substantiated by only three sphere tests, whereas the implosion failure expression (Equation 6) was supported by 27 tests. However, the presence of an in-plane cracking failure mode prior to implosion was strongly evident from strain data, and the development of the expression to predict the pressure at in-plane cracking was rational. Hence, the authors recommend that tentative, generalized predictions on the depth capability of concrete spheres in the ocean be based upon the pressure at initiation of in-plane cracking, and that concrete be considered as a construction material for underwater structures for use above the depth of 3,000 feet.

Appendix

SPECIMEN FABRICATION AND TEST PROCEDURE

SPECIMEN DESCRIPTION

Dimensions

Test specimens were concrete spheres having a constant outside diameter of 16 inches with inside diameters of 8, 10, 12 and 14 inches. Dimensional tolerances on the diameters were held to within $\pm 1/32$ inch.

Material

Type II, low heat of hydration, portland cement and San Gabriel river aggregate were the concrete constituents. Aggregate proportions are outlined in Table 4. The water/cement ratio was 0.70 by weight, and the aggregate/cement ratio was 3.30 by weight. Concrete control cylinders, 3 x 6 inches, attained a uniaxial compressive strength of approximately 6,000 psi in a curing period of 28 days. The curing conditions were 14 days at 100% RH and 73°F and 14 days at room conditions.

Table 4. Aggregate Proportions of Concrete

Passing Screen No.	Retained on Screen No.	Percent Retained
4	8	29.6
8	16	20.8
16	30	14.7
30	50	10.3
50	100	7.3
100	pan	17.3
Total		100.0

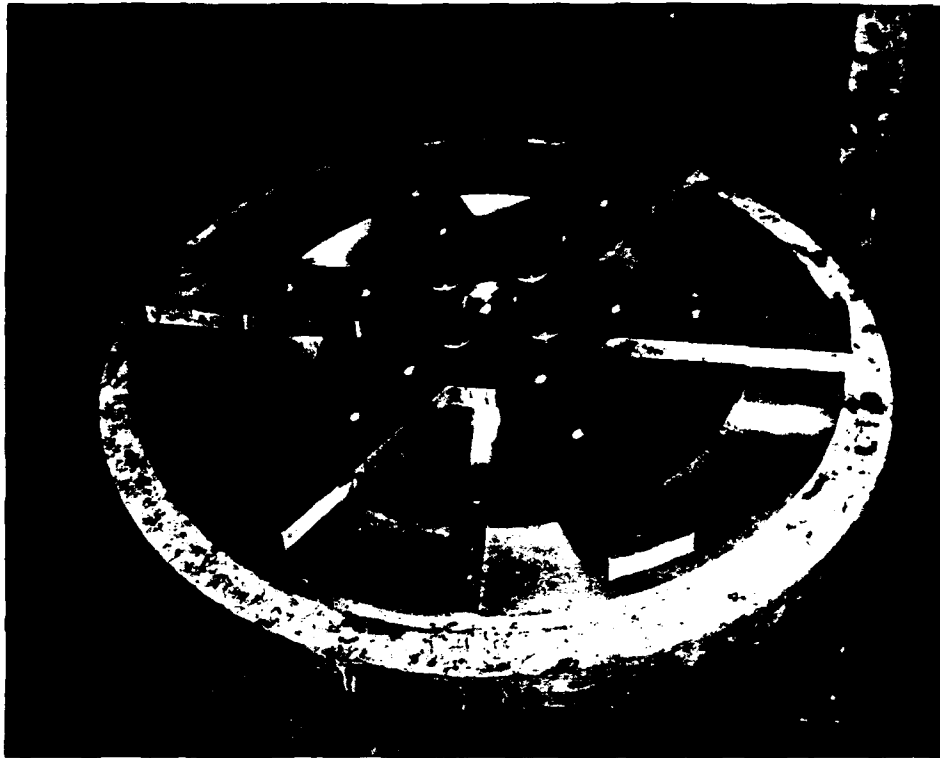


Figure 18. Mold for casting 8-inch-ID, 4-inch wall thickness concrete hemispheres.

Casting

Concrete hemisphere sections were cast in a rigid aluminum mold. Figure 18 shows the assembled mold ready for casting concrete, while Figure 19 shows the various interior molds for the construction of hemispheres with different wall thicknesses. The molds were prepared for casting by initially spraying the aluminum with clear enamel paint and then applying a coat of silicone grease.

An external form vibrator was attached to the underside of the mold and was in operation throughout casting of the concrete. The concrete was mixed in a pan-type mixer for a total of 3.0 minutes and then slowly placed into the mold, usually within the next 4 minutes.

The day after casting, the hemisphere was removed from the mold and the interior surface was usually pitted with numerous small air pockets. These voids were fully exposed by rubbing down the surface with steel wool, and then the voids were filled with a cement paste consisting of Type III portland cement and pan-size aggregate in a ratio of 1:1 with only enough water to form a workable mix.

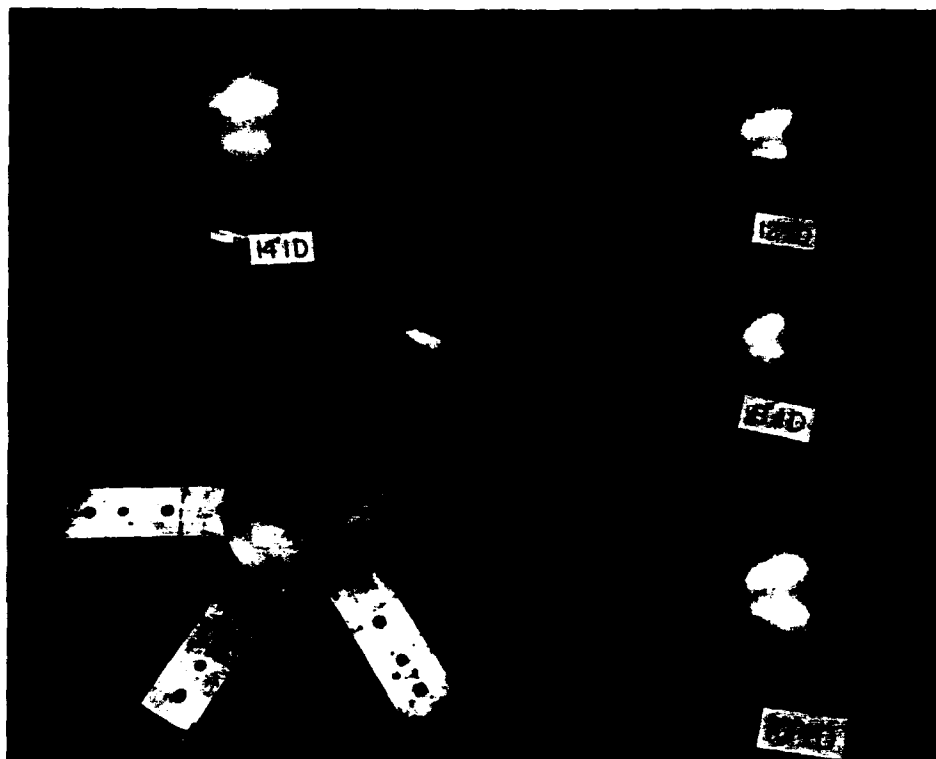


Figure 19. Interior molds for concrete hemispheres.

Fabrication

Spheres were fabricated by bonding together two hemisphere sections with an epoxy adhesive. Each section had its annular mating surface ground smooth by rotating the hemisphere on a sheet of plate glass which was covered with water and no. 60 silica carbide grit. The mating surfaces were then cleaned and etched with 10% hydrochloric acid solution to assure good bond between the epoxy and concrete. The final thickness of the epoxy joint was 1/32 to 1/16 inch. All spheres were waterproofed by coating the exterior surface with three applications of a waterproofing epoxy.

A schematic diagram of a fabricated concrete sphere is shown in Figure 20. The sphere was attached to the head of the pressure vessel by a steel, through-hull penetration located at the apex of the top hemisphere and bonded to the concrete with epoxy. A hole through the middle of the penetration provided atmospheric pressure to the interior of the sphere.

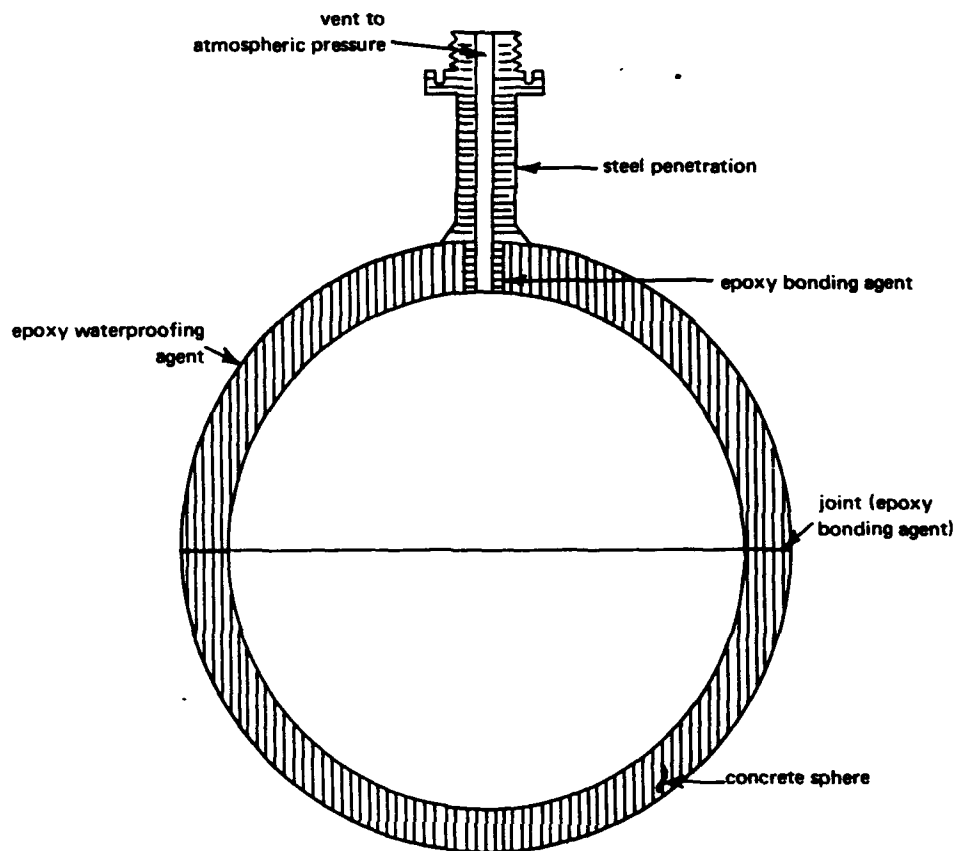


Figure 20. Schematic diagram of concrete sphere assembled for testing.

TEST PROCEDURE

The concrete spheres were tested to failure in an 18-inch-ID pressure vessel having an operational capability of 20,000 psi. Freshwater was used as the pressurizing medium. Hydrostatic pressure loading was applied at a constant rate of 100 psi/min until implosion occurred, and the implosion pressure was recorded. Implosion was signaled by a sharp noise and a rapid decrease in hydrostatic pressure.

The fragments of the imploded spheres were removed from the pressure vessels and inspected for in-plane cracking of the wall. Figures 21 through 24 show the relative size of the fragments of the test specimens.



Figure 21. Some fragments of sphere 35, t/D_0 ratio 0.0625.



Figure 22. Some fragments of sphere 36, t/D_0 ratio 0.1250.

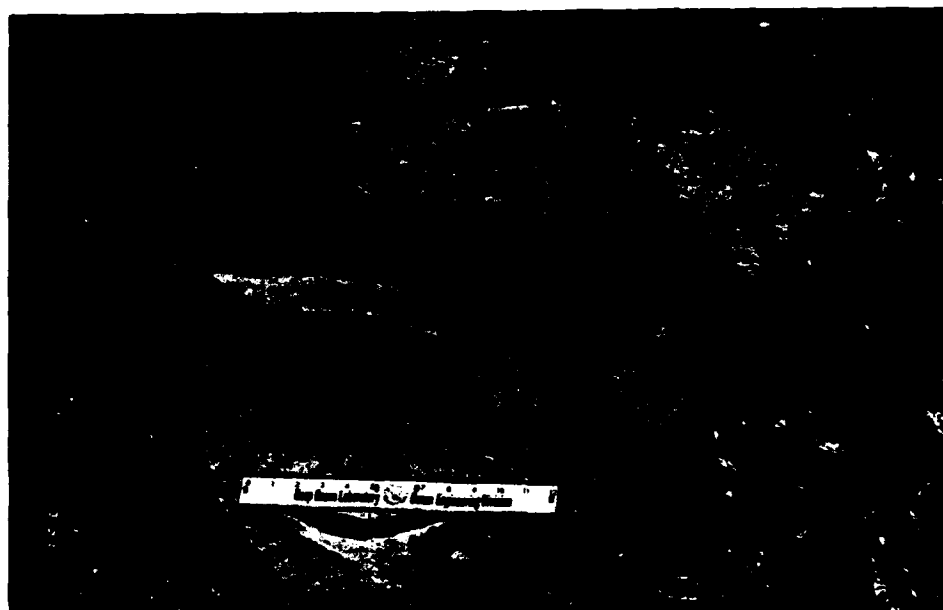


Figure 23. Some fragments of sphere 37, t/D_0 ratio 0.1875.

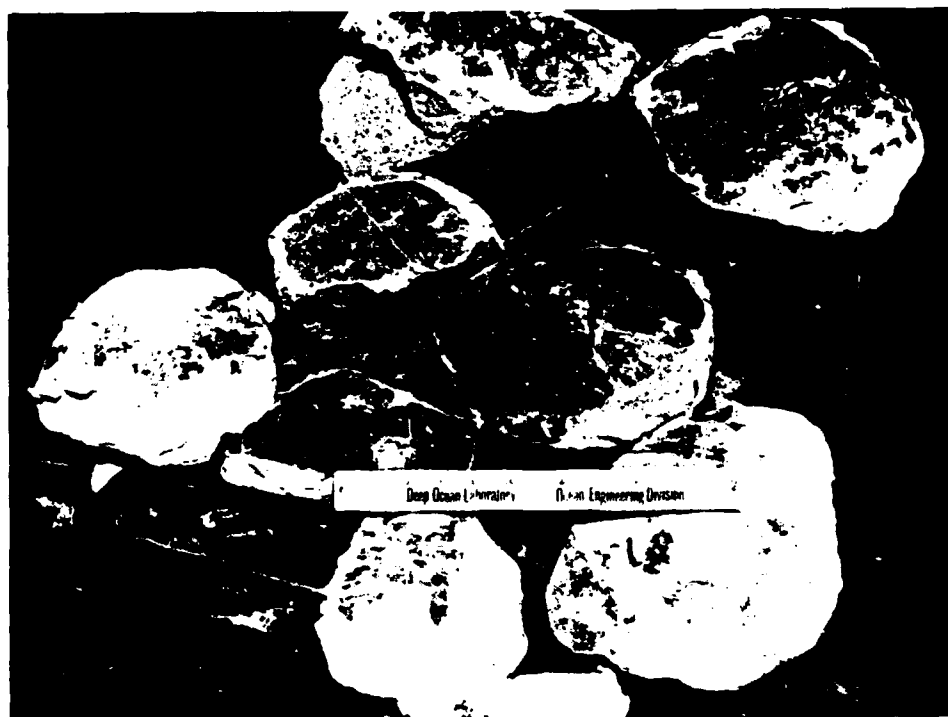


Figure 24. Some fragments of sphere 38, t/D_0 ratio 0.2500.

REFERENCES

1. C. M. Wakeman, et al. "Use of concrete in marine environments," American Concrete Institute, Journal, Proceedings, vol. 54, no. 10, Apr. 1958, pp. 841-856.
2. Naval Civil Engineering Laboratory. Technical Report R-517: Behavior of spherical concrete hulls under hydrostatic loading, pt. I. Exploratory investigation, by J. D. Stachiw and K. O. Gray. Port Hueneme, Calif., Mar. 1967. (AD 649290)
- 3.———. Technical Report R-547: Behavior of spherical concrete hulls under hydrostatic loading, pt. II. Effect of penetrations, by J. D. Stachiw. Port Hueneme, Calif., Oct. 1967. (AD 661187)
- 4.———. Technical Report R-588: Behavior of spherical concrete hulls under hydrostatic loading, pt. III. Relationship between thickness-to-diameter ratio and critical pressures, strains, and water permeation rates, by J. D. Stachiw and K. Mack. Port Hueneme, Calif., June 1968. (AD 835492L)
5. R. J. Roark. Formulas for stress and strain, 4th ed. New York, McGraw-Hill, 1965.
6. G. S. Robinson. "Behavior of concrete in biaxial compression," American Society of Civil Engineers, Proceedings, Journal of the Structural Division, vol. 93, no. 1, Feb. 1967, pp. 71-86.
7. G. W. D. Vile. "Strength of concrete under short-term static biaxial loading," paper presented at International Conference on the Structure of Concrete and its Behaviour Under Load, London, England, Sept. 1965. (Paper no. F2)
8. Brookhaven National Laboratory. Report BNL-50134: Concrete-polymer materials. First Topical Report, by M. Steinberg, et al. Upton, N. Y., Dec. 1968. (Also Bureau of Reclamation, GEN. REP.-41, Denver, Col.)

DISTRIBUTION LIST

SNDL Code	No. of Activities	Total Copies	
—	1	20	Defense Documentation Center
FKAIC	1	10	Naval Facilities Engineering Command
FKNI	13	13	NAVFAC Engineering Field Divisions
FKN5	9	9	Public Works Centers
FA25	1	1	Public Works Center
—	14	14	RDT&E Liaison Officers at NAVFAC Engineering Field Divisions and Construction Battalion Centers
—	350	350	NCEL Special Distribution List No. 9 for persons and activities interested in reports on Deep Ocean Studies

LIST OF SYMBOLS

D_o	Outside diameter of sphere (in.)
f'_c	Uniaxial compressive strength of concrete control cylinder (psi)
P_i	Pressure inside sphere (psi)
P_{im}	Externally applied hydrostatic pressure to cause implosion of sphere (psi)
P_o	Pressure outside sphere (psi)
P_{pi}	Pressure at initiation of in-plane cracking (psi)
r	Radius of sphere under consideration (in.)
r_i	Inside radius of sphere (in.)
r_o	Outside radius of sphere (in.)
S	Stress in sphere wall thickness (psi)
S_r	Radial stress in sphere wall thickness (psi)
S_{r_i}	Radial stress at inside surface of sphere wall thickness (psi)
S_{r_o}	Radial stress at outside surface of sphere wall thickness (psi)
S_t	Tangential stress in sphere wall thickness (psi)
S_{t_i}	Tangential stress at inside surface of sphere wall thickness (psi)
S_{t_o}	Tangential stress at outside surface of sphere wall thickness (psi)
t	Wall thickness of sphere (in.)
ρ	Density of concrete (lb/ft ³)

Naval Civil Engineering Laboratory

INFLUENCE OF END-CLOSURE STIFFNESS ON
BEHAVIOR OF CONCRETE CYLINDRICAL HULLS
SUBJECTED TO HYDROSTATIC LOADING, by L. F. Kahn
TR-740 53 p. illus October 1971 Unclassified

1. Concrete hulls I. 3.1610-1

Twelve model concrete cylindrical hulls were subjected to hydrostatic loading to determine the influence of end-closure stiffness on implosion pressure and strain behavior of the cylinders. Results showed that variation of end-closure stiffness did not reduce the implosion pressure below that of a cylinder with a free end condition or below the implosion pressure predicted by elastic thick-wall theory. To vary the closure stiffness, concrete hemisphere and steel plate end closures were used to simulate free, pinned, beveled, and fixed end conditions. Strain variations along the length of the cylinders indicated that the influence of the closure was limited to a distance of one diameter from the closure. Recommendations are presented to aid in the design of concrete cylindrical hulls.

Naval Civil Engineering Laboratory

INFLUENCE OF END-CLOSURE STIFFNESS ON
BEHAVIOR OF CONCRETE CYLINDRICAL HULLS
SUBJECTED TO HYDROSTATIC LOADING, by L. F. Kahn
TR-740 53 p. illus October 1971 Unclassified

1. Concrete hulls I. 3.1610-1

Twelve model concrete cylindrical hulls were subjected to hydrostatic loading to determine the influence of end-closure stiffness on implosion pressure and strain behavior of the cylinders. Results showed that variation of end-closure stiffness did not reduce the implosion pressure below that of a cylinder with a free end condition or below the implosion pressure predicted by elastic thick-wall theory. To vary the closure stiffness, concrete hemisphere and steel plate end closures were used to simulate free, pinned, beveled, and fixed end conditions. Strain variations along the length of the cylinders indicated that the influence of the closure was limited to a distance of one diameter from the closure. Recommendations are presented to aid in the design of concrete cylindrical hulls.

Naval Civil Engineering Laboratory

INFLUENCE OF END-CLOSURE STIFFNESS ON
BEHAVIOR OF CONCRETE CYLINDRICAL HULLS
SUBJECTED TO HYDROSTATIC LOADING, by L. F. Kahn
TR-740 53 p. illus October 1971 Unclassified

1. Concrete hulls I. 3.1610-1

Twelve model concrete cylindrical hulls were subjected to hydrostatic loading to determine the influence of end-closure stiffness on implosion pressure and strain behavior of the cylinders. Results showed that variation of end-closure stiffness did not reduce the implosion pressure below that of a cylinder with a free end condition or below the implosion pressure predicted by elastic thick-wall theory. To vary the closure stiffness, concrete hemisphere and steel plate end closures were used to simulate free, pinned, beveled, and fixed end conditions. Strain variations along the length of the cylinders indicated that the influence of the closure was limited to a distance of one diameter from the closure. Recommendations are presented to aid in the design of concrete cylindrical hulls.

Naval Civil Engineering Laboratory

INFLUENCE OF END-CLOSURE STIFFNESS ON
BEHAVIOR OF CONCRETE CYLINDRICAL HULLS
SUBJECTED TO HYDROSTATIC LOADING, by L. F. Kahn
TR-740 53 p. illus October 1971 Unclassified

1. Concrete hulls I. 3.1610-1

Twelve model concrete cylindrical hulls were subjected to hydrostatic loading to determine the influence of end-closure stiffness on implosion pressure and strain behavior of the cylinders. Results showed that variation of end-closure stiffness did not reduce the implosion pressure below that of a cylinder with a free end condition or below the implosion pressure predicted by elastic thick-wall theory. To vary the closure stiffness, concrete hemisphere and steel plate end closures were used to simulate free, pinned, beveled, and fixed end conditions. Strain variations along the length of the cylinders indicated that the influence of the closure was limited to a distance of one diameter from the closure. Recommendations are presented to aid in the design of concrete cylindrical hulls.

Unclassified

Security Classification

DOCUMENT CONTROL DATA - R & D		
<i>Security classification of title, body of abstract and indexing annotation must be entered when the overall report is classified</i>		
1. ORIGINATING ACTIVITY (Corporate author) Naval Civil Engineering Laboratory Port Hueneme, California 93041		2a. REPORT SECURITY CLASSIFICATION Unclassified
		2b. GROUP
3. REPORT TITLE FAILURE OF THICK-WALLED CONCRETE SPHERES SUBJECTED TO HYDROSTATIC LOADING		
4. DESCRIPTIVE NOTES (Type of report and inclusive dates) Not final; June 1968-January 1969		
5. AUTHOR(S) (First name, middle initial, last name) H. H. Haynes and R. A. Hoofnagle		
6. REPORT DATE May 1970	7a. TOTAL NO. OF PAGES 33	7b. NO. OF REFS 8
8a. CONTRACT OR GRANT NO. b. PROJECT NO 56-015 c. d.		9a. ORIGINATOR'S REPORT NUMBER(S) TR-679 9b. OTHER REPORT NO(S) (Any other numbers that may be assigned this report)
10. DISTRIBUTION STATEMENT This document has been approved for public release and sale; its distribution is unlimited.		
11. SUPPLEMENTARY NOTES		12. SPONSORING MILITARY ACTIVITY Naval Facilities Engineering Command Washington, D. C.
13. ABSTRACT <p>Two modes of failure for hollow concrete spheres subjected to hydrostatic pressure loadings are discussed, and the experimental results are presented. The first mode of failure was crack development in the plane of the concrete wall, and the second mode was implosion. From experiments using 16-inch-OD spheres, the difference between the pressures at failure for the two modes ranged from 0 to 50%. Expressions to predict the pressures at initiation of in-plane cracking of the concrete wall and the pressures at implosion are presented.</p>		

Security Classification

14	KEY WORDS	LINK A		LINK B		LINK C	
		ROLE	WT	ROLE	WT	ROLE	WT
	Materials						
	Underwater construction						
	Concrete						
	Hollow spheres						
	Implosion pressure						
	Failure modes						

Technical Report

R 774



Sponsored by

NAVAL FACILITIES ENGINEERING COMMAND

September 1972

NAVAL CIVIL ENGINEERING LABORATORY

Port Hueneme, California 93043



BEHAVIOR OF 66-INCH CONCRETE SPHERES UNDER
SHORT- AND LONG-TERM HYDROSTATIC LOADING

Approved for public release; distribution unlimited.

BEHAVIOR OF 66-INCH CONCRETE SPHERES UNDER SHORT- AND LONG-TERM HYDROSTATIC LOADING

Technical Report R-774

3.1610

by

H. H. Haynes and L. F. Kahn

ABSTRACT

Fourteen unreinforced concrete and mortar spheres, 66 inches in outside diameter (OD) and 4.125 inches in wall thickness, were subjected to simulated deep-ocean loading conditions. The average short-term implosion pressure for wet-concrete spheres was 2,350 psi and for the dry-concrete spheres was 2,810 psi; the average uniaxial compressive strength of the concrete was respectively 7,810 psi and 9,190 psi. From control cylinders, it was found that the uniaxial compressive strength of wet concrete was 10% weaker than that of dry concrete. The ratio of implosion pressure to compressive strength, P_{im}/f'_c , was nearly equal for the wet- and dry-concrete spheres at 0.301 and 0.306. The implosion pressures for the 66-inch-OD concrete spheres could be predicted conservatively from an empirical equation developed from 16-inch-OD mortar spheres. The equation was not valid for 66-inch-OD *mortar* spheres, which were found 30% weaker in implosion strength than the 66-inch-OD *concrete* spheres.

Under long-term loading, the concrete spheres failed by static fatigue where the relation between level of sustained pressure and time to implosion was similar to that known for concrete under uniaxial loading. Wet-concrete spheres under seawater pressure as high as 1,670 psi showed an average D'Arcy's permeability coefficient, K_c , of 0.13×10^{-12} ft/sec; this K_c value was also similar to that known for concrete under freshwater pressure as high as 400 psi. Design guides were developed to predict the short- and long-term implosion pressures and permeability rates of concrete spheres.

Approved for public release; distribution unlimited.

Copies available at the National Technical Information Service (NTIS),
Sills Building, 5285 Port Royal Road, Springfield, Va. 22151

CONTENTS

	page
INTRODUCTION	1
EXPERIMENTAL PROGRAM	1
SCOPE	1
FABRICATION OF SPECIMENS	3
TEST PROCEDURE	7
RESULTS AND ANALYSIS	9
SHORT-TERM BEHAVIOR	9
Implosion	9
Deformation	11
Comparison With 16-Inch-OD Spheres	19
LONG-TERM BEHAVIOR	26
Time to Implosion	26
Implosion Failure	30
Effect of Sustained Loading on Implosion Pressure	31
Deformation Under Long-Term Loading	32
Permeability	37
FINDINGS	44
CONCLUSIONS	45
DESIGN GUIDES	46
DESIGN RECOMMENDATIONS	46
EXAMPLE DESIGN PROBLEM	47
Wall Thickness	47
Life of Structure	48
Water Permeation	48

APPENDIXES

A – Concrete And Mortar Mix Designs	49
B – Mechanical Properties of Concrete And Mortar Control Cylinders	51
C – Effect of Control Cylinder Size on Compressive Strength	52
D – Post-Implosion Views of Concrete And Mortar Spheres . .	55
E – Development of Implosion Equation For 16-Inch-OD Mortar Spheres	65
F – Long-Term Strain Response of Concrete Spheres Subjected to Sustained Load	67
G – Miscellaneous Tests on 66-Inch-OD Mortar Spheres	76

REFERENCES	84
----------------------	----

INTRODUCTION

The objective of this experimental program was to determine the behavior of large model concrete spheres subjected to short- and long-term hydrostatic loading conditions. The purpose for the study was to generate data that would aid in developing design guides for utilizing concrete as a construction material for undersea pressure-resistant structures.

The Naval Facilities Engineering Command (NAVFAC) sponsored this research to advance the state of concrete technology related to undersea structures. Portland cement concrete exhibits several qualities that make the material highly desirable for ocean structures. Concrete is highly durable in the seawater environment and is low in cost—both features are good advantages for massive structures with long-term undersea missions. Also, complex structural shapes of double curvature, such as spheres, are fabricated rather easily (even mass-produced) with use of concrete materials.

The Naval Civil Engineering Laboratory (NCEL) has been conducting research on pressure-resistant concrete spheres and cylinders since 1965.¹⁻⁵ All this research has been performed on specimens of 16-inch outside diameter (OD) and 1-, 2-, 3-, and 4-inch wall thicknesses. These investigations tested over 50 model spheres,* and the results showed that concrete was structurally capable of being used as a deep-ocean construction material. The maximum operational depth appeared to be 3,000 feet for a buoyant concrete spherical structure.

EXPERIMENTAL PROGRAM

SCOPE

This experimental program consisted of hydrostatically testing 14 unreinforced concrete and mortar spheres, 66 inches in OD and 4.125 inches in wall thickness (t/D_o ** = 0.0625). Table 1 presents a summary of the

* Over 25 model cylindrical structures have been tested.

** Ratio of wall thickness to outside diameter.

specimens. Eleven of the spheres were fabricated from a concrete with 3/4-inch-maximum-size aggregate and were subjected to short- or long-term loading with the concrete either dry or wet.* Three spheres were fabricated of mortar (small-aggregate concrete) and were tested under short-term hydrostatic loading with the mortar dry.

Table 1. Specimen Summary

Sphere Designation ^a	Wall Material	Condition of Wall Prior to Test	Type of Test	Instrumentation	
				Strain Gages	Change-in-Volume
CDS-1	concrete	dry	short-term	yes	yes
CDS-2	concrete	dry	short-term	no	yes
CWS-3	concrete	wet	short-term	yes	yes ^b
CWS-4	concrete	wet	short-term	no	yes
CWL-5	concrete	wet	long-term	yes	yes
CWL-6	concrete	wet	long-term	yes	yes
CWL-7	concrete	wet	long-term	yes	yes
CWL-8	concrete	wet	long-term	yes	yes
CWL-9	concrete	wet	long-term	yes	yes
CDL-10	concrete	dry	long-term	yes	yes
CDL-11	concrete	dry	long-term	yes	yes
MDS-1	mortar	dry	short-term	no	yes
MDS-2	mortar	dry	short-term	no	yes
MDS-3	mortar	dry	short-term	yes	yes

^a For example: CDS means Concrete Dry Short-term load; CWL means Concrete Wet Long-term load; MDS means Mortar Dry Short-term load.

^b Specimen leaked, so change-in-volume measurements were not accurate.

The deformation behavior of some spheres was recorded by using strain gages or by measuring the change in volume of the specimen. The rate of seawater permeation through the concrete wall was obtained for certain spheres under long-term loading. Implosion data for all specimens were recorded and compared with the behavior of 16-inch-OD by 1-inch-wall-thickness ($t/D_o = 0.0625$) mortar spheres; Figure 1 gives a comparison of size between the small and large models.

* In this report "wet concrete" means hardened concrete that has been saturated with seawater.



Figure 1. Comparison of size between spheres of 66-inch OD with 4.125-inch wall thickness and 16-inch OD with 1.0-inch wall thickness.

FABRICATION OF SPECIMENS

Unreinforced hemispheres were cast of concrete or mortar by use of a steel mold (Figure 2). The day after the concrete was poured, the mold was disassembled to remove the hemisphere (Figure 3). To moist-cure the concrete, the hemisphere was wrapped first in wet burlap and then in polyethylene film. Nine 6 x 12-inch control cylinders were cast with each concrete hemisphere; six of the cylinders were cured inside the hemisphere enclosure, and three cylinders were wrapped in wet burlap and polyethylene film and cured next to the hemisphere enclosure. The latter cylinders were tested at an age of 7 days. Each hemisphere, with six corresponding cylinders, underwent 28 days' moist-curing at ambient temperature inside an open building and an additional 28 days' curing at room conditions. Subsequently, the hemispheres were placed outdoors in an unshaded location.

The mortar hemispheres underwent a different curing procedure. The hemispheres were wrapped in polyethylene film, without wet burlap surrounding the mortar, but with approximately 8 gallons of water ponded at the bottom of the hemisphere enclosure; they were cured outside in an unshaded location for the first 28 days, after which the polyethylene was removed. Six 3 x 6-inch control cylinders were cast with each mortar hemisphere and were cured inside the hemisphere enclosure.



Figure 2. Mold for casting concrete and mortar hemispheres.



Figure 3. Hemisphere being removed from mold the day after cast.

When the hemispheres were over 60 days old, such operations as applying strain gages, epoxy-bonding end penetrators into place, or water-proofing the interior surface were performed. Finally, to fabricate a sphere, two hemispheres were bonded together with an epoxy adhesive (Figure 4).

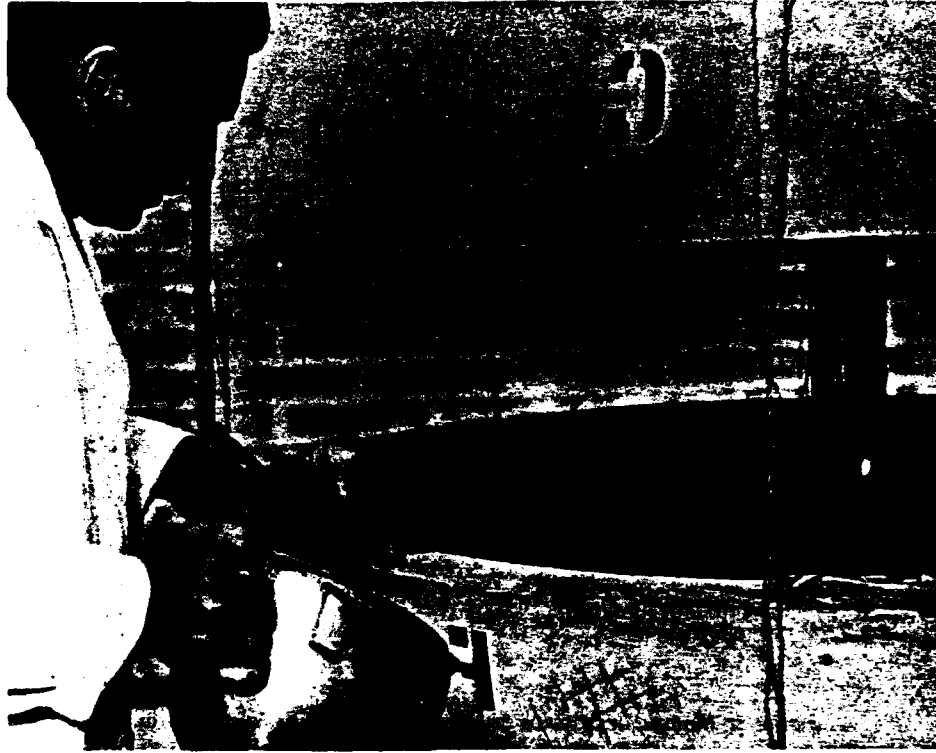


Figure 4. Epoxy adhesive used to bond hemispheres together to form sphere.

Mix design information on the concrete and mortar is contained in Appendix A. The concrete was manufactured at a local batch plant and delivered via transit mix truck, whereas the mortar was batched and mixed in-house. All the concrete hemispheres were X-rayed to ensure that potentially deleterious inclusions were not present in the wall. Of 24 hemispheres, two were rejected—the first because of an excessive number of small air pockets in one general location and the second because of a few shrinkage cracks concentrated around one location. Shrinkage cracks were rarely observed in any of the other specimens. The mortar hemispheres were not X-rayed.

A concrete hemisphere was measured to obtain accurate values of the sphere dimensions and to determine out-of-roundness. Radius measurements were made on the inside of the outer steel mold and on the inside of a concrete

hemisphere. As shown in Figure 5, the measuring device had an adjustable arm to obtain inside and outside radius measurements to the nearest one-thousandth of an inch with use of an Ames dial.

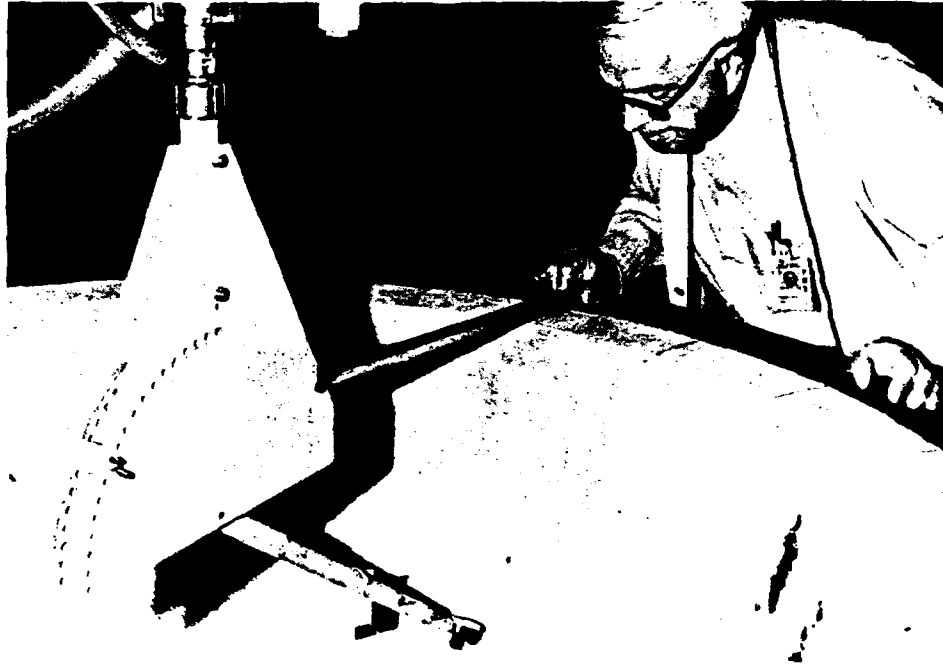


Figure 5. Method and device used to obtain radius measurements.

Wall thickness values at 432 locations were calculated as the difference between interior and exterior radii. A statistical analysis of the data yielded the average hemisphere dimensions given in Table 2. In summary, the mean outside diameter was 65.886 inches and the mean wall thickness was 4.124 inches.

The out-of-roundness deviations are also presented in Table 2, where the maximum variation of the radius is presented as a percentage of the mean wall thickness. Krenzke and Kieman⁶ employed this method to determine local out-of-roundness. They found that a near-perfect sphere was one that had a local variation in dimension of less than 3% of the wall thickness. The maximum local variation of the radius for the concrete sphere was on the exterior surface and was smaller than the average radius by 5.94% of the wall thickness.

Table 2. Hemisphere Dimensions and Out-of-Roundness Variations

Item	Mean Dimension (in.)	Standard Deviation		Maximum Local Variation	
		Measured (in.)	Percent of Wall Thickness	Measured (in.)	Percent of Wall Thickness
Interior radius	28.820	±0.093	±2.26	+0.145 -0.213	+3.51 -5.16
Exterior radius	32.943	±0.083	±2.01	+0.150 -0.247	+3.64 -5.94
Wall thickness	4.124	±0.060	±1.45	+0.181 -0.165	+4.26 -3.90

TEST PROCEDURE

The concrete spheres were tested in NCEL's 72-inch-ID (inside diameter) pressure vessel. Figure 6 shows a concrete sphere rigged for testing being lowered into the vessel.

The interior of the sphere was vented directly to the atmosphere via the top penetrator, thus ensuring that atmospheric pressure was always present in the structure interior. Strain gage wires were led through the penetrator and pressure vessel head to a data acquisition system.

Each sphere's interior was filled with water. The purpose was twofold: firstly, to reduce the shock forces created by implosion and, secondly, to measure the change in volume of the sphere under load. By measuring the volume of water displaced from the interior of the specimen, as shown in Figure 7, data were obtained on the change in volume of the structure under load.

The procedure for obtaining wet-concrete walls before testing was to place an uncoated sphere on the bottom of the pressure vessel and allow the seawater to fill the inside of the sphere, and then apply hydrostatic pressure. The pressure was maintained usually for 7 days at 500 psi or until the pressure became constant and showed no decrease, thus indicating that the air pockets in the concrete were filled with water. The exterior and interior walls of dry-concrete spheres were waterproofed with an epoxy or phenolic coating.

The hydrostatic load was applied to the specimens at a pressurization rate of 100 psi/min. Implosion of the concrete spheres was abrupt and loud. Pressure dropoff was almost instantaneous as the seawater inside the vessel forced its way through the top penetrator to the vessel exterior. The failed specimens were removed from the vessel, and the fragmented spheres were inspected for failure location and unusual crack patterns.

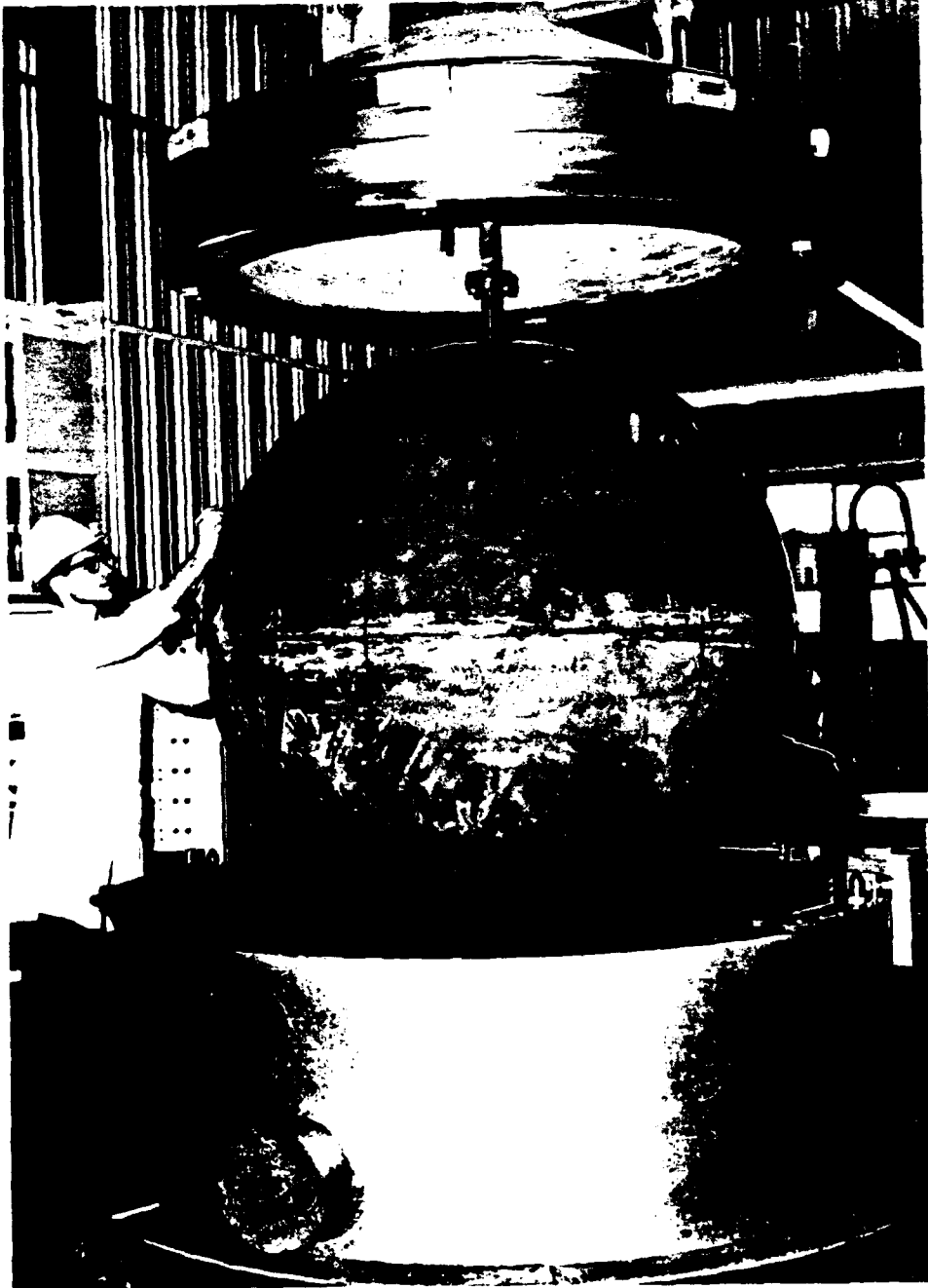


Figure 6. Concrete sphere prepared for test in 72-inch-ID pressure vessel.

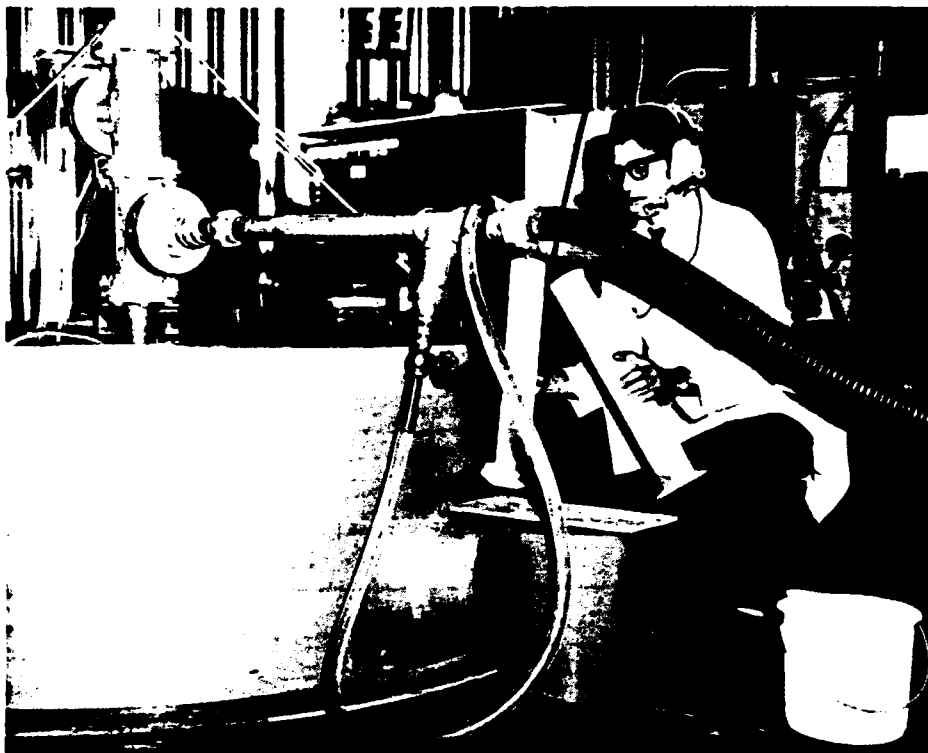


Figure 7. Procedure for collecting displaced water from sphere interior.

RESULTS AND ANALYSIS

SHORT-TERM BEHAVIOR

Implosion

Implosion test results are presented in Table 3. The concrete spheres exhibited considerably higher implosion pressures, P_{im} , than the mortar spheres for similar uniaxial compressive strengths, f'_c ; average values of the nondimensional strength parameter, P_{im}/f'_c , were 0.306 and 0.301 for dry- and wet-concrete spheres, respectively. The difference between dry- and wet-concrete spheres was not found significant in terms of P_{im}/f'_c ratio; however, the uniaxial compressive strength of 6 x 12-inch control cylinders (from specimens CWS-3 through CWL-9, see Appendix B) was reduced an average of 10% by wetting the concrete. This reduction in strength caused the wet spheres

to implode at lower pressures, directly proportional to the strength decrease. The average implosion pressures for the dry- and wet-concrete spheres were 2,810 and 2,350 psi for uniaxial concrete strengths of 9,190 and 7,810 psi, respectively.

Table 3. Implosion Test Results

Sphere Designation	Wall Material	Condition of Wall	Implosion Pressure, P_{im} (psi)	Uniaxial Compressive Strength, f'_c (psi) ^a	P_{im}/f'_c Ratio
CDS-1	concrete	dry	2,860	9,250	0.309
CDS-2	concrete	dry	2,755	9,120	0.302
Average					0.306
CWS-3	concrete	wet	2,500	7,960 (9,010) ^b	0.314
CWS-4	concrete	wet	2,205	7,660 (8,270) ^b	0.288
Average					0.301
MDS-1	mortar	dry	1,960	8,830	0.222
MDS-2	mortar	dry	1,730	8,010	0.216
MDS-3	mortar	dry	1,780	9,150	0.195
Average					0.211

^a Strengths were from control cylinders (six 6 x 12-inch cylinders for dry concrete, three 6 x 12-inch cylinders for wet concrete, and six 3 x 6-inch cylinders for the mortar) that corresponded to the weakest hemisphere of the sphere.

^b Dry-concrete strength from three 6 x 12-inch control cylinders.

The mortar spheres had an average P_{im}/f'_c ratio of 0.211, approximately 30% less than that of the concrete spheres.

The mechanical properties of the control cylinders are given in Appendix B. In general, the concrete and mortar had a uniaxial compressive strength of approximately 8,000 to 9,000 psi; the secant modulus at one-half f'_c was an average of 4.12×10^6 psi for concrete and 3.45×10^6 psi for mortar. The moduli of wet and dry concrete were found to be approximately the same.

Results of controlled tests on 3 x 6-inch and 6 x 12-inch specimens showed the effect of control cylinder size on the compressive strengths of concrete and mortar to be insignificant. These results are presented in Appendix C. Hence, the compressive strength, f'_c , used in this report was not modified for changes in control cylinder size between 3 x 6-inch mortar cylinders and 6 x 12-inch concrete cylinders.

A view of a typical imploded sphere under short-term loading is shown in Figure 8; post-implosion views of the other specimens are shown in Appendix D. The specimens failed because the sphere had "flat spots" that produced higher than average stresses at those locations and eventually caused the concrete wall to fail in compression—shear. The typical concrete compression—shear failure occurred along one arc of the sphere and was usually 2 to 4 feet in length. Figure 9 shows a mortar sphere fragment that revealed the compression—shear angle. For most specimens, the shear angle ranged from 30 to 40 degrees from a line tangent to the exterior surface of the sphere.

After the failure shear plane was formed, the instantaneous release of strain energy in the wall coupled with the implosion shock forces usually caused the concrete to break in many places. These secondary cracks were normal to the exterior surface. Figure 9 also shows the secondary cracks.

Figure 10 shows a secondary crack that crossed the equatorial joint. Note that the joint is hardly discernible. It appeared the effect of the joint on the structural behavior of the sphere was not significant and did not lower the implosion pressure.

Deformation

Strain. Concrete spheres CDS-1 and CWS-3 were instrumented with 12 interior and 12 exterior gages, as shown in the layout of Figure 11. Average interior and exterior strain behaviors for the dry-concrete sphere, CDS-1, are plotted in Figures 12 and 13. Strain data from wet-concrete sphere CWS-3 were considered unreliable and are not presented. (Wet-concrete strain data are given in the long-term behavior section.)

The strain gage layout for the mortar sphere, MDS-3, was quite different from that for the concrete spheres. Twelve 60-degree rosettes were placed uniformly on each interior and exterior surface (a total of 72 single gages). Figure 14 shows a portion of the gage layout. The average interior and exterior behaviors of the mortar sphere are shown in Figures 15 and 16.

Classical elastic theory for thick-walled spheres predicted that the interior strain should have been approximately 15% greater than the exterior strain. Results from the dry-concrete and mortar spheres showed that the interior strain was greater than the exterior strain by 18 and 13%, respectively, when the specimens were near implosion.

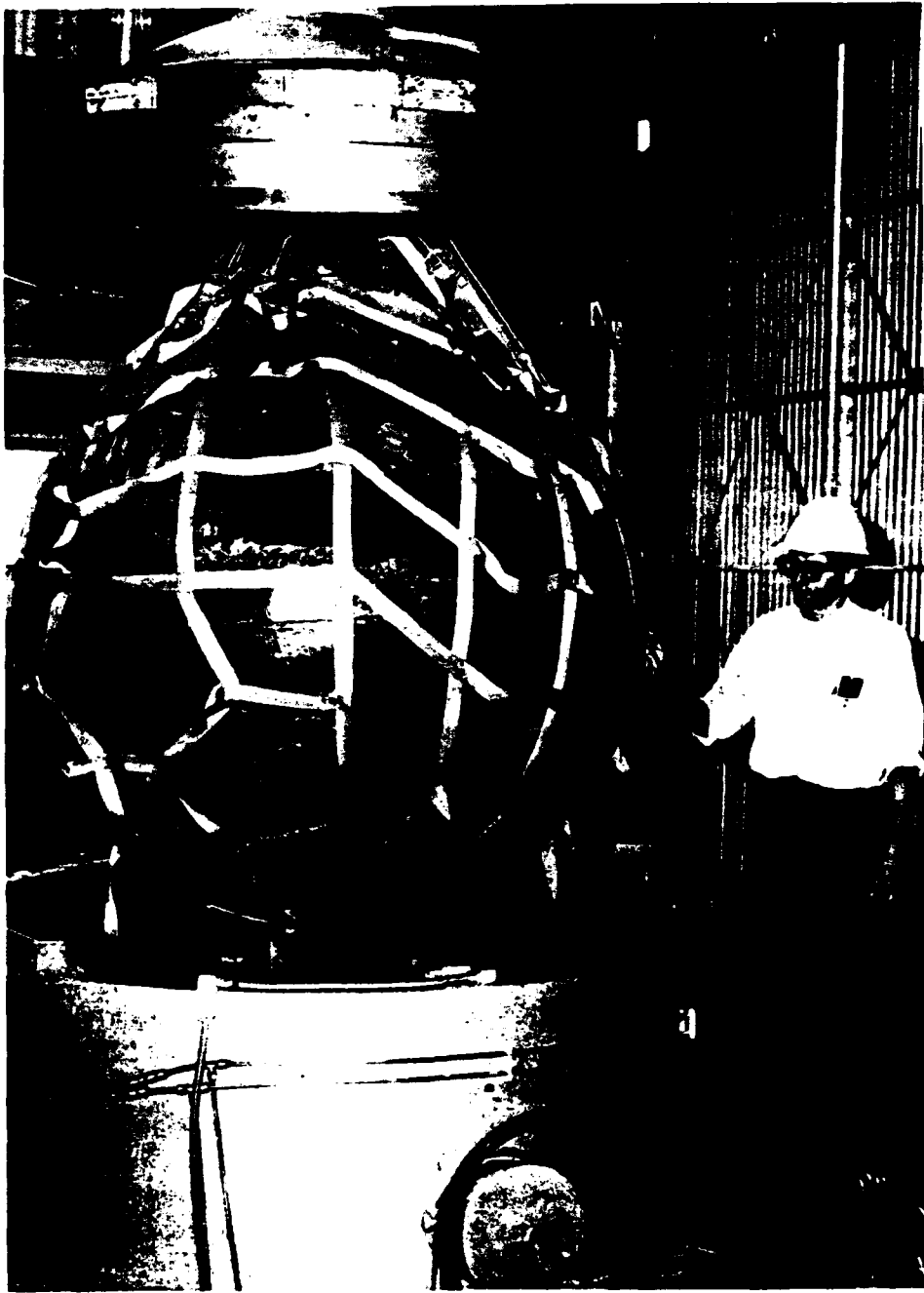


Figure 8. Sphere CDS-1 after implosion failure under short-term loading.



Figure 9. Sphere MDS-3 fragment that shows compression—shear failure angle.



Figure 10. Finger points to epoxy joint between hemispheres.

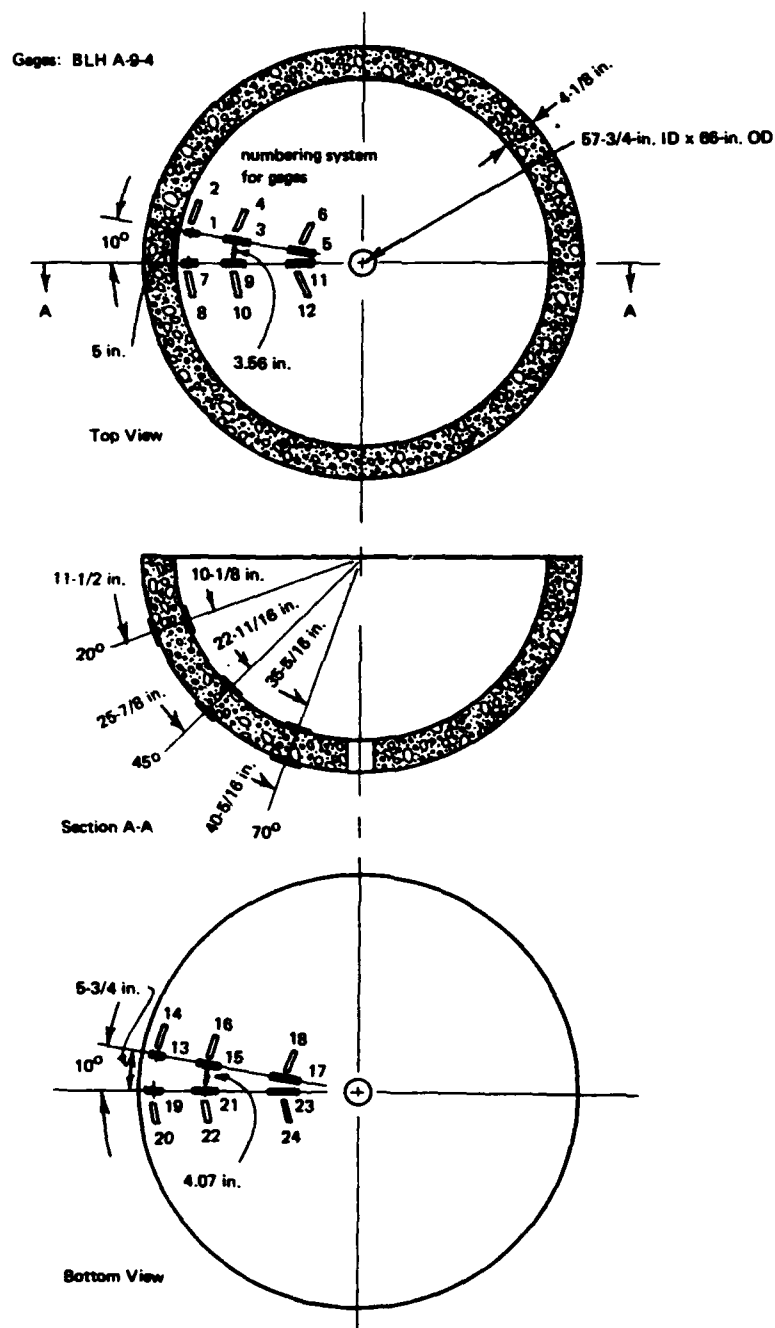


Figure 11. Strain gage layout for spheres CDS-1 through CWL-6. Spheres CWL-7 through CDL-11 had gages placed in locations 1 through 6 only.

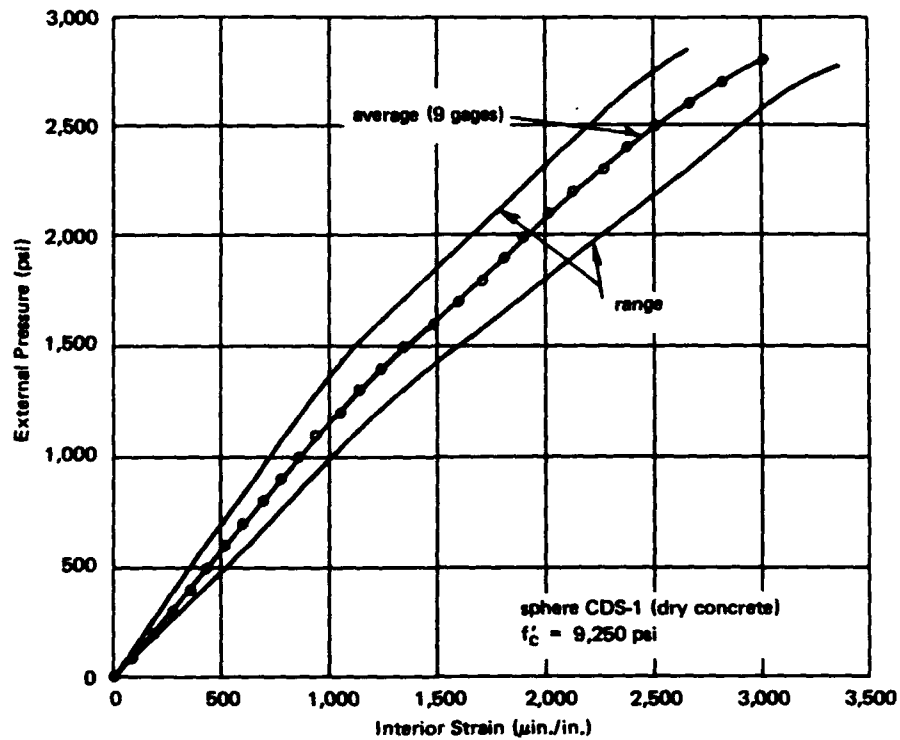


Figure 12. Interior strain behavior of sphere CDS-1.

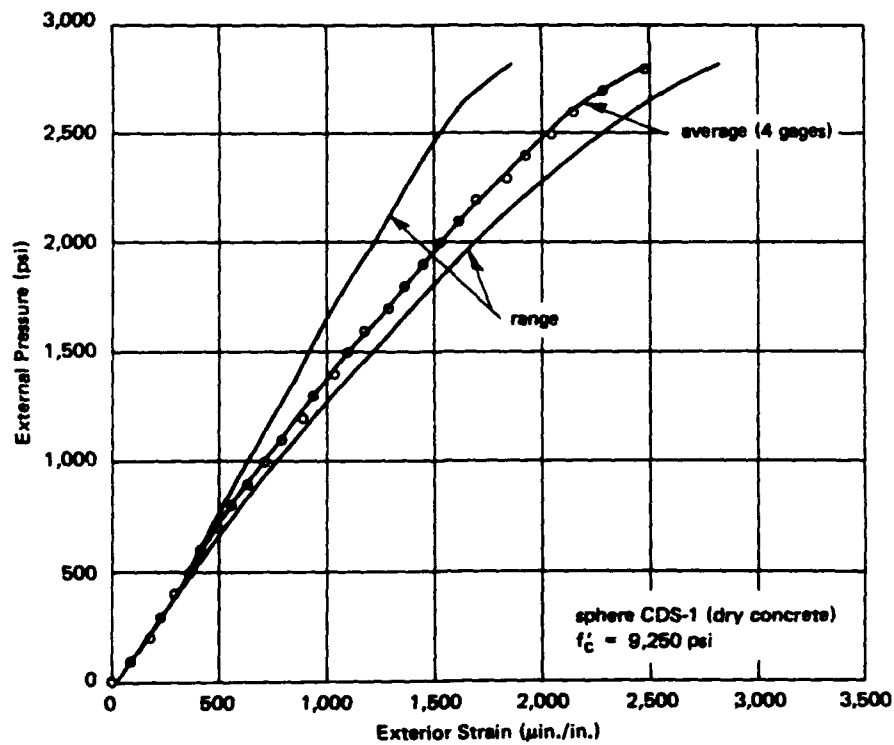


Figure 13. Exterior strain behavior of sphere CDS-1.



Figure 14. Rosette layout on interior of bottom hemisphere of sphere MDS-3.

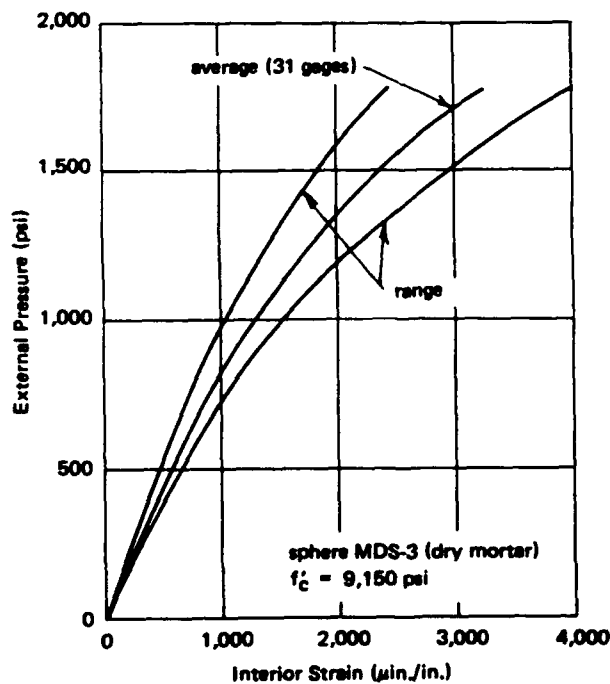


Figure 15. Interior strain behavior of sphere MDS-3.

A study of the individual gage behavior of mortar sphere MDS-3 revealed that the location of the compression-shear failure of the concrete occurred between a rosette that recorded the highest compressive strains and another rosette that recorded the highest tangential shear strains. The failure location on the sphere in relation to the rosettes is shown in Figure 17. The rosette recording high compressive

strain (strain on the order of $4,300 \mu\text{in./in.}$ compared with the average strain of $2,600 \mu\text{in./in.}$) signified that the rosette was at or near the center of a flat spot where curvature was decreasing; whereas the rosette recording high tangential shear strain signified that the rosette was on the edge of the flat spot where the curvature was increasing in one direction. Hence, the concrete failure occurred within a flat spot locality.

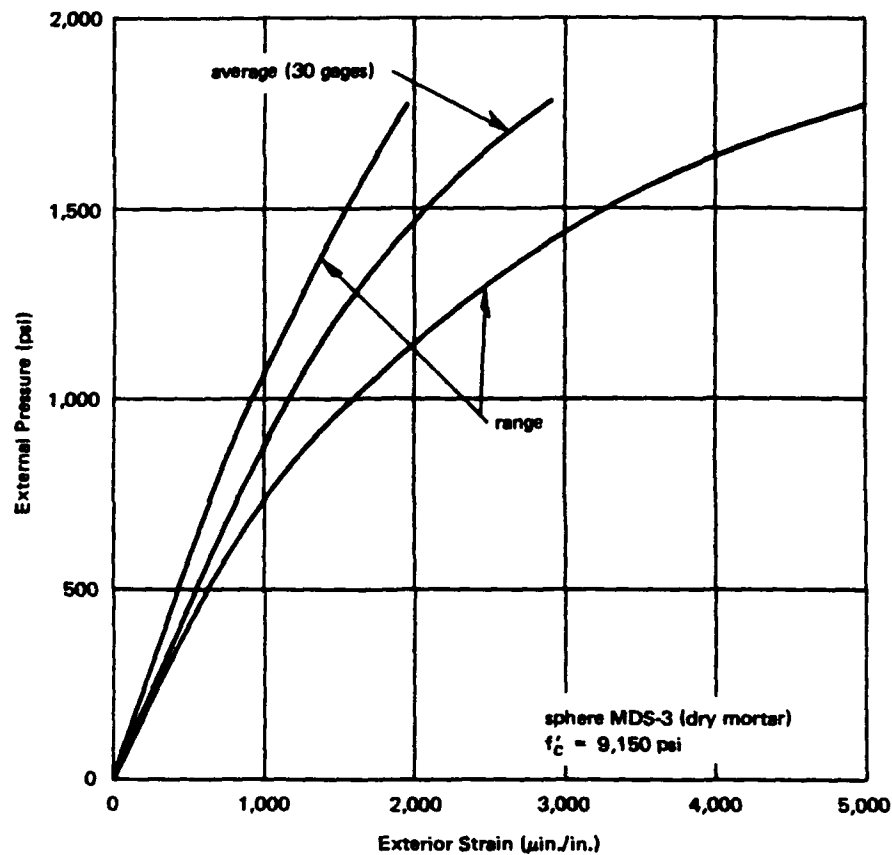


Figure 16. Exterior strain behavior of sphere MDS-3.

Change in Volume. The spheres decreased in volume as the hydrostatic pressure was increased. A direct measure of the change in interior volume was obtained by collecting water displaced from the sphere interior. By assuming that the sphere deformed uniformly under hydrostatic loading, the change-in-volume measurements were directly related to interior strain values. For the spheres, the accuracy of displaced-water measurements was $\pm 3.53 \times 10^{-4} \text{ ft}^3$ ($\pm 10 \text{ ml}$), which represented approximately $\pm 2 \mu\text{in./in.}$ of interior strain.

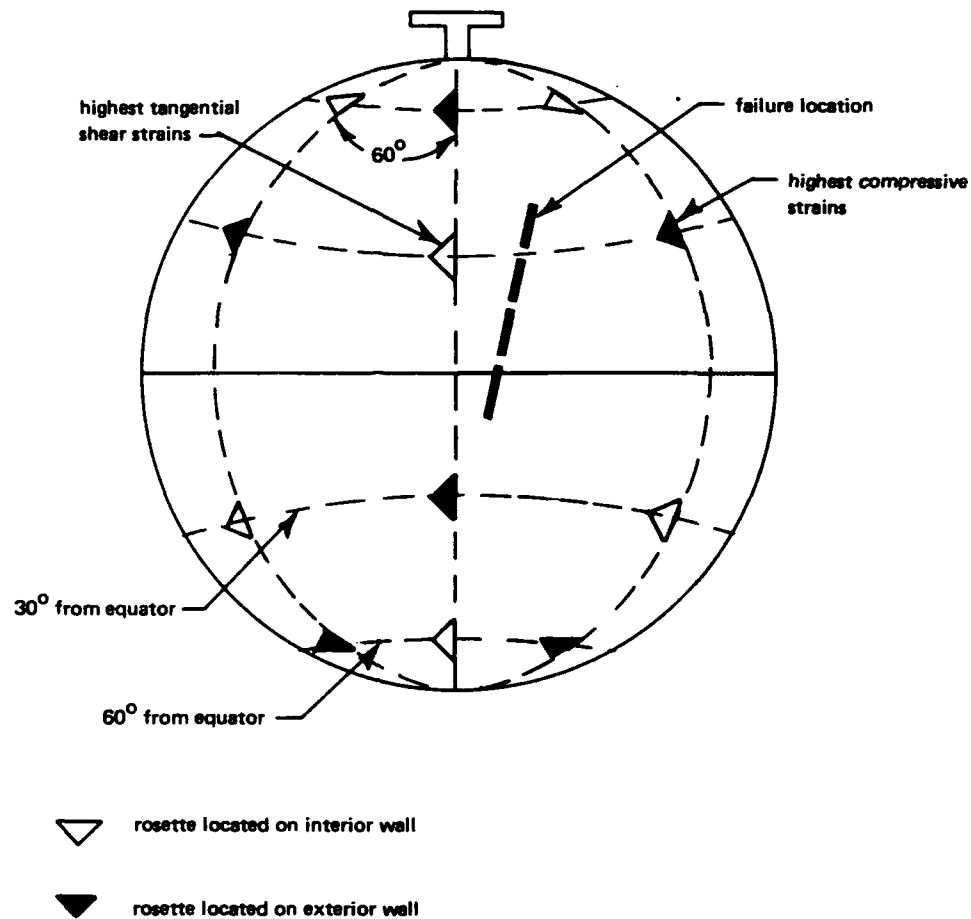


Figure 17. Compression—shear failure location for sphere MDS-3 shown in relation to rosettes recording highest tangential shear and highest compressive strains.

Figures 18 and 19 show the short-term change-in-volume behavior of the concrete and mortar spheres. For the dry-concrete and mortar spheres the maximum change in volume was fairly constant at approximately 1% of the total interior volume. This indicated that the implosion failure of the spheres was defined by a strain criterion based on out-of-roundness. The out-of-roundness for the concrete and mortar spheres was the same because the same mold was used to fabricate the hemispheres. The change-in-volume behavior of only one wet-concrete sphere (CWS-4) was obtained, and this sphere imploded at an ultimate change in volume 25% less than the dry-concrete spheres.

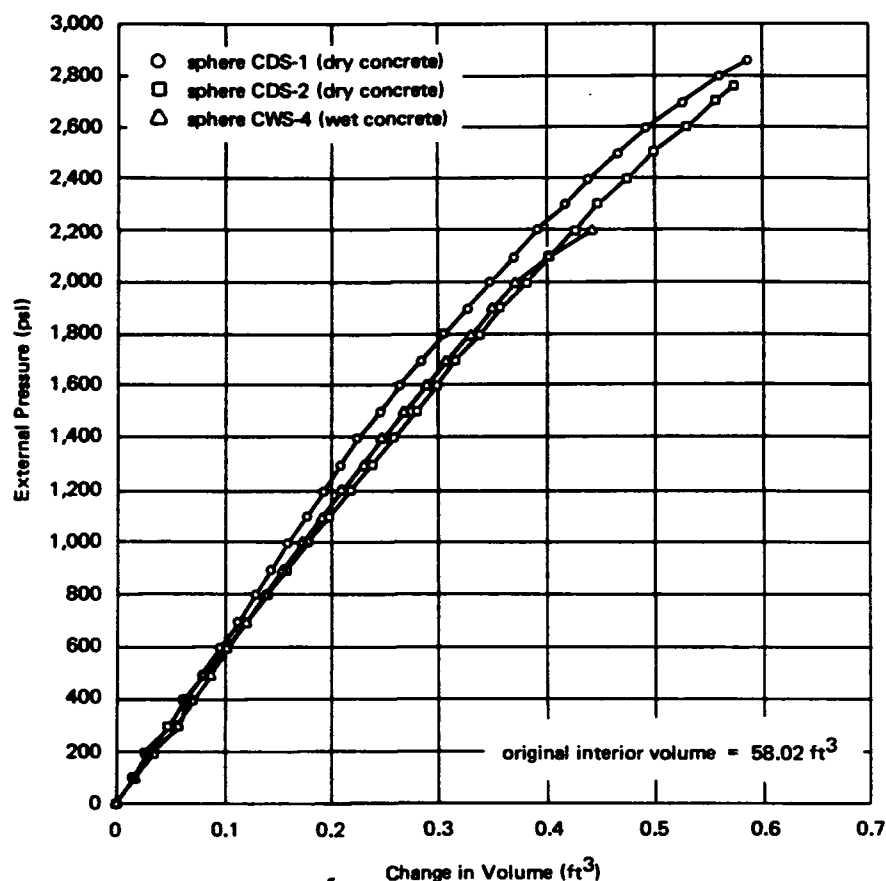


Figure 18. Change-in-volume behavior for wet- and dry-concrete spheres.

Change-in-volume measurements were converted into interior strain values and then compared to strain gage averages for two specimens, CDS-1 and MDS-3 (Figures 20 and 21). Excellent agreement was found between change-in-volume and average strain behavior; thus, the change-in-volume behavior was used as a reliable indication of interior strain behavior on the other specimens that were not with instrumented strain gages.

Comparison With 16-Inch-OD Spheres

Considerable research on 16-inch-OD mortar spheres has been previously conducted at NCEL.¹⁻⁴ The 66-inch specimens were directly scaled from one particular model size, 16-inch OD by 1-inch wall thickness; the t/D_o ratio for both size specimens was 0.0625. Five 16-inch-OD spheres were tested under short-term loading conditions very similar to those for the 66-inch-OD specimens.

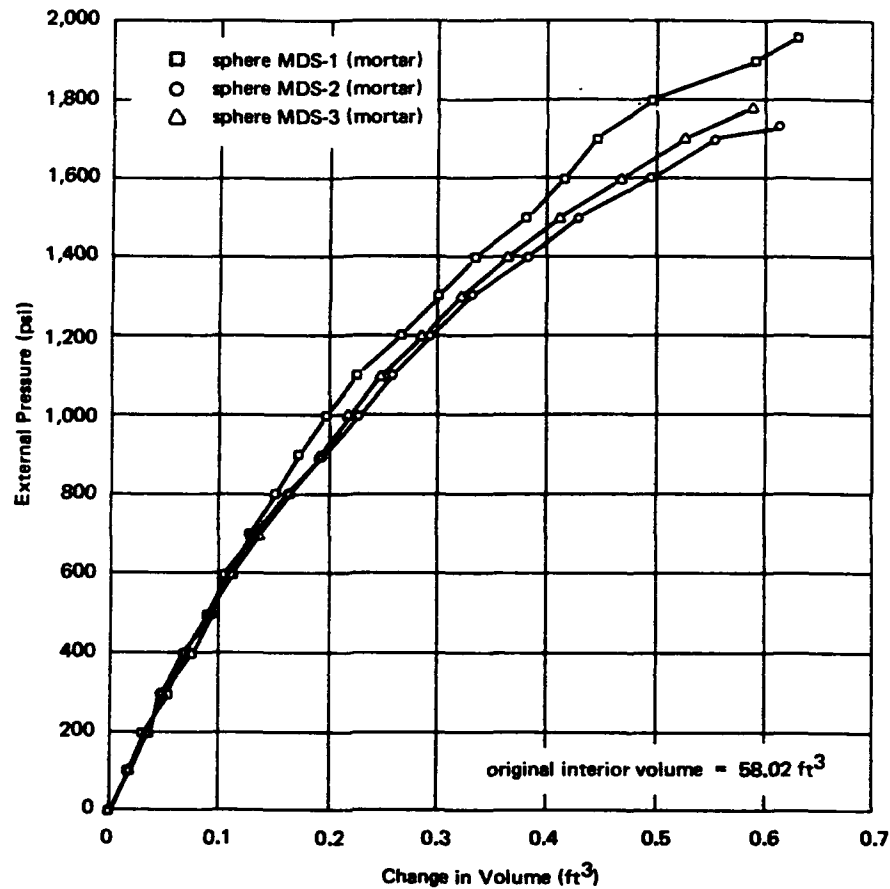


Figure 19. Change-in-volume behavior for dry-mortar spheres.

Implosion. Table 4 compares the implosion results for the different spheres. The 66-inch concrete spheres had an average P_{im}/f'_c ratio 3% greater than that of the 16-inch mortar spheres; whereas the 66-inch mortar spheres had an average P_{im}/f'_c ratio 28% less than that of the 16-inch mortar spheres. An empirical equation was developed in earlier work to predict the implosion pressures for 16-inch-OD spheres of various t/D_o ratios between 0.06 and 0.25 (Appendix E summarizes this development). The equation is

$$P_{im} = \left[5.02 \left(\frac{t}{D_o} \right) - 0.038 \right] f'_c \quad (1)$$

where P_{im} = implosion pressure (psi)

t = wall thickness (in.)

D_o = outside diameter (in.)

f'_c = ultimate uniaxial compressive strength from 3 x 6-inch control cylinders (psi)

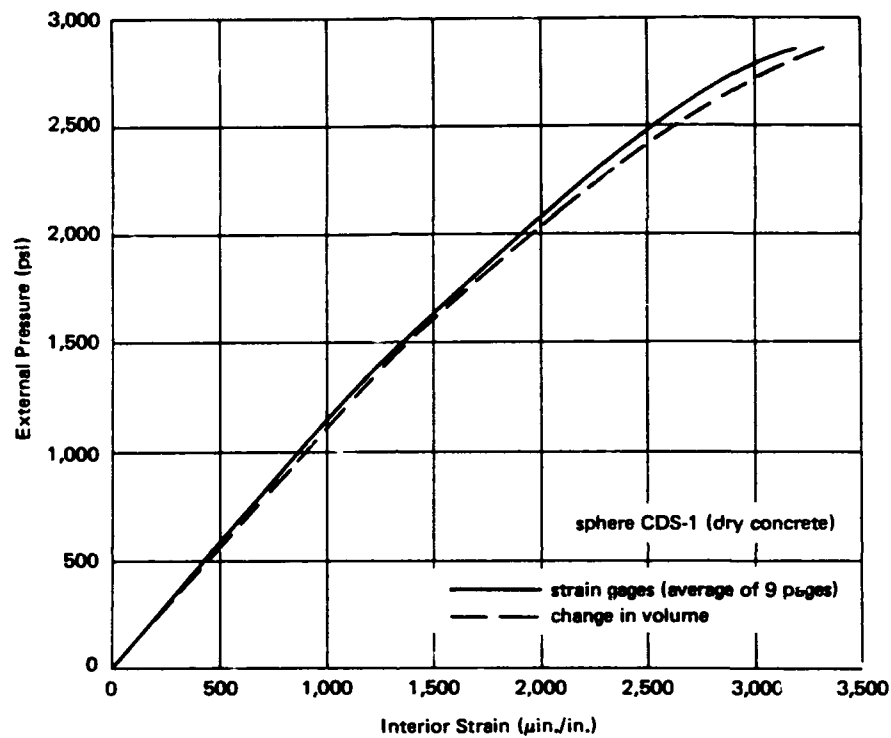


Figure 20. Comparison of interior strains obtained from electrical resistance strain gages and change-in-volume measurements for sphere CDS-1.

By use of Equation 1, predictions were made of the implosion pressures for 66-inch-OD spheres. Figure 22 shows that for the 66-inch *concrete* spheres the predictions were conservative to the same degree as that for the 16-inch mortar spheres. However, for the 66-inch *mortar* spheres, the predicted implosion pressures were considerably higher than the actual implosion pressures.

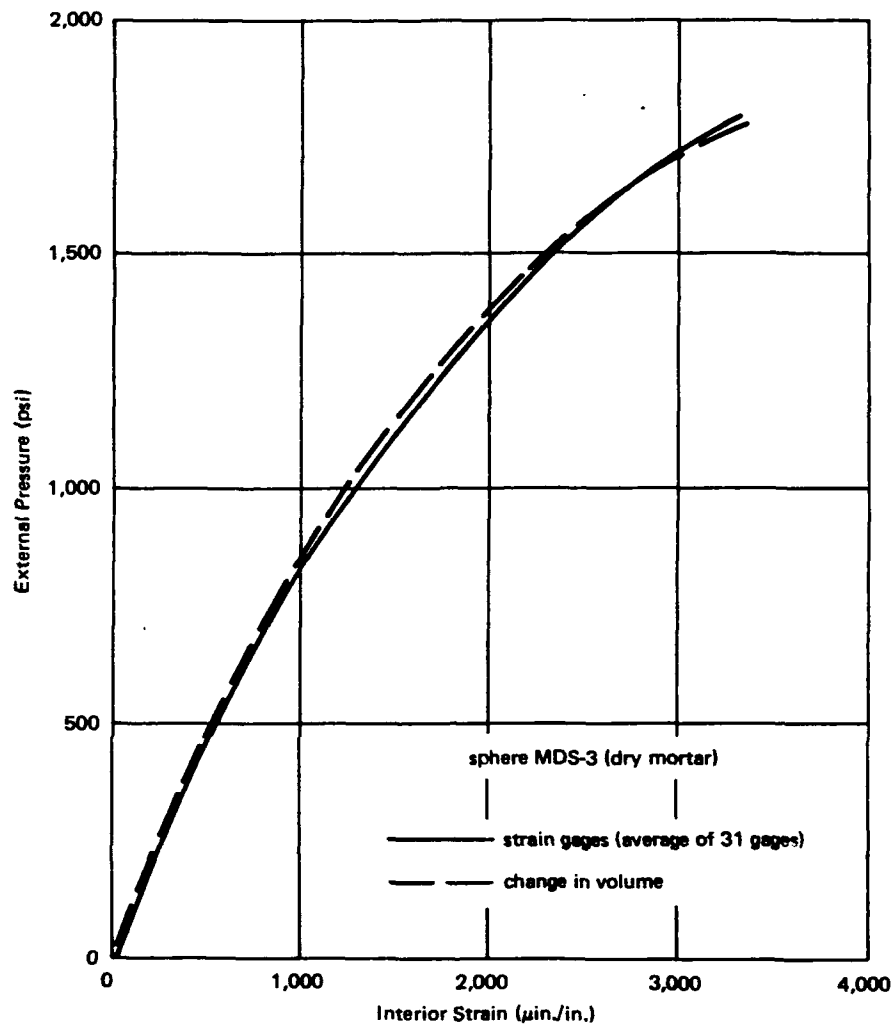


Figure 21. Comparison of interior strains obtained from electrical resistance strain gages and change-in-volume measurements for sphere MDS-3.

Strain. The average strain behaviors for the different 16- and 66-inch-OD spheres are shown in Figure 23. To obtain the mean interior strain behavior for the 66-inch-OD spheres of concrete and mortar, change-in-volume and strain gage data were averaged together. Two 16-inch-OD spheres compose the average for the smaller models. The ordinate of the figure, ratio of external pressure to concrete compressive strength (P/f'_c), is a nondimensional parameter that aids in comparing the different specimens because the effect of a varying compressive strength between specimens has been removed.

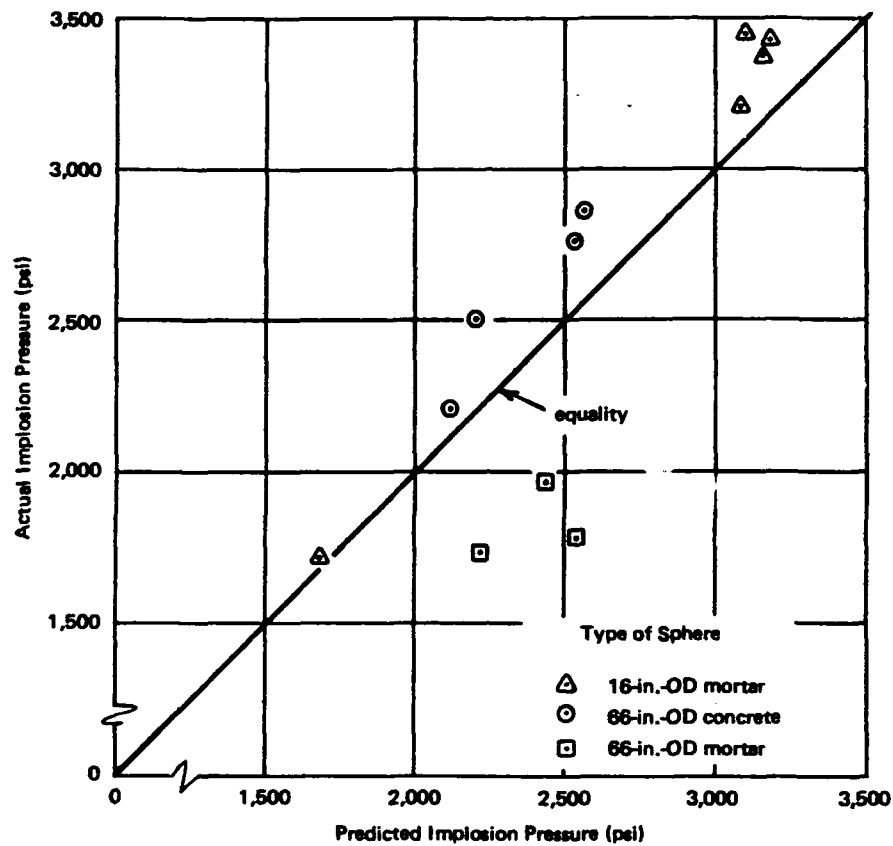


Figure 22. Comparison of actual with predicted implosion pressure for short-term loaded spheres by use of Equation 1.

Table 4. Comparison of Implosion Results

Sphere Size		Implosion Results				
Outside Diameter (in.)	Wall Thickness (in.)	Material	No. of Specimens	Ratio of Implosion Pressure to Compressive Strength, P_{im}/f'_c	Standard Deviation (Coefficient of Variation)	Implosion Ratio, $\frac{66\text{-in. spheres}}{16\text{-in. spheres}}$
16	1	mortar	5	0.294	0.009 (3.1%)	—
66	4.125	concrete	4	0.303	0.011 (3.6%)	1.03
66	4.125	mortar	3	0.211	0.012 (5.7%)	0.72

Note: t/D_o , ratio of wall thickness to outside diameter, was constant at 0.0625.

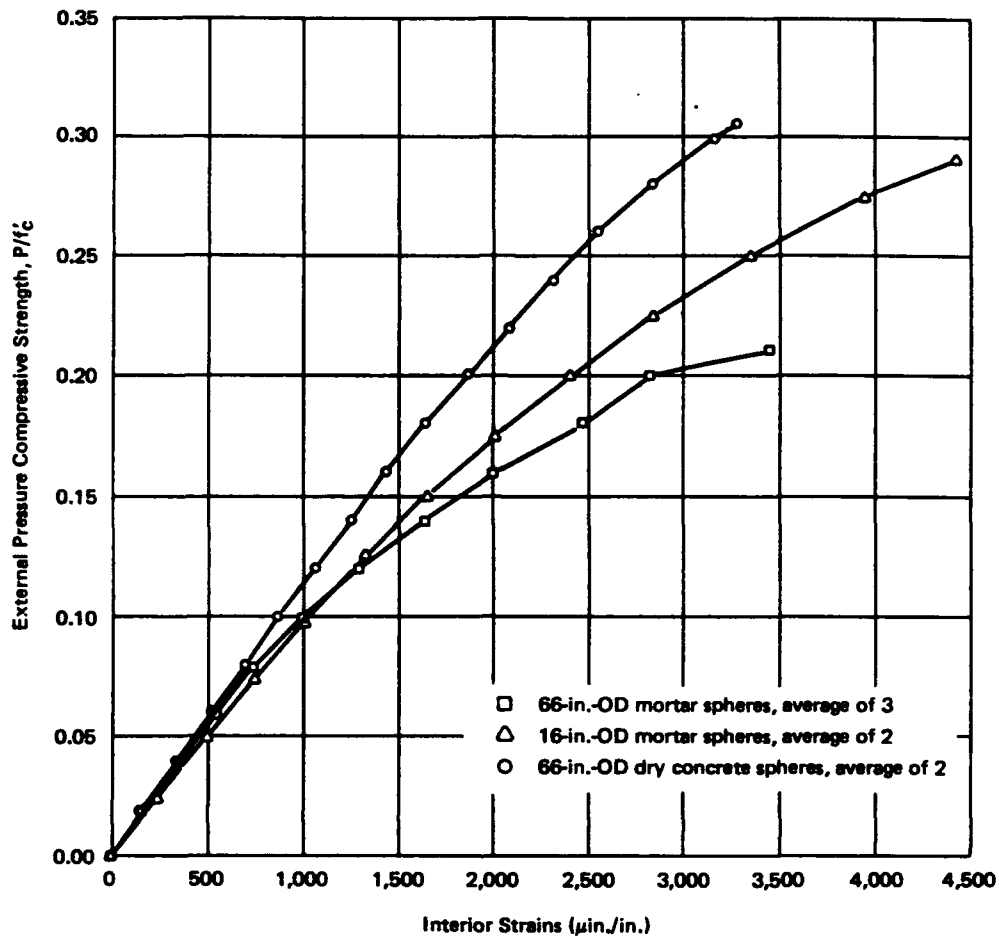


Figure 23. Comparison of interior strains for dry-concrete and mortar 66- and 16-inch-OD spheres.

The range of strain behavior between the various sizes of spheres was substantial. The 66-inch-OD concrete spheres were noticeably stiffer than the 16-inch-OD mortar spheres; the 66-inch mortar spheres showed the lowest stiffness.

Of interest is a comparison of the ultimate strain between the large concrete spheres and the smaller mortar spheres. The ultimate strain of the 66-inch spheres was approximately 3,400 $\mu\text{in./in.}$, whereas that of the 16-inch spheres was approximately 4,400 $\mu\text{in./in.}$ This difference could represent the effect of out-of-roundness. The 16-inch spheres were fabricated to a radius tolerance of 3% of the wall thickness; the 66-inch spheres had a radius tolerance of 6% of the wall thickness. Perhaps if the larger spheres had had better dimensional tolerances the spheres could have experienced higher ultimate strains and consequently attained higher implosion pressures.

Discussion. The large concrete spheres showed a higher P_{im}/f'_c ratio and a stiffer strain response to pressure load than did the 16-inch mortar spheres. It therefore appears safe to assume that Equation 1 is applicable for predicting the implosion pressure for *concrete* spheres larger than 16 inches OD.

The "weak" structural performance of the 66-inch *mortar* spheres could be attributed to two causes: size effect and poor curing of the mortar hemispheres.

Size effect is a phenomenon exhibited by certain materials that relates to the apparent decrease in strength with corresponding increase in specimen size. The most frequently used parameter to evaluate size effect is the volume of material in the test specimen. For the spheres, the material volume ratio between the 16- and 66-inch-OD sizes was 70.1. Past work on solid concrete cylinders⁷ and cubes⁸ has shown a decrease in strength of 13 and 15%, respectively, for a volume ratio of 70. However, size effect has been observed to decrease for higher strength concretes. The past work used concretes of 3,000 to 7,000 psi, whereas the sphere studies used mortar having a strength from 8,000 to 11,000 psi. Also, as shown in Appendix C, no size effect was observed between 3 x 6- and 6 x 12-inch control cylinders fabricated of the concrete and mortar used in this study. Therefore, it strongly appears that the size effect between the 66- and 16-inch mortar spheres should have been less than 13%. Furthermore, it should also be noted that there was no apparent size effect between the 66-inch concrete spheres and 16-inch mortar spheres.

The curing condition for the 66-inch mortar hemispheres appears to have been detrimental to the mechanical properties of the mortar. The large mortar hemispheres were wrapped in polyethylene film (plastic sheet) with water ponded on the bottom and were cured in an unshaded location. On inspection of the hemispheres during curing, it was observed that the mortar near the equator on the exterior surface appeared dry. In this region, the polyethylene film was in direct contact with the concrete and prevented free moisture from wetting the concrete surface. All other locations on the hemisphere appeared wet; thus the mortar on the exterior surface next to the equator might not have cured like the remainder of the hemisphere.

The differential shrinkage which occurred between the dry exterior and wet interior surfaces could have caused microcracks to form within the hemisphere wall. This condition of differential shrinkage would have been aggravated because of the large surface-to-volume ratio of the hemisphere and because large aggregate and steel reinforcement were not present to assist in restraining shrinkage. Visible shrinkage cracks were not detected on the exterior surface before testing; yet internal microcracks were probably present.

The strain behavior of the large mortar spheres, as shown in Figure 23, revealed that microcrack development was more pronounced at earlier loads than for the smaller spheres; the relationship of P_{im}/f'_c ratio versus strain for

the larger spheres deviated from linearity at lower loads than those for the smaller spheres. From these data, it appeared shrinkage microcracks were present.

The authors believe that the principal cause of the low implosion pressures and highly nonlinear strain behavior of the 66-inch mortar spheres compared with that of the 16-inch spheres was the poor curing condition of the larger specimens.

LONG-TERM BEHAVIOR

Seven spheres were tested under long-term hydrostatic loading to determine the time to implosion, time—deformation behavior, difference in long-term response between wet- and dry-concrete spheres, and concrete permeability. Spheres CWL-5 through CWL-9 were not waterproofed, whereas spheres CDL-10 and CDL-11 were coated with a waterproofing compound (Phenoline 300 orange primer and top coat).

Five spheres (CWL-5, CWL-7, CWL-8, CWL-9, and CWL-10) were pressurized to sustained loadings until the spheres imploded; two spheres (CWL-6 and CDL-11) were pressurized to sustained loadings for periods of 1,000 and 500 hours, respectively, at which times the loadings were increased at a rate of 100 psi/min until implosion occurred. Spheres CWL-5 and CWL-9 were subjected to two levels of sustained pressure—the first level designed to secure deformation and permeability data at low pressure loads and the second level to determine time to implosion. The tests at the first pressure level were designated CWL-5A and CWL-9A; at the second level they were CWL-5B and CWL-9B.

Time to Implosion

Table 5 summarizes the long-term implosion results. The pressure levels were 20, 50, 80, 85, and 90% of the spheres' predicted implosion pressures (P_{pim}). The average value of $P_{im}/f'_c = 0.301$ was used to predict the implosion pressure for the wet-concrete spheres (CWL-5 through CWL-9), and the average value of $P_{im}/f'_c = 0.306$ was used for the dry-concrete sphere (CDL-10 and CDL-11). The time-to-implosion data are shown in Figure 24 as the ratio of sustained pressure to predicted implosion pressure, P_s/P_{pim} , versus time. Also presented are data by Rüschi⁹ on concrete under sustained uniaxial compression and the results of sustained pressure tests on 16-inch-OD x 1-inch-wall-thickness spheres.¹⁰ A straight line was fitted through Rüschi's

data and another line through the 66-inch-OD sphere results;* both wet- and dry-concrete sphere results were included. The equations of the lines for the uniaxially loaded specimens and the 66-inch concrete spheres respectively are as follows:

$$\frac{\sigma_s}{f'_c} = 0.925 - 0.0356 \log_{10} T \quad (2)$$

$$\frac{P_s}{P_{pim}} = 0.908 - 0.0360 \log_{10} T \quad (3)$$

where σ_s = sustained uniaxial compressive stress (psi)
 f'_c = ultimate uniaxial compressive strength (psi)
 T = time to implosion (hr)
 P_s = sustained hydrostatic pressure (psi)
 P_{pim} = predicted implosion pressure (psi)

The slopes of the lines were essentially the same, which indicated that the creep failure mechanisms of the concrete in the different tests were similar. The probable cause for the difference between the lines was the higher-than-average stresses at out-of-roundness locations on the sphere. Those areas of high stress strained with time at a greater rate than did the areas of average stress; hence the spheres would implode earlier than would uniaxially loaded cylinders, in which stress redistribution occurs. The small spheres that were less out-of-round than the 66-inch-OD spheres failed (with one exception) with good agreement to Rüschi's data.

The general agreement between results implied that the concrete spheres under the unique loading condition of uniform hydrostatic pressure behaved in a manner similar to the known behavior of concrete. The authors tentatively recommend that Equation 3 be used to approximate the expected life of concrete spherical structures and that the maximum applied pressure should not be greater than 70% of the predicted implosion pressure.** At 70%, Equation 3 yields an expected life of 68 years.

* Results from spheres CWL-6 and CDL-11 were used in fitting the straight line by assuming that the spheres imploded at 1,000 and 500 hours respectively. This was a conservative assumption.

** Present state of the art suggests that concrete under sustained uniaxial load should not be subjected to over 70% of the ultimate concrete compressive strength.^{11, 12, 13}

Table 5. Summary of Long-Term Implosion Results

Sphere Designation ^a	Sustained Pressure, P_s (psi)	Predicted Implosion Pressure, P_{plm} (psi)	P_s/P_{plm} (%)	Time to Implosion (hr)	Duration of Test (hr)	Implosion Pressure After Sustained Pressure Resisted
CWL-5A	505	2,530	20	— ^b	1,000.00	3,005 ^c
CWL-5B	2,278	2,530	90	2.90	2.90	
CWL-6	1,670	2,090	80	—	1,003.00	
CWL-7	1,942	2,160	90	0.95	0.95	
CWL-8	1,845	2,170	85	10.78	10.78	2,740 ^c
CWL-9A	1,120	2,240	50	— ^b	500.00	
CWL-9B	1,904	2,240	85	90.00	90.00	
CDL-10	2,450	2,880	85	3.97	3.97	
CDL-11	2,064	2,428	85	—	500.00	

^a Spheres CWL-5 through CWL-9 were wet-concrete spheres; spheres CDL-10 and CDL-11 were dry-concrete spheres.

^b Spheres CWL-5A and CWL-9A were under low sustained pressure for permeability data—not implosion data. To obtain implosion data, the sustained pressure was increased to a higher level; that test was designated sphere CWL-5B and CWL-9B.

^c Spheres CWL-6 and CDL-11 did not implode under sustained pressure, so the test was terminated by raising the pressure at the rate of 100 psi/min to implosion.

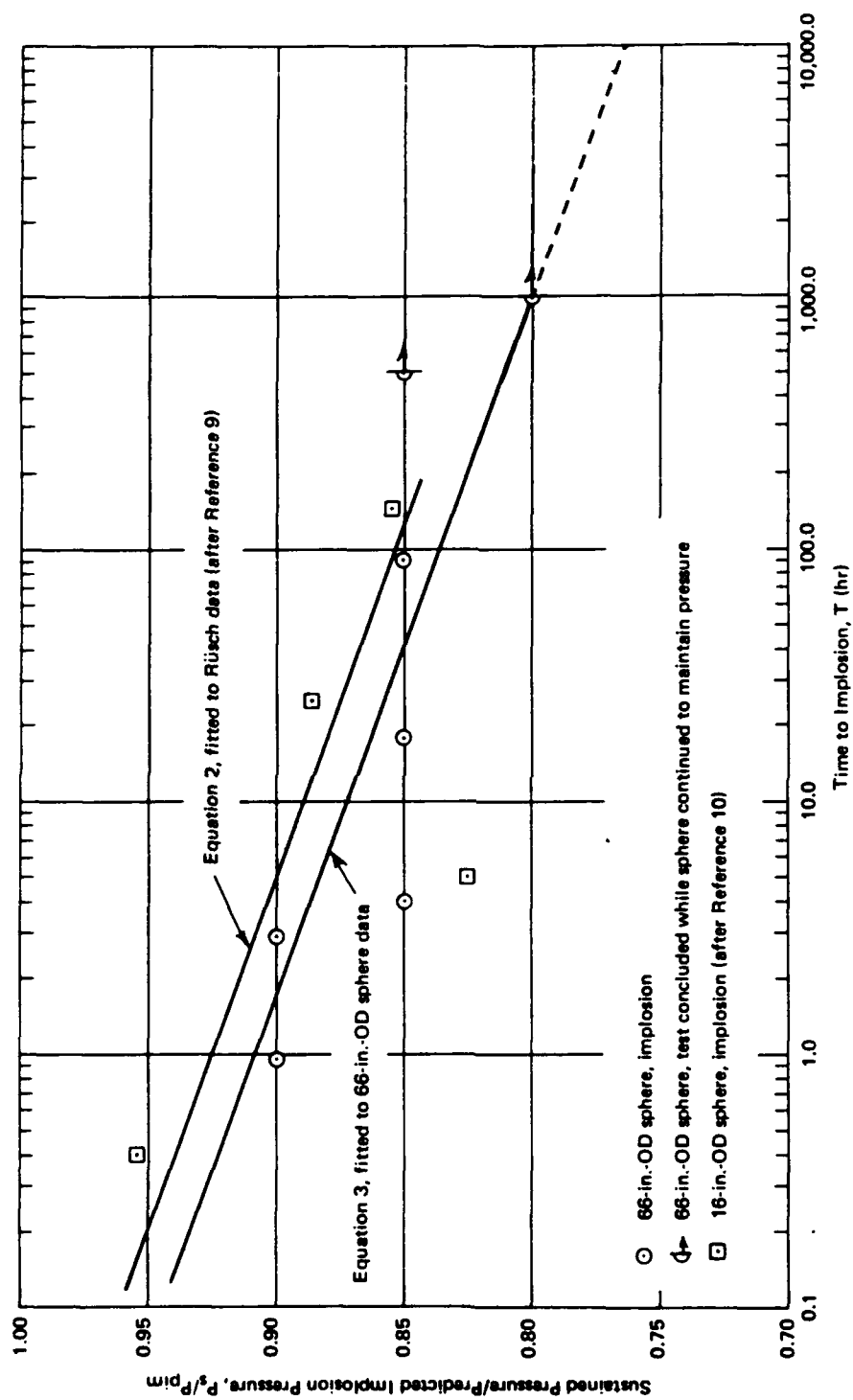


Figure 24. Ratio of applied pressure to predicted implosion pressure as function of the logarithm of time to implosion.

Implosion Failure

Spheres under long-term loading failed in a manner similar to that of those under short-term loading; a typical concrete compression—shear zone was formed. Unlike spheres in the short-term tests, spheres that imploded under sustained load did not fracture into many segments (Figure 25), and in-plane cracks were considerably more evident in the failure zone (Figures 26 and 27).



Figure 25. Localized failure of sphere CWL-7 shows compression—shear zone that circumscribes three-quarters of the hole.

Studies of the short-term behavior of 16-inch-OD spheres clearly showed the formation of in-plane cracking in spheres with t/D_o ratios of 0.125 and greater.⁴ These cracks were due to tensile radial strains. The 16- and 66-inch-OD spheres having a t/D_o of 0.0625 and subjected to short-term loading did not exhibit visible in-plane cracks.

It appears that a combination of two factors caused in-plane cracking in the 66-inch-OD sphere under long-term loadings. These factors are: (1) concrete under biaxial and triaxial compression fails by forming cracks in

planes parallel to the maximum principal stresses, which for spheres under hydrostatic loading is in the plane of the wall thickness; and (2) the stress at the interior surface of the spheres was greater than at the exterior, thus creep was greater at the interior than at the exterior. This difference in creep strain rate between the interior and exterior produced an additional radial tensile strain across the wall; this condition resulted in the development of tensile cracks within the plane of the wall thickness.



Figure 26. Failure zone of sphere CWL-5, showing results of in-plane cracking. Approximately 1 inch of the exterior surface is removed.

Effect of Sustained Loading on Implosion Pressure

Spheres CWL-6 and CDL-11 were pressurized to implosion after a sustained pressure of 80 and 85% of P_{pim} did not result in a static fatigue failure after 1,000 and 500 hours, respectively. The implosion pressures, after the sustained loads were resisted, for spheres CWL-6 and CDL-11, were 44 and 13% greater than the predicted pressure. The sustained load did not adversely affect the implosion pressure of either wet- or dry-concrete sphere. This general result agreed with results of experiments on concrete cylinders

under uniaxial loads; these results demonstrated an approximate 4% strength increase for both wet and dry specimens after 5 months of sustained load at 22% of the short-term strength.¹⁴



Figure 27. In-plane cracks are evident around failure zone of sphere CWL-9 loaded to 85% P_{pim} .

The finding implied that the predicted implosion pressure will not be lowered and may even be increased when spheres are loaded to sustained pressures that do not cause static fatigue failure.

Deformation Under Long-Term Loading

Deformation of the spheres under long-term loading was monitored with electrical resistance strain gages and change-in-volume measurements. Spheres CWL-5 and CWL-6 had interior and exterior gages as shown in Figure 11; spheres CWL-7 through CDL-11 had only six interior gages, located at positions 1 through 6 in Figure 11.

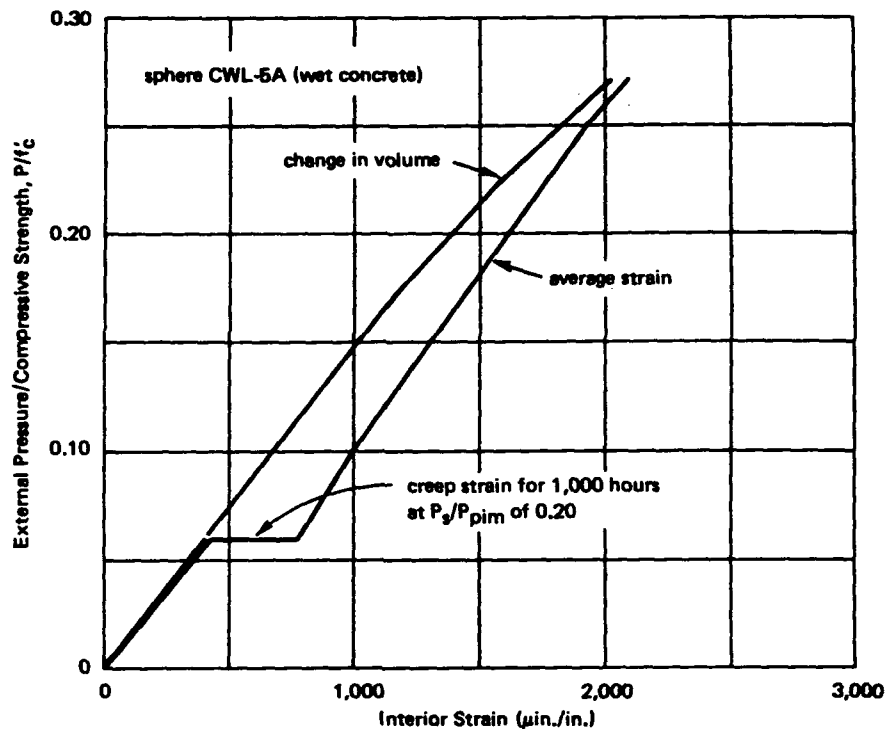


Figure 28. Interior strain behavior for sphere CWL-5.

Strain During Increasing Loading. Figures 28 through 34 present P/f'_c versus the average interior strain and change-in-volume strain for spheres CWL-5 through CDL-11 as the pressure was increased at a rate of 100 psi/min. For most of the specimens (CWL-6, CWL-8, CWL-9A, CWL-9B, CDL-10, and CDL-11) the change-in-volume strains indicated the same deformation behavior as the average interior strain gages.

Four spheres underwent two stages of pressurization—the first pressurization stage to a sustained load held for 500 or 1,000 hours and the second pressurization stage to a higher sustained load (spheres CWL-5 and CWL-9) or to implosion (spheres CWL-6 and CDL-11). Figures 28, 29, 32, and 34 show that each sphere became stiffer after the period of sustained load. The stiffness increase was not caused solely by further hydration of the cement, because both the wet-concrete spheres (CWL-5, CWL-6 and CWL-9) and the dry-concrete sphere (CDL-11) showed similar stiffness increases. This stiffness increase might have been a result of compaction of the concrete because of creep.

Results of experiments on concrete cylinders under sustained uniaxial load also showed that both wet and dry concrete exhibited an increase in elastic modulus after periods of sustained load.¹⁴

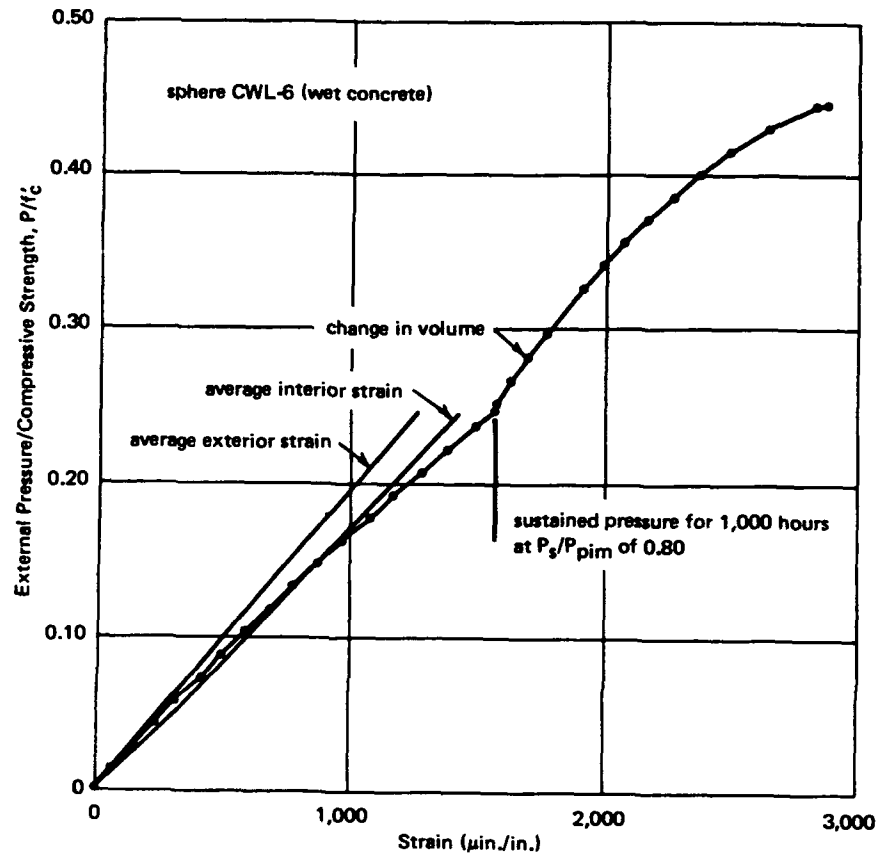


Figure 29. Strain behavior for sphere CWL-6.

Strain During Sustained Loading. The strain behavior of the spheres under sustained loading has been summarized in Figures 35 and 36, in which the average interior strain is shown as a function of log time. A series of straight lines closely fit the strain-versus-log-time data. Strain response versus rectilinear time for individual sphere tests is given in Appendix F; these figures show typical concrete creep behavior.

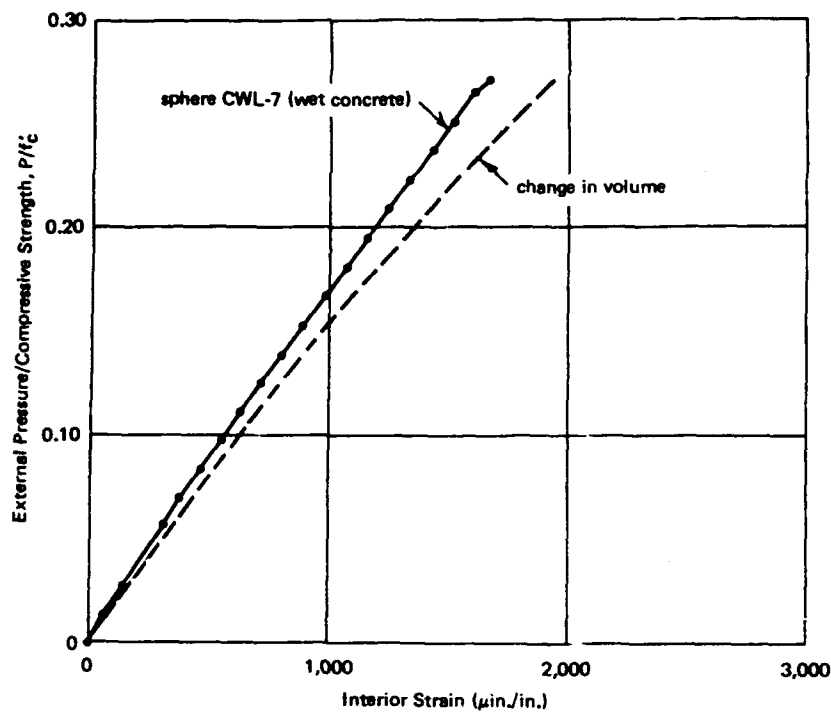


Figure 30. Interior strain behavior for sphere CWL-7.

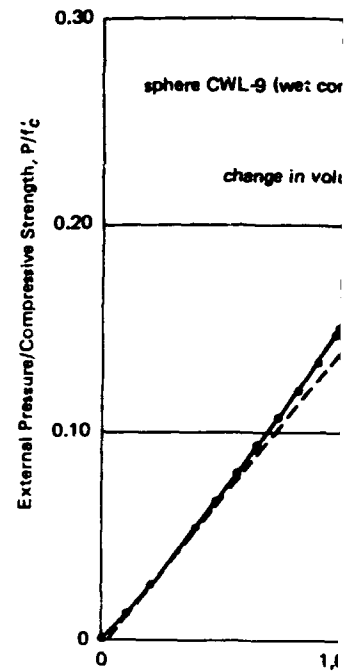


Figure 32. Interior strain behavior for sphere CWL-9.

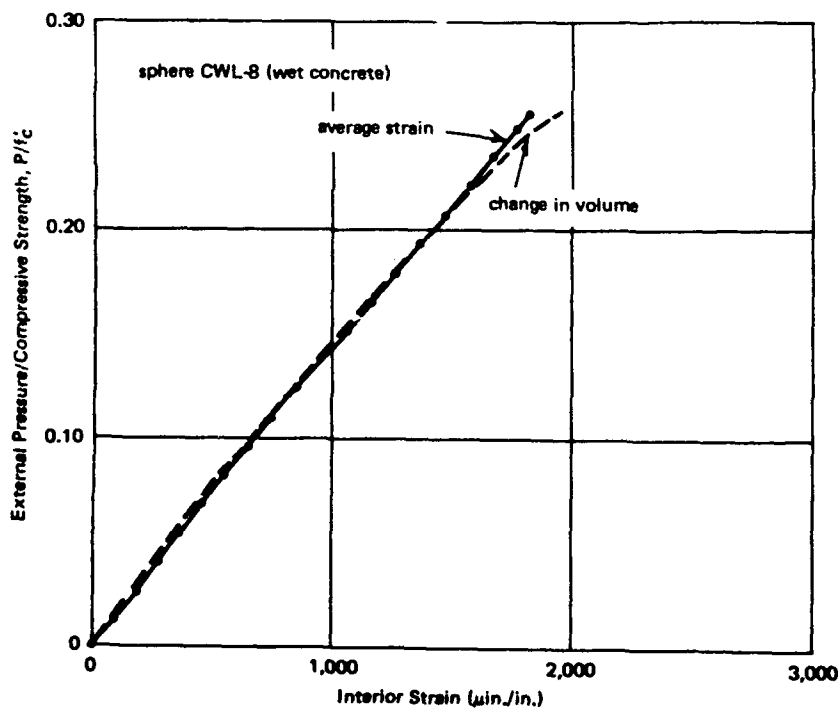


Figure 31. Interior strain behavior for sphere CWL-8.

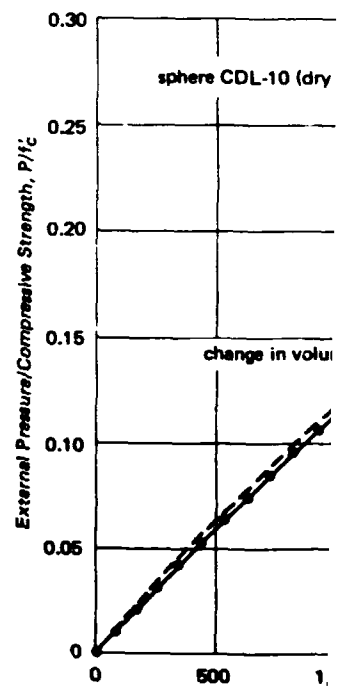
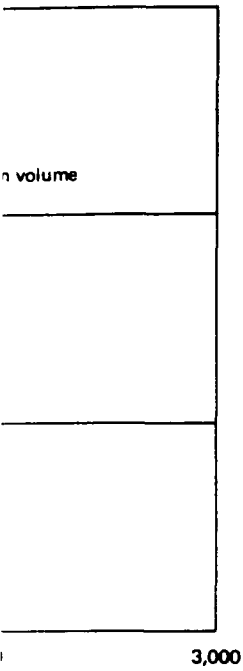
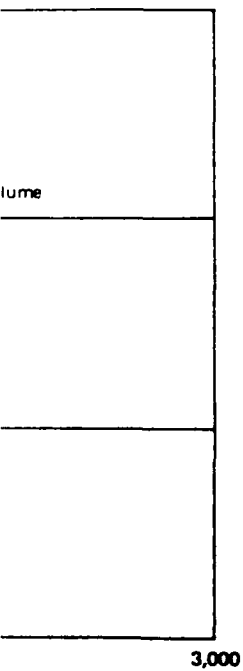


Figure 33. Interior strain behavior for sphere CDL-10.



ere CWL-7.



re CWL-8.

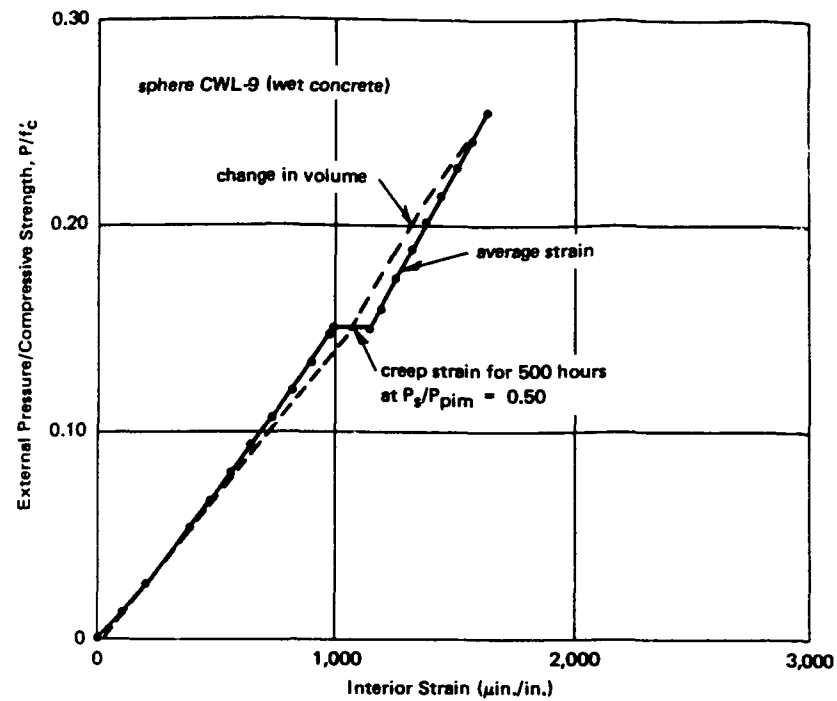


Figure 32. Interior strain behavior of sphere CWL-9.

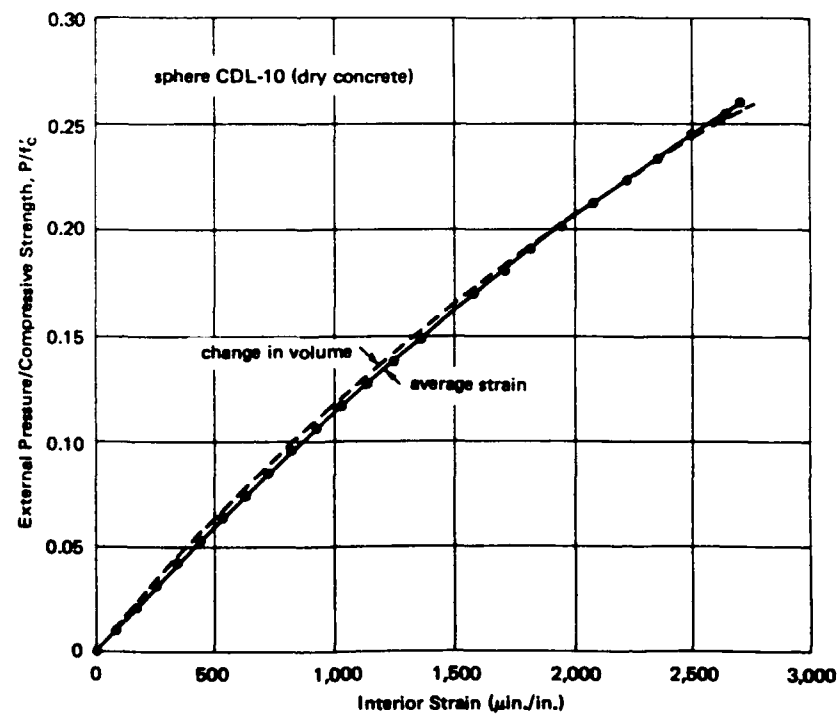


Figure 33. Interior strain behavior for sphere CDL-10.

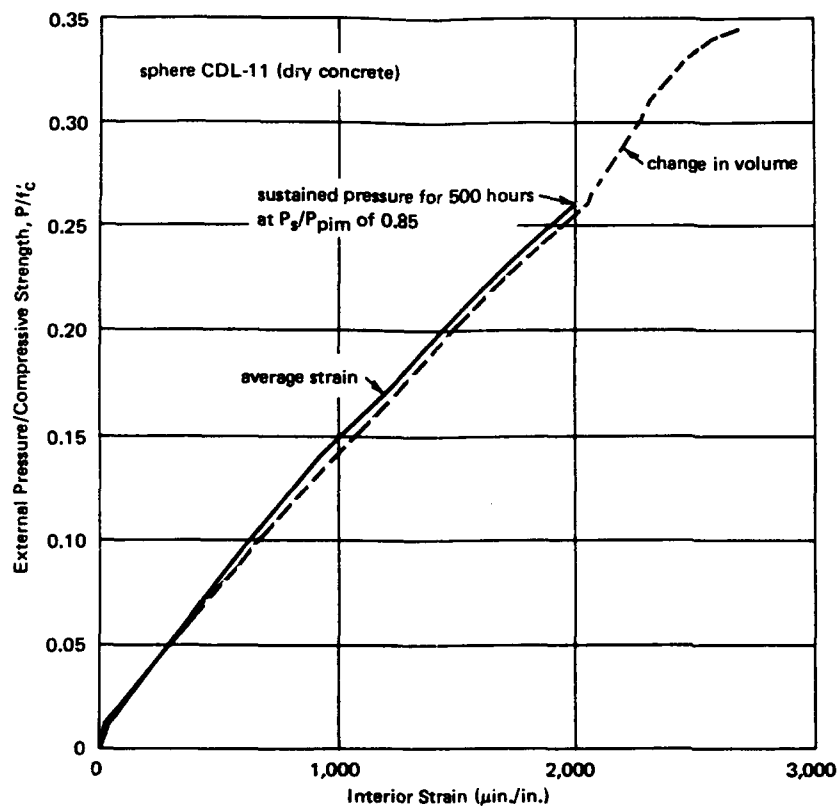


Figure 34. Interior strain behavior of sphere CDL-11.

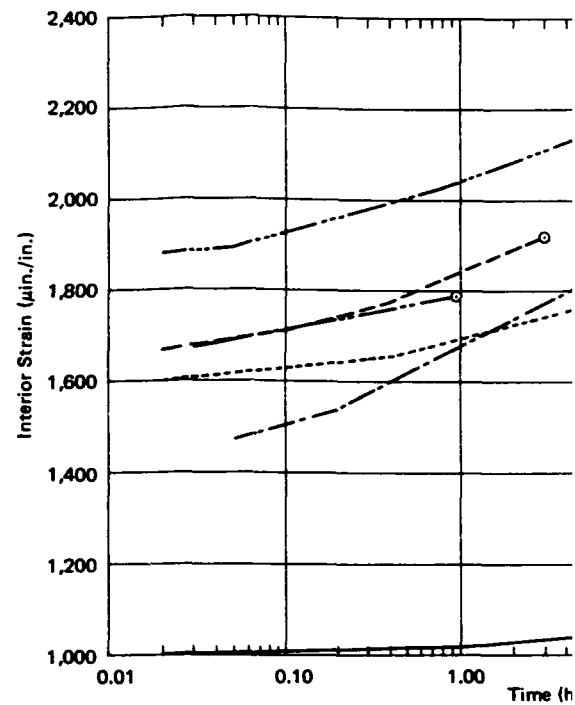


Figure 35. Interior creep strain behavior for sphere CDL-11.

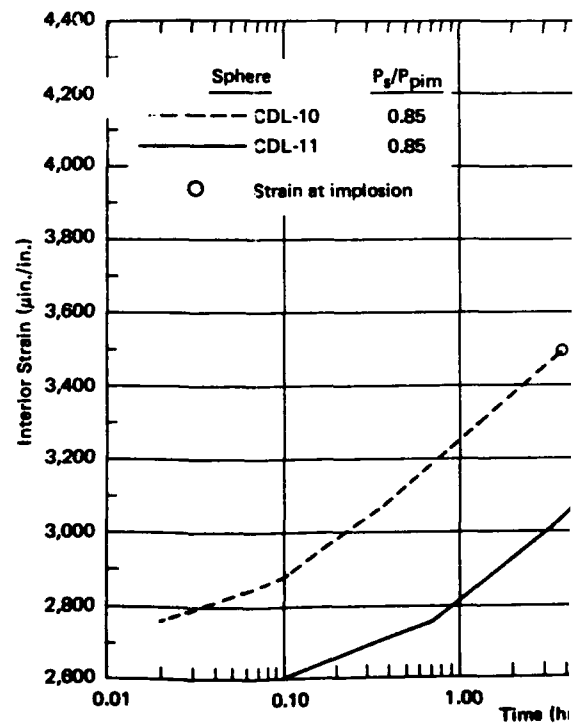


Figure 36. Interior creep strain behavior for sphere CDL-10 and CDL-11.

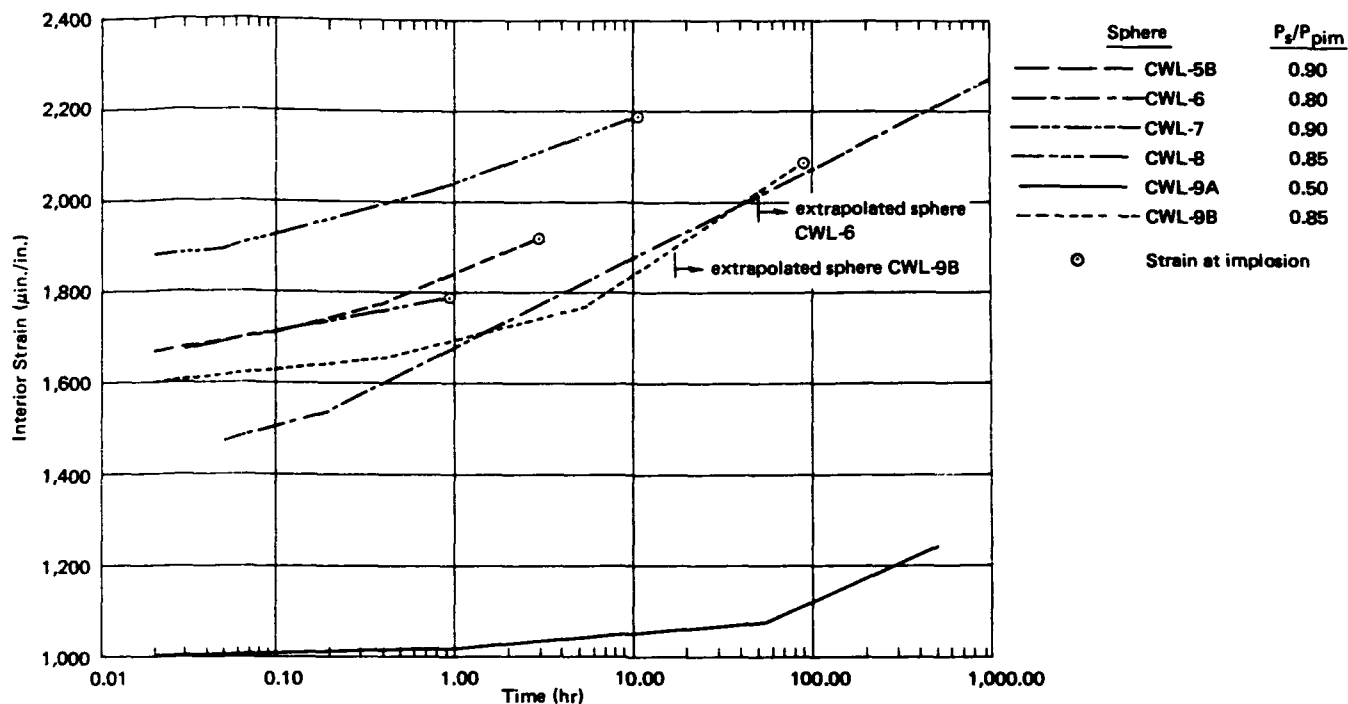


Figure 35. Interior creep strain behavior for spheres CWL-5 through CWL-9.

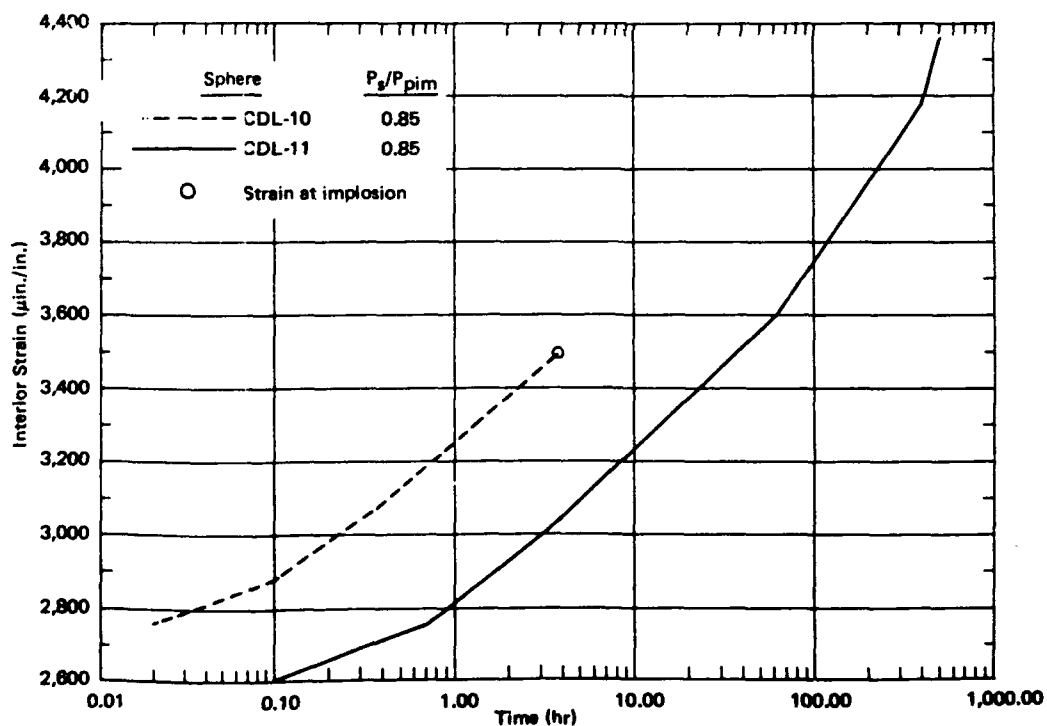


Figure 36. Interior creep strain behavior for spheres CDL-10 and CDL-11.

The principal feature shown by Figures 35 and 36 is that the creep strain of the dry-concrete spheres was considerably greater in magnitude and in rate than that of the wet-concrete spheres under the same pressure. This result agrees with the finding of 16-inch-OD mortar spheres under sustained load equal to 50% of the predicted implosion pressure; the dry-mortar sphere had a higher creep rate and total strain than a wet-mortar sphere.¹⁰ Also, tests of concrete cylinders under uniaxial sustained loads equal to 50% of their ultimate strength have shown that at 50% relative humidity the creep strain is more than twice that at 100% relative humidity.¹⁵ Other investigators have shown that, although the creep rate of dry concrete is initially higher than that of wet concrete, the rates become approximately equal after several years of sustained load.¹² In general, results of the creep strain behavior of the concrete spheres agreed with past research on the creep of concrete under uniaxial sustained loads.

The maximum strain at failure varied considerably for the various spheres. For the wet-concrete specimens that imploded after time under load, the specimens subjected to 90% P_{pim} (spheres CWL-5B and CWL-7) had ultimate strains lower than those at 85% P_{pim} . This finding agreed with results by Sell¹¹ that indicated that dry concrete showed lower ultimate strains when subjected to higher sustained uniaxial loads.

Permeability

The permeability of the five wet-concrete spheres to seawater was determined by measuring the quantity of water flowing out of the spheres with time. (The spheres were filled with water at zero pressure loading so water flowing out of the sphere at the top penetrator was collected and measured.) The water outflow was plotted versus time with zero time beginning when constant pressure was attained (Figures 37 through 40). Although the outflow was a combined result of viscous deformation and concrete permeability, the outflow due to permeability was orders of magnitude greater than that due to deformation when tests continued for over 100 hours.

Previous studies by the Bureau of Reclamation¹⁶ have shown that concrete permeability can be formulated using D'Arcy's law for viscous flow. D'Arcy's permeability coefficient can be expressed as follows for the spheres:

$$K_c = \frac{qt}{Ah} \quad (4)$$

where K_c = permeability coefficient of concrete (ft/sec)

q = rate of permeability (quantity of seawater that permeated into sphere interior per unit time) (ft³/sec)

t = wall thickness (ft)

A = exterior surface area of sphere (ft²)

h = pressure head (ft)

The Bureau experiments¹⁶ showed that the permeability of concrete decreased with time; however, the permeability coefficients were determined by drawing straight-line tangents to curves of water outflow versus time. Similarly, straight-line tangents were drawn for the concrete spheres on Figures 37 through 40 in such a manner that the slope of the line best approximated the general outflow-versus-time curve.

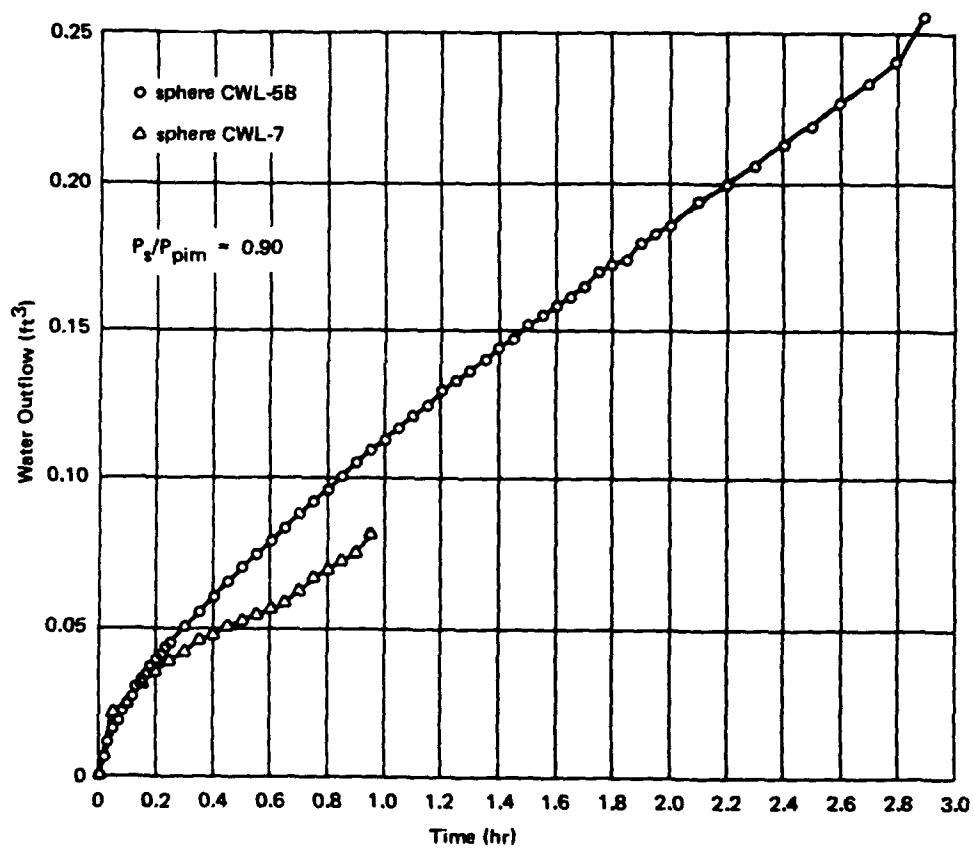


Figure 37. Water outflow versus time for spheres CWL-5B and CWL-7 under sustained pressure of 90% P_{pim} .

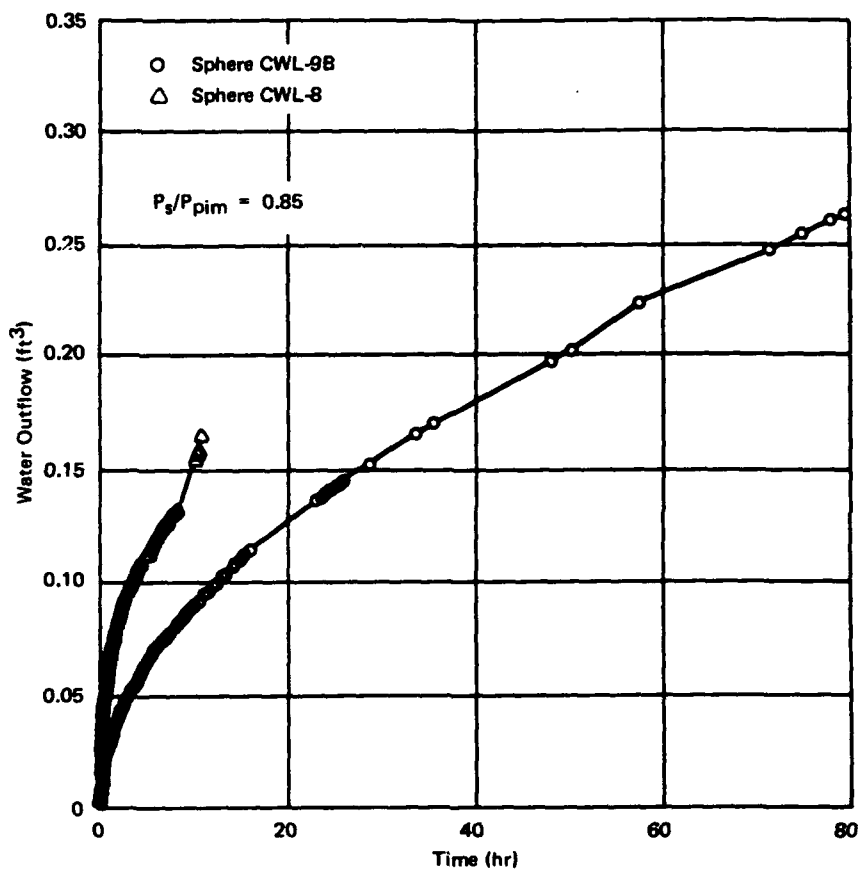


Figure 38. Water outflow versus time for spheres CWL-8 and CWL-9B under sustained pressure of 85% P_{pim} .

The experimental K_c values for the spheres are listed in Table 6. Lower K_c values were found when the time at which K_c was determined was greater (except for sphere CWL-5A).

The rate of outflow for sphere CWL-5A was nearly constant with time; this behavior was different from that of the other specimens. The total amount of outflow was an order of magnitude greater than that for spheres CWL-6 and CWL-9. The constant rate and larger outflow indicated that sphere CWL-5 had a small leak somewhere in the hull. (From experience, we suspect that the leak was most probably at an epoxy-concrete interface.)

An average K_c value of 0.13×10^{-12} ft/sec was determined for the concrete in spheres CWL-6 and CWL-9A; both specimens were tested for periods longer than 500 hours. This mean K_c value was compared with an estimated K_c value from previous work. One estimate was obtained by

extrapolating curves¹⁶ for concretes of various mixes similar to the concrete mix used in this study; the approximated K_c was 0.40×10^{-12} ft/sec. Another estimate was obtained by proportionately reducing the permeability of large-aggregate concrete to the permeability of 3/4-inch-aggregate concrete;¹⁷ this approximate K_c value was also 0.40×10^{-12} ft/sec. The similarity between the two estimates is surprising, because the variation in K_c for identical concretes is often greater than an order of magnitude. Likewise, these estimated K_c values were only three times as great as the mean K_c value for this study. Hence, the concrete in this study, which was subjected to pressure as high as 1,670 psi, showed permeability coefficients similar to those of concrete subjected to pressure as high as 400 psi.

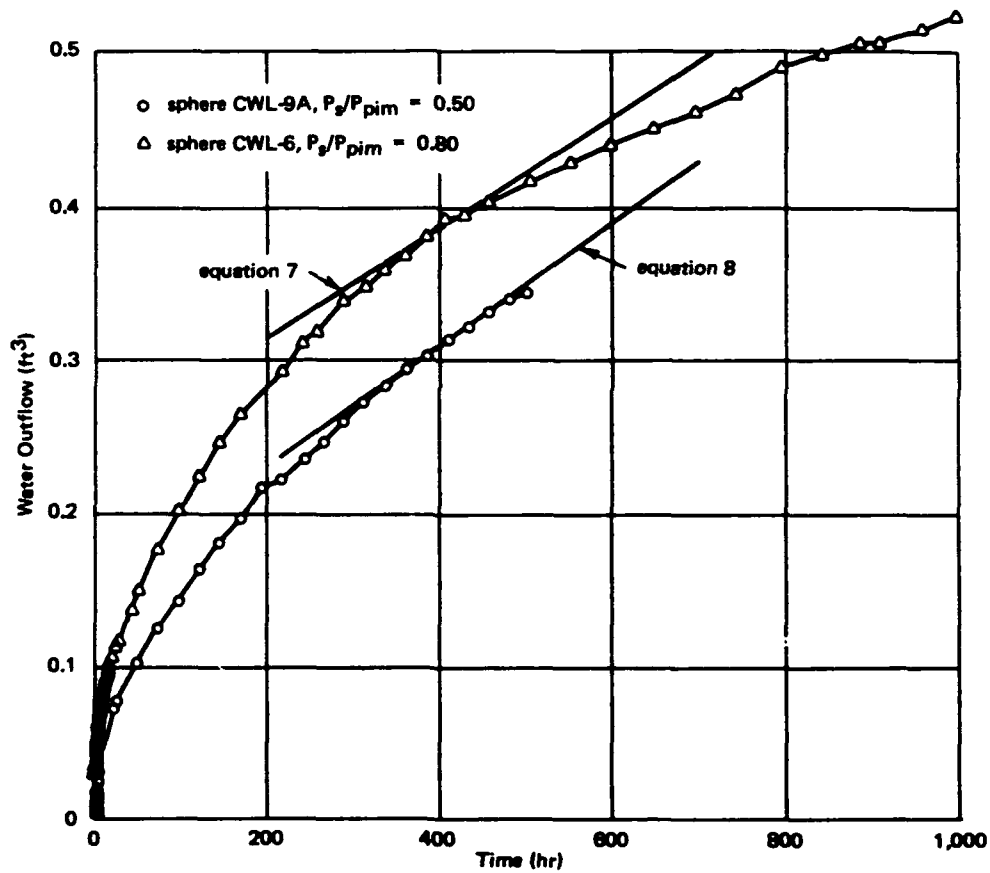


Figure 39. Water outflow versus time for spheres CWL-6 and CWL-9A under sustained pressures of 80 and 50% P_{pim} , respectively.

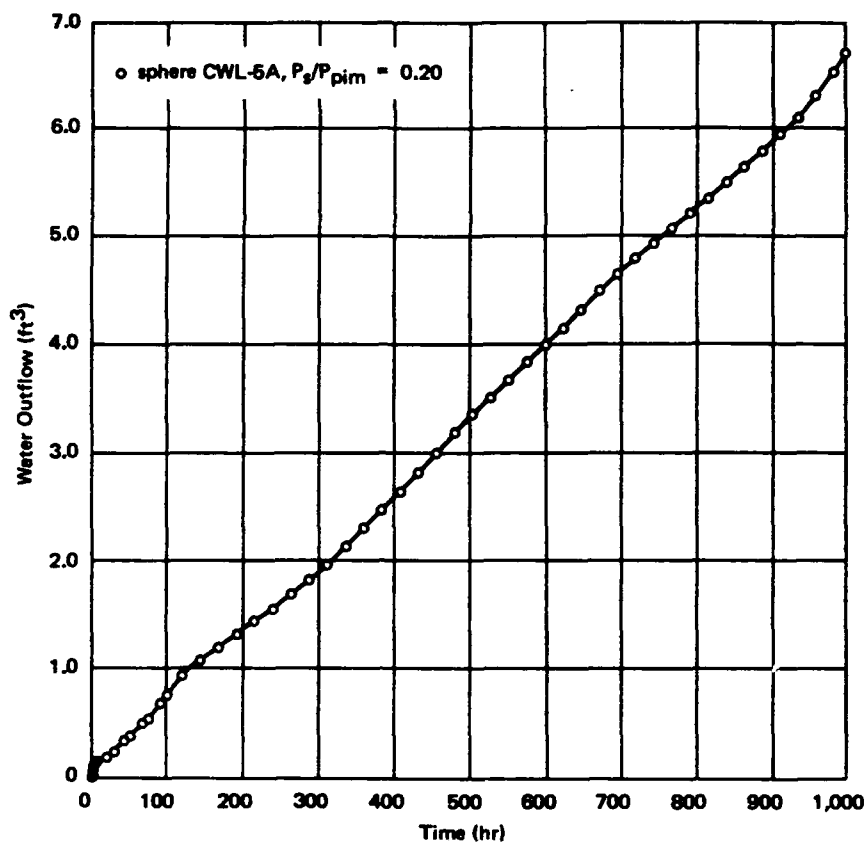


Figure 40. Water outflow versus time for sphere CWL-5A under sustained pressure of 20% P_{pim} .

Table 6. Permeability Coefficients

Sphere No.	Ratio of Sustained Pressure to Predicted Implosion Pressure, P_s/P_{pim} (%)	Sustained Pressure, P_s (psi)	Duration of Test (hr)	Time When K_c Calculated (hr)	D'Arcy's Permeability Coefficient K_c (ft/sec $\times 10^{-12}$)
CWL-5A	20	505	1,000	500.0	5.90
CWL-5B	90	2,278	3	1.8	13.50
CWL-6	80	1,670	1,000	400.0	0.10
CWL-7	90	1,942	1	0.5	10.00
CWL-8	85	1,845	11	7.0	1.38
CWL-9A	50	1,120	500	400.0	0.16
CWL-9B	85	1,904	90	50.0	0.50

Note: Average K_c value of concrete spheres was taken as 0.13×10^{-12} ft/sec. This was the result of averaging spheres CWL-6 and CWL-9A, used because these spheres were under sustained loading for 500 hours or more. Permeability coefficient for sphere CWL-5A, also under sustained loading for more than 500 hours, was not included in the average because rate of water outflow, q , was typical of a sphere with a leak.

The water outflow for spheres CWL-6 and CWL-9A was plotted versus log time in Figure 41. There appeared to be a linear relation between water outflow and log time after 200 hours for both spheres. The equations of the straight lines are

for sphere CWL-6,

$$\Delta = 0.114 \log(T - 99) + 0.184 \quad (5)$$

and for sphere CWL-9A,

$$\Delta = 0.122 \log(T - 99) + 0.095 \quad (6)$$

where Δ = water outflow equal to rate of outflow, q , times time, T (ft^3)

T = time (hr)

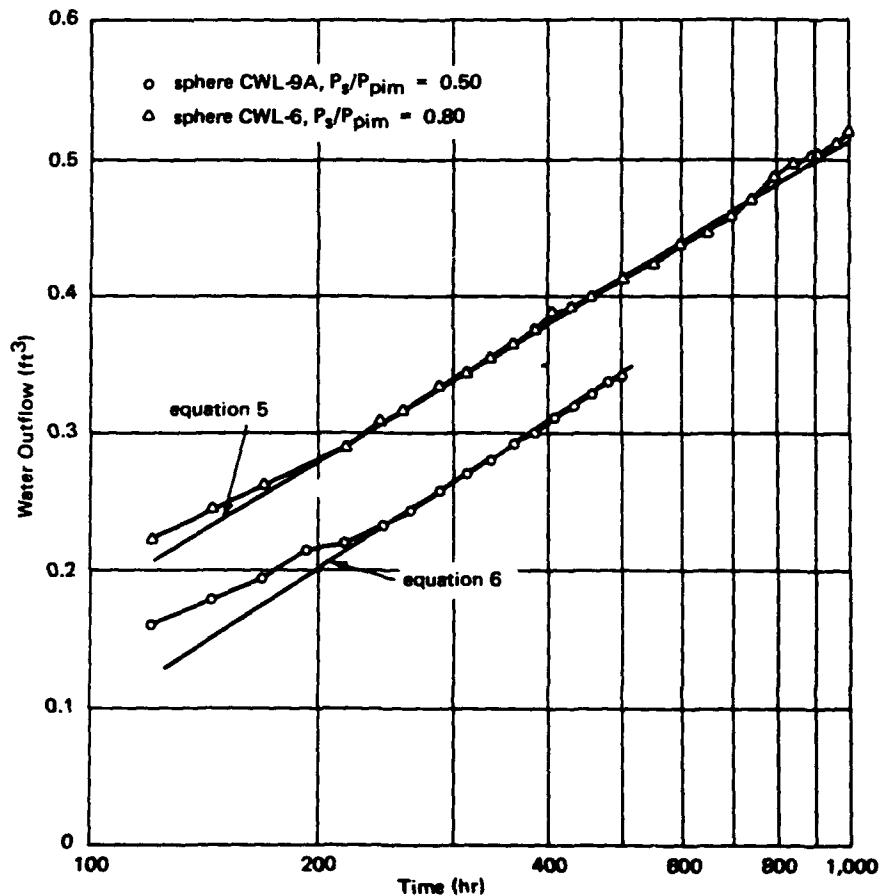


Figure 41. Water outflow versus log time for spheres CWL-6 and CWL-9A under sustained pressures of 80 and 50% P_{pim} , respectively.

Similar equations for water outflow were developed for the straight-line tangents shown on Figure 39 for spheres CWL-6 and CWL-9A; these relations are

for sphere CWL-6,

$$\Delta = 0.000364 T + 0.244 \quad (7)$$

and for sphere CWL-9A,

$$\Delta = 0.000399 T + 0.155 \quad (8)$$

These rectilinear functions, Equations 7 and 8, are based on D'Arcy's law of viscous flow.

To compare the logarithmic and rectilinear relations, the total outflow was computed for periods of 1 and 10 years; these quantities are listed in Table 7. The predicted differences in outflow are significant, particularly for the 10-year period.

Table 7. Predicted Seawater Permeation of Spheres CWL-6 and CWL-9A After 1 and 10 Years

Sphere	Sustained Pressure, P_s (psi)	Total Water Permeation (ft ³)			
		After 1 Year		After 10 Years	
		Logarithmic Relation	D'Arcy Relation	Logarithmic Relation	D'Arcy Relation
CWL-6	1,670	0.63 ^a	3.42 ^c	0.75 ^a	32.08 ^c
CWL-9A	1,120	0.58 ^b	3.64 ^d	0.70 ^b	35.09 ^d

Note: Total interior volume of sphere is 58.02 ft³.

^a Equation 5.

^b Equation 6.

^c Equation 7.

^d Equation 8.

Additional data are being collected on water permeation of concrete spheres from ocean tests that will continue for up to 10 years. The logarithmic relation may prove the more accurate because it accounts for the decrease of permeation with time. Yet, past experience has indicated that the D'Arcy function has reliably estimated the permeability of concrete to freshwater. Data from a mortar sphere submerged at 120 feet for one year are given in Appendix G and support the D'Arcy approach. It is hoped that the long-term ocean tests on the spheres will help decide which approach is more accurate in predicting long-term permeability of concrete to seawater.

A decrease in permeability with time may result from two factors.

1. In the presence of water, the cement undergoes further hydration, which results in smaller pore sizes between cement gels. This decrease in porosity causes a corresponding decrease in flow.¹⁸

2. As the seawater, which is high in mineral content—including $\text{Ca}(\text{HCO}_3)_2$ —begins permeating the concrete, the water may form a thin, impervious shell of CaCO_3 on the interior surface where the pore pressure is low. Also, materials such as $\text{Mg}(\text{OH})_2$ and CaCO_3 are precipitated within the pores of the concrete.¹⁹ Both the formation of the CaCO_3 shell and the precipitation of minerals in the pores decrease the permeability.

If the porosity of the concrete continues to decrease because of cement hydration and deposition of minerals, the logarithmic relations (Equations 5 and 6) may be valid in predicting long-term flow. But as water flows through the concrete, it dissolves materials from the cement, particularly CaO ;¹⁹ the reduction in CaO would tend to increase porosity and, thus, offset the decreases. Therefore, at present the authors propose that the D'Arcy flow relation, Equation 4, be used to predict the permeability of concrete spheres; such a relation is conservative for design purposes.

FINDINGS

1. Under short-term loading, six concrete spheres, 66 inches in OD and 4.125 inches in wall thickness, showed an average ratio of implosion pressure to concrete control cylinder strength (P_{im}/f'_c) of 0.303. This ratio was 3% greater than that for 16-inch-OD mortar spheres tested in previous investigations and was 30% greater than that for the 66-inch-OD mortar spheres. The average implosion pressure for the wet-concrete spheres was 2,350 psi ($f'_c = 7,810$ psi) and for the dry-concrete spheres was 2,810 psi ($f'_c = 9,185$ psi). The difference in implosion pressure was the result of differences in concrete

compressive strength. The uniaxial compressive strength of wet-concrete control cylinders was 10% less than the compressive strength of companion dry-concrete cylinders.

2. The implosion equation, Equation 1, developed from previous tests on 16-inch-OD spheres conservatively predicted within 9% the implosion pressures of 66-inch-OD concrete spheres.
3. Concrete spheres under high levels of sustained hydrostatic loading failed by static fatigue, and the curve of time to implosion versus level of sustained load for the spheres was approximately 2% lower than the known behavior of concrete tested under uniaxial loading.
4. At equivalent P_{im}/f'_c ratios, the creep strain of dry-concrete spheres under long-term loading was greater in rate and in magnitude than that of wet-concrete spheres.
5. D'Arcy's permeability coefficient (K_c) was found to be an average 0.13×10^{-12} ft/sec for concrete spheres under hydrostatic head as high as 3,760 ft; this K_c value was similar to known values for concrete under a pressure head lower than 900 feet.
6. Spheres subjected to sustained loads that did not cause static fatigue failure showed an increase in implosion pressure over that predicted from the short-term tests.

CONCLUSIONS

1. The response of 66-inch-OD concrete spheres to short-term hydrostatic loading has shown that the previous test data on 16-inch-OD mortar models are accurate to within 9% in predicting the behavior of larger scale specimens and may be used to aid in establishing design criteria.
2. In both the short- and long-term tests it was found that allowing the concrete to become saturated with seawater lowered the strength of the concrete but otherwise did not adversely affect the behavior of the structure compared with that of dry-concrete spheres.
3. The test results on permeability and creep deformation of spheres under sustained loading have shown that the behavior of the concrete was similar to the known behavior of uniaxially loaded concrete specimens.
4. The authors do not hesitate to recommend that concrete structures be used to depths of 1,000 feet. It is anticipated that with additional knowledge from on-going tests buoyant concrete spheres can be used to 3,000 feet.

5. This study, together with the earlier studies on concrete spheres, has clearly shown that concrete is an applicable material for the construction of undersea structures. With this developed knowledge of the behavior of concrete spheres and by applying present-day concrete technology, spherical concrete hulls can be safely designed and employed for undersea applications.

DESIGN GUIDES

DESIGN RECOMMENDATIONS

1. It is recommended that Equation 1 be used to predict the short-term implosion pressure of concrete spheres:

$$P_{im} = \left[5.02 \left(\frac{t}{D_o} \right) - 0.038 \right] f'_c \quad (1)$$

where P_{im} = implosion pressure (psi)

t = wall thickness (in.)

D_o = outside diameter (in.)

f'_c = ultimate uniaxial concrete compressive strength (psi)

The concrete strength, f'_c , should be determined from wet-concrete control cylinders if the structure will not be completely waterproofed.

2. For concrete spheres under sustained pressure loads, Equation 3 may be used to estimate the time to implosion for the sphere:

$$P_s/P_{pim} = 0.908 - 0.0360 \log_{10} T \quad P_s/P_{im} \leq 0.70 \quad (3)$$

or

$$\log_{10} T = 25.2 - 27.8 \frac{P_s}{P_{pim}}$$

where P_s = sustained hydrostatic pressure (psi)

P_{pim} = predicted implosion pressure (same as P_{im} in Equation 1)
(psi)

T = time to implosion (hr)

3. The permeation of seawater through the concrete wall of the spheres under hydrostatic loading may be conservatively predicted by use of D'Arcy's law for viscous flow:

$$q = K_c \frac{A h}{t} \quad (4)$$

where q = rate of permeability (quantity of seawater that permeated into sphere interior per unit time) (ft³/sec)

K_c = coefficient of permeability (ft/sec)

A = exterior surface area of sphere (ft²)

h = pressure head (ft)

t = wall thickness (ft)

The K_c for the particular concrete to be used may be determined from past references on concrete permeability, such as Reference 16. The value of K_c found for the concrete used in this study was 0.13×10^{-12} ft/sec.

EXAMPLE DESIGN PROBLEM

Given data are a spherical hull with a 50-foot ID, a net buoyancy of 250 tons, and an operational depth of 1,000 feet. A safety factor of three is assumed on the hull. Determine the wall thickness, estimated life of the structure, and rate of water permeation into the structure.

Wall Thickness

Design the wall thickness based on buoyancy requirement and then check the implosion depth for the hull.

$$(a) \text{ Displacement of hull} = (64 \text{ lb/ft}^3) (\pi/6) (D_o^3) = 33.51 D_o^3$$

$$(b) \text{ Weight of hull} = (150 \text{ lb/ft}^3) (\pi/6) [D_o^3 - (50 \text{ ft})^3] \\ = 78.54 D_o^3 - 9,817,500$$

$$(c) \text{ Displacement} - \text{weight} = \text{buoyancy} = (250 \text{ tons}) (2,000 \text{ lb/ton}) \\ = 500,000 \text{ lb}$$

Substitute (a) and (b) into (c),

$$(d) \quad 33.51 D_o^3 - 78.54 D_o^3 - 9,817,500 = 500,000$$

$$D_o = 59.15 \text{ ft}$$

$$(e) \quad \text{Wall thickness, } t = (D_o - D_i)/2 = (59.15 - 50.00)/2 = 4.57 \text{ ft}$$

Determine implosion pressure from Equation 1, using $f'_c = 8,000$ psi

$$(f) \quad \text{Implosion pressure, } P_{im} = [5.02 (4.57/59.15) - 0.038] 8,000 \\ = 2,800 \text{ psi}$$

$$(g) \quad \text{Implosion depth} = (2,800 \text{ psi}) (2.25 \text{ ft/psi}) = 6,300 \text{ ft}$$

$$(h) \quad \text{Safety factor} = \text{implosion depth/operational depth} \\ = 6,300/1,000 = 6.3$$

Assumed safety factor of 3.0 is less than 6.3.

Use $t = 4.57$ ft

Life of Structure

Substitute into Equation 3 using P_s of 445 psi and P_{pim} of 2,800 psi.

$$(i) \quad \log_{10} T = 25.2 - 27.8(445/2,800) = 20.8$$

$$(j) \quad T = 6.3 \times 10^{20} \text{ hr or } 7.2 \times 10^{16} \text{ yr}$$

Time to implosion is not a critical factor.

Water Permeation

Substitute into Equation 4 using $K_c = 0.13 \times 10^{-12}$ ft/sec.

$$(k) \quad \text{Rate of permeability, } q = [(0.13 \times 10^{-12} \text{ ft/sec}) (\pi) (59.15 \text{ ft})^2 \\ (1,000 \text{ ft})]/4.57 \text{ ft} \\ = 3.13 \times 10^{-7} \text{ ft}^3/\text{sec or } 8.85 \text{ ft}^3/\text{yr}$$

Appendix A

CONCRETE AND MORTAR MIX DESIGNS

The concrete and mortar mix designs are given in Tables A-1 and A-2.

The concrete was transit-mixed with final determination of water content based on workability. The slump was $1\frac{1}{2} \pm \frac{3}{4}$ inches. The cement factor was 733 lb/yd³ (7.8 bags/yd³), and the unit weight of the concrete was 145 lb/ft³.

The mortar was mixed in the laboratory, and the same absolute quantities of constituents were used for each batch. Slump values ranged from 1 to $3\frac{1}{2}$ inches. The cement factor was 825 lb/yd³ (8.8 bags/yd³), and the unit weight of the mortar was 140 lb/ft³.

Table A-1. Concrete Mix Design

Portland cement, type II, low-alkali
 Santa Clara River aggregate
 Water/cement ratio = 0.41
 Sand/cement ratio = 1.85
 Coarse-aggregate/cement ratio = 2.28
 Water-reducing admixture—2 oz/sack of Plastiment

Material	Aggregate Gradation		
	Sieve Size Designation	Percentage Retained	
		Individual	Cumulative
Sand	3/8-inch	0	0
	no. 4	2	2
	no. 8	11	13
	no. 16	17	30
	no. 30	28	58
	no. 50	28	86
	no. 100	11	97
	pan	3	100
Coarse aggregate	3/4-inch	0	0
	3/8-inch	70	70
	no. 4	30	100

Table A-2. Mortar Mix Design

Portland cement, type III, high early strength

San Gabriel River Wash aggregate

Water/cement ratio = 0.55

Sand/cement ratio = 3.30

Material	Aggregate Gradation		
	Sieve Size Designation	Percentage Retained	
		Individual	Cumulative
Sand	no. 4	0	0
	no. 8	29.6	29.6
	no. 16	20.8	50.4
	no. 30	14.7	65.1
	no. 50	10.3	75.4
	no. 100	7.3	82.7
	pan	17.3	100.0

Appendix B

MECHANICAL PROPERTIES OF CONCRETE AND MORTAR CONTROL CYLINDERS

Table B-1. Control Cylinder Data

Hemisphere No.	Compressive Strength, f'_c (psi)		Secant Modulus at One-Half f'_c of Dry Concrete, E_s (psi x 10 ⁶)	Poisson's Ratio	Age at Test (days)
	Dry Concrete	Wet Concrete			
CDS-1a	9,250	—	4.63	0.24	169
CDS-1b	9,430	—	4.21	0.24	162
CDS-2a	9,120	—	4.31	0.24	121
CDS-2b	9,190	—	4.69	0.24	119
CDS-3a	9,010	7,960	—	—	210
CDS-3b	9,000	8,450	—	—	203
CDS-4a	8,270	7,660	4.00	—	195
CDS-4b	9,570	7,840	4.30	—	171
CWL-5a	8,130	7,900	3.83	0.16	259
CWL-5b	8,840	8,590	4.27	0.22	250
CWL-6a	8,110	6,740	3.94	0.20	331
CWL-6b	9,230	7,330	4.06	0.18	317
CWL-7a	7,640	7,170	3.90 ^a	0.14	351
CWL-7b	8,790	8,060	3.96 ^a	0.17	344
CWL-8a	9,300	7,820	3.81	0.20	366
CWL-8b	8,470	7,210	3.72	0.15	361
CWL-9a	8,220	7,770	4.11	0.25	429
CWL-9b	8,230	7,440	3.81	0.21	427
CDL-10a	9,950	—	3.95	0.18	107
CDL-10b	9,420	—	4.09	0.22	105
CDL-11a	7,940	—	3.85	0.18	526
CDL-11b	8,320	—	3.86	0.20	512
MDS-1a	8,830	—	3.80	0.19	127
MDS-1b	10,480	—	3.43	0.20	105
MDS-2a	8,770	—	3.05	0.13	122
MDS-2b	8,010	—	3.63	0.19	129
MDS-3a	9,150	—	3.70	0.22	146
MDS-3b	9,750	—	3.10	0.14	140

^a When an extensometer was used, CWL-7a had a dry-concrete E_s of 3.55 psi and a wet-concrete E_s of 3.37 psi; CWL-7b had a dry-concrete E_s of 3.58 psi and wet-concrete E_s of 3.68 psi.

Appendix C

EFFECT OF CONTROL CYLINDER SIZE ON COMPRESSIVE STRENGTH

Tests were performed on 3 x 6- and 6 x 12-inch control cylinders to determine the effect of specimen size on the compressive strength. Six specimens of mortar and six of concrete were cast in 3 x 6- and 6 x 12-inch cylinders. The specimens were moist-cured for the first 28 days. The mortar specimens were wrapped in wet burlap and then in polyethylene film. The concrete specimens were placed in a 100% relative humidity water-mist enclosure located outdoors. The remainder of the curing period was at room conditions. At age 90 days the specimens were tested under uniaxial compression.

Table C-1 summarizes the results. The larger specimens showed a slight decrease in strength as compared with the smaller specimens for both the concrete and mortar; however, the decrease in strength was not statistically significant. It was concluded that for the high-strength concrete and mortar used in this study, the compressive strength, f'_c , was unaffected by the size of the control cylinder specimens (either 3 x 6 or 6 x 12 inches).

The stress-strain behavior for the specimens is shown in Figures C-1 and C-2. The behavior for large and small cylinders was essentially the same; again, any differences were not statistically significant.

Table C-1. Effect of Specimen Size on Control Cylinder Strength

Material	Size of Control Cylinder (in.)	Uniaxial Compressive Strength ^a (psi)	Standard Deviation (psi)	Difference in Strength ^b (%)	Statistically Significant ^c	Secant Modulus at One-Half f'_c , E_s ^d (psi x 10 ⁶)
Mortar	3 x 6	9,470	280	1.90	no	3.72
	6 x 12	9,290	240			3.98
Concrete	3 x 6	8,840	380	0.57	no	4.02
	6 x 12	8,790	340			4.18

^a Average of six specimens.

^b Percent difference = $\frac{(f'_c)_{3 \times 6} - (f'_c)_{6 \times 12}}{(f'_c)_{3 \times 6}} \times 100$.

^c "t" test at 95% level with 10 degrees of freedom.

^d Average of three specimens.

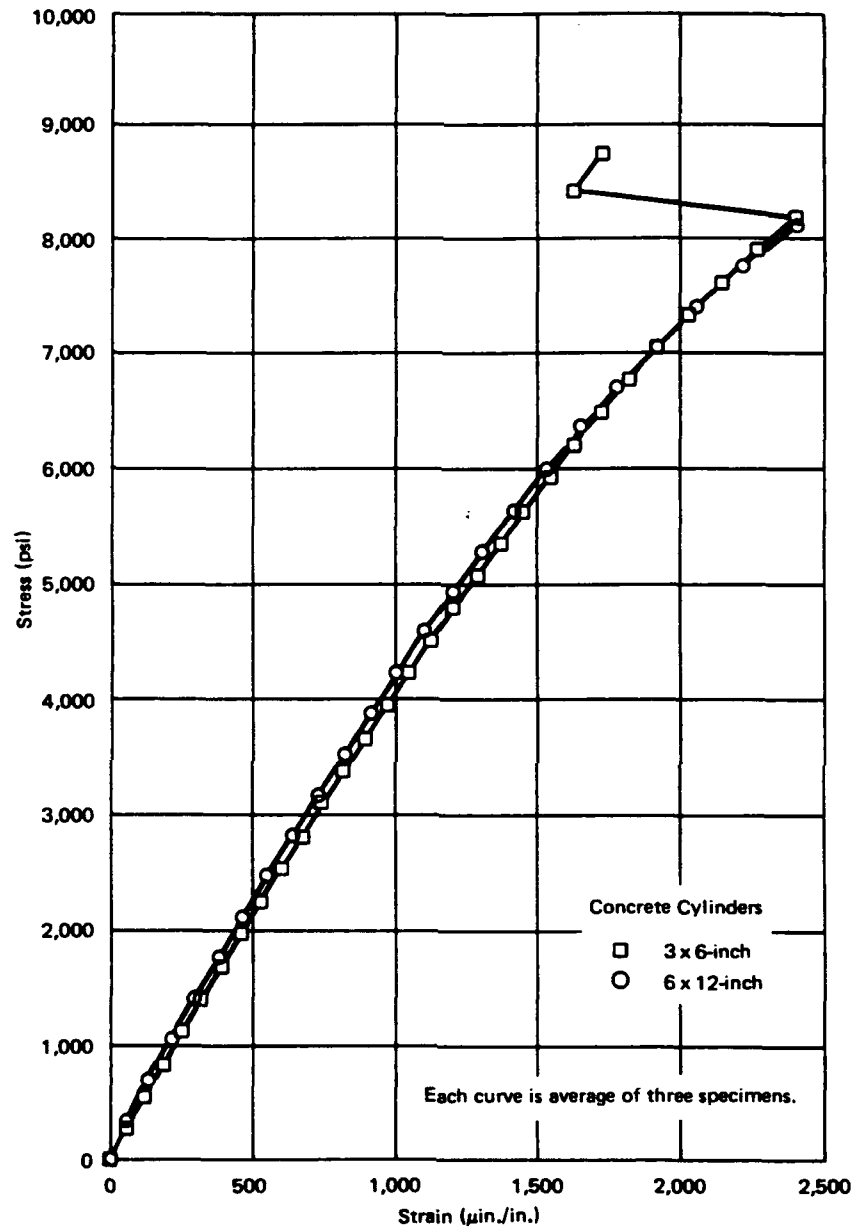


Figure C-1. Stress-strain behavior of 3 x 6- and 6 x 12-inch concrete control cylinders.

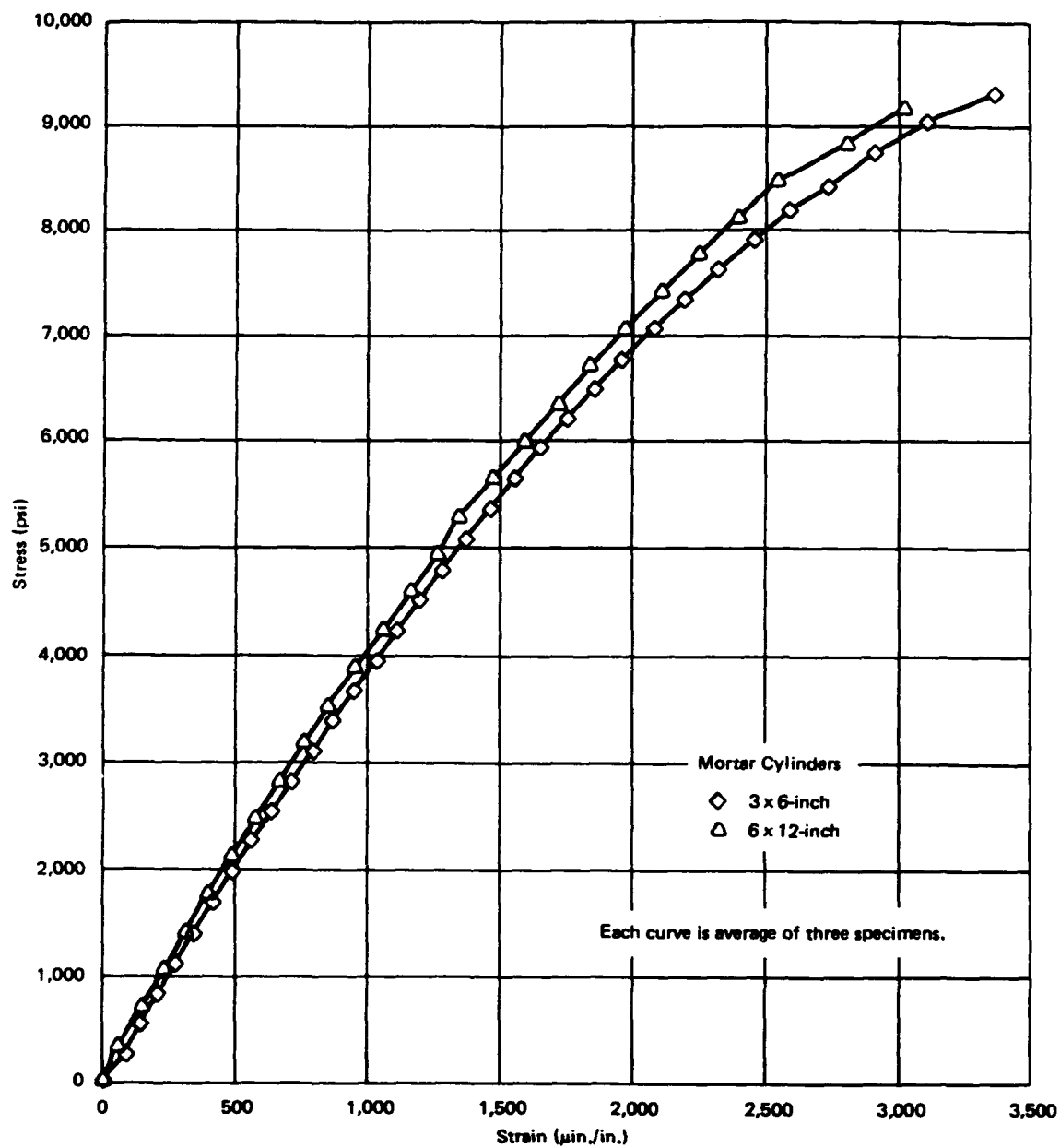


Figure C-2. Stress—strain behavior of 3 x 6- and 6 x 12-inch mortar control cylinders.

Appendix D

POST-IMPLOSION VIEWS OF CONCRETE AND MORTAR SPHERES

Figures D-1 through D-13 show all the concrete and mortar spheres, except CWL-8, after implosion. The reader is reminded that the spheres were filled with water during the test. This procedure saved the specimens from being completely fragmented by the violent shock forces associated with implosion, and thus enabled an inspection of the failure zone.



Figure D-1. Post-implosion view of sphere CDS-1.



Figure D-2. Post-implosion view of sphere CDS-2.

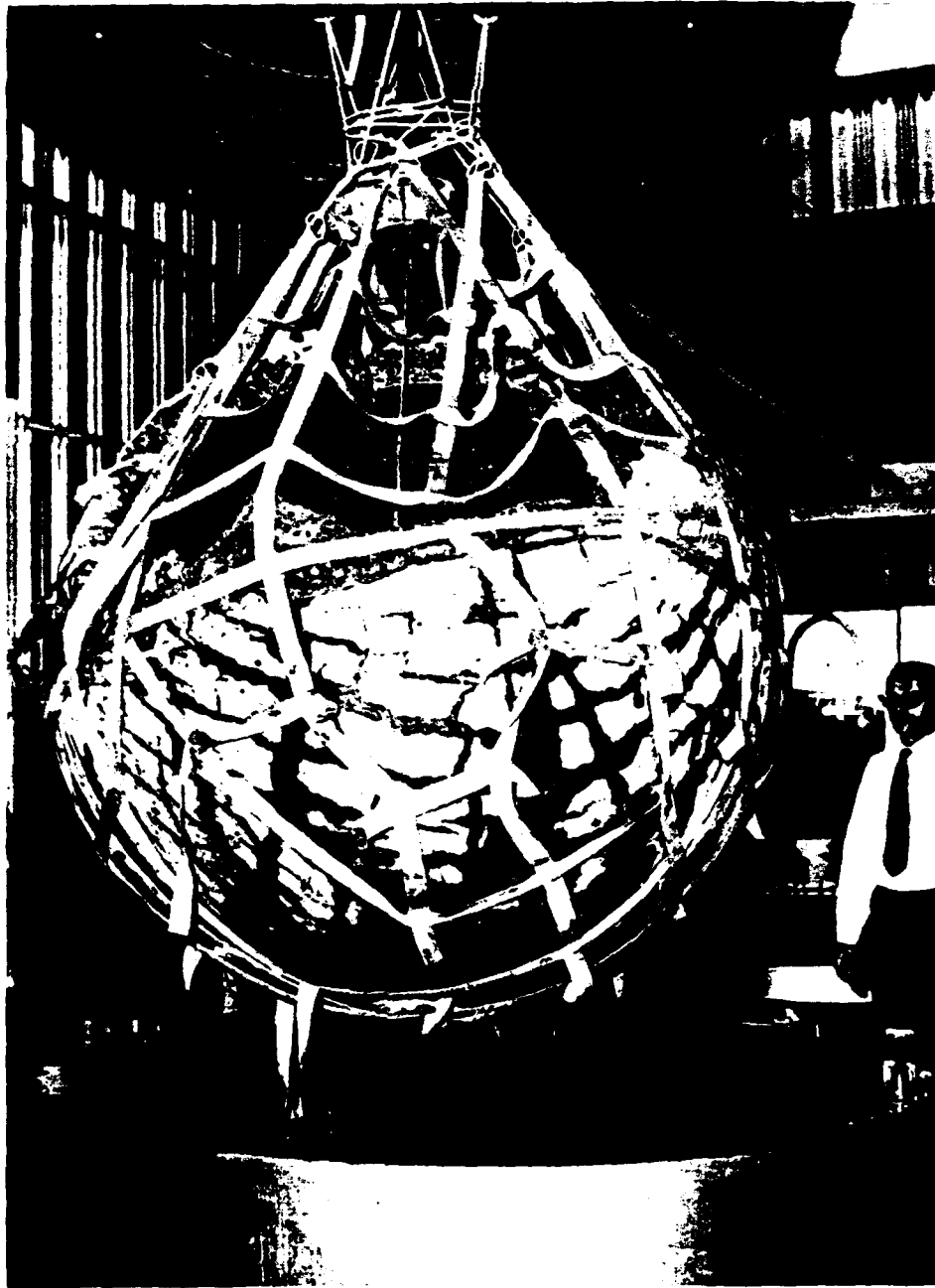


Figure D-3. Post-implosion view of sphere CWS-3.



Figure D-4. Post-implosion view of sphere CWS-4. The epoxy-joint failure occurred after the compression—shear failure.

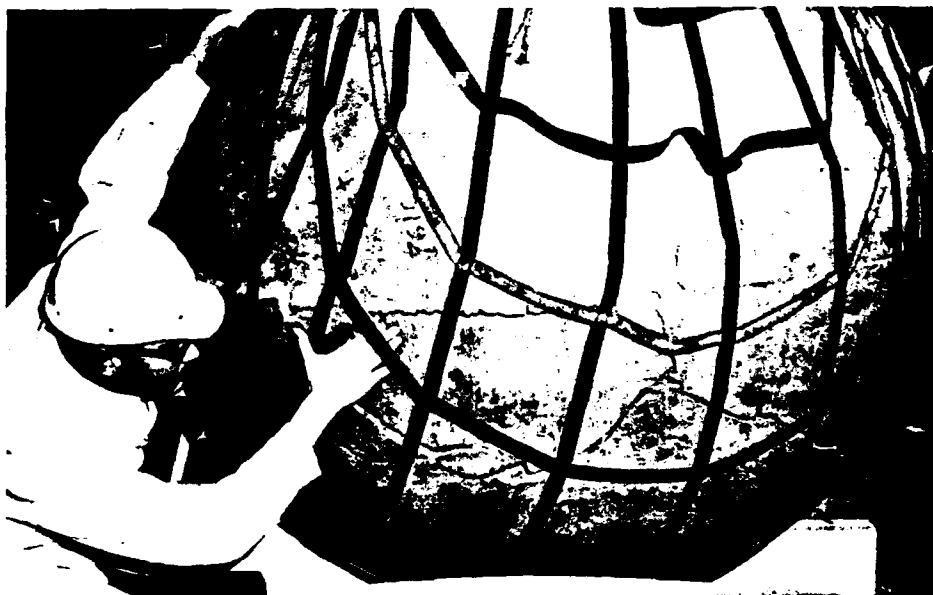


Figure D-5. Post-implosion view of sphere MDS-1.

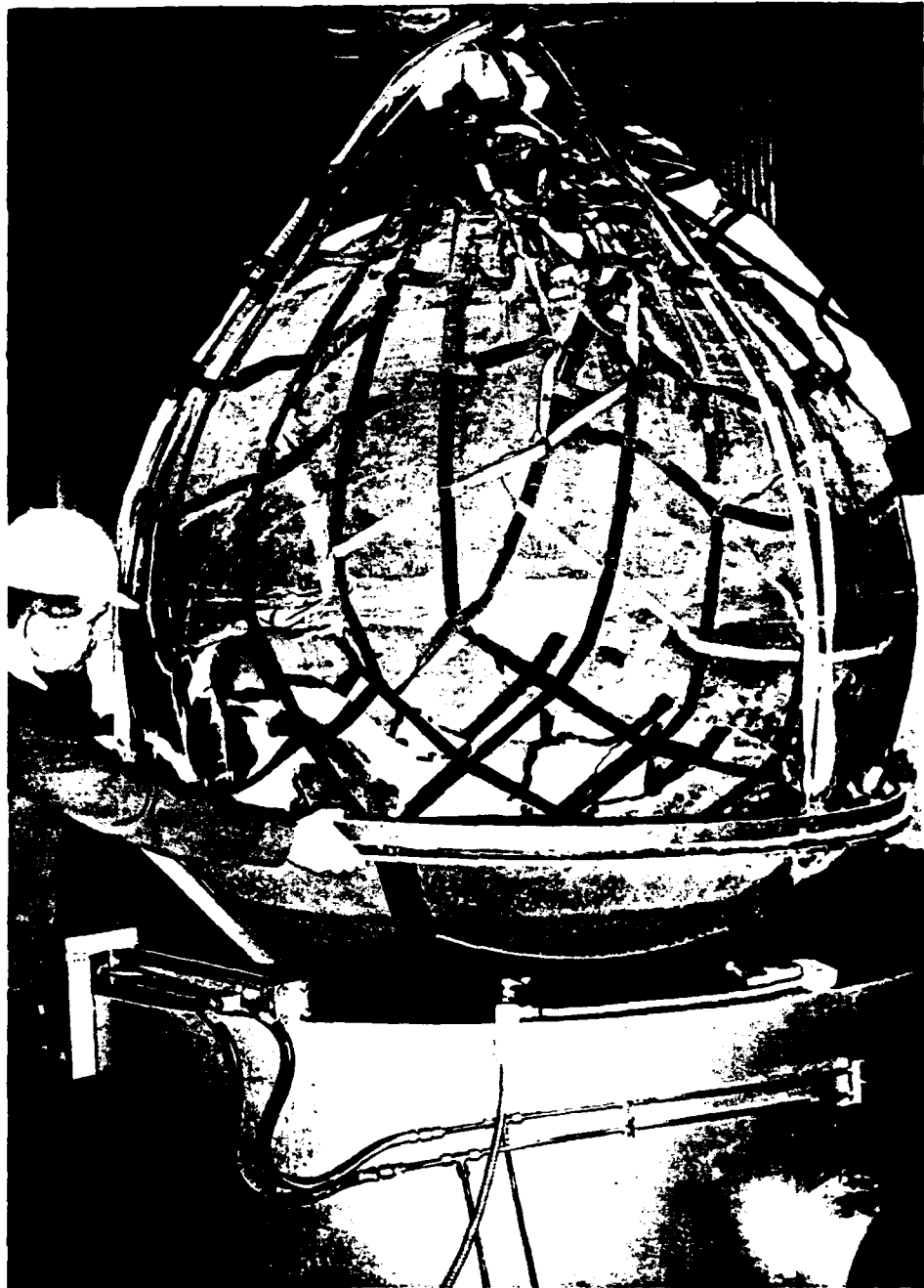


Figure D-6. Post-implosion view of sphere MDS-2.



Figure D-7. Post-implosion view of sphere MDS-3.

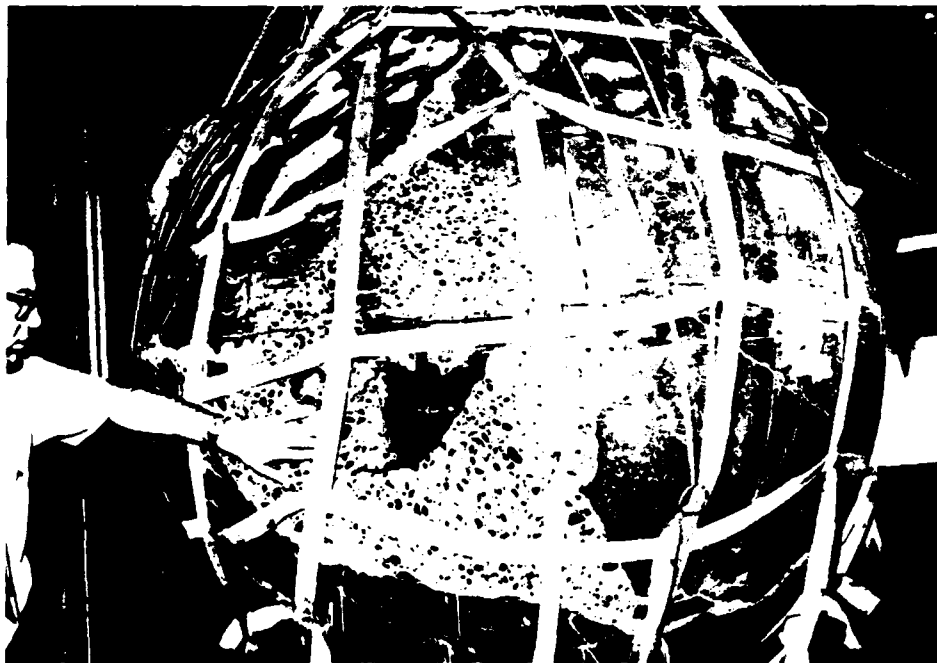


Figure D-8. Post-implosion view of sphere CWL-5. Note MgCROH seeping from cracks. This material apparently precipitated from seawater during a 3-day interval between implosion of sphere and removal of sphere from pressure vessel.

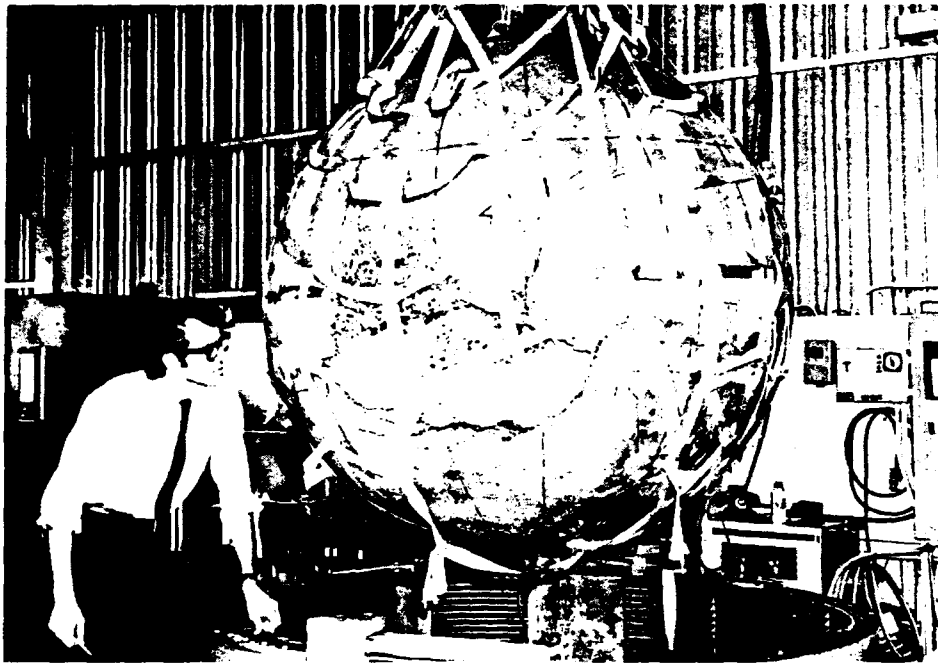


Figure D-9. Post-implosion view of sphere CWL-6.



Figure D-10. Post-implosion view of sphere CWL-7.

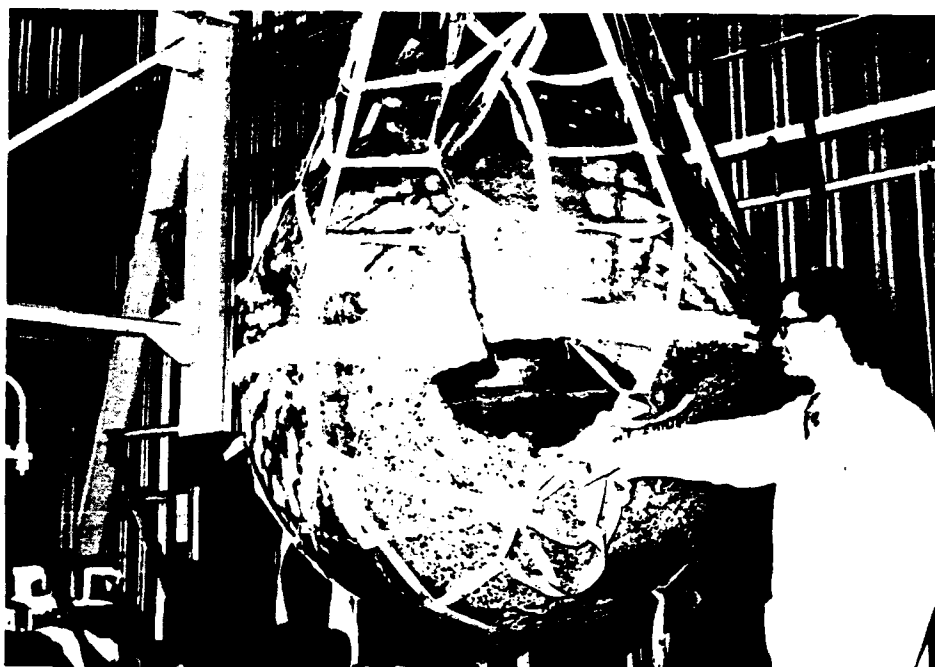


Figure D-11. Post-implosion view of sphere CWL-9.



Figure D-12. Post-implosion view of sphere CDL-10.



Figure D-13. Post-implosion view of sphere CDL-11.

Appendix E

DEVELOPMENT OF IMPLOSION EQUATION FOR 16-INCH-OD MORTAR SPHERES

Seventeen 16-inch-OD mortar spheres were tested under short-term hydrostatic loading at a pressurization rate of 100 psi/min. These specimens had ratios of wall thickness to outside diameter (t/D_o) of 0.0625, 0.1250, 0.1875, or 0.2500, which corresponded to wall thicknesses of 1, 2, 3, and 4 inches.

Table E-1 gives the implosion results for the specimens, and Figure E-1 shows that the relationship between P_{im}/f'_c and t/D_o was a straight-line function. A least-squares analysis gave the following empirical equation as the best-fit curve:

$$P_{im} = \left[5.02 \left(\frac{t}{D_o} \right) - 0.038 \right] f'_c \quad (E-1)$$

Equation E-1 differs slightly from a similar equation presented in previous reports; Equation E-1 is more accurate because of further data evaluation.* From additional research, it was found to be more accurate to use the f'_c value of the weaker hemisphere in the P_{im}/f'_c ratio; hence, this is the major improvement incorporated into Equation E-1.

Table E-1. Implosion Results for 16-Inch-OD Mortar Spheres

Sphere No.	Ratio of Wall Thickness to Outside Diameter, t/D_o	Implosion Pressure, P_{im} (psi)	Compressive Strength, f'_c (psi) ^a	P_{im}/f'_c
18	0.0625	3,375	11,480	0.294
19		3,450	11,220	0.307
20		3,420	11,510	0.297
21		3,240	11,190	0.290
35		1,710	6,090	0.281
				Average 0.294

continued

* Data incorporated in the development of the earlier implosion equation, $P_{im} = 4.8(t/D_o)$, included specimens with large steel penetrations, specimens tested under a pressurization rate of 1,000 psi/min, and values of f'_c that were the average compressive strength of the two hemispheres composing the sphere.

Table E-1. Continued

Sphere No.	Ratio of Wall Thickness to Outside Diameter, t/D_o	Implosion Pressure, P_{im} (psi)	Compressive Strength, f'_c (psi) ^a	P_{im}/f'_c
23	0.1250	5,720	11,050	0.517
24		6,330	11,040	0.573
25		6,590	10,760	0.612
36		3,375	5,750	0.587
				Average 0.572
27	0.1875	9,250	10,370	0.892
28		9,170	10,370	0.884
29		9,500	11,520	0.825
37		5,280	5,990	0.882
				Average 0.871
31	0.2500	13,900	10,910	1.270
32		13,570	10,900	1.245
33		13,550	10,790	1.255
38		7,370	6,080	1.212
				Average 1.246

^a Compressive strength of weakest hemisphere based on uniaxial tests on 3 x 6-inch control cylinders.

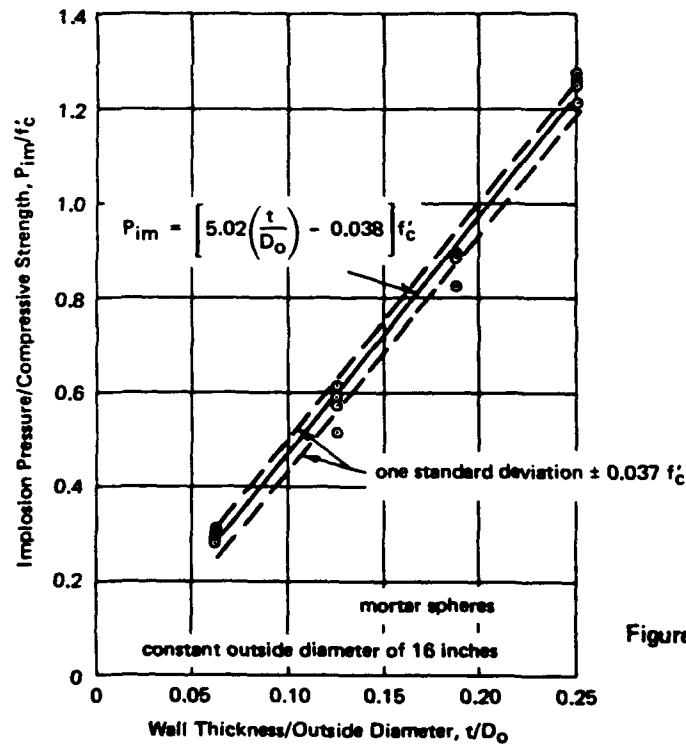


Figure E-1. Empirical equation to predict implosion pressures of small concrete spheres.

Appendix F

LONG-TERM STRAIN RESPONSE OF CONCRETE SPHERES SUBJECTED TO SUSTAINED LOAD

Figures F-1 through F-9 present the long-term strain response of spheres CWL-5 through CDL-11 under sustained loading. Except for Figure F-1, the data from individual strain gages have been given; in most cases, the average strain behavior is also shown.

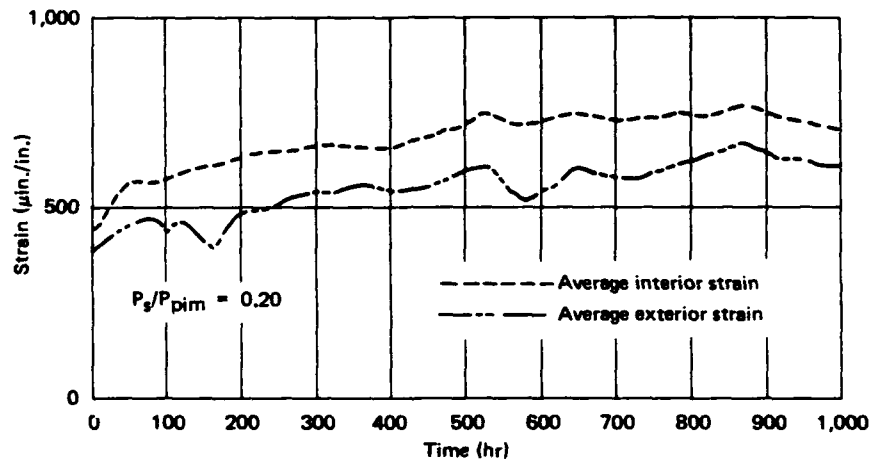


Figure F-1. Sphere CWL-5A under sustained pressure of 20% P_{pim} .

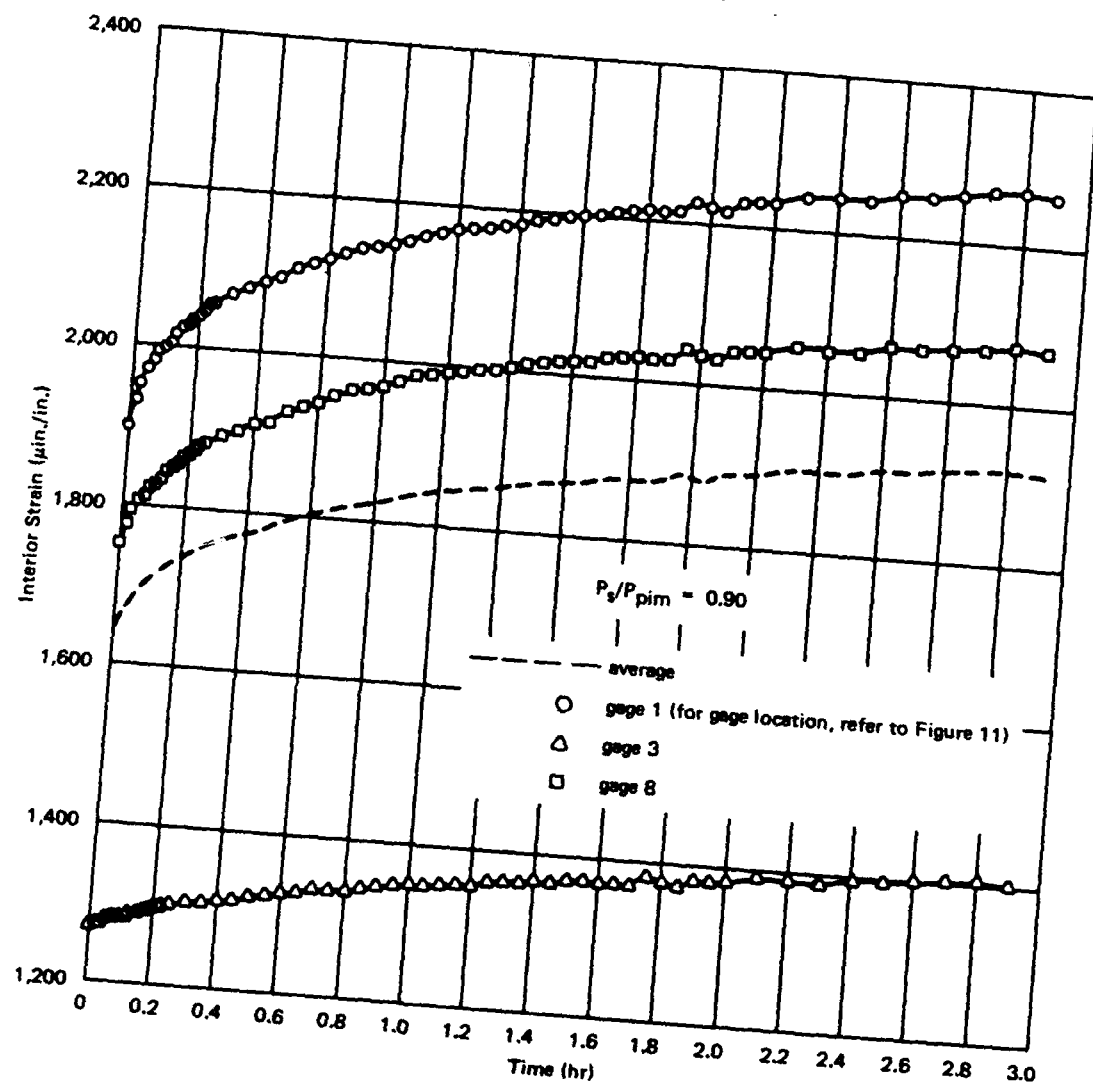


Figure F-2. Sphere CWL-5B under sustained pressure of 90% P_{pim} .

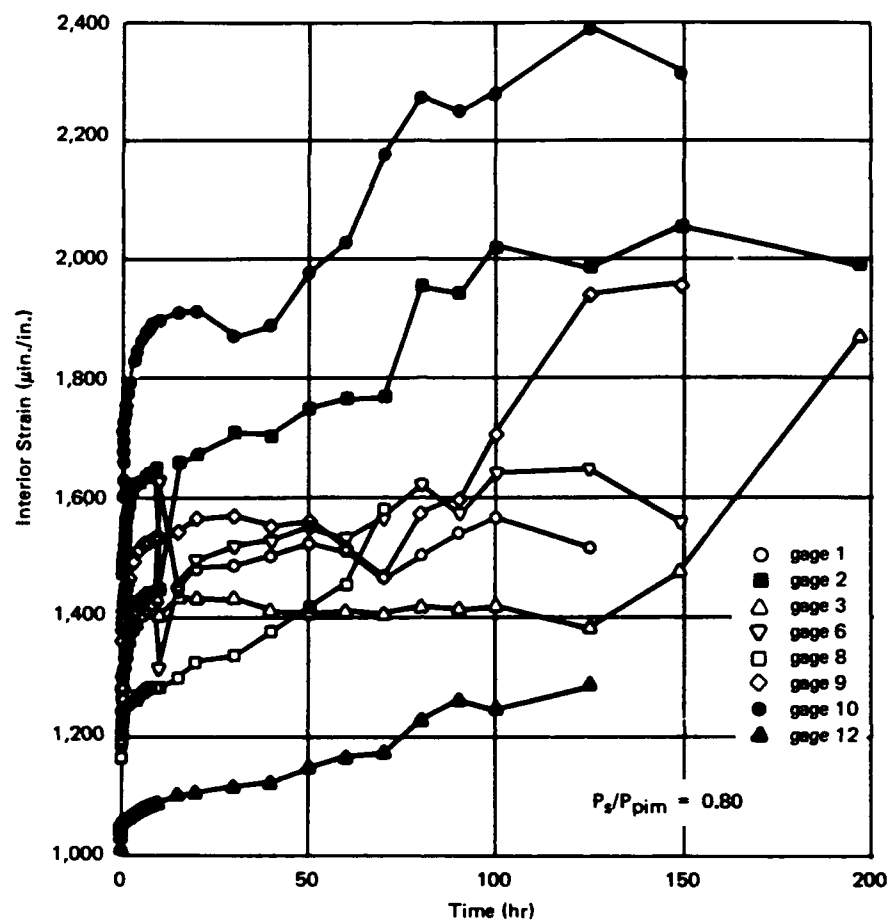


Figure F-3. Sphere CWL-6 under sustained pressure of 80% P_{pim} .

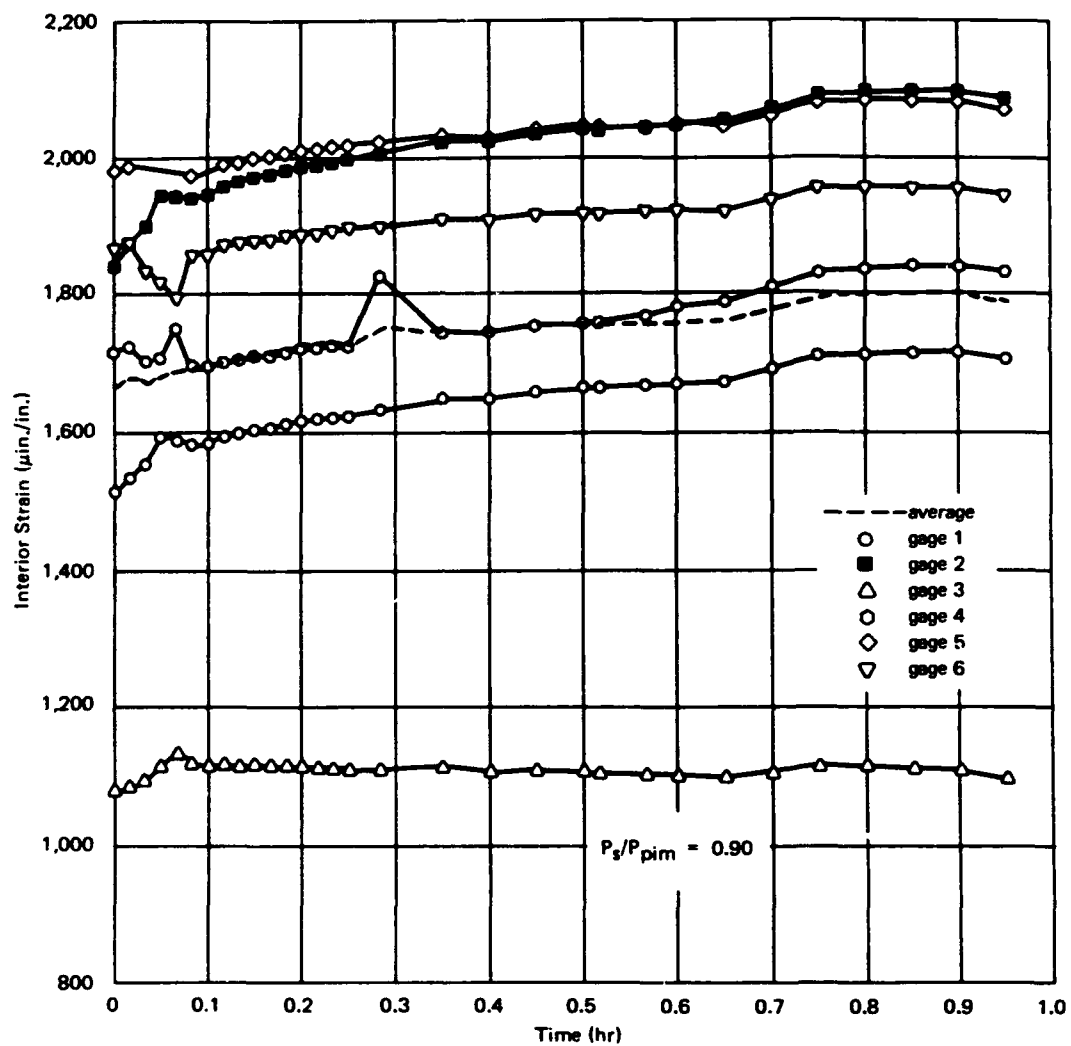


Figure F-4. Sphere CWL-7 under sustained pressure of 90% P_{pim} .

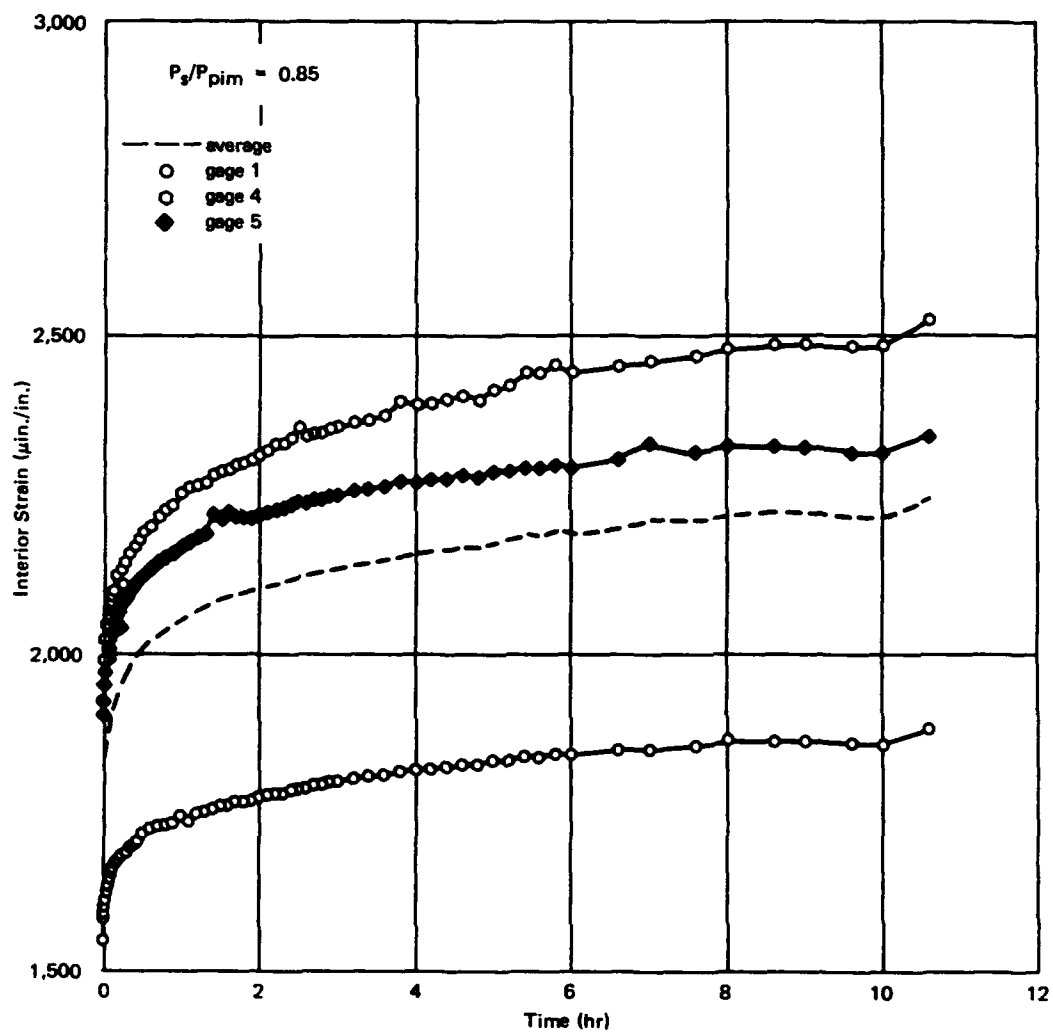


Figure F-5. Sphere CWL-8 under sustained pressure of 85% P_{pim} .

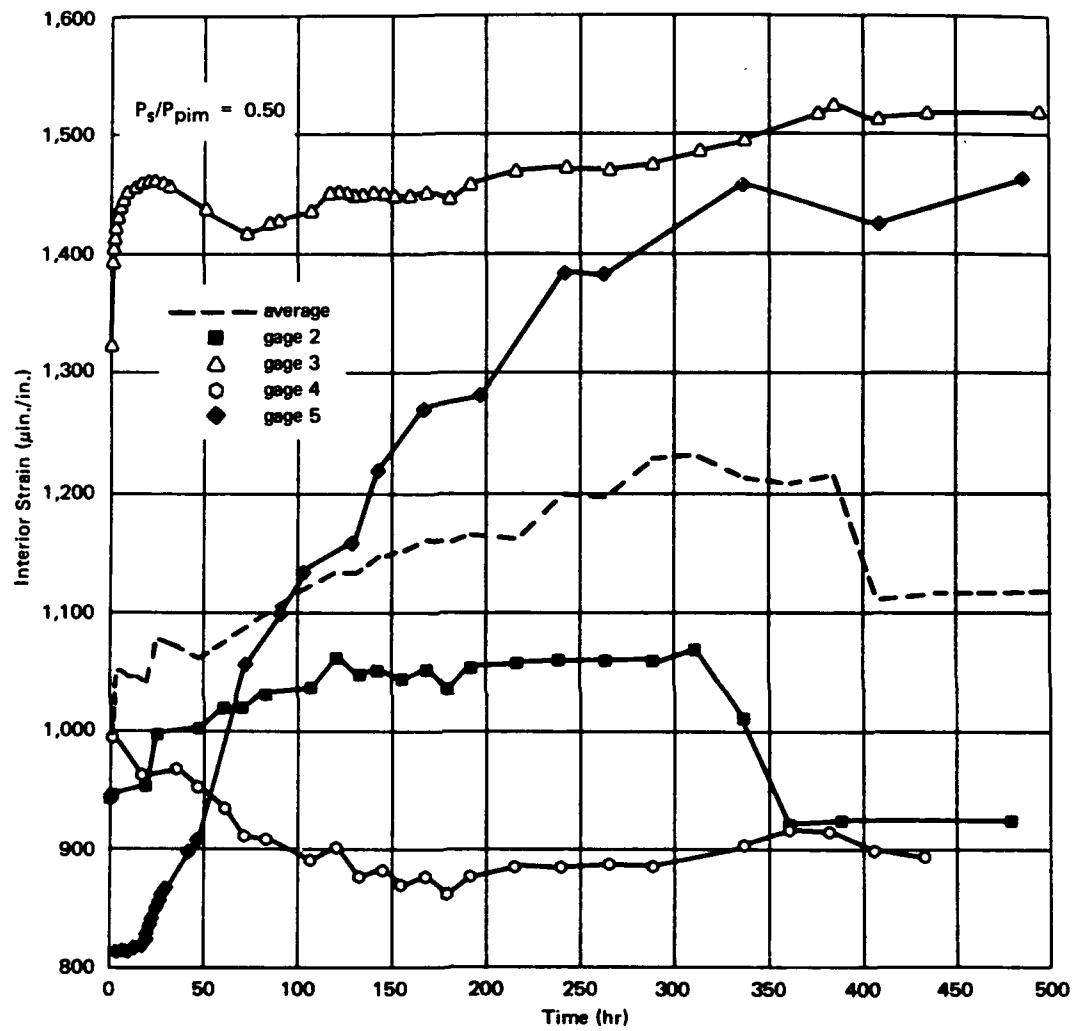


Figure F-6. Sphere CWL-9A under sustained pressure of 50% P_{pim} .

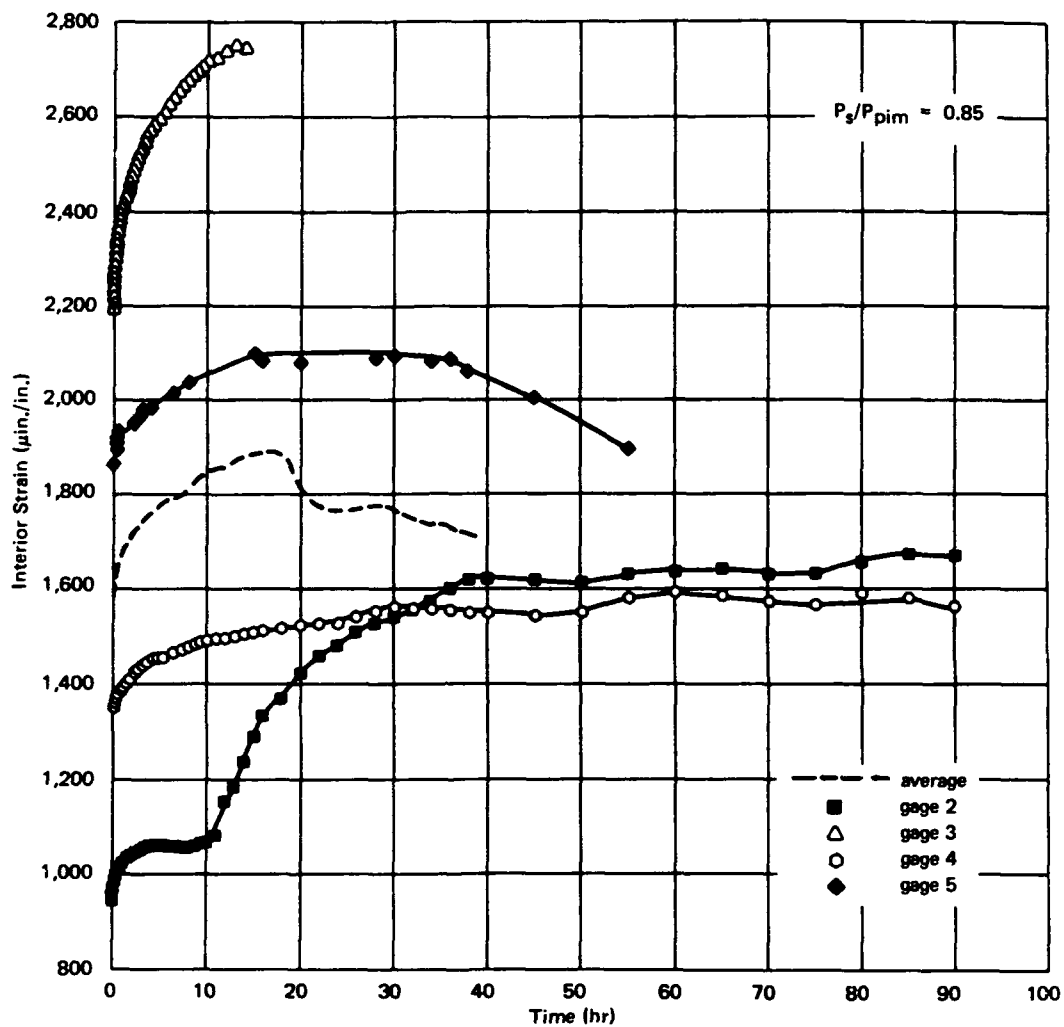


Figure F-7. Sphere CWL-9B under sustained pressure of 85% P_{pim} .

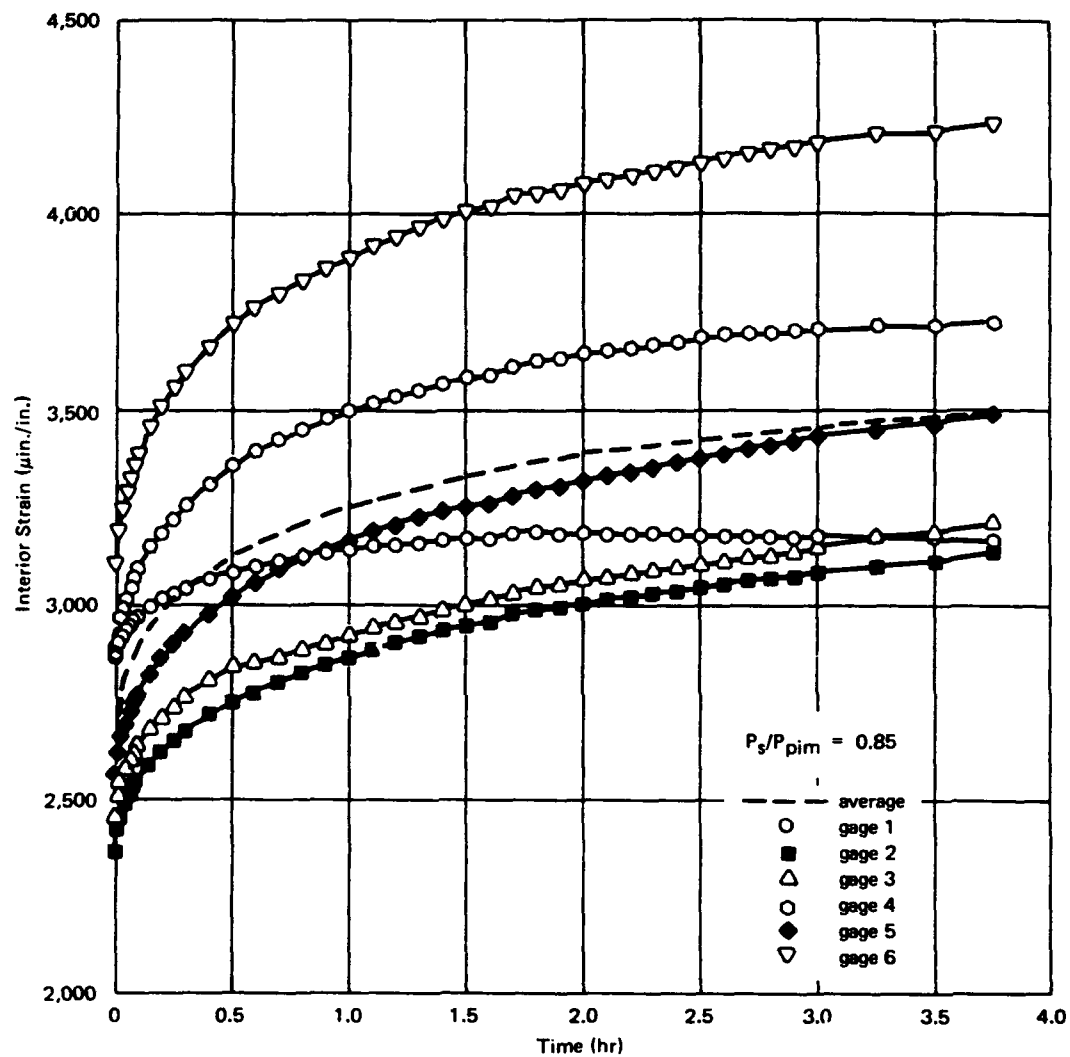


Figure F-8. Sphere CDL-10 under sustained pressure of 85% P_{pim} .

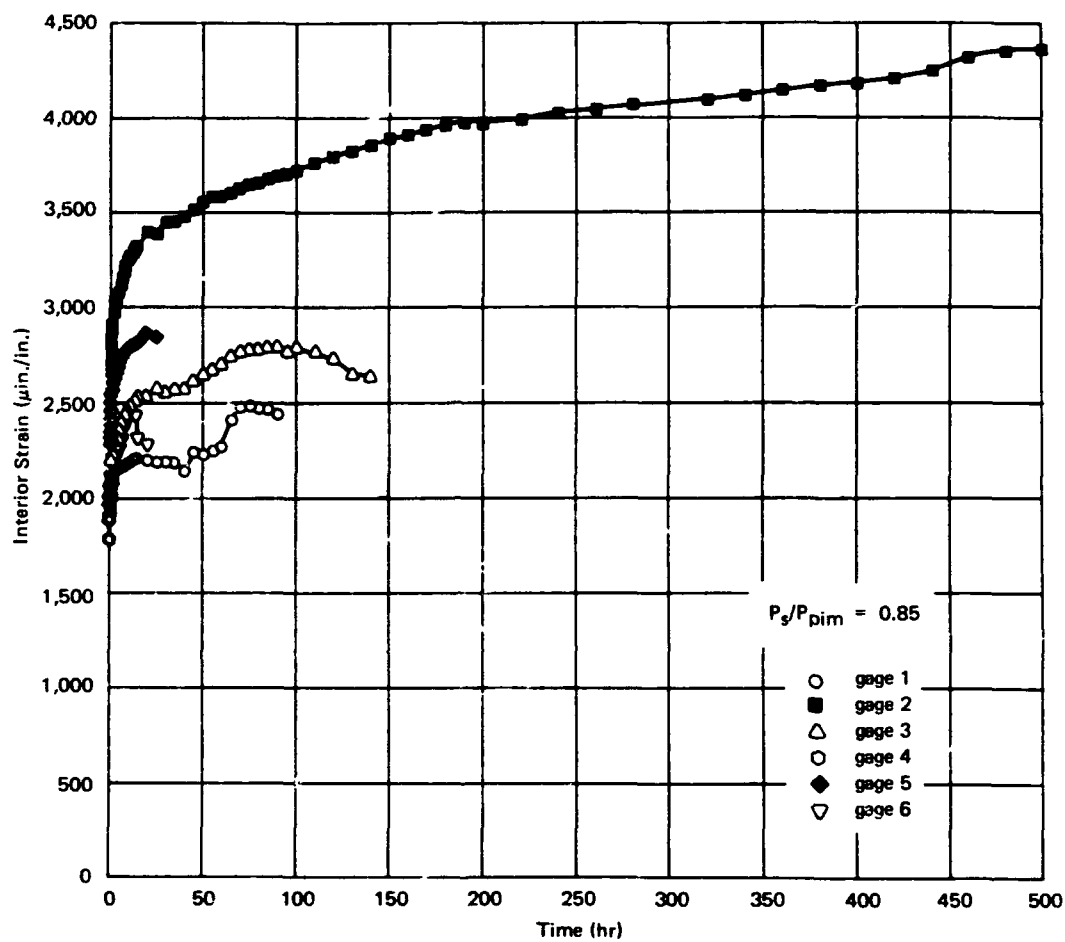


Figure F-9. Sphere CDL-11 under sustained pressure of 85% P_{pim} .

Appendix G

MISCELLANEOUS TESTS ON 66-INCH-OD MORTAR SPHERES

Exploratory tests were performed on three mortar spheres, 66 inches in OD and 4.125 inches in wall thickness. These spheres were constructed in the same manner as the mortar spheres described in the main body of the report. The first sphere, MDS-X1, was a trial specimen; the second, MDL-X2, was used in ocean tests to study the hydrodynamic characteristics of a sphere and to determine the durability and permeability of a mortar sphere located on the seafloor; and the third, MDL-X3, was constructed with a mechanical lock joint at its equator to investigate the influence of a stiff joint on the sphere under sustained loading.

TRIAL SPHERE TEST

The trial sphere, MDS-X1, was the first 66-inch-OD sphere fabricated and tested under hydrostatic load. The major reason that the results are presented herein is that the specimen was fabricated from two hemispheres that did not meet high quality-control standards; yet the implosion pressure was equivalent to that of the good specimens.

The bottom hemisphere of the sphere was the first of all hemispheres cast. Procedural difficulties were encountered during the casting operation, and it required over an hour to complete the operation. Also, during removal of the forms, an unusually large chip of concrete broke away from the edge of the hemisphere (as shown in Figure G-1).

The top hemisphere did not meet high standards because during a handling maneuver in which the hemisphere was being turned over a steel pad-eye broke and the hemisphere fell to the concrete pavement. The distance of the fall was approximately 2 feet and the point of impact of the hemisphere was approximately 20 degrees down from the equator. No visible damage was observed other than a large chip of concrete from the equator (as shown in Figure G-2).

The chipped equators were repaired for both hemispheres and later the two hemispheres were bonded together to form a sphere. This sphere was the first specimen tested in the 72-inch-ID pressure vessel; the test procedure was similar to that for the other spheres except that change-in-volume measurements were not taken.



Figure G-1. Bottom hemisphere of trial sphere MDS-X1.



Figure G-2. Top hemisphere of trial sphere MDS-X1.

The implosion pressure, P_{im} , for the trial sphere was 1,820 psi and the uniaxial concrete strength, f'_c , was 8,910 psi. These results yielded a P_{im}/f'_c ratio of 0.204. This value is within the standard deviation of the test results from the other better quality mortar spheres whose average P_{im}/f'_c was 0.211 ± 0.012 .



Figure G-3. Post-implosion view of trial sphere MDS-X1 showing compression—shear failure zone.

Figure G-3 shows the compression—shear zone of the failed specimen. The failure zone ran parallel to the equator for a length of 64 inches and the average angle for the sheared concrete surface was 36 degrees to a line tangent to the exterior surface.

In summary, the trial sphere appeared to behave similar to the better quality mortar spheres although the trial sphere was fabricated from damaged hemispheres.

OCEAN DYNAMIC AND PERMEABILITY TESTS

Sphere MDL-X2 had been used in various ocean tests. The main objective of the first ocean test was to study the dynamic characteristics of a large object of various weights sliding up and down a taut wire. The concrete sphere was used as the test object. The sphere was made negatively buoyant by 800 and 2,400 pounds by hanging steel plates from a framework surrounding the sphere (Figure G-4).

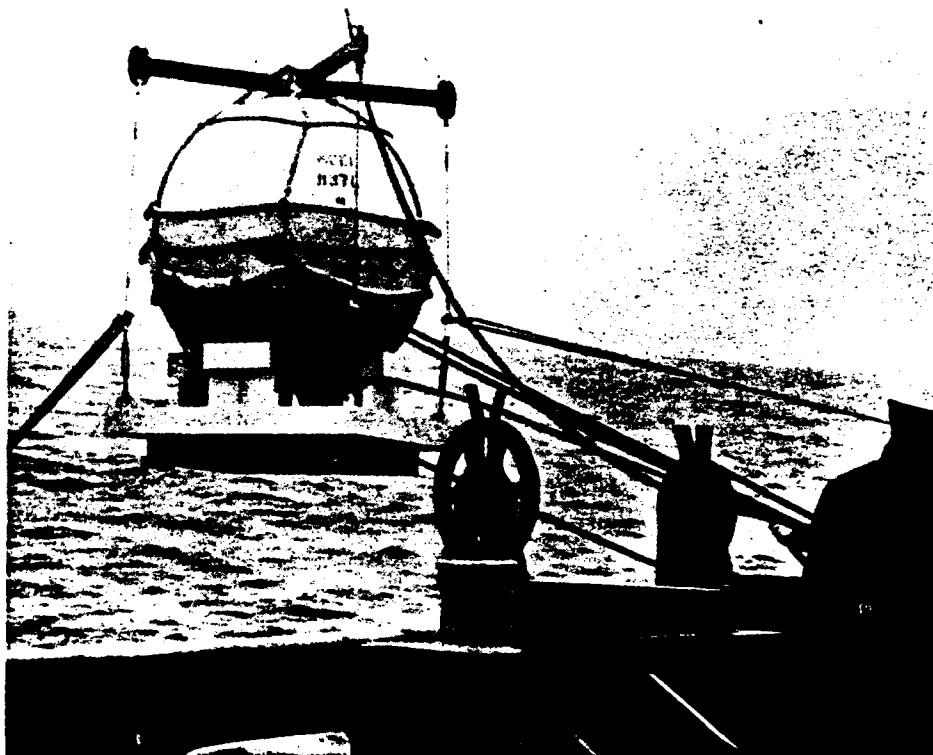


Figure G-4. Sphere MDL-X2 undergoing ocean dynamic test.

The hydrostatic loading conditions which the sphere experienced were one cycle to 800 feet, where the sphere remained at depth for approximately 30 minutes, and eight additional short-duration cycles to 800 feet. The sphere did not appear to be harmed by the tests.

The second ocean test was the emplacement of this sphere on the seafloor off Pitas Point, Calif., at a 120-foot depth to study the durability and permeability of the mortar to the seawater environment. Navy divers

inspected the sphere an average of once every 2 months to report the degree of fouling on the concrete and whether or not the sphere was still positively buoyant.

The sphere was able to float within the framework as shown in Figure G-4, and a diver could determine whether the sphere was buoyant or not by inserting his hand between the sphere and the cradle. To become negatively buoyant the sphere would have had to take on approximately 23 cubic feet of water; the equivalent of 40% of the interior volume.

After 12 months' submergence at 120 feet, the sphere was retrieved from the ocean (Figure G-5). Little fouling and few barnacles were present on the concrete. No evidence of rock-boring mollusks was observed.



Figure G-5. Sphere MDL-X2 being retrieved from 120-foot depth after 12 months continuous submergence.

The quantity of water that permeated the concrete to the interior was a total of 0.60 ft^3 ; D'Arcy's permeability constant, K_c , was calculated as $0.58 \times 10^{-12} \text{ ft/sec}$. This value was within the same order of magnitude as the K_c value for the concrete spheres. The salt content of the water on the interior was typical of that of the seawater in the Pitas Point area.

SPHERE WITH A MECHANICAL EQUATORIAL JOINT

Sphere MDL-X3 was constructed with a steel mechanical lock joint at the equator between the two hemispheres.²⁰ Such a mechanical joint permitted the sphere to be opened and closed repeatedly, so that the capsule could have been used for a variety of oceanographic applications. The objective of the hydrostatic test was to determine if the stiff steel joint affected the strength of the sphere under sustained loading conditions in a manner similar to that in previous research with 16-inch-OD mortar spheres.²⁰

The joint was made of two 1/2-inch-thick steel rings epoxy-bonded to each hemisphere; steel dowel pins set into the concrete aided in the attachment (Figure G-6). The hemispheres were joined by bolting the steel rings together (Figure G-7); an O-ring between the rings sealed the joint.

The sphere was tested under a sustained pressure of 83% P_{pim} (P_{pim} calculated for an unjointed sphere) and had a time to implosion of 4 hours. The concrete compressive strength was 7,720 psi, and the sustained pressure was 1,630 psi.



Figure G-6. View of mechanical joint ring with anchor pins epoxy-bonded into drilled holes in the hemisphere.

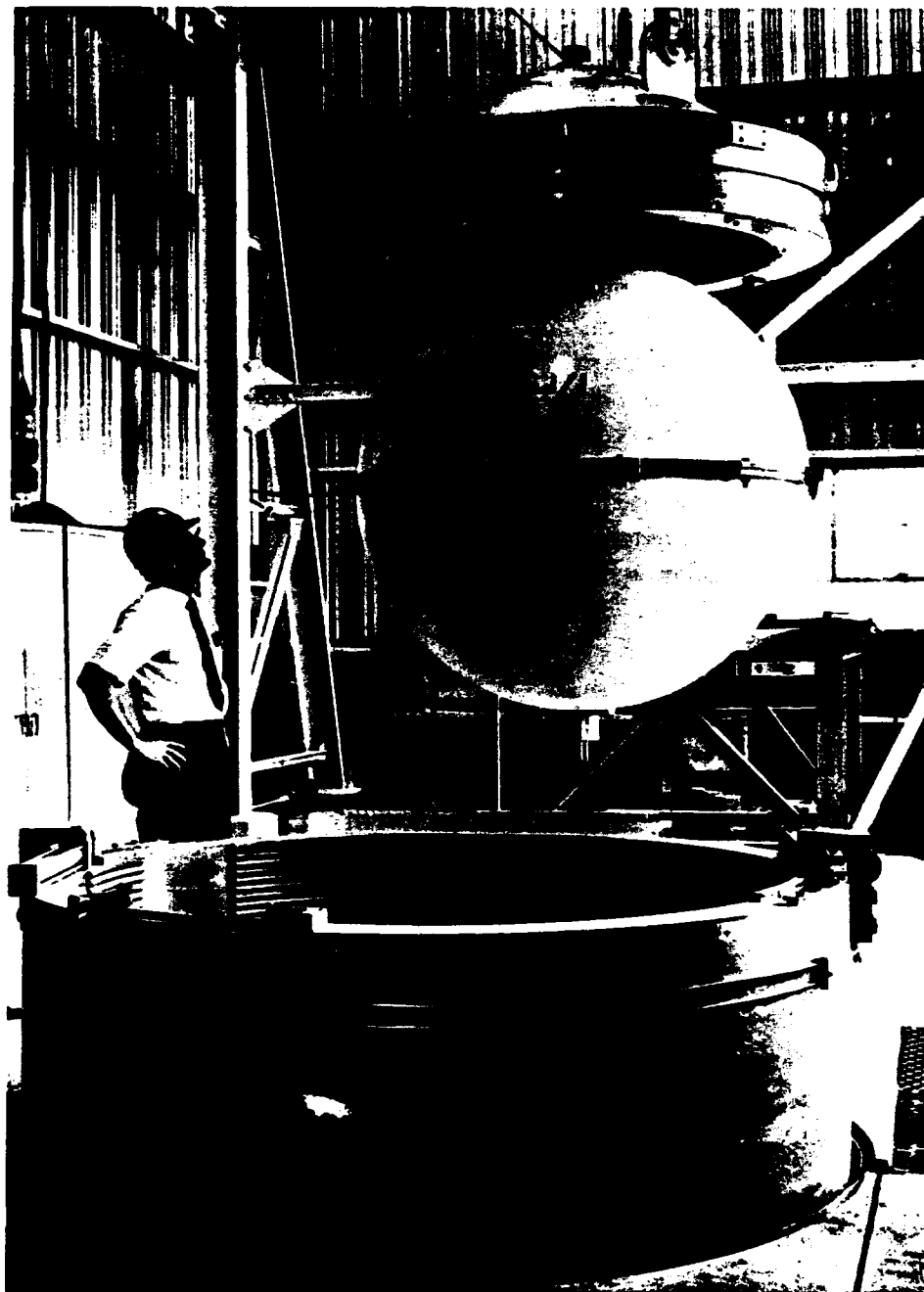


Figure G-7. Sphere MDL-X3 being lowered into pressure vessel for hydrostatic test.

A comparison of results from tests of sphere MDL-X3 with those of the concrete spheres, presented in Figure 24, showed that sphere MDL-X3 failed in less time than did the concrete spheres. The concrete spheres had a range of time to implosion from 4 to 500 hours with the log-time average at approximately 100 hours.

The inclusion of a stiff steel joint at the equator did reduce the long-term strength of the 66-inch mortar spheres, but not severely. A quantitative decrease in strength cannot be defined from this single test. Previous work on 16-inch-OD mortar spheres²⁰ showed that stiff equatorial joint rings reduced the short-term implosion pressure as much as 27%.

REFERENCES

1. Naval Civil Engineering Laboratory. Technical Report R-517: Behavior of spherical concrete hulls under hydrostatic loading, pt. 1. Exploratory investigation, by J. D. Stachiw and K. O. Gray. Port Hueneme, Calif., Mar. 1967. (AD 649290)
- 2.———. Technical Report R-547: Behavior of spherical concrete hulls under hydrostatic loading, pt. 2. Effect of penetrations, by J. D. Stachiw. Port Hueneme, Calif., Oct. 1967. (AD 661187)
- 3.———. Technical Report R-588: Behavior of spherical concrete hulls under hydrostatic loading, pt. 3. Relationship between thickness-to-diameter ratio and critical pressures, strains, and water permeation rates, by J. D. Stachiw and K. Mack. Port Hueneme, Calif., June 1968. (AD 835492L)
- 4.———. Technical Report R-679: Failure of thick-walled concrete spheres subjected to hydrostatic loading, by H. H. Haynes and R. A. Hoofnagle. Port Hueneme, Calif., May 1970. (AD 708011)
- 5.———. Technical Report R-696: Influence of length-to-diameter ratio on behavior of concrete cylindrical hulls under hydrostatic loading, by H. H. Haynes and R. J. Ross. Port Hueneme, Calif., Sept. 1970. (AD 713088)
6. David W. Taylor Model Basin. Report 1757: The effect of initial imperfections on the collapse strength of deep spherical shells, by M. A. Krenzke and T. J. Kiernan. Washington, D. C., Feb. 1965. (AD 612100)
7. R. F. Blanks and C. C. McNamara. "Mass concrete tests in large cylinders," American Concrete Institute, Journal, Proceedings, vol. 31, Jan.-Feb. 1935, pp. 280-303.
8. A. M. Neville. "Some aspects of the strength of concrete," Civil Engineering and Public Works Review, vol. 54, no. 640, Nov. 1959, pp. 1308-1310.
9. H. Rüsck. "Physikalische Fragen der Betonpruefung (Physical problems in the testing of concrete)," Zement-Kalk-Gips, vol. 12, no. 1, Jan. 1959, pp. 1-9. (Available as translation no. 61-18968 from National Translation Center, Chicago, Ill.)
10. Naval Civil Engineering Laboratory. Letter Report: Preliminary experiments on 16-inch-OD spherical concrete hulls under sustained hydrostatic loading, by L. F. Kahn and H. M. Kusano. Port Hueneme, Calif., Apr. 1971.

11. R. Sell. "Investigations into the strength of concrete under sustained load," RILEM Bulletin, no. 5, Dec. 1959, pp. 5-13.
12. A. M. Neville and B. L. Meyers. "Creep of concrete: Influencing factors and predictions," in Symposium on creep of concrete. Detroit, Mich., American Concrete Institute, 1964, pp. 1-33. (ACI SP-9)
13. American Concrete Institute. Committee 318. Building code requirements for reinforced concrete (ACI 318-63). Detroit, Mich., June 1963, sect. 1506.
14. R. E. Davis and H. E. Davis. "Flow of concrete under the action of sustained loads," American Concrete Institute, Proceedings, vol. 27, 1931, pp. 837-901.
15. Naval Civil Engineering Laboratory. Technical Report R-333-1: Study of creep in concrete, phase 1. I-beam, by J. R. Keeton. Port Hueneme, Calif., Jan. 1965. (AD 610550)
16. A. Ruettgers, E. N. Vidal, and S. P. Wing. "An investigation of the permeability of mass concrete with particular reference to Boulder Dam," American Concrete Institute, Journal, Proceedings, vol. 31, Mar.-Apr. 1935, pp. 382-416.
17. ———. Discussion of the paper, "An investigation of the permeability of mass concrete with particular reference to Boulder Dam," American Concrete Institute, Journal, Proceedings, vol. 32, Jan.-Feb. 1936, pp. 378-389.
18. M. Mary. Discussion of the paper, "An investigation of the permeability of mass concrete with particular reference to Boulder Dam," by A. Ruettgers, E. N. Vidal, and S. P. Wing, American Concrete Institute, Journal, Proceedings, vol. 32, Sept.-Oct. 1935, pp. 125-129.
19. S. L. Meyers. Discussion of the paper, "An investigation of the permeability of mass concrete with particular reference to Boulder Dam," by A. Ruettgers, E. N. Vidal, and S. P. Wing, American Concrete Institute, Journal, Proceedings, vol. 32, Nov.-Dec. 1935, pp. 230-233.
20. Naval Civil Engineering Laboratory. Technical Report R-735: Influence of stiff equatorial rings on concrete spherical hulls subjected to hydrostatic loading, by L. F. Kahn and J. D. Stachiw. Port Hueneme, Calif., Aug. 1971. (AD 731352)

DISTRIBUTION LIST

SNDL Code	No. of Activities	Total Copies	
—	1	12	Defense Documentation Center
FKAIC	1	10	Naval Facilities Engineering Command
FKNI	6	6	NAVFAC Engineering Field Divisions
FKN5	9	9	Public Works Centers
FA25	1	1	Public Works Center
—	9	9	RDT&E Liaison Officers at NAVFAC Engineering Field Divisions and Construction Battalion Centers
—	389	389	NCEL Special Distribution List No. 9 for persons and activities interested in reports on Deep Ocean Studies

<p>Naval Civil Engineering Laboratory BEHAVIOR OF 66-INCH CONCRETE SPHERES UNDER SHORT- AND LONG-TERM HYDROSTATIC LOADING, by H. H. Haynes and L. F. Kahn TR-774 86 p. illus September 1972 Unclassified</p>	<p>1. Hollow concrete spheres—Implosion and deformation I. 3.1610</p> <p>Fourteen unreinforced concrete and mortar spheres, 66 inches in outside diameter (OD) and 4.125 inches in wall thickness, were subjected to simulated deep-ocean loading conditions. The average short-term implosion pressure for wet-concrete spheres was 2,350 psi and for the dry-concrete spheres was 2,810 psi; the average uniaxial compressive strength of the concrete was respectively 7,810 psi and 9,190 psi. From control cylinders, it was found that the uniaxial compressive strength of wet concrete was 10% weaker than that of dry concrete. The ratio of implosion pressure to compressive strength, P_{im}/f'_c, was nearly equal for the wet- and dry-concrete spheres at 0.301 and 0.306. The implosion pressures for the 66-inch-OD concrete spheres could be predicted conservatively from an empirical equation developed from 16-inch-OD mortar spheres. The equation was not valid for 66-inch-OD mortar spheres, which were found 30% weaker in implosion strength than the 66-inch-OD concrete spheres. Under long-term loading, the concrete spheres failed by static fatigue where the relation between level of sustained pressure and time to implosion was similar to that known for concrete under uniaxial loading. Wet-concrete spheres under seawater pressure as high as 1,670 psi showed an average D'Arcy's permeability coefficient, K_c, of 0.13×10^{-12} ft/sec; this K_c value was also similar to that known for concrete under freshwater pressure as high as 400 psi. Design guides were developed to predict the short- and long-term implosion pressures and permeability rates of concrete spheres.</p>
<p>Naval Civil Engineering Laboratory BEHAVIOR OF 66-INCH CONCRETE SPHERES UNDER SHORT- AND LONG-TERM HYDROSTATIC LOADING, by H. H. Haynes and L. F. Kahn TR-774 86 p. illus September 1972 Unclassified</p>	<p>1. Hollow concrete spheres—Implosion and deformation I. 3.1610</p> <p>Fourteen unreinforced concrete and mortar spheres, 66 inches in outside diameter (OD) and 4.125 inches in wall thickness, were subjected to simulated deep-ocean loading conditions. The average short-term implosion pressure for wet-concrete spheres was 2,350 psi and for the dry-concrete spheres was 2,810 psi; the average uniaxial compressive strength of the concrete was respectively 7,810 psi and 9,190 psi. From control cylinders, it was found that the uniaxial compressive strength of wet concrete was 10% weaker than that of dry concrete. The ratio of implosion pressure to compressive strength, P_{im}/f'_c, was nearly equal for the wet- and dry-concrete spheres at 0.301 and 0.306. The implosion pressures for the 66-inch-OD concrete spheres could be predicted conservatively from an empirical equation developed from 16-inch-OD mortar spheres. The equation was not valid for 66-inch-OD mortar spheres, which were found 30% weaker in implosion strength than the 66-inch-OD concrete spheres. Under long-term loading, the concrete spheres failed by static fatigue where the relation between level of sustained pressure and time to implosion was similar to that known for concrete under uniaxial loading. Wet-concrete spheres under seawater pressure as high as 1,670 psi showed an average D'Arcy's permeability coefficient, K_c, of 0.13×10^{-12} ft/sec; this K_c value was also similar to that known for concrete under freshwater pressure as high as 400 psi. Design guides were developed to predict the short- and long-term implosion pressures and permeability rates of concrete spheres.</p>
<p>Naval Civil Engineering Laboratory BEHAVIOR OF 66-INCH CONCRETE SPHERES UNDER SHORT- AND LONG-TERM HYDROSTATIC LOADING, by H. H. Haynes and L. F. Kahn TR-774 86 p. illus September 1972 Unclassified</p>	<p>1. Hollow concrete spheres—Implosion and deformation I. 3.1610</p> <p>Fourteen unreinforced concrete and mortar spheres, 66 inches in outside diameter (OD) and 4.125 inches in wall thickness, were subjected to simulated deep-ocean loading conditions. The average short-term implosion pressure for wet-concrete spheres was 2,350 psi and for the dry-concrete spheres was 2,810 psi; the average uniaxial compressive strength of the concrete was respectively 7,810 psi and 9,190 psi. From control cylinders, it was found that the uniaxial compressive strength of wet concrete was 10% weaker than that of dry concrete. The ratio of implosion pressure to compressive strength, P_{im}/f'_c, was nearly equal for the wet- and dry-concrete spheres at 0.301 and 0.306. The implosion pressures for the 66-inch-OD concrete spheres could be predicted conservatively from an empirical equation developed from 16-inch-OD mortar spheres. The equation was not valid for 66-inch-OD mortar spheres, which were found 30% weaker in implosion strength than the 66-inch-OD concrete spheres. Under long-term loading, the concrete spheres failed by static fatigue where the relation between level of sustained pressure and time to implosion was similar to that known for concrete under uniaxial loading. Wet-concrete spheres under seawater pressure as high as 1,670 psi showed an average D'Arcy's permeability coefficient, K_c, of 0.13×10^{-12} ft/sec; this K_c value was also similar to that known for concrete under freshwater pressure as high as 400 psi. Design guides were developed to predict the short- and long-term implosion pressures and permeability rates of concrete spheres.</p>

Unclassified

Security Classification

DOCUMENT CONTROL DATA - R & D		
<i>(Security classification of title, body of abstract and indexing annotation must be entered when the overall report is classified)</i>		
1. ORIGINATING ACTIVITY (Corporate author)		2a. REPORT SECURITY CLASSIFICATION
Naval Civil Engineering Laboratory Port Hueneme, California 93043		Unclassified
		2b. GROUP
3. REPORT TITLE		
BEHAVIOR OF 66-INCH CONCRETE SPHERES UNDER SHORT- AND LONG-TERM HYDROSTATIC LOADING		
4. DESCRIPTIVE NOTES (Type of report and inclusive dates)		
Not final; June 1968 - July 1971		
5. AUTHOR(S) (First name, middle initial, last name)		
H. H. Haynes and L. F. Kahn		
6. REPORT DATE	7a. TOTAL NO. OF PAGES	7b. NO. OF REFS
September 1972	86	20
8a. CONTRACT OR GRANT NO.	8b. ORIGINATOR'S REPORT NUMBER(S)	
b. PROJECT NO 3.1610	TR-774	
c.	8c. OTHER REPORT NO(S) (Any other numbers that may be assigned this report)	
d.		
10. DISTRIBUTION STATEMENT		
Approved for public release; distribution unlimited.		
11. SUPPLEMENTARY NOTES		12. SPONSORING MILITARY ACTIVITY
		Naval Facilities Engineering Command Washington, D. C. 20390
13. ABSTRACT		
<p>Fourteen unreinforced concrete and mortar spheres, 66 inches in outside diameter (OD) and 4.125 inches in wall thickness, were subjected to simulated deep-ocean loading conditions. The average short-term implosion pressure for wet-concrete spheres was 2,350 psi and for the dry-concrete spheres was 2,810 psi; the average uniaxial compressive strength of the concrete was respectively 7,810 psi and 9,190 psi. From control cylinders, it was found that the uniaxial compressive strength of wet concrete was 10% weaker than that of dry concrete. The ratio of implosion pressure to compressive strength, P_{im}/f'_c, was nearly equal for the wet- and dry-concrete spheres at 0.301 and 0.306. The implosion pressures for the 66-inch-OD concrete spheres could be predicted conservatively from an empirical equation developed from 16-inch-OD mortar spheres. The equation was not valid for 66-inch-OD mortar spheres, which were found 30% weaker in implosion strength than the 66-inch-OD concrete spheres.</p> <p>Under long-term loading, the concrete spheres failed by static fatigue where the relation between level of sustained pressure and time to implosion was similar to that known for concrete under uniaxial loading. Wet-concrete spheres under seawater pressure as high as 1,670 psi showed an average D'Arcy's permeability coefficient, K_c, of 0.13×10^{-12} ft/sec; this K_c value was also similar to that known for concrete under freshwater pressure as high as 400 psi. Design guides were developed to predict the short- and long-term implosion pressures and permeability rates of concrete spheres.</p>		

DD FORM 1473

1 NOV 65

(PAGE 1)

S/N 0101-807-6801

Unclassified

Security Classification

Unclassified
Security Classification

14 KEY WORDS	LINK A		LINK B		LINK C	
	ROLE	WT	ROLE	WT	ROLE	WT
Concrete spheres						
Mortar spheres						
Spherical hulls						
Hydrostatic tests						
Implosion pressure						
Deformation of spheres						
Strain in spheres						
Pressurization tests						
Undersea concrete spheres						
Unreinforced concrete spheres						
Long-term loading						
Short-term loading						

DD FORM 1473 (BACK)
(PAGE 2)

Unclassified
Security Classification

Technical Report

R 805

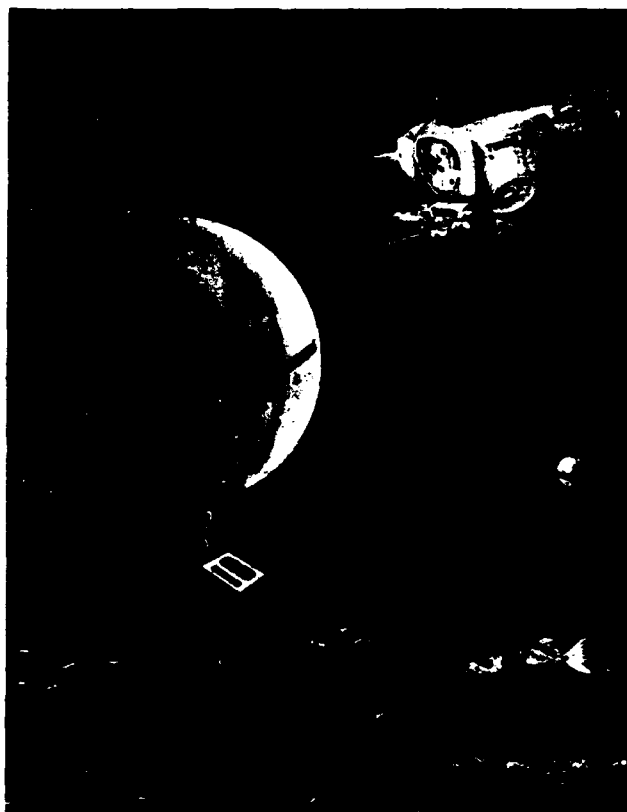


Sponsored by

NAVAL FACILITIES ENGINEERING COMMAND

March 1974

CIVIL ENGINEERING LABORATORY
NAVAL CONSTRUCTION BATTALION CENTER
Port Hueneme, California 93043



Navy submersible TURTLE
performing inspection of
concrete spheres.

LONG-TERM DEEP-OCEAN TEST OF CONCRETE SPHERICAL STRUCTURES—

Part I: Fabrication, Emplacement, and Initial Inspections

by Harvey H. Haynes

Approved for public release; distribution unlimited.

Unclassified

SECURITY CLASSIFICATION OF THIS PAGE (When Data Entered)

REPORT DOCUMENTATION PAGE		READ INSTRUCTIONS BEFORE COMPLETING FORM
1. REPORT NUMBER TR-805	2. GOVT ACCESSION NO.	3. RECIPIENT'S CATALOG NUMBER
4. TITLE (and Subtitle) LONG-TERM DEEP-OCEAN TEST OF CONCRETE SPHERICAL STRUCTURES-Part I: Fabrication, Emplacement, and Initial Inspections		5. TYPE OF REPORT & PERIOD COVERED Not final; July 1971-June 1973
		6. PERFORMING ORG. REPORT NUMBER
7. AUTHOR(s) Harvey H. Haynes		8. CONTRACT OR GRANT NUMBER(s)
9. PERFORMING ORGANIZATION NAME AND ADDRESS CIVIL ENGINEERING LABORATORY Naval Construction Battalion Center Port Hueneme, California 93043		10. PROGRAM ELEMENT PROJECT, TASK AREA & WORK UNIT NUMBERS 3.1610
11. CONTROLLING OFFICE NAME AND ADDRESS Naval Facilities Engineering Command Alexandria, VA 22332		12. REPORT DATE March 1974
		13. NUMBER OF PAGES 43
14. MONITORING AGENCY NAME & ADDRESS (if different from Controlling Office)		15. SECURITY CLASS (of this report) Unclassified
		15a. DECLASSIFICATION DOWNGRADING SCHEDULE
16. DISTRIBUTION STATEMENT (of this Report) Approved for public release; distribution unlimited.		
17. DISTRIBUTION STATEMENT (of the abstract entered in Block 20, if different from Report)		
18. SUPPLEMENTARY NOTES		
19. KEY WORDS (Continue on reverse side if necessary and identify by block number) Concrete structures, pressure-resistant structures, concrete spheres, permeability, implosion, submerged concrete structures, seawater permeability of concrete, long-term loading, unreinforced concrete.		
20. ABSTRACT (Continue on reverse side if necessary and identify by block number) This report summarizes the fabrication, emplacement and inspections during the first 1.2 years of submergence of eighteen 66-inch-OD concrete spheres. The spheres are located 4 miles south of Santa Cruz Island, California, in depths of water from 1,840 to 5,075 feet. The purpose of the test is to collect data on time-dependent failure, permeability and durability of concrete pressure-resistant structures. Findings from the inspections showed that two spheres located at the depths of 3,725 and 4,330 feet had imploded and that the		

DD FORM 1 JAN 73 1473

EDITION OF 1 NOV 65 IS OBSOLETE

Unclassified

SECURITY CLASSIFICATION OF THIS PAGE (When Data Entered)

Unclassified

SECURITY CLASSIFICATION OF THIS PAGE(When Data Entered)

20. Continued

quantity of seawater which permeated through the concrete for phenolic-coated spheres was about 0.8 cu ft and for uncoated spheres it was about 1.6 cu ft. This test program is planned to continue through 1981 (total of 10 years).

Unclassified

SECURITY CLASSIFICATION OF THIS PAGE(When Data Entered)

CONTENTS

	page
INTRODUCTION	1
TEST DESCRIPTION	1
FABRICATION	2
EMPLACEMENT	5
INSPECTIONS	10
RESULTS	10
Implosion	10
Permeability	13
SUMMARY	16
ACKNOWLEDGMENTS	17
REFERENCES	18
APPENDIXES	
A – Concrete Materials	19
B – Soil Properties	27
C – Compressive Strength of Concrete for Sphere 3	28
D – Calculation of Seawater Intake	31
LIST OF SYMBOLS	35

INTRODUCTION

Numerous experimental studies have been performed at the Civil Engineering Laboratory (CEL)^a on the behavior of concrete structures under hydrostatic loading [1-11].^b These studies have shown that concrete is well suited as a construction material for pressure-resistant structures to depths of 3,000 feet. The empirical data were obtained from test specimens subjected to relatively short-term loading conditions where the longest loading-period for any specimen was 42 days. This series of ocean tests was conducted to supplement the earlier research by providing data on concrete structures subjected to in-situ deep-ocean conditions for periods of up to 10 years.

The objectives of the test program were to obtain design information on time-dependent failure, permeability, and durability of the concrete spheres. Data on time-dependent failure will permit a rational factor of safety to be applied to pressure-resistant structures; data on seawater permeability of concrete will allow predictions of the quantity of water to be expected to penetrate to the structure's interior; and data on the durability of plain and steel reinforced concrete will determine such factors as strength changes with time, chemical composition changes of the concrete, and steel corrosion problems.

TEST DESCRIPTION

Eighteen, 66-inch-OD concrete spheres were placed in the ocean at depths ranging from 1,840 to 5,075 feet (Table 1). This depth range corresponds to a sustained pressure-to-short-term implosion pressure

ratio, P_s/P_{im} ,^c of 0.36 to 0.83. It was anticipated that the spheres subjected to a P_s/P_{im} ratio of 0.70 or greater would implode with time [8]; therefore, the six spheres at greatest depths were equipped with clocks that would count days in periods up to three years. If a sphere imploded, the clock would record the day of failure.

Permeability data will be gathered using the following method: the spheres are buoyant by approximately 1,000 pounds and are tethered 32 feet off the seafloor by a 2-1/4-inch-diameter chain. As seawater permeates the concrete, the weight of the sphere will increase. The reduced buoyancy of the sphere means less chain can be suspended off the seafloor, so the sphere moves closer to the seafloor. A change in height of one chain link (2-1/4-inch chain) corresponds to 0.5 cu ft of seawater which has permeated to the hull interior.

The permeability rate of seawater through waterproofed and nonwaterproofed concrete will be determined. Eight spheres were coated on the exterior with a two-part phenolic coating; another eight spheres remained uncoated. All sixteen of these permeability specimens were of unreinforced concrete. The remaining two spheres were reinforced with conventional steel bars of 0.5-inch diameter. The reinforcement was covered with 1 or 2.5 inches of concrete. Also, one-half of the exterior of each sphere was coated with the phenolic compound while the other half remained uncoated.

The durability of the concrete will be studied by determining the changes in strength and chemical composition with time. The concrete compressive strengths will be obtained from core specimens drilled from 14 x 18 x 18-inch blocks. Blocks are located with the spheres in the deep ocean and on land,

^a Formerly the Naval Civil Engineering Laboratory; now a detachment of the Naval Construction Battalion Center, Port Hueneme, California.

^b Numbers in brackets indicate references.

^c The short-term implosion pressure, P_{im} , is calculated by the following empirical equation [8]:

$$P_{im} = [5.02(\nu/D_o) - 0.038] f'_c$$

Table 1. Test Description

Sphere No.	Depth (ft)	P_s/P_{im}^a	Concrete Water-proofed	Comments
1	5,075	0.83	Yes	clock inside sphere
2	4,875	0.80	Yes	clock inside sphere
3	4,330	0.72	Yes	clock inside sphere
4	4,185	0.81	No	clock inside sphere
5	4,100	0.78	No	clock inside sphere
6	3,875	0.70	No	clock inside sphere
7	3,725	0.58	Yes	
8	3,665	0.60	Yes	
9	3,295	0.62	No	
10	3,190	0.56	No	
11	3,140	0.50	Yes	
12	2,790	0.55	No	
13	2,635	0.41	Yes	
14	2,440	0.44	Yes	
15	2,300	0.43	No	
16	2,120	0.40	No	
17	1,980	0.38	<i>b</i>	steel reinforcement in walls
18	1,840	0.36	<i>b</i>	steel reinforcement in walls

^a Sustained pressure-to-short-term implosion pressure ratio.

^b One hemisphere is waterproofed while the other hemisphere is not waterproofed.

exposed to ambient conditions. Chemical composition changes of the concrete will be determined by comparing x-ray diffraction patterns with those of the concrete at age 20 months.

FABRICATION

Concrete hemisphere sections were cast in a steel mold and the following day were removed from the mold. Twelve 6 x 12-inch-long control cylinders and one 14 x 18 x 18-inch control block of concrete were also cast with each hemisphere.

Moist-curing of the hemisphere, six control cylinders, and the control block was accomplished by wrapping the specimens in wet burlap and then in polyethylene film: the remaining six control cylinders were placed in the fog room. Moist-curing continued for 28 days at ambient temperature inside an open building followed by 28 days of room-curing conditions, and then on-land field-curing conditions.

After several weeks of field curing, the hemispheres were prepared for assembly into spheres. The equatorial edges were ground flat by using a large steel plate, and silica carbide grit and water as the cutting agent. A titanium hull penetration at the apex



Figure 1. Fabrication of spheres.

of each hemisphere was epoxy-bonded into place. The exterior surfaces of the hemispheres were lightly sand blasted and a two-part phenolic compound (Phenoline No. 300) was applied.^d Finally, to fabricate a sphere two hemispheres were bonded together with an epoxy adhesive (Furane Epocast 8288). Figure 1 shows several of these operations.

All of the spheres had the same dimensions and variations in out-of-roundness. Extensive measurements [8] were taken on one hemisphere, and Table 2 summarizes the dimensions. In summary, the mean outside diameter was 65.886 inches and the mean wall thickness was 4.124 inches.

Conventional 1/2-inch-diameter steel reinforcing bars were embedded in the concrete of two spheres. Arrangement of the steel bars is shown in Figure 2. Alternate longitudinal bars had a nominal concrete cover of 1 or 2.5 inches; however, in certain locations near the apex the minimum cover was as low as 0.5 inch.

Clocks were placed in Spheres 1 through 6 to record the day of implosion, if the sphere should fail. The clock records days on a counter and has a projected life of 3 years.^e Figure 3 shows the clock and its pressure housing which was a 4-inch-OD pipe section. The pipe was attached to the top penetrator of the sphere.^f

^d Pinholes existed in the final waterproof coating at a rate of approximately 1 per 2 sq in.

^e For zero time in the ocean, the clocks read 41 days for Spheres 1-3, and 38 days for Spheres 4-6.

^f Upon retrieval, safety precautions should be followed in handling the pressure housing because water at high pressure could be inside. Prior to opening, drill a 1/8-inch-diameter hole through the steel wall to relieve any internal pressure.

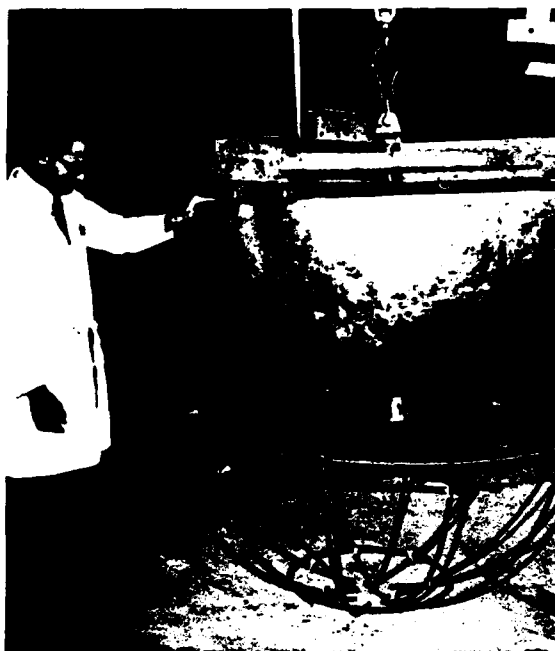


Figure 2. Arrangement of steel bar reinforcement for Spheres 17 and 18.



Figure 3. Clock mechanism and its 4-in.-OD pressure housing.

Table 2. Hemisphere Dimensions and Out-of-Roundness Variations

Item	Mean Dimension (in.)	Standard Deviation		Maximum Local Variation	
		Measured (in.)	Percent of Wall Thickness	Measured (in.)	Percent of Wall Thickness
Interior radius	28.820	± 0.093	± 2.26	+0.145 -0.213	+3.51 -5.16
Exterior radius	32.943	± 0.083	± 2.01	+0.150 -0.247	+3.64 -5.94
Wall thickness	4.124	± 0.060	± 1.45	+0.181 -0.165	+4.26 -3.90

Power was supplied to the clock from dry-cell batteries placed in a watertight, but not pressure-resistant container located at the bottom of the sphere. When implosion occurs, the batteries are destroyed or shorted, and the lead wires running to the clock are broken.

Final assembly of the spheres is shown in Figures 4 and 5. The descriptive information on Figure 5 gives important details on the assembly.

Documentation of the concrete material is given in Appendix A. The mix proportions, compressive strengths, cement compositions, and x-ray diffraction

patterns of the concrete are presented. In general, the concrete was made from a high-quality mix design where the cement factor was 7.8 sacks per cu yd and water-cement ratio was 0.40; the compressive strength at 28 days was an average 7,660 psi.

Disposition of the control cylinders and blocks is as follows: of the six control cylinders placed in the fog room, three were tested at 28 days; their compressive strengths are given in Appendix A, Table A-2. The remaining three control cylinders will stay in the fog room and will be tested when the spheres are retrieved from the ocean. Three of the six control cylinders cured with the hemisphere were tested at age 28 days and the remaining three were tested approximately one month prior to emplacing the spheres in the ocean (Table A-2); these later tests gave the compressive strength used in calculating the short-term implosion pressure, P_{im} . There were two control blocks per sphere; one block went with the sphere into the ocean and the other block stayed on land, located within 50 yards of the ocean. Both blocks will be cored and tested when the sphere is retrieved.

EMPLACEMENT

The spheres were emplaced in the ocean 4 miles south of Santa Cruz Island, California (Figure 6), on 23 September 1971. The method of emplacing the spheres (Figure 7) was as follows: a barge loaded with the spheres (Figure 7) was towed by a surface vessel (*USNS Gear*) which maintained a constant course over a location where the seafloor increased in depth at a fairly uniform rate. At predetermined depths, the appropriate sphere was pushed overboard to free-fall to the seafloor. The method worked well with most of the spheres landing within a few hundred yards of the target location. Final location of the spheres is given in Table 3. Figure 8 shows a plan view and Figure 9 a profile view of the sphere locations.

Water samples were obtained from the depth of 2,530 feet and gave the following data: temperature of 5.33°C, salinity of 34.41 ppt, pH of 7.2, oxygen content of 0.06 ml/l, and velocity of sound of 1,483.9 m/sec. A water sample from 4,740 feet gave a temperature of 5.16°C and a pH of 7.0.

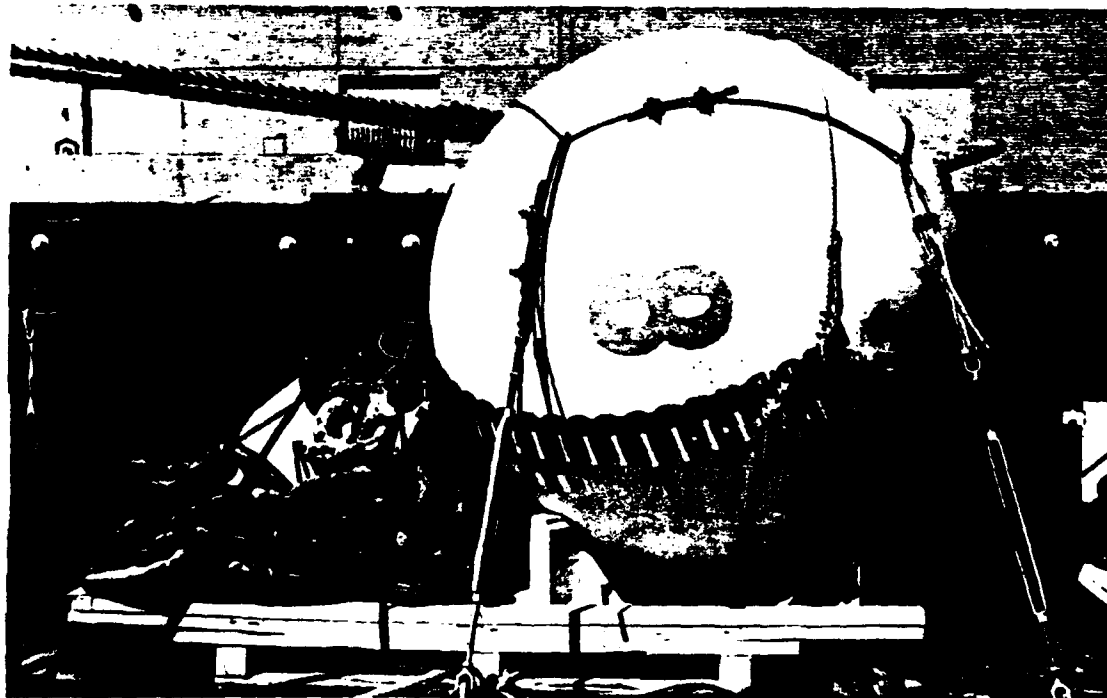


Figure 4. Final assembly of sphere.

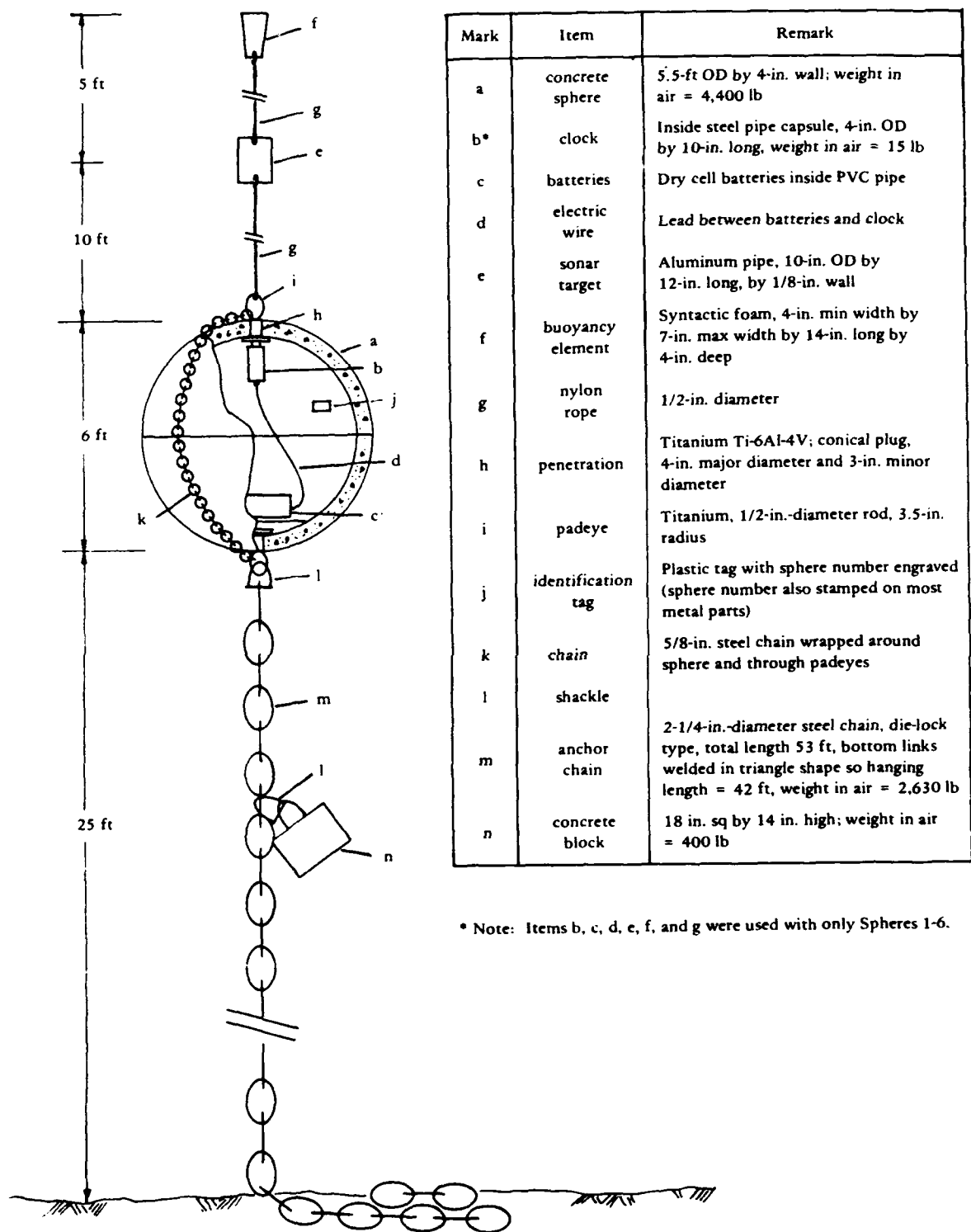


Figure 5. Details of sphere assembly.

Table 3. Location of Spheres

Sphere No.	Surface Location at Launch				Seafloor Location Found by <i>Turtle</i>				Depth (ft)	Sphere No.
	Lorac Coordinates		Distance Between Spheres (yd)	Azimuth Between Spheres (^o T)	Lorac Coordinates		Distance Between Spheres (yd)	Azimuth Between Spheres (^o T)		
	G	R			G	R				
1	479.6 ^a	324.4							5,075	1
2	481.5	320.0	680	346					4,875	2
3	489.9	305.2	2,400	340	490.0	302.0			4,330	3
4	491.4	302.6	600	341	491.0	299.2	400	349	4,185	4
5	492.6	300.8	200	340					4,100	5
6	501.9	284.3	2,650	344					3,875	6
7	503.2	282.2	400	344	500.0	280.9			3,725	7
8	506.6	277.1	900	343	504.7	277.2	800	326	3,665	8
9	511.2	268.0	1,580	350	509.0	265.5	1,920	352	3,295	9
10	511.7	266.6	280	350	511.7	264.4	380	309	3,190	10
11	516.0	259.3	1,250	345	516.0	258.0	1,180	346	3,140	11
12	524.4	250.8	1,720	337	523.5	249.5	1,650	339	2,790	12
13	527.0	248.0	540	337	532.5 ^b	249.7	970	280	2,635	13
14	528.8	244.4	650	347	536.1 ^b	246.8	630	332	2,440	14
15	530.2	242.4	400	355	534.6	242.6	700	23	2,300	15
16	531.7	240.8	300	345	535.0	239.5	550	5	2,120	16
17	533.0	239.4	300	324	535.0	238.3	200	10	1,980	17
18	534.0 ^c	238.3	200	352	535.3	237.5	200	347	1,840	18

^a Geographic coordinates 33°49'15"N by 119°33'30"W.^b These locations may be in error.^c Geographic coordinates 33°56'15"N by 119°36'15"W.

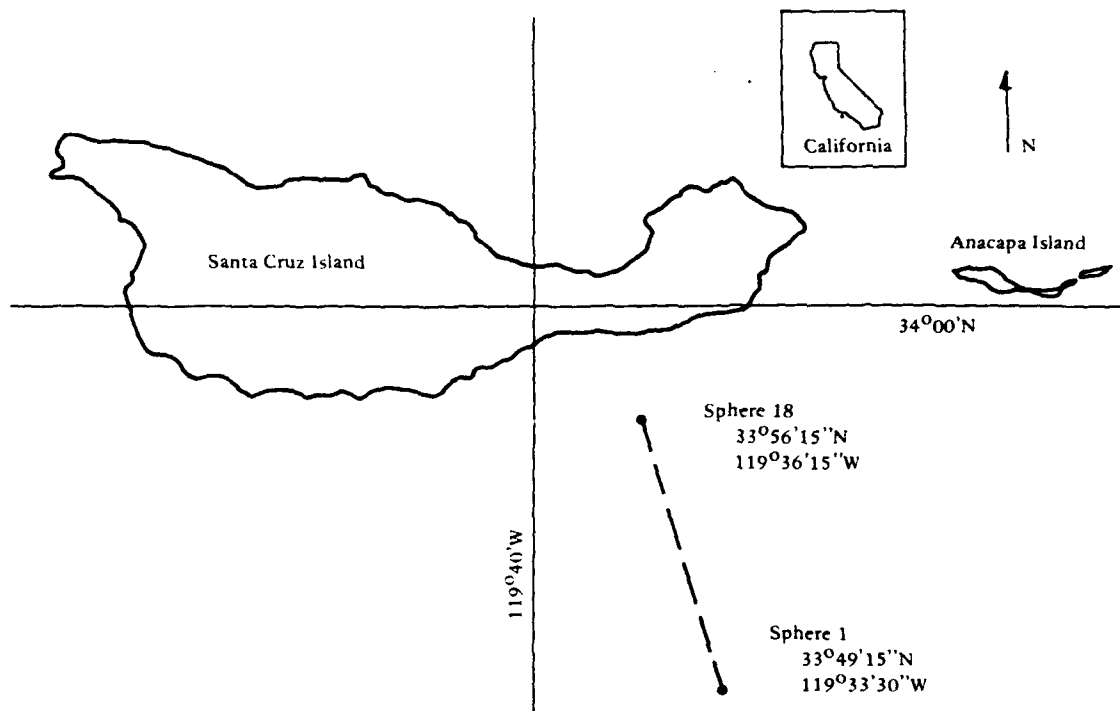


Figure 6. Location of spheres off California coast.



Figure 7. Spheres rigged on barge in preparation for free-fall launch.

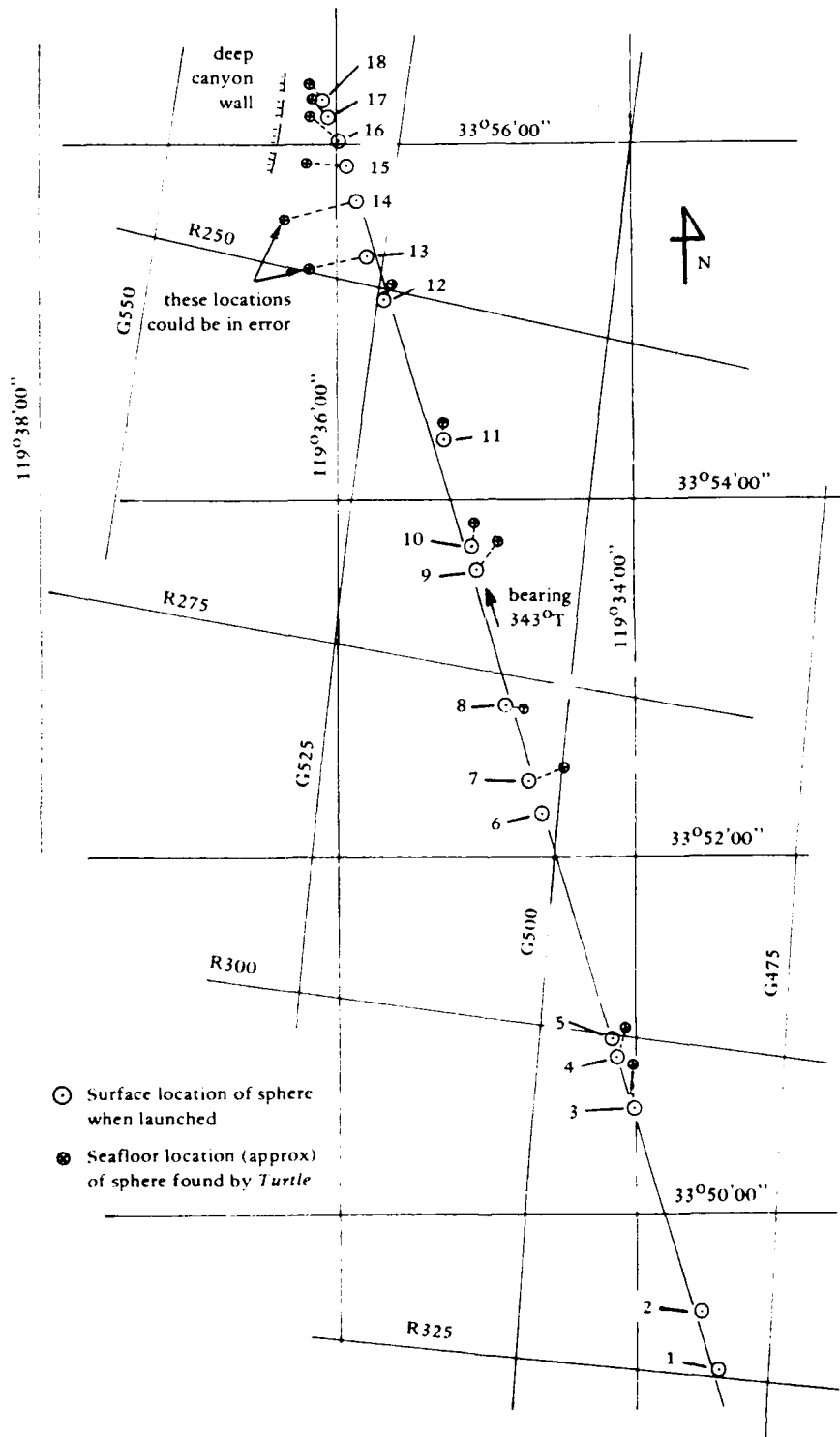


Figure 8. Plan view of sphere location.

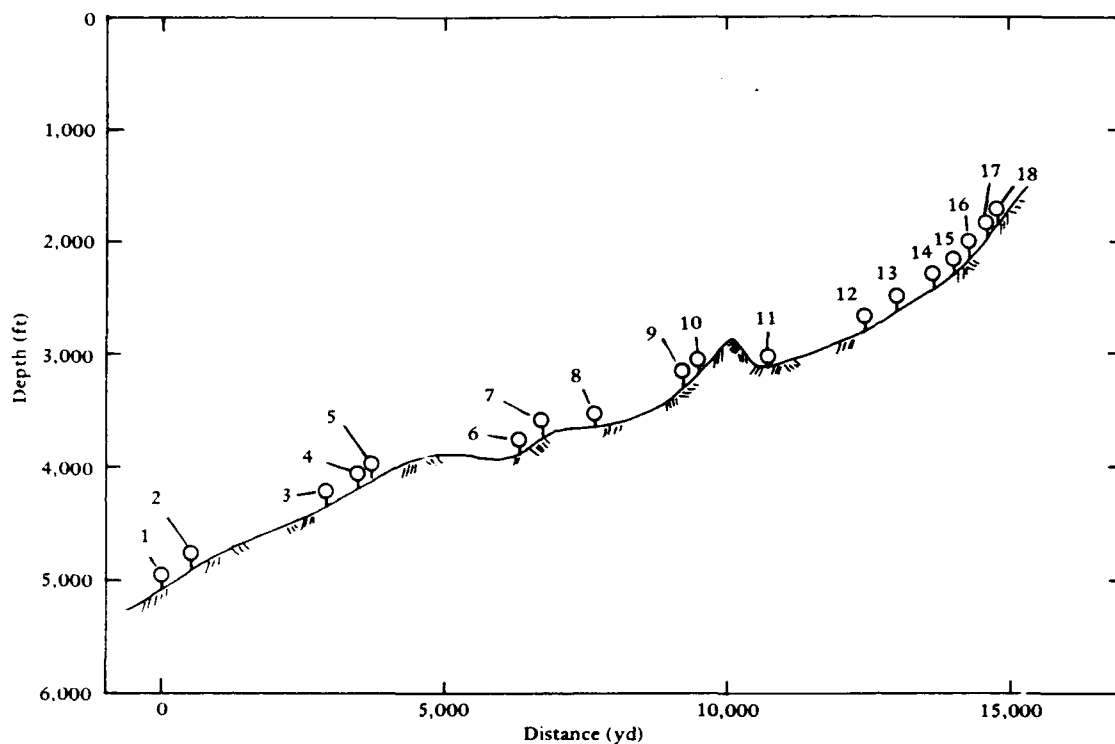


Figure 9. Bottom profile at sphere location directly below surface launch.

A soil sample was obtained at the depth of 4,100 feet near Sphere 5. Data from the core are presented in Appendix B, Table B-1.

INSPECTIONS

Three inspection visits have been made to view as many spheres as possible. Of the 18 spheres, 15 have been viewed once, and of those 15, five have been viewed twice.

The first and third inspections were made by the Naval Submarine Development Group One using the submersible *Turtle*. The second inspection was made by Scripps Institution of Oceanography using the Remote Underwater Manipulator (RUM).

Turtle is a manned submersible capable of operating to depths of 6,500 feet. During the inspections with the submersible, however, those spheres at depths greater than 3,800 feet were not inspected because of the possibility of implosion of a test sphere. Investigators with the *Turtle* were

successful in inspecting Spheres 7-18. The spheres at greater depths (1-6) were to be inspected with the unmanned RUM vehicle. Within the time available for the inspection cruise with RUM, Spheres 3-5 were inspected successfully; the remaining spheres (1, 2, and 6) have not been inspected.

Data collected during the inspections are given in Table 4. The chain link count is the number of links of chain suspended off the seafloor by the buoyant spheres. If a sphere was found imploded or if anything unusual was observed, this information was recorded. Figures 10 and 11 show an uncoated sphere and a coated sphere tethered off the seafloor.

RESULTS

Implosion

Two spheres, 3 and 7, have imploded. Fragments of Sphere 3 were observed during the RUM inspection to be scattered over an area of what appeared to

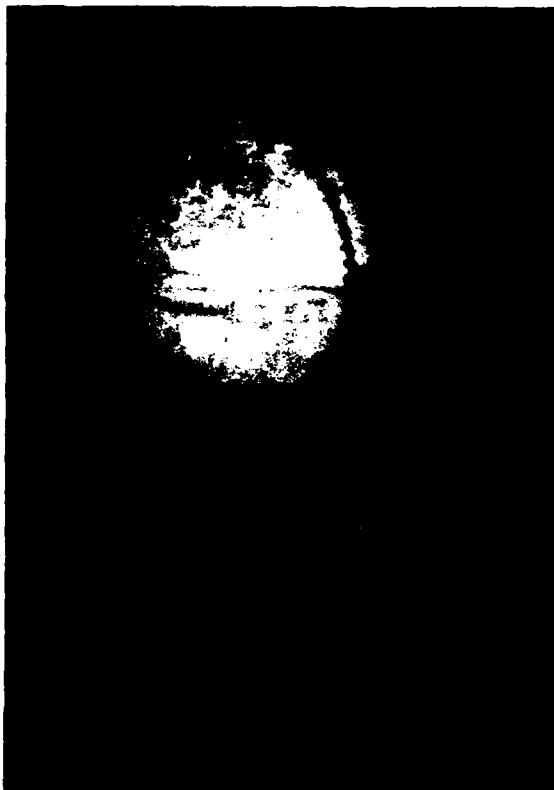


Figure 10. View of uncoated sphere (No. 12) at a depth of 2,790 feet after 431 days.

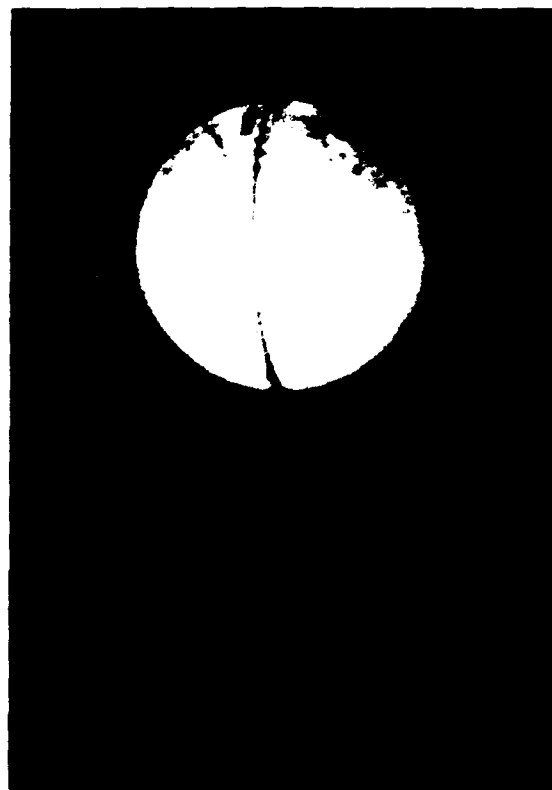


Figure 11. View of coated sphere (No. 13) at a depth of 2,635 feet after 431 days. Material on top of sphere is sediment. Nylon rope on left side of sphere was used to secure 5/8-in. chain around sphere (see Figure 4).

be a 25-yard radius. To retrieve the clock, the manipulator on RUM picked up the 5/8-inch chain to which the clock was attached. Once on the surface, it was learned that the clock was not retrieved. Implosion forces must have "blown" the clock off the chain. Hence, the time to implosion for Sphere 3 was not obtained; however, from information obtained during the third inspection it has been deduced that the sphere imploded during descent. The *Turtle* operators thoroughly searched the Sphere 3 site for the clock, which was not located, but observations showed that fragments of concrete were spread over a radius of 50 yards. Also, the anchor chain was not at the center of debris or at the location of highest fragment density. This information

meant that the sphere probably imploded during descent which allowed the fragments to disperse.

In the case of Sphere 7, the fragments were all located within a 10-yard radius. Sphere 7 did not contain a clock, so the time to implosion is between 1 and 431 days.

For Spheres 3 and 7, the P_s/P_{im} ratio was 0.72 and 0.58, respectively. This level of long-term loading was considered relatively low for implosion to occur. However, seven other spheres are subjected to P_s/P_{im} ratios greater than 0.58, four of which have been inspected and are performing well.

The concrete control block for Sphere 3 was retrieved. The compressive strengths of this block and other control specimens stored at on-land field

Table 4. Inspection Data

Sphere No.	Chain Link Count ^a at—				Time to Implosion (days)	Comments
	Emplacement (By: CEL Date: 23 Sep 71 Time: 0 days)	Inspection No. 1 (By: Turtle Date: 4 Mar 72 Time: 163 days)	Inspection No. 2 (By: RUM Date: 26 Aug 72 Time: 340 days)	Inspection No. 3 (By: Turtle Date: 1 Dec 72 Time: 431 days)		
1	29.7 ^b	—	—	—	—	
2	29.7	—	—	—	—	
3	29.4	—	imploded	—	0	
4	29.4	—	23	—	—	Insp. No. 3, observed sphere intact and floating high.
5	29.6	—	21	—	—	
6	29.6	—	—	—	—	
7	31.5	—	—	imploded	1-431	
8	31.5	—	—	0	—	Insp. No. 3, sphere intact but on seafloor.
9	31.6	—	—	—	—	Insp. No. 3, chain tangled on block.
10	31.6	—	—	24	—	
11	38.0	—	—	31	—	
12	32.1	—	—	24	—	
13	32.1	28	—	28	—	
14	48.4	39	—	39	—	
15	32.2	26	—	25	—	
16	31.8	26	—	25	—	
17	32.6	29	—	28	—	
18	32.6	—	—	25	—	

^a Number of links suspended off seafloor by buoyant sphere.

^b Calculated number of links suspended off seafloor by sphere with concrete at room dry condition.

conditions and fog-room conditions are given in Appendix C. The control block from Sphere 7 was not retrieved as the *Turtle* was not rigged for a retrieval operation.

Permeability

The method used to determine the permeability of seawater through the concrete walls produced a fairly accurate indication of in-situ permeability behavior of the spheres. This method used the change in number (reduced number) of chain links to calculate the gain in weight of the sphere due to seawater intake. The accuracy of the quantitative results depend on several approximations; these are discussed in Appendix D. The accumulative effect of these approximations is estimated to be a maximum of ± 0.8 cu ft of seawater. This error can be reduced to ± 0.3 cu ft by comparing the change in link counts from actual inspections instead of using the calculated link count from zero days.

Table 5 gives the total quantity of seawater intake, Q , for the different time intervals between emplacement and inspections. Seawater intake includes the seawater absorbed by the concrete and the seawater that permeated through the concrete. Figure 12 shows the Q versus time behavior. Three items of interest are observed. One item is that the uncoated concrete spheres have a greater Q than the coated spheres; after 431 days, the coated spheres showed an average Q of about 2.6 cu ft and the uncoated spheres about 3.6 cu ft. Another item is that the spheres which have been inspected twice showed a considerable decrease in the rate of seawater intake. The last item is that Q increased for specimens at greater depth, but the increase was not pronounced.

The actual quantity of seawater permeating the wall, Q_p , was estimated by subtracting the quantity of absorbed seawater from the total seawater intake. Earlier work on 66-inch-OD spheres [8] showed that the concrete (same concrete as used in this study) absorbed approximately 3 percent by weight (or 7 percent by volume) of seawater. This corresponds to 2.0 cu ft of seawater absorbed by the concrete. Table 5 shows the Q_p values for the different time intervals. At 431 days, the average Q_p for the coated spheres was 0.8 cu ft and for the uncoated spheres was 1.6 cu ft.

Reference 8 reports permeability results from two 66-inch-OD concrete spheres subjected to seawater hydrostatic pressure tests. The permeability data are shown in Table 6. D'Arcy's permeability coefficient, K_c , was determined from the data as an average of 0.13×10^{-12} ft/sec. D'Arcy's permeability coefficient can be expressed as follows for the spheres:

$$K_c = \frac{Q_p t}{T A h} \quad (1)$$

where K_c = permeability coefficient, ft/sec

Q_p = quantity of permeability seawater, cu ft

T = time, sec

t = wall thickness, ft

A = exterior surface area, cu ft

h = depth (or pressure head), ft

Using the K_c value of 0.13×10^{-12} ft/sec as a baseline, the data from the spheres in the ocean can be compared to that from the pressure vessel tests. Table 5 lists the K_c values for the ocean spheres. In all cases, the permeability coefficient was lower for the spheres in the ocean than for the spheres in the pressure vessels. The average K_c values for the coated spheres were 0.06×10^{-12} ft/sec at 163 days and 0.02×10^{-12} ft/sec at 431 days, and for the uncoated spheres were 0.11×10^{-12} ft/sec at 163 days and 0.06×10^{-12} ft/sec at 431 days. Other K_c values were those attained between the time interval of 163 to 431 days; for the coated spheres, no increase in Q_p was observed, so K_c was zero, and for the uncoated spheres the average K_c was 0.04×10^{-12} ft/sec.

The permeability data from the pressure vessel tests showed that a straight line curve of Q_p versus $\log T$ fit the data with fair accuracy. The empirical semi-log relations^R for one sphere (specimen CWL-9A) at a simulated depth of 2,520 ft was:

$$Q_p = 0.34 \log_{10} T - 0.11 \quad (2)$$

^R Equations 2 and 3 are presented in this report with time, T , in days. These equations are different from those in Reference 8 which give time, T , in hours.

Table 5. Permeability Data

Sphere No.	Concrete Water-proofed	Depth (ft)	Change in Link Count, ΔL , and Total Seawater Intake, Q , for--						Seawater Permeating Interior, Q_p , ^a and D'Arcy's Permeability Coefficient, K_c , for--					
			0-163 Days		0-340 Days		0-431 Days		163-431 Days		0-163 Days		0-340 Days	
			ΔL (links)	Q (cu ft)	ΔL (links)	Q (cu ft)	ΔL (links)	Q (cu ft)	ΔL (links)	Q (cu ft)	K_c ft/sec $\times 10^{-12}$	Q_p (cu ft)	K_c ft/sec $\times 10^{-12}$	Q_p (cu ft)
4	no	4,185	-	-	6.4	3.1	-	-	-	-	-	1.1	0.03	-
5	no	4,100	-	-	8.6	4.2	-	-	-	-	-	2.2	0.07	-
10	no	3,190	-	-	-	-	7.6	3.7	-	-	-	-	-	-
11	yes	3,140	-	-	-	-	7.0	2.8	-	-	-	-	0.05	-
12	no	2,790	-	-	-	-	8.1	3.9	-	-	-	-	0.02	-
13	yes	2,635	4.1	2.0	-	-	4.1	2.0	0	0	0	-	0.07	-
14	yes	2,440	9.4	3.1	-	-	9.4	3.1	0	1.1	0.12	-	0	0
15	no	2,300	6.2	3.0	-	-	7.2	3.5	1.0	1.0	0.11	-	0.04	0
16	no	2,120	5.8	2.8	-	-	6.8	3.3	1.0	0.8	0.10	-	0.06	0.5
17	half/half	1,980	3.6	1.5	-	-	4.6	1.9	1.0	0.4	-	-	0.06	0
18	half/half	1,840	-	-	-	-	7.6	3.1	-	-	-	-	0.07	-

^a To obtain seawater permeability, Q_p , the seawater absorbed by the concrete was estimated as 2.0 cu ft and was subtracted from the total seawater intake, Q .

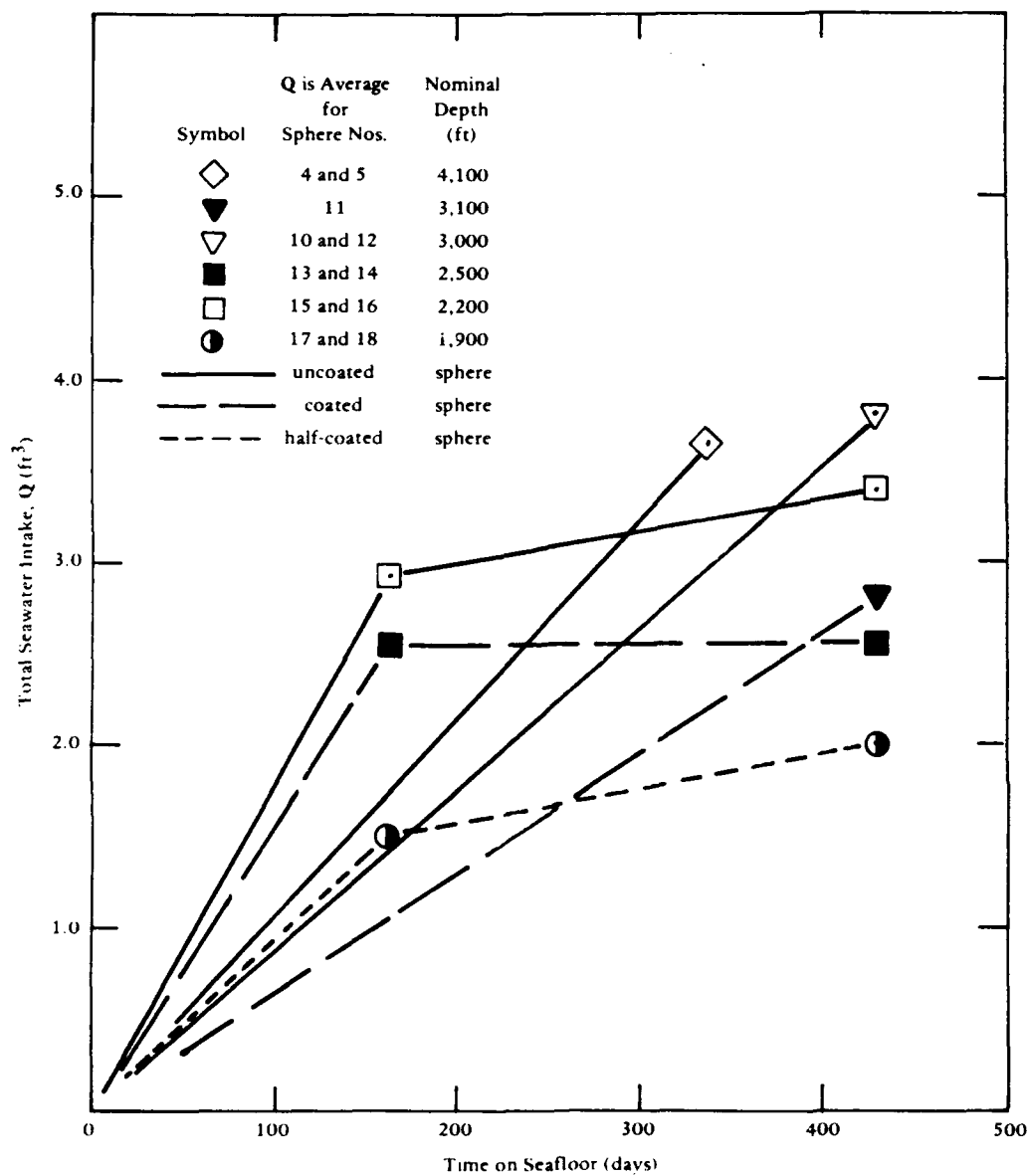


Figure 12. Total seawater intake of concrete spheres.

and for another sphere (specimen CWL-6) at a simulated depth of 3,760 feet it was:

$$Q_p = 0.32 \log_{10} T - 0.01 \quad (3)$$

where T is time (days).

Figure 13 shows a comparison between D'Arcy's equation, Equation 1, using $K_c = 0.13 \times 10^{-12}$ ft/sec and the empirical equations, Equations 2 and 3. Data from the ocean spheres are shown to be bracketed by the D'Arcy and empirical semi-log relations. D'Arcy's

relation assumes a constant rate of permeability, whereas the extrapolation of the empirical semi-log relation assumes a decreasing rate with time. It is not apparent at this time which approach defines the permeability behavior of the concrete spheres. Additional data from inspections are required.

Sphere 8 was found intact but sitting on the seafloor after 431 days. A total seawater intake of 15.3 cu ft or more was required to overcome the positive buoyancy of the sphere. This quantity of seawater was three to four times that of the other

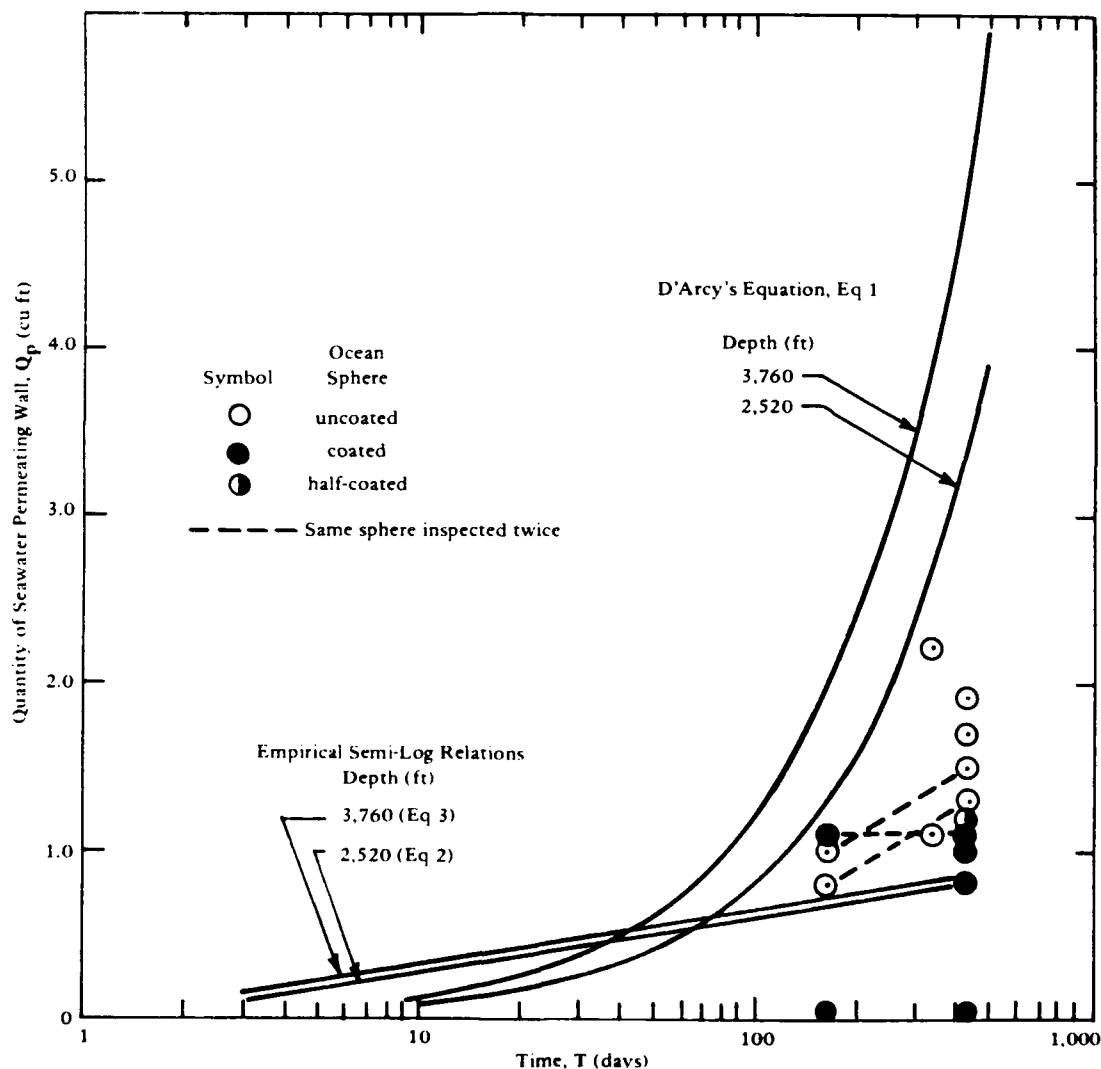


Figure 13. Comparison of ocean sphere permeability data with the D'Arcy equation and the empirical semi-log relations as given in Reference 8.

Table 6. Permeability Data (After Haynes and Kahn [8])

Specimen No.	Simulated Depth (ft)	Time (days)	Permeability, Q_p (cu ft)	D'Arcy's Permeability Coefficient, K_c (ft/sec $\times 10^{-12}$)
CWL-9A	2,520	21	0.34	0.16
CWL-6	3,760	42	0.52	0.10

NOTE: Spheres started the test having the concrete in a wet condition. The procedure for obtaining wet-concrete walls was to place an uncoated sphere on the bottom of the pressure vessel and allow the seawater to fill the inside of the sphere, and then apply hydrostatic pressure. The pressure was maintained usually for 7 days at 500 psi or until the pressure became constant and showed no decrease, thus indicating that the voids of more significant size were filled with water.

spheres, so it was evident that Sphere 8 leaked. Experience in fabricating concrete spheres has shown that periodically a specimen leaked at a concrete-epoxy joint.

SUMMARY

Of the original eighteen spheres emplaced at depths between 1,840 and 5,075 ft, fifteen spheres have been inspected at least once. Of the spheres that were inspected, the one at greatest depth was at 4,185 feet, and was performing well after 431 days. Two spheres have imploded; one sphere imploded during emplacement to the depth of 4,330 feet and the other sphere imploded during the time interval of 1 to 431 days at a depth of 3,725 feet.

The quantity of seawater that had permeated through the concrete walls was about 0.8 cu ft for the coated spheres (waterproofed concrete) and 1.6 cu ft for the uncoated spheres (non-waterproofed concrete).

D'Arcy's permeability coefficient, K_c , was on the average 0.02×10^{-12} ft/sec for the coated spheres and 0.06×10^{-12} ft/sec for the uncoated spheres between the time interval of 0 to 431 days on the seafloor. These K_c values were less than the K_c value of 0.13×10^{-12} ft/sec obtained from pressure vessel tests on similar uncoated spheres for time intervals up to 42 days [8].

The concrete spheres are to remain in the ocean through 1981 with periodic inspections to determine implosion and permeability data.

ACKNOWLEDGMENTS

The author wishes to acknowledge the assistance of Mr. L. F. Kahn during the planning and fabrication stages, of Mr. N. D. Albertsen in emplacing the spheres in the ocean, of Mr. P. C. Zubiate as senior project technician, and of Mr. D. W. Widmayer in fabricating the spheres.

REFERENCES

1. Naval Civil Engineering Laboratory. Technical Report R-517: Behavior of spherical concrete hulls under hydrostatic loading, pt. 1. Exploratory investigation, by J. D. Stachiw and K. O. Gray. Port Hueneme, CA, Mar. 1967. (AD649290)
2. ———. Technical Report R-547: Behavior of spherical concrete hulls under hydrostatic loading, pt. 2. Effect of penetrations, by J. D. Stachiw. Port Hueneme, CA, Oct 1967. (AD661187)
3. ———. Technical Report R-588: Behavior of spherical concrete hulls under hydrostatic loading, pt. 3. Relationship between thickness-to-diameter ratio and critical pressures, strains, and water permeation rates, by J. D. Stachiw and K. Mack. Port Hueneme, CA, Jun. 1968. (AD835492L)
4. ———. Technical Report R-679: Failure of thick-walled concrete spheres subjected to hydrostatic loading, by H. H. Haynes and R. A. Hoofnagle. Port Hueneme, CA, May 1970. (AD708011)
5. ———. Technical Report R-696: Influence of length-to-diameter ratio on behavior of concrete cylindrical hulls under hydrostatic loading, by H. H. Haynes and R. J. Ross. Port Hueneme, CA, Sep. 1970. (AD713088)
6. ———. Technical Report R-735: Influence of stiff equatorial rings on concrete spherical hulls subjected to hydrostatic loading, by L. F. Kahn and J. D. Stachiw. Port Hueneme, CA, Aug. 1971. (AD731352)
7. ———. Technical Report R-740: Influence of end-closure stiffness on behavior of concrete cylindrical hulls subjected to hydrostatic loading, by L. F. Kahn. Port Hueneme, CA, Oct. 1971. (AD732363)
8. ———. Technical Report R-774: Behavior of 66-inch concrete spheres under short and long term hydrostatic loading, by H. H. Haynes and L. F. Kahn. Port Hueneme, CA, Sep. 1972. (AD748584)
9. ———. Technical Report R-785: Hydrostatic loading of concrete spherical hulls reinforced with steel liners, by H. H. Haynes, G. L. Page and R. J. Ross. Port Hueneme, CA, Apr. 1973. (AD 759684)
10. ———. Technical Report R-790: Influence of compressive strength and wall thickness on behavior of concrete cylindrical hulls under hydrostatic loading, by N. D. Albertsen. Port Hueneme, CA. June 1973.
11. ———. Technical Note N-——: Influence of steel bar reinforcement on the behavior of concrete spherical hulls, by N. D. Albertsen. Port Hueneme, CA. (To be published.)
12. Informal correspondence, J. Baker, Graduate student, University of California, Berkeley, CA, letter of 8 February 1973, to H. H. Haynes, Naval Civil Engineering Laboratory, Port Hueneme, CA.
13. Amelyanovich, K. K., Verbitsky, V. D., and Sintsov, G. M., "Results of research into performance of concrete and reinforced concrete members under high pressure head," in *Proceedings of Federation Internationale de la Precontrainte (FIP) Symposium on Concrete Sea Structures*, Tbilisi, USSR, Sep. 1972. [Translated London, 1972.]

Appendix A

CONCRETE MATERIALS

The mix design for the concrete is given in Table A-1. Transit-mix trucks delivered the concrete, and final determination of water content was based on workability. Table A-2 gives the properties of the fresh concrete; average values were (1) water-to-cement ratio of 0.40, (2) slump of 1-1/2 inches, (3) air content of 2.4 percent by volume, and (4) unit weight of 145.2 lb/cu ft.

Compressive strength of the concrete at age 28 days (Table A-2) averaged 7,660 psi for the fog-room-cured specimens and 7,690 psi for the on-land field-cured specimens (moist-cured in wet burlap and wrapped in plastic for first 28 days). The compressive strength of the concrete at ages varying from 45 to 174 days was obtained prior to emplacing the spheres in the ocean (Table A-2). These strengths were used to calculate the short-term implosion pressure of the spheres (the compressive strength of the weaker hemisphere was used) so that projected emplacement depths could be calculated. For the uncoated spheres, the control cylinders were saturated with seawater prior to testing. The method of saturation was to place the specimen in a pressure vessel and apply 500 psi pressure for 7 days. The strength of saturated concrete has been found to be 10% lower than room-dry concrete [8]. The coating was assumed to maintain the concrete in a dry condition, so the control cylinders were tested in a dry condition.

Table A-3 is a copy of a typical mill test report on the portland cement used by the transit-mix supplier, Southern Pacific Milling, during the fabrication of the hemispheres. All of the cement meets ASTM specification C-150-70, Type II, Low Alkali, Portland Cement.

X-ray diffraction patterns for three concrete blocks, W-15, W-39, and W-41, were obtained (Figures A-1 through A-3) for documentation of the chemical composition of the concrete at the early stages of the test program. At the end of the test program, which could be many years away, samples of concrete can be analyzed to determine whether or not the concrete has been attacked by the sulphates in seawater. Table A-4 gives the diffraction angle (2θ) of the expected intensity peaks for concrete attacked and unattacked by sulphates in seawater [12].

Table A-1. Concrete Mix Design

Portland cement, Type II, low-alkali
 Santa Clara River aggregate
 Water-to-cement ratio = 0.41
 Sand-to-cement ratio = 1.85
 Coarse aggregate-to-cement ratio = 2.28
 Water-reducing admixture = 2 oz/slack of Plastiment

Material	Aggregate Gradation		
	Sieve Size Designation	Percentage Retained	
		Individual	Cumulative
Sand	3/8 inch	0	0
	no. 4	2	2
	no. 8	11	13
	no. 16	17	30
	no. 30	28	58
	no. 50	28	86
	no. 100	11	97
	pan	3	100
Coarse aggregate	3/4 inch	0	0
	3/8 inch	70	70
	no. 4	30	100

Table A-2. Concrete Control Cylinder Data

Sphere No.	Hemisphere No. ^d	Characteristics of Fresh Concrete Cylinders				Compressive Strength, f'_c at 28 Days (psi)			Age, Condition, and Compressive Strength, f'_c Prior to Ocean Emplacement		
		Water-to-Cement Ratio	Slump (in.)	Air Content by Volume (%)	Density (lb/cu ft)	Wrapped Wet Burlap and Plastic ^b	Fog Room ^b	Age (days)	Condition of Concrete ^c	f'_c (psi)	
1	W-4 W-35	0.42 0.41	3/4 1-1/4	2.3 2.2	146.0 145.2	7,300 8,070	8,520 8,070	174 65	dry dry	8,940 9,360	
2	W-8 W-7	— 0.38	1-1/4 1-1/2	2.2 2.2	146.4 145.2	8,050 7,590	8,250 7,940	164 162	dry dry	9,950 8,970	
3	W-16 ^d W-15	0.38 0.38	1-3/4 1-1/4	2.1 2.3	145.1 147.8	7,940 7,260	8,400 8,520	132 134	dry dry	9,650 8,840	
4	W-6 W-5	0.41 0.43	1/4 1-1/4	5.8 2.7	138.3 146.4	8,470 7,310	8,760 8,050	170 172	wet wet	8,320 7,600	
5	W-10 W-9	0.44 0.40	1-1/4 1-1/4	2.5 2.1	144.9 146.1	7,210 7,620	7,730 8,240	156 158	wet wet	8,090 7,690	
6	W-14 W-13	0.42 0.41	1-1/4 1-1/2	2.2 2.6	147.0 148.0	8,100 7,960	8,580 8,060	143 144	wet wet	8,510 8,370	
7	W-20 W-17	0.39 0.36	1-1/2 2	2.7 2.1	143.9 147.2	7,720 7,370	7,660 7,750	117 126	dry dry	9,530 9,480	
8	W-22 W-19	0.41 0.38	1-1/4 1-3/4	2.5 2.2	144.1 145.2	7,690 7,940	7,520 8,410	111 119	dry dry	9,030 9,380	
9	W-28 W-25	0.42 0.38	1-3/4 1-3/4	1.6 2.1	147.0 145.2	6,970 7,890	6,920 8,070	94 104	wet wet	7,820 8,740	
10	W-30 W-27	0.39 0.42	1-1/2 1-1/4	2.1 2.3	145.6 146.2	7,950 7,620	8,190 7,900	88 97	wet wet	8,560 8,330	
11	W-24 W-21	0.38 0.36	1-1/2 1-3/4	2.1 2.4	145.2 146.0	7,670 7,670	7,540 7,720	103 113	dry dry	9,820 9,190	
12	W-32 W-29	0.40 0.40	1-1/2 1-3/4	2.4 1.7	145.8 146.0	7,510 7,030	7,570 7,240	80 89	wet wet	8,390 7,430	
13	W-26 W-23	0.39 0.39	1-1/4 1-1/4	2.3 2.7	145.0 143.9	7,990 7,860	8,070 7,640	98 105	dry dry	10,210 9,370	

continued

Table A-2. Continued

Sphere No.	Hemisphere No. ^a	Characteristics of Fresh Concrete Cylinders				Compressive Strength, f'_c at 28 Days (psi)		Age, Condition, and Compressive Strength, f'_c Prior to Ocean Emplacement		
		Water-to-Cement Ratio	Slump (in.)	Air Content by Volume (%)	Density (lb/cu ft)	Wrapped Wet Burlap and Plastic ^b	Fog Room ^b	Age (days)	Condition of Concrete ^c	f'_c (psi)
14	W-12 ^d	0.42	1-1/4	3.2	136.6	6,730	6,990	144	dry	8,170
	W-11	0.43	3/4	-	-	7,440	7,550	148	dry	9,200
15	W-34	0.37	1-1/2	2.1	145.6	7,800	8,170	74	wet	7,830
	W-31	0.38	1-1/4	2.0	146.4	7,880	7,810	82	wet	8,740
16	W-36	0.38	1-1/2	2.3	145.4	7,520	7,220	67	wet	7,780
	W-33	0.41	1-1/2	2.4	145.8	8,050	7,930	75	wet	8,340
17	W-39	-	1-1/4	2.1	145.4	7,690	8,050	51	dry	9,050
	W-40	-	1-1/2	2.0	145.8	7,740	7,730	52	wet	7,730
18	W-41	-	1-1/2	2.6	144.3	7,600	8,620	48	dry	8,770
	W-42	-	1-1/2	2.5	144.5	7,810	7,970	45	wet	7,590

^a Hemisphere number listed first refers to the top hemisphere of the sphere.^b Average of three 6 x 12-in.-long control cylinders.^c Dry refers to cylinders from on-land field conditions.^d Wet refers to cylinders placed in seawater under 500 psi for 7 days.^e Some expanded shale aggregate found in cylinder.

Table A-3. Copy of Mill Test Report on Cement

<p>PACIFIC WESTERN INDUSTRIES, INC. LOS ROBLES CEMENT DIVISION POST OFFICE BOX 1247 • (805)248-6733 LEBEC, CALIFORNIA 93243</p> <p>MILL TEST REPORT</p> <p>We certify that 17,982 bbls. of LOS ROBLES Portland Cement in Silo or Lot No. 1-802 has the following chemical and physical characteristics as tested in our plant laboratory:</p>																																																																			
<p>CHEMICAL ANALYSIS:</p> <table style="width: 100%; border-collapse: collapse;"> <tr><td>Silicon Dioxide, SiO₂</td><td style="text-align: right;">22.28</td><td style="text-align: right;">%</td></tr> <tr><td>Aluminum Oxide, Al₂O₃</td><td style="text-align: right;">4.62</td><td style="text-align: right;">%</td></tr> <tr><td>Ferric Oxide, Fe₂O₃</td><td style="text-align: right;">3.04</td><td style="text-align: right;">%</td></tr> <tr><td>Calcium Oxide, CaO</td><td style="text-align: right;">64.24</td><td style="text-align: right;">%</td></tr> <tr><td>Magnesium Oxide, MgO</td><td style="text-align: right;">1.46</td><td style="text-align: right;">%</td></tr> <tr><td>Sulphur Trioxide, SO₃</td><td style="text-align: right;">2.73</td><td style="text-align: right;">%</td></tr> <tr><td>Loss on Ignition</td><td style="text-align: right;">1.38</td><td style="text-align: right;">%</td></tr> <tr><td>Insoluble</td><td style="text-align: right;">0.05</td><td style="text-align: right;">%</td></tr> <tr><td>Alkalies, Comb. as Na₂O</td><td style="text-align: right;">0.42</td><td style="text-align: right;">%</td></tr> </table> <p>POTENTIAL COMPOUNDS:</p> <table style="width: 100%; border-collapse: collapse;"> <tr><td>3 CaO.SiO₂</td><td style="text-align: right;">49.0</td><td style="text-align: right;">%</td></tr> <tr><td>2 CaO.SiO₂</td><td style="text-align: right;">26.9</td><td style="text-align: right;">%</td></tr> <tr><td>3 CaO.Al₂O₃</td><td style="text-align: right;">7.1</td><td style="text-align: right;">%</td></tr> <tr><td>4 CaO.Al₂O₃.Fe₂O₃</td><td style="text-align: right;">9.2</td><td style="text-align: right;">%</td></tr> </table>	Silicon Dioxide, SiO ₂	22.28	%	Aluminum Oxide, Al ₂ O ₃	4.62	%	Ferric Oxide, Fe ₂ O ₃	3.04	%	Calcium Oxide, CaO	64.24	%	Magnesium Oxide, MgO	1.46	%	Sulphur Trioxide, SO ₃	2.73	%	Loss on Ignition	1.38	%	Insoluble	0.05	%	Alkalies, Comb. as Na ₂ O	0.42	%	3 CaO.SiO ₂	49.0	%	2 CaO.SiO ₂	26.9	%	3 CaO.Al ₂ O ₃	7.1	%	4 CaO.Al ₂ O ₃ .Fe ₂ O ₃	9.2	%	<p>FINENESS:</p> <table style="width: 100%; border-collapse: collapse;"> <tr><td>Blaine, Sq. Cm. per Gram</td><td style="text-align: right;">3476</td></tr> <tr><td>Wagner, Sq. Cm. per Gram</td><td></td></tr> </table> <p>SOUNDNESS:</p> <table style="width: 100%; border-collapse: collapse;"> <tr><td>Autoclave, Percent Expansion</td><td style="text-align: right;">.000</td></tr> </table> <p>TIME OF SETTING:</p> <table style="width: 100%; border-collapse: collapse;"> <tr><td>Vicat</td><td style="text-align: right;">1 hrs.</td><td style="text-align: right;">45 min.</td></tr> <tr><td>Gilmore, Initial Set</td><td style="text-align: right;">2 hrs.</td><td style="text-align: right;">50 min.</td></tr> <tr><td>Final Set</td><td style="text-align: right;">4 hrs.</td><td style="text-align: right;">30 min.</td></tr> </table> <p>COMPRESSIVE STRENGTH:</p> <table style="width: 100%; border-collapse: collapse;"> <tr><td>1 day</td><td style="text-align: right;">1552</td><td style="text-align: right;">psi</td></tr> <tr><td>3 days</td><td style="text-align: right;">2838</td><td style="text-align: right;">psi</td></tr> <tr><td>7 days</td><td style="text-align: right;">4411</td><td style="text-align: right;">psi</td></tr> <tr><td>28 days</td><td style="text-align: right;">6802</td><td style="text-align: right;">psi</td></tr> </table>	Blaine, Sq. Cm. per Gram	3476	Wagner, Sq. Cm. per Gram		Autoclave, Percent Expansion	.000	Vicat	1 hrs.	45 min.	Gilmore, Initial Set	2 hrs.	50 min.	Final Set	4 hrs.	30 min.	1 day	1552	psi	3 days	2838	psi	7 days	4411	psi	28 days	6802	psi
Silicon Dioxide, SiO ₂	22.28	%																																																																	
Aluminum Oxide, Al ₂ O ₃	4.62	%																																																																	
Ferric Oxide, Fe ₂ O ₃	3.04	%																																																																	
Calcium Oxide, CaO	64.24	%																																																																	
Magnesium Oxide, MgO	1.46	%																																																																	
Sulphur Trioxide, SO ₃	2.73	%																																																																	
Loss on Ignition	1.38	%																																																																	
Insoluble	0.05	%																																																																	
Alkalies, Comb. as Na ₂ O	0.42	%																																																																	
3 CaO.SiO ₂	49.0	%																																																																	
2 CaO.SiO ₂	26.9	%																																																																	
3 CaO.Al ₂ O ₃	7.1	%																																																																	
4 CaO.Al ₂ O ₃ .Fe ₂ O ₃	9.2	%																																																																	
Blaine, Sq. Cm. per Gram	3476																																																																		
Wagner, Sq. Cm. per Gram																																																																			
Autoclave, Percent Expansion	.000																																																																		
Vicat	1 hrs.	45 min.																																																																	
Gilmore, Initial Set	2 hrs.	50 min.																																																																	
Final Set	4 hrs.	30 min.																																																																	
1 day	1552	psi																																																																	
3 days	2838	psi																																																																	
7 days	4411	psi																																																																	
28 days	6802	psi																																																																	
<p>THIS CEMENT MEETS OR EXCEEDS THE FOLLOWING DESCRIBED SPECIFICATIONS:</p> <p>ASTM: <u>C-150-70 Type II Low Alkali</u></p> <p>FEDERAL: <u>SS-C-192g Type II Low Alkali</u></p> <p>CALIFORNIA: <u>State Div. of Hwys. Std. Spec. 90-2.01 Mod. Type II Low Alkali</u></p> <p>OTHER: _____</p>																																																																			
<p>MAIN OFFICE:</p> <p>3810 Wilshire Boulevard Los Angeles, California 90005 (213) 381-3181</p>	<p style="text-align: right;"><i>Pacific Western Industries, Inc.</i></p> <p>BY: _____ 4-2-71 CHIEF CHEMIST DATE</p>																																																																		

Table A-4. Expected Intensity Peaks [12] From X-Ray Diffraction Analysis of Concrete Attacked and Unattacked by Seawater

Diffraction Angle (2θ) at Intensity Peak (deg)	Material	Remarks
Concrete Attacked by Sulfates in Seawater		
9.1 15.8	Ettringite, 3CaOAl ₂ O ₃ ·3CaSO ₄ ·32H ₂ O	May not be present. Very soluble, may not be present. Due to carbonation. Formed at cold temperatures, may not be present.
11.2	Hydrocalumite, Ca ₁₆ Al ₁₈ (OH) ₅₄ CO ₃ ·21H ₂ O	
11.7	Gypsum, CaSO ₄ ·2H ₂ O	
29.4	Calcite, CaCO ₃	
26.2 27.2	Aragonite, CaCO ₃	
Concrete Unattacked		
18.1 34.1	Lime, Ca(OH) ₂	Created from hydrated cement.
broad peak ~28-33	Tobermorite gel	Created from hydrated cement.
32.3 32.7 33.1	C ₃ S C ₃ S and C ₂ S C ₃ A	Traces of unhydrated cement, usually hard to see in older concrete.
29.4	Calcite, CaCO ₃	Due to carbonation.
10.5 20.9 26.6 ^a 27.8	Aggregates	Some of the larger peaks from the aggregate.

^a Quartz aggregate.

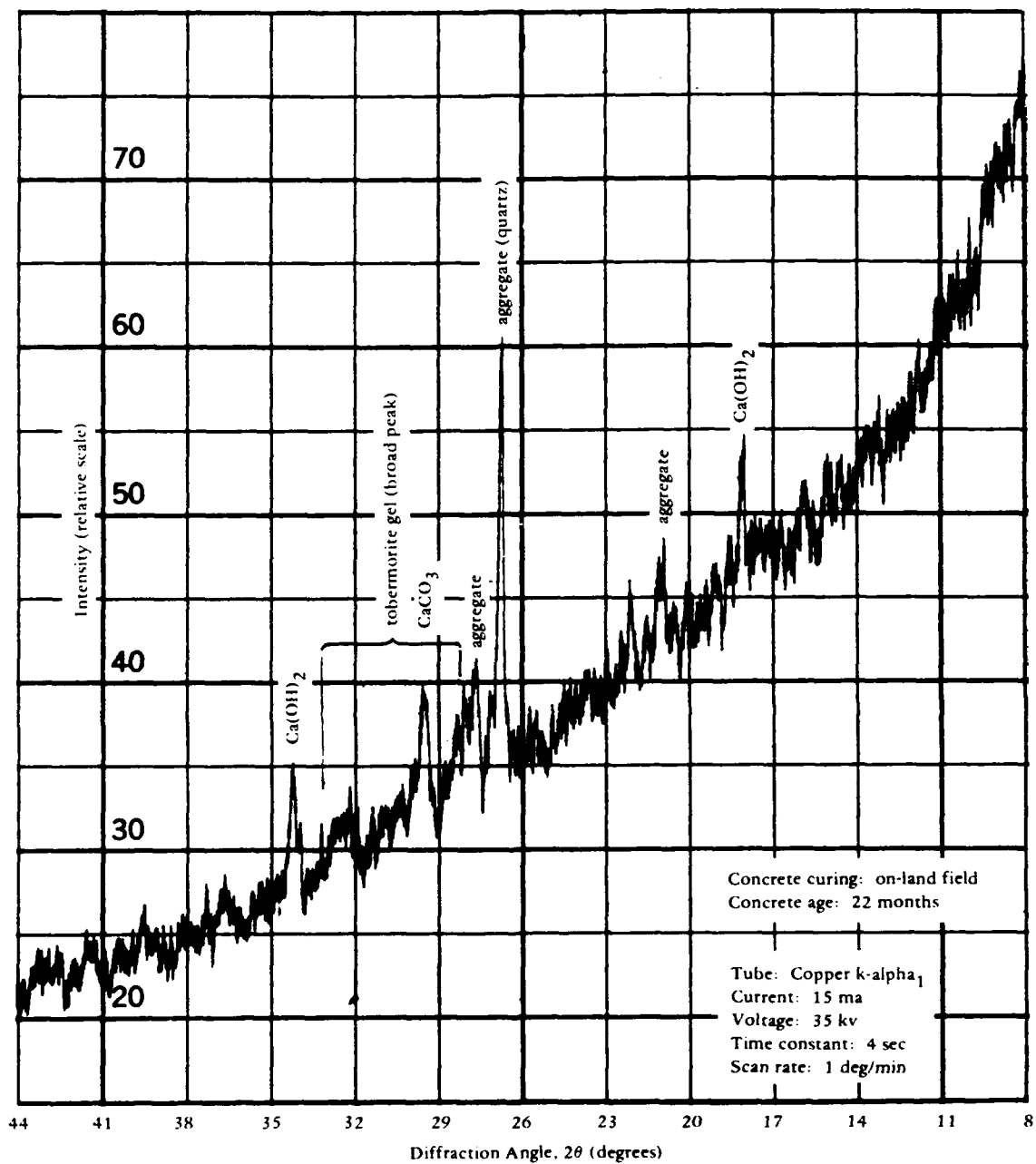


Figure A-1. X-ray diffraction pattern for concrete from W-15 control block.

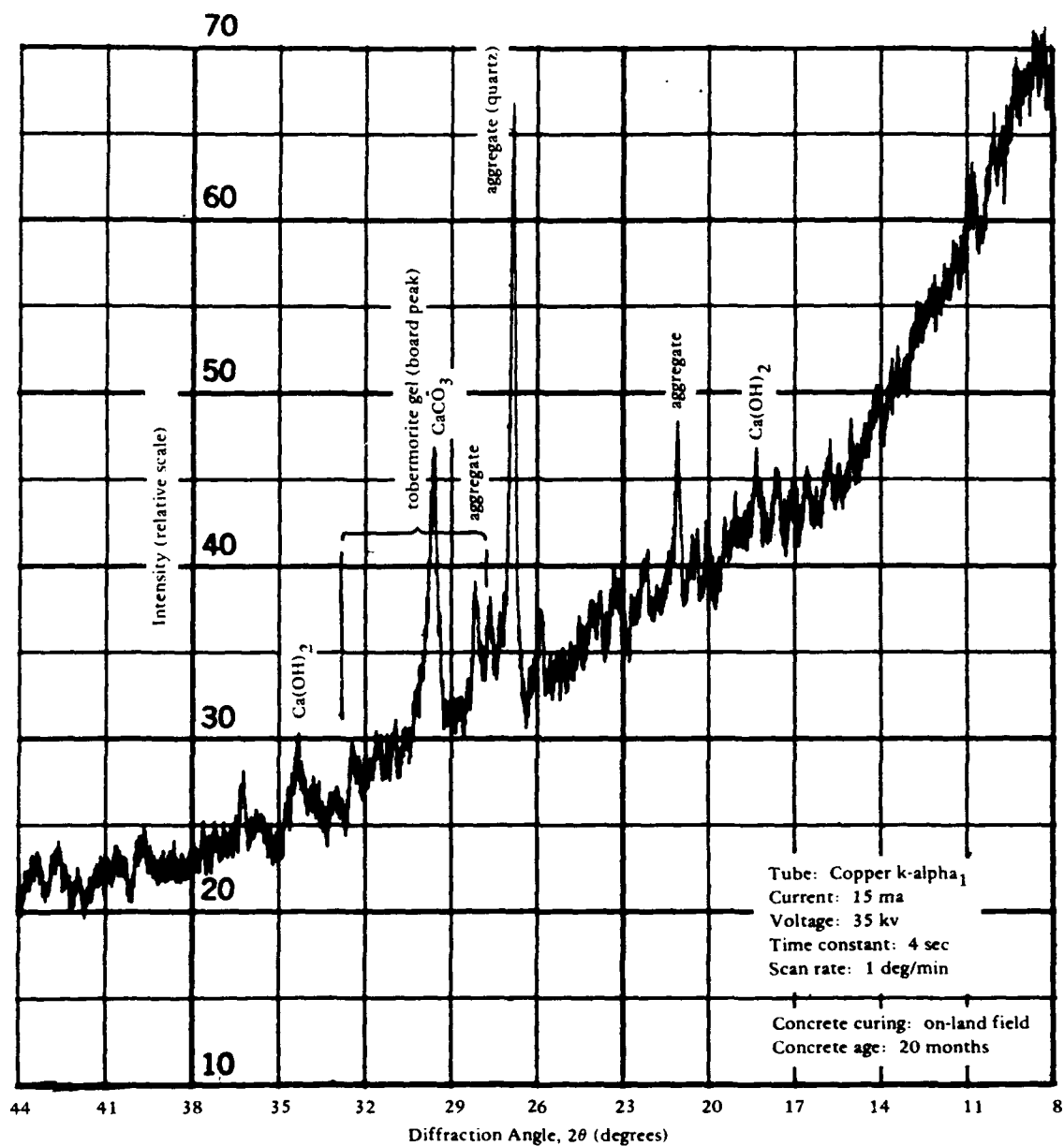


Figure A-2. X-ray diffraction pattern for concrete from W-39 control block.

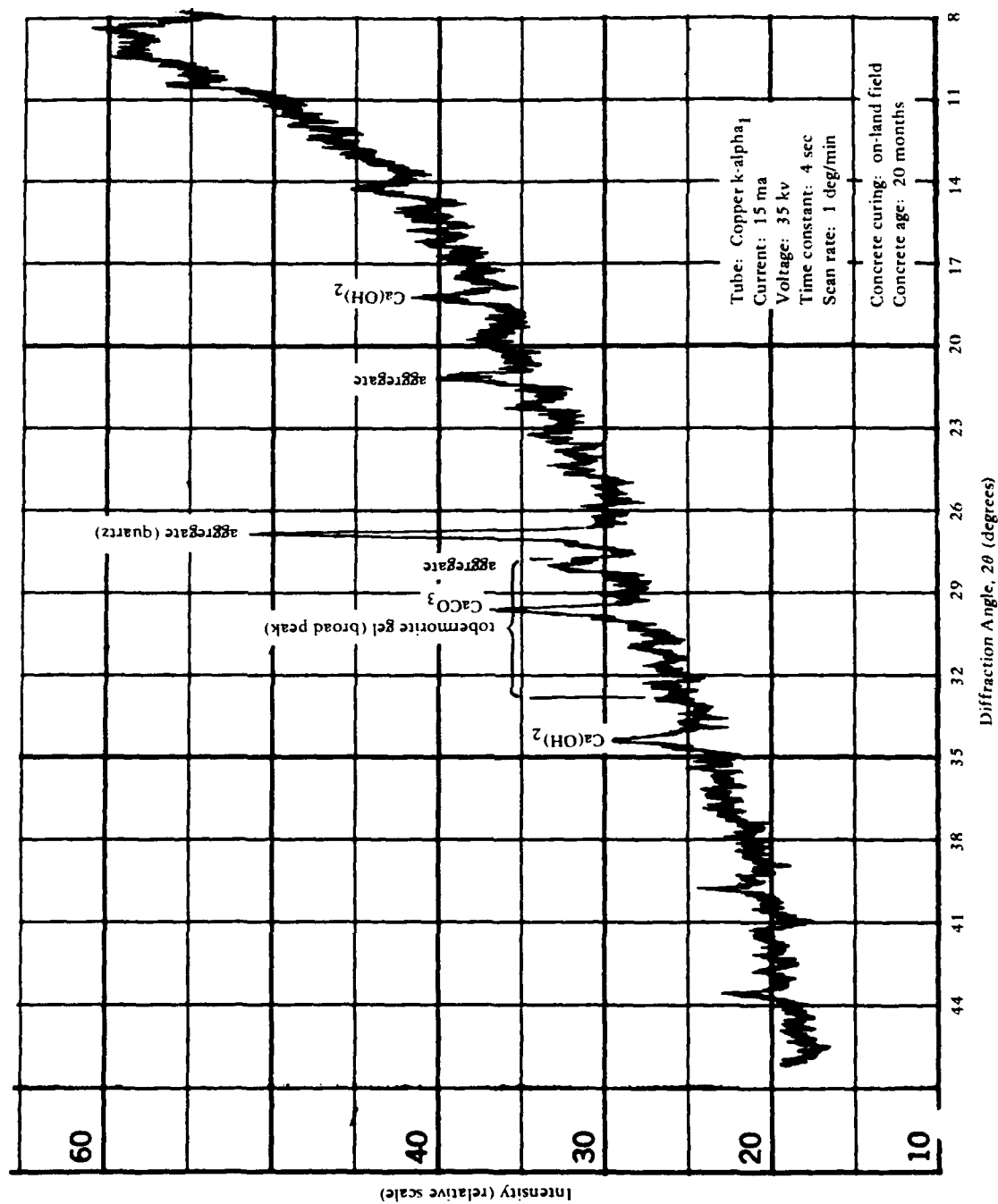


Figure A-3. X-ray diffraction pattern for concrete from W-41 control block.

Appendix B

SOIL PROPERTIES

Table B-1. Soil Data

(Core specimen obtained at 4,100 feet near Sphere 5; core diameter was 2.75 inches.)

Item	Properties of Soil Sample From Core by Intervals		
	0-3 In.	6-9 In.	13-16 In.
Bulk wet density (pcf)	90.64	94.53	94.20
Water content (%)	82.69	83.39	85.54
Vane shear strength (psi)	0.296	1.074	1.431
Remolded shear strength (psi)	0.037	0.394	0.566
Sensitivity	8.0	2.7	2.5
Liquid limit	81.7	91.0	112.3
Plastic limit	42.3	39.9	42.5
Plasticity index	39.4	51.1	69.8
Specific gravity	2.63	2.57	2.61
Unified soil classification	MH	MH	CH
Type of soil	silt	silt	clay-silt

Appendix C

COMPRESSIVE STRENGTH OF CONCRETE FOR SPHERE 3

Even though Sphere 3 imploded on descent to the seafloor, the control block of concrete was not retrieved until 340 days later. This control block was fabricated of the same concrete as one of the sphere's hemispheres, W-16. This concrete experienced a history of 172 days of on-land field curing and 340 days of in-ocean field curing.

The other hemisphere, W-15, had a corresponding control block that was continuously stored out-of-doors; hence, this concrete underwent a continuous 514 days of on-land field curing. Simultaneously, three 6 x 12-inch-long cylinders for both hemispheres underwent continuous fog room curing.

The compressive strengths for the concrete are shown in Table C-1 and Figure C-1. The fog-cured concrete increased 23 percent in average strength, from 8,460 to 10,420 psi. The on-land field-cured concrete leveled off in strength at an average of 8,650 psi after 134 days. The in-ocean field-cured concrete decreased in strength from an average of 9,650 psi after 132 days of on-land curing to an average of 7,600 psi after 340 days in the ocean; this was a 21 percent decrease in strength. Wetting of the dry concrete would account for 10 percent of the decrease [8]; perhaps under the long-term hydrostatic pressure the total decrease in strength was due to saturation of the concrete. Previous work by Russians [13] showed a decrease in compressive strength of 28 percent due to saturating dry concrete under high hydrostatic pressure; however, the test procedure used to obtain the saturated concrete was not discussed.

Concrete from block W-16 was analyzed by x-ray diffraction techniques. It was found that the concrete was not attacked by the seawater.

Table C-1. Control Cylinder Data for Sphere 3

Hemisphere	Curing Condition	Total Age (days)	Saturated With Seawater Prior to Test	Number of Control Specimens	Compressive Strength, f'_c (psi)	Coefficient of Variation (%)
W-15	Fog Room	28	no	3	8,520	—
	Field ^a	28	no	3	7,260	—
	With Hemisphere ^a	134	no	3	8,840	—
	Fog Room	514	no	3	10,470	3.9
	Field at CEL ^{a, b}	514	no	4	8,650	3.7
W-16	Fog Room	28	no	3	8,400	—
	Field ^a	28	no	3	7,940	—
	With Hemisphere ^a	132	no	3	9,650	—
	Fog Room	512	no	3	10,360	1.5
	In Ocean ^{a, b} (at 4,400 ft for 341 days)	512	yes	4	7,600	4.0

^a First 28 days: moist-cured in wet burlap wrapped in plastic sheeting.

^b 6 x 12-in.-long cylinders cored from block 18 x 18 x 14 inches.

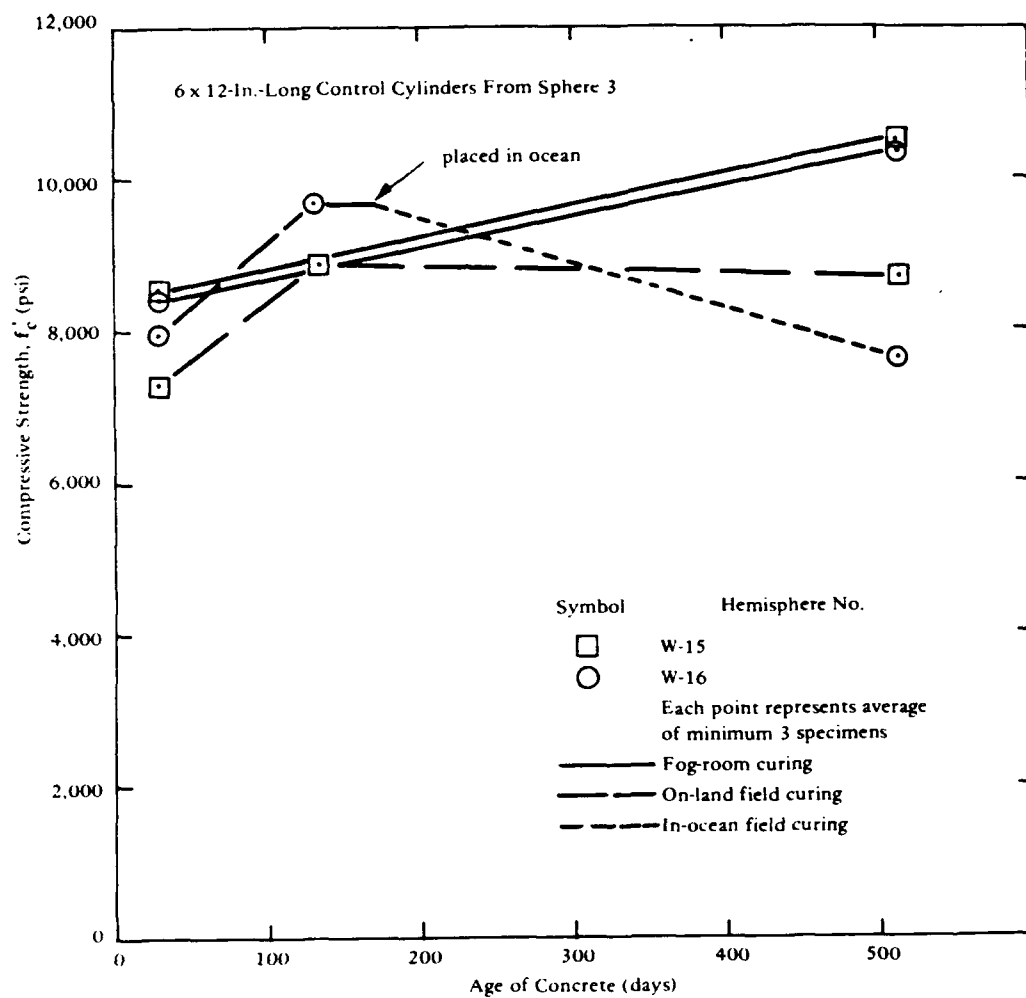


Figure C-1. Compressive strength of concrete for Sphere 3.

Appendix D

CALCULATION OF SEAWATER INTAKE

The method used to calculate the total quantity of seawater intake by the spheres depends on obtaining the change in number of chain links suspended off the seafloor by a sphere. The reduction in number of links is converted into quantity of seawater intake, Q . The accuracy of determining Q is dependent on several approximations.

One approximation is the criterion by which the submersible operators counted the chain links. They counted only whole links; or, in other words, the bottom-most link counted was the one in a vertical position.

Another approximation is estimating the original number of links suspended off the seafloor when the spheres had dry-concrete walls. The associated calculations are shown below, in part, and are completed in Table D-1.

Buoyancy of Hull

Dimensions $D_o = 65.886$ inches and $D_i = 57.640$ inches

Weight of Displaced Seawater, W_D

$W_D = 64 \text{ pcf} (86.64 \text{ cu ft}) = 5,545 \text{ lb}$

Weight of Concrete Sphere, W_C

$W_C = 145.2 \text{ pcf} (28.625 \text{ cu ft}) = 4,156 \text{ lb}$

Positive Buoyancy = 1,389 lb for bare concrete hull

In-Water Weight of Components on Spheres

5/8-inch chain	67 lb
Wet-concrete control block	220 lb
Steel components	40 lb
Titanium components	8 lb
Load on Spheres 7-16 (also common load to other spheres)	335 lb
Clock (estimated in air weight)	20 lb
Batteries (estimated in air weight)	40 lb
Common load	+335 lb
Load on Spheres 1-6	395 lb
Steel bar reinforcement (in-water weight)	150 lb
Common load	+335 lb
Load on Spheres 17 and 18	485 lb

Column D in Table D-1 was another approximation. This was the apparent weight gain of the system due to the change in volume of the sphere under load. Using data from Reference 8, it was assumed that the maximum long-term strain for the spheres at greatest depths was 2,500 $\mu\text{in./in.}$ This strain resulted in a

change in volume sufficient to reduce the buoyancy by 40 pounds. For the spheres in shallower water, a proportional buoyancy adjustment was made.

It was estimated that the maximum error in the net positive buoyancy values was ± 50 pounds. In terms of chain links (2-1/4-inch chain), the error was ± 1.5 links; or in terms of seawater intake, the error was ± 0.8 cu ft.

The error associated with permeability reading between inspections is ± 20 pounds, or ± 0.3 cu ft.

Table D-1. Calculation of Number of Links Off Seafloor at Zero Days

Sphere No.	A Positive Buoyancy of Concrete Hull (lb)	B Weight ^a of Components on Hull (lb)	C Weight ^a of Shackles (lb)	D Apparent Weight Gain (lb) ^b	E = A - [B + C + D] Net Positive Buoyancy (lb)	F Chain Size (in.)	G Weight ^a of Each Chain Link (lb/link)	H = E/G Number of Links Off Seafloor
1	1,389	395	28	40	926	2-1/4	31.2	29.7
2	1,389	395	28	40	926	2-1/4	31.2	29.7
3	1,389	395	42	35	917	2-1/4	31.2	29.4
4	1,389	395	42	35	917	2-1/4	31.2	29.4
5	1,389	395	42	30	922	2-1/4	31.2	29.6
6	1,389	395	42	30	922	2-1/4	31.2	29.6
7	1,389	335	42	30	982	2-1/4	31.2	31.5
8	1,389	335	42	30	982	2-1/4	31.2	31.5
9	1,389	335	42	25	987	2-1/4	31.2	31.6
10	1,389	335	42	25	987	2-1/4	31.2	31.6
11	1,389	335	42	25	987	2-1/4	26.0	38.0
12	1,389	335	28	25	1,001	2-1/4	31.2	32.1
13	1,389	335	28	25	1,001	2-1/4	31.2	32.1
14	1,389	335	28	20	1,006	2	20.8	48.4
15	1,389	335	28	20	1,006	2-1/4	31.2	32.2
16	1,389	335	42	20	992	2-1/4	31.2	31.8
17	1,389	485	42	15	847	2-1/8	26.0	32.6
18	1,389	485	42	15	847	2-1/8	26.0	32.6

^a In-water weight.^b Due to change in volume of sphere under load.

LIST OF SYMBOLS

A	Exterior surface area, cu ft
D_i	Inner diameter of concrete sphere, in.
D_o	Outer diameter of concrete sphere, in.
f'_c	Uniaxial compressive strength of concrete, psi
h	Depth (or pressure head), ft
K_c	Permeability coefficient, ft/sec
P_{im}	Short-term implosion pressure, psi
P_s	Sustained pressure, psi
Q	Total quantity of seawater intake, cu ft
Q_p	Quantity of seawater permeating wall of sphere, cu ft
T	Time, sec, hr, days
t	Wall thickness, ft, in.
W_C	Weight of concrete sphere, lb
W_D	Weight of displaced seawater, lb

DISTRIBUTION LIST

SNDL Code	No. of Activities	Total Copies	
—	1	12	Defense Documentation Center
FKAIC	1	10	Naval Facilities Engineering Command
FKNI	6	6	NAVFAC Engineering Field Divisions
FKN5	9	9	Public Works Centers
FA25	1	1	Public Works Center
—	9	9	RDT&E Liaison Officers at NAVFAC Engineering Field Divisions and Construction Battalion Centers
—	209	209	CEL Special Distribution List No. 11 for persons and activities interested in reports on Ocean Engineering
Bernard Willey (Code 385) * Boston Naval Shipyard Boston, MA 02129			Public Works Officer Naval Security Group Activity Winter Harbor, ME 04693
			Public Works Officer U. S. Naval Facility FPO New York 09552
LCDR David A. Cacchione, USN Office of Naval Research, BROFF 495 Summer Street Boston, MA 02210			Public Works Department Box 400 Naval Submarine Base, New London Groton, CT 06340
			Staff Civil Engineer U. S. Naval Air Station Box 35-D FPO New York 09593
Commanding Officer (Code 200) Navy Public Works Center Naval Base Newport, RI 02840			LCDR T. A. Long, Jr., CEC, USN Naval Submarine Base, New London Groton, CT 06340
			RDT&E Liaison Officer Code 102 Northern Division Naval Facilities Engineering Command Philadelphia, PA 19112
President Naval War College Code 22 Newport, RI 02840			Commanding General U. S. Army Electronics Command Attn AMSEL-GG-TD Fort Monmouth, NJ 07703
			Public Works Officer Naval Facility Lewes, DE 19958
Mr. S. Milligan SB 322 Naval Underwater Systems Center Newport, RI 02844			Engineering Director Code 092 Naval Ammunition Depot, Earle Colts Neck, NJ 07722
			Mr. R. B. Allnutt Code 1706 Naval Ship Research & Dev. Center Bethesda, MD 20034
Commander 21st Naval Construction Regiment Davisville, RI 02854			Plastics Technical Evaluation Center SMUPA-VP3 Picatinny Arsenal Dover, NJ 07801
			Mr. M. A. Krenzke Code 172 - Submarine Division Naval Ship Research & Dev. Center Bethesda, MD 20034
Commanding Officer CBC Technical Library Naval Construction Battalion Center Davisville, RI 02854 (2 copies)			Commanding Officer Amphibious Construction Battalion TWO FPO New York 09501
			William F. Gerhold National Bureau of Standards Corrosion Section Washington, DC 20234
Library U. S. Army Cold Regions Research & Eng. Lab. P. O. Box 282 Hanover, NH 03755			LT Ronald A. Milner, CEC, USN U. S. Naval Station Box 9 FPO New York 09540
			A. Maillar Maritime Administration Office of Ship Construction Washington, DC 20235

* All addressees receive one copy unless otherwise indicated.

Chief of Engineers
U. S. Army
DAEN-MCE-D
Washington, DC 20314

Benj. R. Petrie, Jr.
Op-987T8; Staff, Director RDT&E
Room 4B514, Pentagon
Washington, DC 20350

ENS James F. Morrow, CEC, USN
Office of Comptroller of the Navy
Navy Department
Washington, DC 20350

Commander
Naval Supply Systems Command
Headquarters
SUP 0423
Washington, DC 20360

Technical Library, Ships 2052
Naval Ship Systems Command
National Center No. 3
Washington, DC 20362

Commander
Naval Ship Systems Command
Code 00C
Washington, DC 20362

Chief
Bureau of Medicine & Surgery
Research Department
Navy Department
Washington, DC 20372

U. S. Naval Oceanographic Office
Library - Code 3600
Washington, DC 20373

John DePalma
U. S. Naval Oceanographic Office
Code 9233
Washington, DC 20373

Director
Code 2627
Naval Research Laboratory
Washington, DC 20375

Mr. J. P. Walsh
Naval Research Laboratory
Code 8400
Washington, DC 20375

Mr. J. J. Gennari
Naval Research Laboratory
Code 8410
Washington, DC 20375

Director of Navy Laboratories
Room 300, Crystal Plaza Bldg 5
Department of the Navy
Washington, DC 20376

Commanding Officer
Chesapeake Division - Code 03
Naval Facilities Engineering Command
Washington Navy Yard
Washington, DC 20390

CDR L. K. Donovan, CEC, USN
Chesapeake Division
Naval Facilities Engineering Command
Washington Navy Yard
Washington, DC 20390

Commandant
Naval District Washington
Public Works Department-Code 412
Washington, DC 20390

Naval Security Engineering Facility
Technical Library
3801 Nebraska Avenue, NW
Washington, DC 20390

Commandant (M-2/USP/83)
U. S. Coast Guard
400 SW 7th Street
Washington, DC 20590

Commander
Naval Ship Engineering Center
Code 6136
Prince Georges Center
Hyattsville, MD 20782

Commander
Naval Ship Engineering Center
Code 6162
Prince Georges Center
Hyattsville, MD 20782

Technical Library
Naval Ship Engineering Center
622 Center Bldg
Prince Georges Center
Hyattsville, MD 20782

Mr. John B. Alfors
Naval Ship Engineering Center
Code 6101E
Prince Georges Center
Hyattsville, MD 20782

Chief, Marine & Earth Sciences Library
National Oceanic & Atmospheric Admin.
Dept of Commerce
Rockville, MD 20852

M. E. Ringenbach
Engineering Development Lab (C61)
National Oceanic & Atmospheric Admin.
National Ocean Survey
Rockville, MD 20852

Mr. H. A. Perry
Naval Ordnance Laboratory, White Oak
Silver Spring, MD 20910

LCDR Robert D. Smart, CEC, USN
Naval System Engineering Dept
U. S. Naval Academy
Annapolis, MD 21402

Director
Division of Engineering & Weapons
U. S. Naval Academy
Annapolis, MD 21402

Dr Nell T. Monney
Naval Systems Engineering Dept
U. S. Naval Academy
Annapolis, MD 21402

Mr. D. H. Kallas
Annapolis Laboratory
Naval Ship Research & Dev. Center
Annapolis, MD 21402

Library, Code 5642
Annapolis Laboratory
Naval Ship Research & Dev. Center
Annapolis, MD 21402

Commanding Officer
U. S. Army Mobility Equip. R&D Center
Attn: SMEFB-HPC (Mr. Cevasco)
Fort Belvoir, VA 22060

U.S. Army Coastal Eng. Research Center
Kingman Building
Fort Belvoir, VA 22060

U.S. Army Coastal Eng. Research Center
R.A. Jachowski
Kingman Building
Fort Belvoir, VA 22060

Facilities Officer
Code 108
Office of Naval Research
800 North Quincy Street
Arlington, VA 22217

LCDR G. E. Shank, CEC, USN
Office of Naval Research
Ocean Technology Program
800 North Quincy Street
Arlington, VA 22217

Dr Nicholas Perrone
Code 439
Office of Naval Research
800 North Quincy Street
Arlington, VA 22217

Dr Alexander Malahoff
Code 483
Office of Naval Research
800 North Quincy Street
Arlington, VA 22217

LCDR J.H. Osborn, CEC, USN
Chief of Naval Material (MAT 03414)
c/o Oceanographer of the Navy
200 Stovall Street
Alexandria, VA 22332

Oceanographer of the Navy
Attn: Code N712
200 Stovall Street
Alexandria, VA 22332

CAPT Pharo A. Phelps, CEC, USN
Naval Facilities Engineering Command
200 Stovall Street
Alexandria, VA 22332

Dr. Michael Yachnis
Code 04B
Naval Facilities Engineering Command
200 Stovall Street
Alexandria, VA 22332

CDR G.H. Gans, Jr., CEC, USN
Code 042
Naval Facilities Engineering Command
200 Stovall Street
Alexandria, VA 22332

Commander
Code 0436B
Naval Facilities Engineering Command
200 Stovall Street
Alexandria, VA 22332

CDR Walter J. Eager, CEC, USN
Code PC-2
Naval Facilities Engineering Command
200 Stovall Street
Alexandria, VA 22332

Mr. C.R. Odden
Code PC-2
Naval Facilities Engineering Command
200 Stovall Street
Alexandria, VA 22332

Commanding Officer
Navy Public Works Center
Norfolk, VA 23511

RDT&E Liaison Officer
Code 09P2
Atlantic Division
Naval Facilities Engineering Command
Norfolk, VA 23511 (2 copies)

Staff Civil Engineer
Commander Service Force
U. S. Atlantic Fleet
Norfolk, VA 23511

Director
Amphibious Warfare Board
Naval Amphibious Base, Little Creek
Norfolk, VA 23521

Commandant
U.S. Army Logistics Management Center
Attn: DLSIE
Fort Lee, VA 23801

Public Works Officer
Naval Hospital
Camp Lejeune, NC 28542

RDT&E Liaison Officer
Southern Division - Code 90
Naval Facilities Engineering Command
P. O. Box 10068
Charleston, SC 29411

LCDR G. W. Callender, Jr., CEC, USN
NROTC Unit
Georgia Institute of Technology
Atlanta, GA 30332

Public Works Officer
Naval Coastal Systems Laboratory
Panama City, FL 32401

Mr. R. E. Elliott
Code 710
Naval Coastal Systems Laboratory
Panama City, FL 32401

Library Branch
Army Eng. Waterways Experiment Station
Vicksburg, MS 39180

Army Construction Eng. Research Lab.
ATTN Library
P.O. Box 4005
Champaign, IL 61820

Commanding Officer - Eng. Div.
MRD - Corps of Engineers
Department of the Army
P. O. Box 103, Downtown Station
Omaha, NE 68101

Public Works Officer
Naval Air Station, New Orleans
Belle Chasse, LA 70037

Public Works Officer
Naval Ammunition Depot
McAlester, OK 74501

LT H. S. Stevenson, CEC, USN
Texas A & M University
2304 Truman Street
Bryan, TX 77801

Dr. Arthur R. Laufer
Office of Naval Research, BROFF
1030 East Green Street
Pasadena, CA 91106

Officer in Charge
Pasadena Lab. - Naval Undersea Center
Attn Technical Library
3202 E. Foothill Blvd
Pasadena, CA 91107

Public Works Officer
Marine Corps Base
Camp Pendleton, CA 92055

Mr. H. R. Talkington
Code 65
Naval Undersea Center
San Diego, CA 92132

Dr J. D. Stachiw
Code 6505
Naval Undersea Center
San Diego, CA 92132

Mr. R. E. Jones
Code 65402
Naval Undersea Center
San Diego, CA 92132

Technical Library
Code 1311
Naval Undersea Center
San Diego, CA 92132

Director
San Diego Branch
Western Division
Naval Facilities Engineering Command
San Diego, CA 92132

Public Works Officer
Code 75
Naval Undersea Center
San Diego CA 92132

Public Works Officer
Naval Air Station
North Island
San Diego, CA 92135

Staff Civil Engineer
Naval Station
San Diego, CA 92136

Commanding Officer
Navy Public Works Center
Naval Base
San Diego, CA 92136

Commanding Officer
Naval Missile Center
Code 5632.2, Technical Library
Point Mugu, CA 93042

Office of Patent Counsel
Code PC (Box 40)
Naval Missile Center
Point Mugu, CA 93042

Librarian, Code 9215
Construction Equipment Department
Naval Construction Battalion Center
Port Hueneme, CA 93043

Commanding Officer
Code 155
Naval Construction Battalion Center
Port Hueneme, CA 93043

Technical Library - Code C35
Naval School
Civil Engineer Corps Officers
Bldg 44
Port Hueneme, CA 93043

Commander
31st Naval Construction Regiment
Naval Construction Battalion Center
Port Hueneme, CA 93043 (2 copies)

Commander (Code 753)
Technical Library
Naval Weapons Center
China Lake, CA 93555

Superintendent
Attn Library (Code 2124)
Naval Postgraduate School
Monterey, CA 93940

Dr Edward B. Thornton
Department of Oceanography
Naval Postgraduate School
Monterey, CA 93940

Commanding Officer
Western Division - Code 09PA
Naval Facilities Engineering Command
P. O. Box 727
San Bruno, CA 94066

Commanding Officer
Western Division - Code 04
Naval Facilities Engineering Command
P. O. Box 727
San Bruno, CA 94066

Commanding Officer
Western Division - Code 04B
Naval Facilities Engineering Command
P. O. Box 727
San Bruno, CA 94066

Commanding Officer
Western Division - Code 05
Naval Facilities Engineering Command
P. O. Box 727
San Bruno, CA 94066

Commanding Officer
Western Division - Code 20
Naval Facilities Engineering Command
P. O. Box 727
San Bruno, CA 94066

Public Works Officer
Naval Station
Treasure Island
San Francisco, CA 94130

Asst. Resident OIC of Construction
Bldg 506
Hunters Point Naval Shipyard
San Francisco, CA 94135

Public Works Department (183)
Naval Air Station
Alameda, CA 94501

Supervisor of Salvage
West Coast Representative
4300 Eastshore Highway
Emeryville, CA 94608

Director, Engineering Division
Officer in Charge of Construction
Naval Facilities Engineering Command
Contracts, Southwest Pacific
APO San Francisco 96528

Headquarters
Kwajalein Missile Range
Box 26, Attn SSC-RKL-C
APO San Francisco 96555

Commanding Officer
Mobile Construction Battalion TEN
FPO San Francisco 96601

Operations Officer
Naval Construction Battalions
U. S. Pacific Fleet
FPO San Francisco 96610

Commander
Pacific Division
Naval Facilities Engineering Command
FPO San Francisco 96610

RDT&E Liaison Officer
Pacific Division - Code 403
Naval Facilities Engineering Command
FPO San Francisco 96610

Mr. T. M. Ishibashi
Navy Public Works Center
Engineering Department - Code 200
FPO San Francisco 96610

Public Works Officer
U. S. Naval Station
Box 15
FPO San Francisco 96614

Mr. D. K. Moore
Hawaii Laboratory
Naval Undersea Center
FPO San Francisco 96615

Officer in Charge of Construction
Naval Facilities Engineering Command
Contracts, Marianas
FPO San Francisco 96630

LT G.D. Cullison, CEC, USN
771 Murray Dr.
Honolulu, HI 96818

Engineering Library, Code 202.5
Puget Sound Naval Shipyard
Bremerton, WA 98314

Commanding Officer
U. S. Navy Public Works Center
Box 13
FPO Seattle 98762

Commanding Officer
U.S. Naval Air Facility
Box 15
FPO Seattle 98767

Colleges, etc

Prof. W. E. Heronemus
Civil Engineering Dept
University of Massachusetts
Amherst, MA 01002

MIT Libraries
Technical Reports - Room 14 E-210
Massachusetts Institute of Technology
Cambridge, MA 02139

LCDR James W. Eckert, CEC, USN
NROTC/NAU
Massachusetts, MA 02139

Robert V. Whitman
Room 1-253
Massachusetts Institute of Technology
Cambridge, MA 02139

Mrs. A. P. Richards
Biological Sciences
William F. Clapp Labs - Battelle
Washington Street
Duxbury, MA 02332

Document Library L0-206
Woods Hole Oceanographic Institution
Woods Hole, MA 02543

Pell Marine Science Library
University of Rhode Island
Narragansett Bay Campus
Narragansett, RI 02882

Prof. R. W. Corell
Mechanical Engineering Dept.
Kingsbury Hall
University of New Hampshire
Durham, NH 03824

Kline Science Library
Kline Biology Tower, Room C-8
Yale University
New Haven, CT 06520

M. Schupack
Schupack Associates
300 Broad Street
Stamford, CT 06901

Mr. Willard J. Pierson, Jr.
University Institute of Oceanography
c/o The Bronx Community College
West 181st Street and University Ave.
Bronx, NY 10453

Reprint Custodian
Dept. of Nautical Science
U. S. Merchant Marine Academy
Kings Point, NY 11024

Dept of Civil Engineering
State University of New York
At Buffalo
Buffalo, NY 14214

Mr. R. F. Snyder
Ordnance Research Laboratory
Pennsylvania State University
State College, PA 16801

Mr. William H. Gotolski
Pennsylvania State University
212 Sackett Bldg
University Park, PA 16802

Professor Adrian F. Richards
Marine Geotechnical Laboratory
Lehigh University
Bethlehem, PA 18015

Associate Librarian
Mart Science & Engineering Library
Lehigh University
15 E. Packer Avenue
Bethlehem, PA 18015

Dr Hsuan Yeh
Towne School of Civil & Mechanical Eng.
University of Pennsylvania
Philadelphia, PA 19104

Professor E. Chesson
132 DuPont Hall
Newark, DE 19711

Professor Raymond R. Fox
Nuclear Defense Design Center
School of Engineering & Applied Science
The George Washington University
Washington, DC 20006

T. W. Mermel
4540 43rd Street, NW
Washington, DC 20016

Library of Congress
Science & Technology Division
Washington, DC 20540

Research Library
Chesapeake Bay Institute
The John Hopkins University
Macauley Hall
Baltimore, MD 21218

W. F. Searle, Jr.
National Academy of Engineering
808 Timber Branch Parkway
Alexandria, VA 22302

Public Documents Department
Wm. R. Perkins Library
Duke University
Durham, NC 27706

Dr Aleksandar S. V. sic
Department of Civil Engineering
Duke University
Durham, NC 27706

Dr Bruce Muga
Dept of Civil Engineering
Duke University
Durham, NC 27706

Dr Wm F. Brumund
School of Civil Engineering
Georgia Institute of Technology
Atlanta, GA 30332

Professor J. P. Hartman
Dept of Civil Eng. & Environ. Sciences
Florida Technological University
Orlando, FL 32816

Dr Charles E. Lane
Institute of Marine Science
University of Miami
Coral Gables, FL 33146

Dr R. F. McAllister
Professor of Oceanography
Florida Atlantic University
Boca Raton, FL 33432

C. R. Stephan
Florida Atlantic University
Department of Oceanography
Boca Raton, FL 33432

Lorenz G. Straub Memorial Library
St Anthony Falls Hydraulic Laboratory
Mississippi River at 3rd Ave. SE
Minneapolis, MN 55414

Dr R. C. Jordan
Dept of Mechanical Engineering
University of Minnesota
Minneapolis, MN 55455

Library
Portland Cement Association
Research & Development Laboratories
5420 Old Orchard Road
Skokie, IL 60076

Dr N. M. Newmark
1114 Civil Engineering Bldg
University of Illinois
Urbana, IL 61801

Professor W. J. Hall
1108 Civil Engineering Bldg
University of Illinois
Urbana, IL 61801

Dr M. T. Davisson
2217 Civil Engineering Bldg
University of Illinois
Urbana, IL 61801

Metz Reference Room
Civil Engineering Dept
B106 Civil Engineering Bldg
University of Illinois
Urbana, IL 61801

Acquisition Dept - Serials Section
University of Nebraska Libraries
Lincoln, NE 68508

Robert D. Tent
Undersea Services Division
Fluor Ocean Services Inc
P. O. Drawer 310
Houma, LA 70360

Department of Oceanography
Texas A & M University
College Station, TX 77843

Civil Engineering Dept
Texas A & M University
College Station, TX 77843

R. C. Dehart
Southwest Research Institute
8500 Culebra Road
San Antonio, TX 78228

Director
Institute of Marine Science
The University of Texas
Port Aransas, TX 78373

Professor M. M. Ayoub
Dept of IE
Texas Technological University
Lubbock, TX 79409

Dr Bernard C. Abbott
Allan Hancock Foundation
University of Southern California
Los Angeles, CA 90007

Director
Catalina Marine Science Center
University of Southern California
Los Angeles, CA 90007

Aerospace Corporation
Acquisitions Group
P. O. Box 92957
Los Angeles, CA 90009

Dr Young C. Kim
Dept of Civil Engineering
Calif. State University, Los Angeles
Los Angeles, CA 90032

TRW Systems
Attn P. L. Dai R1/2178
1 Space Park
Redondo Beach, CA 90278

Mr. C. C. Mow
The Rand Corporation
1700 Main Street
Santa Monica, CA 90401

Dr. Armas Laupa
The Rand Corporation
1700 Main Street
Santa Monica, CA 90406

Robert Q. Palmer
P.O. Box 7707
Long Beach, CA 90807

Dr C. V. Chelapati
Calif. State University, Long Beach
Long Beach, CA 90840

Keck Reference Room (107-78)
136 W. M. Keck Laboratory
Calif. Institute of Technology
Pasadena, CA 91109

Oceanic Library & Info. Center
P. O. Box 2369
La Jolla, CA 92037

Dr John F. Peel Brahtz
P. O. Box 825
La Jolla, CA 92037

Mr. F. Simpson
Lockheed Ocean Laboratory
3380 No. Harbor Blvd
San Diego, CA 92101

Dr F. N. Spiess
Marine Physical Laboratory of the
Scripps Institution of Oceanography
University of California
San Diego, CA 92152

Dr Victor C. Anderson
Marine Physical Laboratory of the
Scripps Institution of Oceanography
University of California
San Diego, CA 92152

J. Padilla
866 Concord Ave
Ventura, CA 93003

Manager Ocean Systems, MVJG
Lockheed Missiles & Space Co
P. O. Box 504
Sunnyvale, CA 94088

Engineering Library
Stanford University Libraries
Stanford, CA 94305

Mr. Richard G. Luthy
615 Madison Street
Albany, CA 94706

Dept of Naval Architecture
College of Engineering
University of California
Berkeley, CA 94720

Engineering Library
University of California
Berkeley, CA 94720

Michael A. Taylor
Civil Engineering Dept
College of Engineering
University of California, Davis
Davis, CA 95616

Director
Calif. Dept of Navigation & Ocean Dev.
1416 9th Street
Sacramento, CA 95814

Assoc. Professor R. A. Grace
University of Hawaii
Honolulu, HI 96822

LT G. D. Cullison, CEC, USN
771 Murray Dr.
Honolulu, HI 96818

School of Oceanography
Oregon State University
Corvallis, OR 97331

Dr S. R. Murphy
University of Washington
Seattle, WA 98195

Information Officer
United Kingdom Scientific Mission
British Embassy
3100 Massachusetts Ave, NW
Washington, DC

Mrs. Ragna Adolfsson, Librarian
Cement- och Betonginstitutet
Fack 100 44 Stockholm 70
Sweden

Literature Exchange
Cement and Concrete Association
Wexham Springs
SLOUGH SL3 6PL
Bucks, England

Additions

Mr. Austin Kovacs
U.S. Army
Cold Regions Research & Eng. Lab.
P. O. Box 282
Hanover, NH 03755

Mr. John Quirk
Code 710
Naval Coastal Systems Lab.
Panama City, FL 32401

Public Works Dept.
Puget Sound Naval Shipyard
Bremerton, WA 98314

Mr. John R. Saroyan
1320 Carl Avenue
Vallejo, CA 94590

Dr. M. D. Ashton
United Kingdom Scientific Mission
British Embassy
3100 Massachusetts Avenue, NW
Washington, DC 20008

Dr. A. H. Mattock
Department of Civil Engineering
University of Washington
Seattle, WA 98105

Meyer Steinberg
Nuclear Engineering Department
Brookhaven National Laboratory
Upton, NY 11973

Mr. J. H. Walker
Portland Cement Association
Research & Development Laboratories
5420 Old Orchard Road
Skokie, IL 60076

Mr. George Schick
Scripps Institution of Oceanography
University of California
La Jolla, CA 92038

Mr. James Snodgrass
Scripps Institute of Oceanography
University of California
La Jolla, CA 92038

Mr. Sorkin
Naval Ship Systems Command
Code 03421
Washington, DC 20362

Mr. Freund
Naval Ship Systems Command
Washington, DC 20362

George J. Peroni
985 NW 95th Street
Miami, FL 33125

Morris Schupack
Schupack & Associates
2701 Summer Street
Stamford, CT 06905

Mr. Will Foreman
Code 55 204
Naval Weapons Center
China Lake, CA 93555

Wne F. Chang
Department of Civil Engineering
University of Miami
Coral Gables, FL 33124

Adam Whitley III
SEAFERRO Inc.
3701 NW South River Drive
Miami, FL 33142

R. S. Schmid
Marine Development
Bechtel Corporation
50 Beale Street
San Francisco, CA 94111

Walter H. Price
American Cement Technical Center
P.O. Box 832
Riverside, CA 92502

Ben C. Gerwick, Jr.
Civil Engineering Department
University of California, Berkeley
Berkeley, CA 94720

Ralph Warrington
Shell Oil
P.O. Box 127
Metairie, LA 70004

Joseph F. Rynewicz
Lockheed Missile & Space Company
Depart 57-26
Bldg 150
Sunnyvale, CA 94086

Sid Beckowich
Bechtel Incorporated
50 Beale Street
San Francisco, CA 94111

James H. Jennison
Pasadena Laboratory
Naval Undersea Center
3202 E. Foothill Blvd.
Pasadena, CA 91107

CAPT E. B. Mitchell, USN
Code OOC
Naval Ship Systems Command
Washington, DC 20362

Dr. Glen Berg
Department of Civil Engineering
University of Michigan
Ann Arbor, MI 48104

Dr. Lynn Beedle
Department of Civil Engineering
Lehigh University
Bethlehem, PA 18015

Mr. Richard Thless
Undersea Habitat Designers
87 Harris Road
Katonah, NY 10536

Mr. William Gates
Conrad Associates
14656 Oxnard Street
Van Nuys, CA 91401

Dr. J. D. Stachiw
Ocean Technology Department
Code 65
Naval Undersea Center
San Diego, CA 92132

Dr. Bryan Williams
Nuclear Branch
Gulf Radiation Technology
P.O. Box 608
San Diego, CA 92112

Mr. Larry Kahn
2143 Medford Road #2
Ann Arbor, MI 48104

Terrance J. Dahl
Oceanographic Services Inc.
5375 Overpass Road
Santa Barbara, CA 93105

Dr. R. C. Denart
Southwest Research Institute
San Antonio, TX 78205

Joseph J. Carroll
Jaycon Engineers, Inc.
P.O. Box 26656
Houston, TX 77032

Dr. Rudolph Szilard
University of Hawaii
2565 The Mall
Honolulu, HI 96822

CAPT Jack Adams
Director of Public Services-Engineering
Department
City of Cerritos
19400 S. Pioneer Blvd.
Cerritos, CA 90701

Dr. Sidney J. Green
Manager, Applied Mechanics
Terra Tek, Inc.
915 East 4th South
Salt Lake City, UT 94102

E. V. Wright
Dravo Corp.
4800 Grant Avenue
Pittsburgh, PA 15225

Bob Oversmith
Scripps Institute of Oceanography
La Jolla, CA 92037

Dr. Gene Corely
Manager, Structural Section
Portland Cement Association
5420 Old Orchard Road
Skokie, IL 60076

Claude Sellars, Jr.
Shell Development Corporation
3747 Bellaire Blvd.
Houston, TX 77025

Dr. Henning Ottsen (FPO-1)
Chesapeake Division
Naval Facilities Engineering
Command
Washington Navy Yard
Washington, DC 20390

Professor D. Pritz
Civil Engineering Department
University of California, Berkeley
Berkeley, CA 94720

Karl Runge
ESSO Products Research Corp.
P.O. Box 2189
Houston, TX 77001

Boris Bresler
777 Davis Hall
University of California, Berkeley
Berkeley, CA 94720

Robert Cohen
G. E.-RESO
Ocean Systems Program
3198 Chestnut Street
Philadelphia, PA 19101

Loris Gerber
The Prescon Corporation
P.O. Box 2723
Corpus Christi, TX 78403

Paul Lavoie
Engineering Design & Analysis
Laboratory
Kingsbury Hall
University of New Hampshire
Durham, NH 03824

Arvid Grant
Arvid Grant & Associates
1600 E. 4th Avenue
Olympia, WA 98506

Nils D. Olsson
The Prescon Corporation
8E Pennsylvania Avenue
Towson, MD 21128

H. Joe Meheen
Meheen Engineering Company
6464 W. 14th Avenue
Denver, CO 80214

J. Preston Mason
ESSO Production Research Company
Box 2189
Houston, TX 77001

Ron Nordgren
Shell Development Company
P.O. Box 481
Houston, TX 77001

D. M. Roy
The Pennsylvania State University
Materials Research Laboratory
University Park, PA 16802

Dr. Arthur Anderson
Concrete Technology Corporation
Port of Tacoma Road
Tacoma, WA 98421

James R. Lloyd
ESSO Production Research Company
P.O. Box 2189
Houston, TX 77001

S. Clifford Doughty
Construction Engineering Service
843 Crossway Road
Burlingame, CA 94010

Hugh Aiken
Marine Concrete Structures, Inc.
P.O. 607
Metairie, LA 70004

John S. Hollett
Global Marine Development Inc.
5959 West Century Blvd.
Los Angeles, CA 90045

C. M. Wakeman
26803 Basswood Avenue
Palos Verdes Peninsula, CA 90274

A. S. Crandon, Jr.
Dravo Corporation
Eastern Construction Division
4800 Grant Avenue
Pittsburgh, PA 15225

H. Georgi, President
AB HYDROBETONG
Fack 100 52
Stockholm 29, Sweden

Arnfinn Jenssen, Captain
Norwegian Defense Construction Service
Oslo-MIL
Oslo 1, Norway

John H. Creed
Royal Norwegian Council for
Scientific & Industrial Research
Ellingsrudveien 23C
1400 Ski, Norway

Anton Brandtzaeg
Professor of Construction & Harbour
Engineering
Norwegian Technical University
Trondheim, Norway

Dr. J. Dejong
Lockheed Petroleum Services Ltd.
1 Grosvenor Square
New Westminster, B.C., Canada

Dr. R. D. Browne
Head of Materials Research
Laboratory
Taylor Woodrow Construction
Limited
345 Ruislip Road
Southall, Middlesex, England

Napoleon DeMeyer
HAECON
Marathonstraat 12
9000 Gent
Belgium

Frøde Hansen
Harris & Sutherland
38 Whitfield Street
London W1
United Kingdom

Franco Levi
Corso Massimo d'Azeglio 100
10126 Torino
Italy

Kurt Eriksson
VBB
Box 5038
10241 Stockholm
Sweden

Roger LaCroix
56 Fauborg Saint-Honore
75008 Paris
France

Rowland G. Morgan
Department of Civil Engineering
University of Bristol
Bristol BS6 6SX
United Kingdom

Odd E. Gjorv
Department of Civil Engineering
Technical University of Norway
7034 Trondheim
Norway

J. G. Bodhe
24-26 Dalal Street
Fort, Bombay
India

B. H. Spratt
Cement & Concrete Association
Wexham Springs
Slough SL3 6P1
United Kingdom

P. S. Hafskjold
Ing. F. Selmer AS
Post Office Box 256
Oslo, Norway

John D. Holst
Elkem-Spigerverk
Post Office Box 4224
Oslo 4, Norway

M. D. Haxwell
Sir Robert McAlpine & Sons, Ltd.
40 Bernard Street
London WC1
United Kingdom

K.V. Swaminathan
Principal Scientist, Cement
Research Institute of India
M-10 South Extension II
Ring Road
New Delhi 49, India

K. H. Brittain
Chief Technical Consultant-Blue
Circle Group
Cement Marketing Company Ltd.
Portland House, Stag Place
London SW1, United Kingdom

Hans Richard Hansen
DET NORSKE VERITAS
Division of Marine Technology
P.O. Box 6060
Etterstud, Oslo 6, Norway

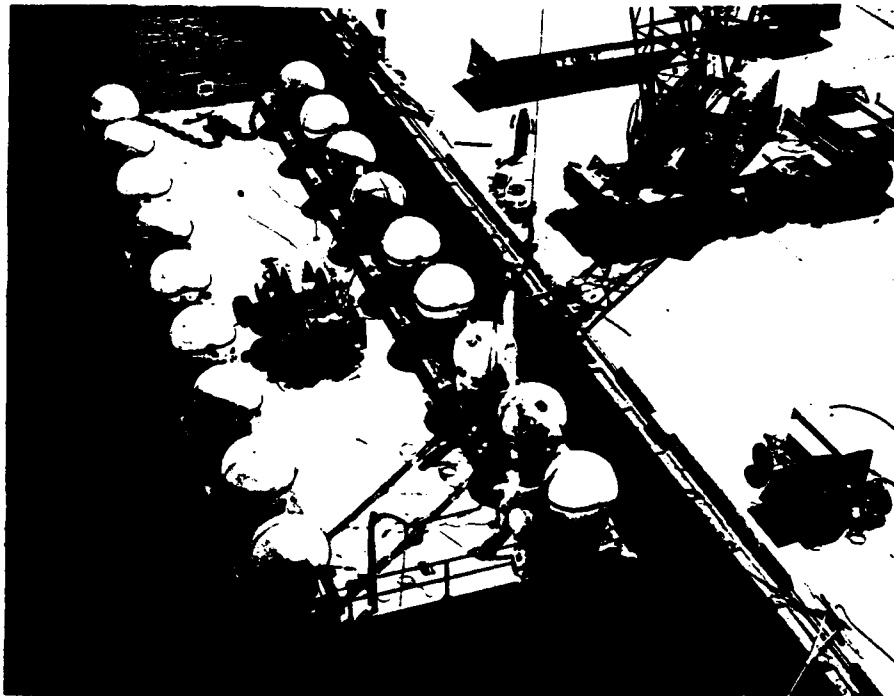
Mr. Knut Hove
DET NORSKE VERITAS
Division of Marine Technology
P.O. Box 6060
Etterstud, Oslo 6, Norway

S. B. Stubbs
Taylor, Woodrow Construction Ltd
345 Ruislip Road
Southall
Middlesex, England

Pierre Launay
Europe-Etudes
66 Route de la Reine
92 Boulegne-Bellancourt

Dr. Munther Haddadin
Royal Scientific Society
Amman, Jordan

<p>Civil Engineering Laboratory LONG-TERM DEEP-OCEAN TEST OF CONCRETE SPHERICAL STRUCTURES. Part I. Fabrication, Emplacement, and Initial Inspections, by Harvey H. Haynes TR-805 43 p. illus March 1974 Unclassified</p> <p>1. Submerged concrete structures 2. Seawater permeability of concrete 1. DOT 3.1610</p> <p>This report summarizes the fabrication, emplacement and inspections during the first 1.2 years of submergence of eighteen 66-inch-OD concrete spheres. The spheres are located 4 miles south of Santa Cruz Island, California, in depths of water from 1,840 to 5,075 feet. The purpose of the test is to collect data on time-dependent failure, permeability and durability of concrete pressure-resistant structures. Findings from the inspections showed that two spheres located at the depths of 3,725 and 4,330 feet had imploded and that the quantity of seawater which permeated through the concrete for phenolic-coated spheres was about 0.8 cu ft and for uncoated spheres it was about 1.6 cu ft. This test program is planned to continue through 1981 (total of 10 years).</p>	<p>Civil Engineering Laboratory LONG-TERM DEEP-OCEAN TEST OF CONCRETE SPHERICAL STRUCTURES. Part I. Fabrication, Emplacement, and Initial Inspections, by Harvey H. Haynes TR-805 43 p. illus March 1974 Unclassified</p> <p>1. Submerged concrete structures 2. Seawater permeability of concrete 1. DOT 3.1610</p> <p>This report summarizes the fabrication, emplacement and inspections during the first 1.2 years of submergence of eighteen 66-inch-OD concrete spheres. The spheres are located 4 miles south of Santa Cruz Island, California, in depths of water from 1,840 to 5,075 feet. The purpose of the test is to collect data on time-dependent failure, permeability and durability of concrete pressure-resistant structures. Findings from the inspections showed that two spheres located at the depths of 3,725 and 4,330 feet had imploded and that the quantity of seawater which permeated through the concrete for phenolic-coated spheres was about 0.8 cu ft and for uncoated spheres it was about 1.6 cu ft. This test program is planned to continue through 1981 (total of 10 years).</p>
<p>Civil Engineering Laboratory LONG-TERM DEEP-OCEAN TEST OF CONCRETE SPHERICAL STRUCTURES. Part I. Fabrication, Emplacement, and Initial Inspections, by Harvey H. Haynes TR-805 43 p. illus March 1974 Unclassified</p> <p>1. Submerged concrete structures 2. Seawater permeability of concrete 1. DOT 3.1610</p> <p>This report summarizes the fabrication, emplacement and inspections during the first 1.2 years of submergence of eighteen 66-inch-OD concrete spheres. The spheres are located 4 miles south of Santa Cruz Island, California, in depths of water from 1,840 to 5,075 feet. The purpose of the test is to collect data on time-dependent failure, permeability and durability of concrete pressure-resistant structures. Findings from the inspections showed that two spheres located at the depths of 3,725 and 4,330 feet had imploded and that the quantity of seawater which permeated through the concrete for phenolic-coated spheres was about 0.8 cu ft and for uncoated spheres it was about 1.6 cu ft. This test program is planned to continue through 1981 (total of 10 years).</p>	<p>Civil Engineering Laboratory LONG-TERM DEEP-OCEAN TEST OF CONCRETE SPHERICAL STRUCTURES. Part I. Fabrication, Emplacement, and Initial Inspections, by Harvey H. Haynes TR-805 43 p. illus March 1974 Unclassified</p> <p>1. Submerged concrete structures 2. Seawater permeability of concrete 1. DOT 3.1610</p> <p>This report summarizes the fabrication, emplacement and inspections during the first 1.2 years of submergence of eighteen 66-inch-OD concrete spheres. The spheres are located 4 miles south of Santa Cruz Island, California, in depths of water from 1,840 to 5,075 feet. The purpose of the test is to collect data on time-dependent failure, permeability and durability of concrete pressure-resistant structures. Findings from the inspections showed that two spheres located at the depths of 3,725 and 4,330 feet had imploded and that the quantity of seawater which permeated through the concrete for phenolic-coated spheres was about 0.8 cu ft and for uncoated spheres it was about 1.6 cu ft. This test program is planned to continue through 1981 (total of 10 years).</p>



R869



TECHNICAL REPORT CIVIL ENGINEERING LABORATORY

Naval Construction Battalion Center, Port Hueneme, California 93043

**LONG-TERM, DEEP-OCEAN TEST OF CONCRETE
SPHERICAL STRUCTURES – Results After 6 Years**

By Harvey H. Haynes and Roy S. Highberg

January 1979

Sponsored by
NAVAL FACILITIES ENGINEERING COMMAND

Approved for public release; distribution unlimited.

Unclassified

SECURITY CLASSIFICATION OF THIS PAGE (When Data Entered)

REPORT DOCUMENTATION PAGE		READ INSTRUCTIONS BEFORE COMPLETING FORM
1. REPORT NUMBER TR-869	2. GOVT ACCESSION NO. DN044053	3. RECIPIENT'S CATALOG NUMBER
4. TITLE (and Subtitle) LONG-TERM, DEEP-OCEAN TEST OF CONCRETE SPHERICAL STRUCTURES - Results After 6 Years		5. TYPE OF REPORT & PERIOD COVERED Not final; Jul 1971 - Mar 1978
		6. PERFORMING ORG. REPORT NUMBER
7. AUTHOR(s) Harvey H. Haynes and Roy S. Highberg		8. CONTRACT OR GRANT NUMBER(s)
9. PERFORMING ORGANIZATION NAME AND ADDRESS Civil Engineering Laboratory Naval Construction Battalion Center Port Hueneme, California 93043		10. PROGRAM ELEMENT PROJECT, TASK AREA & WORK UNIT NUMBERS 63713N, S0397, S0397-SL, 3.1610-1
11. CONTROLLING OFFICE NAME AND ADDRESS Naval Facilities Engineering Command Alexandria, Virginia 22332		12. REPORT DATE January 1979
		13. NUMBER OF PAGES 51
14. MONITORING AGENCY NAME & ADDRESS (if different from Controlling Office)		15. SECURITY CLASS. (of this report) Unclassified
		15a. DECLASSIFICATION DOWNGRADING SCHEDULE
16. DISTRIBUTION STATEMENT (of this Report) Approved for public release; distribution unlimited.		
17. DISTRIBUTION STATEMENT (of the abstract entered in Block 20, if different from Report)		
18. SUPPLEMENTARY NOTES		
19. KEY WORDS (Continue on reverse side if necessary and identify by block number) Concrete structures, pressure-resistant structures, concrete spheres, permeability, implosion, submerged concrete structures, undersea structures, long-term loading, unreinforced concrete.		
20. ABSTRACT (Continue on reverse side if necessary and identify by block number) In 1971, a long-term, deep-ocean test was started on eighteen concrete spheres, 66 inches (1,676 mm) in outside diameter by 4.12 inches (105 mm) in wall thickness. The spheres were placed in the ocean at depths from 1,840 to 5,075 feet (560 to 1,547 m). Over a 6.4-year period, yearly inspections of the spheres by submersibles have provided data on time-dependent failure and permeability. After 5.3 years, three of the spheres were continued		

DD FORM 1473 1 JAN 73 EDITION OF 1 NOV 65 IS OBSOLETE

Unclassified

SECURITY CLASSIFICATION OF THIS PAGE (When Data Entered)

Unclassified

SECURITY CLASSIFICATION OF THIS PAGE(When Data Entered)

20. Continued

retrieved from the ocean for laboratory testing. Data on concrete compressive strength gain, short-term implosion strength of the three retrieved spheres, and permeability and durability of the concrete were obtained. This report summarizes the findings from the laboratory and ocean tests.

Library Card

Civil Engineering Laboratory
LONG-TERM, DEEP-OCEAN TEST OF CONCRETE
SPHERICAL STRUCTURES - Results After 6 Years, by
Harvey H. Haynes and Roy S. Highberg
TR-869 51 pp illus January 1979 Unclassified

1. Undersea concrete structures 2. Concrete spheres 1. 3.1610-1

In 1971, a long-term, deep-ocean test was started on eighteen concrete spheres, 66 inches (1,676 mm) in outside diameter by 4.12 inches (105 mm) in wall thickness. The spheres were placed in the ocean at depths from 1,840 to 5,075 feet (560 to 1,547 m). Over a 6.4-year period, yearly inspections of the spheres by submersibles have provided data on time-dependent failure and permeability. After 5.3 years, three of the spheres were retrieved from the ocean for laboratory testing. Data on concrete compressive strength gain, short-term implosion strength of the three retrieved spheres, and permeability and durability of the concrete were obtained. This report summarizes the findings from the laboratory and ocean tests.

Unclassified

SECURITY CLASSIFICATION OF THIS PAGE(When Data Entered)

CONTENTS

	page
INTRODUCTION	1
BACKGROUND.	1
INSPECTION AND RETRIEVAL	2
RESULTS AND DISCUSSION	8
Concrete Strength Gain	8
Short-Term Loading of Spheres	15
Long-Term Loading of Spheres	26
Permeability	30
Durability	32
FINDINGS	33
SUMMARY.	34
ACKNOWLEDGMENTS	34
REFERENCES	34
APPENDICES	
A - Effect of Drilling Cores on Compressive Strength	37
B - Early Compressive Strength Data of Spheres.	39
C - Moisture Content of Concrete Samples	41
D - Cement Paste Samples Placed in the Ocean	45
E - Microstructure Examination of Concrete	47

INTRODUCTION

In September 1971, a test program was started on concrete spherical structures placed in the deep ocean for long-term testing. This report is the second in a series documenting the study; presented are the test results of the spheres after 6.4 years in the ocean. The first report (Ref 1) covered the fabrication, ocean emplacement, and inspections up to 1.3 years. Details of the test program and the specimens are given in Reference 1.

The technical objectives of the program are to obtain data on time-dependent failure, permeability, and durability of the concrete spherical structures. These data can provide a technology base from which engineering guidelines could be written. Another important aspect of the program was to expose the spheres to real environmental conditions. The test results will aid considerably in establishing confidence and credibility for concrete as a deep-ocean construction material.

BACKGROUND

Eighteen concrete spheres 66 inches (1676 mm) in outside diameter and 4.12 inches (105 mm) in wall thickness were placed in the ocean at depths varying from 1,840 to 5,075 feet (560 to 1,547 m). Sixteen of the spheres were unreinforced concrete, eight of which were coated on the exterior with a phenolic compound to act as a waterproofing agent; the other eight spheres were left

uncoated. The remaining two spheres were lightly reinforced with 0.5-inch (13-mm) diameter steel bars. The reinforcing bars had a concrete cover of 1 and 2.5 inches (25 and 63 mm). Half of the exterior of each of these spheres was coated with the waterproofing agent. The reinforced spheres were to determine whether corrosion problems exist in the deep ocean environment.

The depth range for the spheres corresponds to relative load levels of from 0.36 to 0.83. The relative load level, P_s/P_{im}^P , is defined as the ratio of sustained pressure to predicted short-term implosion pressure.

Time-dependent failure was expected for six of the spheres subjected to the highest load levels; therefore, those spheres were equipped with clock mechanisms to record the day of implosion. If other specimens were to implode, the yearly inspections would discover the failed specimens.

Permeability data were gathered during inspections. The spheres, which were approximately 1,000 pounds (450 kg) buoyant, were tethered 30 feet (10 m) off the seafloor by a 2.25-inch (57-mm) diameter chain. As seawater was absorbed by and permeated through the concrete, the sphere weight increased. The reduced buoyancy of the sphere meant that less chain was suspended off the seafloor. Therefore, change of one chain link corresponded to 0.50 cu ft (14 liters) of seawater being taken on by the sphere.

The concrete mix design was Type II Portland cement, a water-to-cement ratio of 0.41, a sand-to-cement ratio of

1.85, and a coarse-aggregate-to-cement ratio of 2.28. The maximum size aggregate used was 3/4 inch (19 mm).

INSPECTION AND RETRIEVAL

The operations to inspect and retrieve the spheres were conducted by submersibles. The Navy's deep-diving manned submersibles Turtle and Seacraft, operated by the Submarine Development Group One, were used in all but one operation; Scripps Institution of Oceanography used their Remote Underwater Manipulator (RUM) to conduct an inspection in 1972. The last inspection occurred in March 1978.

During each operation, only a limited number of spheres were inspected. Those checked depended on the number of dive days scheduled for the submersible and on weather conditions, which could restrict the actual number of dives. Hence, some spheres have been inspected more frequently than others (Figure 1). Sphere no. 6 has not been inspected as yet. Table 1 summarizes the data obtained during the inspections.

Spheres no. 15 and 17 show chain link counts (the number of links suspended off the seafloor) that increased with time in the ocean. This increase in chain link count was due to inaccuracies in counting links. Turbidity sometimes obscured the links near the seafloor, making it difficult for the submersible operators to get an accurate count. Also, the submersible operators were changed with each dive, which caused variations in the data collection procedure. More reliable data have been obtained during recent inspections because chain link counts were sometimes taken two and three times as a check.

During the sixth inspection in January 1977, Spheres No. 11, 12, and 13 were recovered after 5.3 years in the ocean. Two of the spheres had a waterproof coating and were retrieved from depths of 2,635 and 3,140 feet (803 and 957 m). The other sphere was uncoated and was retrieved from a depth of 2,790 feet (851 m).

The submersible Seacraft made a separate dive to retrieve each sphere. A reel containing 6,000 feet (2,000 m) of 1/2-inch (13-mm) nylon line was attached to the front end of the submersible. A large steel hook was connected on the end of the line. Using a manipulator, the Seacraft attached the hook to the Sphere's tether chain and then payed-out the line as it surfaced. At the water surface, the line was buoyed with a marker. The CEL warping tug was then employed to reel in the line and recover the sphere (Figure 2). Each sphere was subsequently wrapped in wet burlap and plastic sheet to prevent it from drying out.

A surface inspection of the spheres revealed tube worms and a grass-like animal growth on the coated spheres as well as a few small anemones and a grouping of small scallops. The concrete surfaces, whether coated or uncoated, had considerably less grass-like growth than the steel chains (Figure 3). Figures 4 and 5 show a close-up view of the exteriors for a coated and uncoated sphere.

These spheres were subsequently tested in the laboratory where they provided data on the actual quantity of water permeating to the inside of the spheres, the short-term implosion pressure and strain behavior of preloaded spheres, and the chemical compounds present in the concrete.

Table 1. Sphere Inspection Data

Sphere No.	Exterior Surface	Emplacement Depth (ft)	No. of Chain Links Off Seafloor at Start of Test ^a	Inspection No. 1 (Mar 1972, 163 days)		Inspection No. 2 (Aug 1972, 340 days)		Inspection No. 3 (Dec 1972, 431 days)		Inspection No. 4 (Nov 1973, 776 days)		Inspection No. 5 (Oct 1974, 1,120 days)	
				No. of Chain Links Off Seafloor	Permeated Water ^b (ft ³)	No. of Chain Links Off Seafloor	Permeated Water (ft ³)	No. of Chain Links Off Seafloor	Permeated Water (ft ³)	No. of Chain Links Off Seafloor	Permeated Water (ft ³)	No. of Chain Links Off Seafloor	Permeated Water (ft ³)
1	Coated	5,075	29.7										
2	Coated	4,875	29.7										
3	Coated	4,330	29.4			Imploded						Imploded	No count*
4	Uncoated	4,185	29.4			23	0.99					No count*	
5	Uncoated	4,100	29.6			21	2.06					No count*	
6	Uncoated	3,875	29.6										
7	Coated	3,725	31.5										
8	Coated	3,665	31.5					Imploded Intact, but on bottom* Chain tangled*					
9	Uncoated	3,295	31.6										
10	Uncoated	3,190	31.6					24	1.58	24	1.58		
11	Coated	3,140	34 ^c					31	0	31	0		
12	Uncoated	2,790	31.7 ^d					24	1.63	24.5	1.38	24.5	1.38
13	Coated	2,635	32.1					29	0	29	0	29	0
14	Coated	2,440	43 ^c	39	0			39	0	38.5	0	38.25	0
15	Uncoated	2,300	32.2	26	0.89			25	1.38	25.5	1.14	25.75	1.14
16	Uncoated	2,120	31.8	26	0.70			25	1.19	25	1.19	24	1.19
17	Half-coated	1,980	32.6	29	0			28	0			29	0
18	Half-coated	1,840	32.6					25	1.28				

^aOriginal number of links off seafloor calculated from known weights of components.

^bBased on 3% by weight absorption to saturate the concrete.

^cNew chain count based on retrieved sphere data.

^dExtra shackle found on retrieved chain which changed number of links from Reference 1.

^eActual quantity of permeated water was 1.24 ft³.

Table 1. Sphere Inspection Data

Inspection No. 2 (Days)	Inspection No. 3 (Dec 1972, 431 days)		Inspection No. 4 (Nov 1973, 776 days)		Inspection No. 5 (Oct 1974, 1,120 days)		Inspection No. 6 (Jan 1977, 1,945 days)		Inspection No. 7 (Mar 1978, 2,355 days)		Comments
	No. of Chain Links Off Seafloor	Permeated Water (ft ³)	No. of Chain Links Off Seafloor	Permeated Water (ft ³)	No. of Chain Links Off Seafloor	Permeated Water (ft ³)	No. of Chain Links Off Seafloor	Permeated Water (ft ³)	No. of Chain Links Off Seafloor	Permeated Water (ft ³)	
27					Imploded No count*		27	0			*Sphere intact
14 18					No count* No count*		14 18	5.38 3.53			*Sphere intact *Sphere intact Not inspected to date
Intact	Imploded Intact, but on bottom* Chain tangled*						Intact				*Sphere flooded, probably from leak *Chain tangled; could not count links
23 30.5	24 31	1.58 0	24 31	1.58 0			23 30.5*	2.06 0			*Retrieved during Inspection No. 6
24.5	24	1.63	24.5	1.38	24.5	1.38	24.5*	1.38			*Retrieved during Inspection No. 6 ^c
29	29	0	29	0	29	0	29*	0			*Retrieved during Inspection No. 6
38 25	39 25	0 1.38	38.5 25.5	0 1.14	38.25 25.75	0 1.02	38 25	0 1.38	25.75	1.02	
23	25 28	1.19 0	25	1.19	24 29	1.67 0	23	2.16 0	22 29	2.64 0	
21	25	1.28					21	2.91			

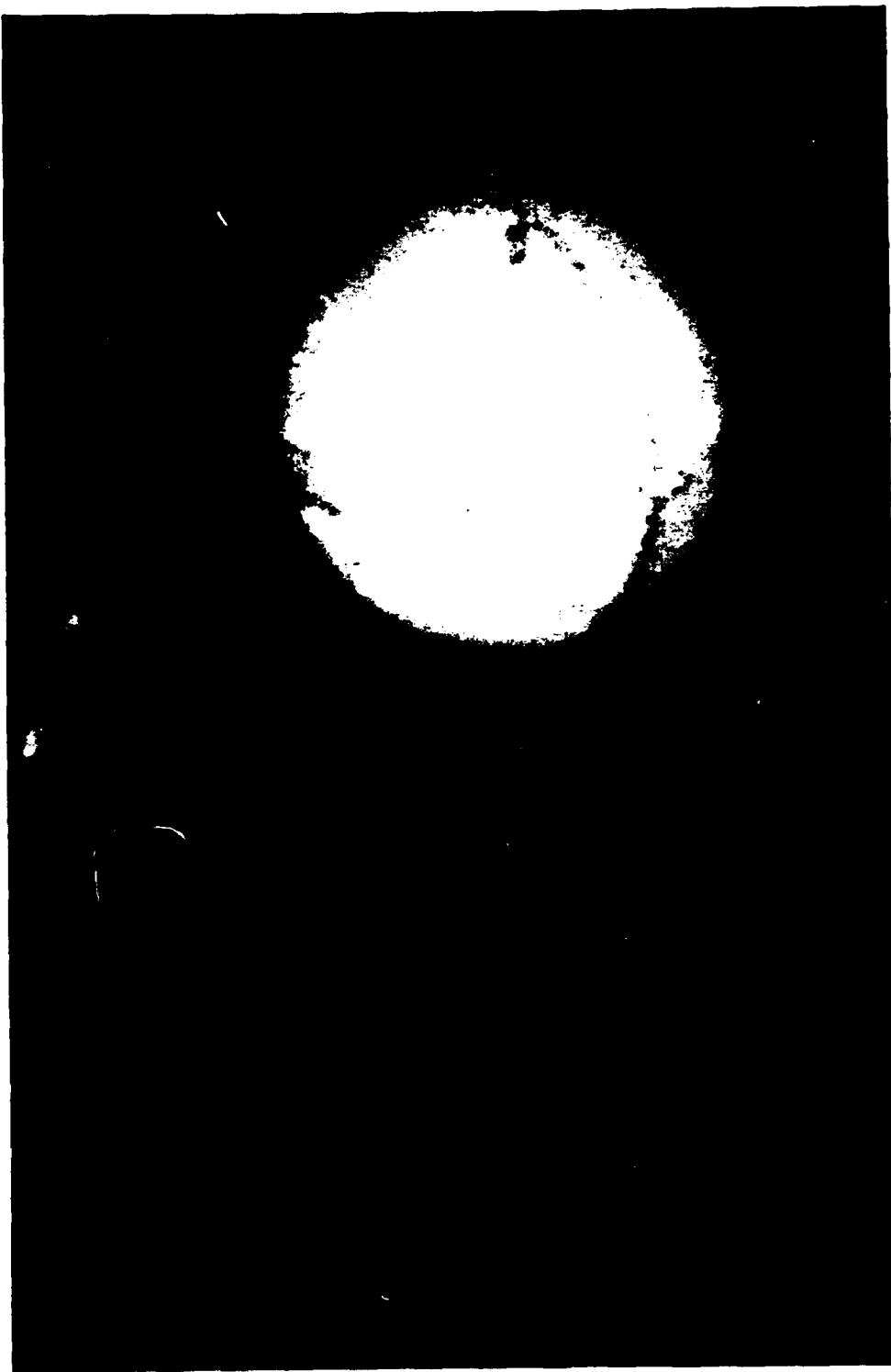


Figure 1. Sphere no. 12 shown after 1 year in the ocean at 2,790 feet (850 m).

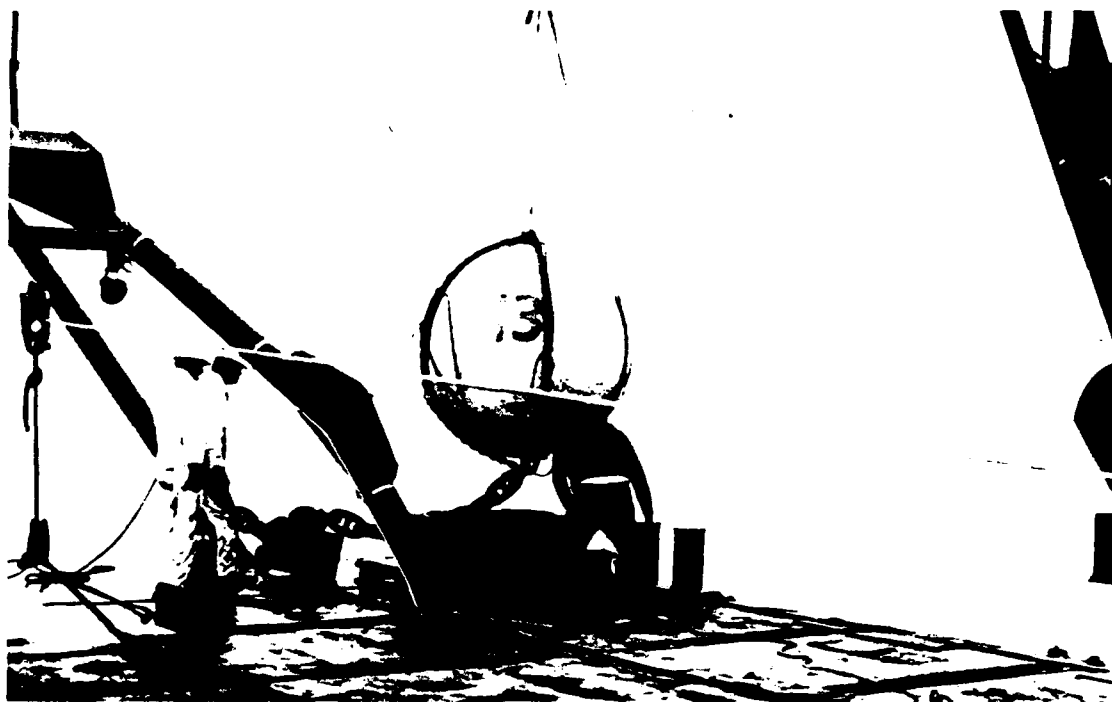


Figure 2. Sphere no. 13 retrieved from depth of 2,635 feet (803 m).



Figure 3. Uncoated concrete block had considerably less grass-like growth than the steel chain.



Figure 4. Sphere no. 13 was a coated sphere, which made the grass-like growth more visible. A technician is collecting scallop samples.

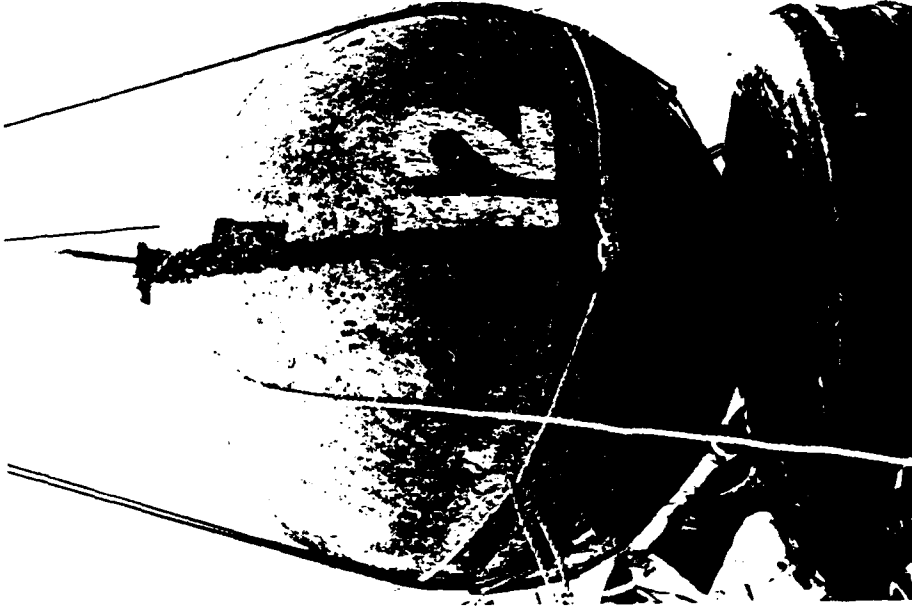


Figure 5. Sphere no. 12 was an uncoated sphere, which made the tubeworms more visible. The grass-like growth is visible on the white numerals.

RESULTS AND DISCUSSION

Concrete Strength Gain

The compressive strength of concrete after curing in the ocean for 1.3 and 5.3 years was obtained from uncoated concrete blocks that were attached to the chain of the spheres (Figure 3). The block size was 14 x 18 x 18 inches (356 x 457 x 457 mm), from which four 6 x 12-inch (152 x 305-mm) cores were drilled. The uniaxial compressive strength of the cores was compared to that of 6 x 12-inch (152 x 305-mm) cast cylinders made from the same batch of concrete and cured under continuous fog room conditions. The strength was also compared to that of on-land cured concrete blocks located about 150 feet (50 m) from the shoreline. These blocks were the same size as those in the ocean, and test specimens were cored from the blocks. The compressive strength results are presented in Table 2.

A strength differential has been observed to occur between cast and cored specimens of the same concrete due to the effect of drilling. The compressive strength of the core specimens in this study was increased by 7% so that it would be equivalent to that of the cast specimens. (Past data supporting the strength adjustment are given in Appendix A). Table 2 presents both the measured strength of the core specimens and the adjusted strength. The following analysis of strength data is based on the adjusted strengths.

The compressive strength gain of concrete in the different curing environments is presented graphically in Figures 6 through 9. Relative strengths are shown where the common denominator is the 28-day fog-cured strength. This strength had a nominal value of 8,000 psi (55 MPa). Reference 1 did not give the coefficients of variation of the

compressive strengths for spheres at 28 days and at the time of emplacement; these data are now given in Appendix B. At 5.6 years of age, the continuously fog-cured concrete showed a relative strength of 1.35 (coefficient of variation was 5.2%). The on-land field-cured concrete showed a relative strength of 1.32 (coefficient of variation was 8.0%), and the ocean-cured concrete a relative strength of 1.15 (coefficient of variation was 9.5%).

The data from the on-land field-cured concrete are interesting but difficult to discuss because the concrete's actual moisture content varied with time. The compressive strength of dry concrete is greater than that of equivalent wet concrete by an average of 20% (Ref 2, 3). The degree of dryness, i.e., the relative humidity of the environment with which concrete is in equilibrium, also influences the compressive strength. For our case, the equilibrium relative humidity was not known. At 5.6 years, spring was starting after a drought year. However, because of the proximity of the concrete blocks to the ocean, the environmental relative humidity was high (100%) most evenings.

Samples were dried in an oven to obtain an indication of how much absorbed water the on-land concrete had in comparison to the fog- and ocean-cured concrete. These data are given in Appendix C. As expected, the on-land concrete contained less moisture than either the fog-cured or ocean-cured concrete. It is likely that if the on-land concrete were soaked in water for several days prior to uniaxial testing, the compressive strength would have decreased. The amount of the decreases would have been an estimated 5 to 15%.

Figure 10 shows a constructed relationship between relative strength and total age for the fog- and ocean-cured concrete. The strength gain

behavior for the fog-cured concrete is consistent with existing knowledge. However, the strength gain behavior for the ocean-cured concrete is unusual and needs discussion.

When a mass of concrete the size of a control cylinder is placed in the ocean under high hydrostatic pressure, water fills the larger size voids within a period of several days. The smaller size voids become filled over a much longer time period. For example, 6 x 12-inch (152 x 305-mm) cylinders under a pressure head of 550 feet (168 m) were still absorbing water after 84 days (Ref 4). Saturated concrete, that is, concrete whose voids are mostly filled with water, has been found previously to have a strength reduction of 10% compared to companion unsaturated concrete. This strength reduction was observed from two different types of tests: (1) specimens were exposed to a pressure head of 1,125 feet (343 m) for 7 days and then tested under uniaxial compression in a laboratory environment (Ref 1, 5); and (2) specimens were placed under a pressure head of 20,000 feet (6,096 m) for 60 days and then loaded axially while in the hydrostatic environment (if the concrete was totally saturated, which was the assumed condition, then this test was a uniaxial compression test) (Ref 4). The cause of these strength reductions was most likely from pore pressure buildup. During uniaxial loading, the water pressure in some of the pores rose slightly, thereby placing an additional component of tensile strain within the specimen that reduced the tensile strength in the radial direction and, consequently, reduced the compressive strength in the axial direction.

In Figure 10, when concrete specimens were placed in the ocean, a decrease in strength of about 10% occurred. At 1.6 years, ocean-cured concrete showed a compressive strength that was still less than the 28-day fog-cured strength. Two alternative paths

are shown in estimating the relationship between the time the concrete was placed in the ocean and 1.6 years. For the lower path, which intersects the datum point at 1.6 years, the initial strength reduction when placed in the ocean had to be greater than 10%. The higher path assumes that the data at time 0.25 years to be accurate and those at 1.6 years to be a "low" result. The data at 1.6 years are from one concrete block, producing four cores with a coefficient of variation of 4.0%.

At 5.6 years, the cement was completely hydrated for both the fog-cured and ocean-cured concrete as determined from x-ray diffraction analysis of the concrete. Hence, the rate of strength gain of the concrete, or the slope of the curve, should be zero. However, strength changes could be occurring due to other chemical composition changes.

Also, at 5.6 years, the ocean-cured concrete showed a compressive strength 15% less than that of the fog-cured concrete. This strength reduction had to be due to a different reason than saturation effect because at this advanced age, both the fog- and ocean-cured concretes are known to be saturated (Ref 4). Therefore, the cause for the lower strength of the ocean-cured concrete as compared to the fog-cured concrete can be speculated as mainly due to the presence of seawater. Magnesium ions in seawater replace some of the calcium ions in calcium silicate hydrate (tobermorite gel). This causes the formation of magnesium silicate hydrate, which is more brittle than calcium silicate hydrate (Ref 6). Specimens of pure cement paste are required in order to determine the presence of magnesium silicate hydrate with a scanning electron microscope. Hence, these concrete samples could not be tested for magnesium silicate hydrate. Appendix D presents an extension to the sphere program which will provide data so that the phenomenon of magnesium ions replacing calcium ions can be studied.

Table 2. Compressive Strength Test Results

Parameter	Concrete Used in Sphere										Average
	No. 3		No. 11		No. 12		No. 13		No. 1		
	W-15 ^a	W-16	W-24	W-21	W-32	W-29	W-26	W-23	W-4	W-35	
Compressive Strength, f'_c (psi)											
Fog cure ^b											
28-day	8,520 (1.5%) ^d	8,400 (1.9%)	7,540 (3.8%)	7,720 (2.7%)	7,570 (0.6%)	7,240 (3.0%)	8,070 (4.5%)	7,640 (2.0%)	8,520 (0.1%)	8,070 (2.1%)	—
Total age											
1.3 yr	10,470 (3.9%)	10,360 (1.5%)	10,960 (3.3%)	10,710 (2.1%)	10,210 (4.2%)	10,160 (2.8%)	10,950 (3.2%)	10,220 (9.6%)	10,410 (3.6%)	10,430 (2.4%)	—
5.6 yr											—
On-land field cure ^c											
1.3 yr (includes 28-day fog cure)	9,260 (8,650) ^e (3.7%)										—
5.6 yr (includes 28-day fog cure)				9,200 (8,600) (2.0%)		10,370 (9,690) (2.9%)		9,760 (9,120) (1.0%)		11,090 (10,360) (3.1%)	—
Ocean cure ^c											
1.3 yr (includes fog cure, on-land field cure, and 341 days submerged)		8,130 (7,600) (4.0%)									—
5.6 yr (includes fog cure, on-land field cure, and 1,950 days submerged)			8,320 (7,780) (3.9%)		9,960 (9,310) (1.9%)		9,060 (8,470) (0.4%)		9,150 (8,550) (1.9%)		—

continued

Table 2. Continued

Parameter	Concrete Used in Sphere										Average
	No. 3		No. 11		No. 12		No. 13		No. 1		
	W-15 ^a	W-16	W-24	W-21	W-32	W-29	W-26	W-23	W-4	W-35	
	Relative Strength										
Total-Age fog cure/28-day fog cure											
1.3 yr	1.229	1.233		1.387	1.349	1.403	1.357	1.338	1.222	1.292	1.350 (5.2%)
5.6 yr											
On-land cure/28-day fog cure											
1.3 yr	1.087			1.192		1.432		1.277		1.374	1.319 (8.0%)
5.6 yr											
Ocean cure/28-day fog cure											
1.3 yr		0.968	1.103		1.316			1.123	1.074		1.154 (9.5%)
5.6 yr											

^aHemisphere section identification.^bAverage of three 6 x 12-inch (152 x 305-mm) cast cylinders.^cAverage of four 6 x 12-inch (152 x 305-mm) core specimens.^dCoefficient of variation.^eUnadjusted core strength with coefficient of variation.

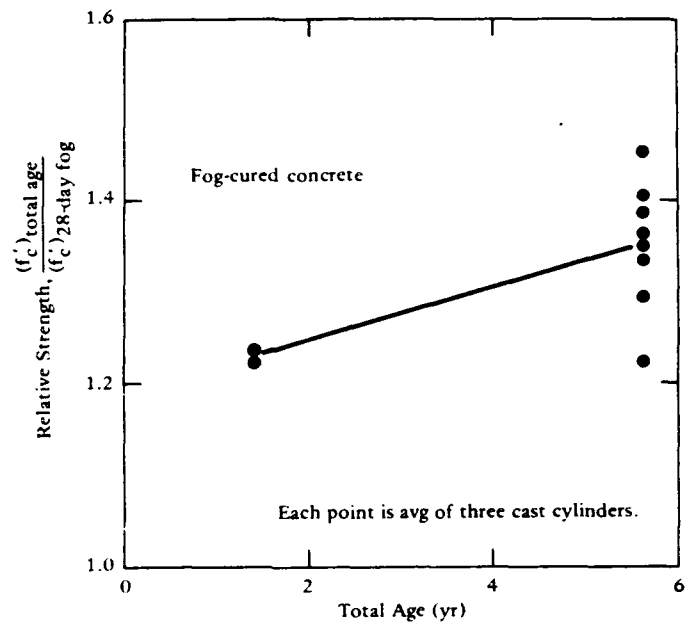


Figure 6. Compressive strength gain of concrete exposed to continuous fog curing.

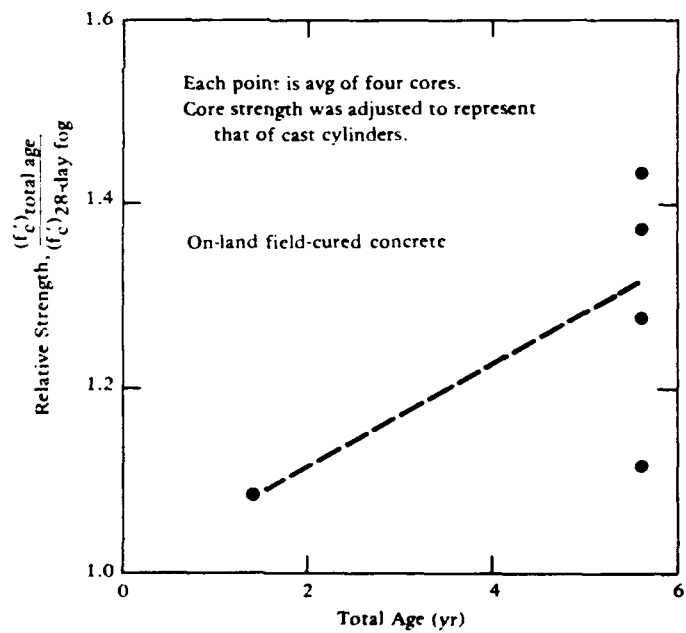


Figure 7. Compressive strength gain of concrete exposed to on-land field curing after initial 28-day fog curing. Location was about 150 feet from ocean.

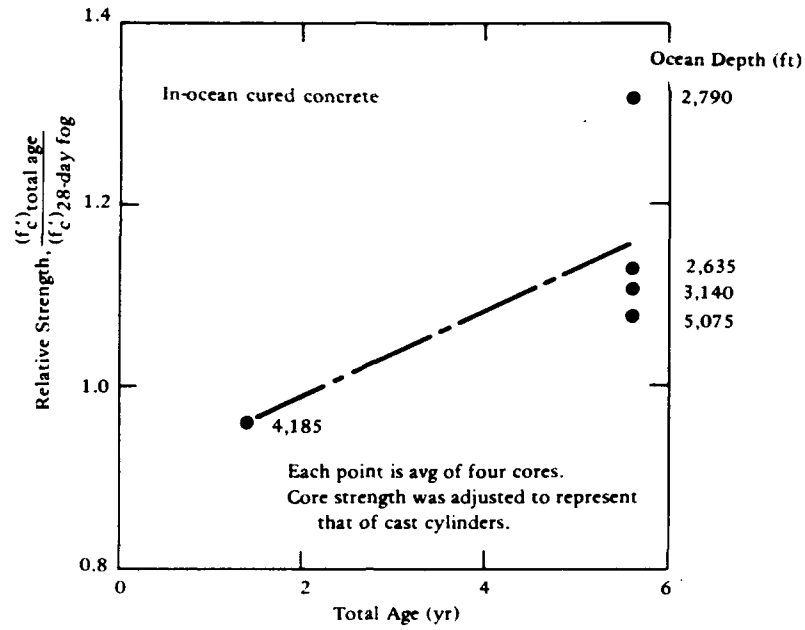


Figure 8. Compressive strength gain of concrete exposed to ocean curing conditions after initial 28-day fog cure and 2 to 5 months of on-land curing.

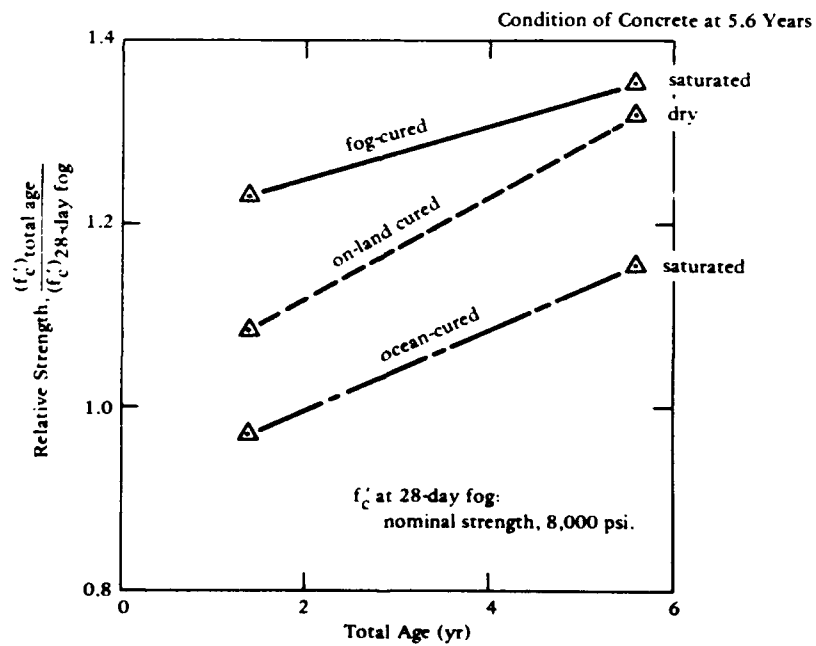


Figure 9. Compressive strength gain of concrete in different environments.

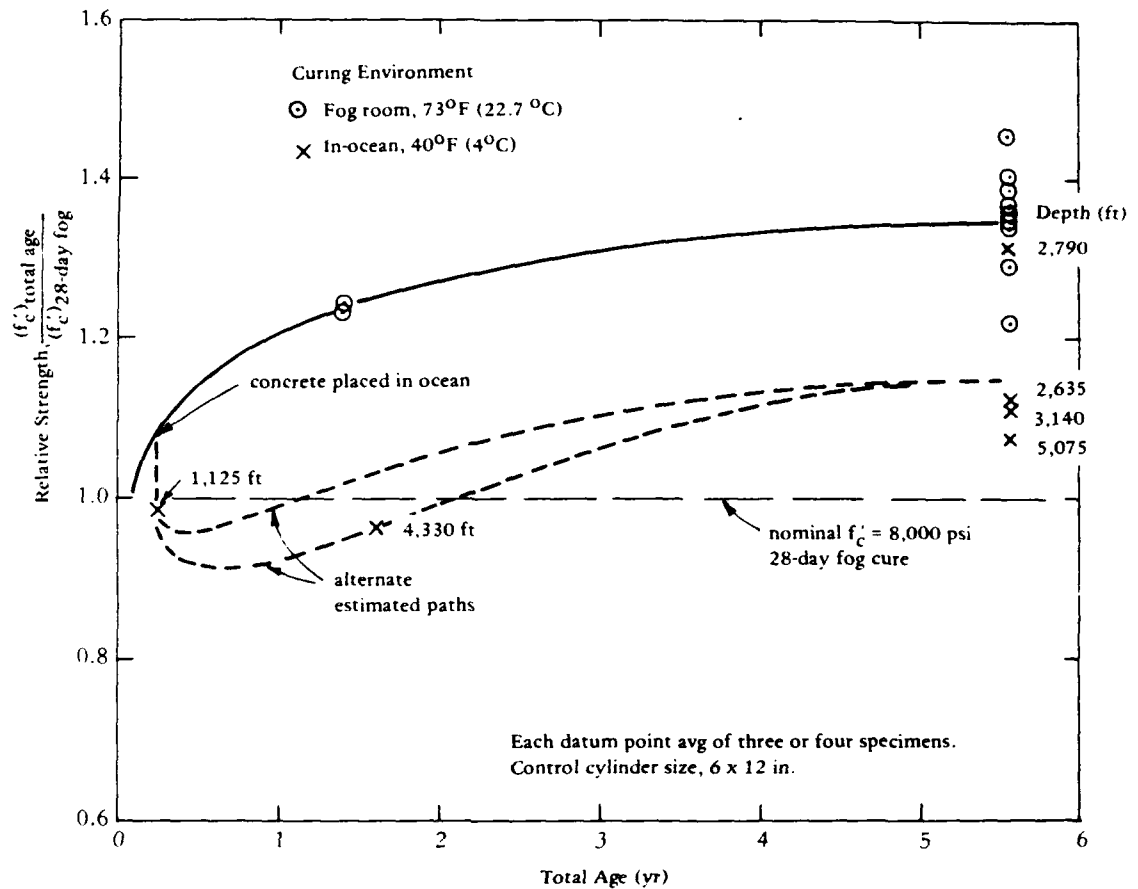


Figure 10. Relative compressive strength of fog-cured and ocean-cured concrete.

It can also be speculated that the cold temperature environment of the ocean had a small effect on retarding full development of strength gain. The ocean temperature was 40F (4C), whereas the fog room environment was 73F (22.8C). Discussion of the long-term effect of a continuous 40F (4C) curing environment was not found in the literature. Lorman (Ref 7) gave limited test results on concrete that set and cured under seawater at 47F (8.3C) compared

to that in a 73F (22.8C) fog environment. After 28 days, the concrete in the cold environment showed a compressive strength that was approximately 10% less than the control concrete.

The important findings from the data are: (1) the ocean-cured concrete required 1 to 2 years in the ocean before regaining a strength equal to its 28-day fog strength; and (2) within the time period of up to 5.3 years, the strength of the concrete in the ocean was 15 to 20% less than that of continuously fog-cured concrete.

These findings raise a question as to the applicability of "concrete strength increases with age" as generally accepted (Ref 8). Massive offshore structures are typically fabricated in a seawater environment. If saturation is considered to occur, then the following interim guide can be used for strength gain with age. The initial 28-day fog-cured strength should be reduced by 10% to account for saturation effects. Subsequent in-situ strength increases with time may depend on the depth at which the concrete is located. Depth is important because it can influence the degree of saturation. At present, data are available at depths of a few thousand feet. For this case, the strength increase relative to the 28-day fog-cured strength appears to be nil at 1 year, 5% at 2 years, and 15% at 5 years.

For cases where the concrete is at a depth of a few hundred feet, it is hard to estimate the strength gain behavior. First, it is unknown how much of the wall thickness will become saturated. It could take months for several feet of thickness to become saturated. If the interior of the structure were to be at a relative humidity of less than 100%, the concrete would never become saturated. However, some of the concrete would be saturated near the outside wall, and that portion would exhibit a strength different from that not saturated. As a guide, the compressive strength should be reduced by 10% to account for saturation effects; then it is probably reasonable to permit a strength increase of 10% at 6 months and 15% at 12 months. These values are conservative from the on-land increase factors of 20% at 6 months, and 24% at 12 months.

Numerous cylinders, both cast and cored, were instrumented with strain gages to determine the elastic modulus and Poisson's ratio of the concrete. Table 3 summarizes the data, and Figures 11 through 14 show the stress-

strain curves. The behavior of cored cylinders is presented as raw data, i.e., it has not been adjusted for drilling effect. The concretes were all linear up to about $0.5 f'_c$. The elastic modulus of ocean-cured concrete was 30% less than that of the continuously fog-cured concrete. Although the elastic modulus was not determined for fog-cured concrete at the age of 28 days, it is reasonable to assume, based on data from similar concrete (Ref 5), that the elastic modulus of the ocean-cured concrete did not change significantly from that of the 28-day fog-cured specimens.

Short-Term Loading of Spheres

Implosion. The three spheres retrieved from the ocean were returned to the Laboratory for short-term loading tests. These tests were conducted in a pressure vessel where the external hydrostatic pressure was increased steadily until implosion.

While in the ocean, these spheres were subjected to a sustained load of about 50% their short-term ultimate strength for a period of 5.3 years. In previous work (Ref 5) identical specimens were tested under short-term loading where the specimens were not exposed to the long-term preloading. Table 4 shows the results from both types of short-term tests, with and without preload. Table 5 summarizes the results.

For the uncoated spheres, the preloaded sphere showed a decrease in implosion strength of about 8% compared to that of the non-preloaded spheres. The compressive strength of the saturated concrete was fairly well-defined for these tests. For the coated spheres, the preloaded spheres showed an increase in implosion strength of about 5% compared to that of the non-preloaded spheres. The actual increase

Table 3. Elastic Moduli and Poisson's Ratio Data

[Test specimen size was 6 x 12 inches (152 x 305 mm)]

Type of Specimen	Total Age	Main Curing Environment	Type of Cylinders	No. of Specimens	Elastic Modulus, E (psi x 10 ⁶)	Poisson's Ratio, ν
Fog-cured	5.6 yr	100% RH; 73°F	cast	24	5.33	0.21
Ocean-cured	5.6 yr (includes initial 28 days in fog room and then 2 to 5 mo of on-land field curing 150 ft from shoreline)	ocean depth, 2,400 to 3,200 ft; 40°F	core	15	3.77 ^a	0.24
On-land	5.6 yr (includes initial 28 days in fog room)	150 ft from shoreline	core	16	4.21 ^a	0.22
	90 days (includes initial 28 days in fog room)	400 ft from shoreline in a building	cast	2	4.12	—

^aElastic modulus determined from unadjusted core data.

in implosion strength may have been greater than the reported 5% due to not defining as accurately the compressive strength for the preloaded spheres as for the other cases. The coated spheres from the ocean had relatively dry concrete. To obtain a compressive strength of dry concrete, the on-land concrete blocks were used. The evaporable moisture content of the on-land blocks was 2.7% by weight, which was less than the 3.5% by weight moisture content for the coated sphere wall (Appendix B). Hence, the compressive strength listed in Table 4 for Spheres no. 11 and 13 may be a little greater than the actual strength of the concrete in the sphere wall. If this potential error was corrected, the effect would be to increase the P_{im}/f'_C ratio for the coated preloaded spheres.

Table 5 shows that for non-preloaded spheres the dry concrete specimens had an implosion strength only

slightly greater than that for the saturated concrete specimens. However, for the preloaded spheres, the dry concrete specimens were at least 14% stronger than the saturated concrete specimens. This difference in strength will be discussed in the next section.

The implosion data are limited. When the implosion strengths of dry and saturated preloaded specimens ($P_{im}/f'_C = 0.299$) were averaged and compared to those of the non-preloaded spheres ($P_{im}/f'_C = 0.304$), it was found that the overall effect of preloading the spheres to a stress level of about 50% their ultimate strength for 5.3 years was quite small.

Views of the imploded spheres are shown in Figures 15 through 18. The visual damage, in terms of fragmentation, is rather mild in comparison to non-preloaded specimens and, in particular, to specimens that have imploded in the

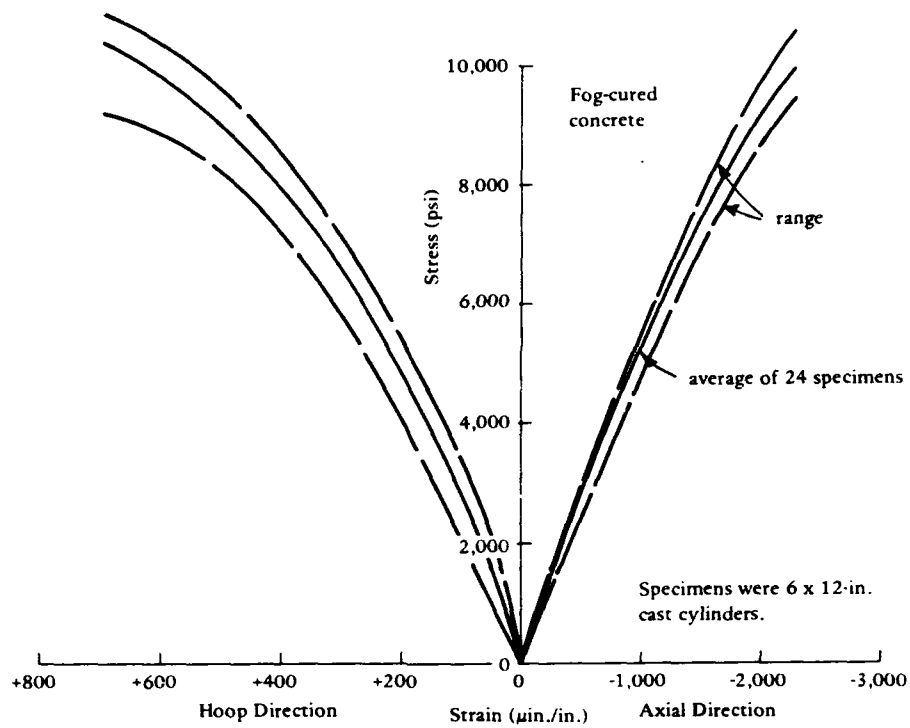


Figure 11. Uniaxial compressive tests of continuously fog-cured concrete for 5.6 years.

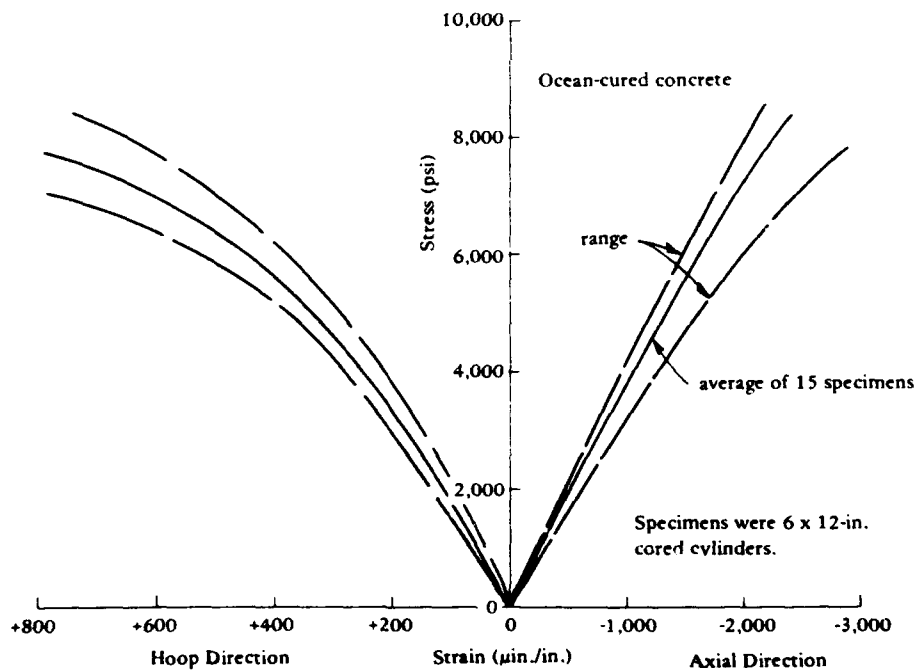


Figure 12. Uniaxial compressive tests of ocean-cured concrete for 5.6 years.

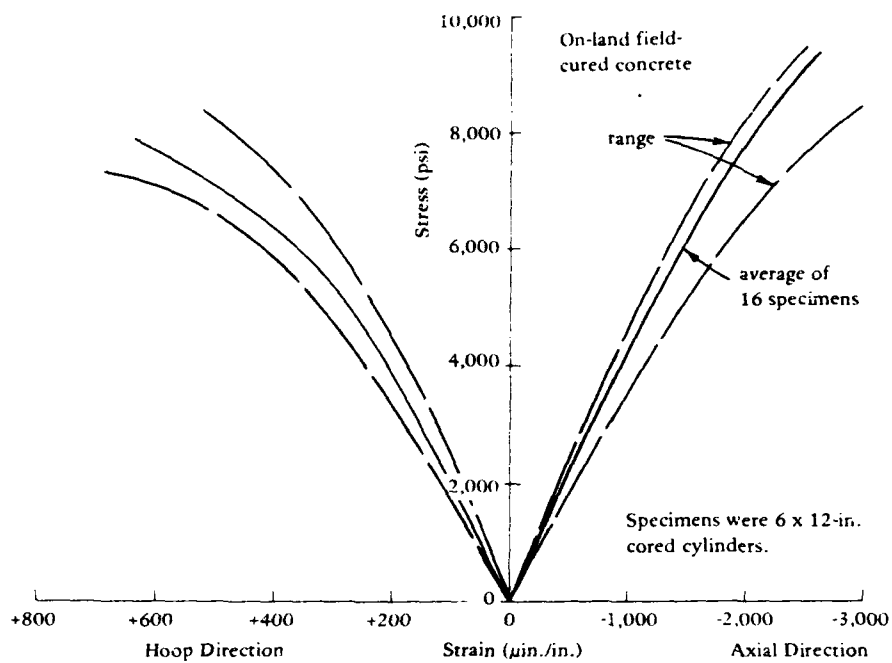


Figure 13. Uniaxial compressive tests of on-land field-cured concrete for 5.6 years.

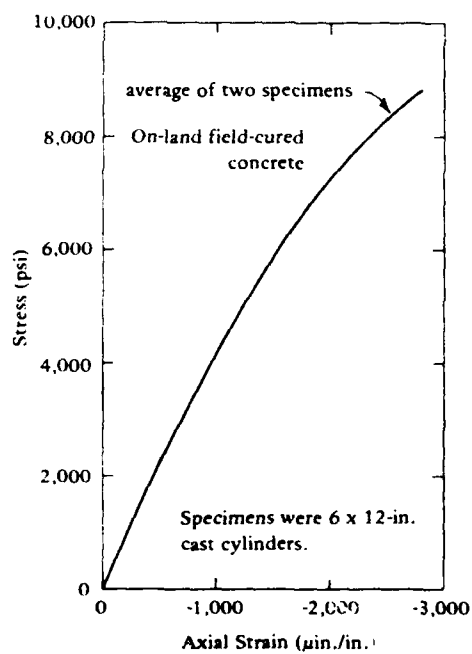


Figure 14. Uniaxial compressive tests of on-land field-cured concrete for 90 days (from Ref 5).

Table 4. Short-Term Loading Results of Concrete Spheres

Description	Sphere Designation	Concrete Condition ^a	Preload Pressure (psi)	Uniaxial Compressive Strength, f'_c (psi)	Implosion Pressure, P_{im} (psi)	Ratio, $\frac{P_{im}}{f'_c}$	Elastic Modulus of Sphere Wall, E (psi $\times 10^6$)
Spheres preloaded in the ocean for 5.3 yr	11	dry	1,400	9,200 ^b	2,970	0.323	5.05
	12	saturated	1,245	9,960 ^c	2,750	0.276	5.20
	13	dry	1,175	9,760 ^b	3,115	0.319	5.05
Non-preloaded spheres (after Reference 5)	CDS-1	dry	0	9,250	2,860	0.309	4.64
	CDS-2	dry	0	9,120	2,755	0.302	4.14
	CWS-3	saturated	0	7,960	2,500	0.314	—
	CWS-4	saturated	0	7,660	2,205	0.288	4.29

^aDry concrete corresponds to coated spheres, and saturated concrete corresponds to uncoated spheres.

^b6 x 12-inch (152 x 305-mm) cylinders cored from on-land field-cured concrete blocks prepared from concrete used in spheres.

^c6 x 12-inch (152 x 305-mm) cylinders cored from the ocean-cured concrete block attached to Sphere No. 12.

Table 5. Summary of Short-Term^a Loading Results

Spheres	Implosion Pressure to Compressive Strength Ratio, P_{im}/f'_c , for Spheres	
	Coated (dry concrete)	Uncoated (saturated concrete)
Preloaded ^b	0.321	0.276
Non-Preloaded (after Ref 5)	0.306	0.301

^aSpheres tested in a pressure vessel.

^bIn the ocean for 5.3 yr.

ocean. The zones of failure for Spheres no. 11 and 12 (Figures 15 and 16) appeared to be from crushing of concrete and were more localized than for the non-preloaded spheres. Sphere no. 13 showed a failure zone (Figures 17 and 18) that was more typical of the non-preloaded spheres. A shear-compression-type failure mode for a section of wall was evident for about 50 inches (130 mm) in length.

The spheres that imploded in the ocean were found totally fragmented. In a pressure vessel, once failure of a sphere began, the pressure load dropped off rapidly. This did not occur in the ocean, and, hence, a sphere was subjected to extremely violent shock forces when the water collapsed the walls. Figure 19 shows the debris on the seafloor for Sphere no. 1 that imploded at a depth of 5,075 feet (1,547 m).

Strain Behavior. Strain behavior for the spheres tested in the pressure vessel was monitored by measuring the quantity of water displaced from the interior of the sphere while under load.* A change of interior volume is a direct function of the change in radius, and the change in radius is a direct function of hoop strain. The displaced water was measured to an accuracy of ± 10 ml, which converted to a strain accuracy of ± 2 in./in. This is applicable only when membrane displacements account for most of the change in volume. Near failure, displacements due to flat-spot development can contribute significantly to the displaced water.

Figure 20 shows the raw data of pressure versus displaced water for the spheres. Other scales show the wall

stress and strains. A similar presentation of results is given in Figure 21 for the non-preloaded spheres (after Ref 5). The dry concrete spheres were able to withstand about 20% more ultimate strain than the saturated spheres before imploding.

It was quite apparent from the data that saturated concrete behaved differently than dry concrete. However, at this time, data do not exist on the stress-strain behavior of concrete control cylinders that are saturated and uniaxially loaded while in a hydrostatic pressure environment. This sphere test program (Figures 20 and 21) provides the first data that show saturated concrete under hydrostatic pressure does not perform as well as similar dry concrete.

Table 4 lists the stiffness, or elastic modulus, for the walls of the spheres. The average modulus value for the three ocean spheres was 5.1×10^6 psi (35.2 GPa); for the non-preloaded spheres, it was 4.4×10^6 psi (30.3 GPa). This difference was due to the effect of the preload and is a well-known effect of concrete creep (Ref 8). For 5.3 years the concrete in the ocean spheres experienced creep under a wall stress of about 5,000 psi.

Concrete creep and a triaxial loading condition explains why the modulus of 5.1×10^6 psi (35.2 GPa) for the wall of the preloaded sphere was greater than that given in Table 3 for the ocean-cured concrete block, where the modulus was 3.77×10^6 psi (26.0 GPa). The concrete block in the ocean was not stressed like the sphere wall; it was saturated with seawater and in a state of equilibrium with the environment.

*This technique was used in Reference 5 with excellent results; the same procedures were applied in these tests.

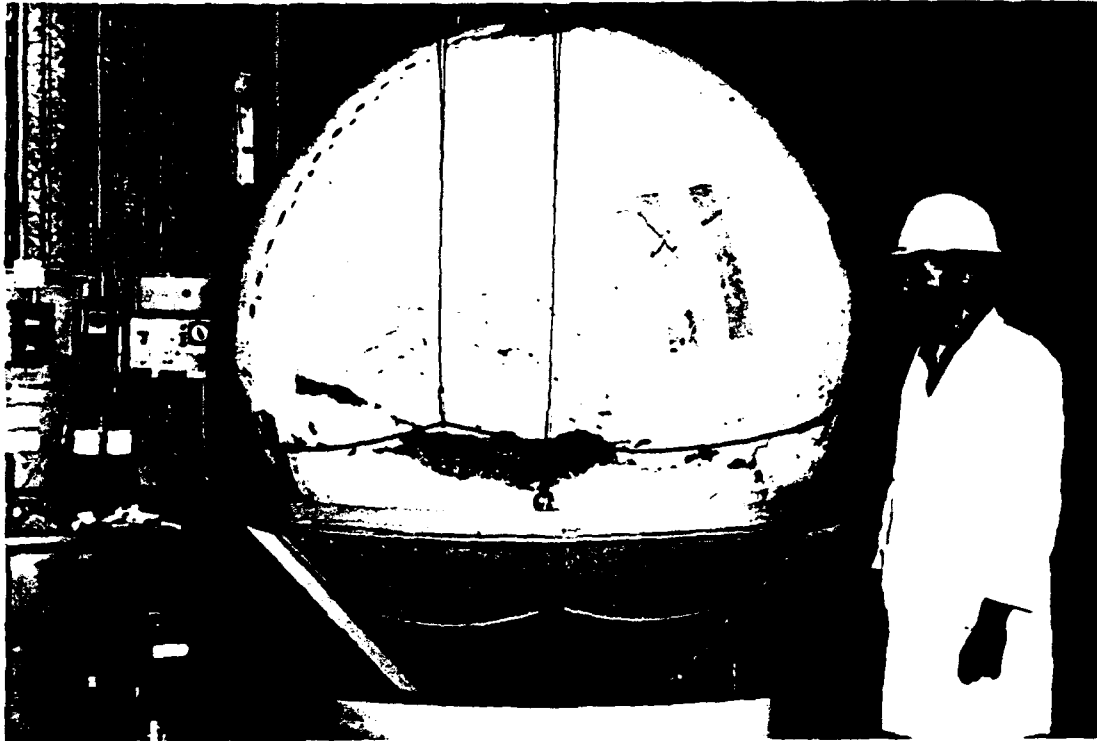


Figure 15. Post-implosion view of Sphere no. 11.

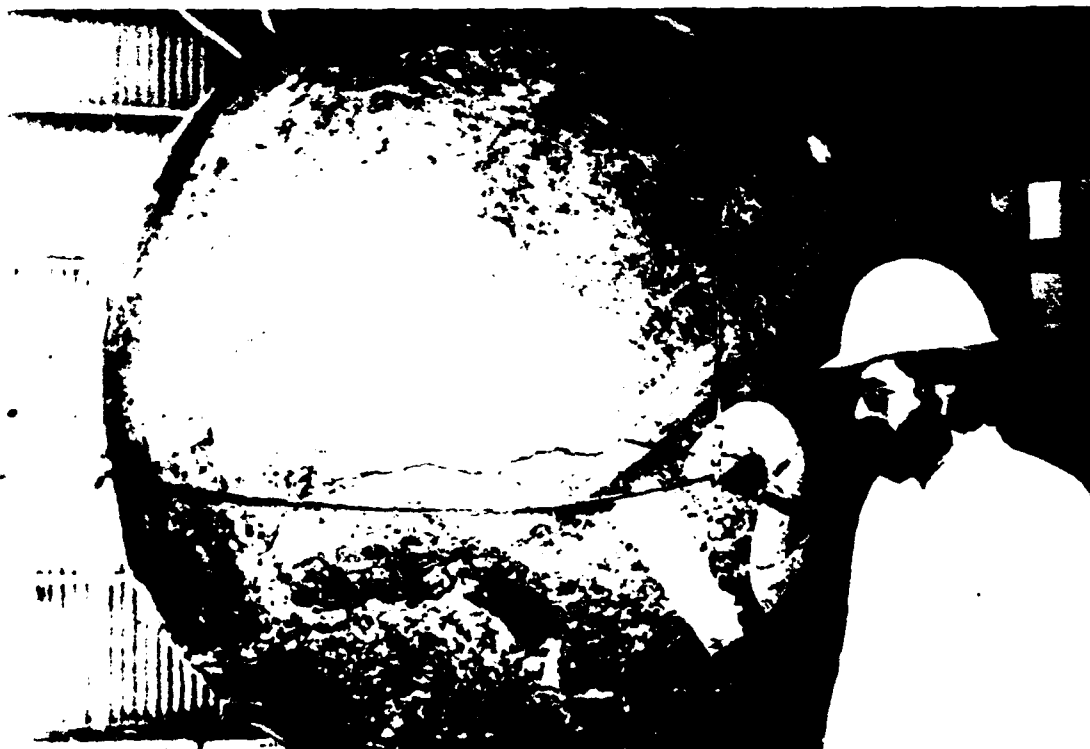


Figure 16. Post-implosion view of Sphere no. 12.



Figure 17. Post-implosion view of Sphere no. 13.



Figure 18. This view of Sphere no. 13 is typical of post-implosion for non-preloaded spheres. The missing concrete was pushed to the interior of the sphere. Shear-compression plane runs from equator to above the numeral 13.



Figure 19. Debris on the seafloor after Sphere no. 1 imploded at a depth of 5,075 feet. The submersible's manipulator arm is seen at the top of the photograph, and the dark area under the arm is vegetation-like growth.

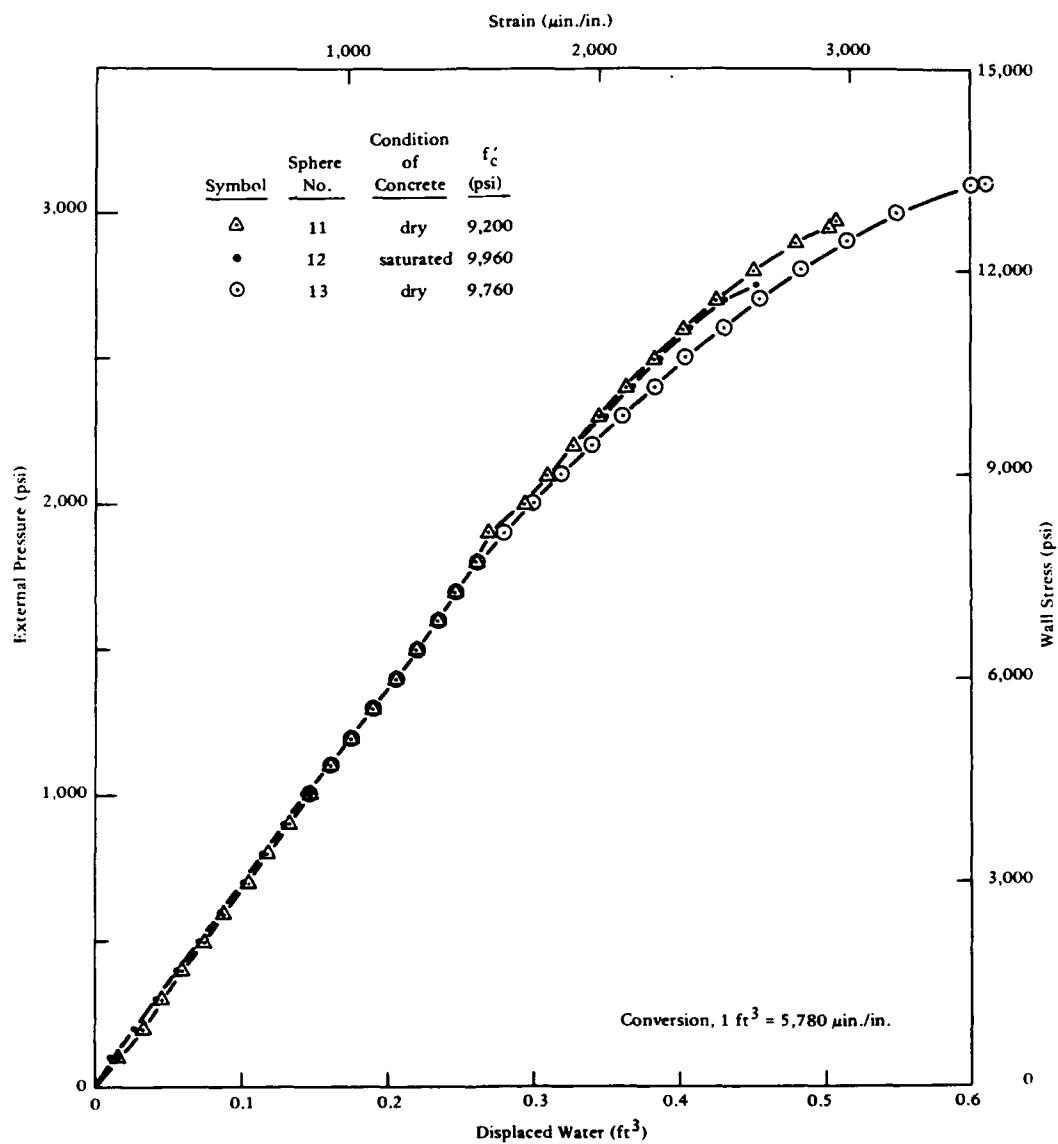


Figure 20. Displaced water versus pressure for short-term implosion of preloaded spheres.

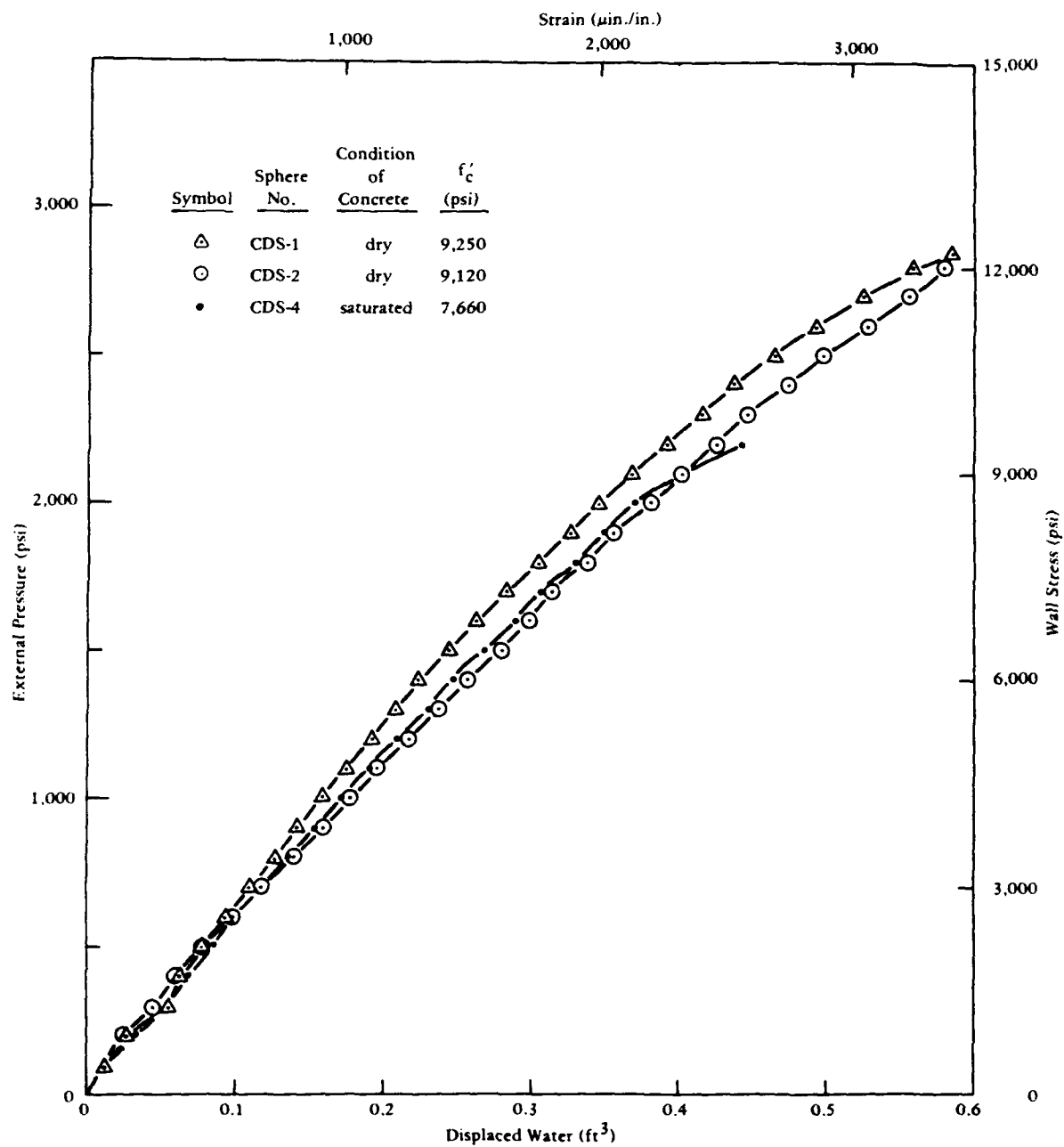


Figure 21. Displaced water versus pressure for short-term implosion of non-preloaded spheres (from Ref 5).

Long-Term Loading of Spheres

Of the original eighteen spheres in the ocean, three spheres have imploded at depth. The time-to-failure for each of the spheres has had to be estimated because the clocks contained in two of them have not been found. Sphere no. 3 evidently imploded on descent to the seafloor at 4,330 feet (1,320 m) because the concrete fragments were widely scattered. Spheres no. 1 and 7 had a time-to-failure that was between the beginning of the test and the day of their first inspection. For these specimens the concrete fragments were in a localized area.

Detailed data for these spheres and the other spheres still intact on the seafloor are given in Table 6. This table also shows the calculations for the relative load level, i.e., the ratio of sustained pressure to the predicted implosion pressure, P_s/P_{im}^p , for each sphere. The relative load level for the spheres changed between the beginning of the test and the 5.3-year period as the concrete became stronger with time. Using data from Figure 7 for dry concrete and Figure 8 for saturated concrete, the 28-day fog cure compressive strength was adjusted to estimate the strength at 5.6 years.

The long-term loading failure behavior for the ocean spheres is shown in Figure 22. Data from spheres tested in a pressure vessel (Ref 5) are also presented in Figure 22 and summarized in Table 7. The results of Stockl (Ref 9) are shown by an average data curve which represents hundreds of tests on uniaxially loaded specimens. With two exceptions, the sphere results are in agreement with Stockl's findings. From his data, it appears that the safe relative load level is about 0.75.

Stockl presented an interesting discussion on long-term loading. When a structure is initially placed under

sustained load, the creep behavior of concrete causes degradation of strength by forming microcracks. At the same time, in the presence of moisture, hydration of cement causes a strengthening of the concrete. Long-term loading to failure occurs when microcracks from creep progress at a faster rate than strengthening from cement hydration. Since creep effects slow down with time, strength gain from cement hydration has a chance to catch up and overtake the creep-induced strength reductions. The rate of cement hydration is dependent upon the amount of free cement available within the concrete before it is placed under sustained load. The practical significance of this condition is that once the "critical duration of load" is over and hydration strengthening occurs at a faster rate than creep damage, the specimen will never fail from creep. The critical duration of sustained load can be days when applied to young concrete and years for old concrete. For the spheres in the ocean, the critical duration of load was probably on the order of months. Hence, according to Stockl, any sphere that has not failed after 5.3 years under sustained load should not fail in the future.

In Figure 22, for Sphere no. 1 (5,075 feet) and Sphere no. 7 (3,725 feet) the time-to-failure is shown as a dashed line. The datum point for the spheres was plotted at 10 days as a conservative estimate. For Sphere no. 3 (4,330 feet), a wide scatter of fragments on the seafloor indicated that the specimen failed during descent.

A valuable supplement to the failure data was the results from the spheres that had not failed. Figure 23 shows the relative load levels for the spheres in the ocean that are still intact. Stockl's curve is shown to lie above the data. The relative load levels experienced by the spheres in the ocean are shown to decrease with time as the strength of concrete increases.

Table 6. Summary of Long-Term Loading Data From Spheres Tested in Ocean

Sphere No.	Condition of Concrete in Sphere	Sustained Pressure in the Ocean, P_s (psi)	Beginning of Ocean Test				At Implosion or Last Inspection				Time to Failure (day)
			Age of Concrete (day)	Uniaxial Compressive Strength, f'_c (psi)	Predicted Implosion Pressure ^a P_{im} (psi)	Relative Load Level, P_s/P_{im}	Age of Concrete (day)	Uniaxial Compressive Strength ^b f'_c (psi)	Predicted Implosion Pressure ^a P_{im} (psi)	Relative Load Level, P_s/P_{im}	
1	dry	2,255	174	8,940	2,710	0.83	1,294 ^c	9,440 ^c	2,860	0.79	1 to 1,120
2	dry	2,165	162	8,970	2,715	0.80	2,112	10,470	3,170	0.68	Intact
3	dry	1,925	134	8,840	2,680	0.72	134	8,840	2,680	0.72	0
4	wet	1,860	172	7,600	2,300	0.81	2,122	9,290	2,815	0.66	Intact
5	wet	1,820	158	7,690	2,330	0.78	2,108	8,920	2,700	0.67	Intact
6	wet	1,720	143	8,370	2,535	0.68	2,093	9,300	2,815	0.61	Never inspected
7	dry	1,655	126	9,480	2,870	0.58	557 ^c	9,480 ^c	2,870	0.58	1 to 430
8	dry	1,630	111	9,030	2,735	0.60	2,061	9,920	3,005	0.54	Intact, but flooded
9	wet	1,465	94	7,820	2,370	0.62	2,027	7,990	2,420	0.61	Intact
10	wet	1,420	97	8,330	2,525	0.56	2,030	9,120	2,765	0.51	Intact
11	dry	1,395	113	9,190	2,785	0.50	2,063	9,950	3,015	0.46	Intact
12	wet	1,240	89	7,430	2,250	0.55	2,022	8,350	2,530	0.49	Intact
13	dry	1,170	105	9,370	2,840	0.41	2,005	10,080	3,055	0.38	Intact
14	dry	1,085	144	8,170	2,475	0.44	2,094	9,220	2,795	0.39	Intact
15	wet	1,020	74	7,830	2,370	0.43	2,024	9,010	2,730	0.37	Intact
16	wet	940	67	7,780	2,355	0.40	2,017	8,330	2,525	0.37	Intact
17	wet	880	52	7,730	2,340	0.38	2,002	8,920	2,700	0.33	Intact
18	wet	820	45	7,590	2,300	0.36	1,995	9,200	2,790	0.29	Intact

^a P_{im} = 0.303 f'_c obtained from short-term loading tests.

^b f'_c is estimated for last inspection by using Figures 7 and 8.

^cRepresents maximum value; sphere imploded sometime during this period.

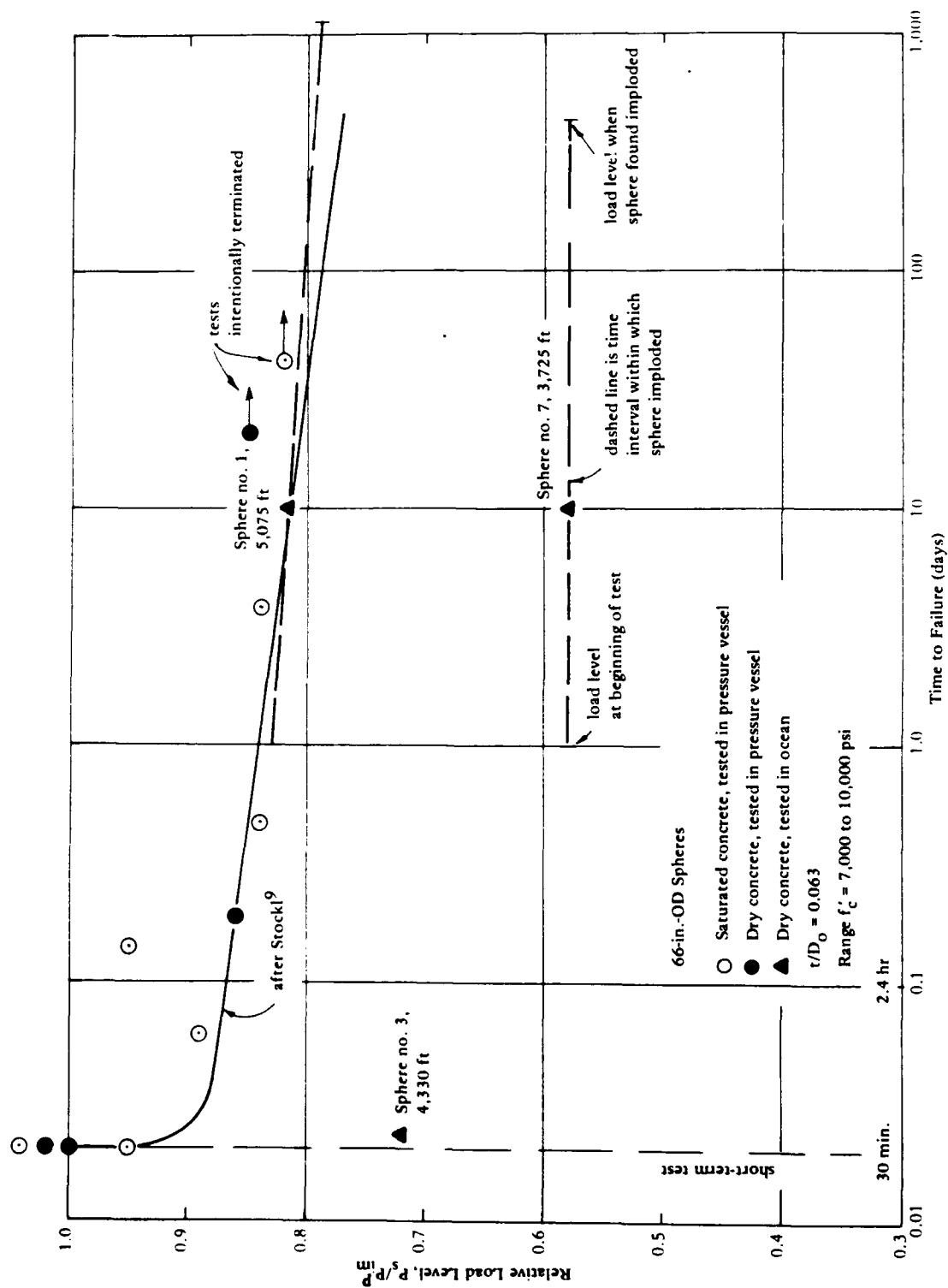


Figure 22. Time to failure of concrete spheres under long-term hydrostatic loading.

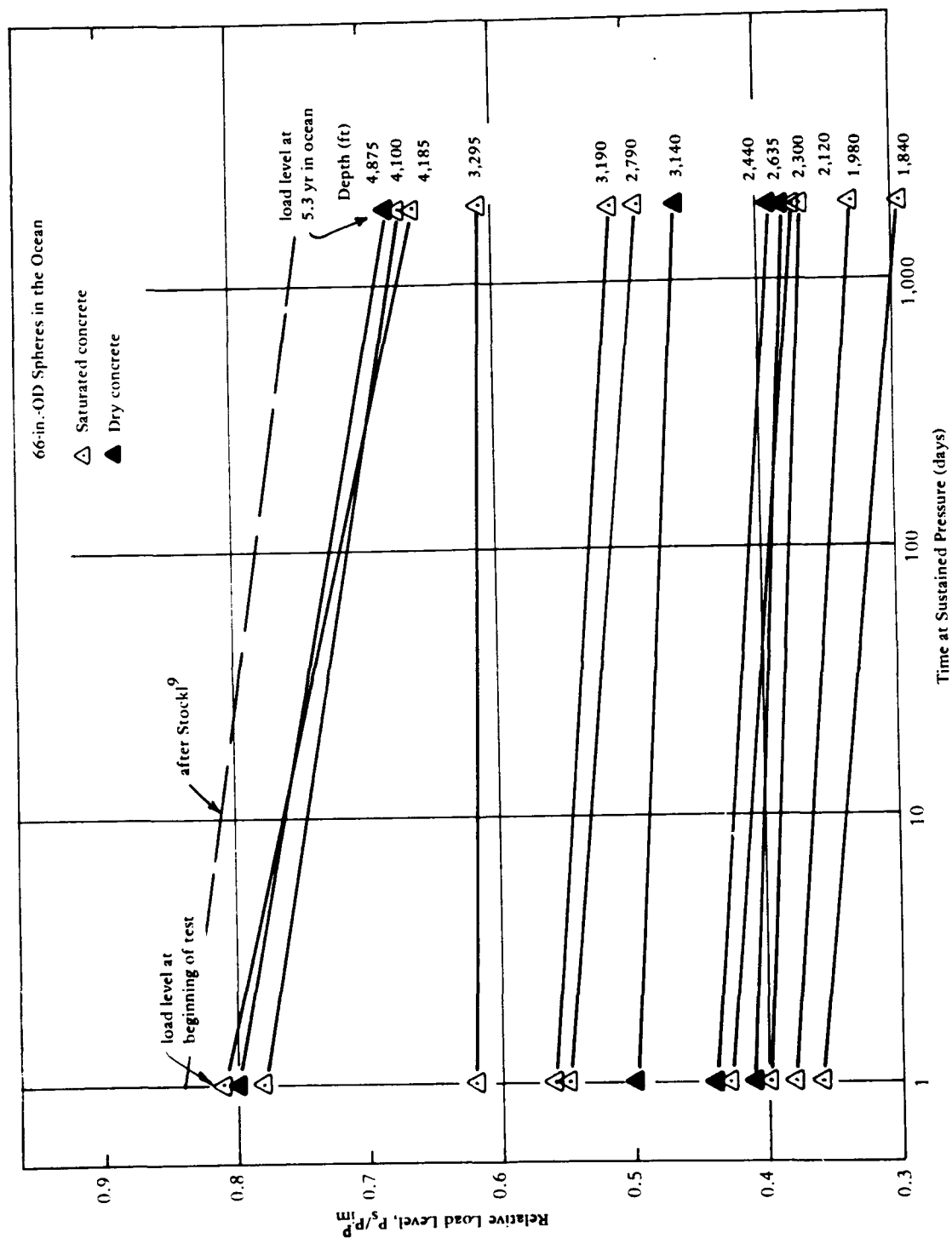


Figure 23. Relative load level for spheres still intact in the ocean.

Table 7. Summary of Long-Term Loading Data From Spheres Tested in Pressure Vessel (after Ref 5)

Sphere No.	Condition of Concrete	Sustained Pressure, P_s (psi)	Uniaxial Compressive Strength, ^a f'_c (psi)	Predicted Implosion Pressure, ^b P_{im} (psi)	Relative Load Level, $\frac{P_s}{P_{im}}$	Time to Failure (day)	Comment
CWL-5B	wet	2,280	7,900	2,395	0.95	0.14 (200 min)	Test intentionally terminated
CWL-6	wet	1,670	6,740	2,040	0.82	41.82	
CWL-7	wet	1,940	7,170	2,170	0.89	0.06 (90 min)	
CWL-8	wet	1,845	7,210	2,185	0.84	0.47 (680 min)	
CWL-9B	wet	1,905	7,440	2,255	0.84	3.77	
CDL-10	dry	2,405	9,420	2,855	0.86	0.19 (270 min)	Test intentionally terminated
CDL-11	dry	2,065	7,940	2,415	0.85	20.92	

^aStrength given for weaker hemisphere.

^b $P_{im} = 0.303 f'_c$ obtained from short-term loading tests.

Permeability

Table 1 gives the change in number of chain links suspended off the seafloor by the spheres. The change in link count was due to a loss of buoyancy by the spheres because of weight gain from water absorption and permeability. The loss of buoyancy was converted to a volume of seawater taken on by the spheres.

Total water intake by a sphere included the quantity of seawater absorbed by the concrete and permeated through the wall. The quantity of seawater absorbed by the concrete was calculated by assuming 3% by weight

absorption. Three percent absorption was determined for identical concrete by extrapolating data obtained at 550 feet (168 m) pressure head for 86 days (Ref 4) to a time period of 3 years when it was estimated that absorption was complete.

For Sphere no. 12, which was uncoated, it was predicted from the chain link count that the interior contained 1.38 cu ft (39 liters) of water. The actual measured volume of water was 1.24 cu ft (35 liters). This close prediction of the actual permeated seawater not only indicates the 3% by weight absorption is a fair estimate, but also that the initial calculations of the original number of chain links suspended

off the seafloor was accurate. In Reference 1 concern was expressed that the original number of links off the seafloor could be in error by ± 1.5 links (equivalent to 0.73 cu ft or 21 liters). With the data from Sphere no. 12, it is now known that that error estimate was too high. A new estimate of error is ± 0.5 link (0.24 cu ft or 7 liters), which is also the error estimate between different inspections.

Figure 24 shows the relationship between total water intake and time in the ocean for all of the spheres (except Spheres no. 17 and 18, which were half coated) where chain link count data were obtained. The coated spheres do not show any evidence of having permeated water. This case is known to be true for Spheres no. 11 and 13. The coated spheres range in depth from 2,440 to 4,875 feet (744 to 1,486 m).

The waterproof coating appeared quite effective. This was an anticipated finding, because the coating was not a complete barrier. Pin-holes or "fish-eye" openings existed in the coating. The coating also bridged air pockets in the wall near the surface; these locations had the coating broken because the water pressure pushed the coating into the air pocket. Water definitely had access to the concrete wall through these openings.

When a hole was drilled in the walls of Spheres no. 11 and 13, the concrete was found to be quite dry in appearance. It is apparent that the pin-hole openings became watertight with time. Continued hydration of cement, microorganisms, and chemical changes were probably some of the causes for the concrete becoming watertight. Whatever the mechanism, it can be speculated that it was functioning in the uncoated concrete

too. From Figure 24, it is shown that, in general, the uncoated concrete spheres became watertight. In less than 1 year, the uncoated spheres absorbed (and permeated) water at a faster rate than the coated spheres. However, after 1 year the additional water intake was quite small.

One method of analyzing permeability results is to apply D'Arcy's viscous flow equation. For a sphere, this equation can be expressed as:*

$$K_C = \frac{Q_p t}{T A_s h} \quad (1)$$

where K_C = permeability coefficient, ft/sec (m/sec)

Q_p = quantity of permeated seawater, ft³ (m³)

T = time (sec)

t = wall thickness, ft (m)

A_s = interior surface area, ft² (m²)

h = pressure head, ft (m)

D'Arcy's theory assumes K_C to be constant with time. However, the permeability results from the spheres show that K_C decreases with time. To account for the change in rate of K_C , a secant K_C is utilized. This is analogous to the secant modulus of elasticity for nonlinear materials such as concrete.

In Figure 25 the secant K_C values are shown as a function of time in the ocean. Data from two spheres tested in a pressure vessel for up to 42 days are included. These spheres were similar to the ones in the ocean. It is interesting

*This expression is different from that given in References 1 and 5 because A_s is now defined as the interior surface area and not as mentioned previously as the exterior surface area. This revised equation will give K_C values 30.6% greater than the previous equation.

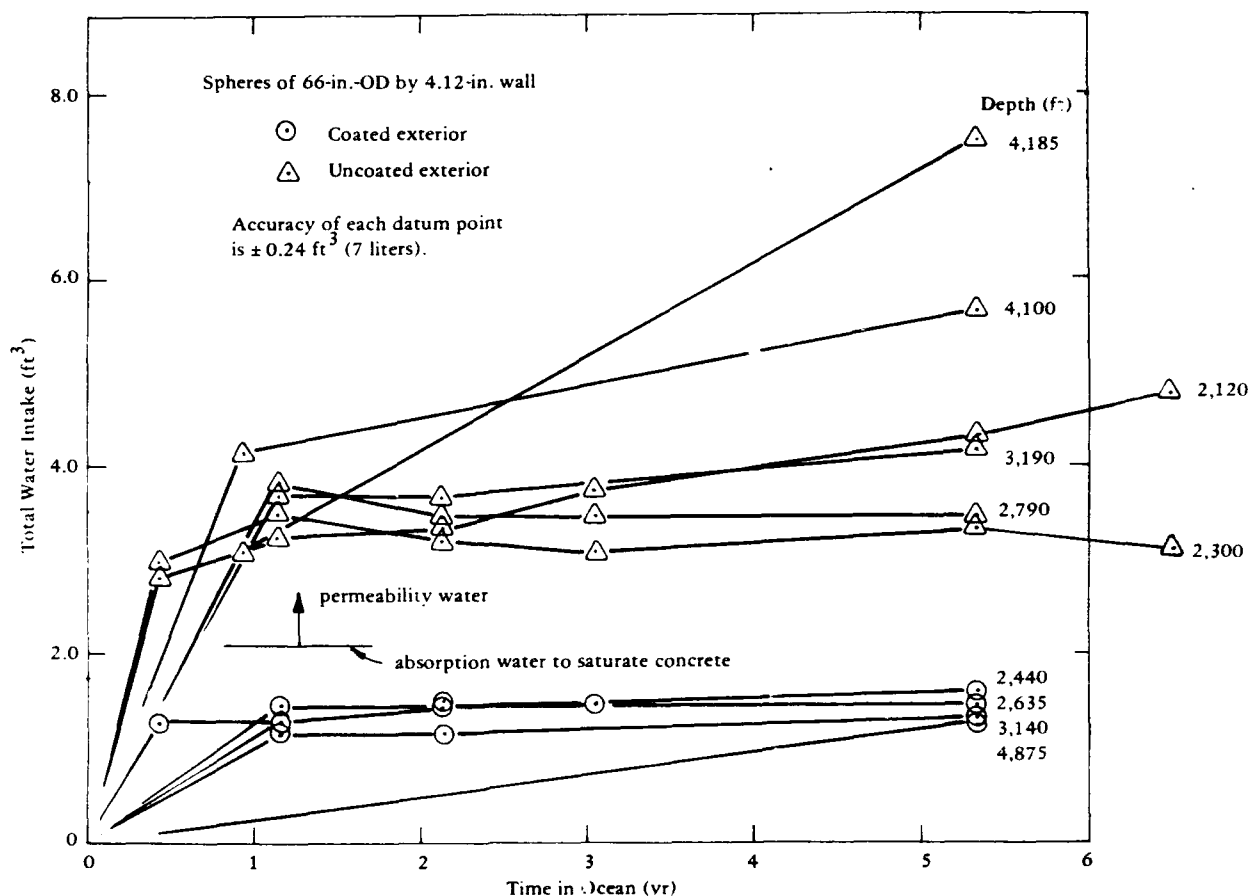


Figure 24. Total water intake for spheres in the ocean for long time periods.

that extrapolations of the pressure vessel test results yield results close to the actual values obtained from the spheres in the ocean.

The data from the spheres compared moderately well with results from Powers et al. (Ref 10) who studied cement pastes. The water-to-cement ratio for the pastes varied from 0.3 to 0.7, and the measured K_C values (initial tangent K_C) ranged from 0.3×10^{-14} to $400 \times 10^{-14} \text{ ft/sec}$ (0.1×10^{-14} to $120 \times 10^{-14} \text{ m/sec}$), respectively.

For a water-to-cement ratio of 0.4, which was equivalent to that for the concrete in the spheres, Power's results showed a K_C of about $3.3 \times 10^{-14} \text{ ft/sec}$

($1.0 \times 10^{-14} \text{ m/sec}$). This was an order of magnitude lower than that for the concrete in the spheres tested in the pressure vessels. Powers did not discuss any indication of permeability results decreasing with time, as was found in this study.

Durability

Samples of 5.6-year-old concrete from the ocean spheres, both coated and uncoated, and from the on-land and continuously fog-cured cylinders were analyzed by x-ray diffraction techniques by Prof. Mehta at the University of California at Berkeley. He determined

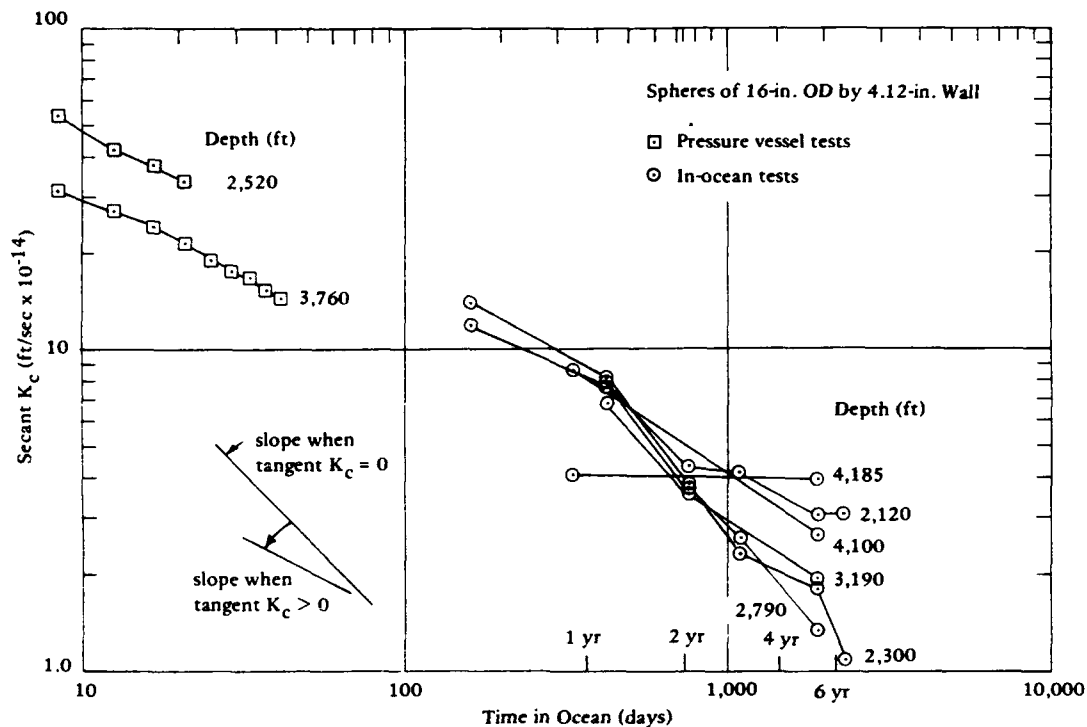


Figure 25. Permeability of uncoated spheres expressed as secant K_c versus time.

the chemical composition of the cement pastes; his report is given in Appendix E. All samples showed that the cement compounds were hydrated. The samples also showed that substantial amounts of calcium hydroxide were present, which indicates the hardened cement pastes were undamaged. No evidence was present of harmful chemical compounds. The ocean concrete remained essentially unaltered from the fog-cured concrete.

FINDINGS

1. Concrete that was placed in the ocean decreased in compressive strength by at least 10% due to saturation. A time period of from 1 to 2 years in the ocean was required to regain a strength equal to that of the 28-day fog-cured strength.
2. After 5.3 years in the ocean, concrete showed a compressive strength that was 15% greater than its 28-day fog-cured

strength. However, this strength was still 15% less than companion concrete continuously fog-cured.

3. Three spheres were retrieved from the ocean where they had been exposed to a preload of 50% of their ultimate strength for 5.3 years. These preloaded spheres were tested in the laboratory under short-term loading and, in general, behaved similarly to that of non-preloaded spheres. Whether preloaded or non-preloaded, the saturated (uncoated) concrete spheres had a tendency to fail at lower pressures than those of dry (coated) concrete spheres.

4. Three of the original eighteen spheres have imploded in the ocean under long-term loading. The remaining spheres have withstood load levels of 0.3 to 0.8 of their predicted short-term strength.

5. The permeability of concrete in uncoated spheres has shown a decrease in rate with time and, in several cases, the permeation of seawater through the concrete wall has stopped. Coated (waterproofed) spheres remained dry on the interior.

6. X-ray diffraction analysis of the fog-cured and ocean-cured concrete has shown the 5.3-year ocean-cured concrete - whether coated or uncoated - to be essentially unchanged from the fog-cured concrete.

SUMMARY

After 6.4 years in the ocean, the long-term test on concrete spheres at deep ocean depths has demonstrated several important factors that will result in design criteria for undersea concrete structures. Those items are listed in the Findings section above. To summarize:

(1) the compressive strength of concrete decreased slightly due to becoming saturated with seawater, (2) the rate of strength gain with time for concrete in the deep ocean was slower than that for concrete cured in a standard fog room, (3) spheres exposed to a load 50% of their short-term strength for 5.3 years behaved in a manner similar to that of spheres that were not exposed to a long-term load, (4) twelve spheres are still in the ocean and are withstanding pressure loads that range from 1,840 to 4,875 feet (560 to 1,486 m), (5) the permeability of uncoated concrete was quite low, (6) if complete watertightness is desired, a waterproof coating was found to be effective, and (7) the durability of concrete in the deep ocean was found to be excellent.

The results from this study show undersea concrete structures to behave exceptionally well at deep ocean depths. The strength, permeability, and durability of the spheres are within or exceed engineering acceptability limits. Confidence in using concrete for undersea structures is substantiated and enhanced by the results of this ocean test. The test is continuing, and additional data will be forthcoming.

ACKNOWLEDGMENTS

The authors wish to acknowledge the able assistance of Mr. Phillip C. Zubieta as the senior project technician for this task from its beginning, and the support and cooperation of the Navy's Submarine Development Group One for its services in conducting the submersible operations.

REFERENCES

1. Civil Engineering Laboratory. Technical Report R-805: Long-term deep ocean

- test of concrete spherical structures - Part I: Fabrication, emplacement, and initial inspections, by Harvey H. Haynes. Port Hueneme, Calif., Mar 1974.
2. H. J. Gilkey. "Rate of air drying effect upon strength of concrete," Concrete, May 1941, pp 4-5.
3. S. E. Pihlajavaara. "A review of some of the main results of research on the aging phenomena of concrete - Effect of moisture conditions on strength, shrinkage, and creep of mature concrete," Cement and Concrete Research, vol 4, 1974, pp 761-771.
4. Civil Engineering Laboratory. Technical Note N-1436: Seawater absorption and compressive strength of concrete at ocean depths, by Harvey H. Haynes, Roy S. Highberg, and Bjorn A. Nordby. Port Hueneme, Calif., Apr 1976; or "Concrete properties at ocean depths," by H. H. Haynes and R. S. Highberg. Journal of the Waterways, Harbors, and Coastal Engineering Division, ASCE, vol 102, no. WW4, Nov 1976, pp 455-470.
- 5.—. Technical Report R-774: Behavior of 66-inch concrete spheres under short- and long-term hydrostatic loading, by H. H. Haynes and L. F. Kahn. Port Hueneme, Calif., Sep 1972. (AD 748584)
6. P. K. Mehta. Correspondence with H. Haynes of 8 August 1977, University of California, Berkeley, Calif.
7. Civil Engineering Laboratory. Technical Report R-673 and R-673S: In-situ strength of subaqueous concrete, by W. R. Lorman. Port Hueneme, Calif., Apr 1971 and Sep 1971.
8. A. M. Neville. Properties of concrete, 2nd ed. Pitman Publishing, New York, N.Y., 1973, p. 259.
9. S. Stockl. "Strength of concrete under uniaxial sustained loading," Concrete for Nuclear Reactors, vol 1, ACI, Special Publication SP-34, 1972, pp 313-326.
10. T. C. Powers et al. "Permeability of portland cement paste," Journal of the American Concrete Institute, Proceedings, vol 51, Nov 1954, pp 285-298.
11. D. L. Bloem. "Concrete strength in structures." American Concrete Institute Journal, Proceedings, vol 65, no. 3, Mar 1968, pp 176-187.
12. R. H. Campbell and R. E. Tobin. "Core and cylinder strengths of natural and lightweight concrete," American Concrete Institute Journal, Proceedings, vol 64, no. 4, Apr 1967, pp 190-195.
13. W. E. Murphy. "Discussion of the paper, 'Contract strength requirements - cores versus in-situ evaluation,' by V. M. Malhotra." American Concrete Institute Journal, Proceedings, vol 74, no. 10, Oct 1977, pp 523-525.

Appendix A

EFFECT OF DRILLING CORES ON COMPRESSIVE STRENGTH

It is generally known that the compressive strength of core specimens obtained from a structure is usually less than that of standard laboratory cast cylinders. This observation is the result of many influencing parameters, one of which is the effect of drilling the core specimens. Other parameters are: curing environment, size of core specimen, and direction of coring compared to casting (to name a few). The specific topic of drilling effect had not been directly addressed in past studies. However, investigations by Bloem (Ref 11) and Campbell and Tobin (Ref 12) gave data suitable for estimating the drilling effect.

Both investigations used concrete slabs that had provisions for making and curing cast cylinders as part of the slab. At the time of test, the cast cylinders were removed from the slab, and then core specimens of the same size as the cast cylinders were drilled from the slab.

The Bloem study used plastic inserts that were set in the slab to make the

cast cylinders; these were subsequently "pushed-out." Both the cast and cored cylinders were soaked for 40 hours prior to testing to insure similar moisture contents. The Campbell and Tobin study used concrete having two cement contents, 5.33 and 7.33 sacks per cu yd. Cast cylinders were made in metallic molds and then placed in holes in the slab. The cast and cored cylinders were soaked prior to testing.

The uniaxial compressive strength data of select test runs are given in Table A-1. The observed effect of drilling is to reduce the strength of the cast cylinders by a factor of 0.93. For this report, the inverse, 1.07, is the factor to increase the strength of cored specimens so that they become equivalent to cast cylinders.

This factor of 1.07 was in close agreement with that of Murphy (Ref 13) who mentioned a factor of 1.06 but did not present test results or the background source.

Table A-1. Compressive Strength Data on Effect of Drilling Cores

Investigator	Size of Specimen (in.)	Type of Cement	No. of Specimens	Compressive Strength at 28 Days for Standard Laboratory Conditions, f'_c (psi)	Test Age (days)	Compressive Strength, f'_c (psi) for -		Core/Cast	Coefficient of Variation (%)
						Cast Cylinders	Cores		
Bloem (Ref 11)	4x6	Type I	3	3,730	3	1,750	1,700	0.971	
			3		7	2,310	2,290	0.991	
			3		28	3,210	3,040	0.947	
			3		91	3,420	3,370	0.985	
			3		364	3,450	3,025	0.877	
								avg 0.954	4.9
	4x6	Type III	3	5,490	3	3,710	3,250	0.876	
			3		7	3,770	3,510	0.931	
			3		28	4,160	3,640	0.875	
			3		91	4,440	4,130	0.930	
			3		364	4,270	3,500	0.820	
								avg 0.886	5.2
	4x6	Type III	3	4,150	1	2,980	2,770	0.930	
			3		3	3,110	2,910	0.936	
			3		7	3,280	3,020	0.921	
			3		28	3,340	3,060	0.916	
			3		91	3,540	3,180	0.898	
					364	3,390	2,850	0.841	
								avg 0.907	3.9
Campbell and Tobin (Ref 12)	6x12	Type II	4	4,515	28	4,150	3,850	0.928	
			4		56	4,195	4,140	0.987	
			4		84	4,660	4,095	0.879	
								avg 0.931	5.8
	6x12	Type II	4	5,870	28	5,280	5,345	1.012	
			4		56	5,460	5,390	0.987	
			4		84	6,000	5,725	0.949	
								avg 0.983	3.2
overall avg								0.932	

Appendix B

EARLY COMPRESSIVE STRENGTH DATA OF SPHERES

Table B-1 lists the uniaxial compressive strength data for all the spheres in a manner similar to that in Reference 1, Table A-2 on Concrete Control Cylinder Data. This new table includes the coefficients of variation.

Table B-1. Early Compressive Strength Data of Spheres

[Each compressive strength value is average of three 6 x 12-in. (152 x 305-mm) cast cylinders.]

Sphere No.	Hemisphere No.	28-Day Fog Cure		Prior to Ocean Emplacement				
		Compressive Strength, f'_c (psi)	Coefficient of Variation (%)	Compressive Strength, f'_c of Wet Concrete (psi)	Coefficient of Variation (%)	Compressive Strength f'_c of Dry Concrete (psi)	Coefficient of Variation (%)	Age (days)
1	W4	8,520	0.1			8,940	1.5	174
	W35	8,070	2.1			9,360	1.5	65
2	W8	8,250	2.9			9,950	3.3	164
	W7	7,940	0.6			8,970	4.5	162
3	W15	8,520	1.5			8,840	1.5	134
	W16	8,400	1.9			9,650	2.0	132
4	W6	8,760	0.7	8,320	5.8			170
	W5	8,050	1.5	7,600	2.7			172
5	W10	7,730	1.1	8,090	2.9			156
	W9	8,240	1.7	7,690	1.7			158
6	W14	8,580	1.8	8,510	1.6			143
	W13	8,060	1.5	8,370	2.6			144
7	W20	7,660	1.7			9,530	2.3	117
	W17	7,550	5.5			9,480	2.3	126
8	W22	7,520	2.2			9,030	1.2	111
	W19	8,410	3.2			9,380	5.7	119
9	W28	6,920	1.8	7,820	5.5			94
	W25	8,070	3.4	8,740	2.7			104
10	W30	8,190	1.2	8,560	4.4			88
	W27	7,900	0.2	8,330	9.6			97
11	W24	7,540	3.8			9,820	5.6	103
	W21	7,720	2.7			9,190	3.3	113
12	W32	7,570	0.6	8,390	6.7			80
	W29	7,240	3.0	7,430	0.6			89
13	W26	8,070	4.5			10,210	5.3	98
	W23	7,640	2.0			9,370	1.2	105
14	W12	6,990	2.1			8,170	1.3	144
	W11	7,550	3.0			9,200	2.0	148
15	W34	8,170	2.3	7,830	4.9			74
	W31	7,810	1.4	8,740	1.9			82
16	W36	7,220	2.0	7,780	1.7			67
	W33	7,930	0.4	8,340	0.3			75
17	W39	8,050	1.1			9,050	4.2	51
	W40	7,730	2.0	7,730	5.0			52
18	W41	8,620	2.3			8,770	5.2	48
	W42	7,970	2.1	7,590	4.3			45

Appendix C

MOISTURE CONTENT OF CONCRETE SAMPLES

Tests were conducted on concrete fragments from ocean-cured spheres and blocks, on-land-cured blocks, and fog-cured cylinders to determine the relative free moisture contents associated with the different curing environments. These data were obtained by drying specimens in a 50% RH, 70F environment for 4 months and then at 130F (55C) for 3 weeks. The data are presented in Table C-1 and Figure C-1.

Moisture contents for the continuously fog-cured cylinders, ocean-cured blocks, and uncoated ocean-cured sphere were similar. The concrete in the coated ocean-cured sphere had a lower moisture content, and the on-land field-cured block had a still lower moisture content.

The moisture content of the concrete in the coated spheres represents the condition of the concrete after the spheres were tested in the pressure vessel. The spheres in the ocean probably had a lower moisture content. This conclusion can be presented because of an observation made during test. Prior

to tests in the pressure vessel, the interior volume of the sphere was filled with water for the purpose of measuring the change in volume of the sphere during pressurization. The interior surface of the sphere was not coated. For Sphere no. 13, the specimen had water in its interior for about 16 hours, at which time it was observed that additional water had to be added to completely fill the interior again. A certain quantity of water was absorbed by the dry concrete before the test. For Sphere no. 11, water was in contact with the dry concrete for only about 4 hours.

In addition to drying some samples, other samples from the ocean-cured blocks and coated sphere wall were saturated in a pressure vessel. When the water gained was added to the water lost, the total water content for the blocks was about 5.13% by weight, and for the coated sphere wall, it was about 5.55% by weight. The average water content was 5.34% by weight, which represents an average void volume in the concrete of 12.5%.

Table C-1. Moisture Content of Concrete

Environmental Condition for Concrete Samples	Samples in Original Condition Placed in Pressure Vessel at 15,000 Psi for 7 Days			Samples in Original Condition Dried-Out by –					
				50% RH, 70°F for 4 Months			Additional 3 Weeks at 130°F		
	Water Gain (% by wt)	No. of Samples	Coefficient of Variation (%)	Water Loss (% by wt)	No. of Samples	Coefficient of Variation (%)	Total Water Loss (% by wt)	No. of Samples	Coefficient of Variation (%)
On-land field-cured for 5.6 yr									
Interior of blocks	–	–	–	0.87	12	21.8	2.61	12	12.3
Exterior of blocks	–	–	–	1.78	4	27.5	2.76	4	16.7
Fog-cured for 5.6 yr	–	–	–	2.47	18	8.9	4.37	18	8.0
Ocean-cured for 5.3 yr									
Blocks (uncoated)	0.83	2	56.6	2.83	8	4.2	4.72	10	5.5
Coated sphere wall	1.61	4	9.9	1.85	4	9.2	3.52	8	8.6
Uncoated sphere wall	–	–	–	2.58	2	3.9	4.27	2	1.2

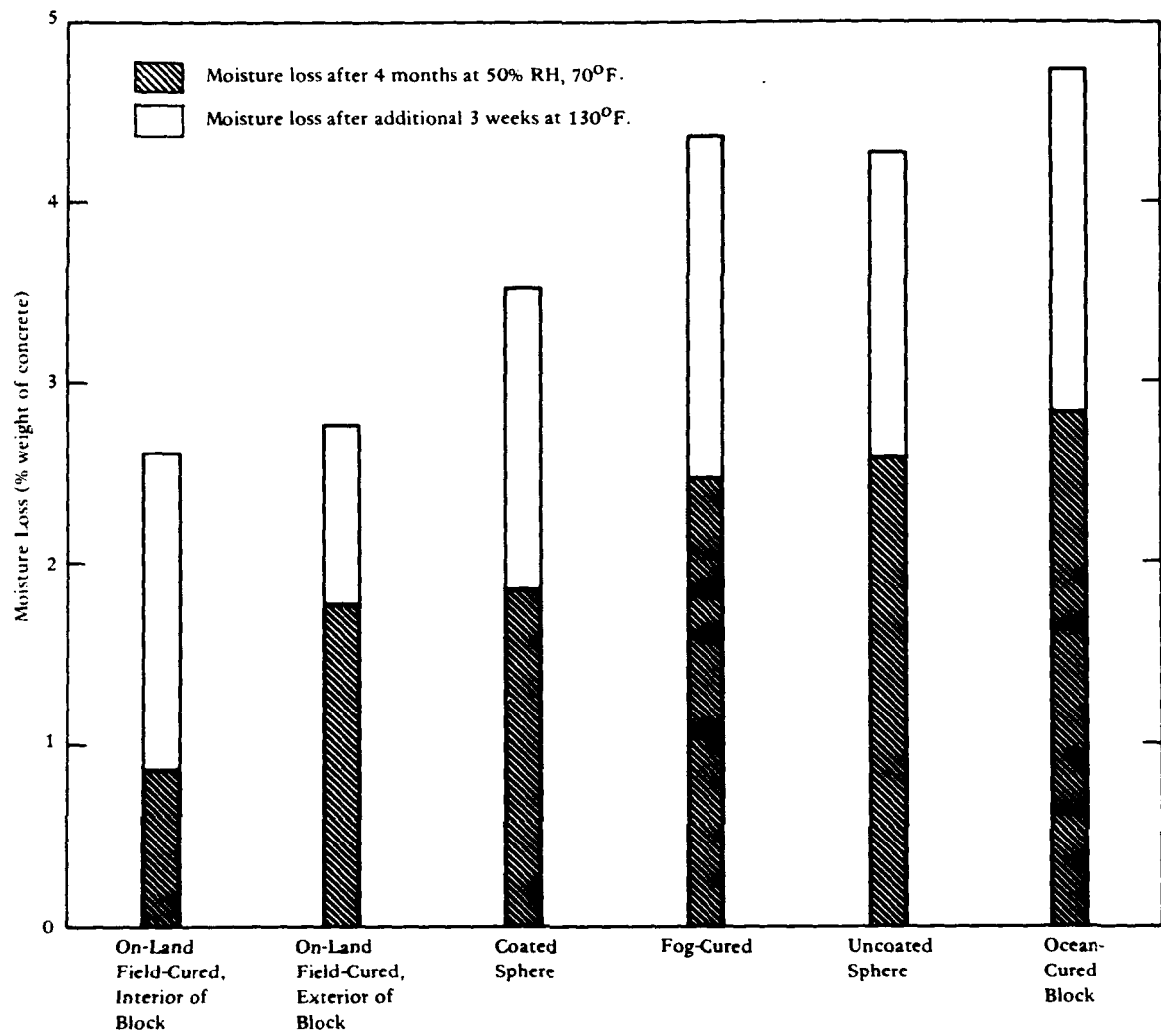


Figure C-1. Moisture content of concrete.

Appendix D

CEMENT PASTE SAMPLES PLACED IN THE OCEAN

To study the phenomenon of magnesium ions replacing calcium ions in tobermorite gel, small neat cement paste samples were mounted on the chain of Spheres no. 15 and 16 on 7 Mar 1978. Ten samples were placed, five at each sphere. The samples were 1 inch in diameter by 2 inches long (25 x 51 mm). They were suspended from a steel bar that was hooked onto the sphere chain. The samples were hung from insulated electrical cables about 1.5 feet (0.5 m) below the bar. Each cable contained a plug-in type connector (Figure D-1). In the future to retrieve a sample, a submersible can use its manipulators to disconnect the plug.

The cement paste samples were prepared on 1 Jan 1978 by Professor P. K. Mehta of the University of California at Berkeley. The paste was made of Type II Portland cement having a water-to-cement ratio of 0.60. The relatively high water-to-cement ratio was used to create a higher-than-normal porosity. The samples were made using a technique that prevented bleeding.

The chemical composition for the cement is given in Table D-1. Comparison samples to those in the ocean were placed in a fog room environment at CEL and the University of California at Berkeley.

Table D-1. Chemical Composition of Portland Cement

Chemical	Percent
SiO ₂	22.36
Al ₂ O ₃	3.75
Fe ₂ O ₃	2.10
CaO	65.89
MgO	1.77
SO ₃	2.29
C ₃ S	63.5
C ₂ S	16.3
C ₃ A	6.4
C ₄ AF	6.4
Blaine, cm ² /g	4,800

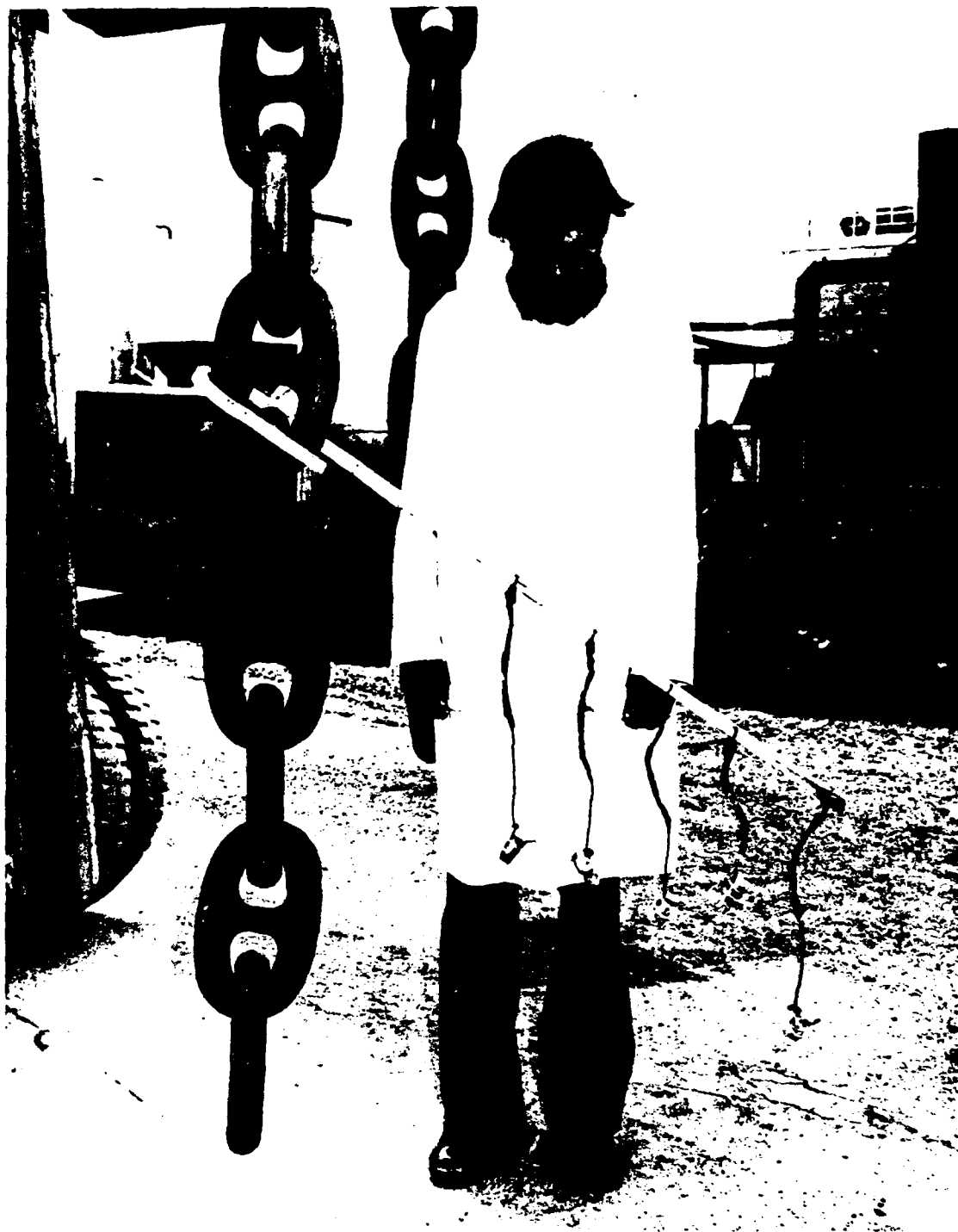


Figure D-1. Arrangement for suspending cement samples from chain of Spheres no. 15 and 16.

Appendix E

MICROSTRUCTURE EXAMINATION OF CONCRETE

by
Prof. P. K. Mehta
University of California, Berkeley

The results of a microstructure examination of the concrete samples listed in Table E-1 are summarized below.

Aggregate pieces from the concrete were carefully separated as much as possible before crushing and grinding the remainder of the sample for x-ray diffraction analysis. All x-ray diffraction analysis work was conducted at 40 kV, 35 mA Cu $k\alpha$.

There was no evidence of unhydrated cement compounds in any of the specimens. This showed that the cement was more or less completely hydrated. All the samples showed substantial amounts of calcium hydroxide, thus indicating that the hardened cement pastes were undamaged in every case. Since large peaks due to quartz and

feldspar emanating from sand were also present, it was not possible to make any estimate of the relative quantities of calcium hydroxide in the different specimens. Concrete samples no. A, B, and C showed small peaks due to ettringite. In no case were peaks large enough to draw any conclusions. Concrete sample no. A (piece from wall of sphere no. 12) differed only in one respect from the others. It showed two small peaks, 2.54 Å and 2.16 Å, which are possibly due to the presence of calcium carboaluminate hydrates. However, these peaks are not very large, and all major peaks due to carboaluminate hydrates were not present. Therefore, it is concluded that the concrete has remained essentially unaltered.

Table E-1. Concrete Samples for Microstructure Examination

Sample No.	Sample Description	Curing History
A	Piece of uncoated wall from hemisphere W-32, which was part of Sphere no. 12.	5.3 yr at 2,790 ft in the ocean
B	Piece of concrete block that was attached to Sphere no. 12. Concrete was from same batch as that of hemisphere W-32.	5.3 yr at 2,790 ft in the ocean
C	Piece of control cylinder that corresponded to hemisphere W-32.	Fog curing, 100% RH, 73°F for 5.6 yr
D	Piece of concrete block that remained exposed to on-land field conditions. Concrete was from same batch as that of hemisphere W-29 (other hemisphere to Sphere no. 12).	Field-cured on land, 150 ft from ocean for 5.6 yr
E	Piece of coated wall from hemisphere W-26, which was part of Sphere no. 13.	5.3 yr at 2,635 ft in the ocean

DISTRIBUTION LIST

ARMY CRREL Library, Hanover NH
 ARMY ENG WATERWAYS EXP STA Library, Vicksburg MS
 BUREAU OF RECLAMATION (J Graham), Denver, CO; G. Smoak, Denver CO
 CNO Code OPNAV 22, Wash DC; Code OPNAV 23, Wash DC; OP-23 (Capt J.H. Howland) Washinton, DC
 COMOCEANSYSPAC SCE, Pearl Harbor HI
 COMSUBDEVGRUONE Operations Offr, San Diego, CA
 DNA (LTCOL J. Galloway), Washington, DC
 DNL Washington DC
 DOE (D Uthus), Arlington, VA; (G. Boyer), Washington, DC; (W. Sherwood) Washington, DC; Dr. Cohen
 DTNSRDC Code 172 (M. Krenzke), Bethesda MD
 DTNSRDC Code 522 (Library), Annapolis MD
 ENVIRONMENTAL PROTECTION AGENCY (Dr. R Dyer), Washington, DC
 MARINE CORPS BASE PWO Camp Lejeune NC
 MARITIME ADMIN (E. Uttridge), Washington, DC
 MCAS CO, Kaneohe Bay HI
 MCRD PWO, San Diego Ca
 NAVCOASTSYSLAB Code 713 (J. Quirk) Panama City, FL; Library Panama City, FL
 NAVEODFAC Code 605, Indian Head MD
 NAVFACENGCOM Code 042 Alexandria, VA; Code 0453 (D. Potter) Alexandria, VA; Code 0454B Alexandria, Va;
 Code 04B (M. Yachnis) Alexandria, VA; Code 04B5 Alexandria, VA
 NAVFACENGCOM - CHES DIV, Code FPO-1 Wash, DC
 NAVOCEANO Code 1600 Bay St. Louis, MS
 NAVOCEANSYSCEN Code 5204 (J. Stachiw), San Diego, CA; San Diego, CA (J. Jennison)
 NAVPGSCOL (Dr. G. Haderlie), Monterey, CA; J. Garrison Monterey CA
 NAVPHIBASE Harbor Clearance Unit Two, Little Creek, VA
 NAVREGMEDCEN SCE, Guam; SCE, Philadelphia PA
 NAVSEASYSKOM (R. Sea), Washington, DC; Code SEA OOC Washington, DC; M. Freund, Washington DC
 NAVSEC Code 6034, Washington DC
 NAVSURFWPCEN J. Honaker, White Oak Lab, Silver Spring, MD
 NAVTECHTRACEN SCE, Pensacola FL
 NAVWARCOL NPT RI President, Newport, RI
 NAVWPNCEN ROICC (Code 702), China Lake CA
 NCBC Code 155, Port Hueneme CA
 NOAA (Dr. T. Mc Guinness) Rockville, MD; (M. Ringenbach), Rockville, MD
 NRL Code 8400 Washington, DC
 NAVOCEANSYSCEN Hawaii Lab (D. Moore), Hawaii; Hawaii Lab (R. Hubbard Jr), Kailua HI
 NUCLEAR REGULATORY COMMISSION T.C. Johnson, Washington, DC
 NUSC Code S332, B-80 (J. Wilcox)
 OCEANAV Mangmt Info Div., Arlington VA
 ONR (Dr. E.A. Silva) Arlington, VA
 SUBRESUNIT OIC Seacliff, San Diego; OIC Turtle, San Diego
 PETRO MARINE ENGINEERS EDI
 U.S. MERCHANT MARINE ACADEMY Kings Point, NY (Reprint Custodian)
 US GEOLOGICAL SURVEY (F Dyhrkopp) Metairie, LA; (R Krah) Marine Oil & Gas Ops, Reston, VA
 USAF SCHOOL OF AEROSPACE MEDICINE Hyperbaric Medicine Div, Brooks AFB, TX
 USNA Ocean Sys. Eng Dept (Dr. Monney) Annapolis, MD; Oceanography Dept (Hoffman) Annapolis MD
 BROOKHAVEN NATL LAB M. Stenberg, Upton NY
 CALIFORNIA STATE UNIVERSITY LONG BEACH, CA (YEN); LOS ANGELES, CA (KIM); Long Beach, CA
 (Kendall)
 CLARKSON COLL OF TECH G. Batson, Potsdam NY
 DAMES & MOORE LIBRARY LOS ANGELES, CA
 DUKE UNIV MEDICAL CENTER B. Muga, Durham NC
 UNIVERSITY OF DELAWARE (Dr. S. Dexter) Lewes, DE
 FLORIDA ATLANTIC UNIVERSITY Boca Raton FL (Ocean Engr Dept
 FLORIDA ATLANTIC UNIVERSITY Boca Raton FL (W. Tessin)

FLORIDA ATLANTIC UNIVERSITY W. Hartt, Boca Raton FL
 FLORIDA TECHNOLOGICAL UNIVERSITY (J Schwalbe) Melbourne, FL
 GEORGIA INSTITUTE OF TECHNOLOGY Atlanta GA (School of Civil Engr., Kahn)
 HOUSTON UNIVERSITY OF (Dr. R.H. Brown) Houston, TX; (Dr. T Yamamoto) Houston, TX
 INSTITUTE OF MARINE SCIENCES Dir. Port Aransas TX
 JOHNS HOPKINS UNIV Rsch Lib, Baltimore MD
 LEHIGH UNIVERSITY BETHLEHEM, PA (MARINE GEOTECHNICAL LAB., RICHARDS); Bethlehem PA
 (Fritz Engr. Lab No. 13, Beedle); D. Chen, Bethlehem PA
 LIBRARY OF CONGRESS WASHINGTON, DC (SCIENCES & TECH DIV)
 MAINE MARITIME ACADEMY (Wyman) Castine ME
 MIT Cambridge MA
 NATL ACADEMY OF ENG. ALEXANDRIA, VA (SEARLE, JR.)
 NORTHWESTERN UNIV Z.P. Bazant Evanston IL
 UNIV. NOTRE DAME Katona, Notre Dame, IN
 OKLAHOMA STATE UNIV (J.P. Lloyd) Stillwater, OK
 MUSEUM OF NATL HISTORY San Diego, CA (Dr. E. Schulenberger)
 SCRIPPS INSTITUTE OF OCEANOGRAPHY San Diego, CA (Marina Phy. Lab. Spiess)
 SEATTLE U Prof Schwaegler Seattle WA
 SOUTHWEST RSCH INST R. DeHart, San Antonio TX
 STANFORD UNIVERSITY Stanford CA (Gene)
 STATE UNIVERSITY OF NEW YORK (Dr. H. Herman) Stony Brook, NY
 TEXAS A&M UNIVERSITY College Station, TX Depts of Ocean, & Meteor; W.B. Ledbetter College Station, TX
 UNIVERSITY OF CALIFORNIA Berkeley CA (B. Bresler); Berkeley CA (D.Pirtz); Berkeley CA (Dept of Naval
 Arch.); Engr Lib., Berkeley CA; M. Duncan, Berkeley CA; P. Mehta, Berkeley CA
 UNIVERSITY OF DELAWARE LEWES, DE (DIR. OF MARINE OPERATIONS, INDERBITZEN); Newark, DE
 (Dept of Civil Engineering, Chesson)
 UNIVERSITY OF HAWAII Honolulu HI (Dr. Szilard)
 UNIVERSITY OF ILLINOIS Metz Ref Rm. Urbana IL; URBANA, IL (NEWARK); Urbana IL (CE Dept. W.
 Gamble)
 UNIVERSITY OF MASSACHUSETTS (Heronemus), Amherst MA CE Dept
 UNIVERSITY OF MICHIGAN Ann Arbor MI (G. Berg); Ann Arbor MI (Richart).
 UNIVERSITY OF NEW HAMPSHIRE DURHAM, NH (LAVOIE)
 UNIVERSITY OF TEXAS AT AUSTIN Austin, TX (Breen)
 UNIVERSITY OF TEXAS MEDICAL BRANCH (Dr. R.L. Yuan) Arlington, TX
 UNIVERSITY OF WASHINGTON (Dr. N. Hawkins) Seattle, WA; Dept of Civil Engr (Dr. Mattock), Seattle WA;
 Seattle WA (E. Linger)
 WOODS HOLE OCEANOGRAPHIC INST. Doc Lib LO-206, Woods Hole MA
 AGBABIAN ASSOC. C. Bagge, El Segundo CA
 ALFRED A. YEE & ASSOC. A. Yee, Honolulu HI
 AMERICAN BUR OF SHIPPING (S Stiensen) New York, NY
 APPLIED TECH COUNCIL R. Scholl, Palo Alto CA
 ARVID GRANT OLYMPIA, WA
 AUSTRALIA A. Eddie, Victoria
 BECHTEL CORP. R. Leonard, San Francisco CA
 BECHTEL INC. San Francisco CA (S. Beckowich)
 BELGIUM Gent (N. De Meyer); HAECON, N.V., Gent
 BRAND INDUS SERV INC. J. Buehler, Hacienda Heights CA
 CANADA (Dr. D.V. Reddy), Newfoundland; Library, Calgary, Alberta; Lockheed Petro. Serv. Ltd, New Westminster
 B.C.; Surveyor, Nenninger & Chenevert Inc., Montreal; W. German, Montreal, Quebec
 CF BRAUN CO Du Bouchet, Murray Hill, NJ
 CHAS. TL MAIN, INC. (R.C. Goyette), Portland, OR
 COLUMBIA GULF TRANSMISSION CO. HOUSTON, TX (ENG. LIB.)
 CONCRETE TECHNOLOGY CORP. TACOMA, WA (ANDERSON)
 CONRAD ASSOC. Van Nuys CA (W. Gates)
 CONTINENT OIL CO O. Maxson, Ponca City, OK
 DENMARK E. Wulff, Svenborg
 DILLINGHAM PRECAST F. McHale, Honolulu HI
 DIXIE DIVING CENTER Decatur, GA
 EXXON PRODUCTION RESEARCH CO Houston, TX (Chao)

FRANCE (J. Trinh) ST-REMY-LES-CHEVREUSE; (P Ozanne), Brest; Dr. Dutertre, Boulogne; L. Pliskin, Paris; P. Jensen, Boulogne; P. Xercavins, Europe Etudes; Roger LaCroix, Paris
 GERMANY C. Finsterwalder, Sapporobogen 6-8
 GLOBAL ASSOCIATES Engr Dept (Scott), Kwajalein
 GULF RAD. TECH. San Diego CA (B. Williams)
 INDIA Shri J. Bodhe, Fort Bombay
 IRELAND P.F. Daly, Dublin
 ITALY M. Caironi, Milan; Torino (F. Levi)
 JAPAN (Dr. T. Asama), Tokyo; M. Kokubu, Tokyo; S. Inomata, Tokyo; S. Shiraishi, Tokyo
 LIN OFFSHORE ENGRG P. Chow, San Francisco CA
 LOCKHEED MISSILES & SPACE CO. INC. L. Trimble, Sunnyvale CA; Mgr Naval Arch & Mar Eng Sunnyvale, CA
 MC CLELLAND ENGINEERS INC Houston TX (B. McClelland)
 MEXICO R. Cardenas
 MOBIL R & D CORP (J Hubbard), Dallas, TX
 NEW ZEALAND New Zealand Concrete Research Assoc. (Librarian), Porirua
 NOLLE, DENTON & ASSOC, INC. (Dr. M Sharples) Houston, TX
 NORWAY E. Gjørvi, Trondheim; F. Manning, Stavanger; J. Creed, Ski; Norwegian Tech Univ (Brandtzaeg), Trondheim; P.S. Hafskjold, Oslo; R. Sletten, Oslo; S. Fjeld, Oslo; Siv Ing Knut Hove, Oslo
 OFFSHORE POWER SYS (S N Pagay) Jacksonville, FL
 PACIFIC MARINE TECHNOLOGY Long Beach, CA (Wagner)
 PORTLAND CEMENT ASSOC. (Dr. E. Hognestad) Skokie, IL; SKOKIE, IL (CORELY); Skokie IL (Rsch & Dev Lib. Lib.)
 PRESTRESSED CONCRETE INST C. Freyermuth, Chicago IL
 SANDIA LABORATORIES (Dr. D.R. Anderson) Albuquerque, NM
 SCHUPACK ASSOC SO. NORWALK, CT (SCHUPACK)
 SHELL OIL CO. HOUSTON, TX (WARRINGTON); I. Boaz, Houston TX
 SOUTH AMERICA B. Contarini, Rio de Janeiro, Brazil; N. Nouel, Valencia, Venezuela
 SPAIN D. Alfredo Paez, Algorta
 SWEDEN Cement & Concrete Research Inst., Stockholm; GeoTech Inst; K. Christenson, Stockholm; Kurt Eriksson, Stockholm
 THE NETHERLANDS Ir Van Loenen, Beverwijk; J. Slagter, Driebergen
 TRW SYSTEMS REDONDO BEACH, CA (DAI)
 UNITED KINGDOM (D. Faulkner) Glasgow, Scotland; (Dr. F.K. Garas), Middlesex; (Dr. P. Montague) Manchester, England; (H.W. Baker) Glasgow, Scotland; (M E W Jones) Glasgow, Scotland; (M J Collard), London; A. Denton, London; British Embassy (Info. Offr), Washington DC; Cambridge U (Dr. C. Morley) Cambridge, GB; Cement & Concrete Assoc Wexham Springs, Slough Bucks; Cement & Concrete Assoc. (Lit. Ex), Bucks; Cement Marketing Co. Ltd. (Brittain) London; D. Lee, London; J. Derrington, London; Library, Bristol; P. Shaw, London; R. Browne, Southall, Middlesex; Sunderland Polytechnic (A.L. Marshall), Great Britain; T. Ridley, London; Taylor, Woodrow Constr (Stubbs), Southall, Middlesex; Univ. of Bristol (R. Morgan), Bristol; W. Crozier, Wexham Springs; Watford (Bldg Rsch Sta, F. Grimer)
 WATT BRIAN ASSOC INC. Houston, TX
 WOODWARD-CLYDE CONSULTANTS PLYMOUTH MEETING PA (CROSS, III)
 BROWN, ROBERT University, AL
 DOBROWOLSKI, J. A. Altadena, CA
 GERWICK, BEN C. JR San Francisco, CA
 JEFFREY LAYTON Bellevue WA
 LAYTON Redmond, WA
 NORWAY B. Nordby, Oslo
 WATT BRIAN ASSOC INC. Houston, TX
 WESTCOTT WM Miami, FL
 WM TALBOT Orange CA

TN-1760

HANDBOOK FOR DESIGN OF UNDERSEA, PRESSURE-RESISTANT CONCRETE STRUCTURES

by

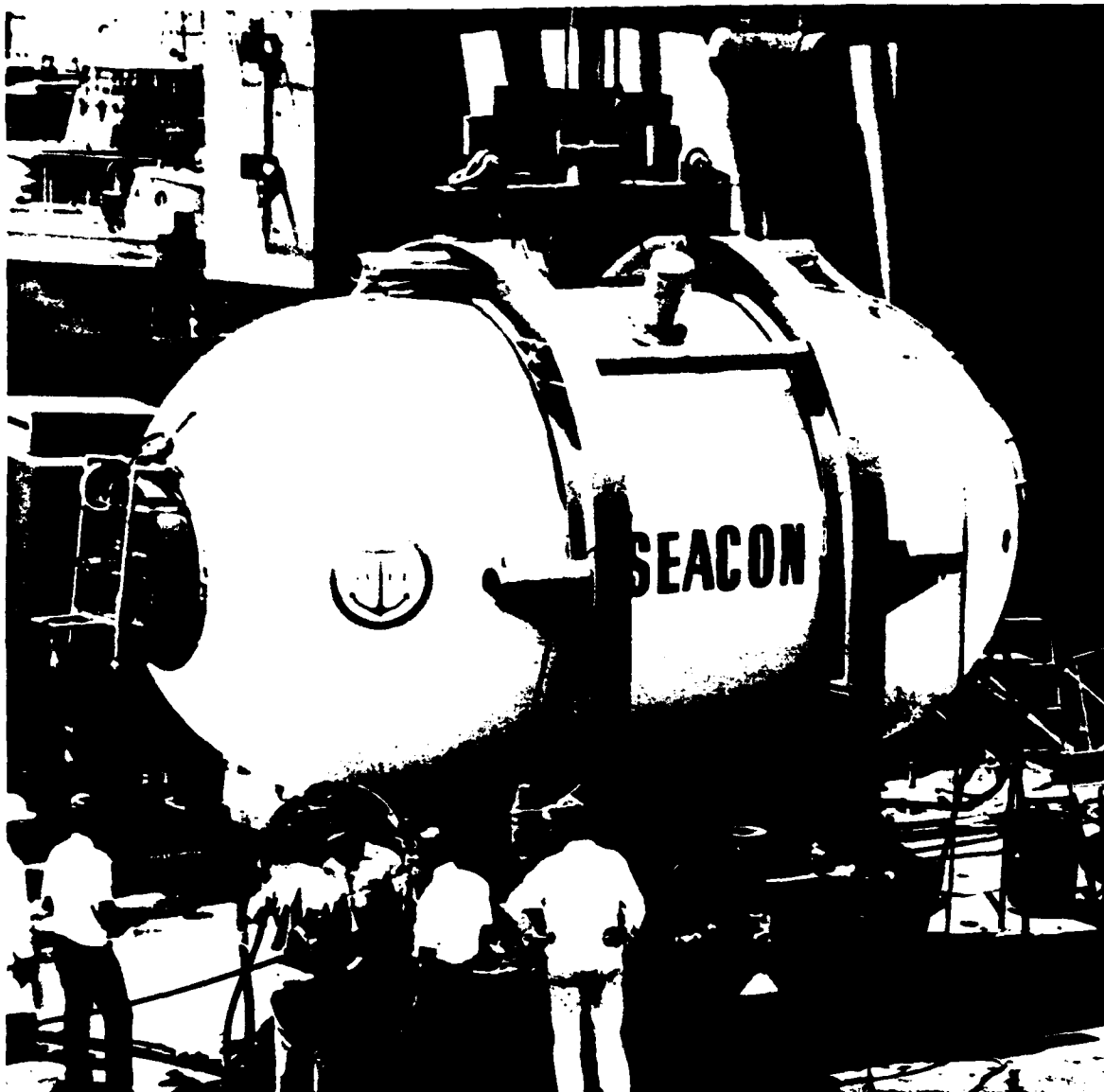
H. H. Haynes and R. D. Rail

October 1986
(First published September 1976)

DEEP OCEAN TECHNOLOGY

NAVAL CIVIL ENGINEERING LABORATORY
PORT HUENEME, CALIFORNIA 93043

Approved for public release; distribution unlimited.



Frontispiece: Concrete cylinder experimental structure, 10-foot OD by 20-foot overall length by 9.5-inch wall thickness, placed on the seafloor at 600-foot water depth for 10.5 months.

Unclassified

SECURITY CLASSIFICATION OF THIS PAGE (When Data Entered)

REPORT DOCUMENTATION PAGE		READ INSTRUCTIONS BEFORE COMPLETING FORM
1 REPORT NUMBER TN-1760	2 GOVT ACCESSION NO. DN044053	3 RECIPIENT'S CATALOG NUMBER
4 TITLE (and Subtitle) HANDBOOK FOR DESIGN OF UNDERSEA, PRESSURE-RESISTANT CONCRETE STRUCTURES		5 TYPE OF REPORT & PERIOD COVERED Not final; Sep 1976 - Jan 1985
		6 PERFORMING ORG. REPORT NUMBER
7 AUTHOR(s) H. H. Haynes and R. D. Rail		8 CONTRACT OR GRANT NUMBER(s)
9 PERFORMING ORGANIZATION NAME AND ADDRESS NAVAL CIVIL ENGINEERING LABORATORY Port Huene, California 93043-5003		10 PROGRAM ELEMENT, PROJECT, TASK AREA & WORK UNIT NUMBERS 63713N; S0397 3.1610-1
11 CONTROLLING OFFICE NAME AND ADDRESS Naval Facilities Engineering Command Alexandria, Virginia 22332		12 REPORT DATE October 1986
		13 NUMBER OF PAGES 97
14 MONITORING AGENCY NAME & ADDRESS (if different from Controlling Office) Naval Sea Systems Command Washington, DC 20362		15 SECURITY CLASS (of this report) Unclassified
		15a DECLASSIFICATION DOWNGRADING SCHEDULE
16 DISTRIBUTION STATEMENT (of this Report) Approved for public release; distribution unlimited.		
17 DISTRIBUTION STATEMENT (of the abstract entered in Block 20, if different from Report)		
18 SUPPLEMENTARY NOTES		
19 KEY WORDS (Continue on reverse side if necessary and identify by block number) Concrete structures, pressure-resistant structures, concrete spheres, concrete cylinders, submerged concrete structures, undersea structures, long-term loading, unreinforced concrete, compressive strength, cyclic loading, implosion, failure mode, durability, structural design		
20 ABSTRACT (Continue on reverse side if necessary and identify by block number) This handbook summarizes the development of concrete pressure-resistant structures for ocean applications and presents the results in the form of design guidelines. The guidelines are based primarily on test results from laboratory and ocean investi- gations of model concrete structures conducted at NCEL over the past two decades; the guides are principally for designing cylindrical and spherical plain (unreinforced) concrete structures to resist the externally applied pressures of hydrostatic loads and thus to be safe		

DD FORM 1473
1 JAN 73

EDITION OF 1 NOV 65 IS OBSOLETE

Unclassified

continued

SECURITY CLASSIFICATION OF THIS PAGE (When Data Entered)

Unclassified

SECURITY CLASSIFICATION OF THIS PAGE(When Data Entered)

20. Continued

from implosion failure. Thin-walled and thick-walled structures are considered.

For predicting implosion pressure of thin-walled cylinders, buckling expressions by Donnell for moderately long cylinders and by Bresse for long cylinders are simplified by incorporating experimentally determined numerical values for the modulus of elasticity and Poisson's ratio of high strength concrete and then modified by an empirically determined plasticity reduction factor. For thin-walled spheres, a conservative buckling expression was developed.

The design approach for predicting implosion pressures of thick-walled cylinders and spheres is based on material failure in the wall of the structure; the predicted failure stress in the structure is related to the standard concrete compressive strength, f'_c , by empirically derived strength increase factors.

Library Card

Naval Civil Engineering Laboratory
HANDBOOK FOR DESIGN OF UNDERSEA, PRESSURE-RESISTANT
CONCRETE STRUCTURES, by H.H. Haynes and R.D. Rail
TN-1760 97 pp illus October 1986 Unclassified

1. Pressure-resistant structures

2. Concrete spheres

I. 3.1610-1

This handbook summarizes the development of concrete pressure-resistant structures for ocean applications and presents the results in the form of design guidelines. The guidelines are based primarily on test results from laboratory and ocean investigations of model concrete structures conducted at NCEL over the past two decades; the guides are principally for designing cylindrical and spherical plain (unreinforced) concrete structures to resist the externally applied pressures of hydrostatic loads and thus to be safe from implosion failure. Thin-walled and thick-walled structures are considered. For predicting implosion pressures of thin-walled cylinders, buckling expressions by Donnell for moderately long cylinders and by Bresse for long cylinders are simplified by incorporating experimentally determined numerical values for the modulus of elasticity and Poisson's ratio of high strength concrete and then modified by an empirically determined plasticity reduction factor. For thin-walled spheres, a conservative buckling expression was developed.

The design approach for predicting implosion pressures of thick-walled cylinders and spheres is based on material failure in the wall of the structure; the predicted failure stress in the structure is related to the standard concrete compressive strength, f'_c , by empirically derived strength increase factors.

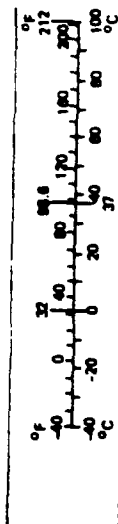
Unclassified

SECURITY CLASSIFICATION OF THIS PAGE(When Data Entered)

CONVERSION FACTORS—INCH-POUND TO SI (METRIC)

Approximate Conversion Factors (E indicates that the factor given is exact)

To convert from	to	multiply by
Length		
inch	millimeter (mm)	25.4 E
foot	meter (m)	0.3048 E
yard	meter (m)	0.9144 E
mile (statute)	kilometer (km)	1.609
Area		
square inch	square centimeter (cm ²)	6.451
square foot	square meter (m ²)	0.0929
square yard	square meter (m ²)	0.8361
Volume (capacity)		
ounce	cubic centimeter (cm ³)	29.57
gallon	cubic meter (m ³)	0.003785
cubic inch	cubic meter (m ³)	16.4
cubic foot	cubic meter (m ³)	0.02832
cubic yard	cubic meter (m ³)	0.7646
Force		
kilogram-force	newton (N)	9.807
kip-force	newton (N)	4448
pound-force	newton (N)	4.448
Pressure or stress (force per area)		
kilogram-force/square meter	pascal (Pa)	9.807
kip-force/square inch (ksi)	megapascal (MPa)	6.895
newton/square meter (N/m ²)	pascal (Pa)	1.000 E
pound-force/square foot	pascal (Pa)	47.88
pound-force/square inch (psi)	kilopascal (kPa)	6.895
Bending moment or torque		
inch-pound-force	newton-meter (Nm)	0.1130
foot-pound-force	newton-meter (Nm)	1.356
meter-kilogram-force	newton-meter (Nm)	9.807
Mass		
ounce-mass (avoirdupois)	gram (g)	28.34
pound-mass (avoirdupois)	kilogram (kg)	0.4536
ton (metric)	megagram (Mg)	1.000
ton (short, 2000 lbm)	megagram (Mg)	0.9072
Mass per volume		
pound-mass/cubic foot	kilogram/cubic meter (kg/m ³)	16.02
pound-mass/cubic yard	kilogram/cubic meter (kg/m ³)	0.5931
pound-mass/gallon	kilogram cubic meter (kg/m ³)	119.8
Temperature		
deg Fahrenheit (F)	deg Celsius (C)	$t_C = (t_F - 32) \times 5/9$
deg Celsius (C)	deg Fahrenheit (F)	$t_F = t_C \times 9/5 + 32$



CONTENTS

	Page
CHAPTER 1. INTRODUCTION	1
1.1 OBJECTIVE	1
1.2 BACKGROUND	2
CHAPTER 2. DESIGN CONSIDERATIONS	5
2.1 CONCRETE MATERIALS	6
2.1.1 Strength	6
2.1.2 Durability	9
2.2 SATURATED CONCRETE	10
2.2.1 Pore Structure of Cement Paste	11
2.2.2 Seawater Absorption	12
2.2.3 Compressive Strength of Saturated Concrete	15
2.2.4 Pressure Cycling Effect	18
2.3 HYDROSTATIC LOADING CONDITIONS	21
2.3.1 Long-Term Loading	21
2.3.2 Cyclic Loading Effect	23
2.3.3 Rapid Loading	25
2.4 REINFORCEMENT	27
2.5 EPOXY ADHESIVE JOINTS	34
2.6 PENETRATIONS	35
2.7 FACTORS OF SAFETY	37
CHAPTER 3. CYLINDRICAL STRUCTURES	39
3.1 THICK-WALLED CYLINDERS	41
3.2 THIN-WALLED CYLINDERS	46
3.2.1 Moderately-Long Cylinders	53
3.2.2 Long Cylinders	54
3.2.3 Out-of-Roundness	55
3.3 DESIGN EXAMPLE, CYLINDRICAL STRUCTURE	58

	Page
CHAPTER 4. SPHERICAL STRUCTURES	61
4.1 THICK-WALLED SPHERE	63
4.2 THIN-WALLED SPHERES	66
4.3 DESIGN EXAMPLE, SPHERICAL STRUCTURE	68
CHAPTER 5. SUMMARY	71
CHAPTER 6. ACKNOWLEDGMENT	73
CHAPTER 7. REFERENCES	75
CHAPTER 8. NOMENCLATURE	83

CHAPTER 1. INTRODUCTION

1.1 OBJECTIVE

This report summarizes the development of concrete pressure-resistant structures for ocean applications and presents the results in the form of design guides. Specifically, the emphasis is on designing concrete spherical and cylindrical structures to withstand implosion failure caused by uniform external hydrostatic pressure loading. Most portions of the design approach are based on experimental data, which have been obtained from laboratory and ocean testing of model concrete structures over the past two decades. Some portions do not have experimental support for the design approach; however, in those cases, extrapolations of the test results have been made in conjunction with theory to give the reader a method for predicting failure that has a quasi-empirical background. This has been done as an alternative to a purely theoretical analysis.

The portions based on experimental studies have been substantially improved in this revised handbook by incorporating additional experimental data and other information obtained in the 10 years since the "Handbook for Design of Undersea, Pressure-Resistant Concrete Structures," was first published in 1976. This is in keeping with the original plan to update the handbook from time-to-time as new information became available. The revisions are included in several ways. For example, information on the uniaxial compressive strength behavior of concrete subjected to long term (to 10.5 years) sustained pressure loading in the ocean, and the behavior of saturated concrete as affected by pore pressure are presented as new sections in Chapter 2. In Chapter 3 an improved method to design cylindrical structures is presented along with simplified design guidelines, for example Figure 3.5. In Chapters 3 and 4, additional data are entered in the curves.

This handbook was prepared as part of the Navy's Deep Ocean Technology Program sponsored by the Naval Sea Systems Command and the Naval Facilities Engineering Command.

1.2 BACKGROUND

In 1966, small model concrete spheres were tested under hydrostatic loading to experimentally determine implosion pressures as compared to theoretically predicted pressures. The results were impressive; for concrete having a uniaxial compressive strength of 10,000 psi, the average circumferential compressive stress in the sphere wall at implosion was 12,500 psi. This 25% higher strength at failure was due, not to any change in the concrete material strength properties, but rather to the geometrical configuration, a sphere, and the loading condition, external hydrostatic pressure. Specifically, the increase in failure strength was the result of the lateral confining stresses caused by the multi-axial compressive loading effects on the wall of the sphere as compared to the uniaxial loading condition of the concrete control specimens (6- x 12-inch cylinders). It was evident from these exploratory tests that concrete could perform well in pressure-resistant undersea structures.

Further studies were conducted on spheres and, later, on cylinders (Ref 1 through 17). The ultimate objectives of the investigations were to determine the maximum depth in the ocean that concrete structures could be safely used and to develop design guides. The results demonstrated the feasibility of near neutrally buoyant concrete structures, having an overall safety factor of three, at depths to 3,000 feet for spheres and 1,500 feet for cylinders. Greater depths are possible if concretes having a compressive strength greater than 10,000 psi are used or if negatively buoyant structures are designed.

During the past 15 years, offshore concrete structures have been used for oil production platforms and storage facilities in the North Sea. This activity has demonstrated the economics and reliability of using concrete in the ocean.

Because of the offshore activity, concrete societies around the world have committed much effort to defining the state-of-the-art and developing recommended standards of practice for concrete ocean structures (Ref 18). The work of these societies will not be repeated herein. As noted this report deals with the special loading case of externally applied hydrostatic pressure. These results have application to concrete floating vessels, offshore platforms, and submerged structures. In addition, hydrostatic pressure loading is a major design load for deep mine shafts and tunnels, and even buried structures subjected to blast overpressures.

Concrete's history is not devoid of examples of submerged pressure-resistant structures. Today many underwater transportation tunnels built of concrete are in operation. A notable example is the BART transbay tube in San Francisco that is 3.5 miles long and located in water 120 feet deep. Interestingly, research related to this report has shown that concrete cylinder structures, such as transportation tubes, can be used to depths 10 times this state-of-the-art depth.

Very large offshore concrete platforms have been built since 1973 for the oil industry in the North Sea. These structures rest on the seafloor with base sections over 300 feet wide and extend above the sea surface with towers having a total height of some 500 feet. The base sections are composed of multiple cells, each cell about 60 feet across and 150 feet high. During construction the cells are employed as pressure-resistant, buoyancy chambers that withstand pressure heads of up to 300 feet. During service the cells are used as oil storage and seawater ballast chambers.

Potential applications in support of military operations are sea-floor storage of fuels, long-term environmental data-gathering stations, and possibly target submarines. Feasibility studies have been conducted on fuel storage facilities (Ref 19) and target submarines (Ref 20). The target submarine study showed that a pressure-resistant hull of concrete would cost 60% that of a similar steel hull.

CHAPTER 2. DESIGN CONSIDERATIONS

The design methods presented in this handbook apply to spherical and cylindrical pressure-resistant structures subjected to hydrostatic loading, that is, to external pressure applied normal to the outside surface of the spheres and cylinders (including both the sides and the ends of the cylinders).

This loading places the wall of the structures in a state of multi-axial compression where the inner surface of the wall is in bi-axial compression and all other portions of the wall are in tri-axial compression. For cylinders, the circumferential (hoop) stress is the largest, the longitudinal (axial) stress is less, and the radial (across the wall) stress is the smallest and varies from zero at the internal surface to the same stress level as the applied pressure at the external surface. In a sphere the circumferential stresses are the same in all great circle directions and, again, the smaller radial stress varies across the wall from zero to the ambient applied pressure.

The applied external pressure is assumed to be uniform in all directions and at all locations on the outer surface of the structure. That is, the difference in hydrostatic head at the top and at the bottom of the structure is small compared to the average hydrostatic head and so is neglected.

Although the dead-weight of the structure itself is an important factor in computing the buoyancy of a structure, it is not included in the stress calculations in these guidelines since it is considered to be small compared to the pressure loading. This was the actual situation in the test programs that produced the data on which the design guidelines are based. Thus, these guidelines can be used for design of concrete structures in which the total pressure is a factor of 20 or greater than the pressure difference between the top and bottom of the

structure. These guidelines do not apply directly to cases in which the top-to-bottom pressure difference is a large percentage (10% or more) of the total pressure, for example, the case of a large structure in relatively shallow water. In such situations these guidelines are useful but must be combined with other approaches to account for the nonsymmetry of loading.

The design guidelines in this handbook are presented in equations and charts. These guidelines provide an initial estimate of the size of a structure for a given depth. Advanced design and analysis techniques must be used to complete a final design, but these techniques need to start from given dimensions. This handbook provides design aids to quickly determine the near final dimensions. It is recommended that, once a structure is sized by these aids and meets the design requirements, a detailed analysis (such as a finite element analysis) be conducted. The analysis should assume a realistic out-of-round geometry and take into account any significant loadings due to dead-weight distribution, pressure differentials, live loads, etc.; it should also model the inelastic behavior of concrete materials.

2.1 CONCRETE MATERIALS

2.1.1 Strength

The compressive strength of concrete, f'_c , used in the design equations of this report is the uniaxial compressive strength of 6- x 12-inch control cylinders tested at the time the structure experiences hydrostatic loading. Because the strength of concrete in the as-loaded condition of an undersea structure is needed, the control cylinders should be tested with the concrete in a wet condition. Mature concrete that has been continuously fog cured is considered to be in a wet condition. If the control cylinders have been cured along with the structure and have become air dried from field exposure, the concrete cylinders should be soaked underwater for 3 days prior to testing. However, as will be explained in following sections, concrete that has

been soaked for 3 days is not necessarily "completely saturated." The strength of concrete in a wet condition is about 10 to 20% lower than concrete in a dry condition (Ref 21). Conversely, concrete in a continuously moist condition will gain in strength with aging; at age 1 year, good quality concrete is approximately 20% stronger than at 28 days.

Information is available on the compressive strength of concrete after long periods of time in a hydrostatic environment as reported in References 15 and 17.

Ocean-exposed concrete blocks (18 x 18 x 14 inches) were retrieved on three occasions: 1 block after 1 year in the ocean, 4 blocks after 5.3 years, and 2 blocks after 10.5 years. Six-inch diameter core samples were taken from the ocean exposed blocks and companion on-land field exposed blocks and then tested, along with fog-room cured cast cylinders, for compressive strength, modulus of elasticity, and Poisson's ratio. Drilled cores are, in general, weaker in compressive strength than cast cylinders of the same concrete; for the following strength comparisons the core strengths are adjusted by increasing the measured core strength by 7% as discussed in Reference 15.

The results are summarized in Figure 2.1, which shows the relative strengths of the concrete in the three environments at total ages of 1.3, 5.6, and 10.8 years. The relative strength is the ratio of the compressive strength of the concrete at a given total age compared to the compressive strength at 28 days of fog-cured specimens.

The continuously fog-cured specimens increased in strength by 23% at 1.3 years, to 35% above the baseline strength at 5.6 years of age, and were still at 35% at 10.8 years. This pattern of rapid strength gain at early ages and then slower gain and a tendency to level off at later ages is typical of concrete.

The on-land field-exposed concrete, tested in the air-dried condition, showed a similar but smaller gain to 5.6 years, as expected, but indicated a loss of strength during the second 5-year period. This drop, which was not expected, may have been due to differences in the concrete's moisture content, due in turn to the outdoor conditions, especially relative humidity and temperature, which varied considerably

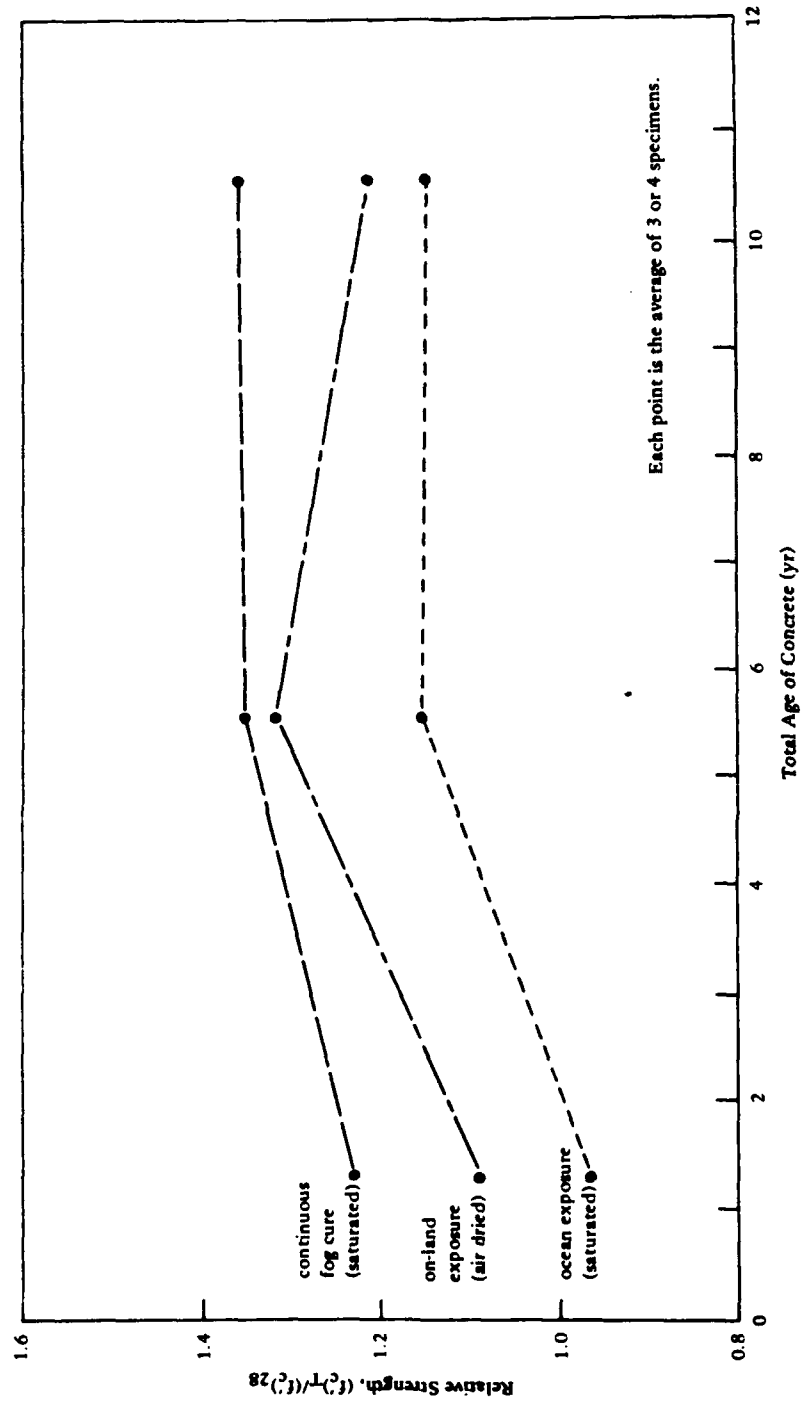


Figure 2.1 Effect of long-term exposure environment on relative compressive strength.*

- * Relative strength is the ratio of the compressive strength of concrete at a given total age after exposure in a given environment compared to the compressive strength of the concrete after 28 days of standard cure in a fog room.

on a daily as well as seasonal basis in contrast to the fog room and the in-ocean conditions which were constant throughout the exposure period.

The most interesting findings are, of course, those of the ocean-exposed concrete. This concrete showed a decrease in strength on first being placed in the ocean. This decrease results from the concrete changing from an air-dry condition at the time of deployment (after its initial 28-day cure the concrete was stored outdoors for several months until deployment) to a saturated condition in the ocean. It is well known that the uniaxial compressive strength of wet (saturated) concrete is 10% or more lower than otherwise comparable dry concrete. However, after the initial loss in strength, the concrete continued to cure in the ocean and gain strength. At 1.3 years age its strength was approximately the same as the reference concrete, by 5.6 years total age it was 15% above the baseline strength, and was still at the same strength level at 10.8 years age. Thus, the ocean exposed concrete, after an initial loss, gained strength and then leveled off at the later age, much the same as the reference fog-cured concrete, but at a lower attained strength.

Thus, for predicting strength changes in saturated concrete in the ocean, the data to date indicate that the strength increase of ocean-exposed concrete relative to the 28-day, fog-cured strength is zero at the end of 1 year, 5% at 2 years, and 15% at 5 to 10 years (Ref 17).

2.1.2 Durability

Good quality concrete that is completely submerged in seawater usually does not experience problems of steel reinforcement corrosion. The seawater that eventually surrounds the reinforcing steel becomes oxygen depleted, and the high pH environment supplied by the cement and the products of hydration of the cement, especially Ca(OH)_2 , acts as an effective method of retarding corrosion.

A potential problem exists in pressure-resistant structures where the interior contains air. Oxygen has access to the walls from inside the structure. Also, the chloride content in the concrete can increase from salts deposited by seawater evaporating on the inside surface thus

promoting corrosion. These problems are accentuated for concrete in the intertidal and splash zones, which are surely the worst environmental conditions to design for durability.

Design criteria include using cement with a suitable tricalcium aluminate (C_3A) content, using concrete with low permeability, and enough concrete cover for the reinforcing steel. The C_3A content should be above 5% but should not exceed 10%, because then the concrete may become vulnerable to deterioration by sulfate attack (Ref 18). Portland cements that meet these specifications are usually Type II or Type V; however, the mill specifications should be used to determine the actual C_3A content. Low permeability is attained for concrete by using: (1) a cement content of 675 lb/yd³ or greater (do not exceed 840 lb/yd³ because of shrinkage or heat hydration problems), (2) a water-to-cement ratio of less than 0.45 (and preferably 0.40 or less), and (3) vigorous but not excessive vibration. The use of pozzolans will also help reduce permeability; however pozzolans should be used only after tests have been made to indicate that there is improved sulphate resistance of the concrete and no decrease in corrosion resistance of reinforcing steel (if present). The recommended concrete cover is 2.5 inches on reinforcing steel and 4 inches on prestressing steel. For specific cases, the cover can be reduced by considering aggregate size, bar diameter, cement factor, water-to-cement ratio, workability of fresh concrete, degree of compaction, smoothness of concrete surface, and other factors.

Rock boring mollusks do not usually attack high quality concrete that is made with non-limestone aggregate. As an example, concrete that was located on the ocean side of the Los Angeles Harbor breakwater in California showed only very mild attack by borers after 67 years. In no place had the borers progressed more than 1/4 inch into the surface (Ref 22).

2.2 SATURATED CONCRETE

An understanding of the pore structure of cement paste helps to understand the behavior of saturated concrete.

2.2.1 Pore Structure of Cement Paste

Cement paste composes about 30% of the volume of a good-quality concrete mixture. Because the paste surrounds each aggregate particle and each entrapped or entrained air void, the characteristics of the paste essentially control the permeability of the concrete.

Hardened concrete is a porous material whose void volume is predominately that of the pore space of the cement paste. In general terms, a well-compacted, non-air-entrained concrete (of water-cement ratio 0.40) has a void volume of about 20% at a young age and 14% at a mature age after good curing conditions; the minimum void volume possible is 10%.

Pore size, rather than pore volume, controls the permeability of concrete. In a hardened cement paste, there are essentially two types of pores: capillary pores and gel pores. In a freshly mixed cement paste, the cement particles are rather evenly distributed due to electrostatic repulsion forces. The spaces occupied by the water in the fresh concrete mix are termed the capillary pore spaces; they are interconnected and range in size from 3×10^{-7} inches to 5×10^{-4} inches in diameter (Ref 23). As each cement grain reacts with water, it forms a calcium-silicate-hydrate gel that surrounds the unhydrated portion of the cement grain. With time, fiber-like chains of molecules, called fibrils, develop from the gel coating (Ref 24). The interstices among the fibrils are the gel pores. Gel pores are extremely small, from 4×10^{-8} inches to 3×10^{-7} inches in diameter.

After a cement grain has fully hydrated, the bulk volume of gel is less than the combined volume of the water and cement from which the gel is formed, but is larger (requires 120% more volume) than the original size of the cement grain (Ref 25). The expansion moves into capillary pores. Thus as hydration occurs, the capillary pore volume decreases while the gel volume (and thus the gel pore volume) is created.

Theoretically, if the original water-cement ratio for a paste were 0.38 or less, the entire capillary pore volume would become occupied with gel. The formation of gel within capillary pores increases tremendously the resistance of water molecules moving through the capillary pores. Excellent permeability characteristics arise for concretes made

with water-cement ratios of 0.40 or less because the capillary pores are essentially interrupted or filled by gel.

2.2.2 Seawater Absorption

A major significance of seawater absorption is that large concrete structures can gain in weight by hundreds of tons over long periods of time. Designers may need to consider this factor for certain types of floating, submerged, or relocatable concrete structures.

Two concrete mixtures were tested for seawater absorption (Ref 26). The first mix was a high-quality concrete having a water-cement ratio of 0.39, and a uniaxial compressive strength of 7,380 psi at 28 days. The second mix was a medium-quality concrete of unknown water-cement ratio (about 0.55); the compressive strength was 4,550 psi at 28 days. Specimens of the high quality concrete mix cured for 3.3 years in two different environments: some were exposed continuously in a controlled moist room environment and some to an outdoor environment. The medium-quality concrete was continuously fog cured and the absorption test started at an age of 19 days.

The specimens, which were 6- x 12-inch control cylinders, were subjected to a pressure head of 550 feet and the absorption of seawater was monitored by measuring the quantity of water added to the pressure vessel.

The results of the fog-cured specimens are shown in Figure 2.2. During 8 days time at sustained pressure, the mature high-quality concrete absorbed a negligible amount of seawater. During a similar length of time, the young medium-quality concrete absorbed about 1.1% by weight and then lost about 13% of the absorbed seawater when the pressure was removed and some internal gases expanded.*

Figure 2.3 shows the data for the mature, high-quality concrete that was field-cured for 3.3 years. After 15 days soaking at 0-foot

*No specimens were evacuated in any of the test programs because that condition is unnatural for usual concrete applications in the ocean.

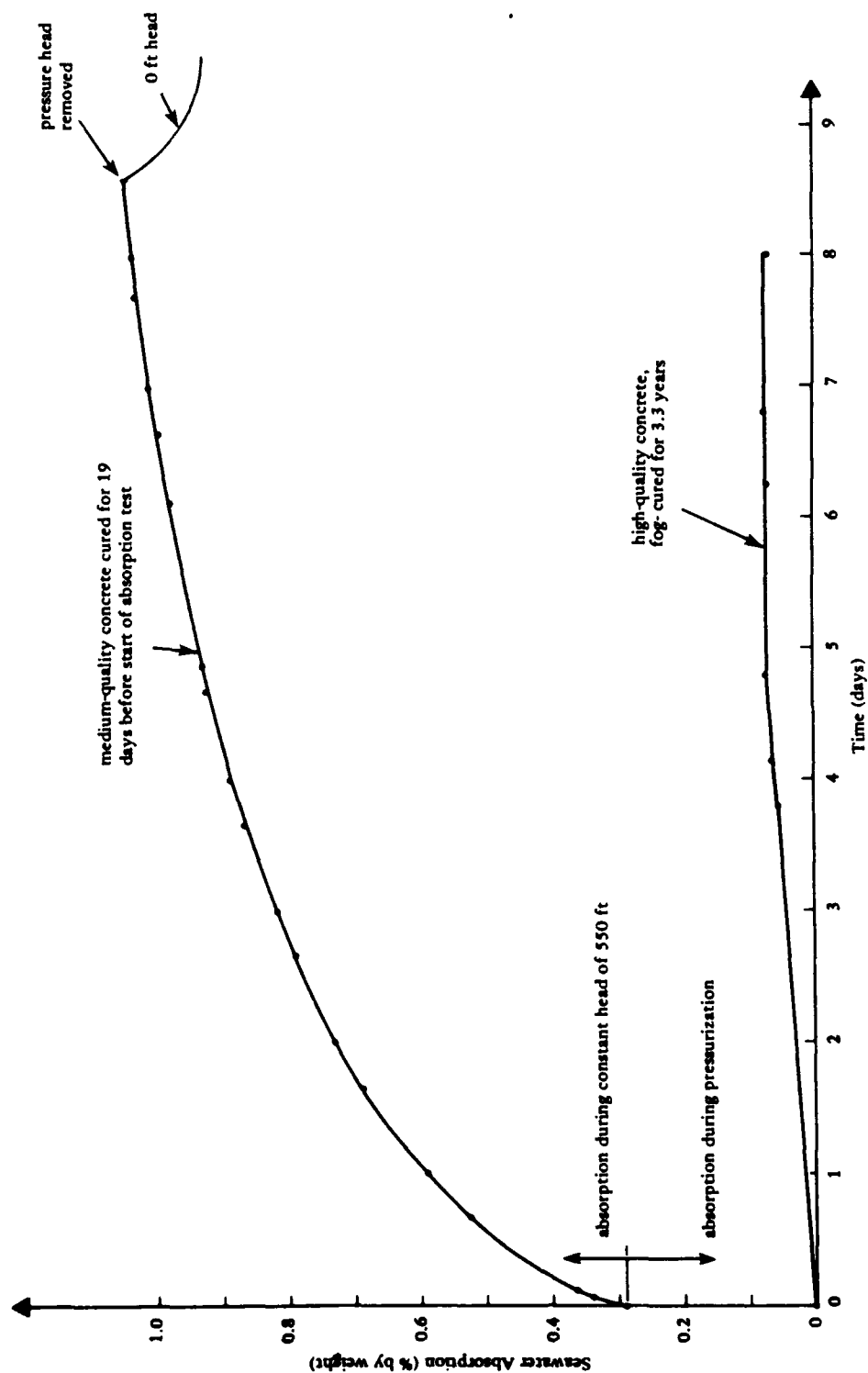


Figure 2.2 Seawater absorption of fog-cured concrete as a function of time under a constant pressure head of 550 feet.

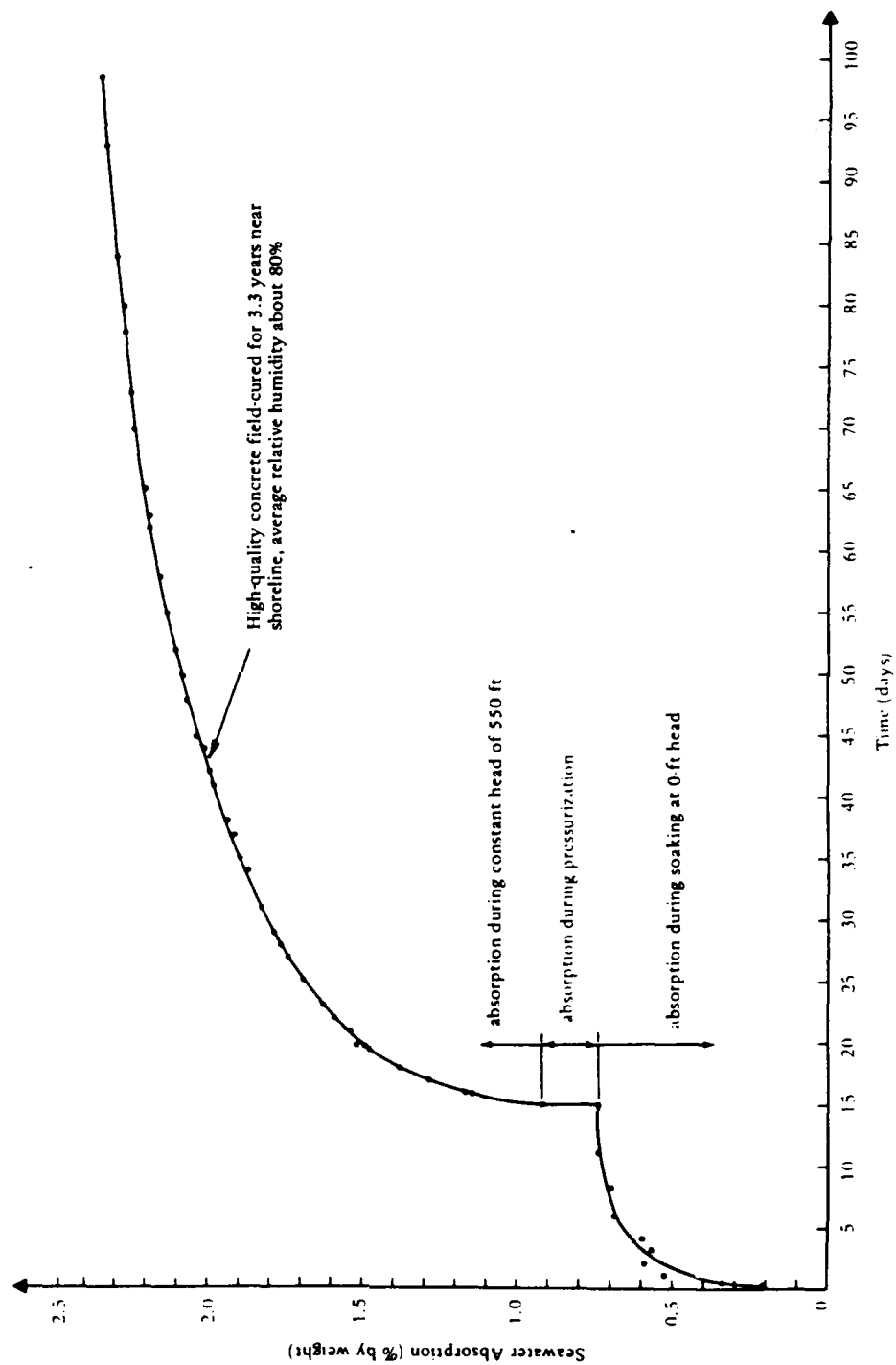


Figure 2.3 Seawater absorption of field-cured concrete as a function of time under a constant pressure head of 550 ft.

head, the concrete appeared to be saturated, but actually was not since more water was absorbed at a 550-foot head. This demonstrates water moving into the gel pores.

The data also illustrate the difficulty of defining "saturated" concrete. At different pressure heads, concrete may become apparently "saturated," yet some gel pores can still be empty.

2.2.3 Compressive Strength of Saturated Concrete

Two types of investigations were conducted on the compressive strength of saturated concrete. During the first investigation mature, high-quality hardened concrete was put into a pressure vessel to saturate the material and then, while at the saturation pressure, a uniaxial compression test (Ref 26) was conducted. During the second investigation freshly mixed concrete, of both high and low strength mixtures, was put into a seawater environment to cure and eventually be tested in uniaxial compression while under the saturation pressure (Ref 27).

The first investigation used a concrete of water-cement ratio of 0.51 and a uniaxial compressive strength of 6,630 psi at 28 days. Specimens were fog cured for 128 days before being placed at pressure heads of 1 foot, 500 feet, and 20,000 feet for about 60 days. The pressure was cycled 4 to 6 times for the 500-foot and 20,000-foot specimens to assist in saturating the concrete.

The results are shown in Figure 2.4. Only the 20,000-foot specimens showed a statistically significant difference in compressive strength from that of the fog-cured specimens. A 10% decrease was recorded. The decrease is attributed to pore pressure build up during the uniaxial test. Under uniaxial load, the change in total volume of the specimen requires that some water be expelled from the specimen. If the rate of loading is faster than internal water can exit the concrete, then a positive pore pressure will develop which can cause a decrease in compressive strength.

The 500-foot specimens showed a 6% increase in strength. The increase could have been due to empty pore space causing the specimen to act as if it were under a small triaxial load from the pressure environment. The 500-foot specimens were not saturated.

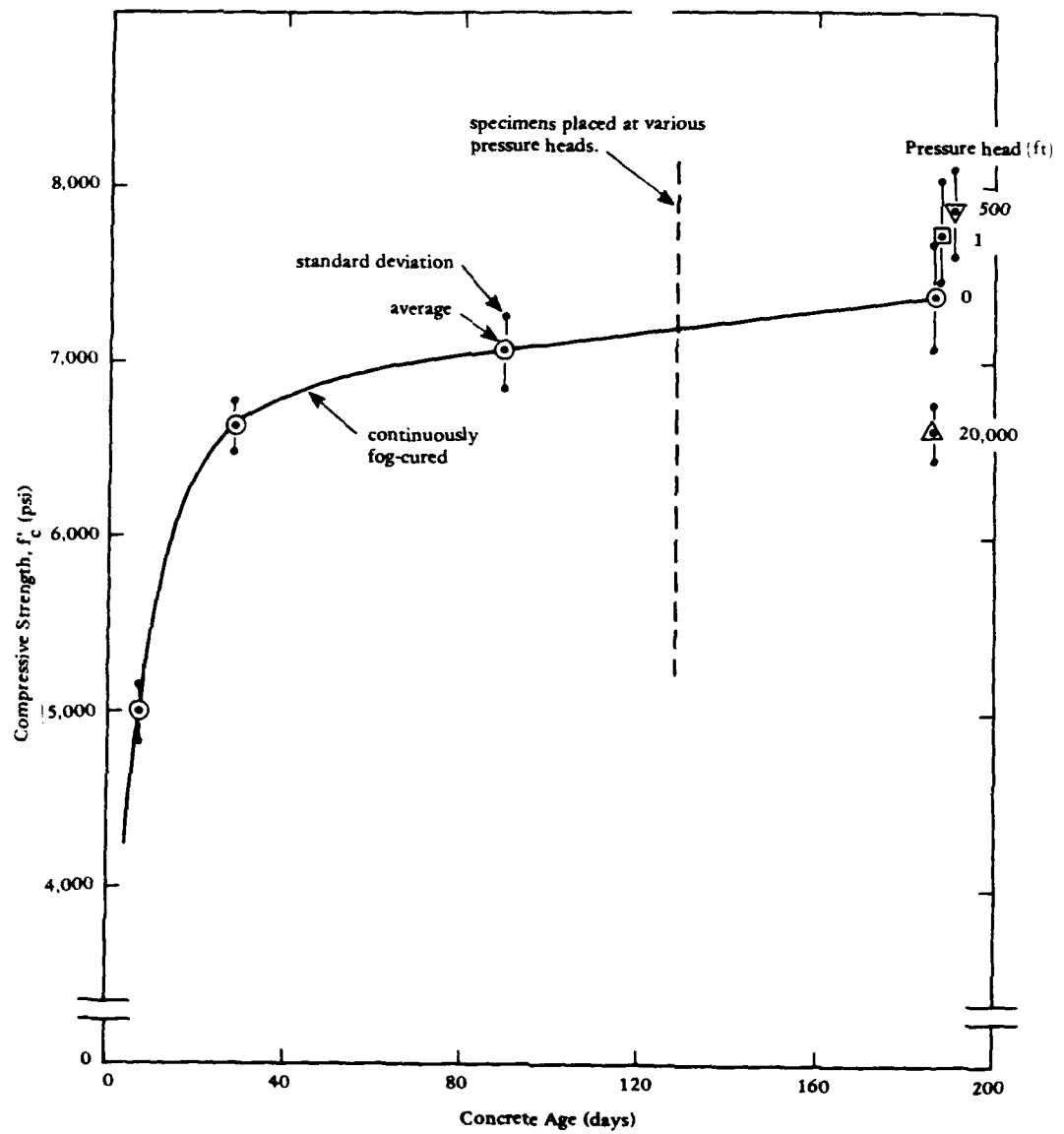


Figure 2.4 Uniaxial compressive strength of concrete tested at various pressure heads.

For the second investigation, specimens of a low-strength concrete mix, which had a water-cement ratio of 0.66 and uniaxial compressive strength of 3,000 psi at 28 days, and a high-strength mix of water-cement ratio of 0.46 and strength of 6,060 psi at 28 days, were placed on the seafloor at a depth of 1,830 feet within 3 hours after mixing before the initial set of the concrete had occurred. After curing in the ocean at 42°F for 11 months, some specimens were returned to the Laboratory, placed again at a pressure head of 1,830 feet for a hold period and then tested under uniaxial compression while at that pressure head. Companion specimens were cured in a fog room at 73°F and others in a tank of continuously circulating fresh seawater at a head of 6 feet at an average of 66°F.

Briefly, the results showed the low-strength concrete increased in uniaxial compressive strength, as compared to the 28-day fog-cured strength, by 28, 28, and 24%, respectively, after 10.8 months of curing in a fog room, 10.2 months in a seawater tank, and 11 months in a deep-ocean environment at 1,830 feet. The differences in strength are not statistically significant, that is, the deep-ocean concrete had a strength essentially equivalent to that of the fog-room and seawater-tank-cured concrete. The high-strength, fog-cured concrete increased in uniaxial compressive strength, as compared to the 28-day fog-cured strength, by 26, 15, and 9% respectively, after 10.8 months of curing in a fog room, 10.2 months in a seawater tank, and 11 months in a deep-ocean environment at 1,830 feet. In this case the differences in strength were statistically significant.

Another group of specimens were retrieved from the ocean after 5 years on the seafloor at a depth of 2,450 feet and tested in the laboratory along with companion specimens that had been continuously cured for the 5 years in a fog room or under a low head (nominally 6 feet) of seawater.

The various specimens were tested in uniaxial compressive strengths under three different conditions: (1) submerged under seawater at the

same pressure (2,450 feet) as the ocean-exposed specimens, (2) under seawater at a low head, and (3) in normal laboratory atmosphere. The results are shown in Figure 2.5 which supplement the findings at concrete ages of 10 to 11 months.

At 5 years age, the low-strength concrete was nearly the same strength that it had been at 10 to 11 months, that is, the low-strength concrete had, essentially, neither gained nor lost strength in the additional 4 years of exposure in the three environments. On the other hand the high-strength concrete continued to gain strength in all three environments. For example, the ocean-exposed concrete averaged more than 30% stronger at 5 years than at 10 to 11 months.

There are several small differences in the strengths of the concretes cured and/or tested in the various environments. For example the low-strength concrete cured and tested (at 5 years age) under high pressure had an average f'_c of 4,100 psi, which is indicative of a reliable, good quality structural concrete, but is about 10% weaker than the companion concrete cured in the near ideal fog room conditions.

However, the main findings of this test series are that, at a given water/cement ratio and a given age (after the first several weeks), the specimens all had similar strengths whether cured or tested submerged at high pressure, submerged at low pressure, or in the air. The differences in performance are primarily due to the well established principles that higher strength is primarily a function of lower water/cement ratio, and the degree of hydration of cement which is a function of age and normally continues (if curing water is available) at a decreasing rate for a number of months up to more than a year, after which the concrete continues to maintain its achieved strength.

2.2.4 Pressure Cycling Effect

Several tests were conducted where concrete was subjected to pressure cycling and then tested under uniaxial compression. This type of test was of interest because a rapid decrease in ambient pressure results in a rapid change in pore pressure of the concrete, a condition which might harm the concrete.

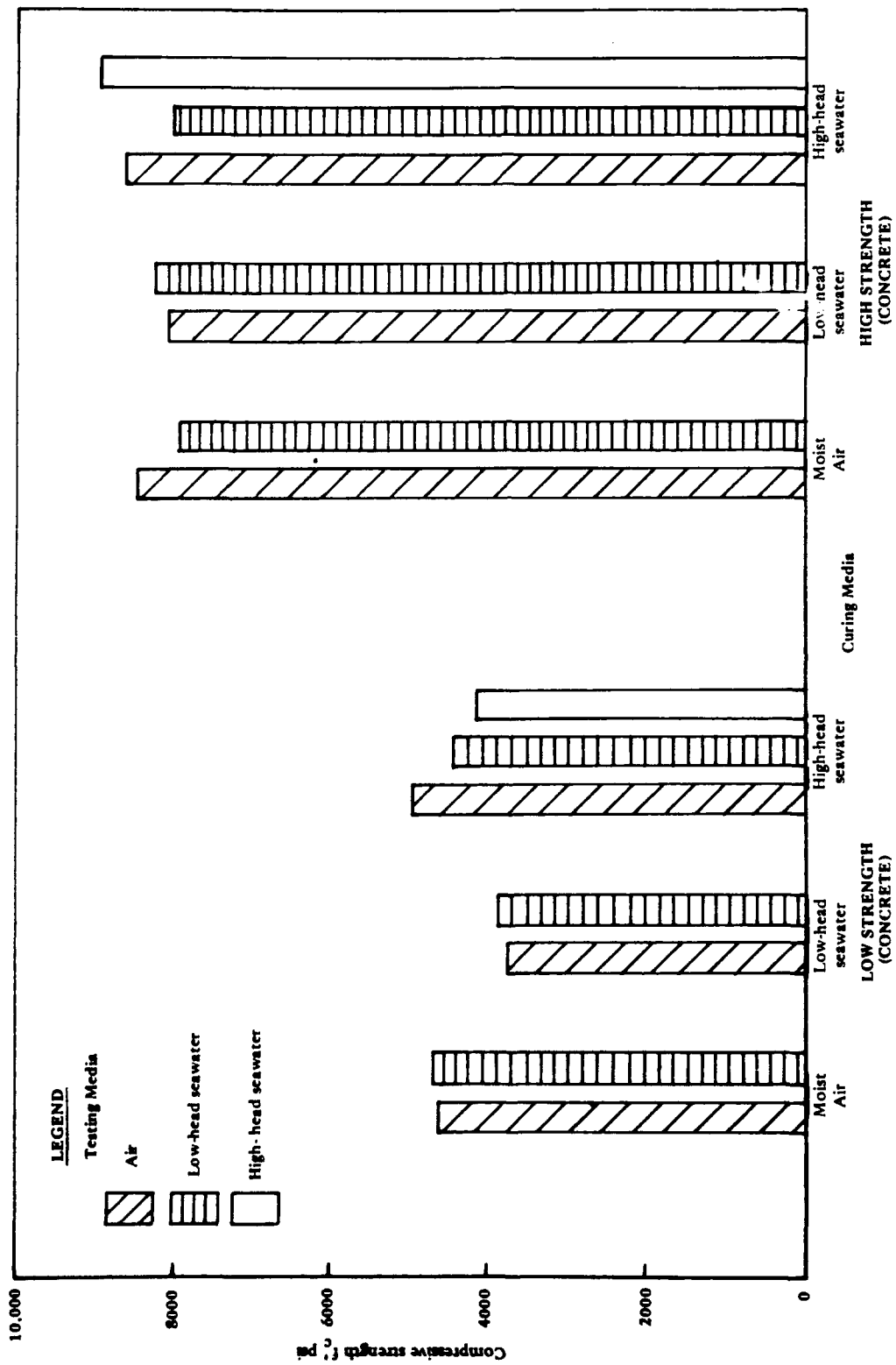


Figure 2.5 Strength of concrete cured and tested in air and seawater at low and high pressure heads.

One test series was part of the program involving freshly mixed concrete placed in the ocean at 1,830 feet. All the specimens, both low-and high-strength mixes, which cured in the ocean for 11 months (and were, therefore, saturated with seawater), underwent three pressure cycles: raised from the seafloor to the surface, placed in a pressure vessel and held at 1,830 feet of head, then removed from the pressure vessel, placed in a compression tester, and then placed back at 1,830 feet of head for the uniaxial test. Each of the pressure cycles was at a rate of 1 foot of head per second (0.4 psi/sec). The strength of these specimens was compared to that of companion specimens that cured in a seawater tank at 6 feet of head. No statistically significant strength differences were observed, so the pressure cycles did not harm the concrete.

Additional ocean-cured specimens of both low- and high-strength mixes were pressure cycled an additional three times at a rate of 10 feet of head per second (4.4 psi/sec). This rate was faster than any concrete structure or object will be raised from the ocean. A practical rate is 1 fps or less. The compressive strength of these specimens was compared to that of the ocean-cured specimens that were exposed to only three cycles of 1 foot of head per second. The strengths were essentially identical, so the faster pressure cycling rate did not harm the specimens.

Another observation that demonstrated that pressure cycling does not harm concrete is the retrieval of two uncoated-concrete spheres from the ocean. One sphere was at 2,790 feet for 5.3 years (Ref 15) and the other sphere at 3,190 feet for 10.5 years (Figure 2.6) (Ref 17). In both cases, after retrieval and a number of hours at atmospheric pressure, the spheres were tested in a pressure vessel to failure by implosion under short-term hydrostatic loading, and behaved similar to spheres that had not been placed in the ocean.

The most significant test of pressure cycling was conducted on six 3- x 6-inch solid, microconcrete cylinders that were exposed to a fresh-water pressure head of 45,000 feet for 6 days (Ref 28). The pressure in the pressure vessel was released within 1 second for a depressurization rate of over 45,000 feet of head per second. This condition was an

extreme test. Upon removal from the pressure vessel, the specimens showed cracking as if large areas of the surface were about to spall. Uniaxial compression tests showed that the specimens had an average strength of 5,900 psi. These strength data were compared to that of six companion specimens that had remained in an air-dried (field-cured) condition; these specimens had a strength of 8,040 psi. The decrease in strength was 27%. The strength reduction included the effect of dry concrete becoming wet, which is 10% or more. Hence, only 17% of the reduction would be attributed to the effect of sudden release of pore pressure. Thus, the damage is considered to be small for the extreme nature of the test.

The reason pressure cycling at reasonable rates does not affect concrete is that little water actually moves in or out of saturated concrete as the pressure environment increases or decreases. The bulk modulus of the concrete is a little larger in value than the bulk modulus of seawater; hence, as the pressure increases, the decrease in volume of a concrete specimen is a little less than that of seawater. So a small quantity of seawater will enter the specimen. Upon pressure decrease, the small quantity of seawater must exit the specimen. This quantity is about 10 to 20% of the quantity that must exit saturated concrete under uniaxial loading. Hence, pressure cycling does not appear harmful to saturated concrete.

2.3 HYDROSTATIC LOADING CONDITIONS

2.3.1 Long-Term Loading

Experimental investigations on the long-term loading behavior of pressure-resistant concrete structures were conducted primarily on spheres, but a few tests were conducted on cylinders. Three spheres of 16 inches (Ref 1) and seven of 66 inches OD (Ref 10), both sizes having t/D_o ratios of 0.063 (Figure 2.7), were tested in pressure vessels to obtain data on their response to continuously sustained loading during the early period (first 20 days) of long-term loading. Eighteen spheres of 66 inches OD, also having a t/D_o ratio of 0.063, were placed in the

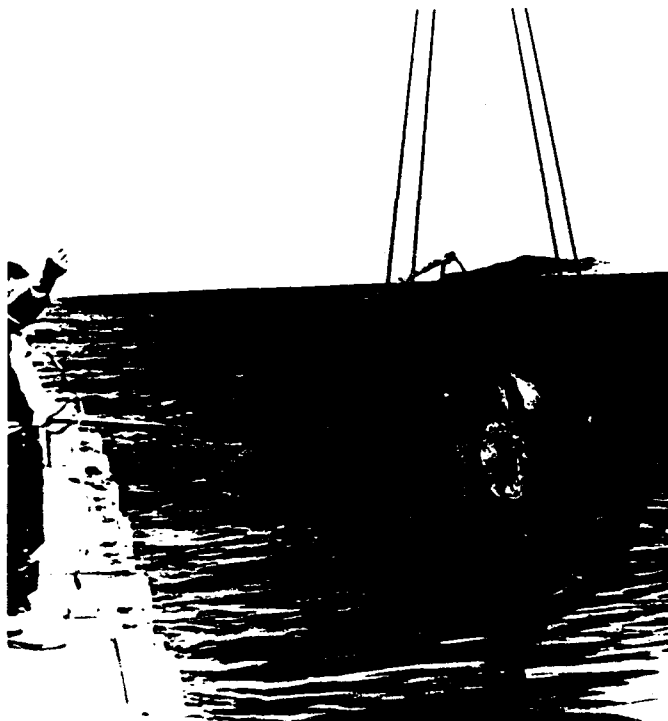


Figure 2.6 Sphere retrieved from 3,190 feet after 10.5 years.



Figure 2.7 Concrete spherical structures, 16-inch and 66-inch OD, used for hydrostatic loading tests conducted in laboratory pressure vessels and in the ocean.

ocean to obtain data for periods up to 13 years and longer (Ref 13, 15, and 17). The spheres were placed in the ocean in 1971; since that time three of the spheres imploded in-situ at or soon after deployment, two spheres flooded without imploding (one soon after deployment with no visible defect, the other due to a small local failure after 8 years in the ocean), five spheres were retrieved from the ocean for laboratory testing, one has never been inspected, and seven are still exposed to long-term loading. The long-term loading data are shown in Figure 2.8.

Three cylindrical specimens, 54 inches OD, with a t/D_o of 0.037 and L/D_o of 2.35, were tested in a pressure vessel (Ref 16 and 29). The data from these tests are also shown in Figure 2.8. A large cylindrical structure (see Frontispiece) of 10 feet OD by 20 feet overall length (10-foot cylinder section plus two hemispherical end caps) was also subjected to long-term loading for 10.5 months in the ocean, but the depth was only 600 feet for a relative load level of about 13% of its short-term strength. The datum from this test is not shown because of the low relative load level (Ref 14).

An average data curve from Stock1 (Ref 29), representing hundreds of uniaxial load tests, is shown in Figure 2.8 for comparison. The results compare favorably. This finding shows that dry and saturated concrete under multiaxial stresses behaves in a manner similar to concrete used for on-land structures. There was no unusual behavior observed for concrete used in the deep ocean as compared to the known behavior of concrete under long-term loading.

2.3.2 Cyclic Loading Effect

Previous work on cyclic loading of confined concrete was quite limited. An investigation, therefore, was conducted on the low-cycle fatigue behavior of fiber reinforced concrete spheres under hydrostatic loading (Ref 30). The spheres were 16 inches OD, with a t/D_o ratio of 0.188.

The concrete mix proportions were a water-cement ratio of 0.43, cement-sand-aggregate proportions of 1:2.55:0.64, and a cement content of 846 lb/yd³. Type II Portland cement was used along with aggregate,

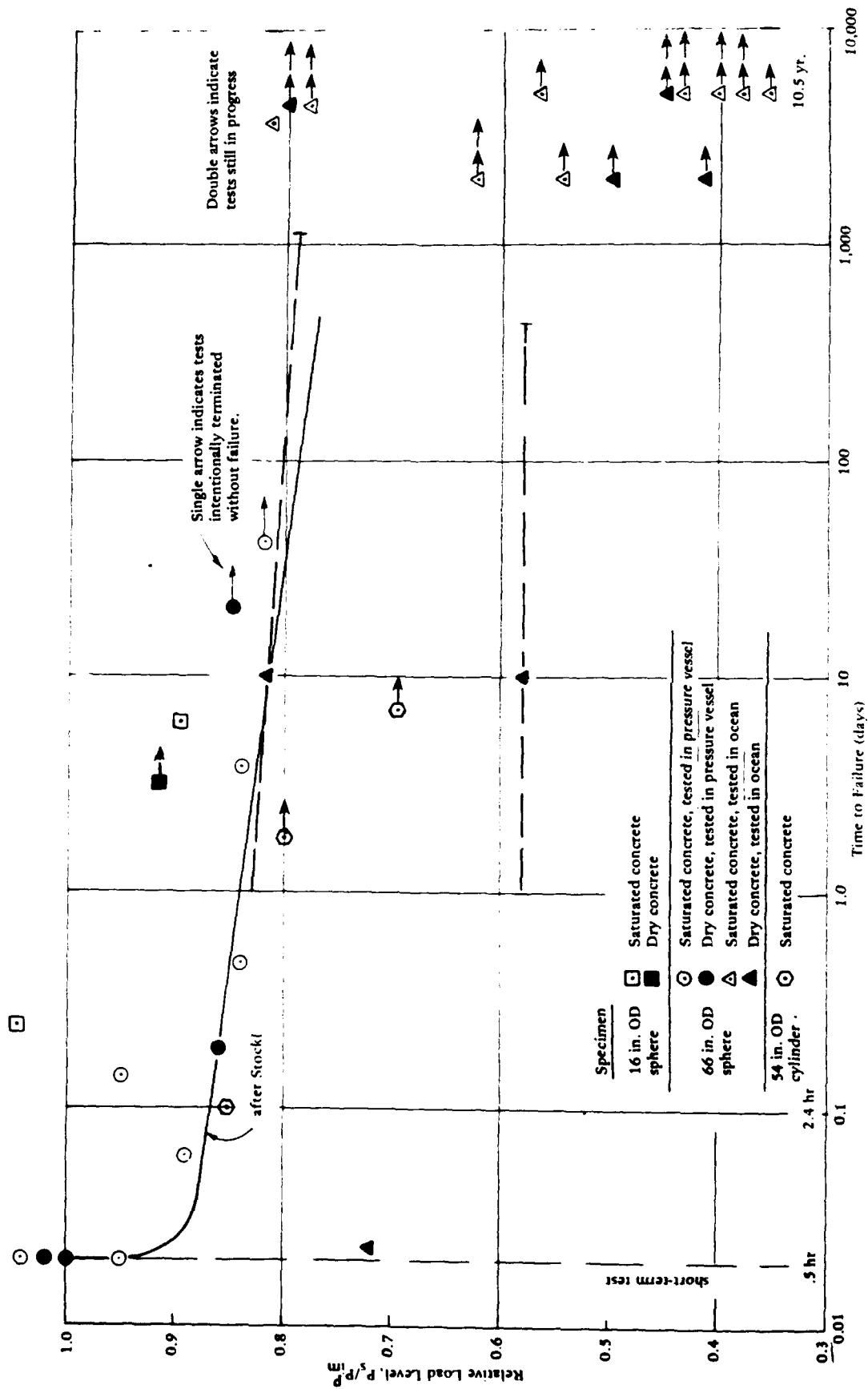


Figure 2.8 Time to failure of concrete spheres and cylinders under long-term hydrostatic loading.

maximum size of 3/8 inch, and a water reducing admixture. Straight steel fibers, 1.5 inches in length and 0.017 inch in diameter, were randomly distributed at a percentage of 1.5% by volume.

The state of stress in the sphere wall varied from biaxial on the inside surface to triaxial elsewhere. The hoop stresses were equal at $\sigma_1 = \sigma_2$ and the radial stress, σ_3 , was an average of $0.3 \sigma_1$. The cyclic hydrostatic load cycled all the stresses. This was in contrast to previous work (Ref 31), using plain concrete solid-cylinders, in which the axial stress, σ_1 , was cycled from 20% to 80 or 90% of the triaxial ultimate strength while the radial stresses, σ_2 and σ_3 , were equal and held constant at stress levels of 9 or 13% of the triaxial ultimate strength.

The test results are shown in Figure 2.9. The spheres showed considerably poorer fatigue behavior compared to the solid cylinders under confinement. This difference in behavior can be explained by the differing stress conditions in the two types of specimens. For the spheres, all wall stresses were cycled, whereas for the cylinders, only the axial stress was cycled. Also, for the spheres, σ_3 was not uniform across the wall but varied from zero at the inner surface to some maximum value at the outer surface.

The sphere results converge rapidly to the uniaxial results (Ref 31 and 32) in Figure 2.9. The uniaxial results should be the lower bound limit of confined concrete fatigue behavior; however, this was not confirmed by the tests.

2.3.3 Rapid Loading

An exploratory test program was conducted on rapidly applying hydrostatic load to concrete spheres (Ref 28). The spheres were 16 inches OD, with a t/D_o ratio of 0.188, and fabricated of plain concrete. The exterior and interior surfaces of the spheres were water-proofed. Previous work on rapid loading effects was conducted only on unconfined concrete solid-cylinder specimens. Testing of spheres under hydrostatic loading provided an opportunity to observe rapid loading effects on confined (unsaturated) concrete.

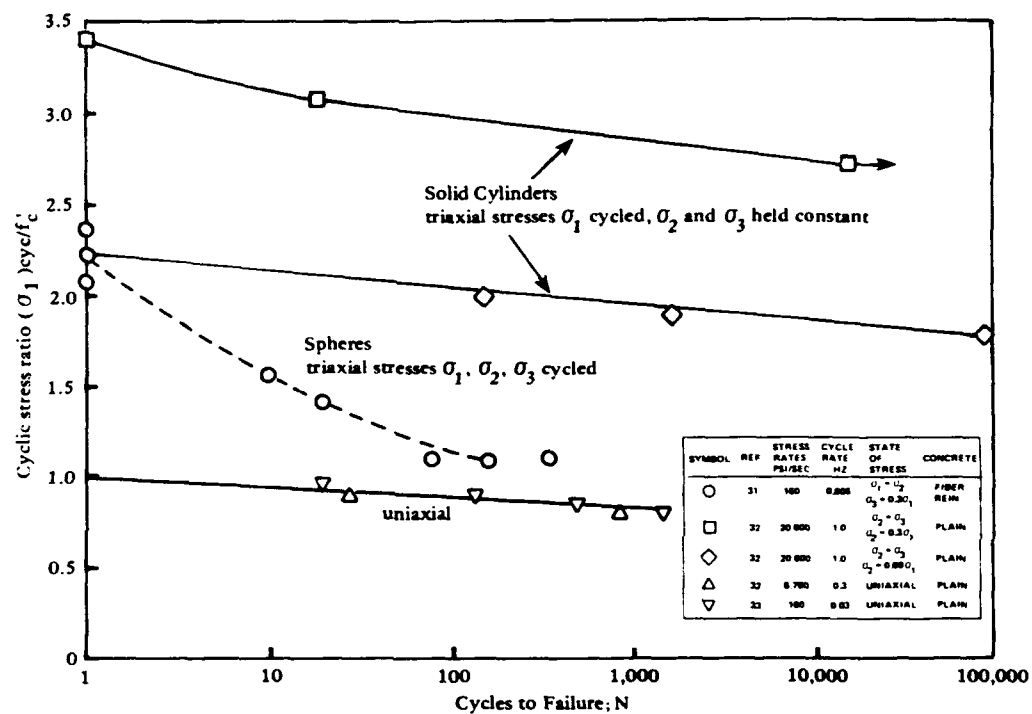


Figure 2.9 Low cycle fatigue behavior of confined and unconfined concrete.

The concrete mix proportions were a water-cement ratio of 0.43, cement-sand-aggregate proportions of 1:2.55:0.64, and a cement content of 846 lb/yd³. Type III Portland cement, modified to plastic cement by the manufacturer, was used along with an aggregate, maximum size of 3/8 inch, and a water reducing admixture.

The test procedure used for creating a rapid hydrostatic load was to apply an equal pressure of 10,000 psi to the interior and exterior of a sphere, and then quickly release the interior pressure, thereby creating a rapidly applied external hydrostatic load. This procedure, modified by decreasing the interior pressure slowly, was used on two spheres and the implosion results compared well with the previous results on spheres subjected to only external hydrostatic loading (Ref 32, 4, and 30). The average implosion pressure for the two statically loaded spheres was 4,420 psi.

The rapid test procedure was used successfully on two spheres. The external load was applied in about 0.007 second and both spheres resisted the maximum available pressure load of 9,600 psi. One sphere held the pressure for about 0.003 second and the other about 0.025 second; hence, the failures were not instantaneous, but rather creep failures.

The strength results are shown in Figure 2.10 as a function of stress rate and in Figure 2.11 as a function of strain rate. The sphere closest to an instantaneous failure showed a strength increase of 2.3 times that of statically loaded spheres. Past work on rapid loading of unconfined concrete showed strength increases on the order of 1.4 times that of the statically loaded specimens (Ref 33, 34, 35, and 36). The improved strength of the spheres demonstrated that confined concrete resisted rapid loads in a manner superior to that of unconfined concrete.

2.4 REINFORCEMENT

Three studies have considered the effects of steel reinforcement on the implosion behavior of spherical structures. Each study investigated a different reinforcement scheme. Cylindrical structures with steel

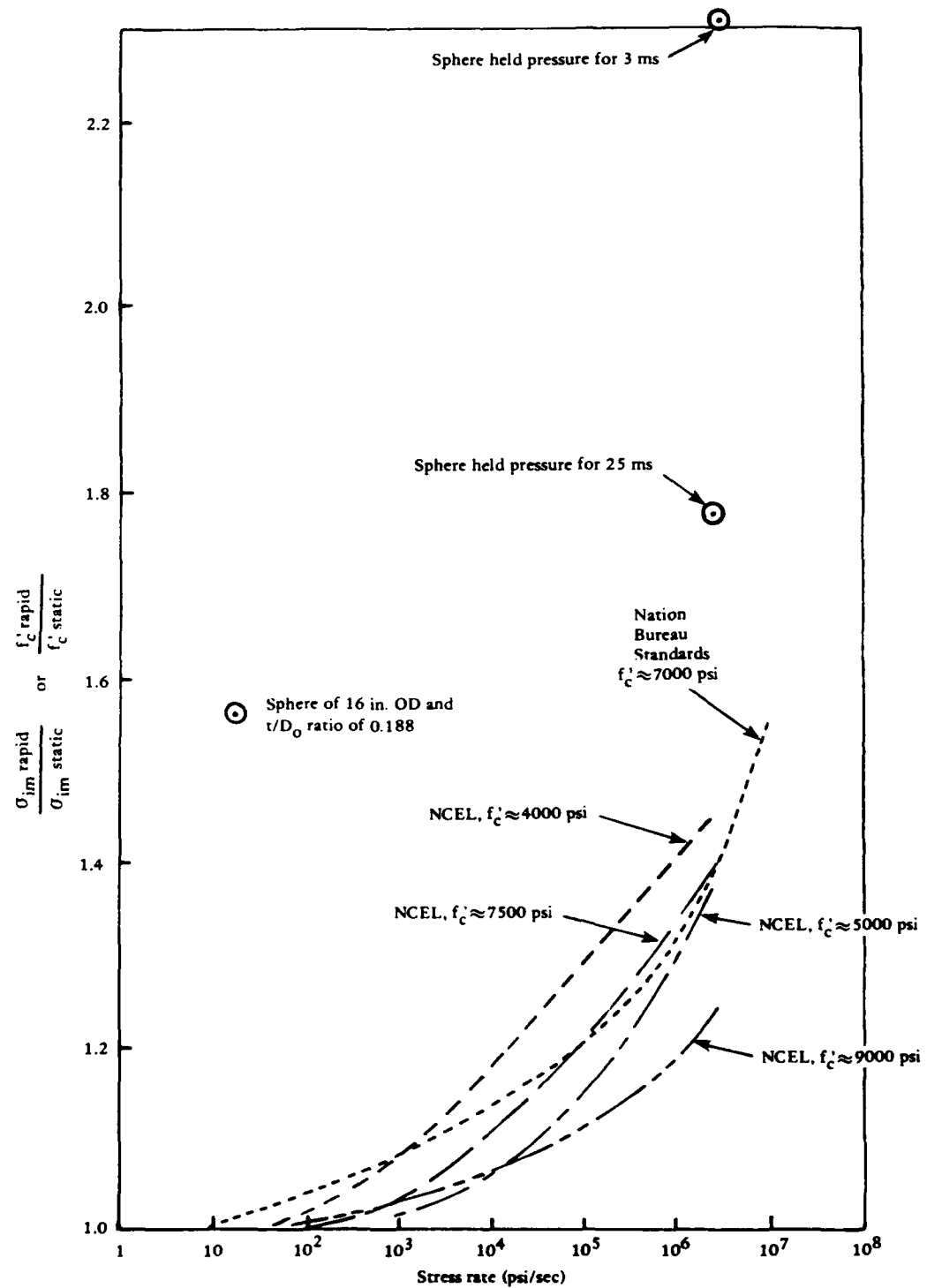


Figure 2.10 Increase in compressive strength as a function of stress rate.

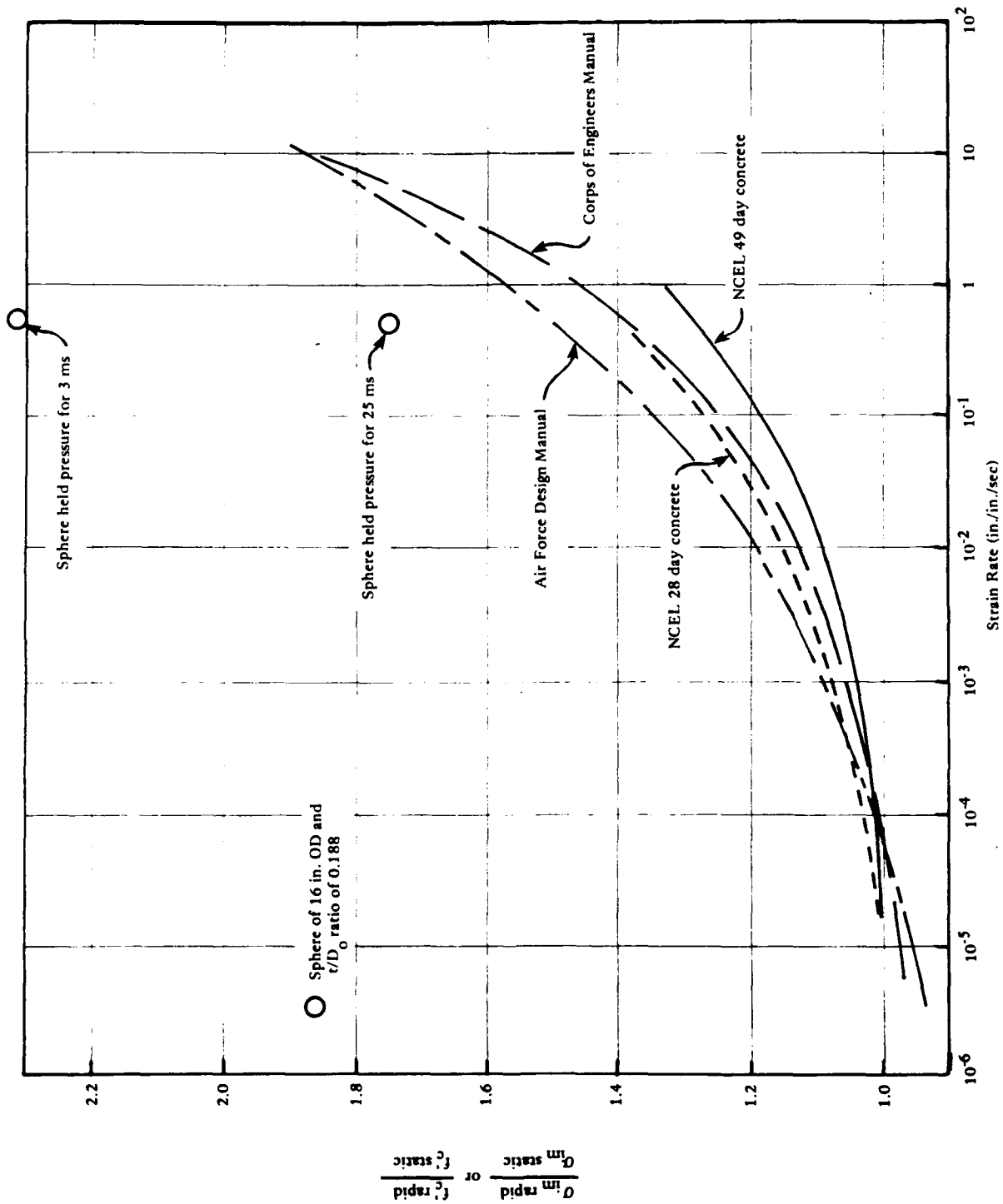


Figure 2.11 Increase in compressive strength as a function of strain rate.

reinforcement have not been investigated, but in general terms the findings from the spherical studies should be applicable.

The first study was on spheres reinforced with steel liners on the inside, on the outside, and on both the inside and outside surfaces (Ref 11). Figure 2.12 shows the 16-inch OD models, which had a t/D_o of 0.063 (for the concrete wall). The quantity of reinforcement varied from 1.8 to 24% by concrete cross-sectional area. Figure 2.13 shows the results of the test program. The implosion strength of the reinforced spheres is presented as the strength relative to that of plain concrete spheres. For a given percentage of steel reinforcement, a liner on both the inside and outside surfaces produced better strength results than if a thicker liner were placed in either the inside or the outside surface.

To substantially increase the implosion strength of concrete spheres required high percentages of reinforcement. For the condition of a liner both on the inside and outside surfaces, a percentage of 12% by area increased the implosion pressure of a plain concrete sphere by a factor of 2.2. On a full-scale structure a percentage of 12% results in thick steel plate. For a 12-foot OD sphere with a t/D_o ratio of 0.063, the thickness of the plate would be about 2.75 inches for a 150,000 psi yield strength steel, which is not a practical design approach.

A more conventional reinforcing scheme was investigated in the second study (Ref 37). Spheres of 32 inches OD with a t/D_o ratio of 0.085 were fabricated with modeled, conventional reinforcing steel cages with percentages of 0.44 and 1.10% by cross-sectional area. Figure 2.14 shows the rebar cage for the higher steel percentage. Implosion results showed that the reinforced spheres failed at relative pressures 5% lower than those for the unreinforced spheres. Near implosion, the interior concrete cover delaminated from the rebar cage. This delamination was not observed for plain concrete spheres of the same wall thickness. The reinforced spheres were fabricated from two hemispheres, and the delamination cracks started at the equatorial joints.

On a full-scale structure, joints would probably not be a problem; however, increases in implosion strength are not anticipated unless the compression steel is tied against lateral movement. Various codes of practice (e.g., Ref 38) require reinforcement be tied if the effect of

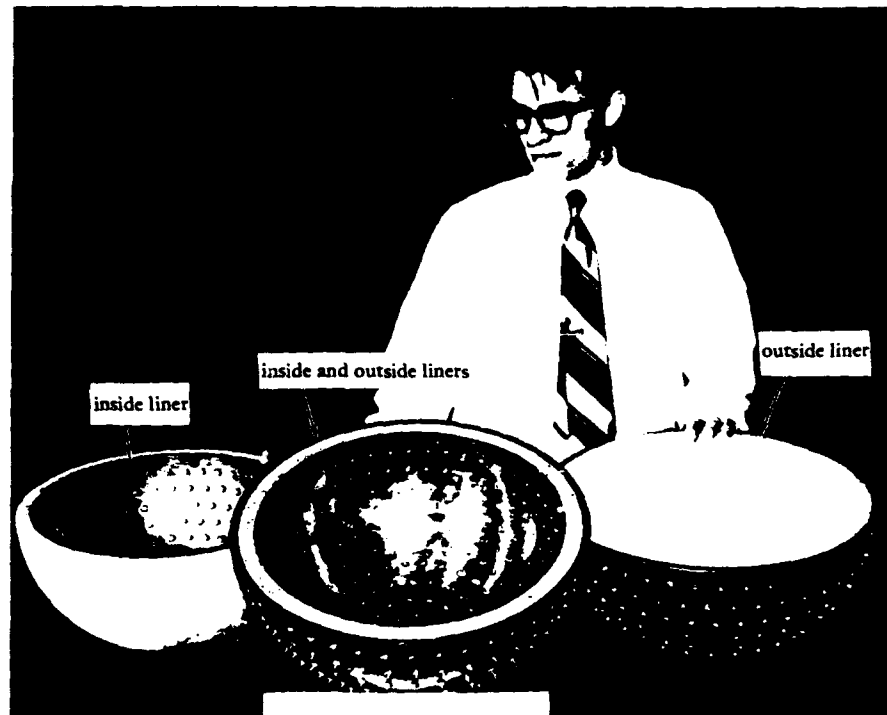


Figure 2.12 Hemisphere sections of steel-lined reinforced concrete spheres. The control (unreinforced) concrete sphere had a $t/D_0 = 0.063$.

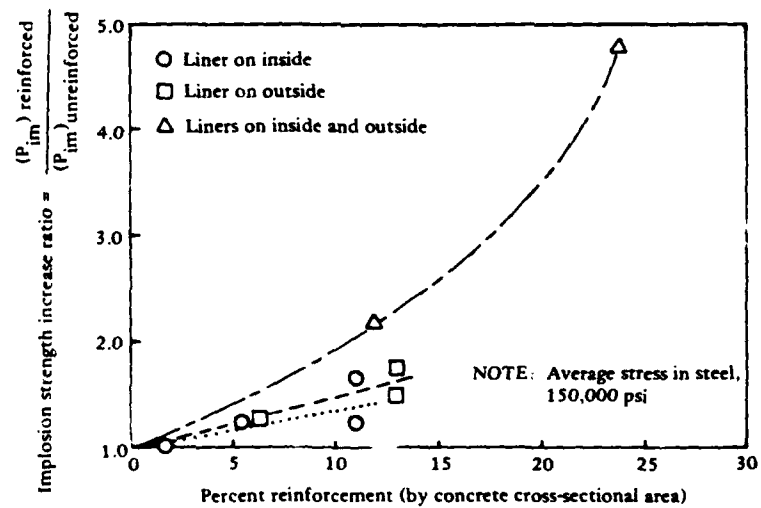


Figure 2.13 The effect of steel-liner reinforcement on the implosion pressure (P_{im}) of thick-walled concrete spheres.



Figure 2.14 Reinforcing cage representing 1.1% steel by area for a concrete sphere of 32-inch OD by 2.71-inch wall thickness.

the reinforcement is to contribute to the strength of a compression member. At operational loads, untied reinforcement will assist in resisting bending displacements caused by out-of-roundness; but, at near failure conditions the untied reinforcement can not be counted on to increase the implosion strength. Hence, when compression reinforcement is not tied, then the member is designed as unreinforced concrete.

The third study was on steel fiber-reinforced-concrete spheres of 16-inch OD, 3-inch wall thickness, and a t/D_o ratio of 0.188 (Ref 39 and 30). Straight steel fibers, 1.5 inches long by 0.017 inch in diameter, were randomly distributed in the concrete at a percentage of 1.5% by volume. The purpose of this study was to investigate cyclic loading effects as discussed earlier. We were also able to compare the static loading strength of three fiber-reinforced spheres to plain concrete spheres of identical size and similar uniaxial concrete compressive strengths. The fiber-reinforced-concrete spheres showed implosion strengths were greater than the plain concrete spheres by a factor of 1.59. This is a substantial increase in implosion strength for a steel reinforcement percentage of only 1.5% by area.

Caution needs to be mentioned regarding steel fiber reinforcement for hydrostatically loaded structures until additional tests can be conducted. A fourth sphere containing steel fiber reinforcement showed an anomalous failure at a pressure 8% lower than plain concrete spheres, a small hole about 1/2 inch in diameter was pushed through the 3-inch thick wall. Perhaps fibers were missing from this region, or perhaps a fiber ball was located in this region.

A somewhat similar failure occurred for a large fiber-reinforced-concrete sphere, 72 inches OD and t/D_o of 0.167 (Ref 40). The reinforcement percentage was 1.5% by area. This sphere was part of an underground blast test program conducted by the Defense Nuclear Agency. After the underground test, which did damage the sphere, the sphere was tested under cyclic hydrostatic loading in a pressure vessel. The failure mode was a 12-inch diameter hole pushed through the 12-inch thick wall in a manner similar to the anomalous failure of the 16-inch OD sphere.

Full-scale concrete structures will require steel reinforcement to resist strains from thermal and shrinkage conditions, loads during construction and transportation stages, moments from discontinuities and out-of-roundness deviations, and other factors. A minimum reinforcement percentage of 0.20% by area should be used.

2.5 EPOXY ADHESIVE JOINTS

Model undersea concrete structures for most of the test programs were fabricated by joining structural components together with an epoxy adhesive. For spheres, two hemispheres were bonded together; for cylinders, end-closures were bonded to the cylinder section. The joints did not appear harmful to the overall behavior. Typically, the initiation of failure did not involve the joints.

The construction approach of bonding elements together was used to bond the hemispherical end closures to a 10-foot diameter by 10-foot long cylinder as shown in Figure 2.15 (Ref 14). The completed structure, which is shown in the Frontispiece, was submerged for 10.5 months at 600 feet and then returned to land. The joints appeared in excellent condition. After being on land for 4.2 years, the structure was again lowered into the ocean, this time to obtain its implosion strength which occurred at 4,700-foot depth. Again, the joints performed well.

When using epoxy adhesives the American Concrete Institute's guidelines (Ref 41) should be considered. Also the manufacturer's recommended practice should be followed. However, not all commercially available epoxy adhesives for concrete perform equally well. In particular, from tests on a number of epoxy materials, it was found that the bond strength for certain epoxies is damaged by the presence of water (Ref 42). Therefore, before using an epoxy for undersea structural applications, bond strength must be determined by tests on concrete elements bonded in a dry (or damp or wet) condition and then subsequently saturated under pressure.

Water-jetting or sand-blasting is required to roughen the concrete's surfaces. The thickness of the epoxy in the joint should be

less than 1/8 inch. For the joint shown in Figure 2.15, the gap between the mating surfaces was less than 1/8 inch for about 75% of the contact area.

2.6 PENETRATIONS

Tests have shown that concrete spherical structures can have small and even relatively large hull penetrations without reducing implosion strength (Ref 2). The recommended design approach is to use a hull penetration having a rigidity equal to or greater than the rigidity of the concrete removed, and having a mating surface between the concrete and the penetration at a spherical angle (taper to the center of the sphere).

This approach was used for large hull penetrations, which represented 40% of the diameter of the hemispheres, that capped the 10-foot OD cylinder described above (Figure 2.16) (Ref 14). The strains in the concrete near the penetrations did not show an increase over that of other locations during the 10.5-month long ocean test at 600 feet. This, however, could have been due to the low stress levels in the wall (approximately $0.2 f'_c$).

For full-scale structures under construction, temporary holes are sometimes required for access to the interior. It is recommended that the edge of the penetration hole have an angle that is tapered to the center of the sphere; or, if that is not possible, the edge should be tapered at an angle that limits shear stresses across the shell thickness to allowable levels. Keyways or ledges around the periphery of the penetration hole should not be used. If concrete is used to fill the hole, then the material should be non-shrinking and have a compressive strength and elastic modulus that is equal to or greater than the concrete in the hull.

Large penetrations in cylindrical hulls have not been investigated. A detailed theoretical analysis using finite elements and a proper constitutive material model for the concrete will produce meaningful results if a large penetration must be located in the cylinder portion

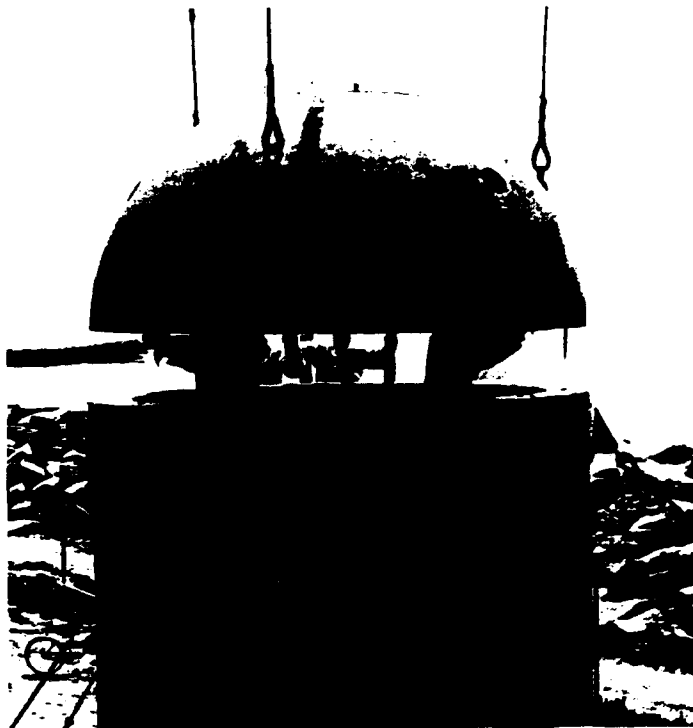


Figure 2.15 Cylindrical structure fabricated by epoxy bonding hemisphere end-closures to cylinder section.

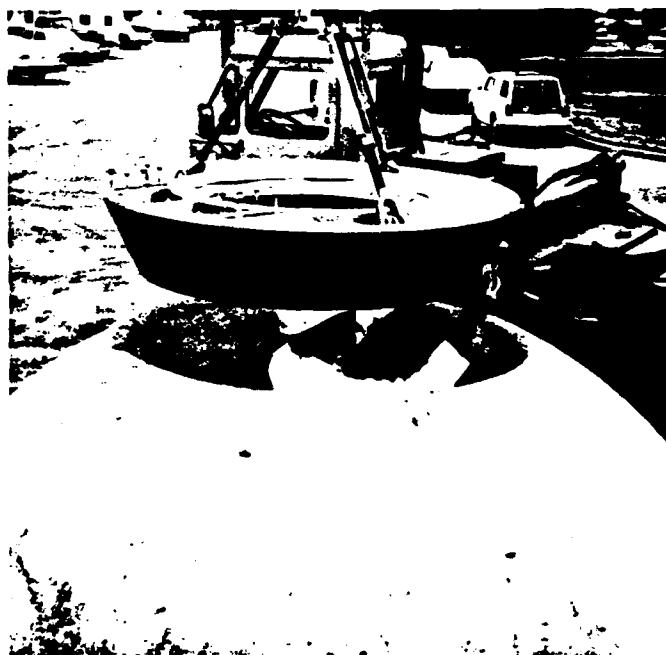


Figure 2.16 Hull penetration in hemisphere end-closure of cylindrical structure represents 40% of the outside diameter of the cylinder.

of the structure. It is preferable, however, to place any large penetrations in the end closures rather than in the wall of the cylinder.

2.7 FACTORS OF SAFETY

The design equations presented in this document to predict implosion pressures of cylindrical and spherical structures require the addition of factors of safety. Factors of safety are applied according to how the structure is to be used.

Different codes of practice have different approaches to assigning factors of safety; however, whatever the approach, the overall factor of safety usually equates to about 2.5 for concrete members under compressive loads (Ref 38 and 43).

The factor of safety is frequently divided into two partial factors: the load factor and the material factor. Without discussing the various codes of practice, these partial factors have the values of about 1.7 for the load factor and about 1.5 for the material factor, and thus, when these factors are multiplied together, the overall factor of safety is approximately 2.5. The load factor accounts for inaccuracies in defining loads, inaccuracies in the design method, variations in construction tolerances, and the importance of the structure (cost and lives involved), and its required reliability. The material factor accounts for variations in concrete strength within the structure and between laboratory and field conditions.

The material factor seldom varies. For undersea structures that are constructed on land or while afloat and then submerged, a material factor of 1.5 is appropriate. If the structure were constructed on the seafloor by tremie placement of concrete, a larger material factor would be warranted. As a guide for the load factor of undersea structures, the value can range from 1.7, if people are not inside the structure, to 2.0 or more if people are inside.

In summary, an overall factor of safety of about 2.5 is proposed for structures that function without people inside and about 3.0, as a minimum, for structures with people inside.

CHAPTER 3. CYLINDRICAL STRUCTURES

Several design approaches are appropriate for cylindrical structures because different geometric configurations behave differently. Analysis methods are presented for thick-walled cylinders, moderately long thin-walled cylinders, and long thin-walled cylinders.

Experimental data exist for each of the geometries. In total, 58 cylinders were tested: 42 had a 16-inch OD (Ref 5, 8, and 12), 15 had a 54-inch OD (Ref 16 and 44), and one had a 121-inch OD (Ref 45). The larger cylinders of 54- and 121-inch diameters generated data of more meaningful quality, probably because they were less sensitive to experimental error. Regardless, data from all cylinder sizes were used in developing the design equations.

The 16-inch OD cylinders are shown in Figure 3.1. These cylinders had various wall thickness-to-diameter, t/D_o , ratios and various length-to-diameter, L/D_o , ratios, so that the wide range of geometric conditions was covered. For the most part, the cylinders were capped with concrete hemispheres of wall thickness equal to that of the cylinder. The concrete uniaxial compressive strengths ranged from 6,000 to 11,000 psi. In general the concrete mix proportions were a water-to-cement ratio between 0.55 and 0.65, an aggregate-to-cement ratio of 3.30, and a cement content of 806 lb/yd³. Type II Portland cement was used. The maximum size of aggregate passed the No. 4 sieve, which means that, technically, the cylinders were cast of mortar (or microconcrete) rather than a concrete mix.

One of the 54-inch OD cylinders is shown in Figure 3.2. These cylinders also had various t/D_o ratios so they ranged from thin- to thick-walled cylinders. Although all of these cylinders had lengths of 134 inches, the two different end conditions (simple-support and free-support) produced test specimens in the "moderately long" (Figure 3.3)

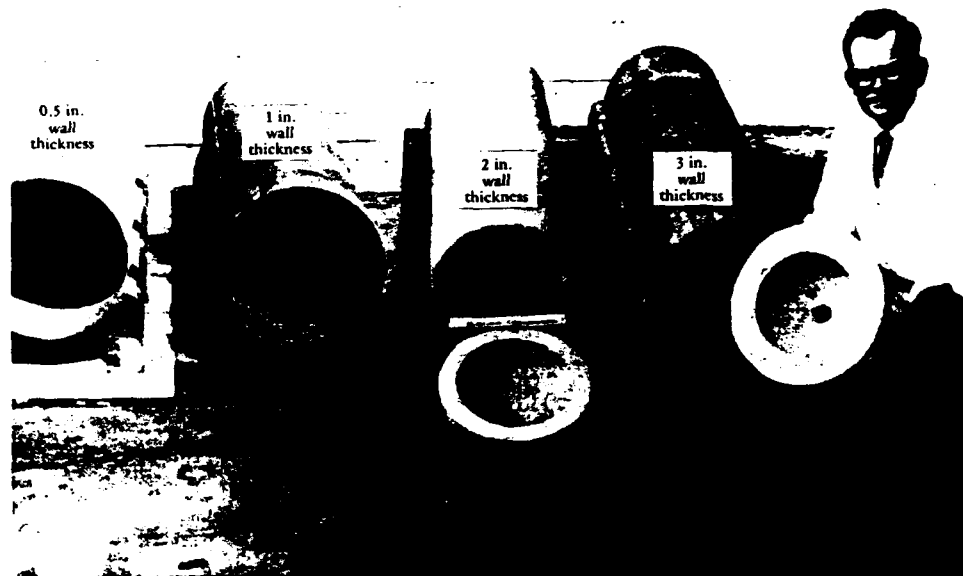


Figure 3.1 16-inch OD concrete test cylinders with various wall thicknesses were tested under hydrostatic loads to implosion.



Figure 3.2 54-inch OD concrete test cylinder. For this series of tests walls were 1.31, 1.97, and 3.39 inches thick.

and "long" thin-walled cylinder categories from the point of view of structural analysis. The concrete uniaxial compressive strengths ranged between nominal 6,500 and 9,500 psi. The mix proportions were a water-to-cement ratio of 0.55, a cement-to-sand-to-aggregate proportion of 1:1.96:2.22, and cement content of 676 lb/yd³. Type II Portland cement was used and the maximum size aggregate was 3/8 inch.

The largest size cylinder, which is shown in the frontispiece and Figure 2.10, was 121 inches OD, 9-1/2-inch wall thickness, and 10 feet long. Thus, the t/D_o ratio was 0.079 and L/D_o was 1.0. The cylinder contained steel reinforcement of 0.70% by area in the hoop direction and in the axial direction. The end closures were concrete hemispheres of wall thickness equal to that of the cylinder. The concrete uniaxial compressive strength was 10,470 psi. The concrete mix proportions were a water-to-cement ratio of 0.40, a cement-to-sand-to-aggregate proportion of 1:1.40:2.50 and a cement content of 734 lb/yd³. Type II Portland cement was used and the maximum size aggregate was 3/4 inch.

Details of test procedures and test results are reported in the appropriate references. Only those data relevant to developing the design approaches are shown herein (Ref 16).

3.1 THICK-WALLED CYLINDERS

The design approach for predicting implosion of thick-walled cylinders is based on material failure of the cylinder wall. Near implosion, the inelastic behavior of concrete along with time-dependent behavior, such as creep, creates a hoop stress distribution across the wall that is modeled more closely by a uniform stress distribution than by an elastic (Lamé) stress distribution. Uniform hoop stress distribution at implosion is expressed by:

$$\sigma_{im} = P_{im} \left(\frac{R_o}{t} \right) \quad (3.1)$$



Figure 3.3(a) Post-implosion view of cylinder.



Figure 3.3(b) Fragments of concrete from failure zone.

where: σ_{im} = average hoop stress in the wall at implosion

P_{im} = implosion pressure

R_o = outside radius of the cylinder

t = average wall thickness

The hoop stress at implosion, σ_{im} , can be expressed as the uniaxial compressive strength of concrete multiplied by a strength factor.

$$\sigma_{im} = k_c f'_c \quad (3.2)$$

where: k_c = strength factor in the circumferential direction
for cylinder structures under hydrostatic loading

f'_c = uniaxial compressive strength of concrete

The term k_c was determined empirically. Figure 3.4 shows k_c as a function of length-to-outside-diameter ratio, L/D_o , for cylinders of various wall-thickness-to-outside-diameter ratio, t/D_o .

For cylinders under external hydrostatic loading, the wall is under biaxial compressive stresses on the inside surface and triaxial compressive stresses at all other locations. The major principal stresses are in the hoop and axial directions, where the hoop stress is about twice the magnitude of the axial stress. The minor principal stress acts radially. If the concrete is considered biaxially loaded, then the hoop-to-axial-stress ratio of 2 increases the compressive strength of concrete by a factor of about 1.25 f'_c (Ref 46). Therefore, k_c values for the cylinders of this program should show a value on the order of 1.25. As a minimum, k_c should be 1.0.

Figure 3.4 shows that short cylinders, those of $L/D_o < 1$, had a k_c around 1.25. However, longer cylinders showed a k_c on the order of 1.0.

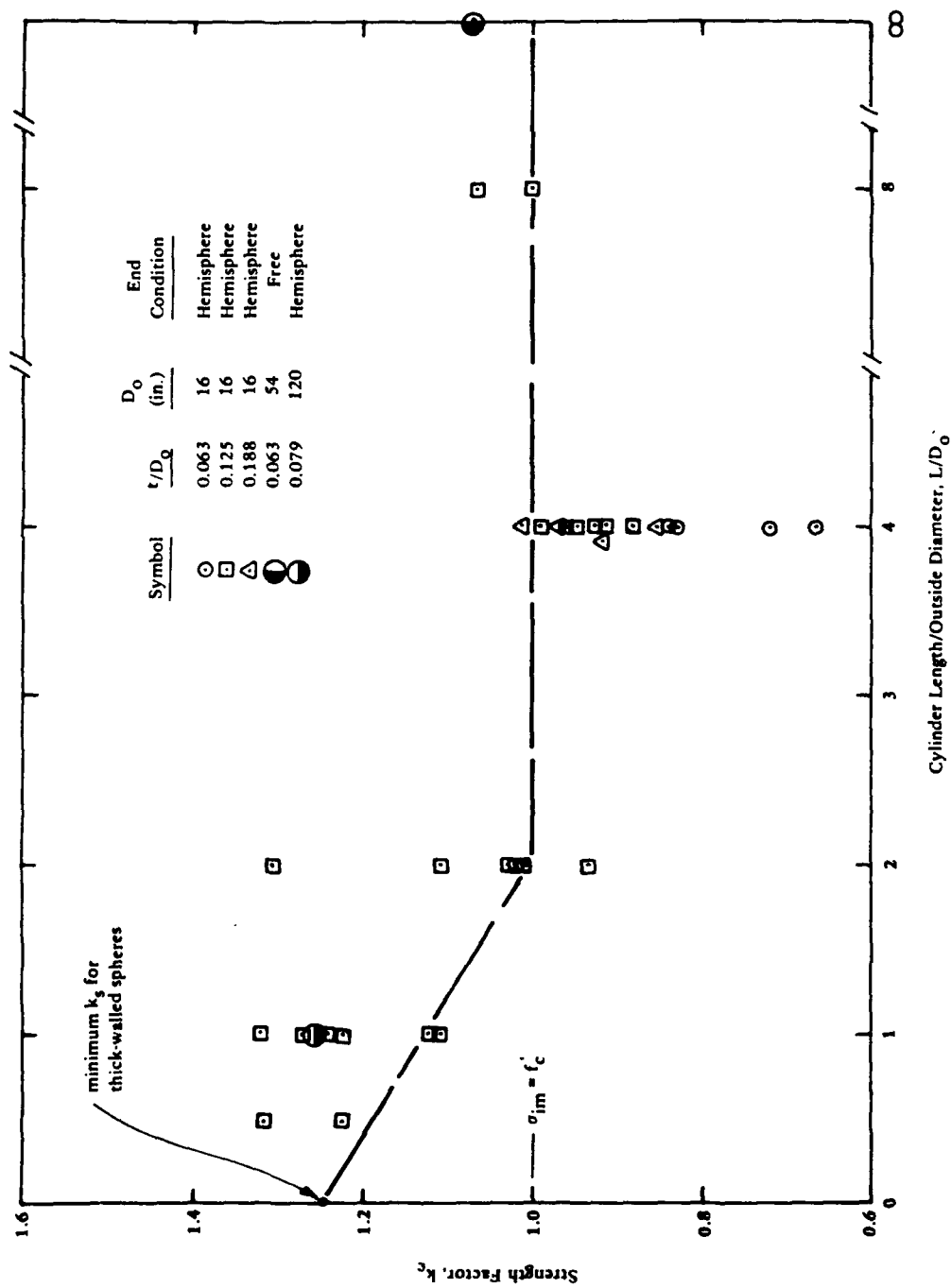


Figure 3.4 Relationship between k_c and L/D_o for thick-walled cylinders.

A decrease in k_c below 1.0 is attributed to an imperfection in the cylinder. An average k_c value of 0.89 was observed at $L/D_o = 4$.*

For design purposes, a $k_c = 1.0$ was selected for cylinders of $L/D_o > 2$. The reader is reminded that this k_c includes the effect of out-of-roundness and experimental error. The reduction in k_c from 1.25 to 1.0, a 20% change, is difficult to assign solely to out-of-roundness effect because thick-walled structures are usually insensitive to small geometric out-of-roundness. The 16-inch OD specimens had the out-of-roundness parameters given in Table 3.1. The specific magnitude of the

Table 3.1. Out-of-Roundness Parameters for 16-Inch OD Cylinders

t/D_o	$\Delta t_{min}/t$	$\Delta R_i/t$	$\Delta R_o/t$
0.03 ^a	0.12	0.12	0.12
0.06 ^b	0.06	0.06	0.06
0.13 ^b	0.03	0.03	0.03
0.19 ^c	0.02	0.02	0.02

^aThin-walled cylinder.

^bBorder between thin- and thick-walled cylinder.

^cThick-walled cylinder.

*Much attention was given to why k_c should be as low as 0.89. If out-of-roundness were the sole cause, then the cylinders showed a decrease in strength of 29% due to out-of-roundness; which is too large an effect for thick-walled cylinders. There is no reason based on engineering mechanics to cause the reduced strength. Some problem related to the fabrication or testing must have been responsible for the low strengths. One procedure that was distinctly different for cylinders with an L/D_o of 4 and 8 was the interior mold. The interior mold was made in segments having a length of $L/D_o = 2$. Cylinders longer than L/D_o of 2 used multiple segments, and it was quite difficult to disassemble the multiple segments to extract the interior mold. If damage was done to the cylinders during this operation, it was not recognized at the time.

out-of-roundness effect could not be determined from the test program; however, the empirical k_c value accounts for whatever out-of-roundness effect that existed. Hence, $k_c = 1.0$ should be a conservative strength factor for design purposes.

Substituting Equation 3.2 into Equation 3.1 and using $R_o = D_o/2$ gives the expression to predict implosion pressure for thick-walled cylinders:

$$P_{im} = 2 k_c f'_c (t/D_o) \quad (3.3)$$

where: $k_c = 1.25 - 0.12 (L/D_o)$ for $(L/D_o) < 2$

$k_c = 1.0$ for $(L/D_o) \geq 2$

Equation 3.3 is shown in Figure 3.5, and is labeled "thick-walled cylinders." Enter the cylinder's L/D_o and t/D_o on the chart to obtain the P_{im}/f'_c ratio. The implosion pressure, P_{im} , can then be calculated by assuming a concrete compressive strength, f'_c .

The effect of different types of end closures on the implosion strength of thick-walled cylinders is small (Ref 8) so this parameter was not included in Equation 3.3.

3.2 THIN-WALLED CYLINDERS

Thin-walled cylinders are divided into two categories: moderately long cylinders and long cylinders. Moderately long cylinders are influenced by end closures that restrain the cylinder from instability failure. Long cylinders are not influenced by end closures and behave as infinitely long cylinders.

The basis for the design approach was to use Donnell's buckling equation for moderately long cylinders (Ref 47) and Bresse's equation for long cylinders (Ref 48). Both equations predict the hoop stresses in the wall of the cylinder at buckling.

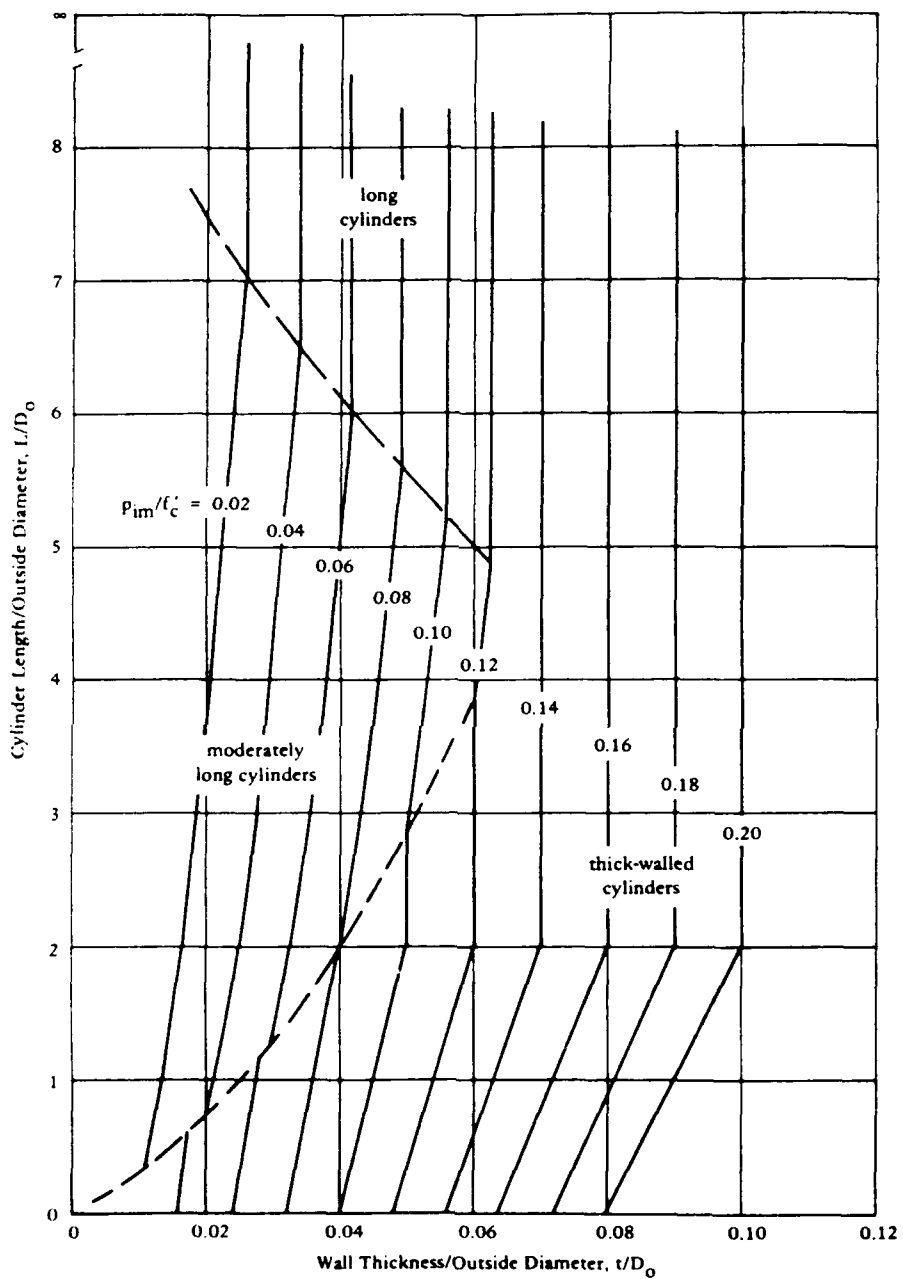


Figure 3.5 Design guide for predicting implosion pressure of concrete cylinder structures.

Note: Enter the chart with known or assumed values for the cylinder's L/D_o and t/D_o ratios to find the P_{im}/f'_c ratio. Select a compressive strength (known or assumed) between 6,000 and 10,000 psi and calculate P_{im} .

Donnell's Equation

$$(\sigma_{im})_D = \frac{0.855 E_c}{(1-\nu^2)^{3/4}} \left(\frac{t}{R}\right)^{3/2} \frac{R}{L} \eta \quad (3.4)$$

where: $(\sigma_{im})_D$ = hoop stress in cylinder wall at implosion, predicted by Donnell's equation

E_c = concrete elastic modulus, psi

L = uninterrupted length of cylinder, in.

R = mean radius, in.

t = wall thickness, in.

η = plasticity reduction factor

ν = Poisson's ratio

and

Bresse's Equation

$$(\sigma_{im})_B = \frac{E_c}{4(1-\nu^2)} \left(\frac{t}{R}\right)^2 \eta \quad (3.5)$$

where: $(\sigma_{im})_B$ = hoop stress in cylinder wall at implosion, predicted by Bresse's equation

Using $\nu = 0.20$ and the approximation $R = D_o/2$, Donnell's equation becomes:

$$(\sigma_{im})_D = \frac{1.25 E_c \eta \left(\frac{t}{D_o}\right)^{1.5}}{L/D_o} \quad (3.6)$$

and Bresse' equation

$$(\sigma_{im})_B = 1.04 E_c \eta \left(\frac{t}{D_o}\right)^2 \quad (3.7)$$

The elastic condition exists when $\eta = 1$.

Figure 3.6 shows the experimental data of the elastic moduli as a function of compressive strength for the concrete used in the 54-inch OD

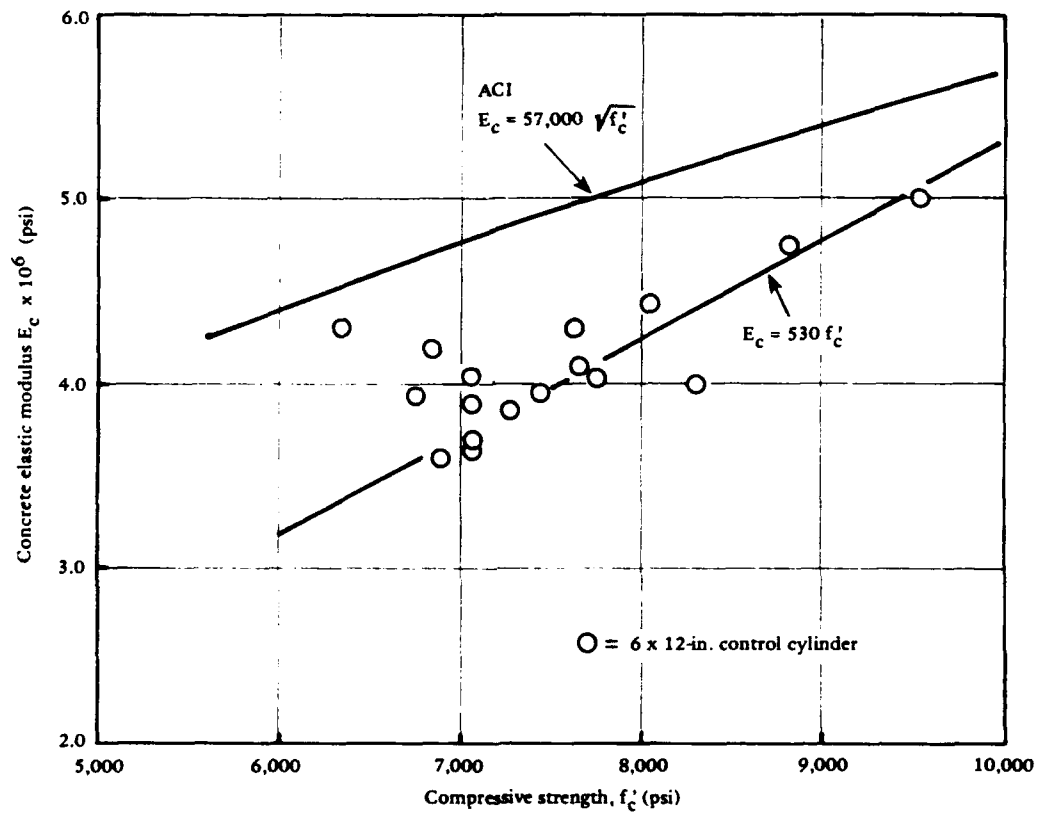


Figure 3.6 Concrete elastic modulus values (obtained as secant modulus up to $0.4 f'_c$) of 54 - inch OD cylinders.

cylinder tests specimens. E_c was obtained experimentally as the secant of the uniaxial compressive stress-strain curves from the beginning up to 40% of ultimate strength. From these data the following empirical expression was developed to predict E_c for concretes in the compressive strength range of 6,000 to 10,000 psi.

$$E_c = 530 f'_c \quad 6,000 \text{ psi} < f'_c < 10,000 \text{ psi}^* \quad (3.8)$$

The American Concrete Institute (ACI) expression for elastic modulus (Ref 39) is shown in Figure 3.6 for comparison. The ACI expression is known to over estimate E_c for high strength concretes (Ref 49).

Equations 3.6 and 3.7 predict the elastic hoop stress at implosion when the plasticity reduction factor, η , is 1.0. When η is less than 1.0, its primary function is to account for inelastic material behavior as E_c deviates from elastic response. For the thin-walled cylinder design approach, η is used in a broader manner. It is the empirical factor to relate Donnell's and Bresse's equations to the test results. Thus η represents more than just inelastic material behavior; it also includes the effects of cylinder out-of-roundness, experimental error, and theoretical equation limitations.

Empirical values were calculated by dividing the experimental hoop stress at implosion (assuming a uniform stress distribution across the wall) by the elastic hoop stress at buckling, Equation 3.6 or 3.7. As the t/D_o ratio increases for thin-walled cylinders, and the failure mode enters the transition region from buckling to material failure, greater inelastic material effects occur and η becomes smaller. This is seen in Figures 3.7, 3.8, and 3.9.

These data are shown in Figure 3.10 where η is a function of the stress level in the cylinder wall at implosion. The fitted inelastic buckling curves of Figures 3.7 and 3.8 were transferred to Figure 3.10

*Outside this range, Equation 3.8 becomes inaccurate, underestimating E_c below 6,000 psi and overestimating E_c above 10,000 psi (Ref 16).

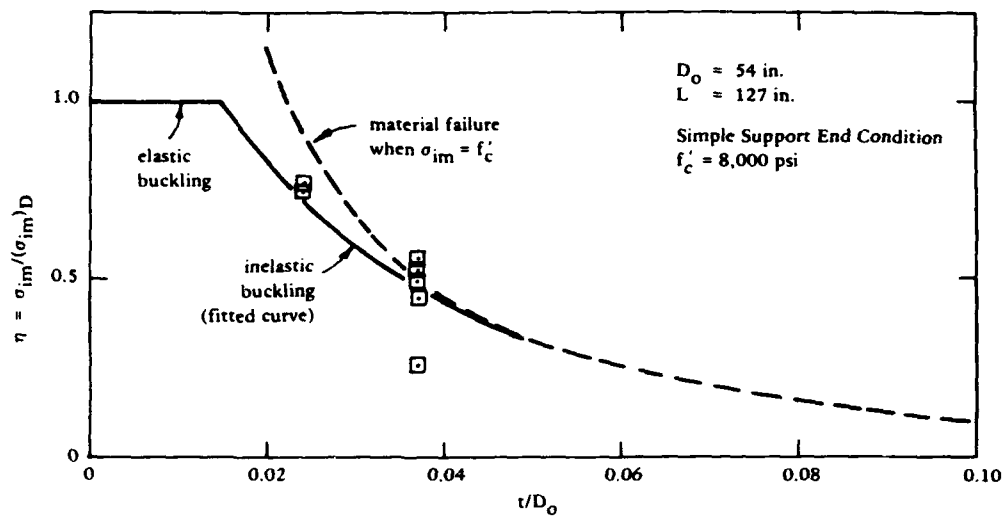


Figure 3.7 Implosion of moderately long cylinders with $D_o = 54$ inches.

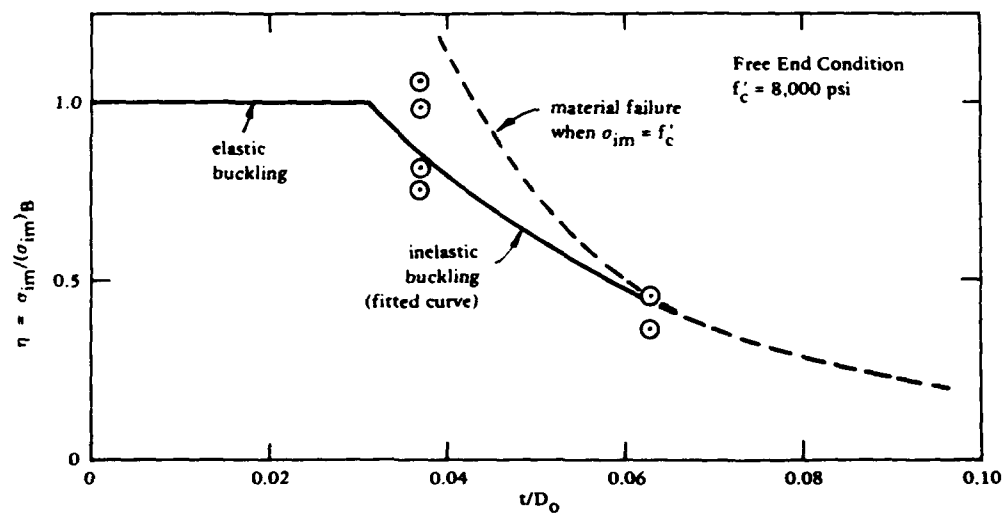


Figure 3.8 Implosion of long cylinders with $D_o = 54$ inches.

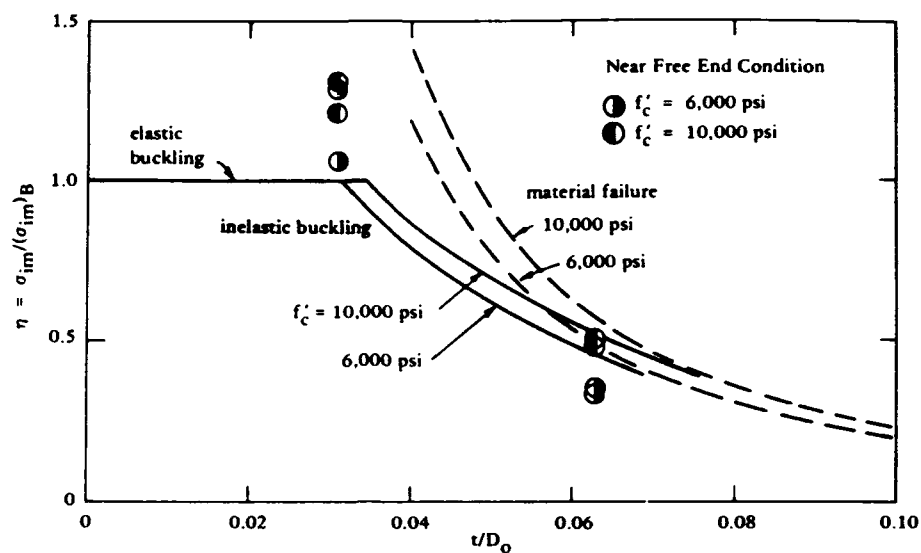


Figure 3.9 Implosion of long cylinders with $D_o = 16$ inch (after Ref. 12).

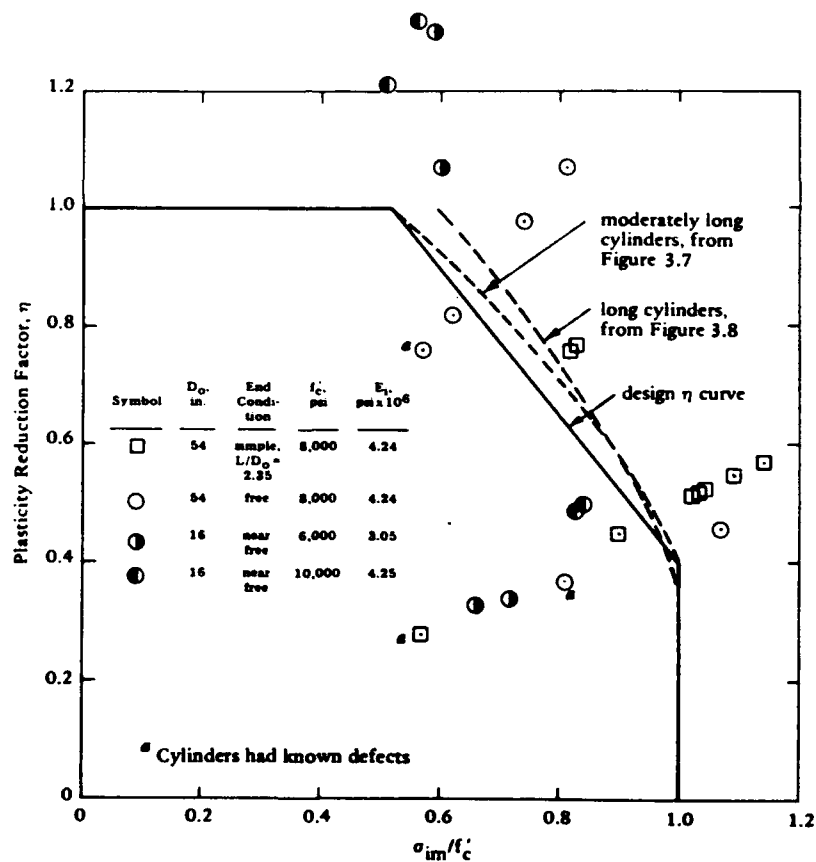


Figure 3.10 Plasticity reduction factor as a function of stress level in cylinder wall at implosion.

and then a design η curve was selected which was applicable to both moderately long and long cylinders. The η expression is:

$$\eta = 1.65 - 1.25 \left(\frac{\sigma_{im}}{f'_c} \right) \quad 0.52 < \frac{\sigma_{im}}{f'_c} < 1.0 \quad (3.9)$$

3.2.1 Moderately-Long Cylinders

The expression to predict implosion pressure for moderately long cylinders was developed as follows.

Equations 3.8 and 3.9 are substituted into Donnell's simplified, equation, Equation 3.6, to yield:

$$\frac{\sigma_{im}}{f'_c} = \frac{1,090 \left(\frac{t}{D_o} \right)^{1.5}}{\frac{L}{D_o} + 830 \left(\frac{t}{D_o} \right)^{1.5}} \quad (3.10)$$

The stress level at implosion, σ_{im}/f'_c , is calculated by knowing the geometry of the cylinder structure. After calculating σ_{im}/f'_c , the following conditions determine the next step:

- a. If $\sigma_{im}/f'_c > 1.0$, a thick-wall analysis is used to predict implosion (Equation 3.3).
- b. If $0.52 < \sigma_{im}/f'_c < 1.0$, then η is calculated by Equation 3.9.
- c. If $\sigma_{im}/f'_c < 0.52$, then $\eta = 1.0$.

If steps (b) or (c) control, the following expression, which predicts the implosion pressure, is used. Equations 3.6 and 3.8 are substituted into Equation 3.1 to obtain:

$$P_{im} = \frac{1,320 \eta f'_c \left(\frac{t}{D_o}\right)^{2.5}}{\frac{L}{D_o}} \quad (3.11)$$

A design chart approach is given in Figure 3.5. Enter the cylinder's L/D_o and t/D_o ratios on the chart to determine the P_{im}/f'_c ratio. The structure is assumed to have a simple support end condition.

For the case of fixed support end conditions, it has been shown analytically (Ref 50) that a 6% implosion strength increase can be expected.

3.2.2 Long Cylinders

The expressions to predict implosion pressure for long cylinders were developed as follows.

Equations 3.8 and 3.9 are substituted into the simplified Bresse's equation, Equation 3.7, to yield:

$$\frac{\sigma_{im}}{f'_c} = \frac{910 \left(\frac{t}{D_o}\right)^2}{1 + 690 \left(\frac{t}{D_o}\right)^2} \quad (3.12)$$

Once the stress level at implosion is calculated, the same conditions for moderately long cylinders hold; that is:

- a. If $\sigma_{im}/f'_c > 1.0$, a thick-wall analysis is used to predict implosion (Equation 3.3).
- b. If $0.52 < \sigma_{im}/f'_c < 1.0$, then η is calculated by Equation 3.9.
- c. If $\sigma_{im}/f'_c < 0.52$, then $\eta = 1.0$.

If steps (b) or (c) control, the following expression, which was developed by substituting Equations 3.7 and 3.8 into Equation 3.1, predicts the implosion pressure:

$$P_{im} = 1,100 \eta f'_c \left(\frac{t}{D_o} \right)^3 \quad (3.13)$$

A design chart approach is given in Figure 3.5. Enter the structure's L/D_o and t/D_o ratio on the chart to determine the P_{im}/f'_c ratio.

3.2.3 Out-of-Roundness

The design chart in Figure 3.5 was developed from theoretical equations that were modified by empirical data. The empirical data were from specimens that had geometric out-of-roundness.

For the 54-inch OD cylinders (Ref 16 and 44), the geometry was extensively measured to define initial out-of-roundness. A summary of the out-of-roundness parameters is given in Table 3.2. This information, however, does not give the complete picture because the location of the thinnest wall thickness coincided with the location of largest radius deviation (or flat spot). Figures 3.11 and 3.12 show the initial geometry. The worst flat spot location was caused by a seam in the exterior casting mold. Displacement recordings taken on the cylinders during hydrostatic loading tests showed that the failure occurred at the worst flat spot location.

Table 3.2. Out-of-Roundness Parameters for 54-Inch OD Cylinders

t/D_o	Out-of-Roundness Parameters		
	$\Delta t_{min}/t$	$\Delta R_i/t$	$\Delta R_o/t$
0.024	0.08	0.04	0.10
0.037	0.06	0.03	0.06
0.063	0.04	0.02	0.03

NOTE: Radius deviations are for radii less than the nominal radii.

Radius deviation scale: 0 0.2 in.

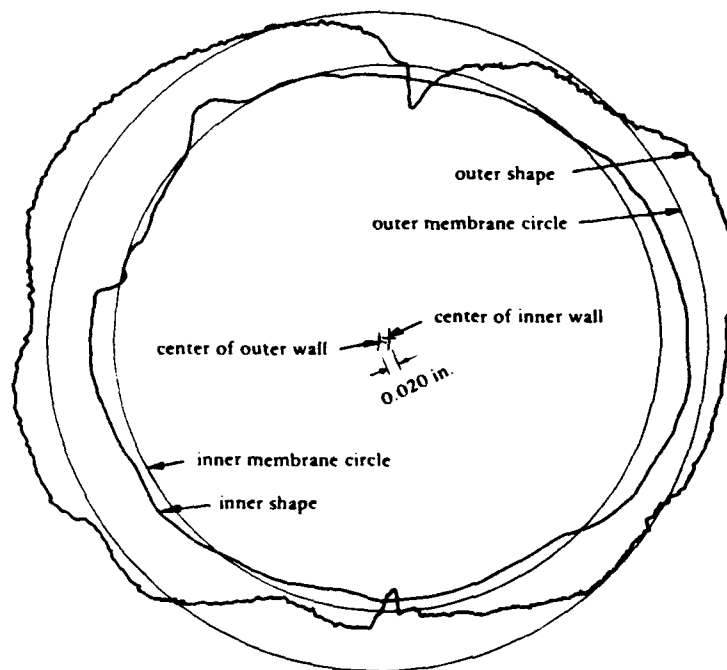


Figure 3.11 Initial cross-section shape showing relative changes in wall thickness and flat spots for a 54 inch OD cylinder having a t/D_o ratio of 0.037.

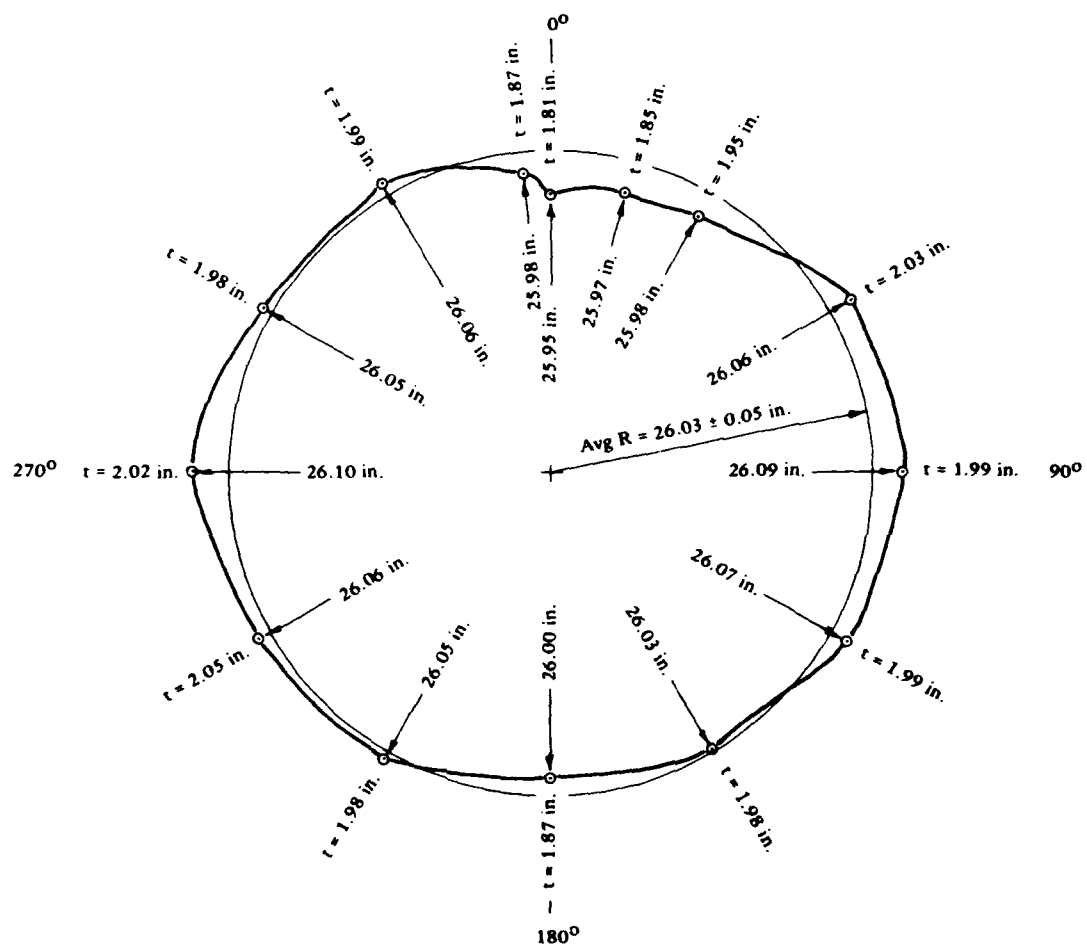


Figure 3.12 Variation in values of wall thickness and mean radius as an average of 54 inch OD cylinders of t/D_o ratio of 0.037.

For full-scale structures, out-of-roundness tolerances can be maintained that are better than those in Table 3.2; therefore, the design chart of Figure 3.5 should be conservative in predicting implosion, in regard to influences from out-of-roundness.

Certain geometries of thin-walled cylinders are more sensitive to axial load effects than other geometries. The curvature parameter, Z , helps to qualitatively define which geometries are sensitive to out-of-roundness deviations (Ref 47).

$$Z = \frac{L^2 \sqrt{1 - \nu^2}}{R t}$$

For concrete, ν is about 0.20 and $\sqrt{1 - \nu^2}$ is approximately 1.0 and thus

$$Z = \frac{L^2}{R t} \quad (3.14)$$

Under hydrostatic loading conditions, cylinders having Z greater than 100 are not sensitive to "normal" deviations in roundness. The out-of-roundness parameters given in Table 3.2 are considered within the limits of "normal" deviations. However, cylinders with Z less than 100 are sensitive to out-of-roundness, and detailed finite element analyses should be performed on those design cases.

3.3 DESIGN EXAMPLE, CYLINDRICAL STRUCTURE

A 100-foot OD, 200-foot long cylindrical structure, which will not be manned, is oriented vertically on the the seafloor at a depth of 500 feet. Hemispheres cap the ends of the cylinder. Seawater ballast fills the structure to a height of 100 feet. Hence, the maximum applied pressure loading is 400 feet or 178 psi. The wall thickness has been preliminarily selected as 3.5 feet and the concrete strength at time of pressure loading as 7,500 psi.

The first step is to determine whether the structure is a moderately long, a long thin-walled, or a thick-walled cylinder. In Figure 3.5, enter an L/D_o of 2.0 and t/D_o of 0.035 to determine that the structure is a moderately long cylinder.

A quick estimate of the implosion strength can be obtained from Figure 3.5. An approximate P_{im}/f'_c is obtained as 0.067

$$P_{im} = 0.067 f'_c = 0.067 (7,500 \text{ psi}) = 502 \text{ psi}$$

Using the design equations to estimate P_{im} requires the following steps:

- The stress level at implosion, σ_{im}/f'_c , for a moderately long cylinder is calculated using Equation 3.10.

$$\frac{\sigma_{im}}{f'_c} = \frac{1,090 (0.035)^{1.5}}{2.0 + 830 (0.035)^{1.5}} = 0.95$$

- When σ_{im}/f'_c is less than 1.0, the plasticity reduction factor, η , is calculated using Equation 3.9.

$$\eta = 1.65 - 1.25 (0.95) = 0.46$$

- Now use the implosion equation, Equation 3.11:

$$P_{im} = \frac{1,320 (0.46) (7,500) (0.035)^{2.5}}{2.0} = 522 \text{ psi}$$

Note that the design chart estimate and the calculated estimate are in reasonable agreement with each other.

The factor of safety is:

$$F.S. = \frac{P_{im}}{P_{operational}} = \frac{522}{178} = 2.93$$

For an unmanned structure, a safety factor of 2.93 is greater than the prescribed 2.5, so the design is adequate. The wall thickness could be revised to a smaller t/D_o ratio, or the concrete strength could be reduced so that the final safety factor was 2.5.

Check the curvature parameter, Z , of Equation 3.14 to determine if this structure is sensitive to out-of-roundness deviations.

$$Z = \frac{L^2}{R t} = \frac{(200)^2}{48.3 (3.5)} = 236 > 100$$

Thus the cylinder is not considered sensitive if normal roundness tolerances are maintained during construction.

CHAPTER 4. SPHERICAL STRUCTURES

Design equations to predict the implosion pressure of thick-walled and thin-walled spheres are presented. Only thick-walled spheres have been tested experimentally.

The experimental specimens were mostly 16-inch OD spheres with t/D_o ratios ranging from 0.062 to 0.25, and concrete compressive strengths ranging from 6,000 to 11,000 psi (Ref 1, 2, 3, and 4). Seventeen of these spheres were tested under short-term loading, i.e., each sphere was placed in a laboratory pressure vessel and the pressure steadily increased until the sphere failed by implosion. The implosion results for these spheres are shown in Figure 4.1. The design approach for thick-walled spheres is based primarily on these data. Larger 32-inch (Ref 37) and 66-inch OD spheres (Ref 10) with t/D_o ratios 0.85 and 0.0625, respectively, were also tested to failure by implosion. The results from the larger sphere tests are also included in Figure 4.1.

For the 16- and 32-inch OD spheres the concrete mix proportions were a water-to-cement ratio between 0.56 and 0.65, an aggregate-to-cement ratio of 3.30, and a cement content of 806 lb/yd³. Type II Portland cement and aggregate passing the No. 4 size sieve were used. For the 66-inch OD spheres, the concrete was manufactured at a local commercial batch plant and transit mixed. The mix proportions were water-to-cement ratio of 0.41, cement-to-sand-to-aggregate proportions of 1:1.85:2.28, and a cement content of 733 lb/yd³. Type II Portland cement, a maximum size aggregate of 3/4 inch, and a water-reducing admixture were used.

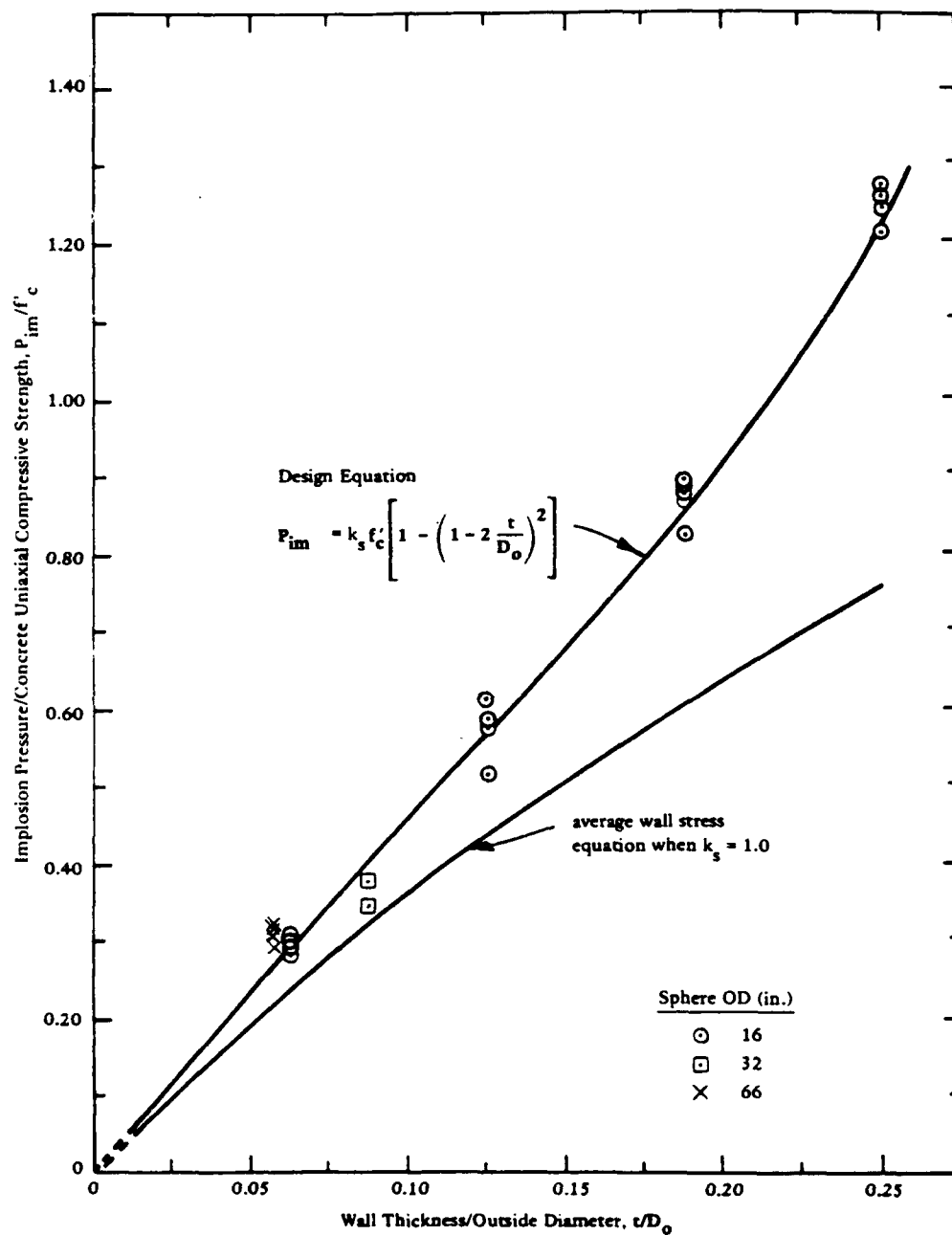


Figure 4.1 Design chart to predict implosion of thick-walled spheres.

4.1 THICK-WALLED SPHERES

The design approach for predicting the implosion pressure of a thick-walled, plain concrete sphere subjected to a uniform external pressure is based on a material failure criterion (not on a buckling failure), viz., the average circumferential ("hoop") compressive stress, σ_{im} , in the sphere wall at the time of implosion of the sphere. The average wall stress is used because, at or near failure, the inelastic behavior of concrete causes redistribution of stresses across the wall thickness. The average hoop stress in the wall of a sphere at implosion due to external pressure can be expressed as:

$$\sigma_{im} = \frac{P_{im}}{1 - \left(1 - 2 \frac{t}{D_o}\right)^2} \quad (4.1)$$

where: σ_{im} = average wall hoop stress at implosion, psi

P_{im} = implosion pressure, psi

t/D_o = wall thickness to OD ratio

Since the sphere wall is in a state of multi-axial compressive stress, σ_{im} should be greater than the uniaxial compressive strength, f'_c , of the concrete. This was confirmed by the implosion tests as shown in Figure 4.1. The empirically determined difference between σ_{im} and f'_c is defined as a design strength factor, k_s , for spherical structures.

$$\sigma_{im} = k_s f'_c \quad (4.2)$$

Figure 4.2 shows k_s as a function of t/D_o ratio. As t/D_o increases, k_s increases exponentially. This is understandable, because as the wall becomes thicker, the state of stress in the wall approaches that of equal triaxial compression. At the limit, when $t/D_o = 0.50$, which is a solid sphere of concrete, the multiaxial state of stress is that of equal triaxial compression, and k_s is a rather large number (say 10 or

100; it's actual value is unknown but it is not infinity). The fitted curve in Figure 4.2 is expressed as:

$$k_s = 1.22 + 0.014 e^{13.5 (t/D_o)} \quad (4.3)$$

To predict implosion of thick-walled spheres, the design equation is obtained by substituting Equation 4.2 into Equation 4.1:

$$P_{im} = k_s f'_c \left[1 - \left(1 - 2 \frac{t}{D_o} \right)^2 \right] \quad (4.4)$$

Equation 4.4 is shown in Figure 4.1, which may be used as a design chart.

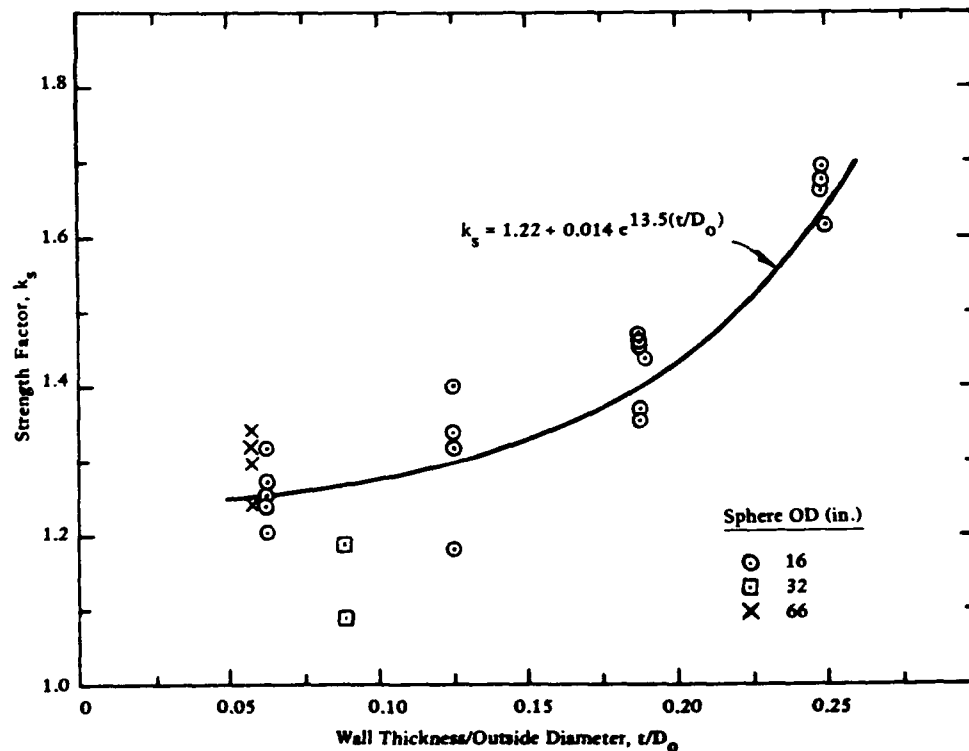


Figure 4.2 Relationship between k_s and t/D_o of thick-walled spheres.

During early work on thick-walled spheres (Ref 4), cracks appeared in the plane of the wall thickness. This cracking was detected before implosion and, therefore, was considered a preliminary failure mode. Two observations were the basis for this proposed failure mode. First, strain gages mounted on the interior of the wall recorded continuously increasing compressive strains until at some pressure the strains started to decrease in magnitude even though the pressure continued to increase; and, second, fragments of imploded spheres having t/D_0 ratios of 0.188 and 0.250 showed distinct in-plane or delamination cracks. In addition, theoretical calculations showed that radial strains were in tension and of magnitudes sufficient to cause cracking. Although data were quite limited, an expression was developed to predict the pressure at initiation of in-plane cracking using Lamé's elastic thick-wall theory equation for calculating stresses on the interior wall modified by a strength factor, k_s , of 1.35. The expression applied only to spheres having a t/D_0 greater than approximately 0.10.

More recent work (Ref 39 and 40) began to raise doubts about the in-plane cracking concept. At present, an explanation of the earlier findings is:

a. The strain gage readings reduced in magnitude because the concrete surface began to crush. The inside concrete surface was under biaxial loading, while all other concrete was under triaxial loadings, so this surface was most susceptible to crushing. Also, the double curvature of the inside surface assisted in physically holding the concrete in place as it progressed into the descending portion of stress-strain behavior (crushing). The earlier results showed that the strain gages started to record reduced strains at the stress level of $1.35 f'_c$. The stress limit for prisms under pure biaxial loading is about $1.25 f'_c$; hence, the inside surface of the concrete sphere had likely reached its ultimate limit.

b. The in-plane cracks, probably, did not develop as the pressure loading was applied, but rather as the load was removed abruptly by implosion. Sphere implosion was sudden; the shock forces at failure combined with the rapid load removal caused tensile microcracks to join into distinct in-plane cracks. Tensile strains existed in the radial direction, and the direction of tensile microcracks would have been parallel to the wall surfaces, or in-plane to the wall surfaces.

To summarize, in-plane cracks are probably not a preliminary failure mode for thick-walled spheres. Rather, the past expression to predict in-plane cracks could be considered to predict the pressure at initiation of crushing of concrete on the inside surface. Crushing does not mean disintegrating or spalling, only that the descending portion of stress-strain behavior has been entered for the biaxially loaded concrete. This expression is:

$$P_{bi} = 0.90 f'_c \left[1 - \left(1 - 2 \frac{t}{D_o} \right)^3 \right], \text{ for } \frac{t}{D_o} \geq 0.10 \quad (4.5)$$

where: P_{bi} = pressure at initiation of crushing of biaxially loaded concrete on inside surface of sphere, psi

Equation 4.5 is shown in Figure 4.3.

4.2 THIN-WALLED SPHERES

Since data were not available on thin-walled spheres, past literature was reviewed for a conservative expression for buckling of spheres. Buchert (Ref 51) applied the following equation, which is adapted herein:

$$P_{im} = 0.18 E_c \eta \left(\frac{t}{R} \right)^2 \quad (4.6)$$

where: E_c = concrete modulus of elasticity, psi

R = mean radius, inch

η = plasticity reduction factor

t = wall thickness, inch

The constant in Equation 4.6 is 15% of the constant in the theoretical elastic buckling expression for spheres; however, it is well known that the elastic buckling pressure is unobtainable by physical models. The reduced constant in Equation 4.6 makes the expression practical.

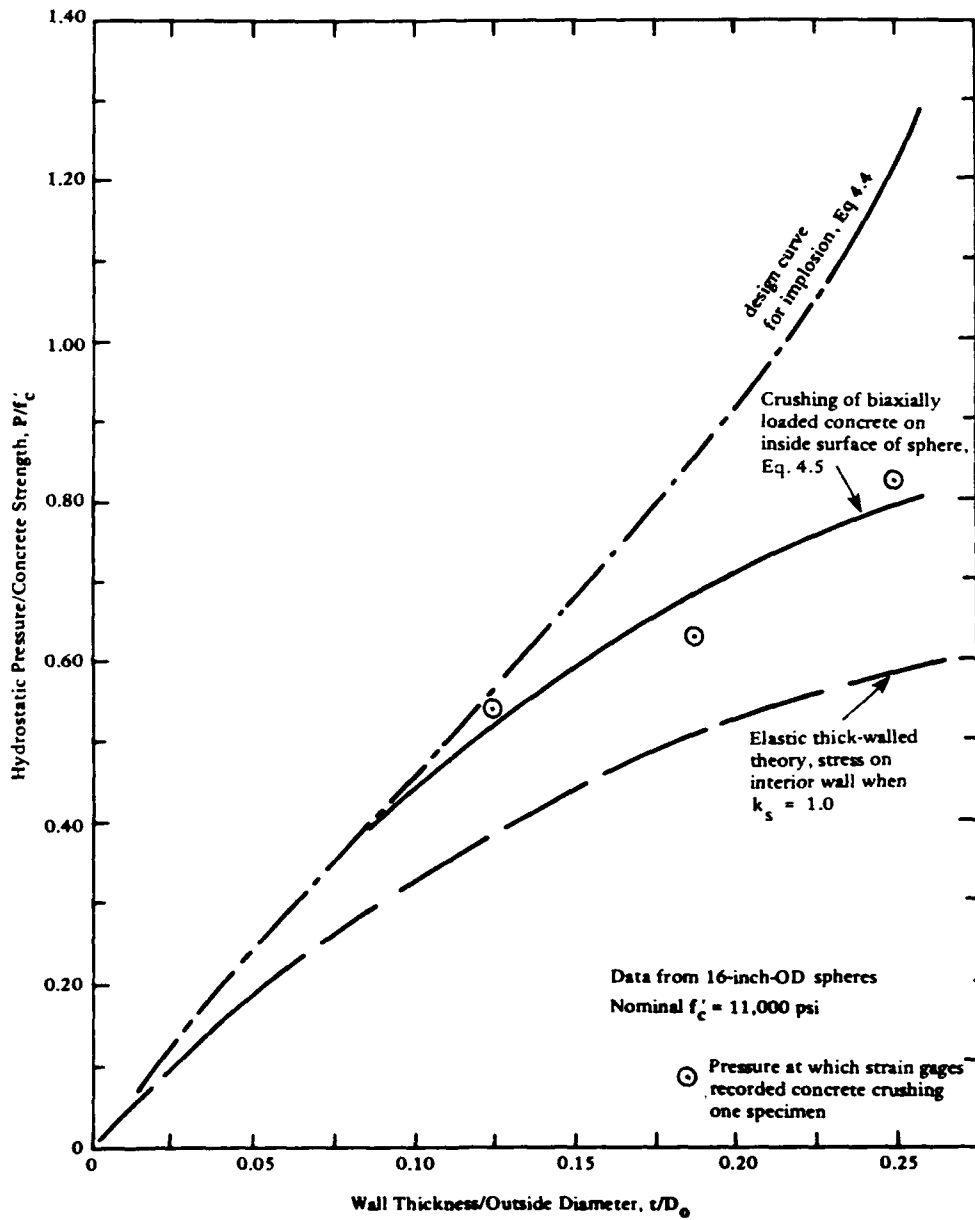


Figure 4.3 Experimental data that indicate the initiation of concrete crushing on the interior surface of thick-walled spheres.

For simplicity, it was assumed that the plasticity reduction factor was the minimum obtained for thin-walled cylinders, $\eta = 0.40$. As t/D_o ratios become smaller, spheres exhibit less inelastic behavior, so η should increase; however the sphere's sensitivity to out-of-roundness will increase. Hence, a conservative approach is to use a consistent η of 0.40. (Note that this is a significant reduction in the value of the plasticity factor ($\eta = 0.70$) recommended in the first edition of this handbook and, therefore, will lead to a more conservative design.)

Also, in a manner similar to that used for the thin-walled cylinders, the empirical expression for concrete modulus of elasticity, $E_c = 530 f'_c$, and the approximation of $R = D_o/2$ are introduced. The design equation to predict implosion for thin-walled spheres thus becomes:

$$P_{im} = 152 f'_c \left(\frac{t}{D_o} \right)^2 \quad (4.7)$$

where: $\frac{t}{D_o} < 0.033$, and $6,000 < f'_c < 10,000$ psi

Figure 4.4, which shows the curve for Equation 4.7, may be used as a design chart.

4.3 DESIGN EXAMPLE, SPHERICAL STRUCTURE

A 100-foot OD spherical structure is required for temporary manned occupation at the 2,000-foot depth in the ocean. Installation procedures require that the structure have a positive buoyancy of about 300 tons.

The following design procedure will determine the concrete compressive strength and sphere wall thickness to meet the above requirements. The reader is cautioned, however, that the buoyancy problem is quite complicated due to water absorption of the concrete,

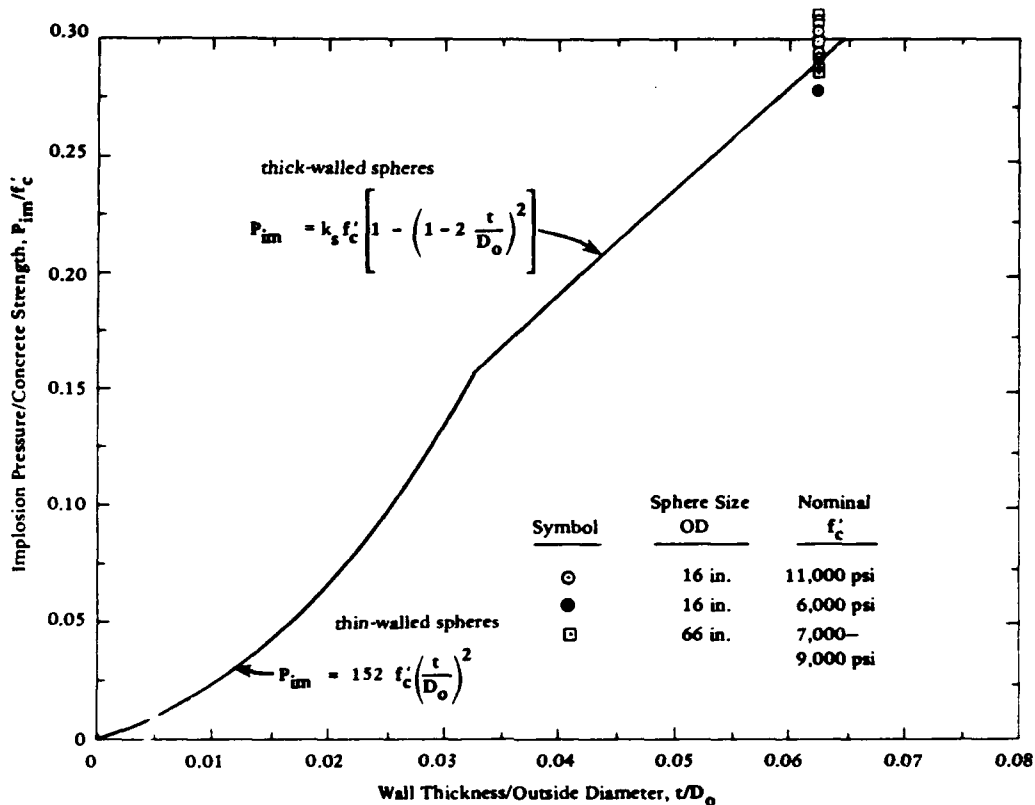


Figure 4.4 Implosion of thin-walled and thick-walled spheres. Experimental data is not available for spheres with a $t/D_o < 0.062$.

volume change of the sphere under load, density changes of the concrete, and other factors. This example will, simplistically, assume a constant 300-ton buoyancy.

The first step is to determine the wall thickness that provides the proper buoyancy for the sphere. Assume that seawater weighs 64 lb/ft³ and concrete 155 lb/ft³.

$$(\text{displaced volume}) - (\text{weight of sphere}) = 300 \text{ tons}$$

$$(64 \text{ pcf}) \frac{\pi}{6} (100)^3 - (155 \text{ pcf}) \frac{\pi}{6} \left[(100)^3 - D_i^3 \right] = 600,000 \text{ lb}$$

Solving for D_i yields:

$$D_i = 84.08 \text{ ft (inside diameter)}$$

Therefore, $t = (100 - 84.08) \frac{1}{2} = 7.96$ ft (wall thickness)

and $\frac{t}{D_o} = 0.08$

The second step is to determine the uniaxial compressive strength of the concrete, f'_c , to give the structure an operational depth of 2,000 feet. The operational pressure, P_{op} , is:

$$P_{op} = 2,000 \text{ ft } (0.445 \text{ psi/ft}) = 890 \text{ psi}$$

The implosion pressure is:

$$P_{im} = (P_{op}) (F.S.)$$

where: F.S. = factor of safety

Use a F.S. of 3.0 for a temporarily manned structure.

$$P_{im} = (890) (3.0) = 2,670 \text{ psi}$$

Use Equation 4.3 to determine k_s and Equation 4.4 to determine f'_c :

$$k_s = 1.22 + 0.014e^{13.5 (t/D_o)} = 1.27$$

$$f'_c = \frac{P_{im}}{k_s \left[1 - \left(1 - 2 \frac{t}{D_o} \right)^2 \right]}$$

$$f'_c = \frac{2,670}{(1.27) \left[1 - (1 - 2 \cdot 0.08)^2 \right]} = 7,140 \text{ psi}$$

which is the compressive strength required at the age when the structure experiences hydrostatic load.

CHAPTER 5. SUMMARY

Test results from laboratory and ocean investigations conducted at NCEL over the past two decades have been condensed into design guides for undersea, pressure-resistant concrete structures. These guides are principally for designing cylindrical and spherical concrete structures to resist the externally applied pressures of hydrostatic loads and thus be safe from implosion failure. Thin-walled and thick-walled structures are considered.

For predicting implosion pressures of thick-walled cylinders, an empirical expression, Equation 3.3, is presented. For thin-walled cylinders, the cases of moderately long, and long cylinders are treated separately. Buckling expressions by Donnell for moderately long cylinders and by Bresse for long cylinders are simplified by incorporating experimentally verified numerical values for the modulus of elasticity and Poisson's ratio of high strength concrete to obtain the design Equations 3.6 and 3.7. These expressions are then modified by an empirically determined plasticity reduction factor. The plasticity reduction factor is presented as a function of the stress level in the cylinder wall at implosion, Equation 3.9. A combined design guide for thick-walled, moderately long, and long cylinders is presented in a chart format in Figure 3.5.

Implosion pressures for thick-walled spheres can be predicted by Equation 4.4, which is an expression based on the average circumferential compressive stress in the concrete sphere wall at the time of failure by implosion. The wall stress is related to the uniaxial compressive strength of concrete by an empirically derived factor. For thin-walled spheres, a conservative buckling expression, Equation 4.7, can be used.

Conservatism has been used in developing these design guides because the technology for submerged concrete structures is relatively

undeveloped. Many concrete technology topics remain to be investigated, and, for that matter, not all the information presented herein has been completely validated. When judgments were made in developing these design guides, engineering knowledge, past experience with concrete used on land and with steel structures under hydrostatic pressure, were conservatively applied. With future research and field experience it is expected that these guidelines will be improved.

CHAPTER 6. ACKNOWLEDGMENT

(Omitted)

(Omitted)

CHAPTER 7. REFERENCES

1. Naval Civil Engineering Laboratory. Technical Report R-517: Behavior of spherical concrete hulls under hydrostatic loading, Part I. Exploratory investigation, by J.D. Stachiw and K.O. Gray. Port Hueneme, Calif., Mar 1967. (AD 649290)
2. _____. Technical Report R-547: Behavior of spherical concrete hulls under hydrostatic loading, Part II. Effect of penetrations, by J.D. Stachiw. Port Hueneme, Calif., Oct 1967. (AD 661187)
3. _____. Technical Report R-588: Behavior of spherical concrete hulls under hydrostatic loading, Part III. Relationship between thickness-to-diameter ratio and critical pressures, straining, and water permeation rates, by J.D. Stachiw and K. Mack. Port Hueneme, Calif., Jun 1968. (AD 8354926)
4. _____. Technical Report R-679: Failure of thick-walled concrete spheres subjected to hydrostatic loading, by H.H. Haynes and R.A. Hoofnagle. Port Hueneme, Calif., May 1970. (AD 708011)
5. _____. Technical Report R-696: Influence of length-to-diameter ratio on the behavior of concrete cylindrical hulls under hydrostatic loading, by H.H. Haynes and R.J. Ross. Port Hueneme, Calif., Sep 1970. (AD 713088)
6. _____. Technical Report R-673 and R-673S: In-situ strength of subaqueous concrete, by W.R. Lorman. Port Hueneme, Calif., Apr 1971 and Sep 1971. (AD 705993 and AD 889084L)

7. _____. Technical Report R-735: Influence of stiff equatorial rings on concrete spherical hulls subjected to hydrostatic loading, by L.F. Kahn. Port Hueneme, Calif., Aug 1971. (AD 731352)
8. _____. Technical Report R-735: Influence of stiff equatorial rings on concrete spherical hulls subjected to hydrostatic loading, by L.F. Kahn and J.D. Stachiw. Port Hueneme, Calif., Aug 1971. (AD 731352)
9. _____. Technical Report R-753: Polymer-impregnated concrete spherical hulls under hydrostatic loading, by H.H. Haynes and N.D. Albertsen. Port Hueneme, Calif., Dec 1971. (AD 736598)
10. _____. Technical Report R-774: Behavior of 66-inch concrete spheres under short-and long-term hydrostatic loading, by H.H. Haynes and L.F. Kahn. Port Hueneme, Calif., Sep 1972. (AD 748584)
11. _____. Technical Report R-785: Hydrostatic loading of concrete spherical hulls reinforced with steel liners, by H.H. Haynes, G.L. Page, and R.J. Ross. Port Hueneme, Calif., Apr 1973. (AD 759684)
12. _____. Technical Report R-790: Influence of compressive strength and wall thickness on behavior of concrete cylindrical hulls under hydrostatic loading, by N.D. Albertsen. Port Hueneme, Calif., Jun 1973. (AD 764054)
13. _____. Technical Report R-805: Long-term deep-ocean test of concrete spherical structures. Part I: Fabrication, emplacement, and initial inspections, by H.H. Haynes. Port Hueneme, Calif., Mar 1974. (AD 777079)
14. _____. Technical Report R-817: Seafloor construction experiment, SEACON I - An integrated evaluation of seafloor construction equipment and techniques, by T. Kretschmer, et al. Port Hueneme, Calif., Feb 1975. (AD A009097)

15. _____. Technical Report R-869: Long-term, deep-ocean test of concrete spherical structures - Results after 6 years, by H.H. Haynes and R.S. Highberg. Port Hueneme, Calif., Jan 1979. (AD A070864)
16. _____. Technical Report R-874: Design for implosion of concrete cylinder structures under hydrostatic loading, by H.H. Haynes. Port Hueneme, Calif., Aug 1979. (AD A078641)
17. _____. Technical Report R-915: Long-term, deep-ocean test of concrete spherical structures - results after 13 years, by R.D. Rail and R.L. Wendt. Port Hueneme, Calif., July 1985. (A 160232)
18. American Concrete Institute. ACI 357-R: Guide for the design and construction of fixed offshore concrete structures. Revised 1985. ACI Committee 357. Detroit, Michigan.
19. Naval Civil Engineering Laboratory. Technical Note N-1360: SEA CACHE: A mobile petroleum, oils, lubricants (POL) seafloor storage and supply system for advanced bases, by N.D. Albertsen and H.H. Haynes. Port Hueneme, Calif., Nov 1974. (AD A004936)
20. B.C. Gerwick, Jr., W. Webster, D. Smith and J.D. Stachiw. Feasibility study for concrete submarine. University of California, Berkely, Calif., Dec 1974.
21. S. Mindess and J.F. Young. Concrete. Prentice-Hall, Englewood Cliffs, N.J., 1981, pp 422-424.
22. Naval Civil Engineering Laboratory. Technical Note N-1308: Compressive strength of 67-year-old concrete submerged in seawater, by H.H. Haynes and P.C. Zubiate, Port Hueneme, Calif., Oct 1973. (AD 772527)

23. G. Verbeck, "Pore structure," Special Technical Publication No. 169-A, Significance of Test and Properties of Concrete and Concrete Making Materials, American Society of Testing and Materials, Philadelphia, Penn., 1966, pp 211-219.
24. D.D. Double, and A. Hellowell, "The solidification of cement," Scientific American, vol 237, no. 1, Jul 1977, pp 82-90.
25. T.C. Powers, "The nature of concrete," Special Technical Publication No. 169-A, Significance of Tests and Properties of Concrete and Concrete Making Materials, American Society of Testing and Materials, Philadelphia, Penn., 1966, pp 61-72.
26. Naval Civil Engineering Laboratory. Technical Note N-1436: Seawater absorption and compressive strength of concrete at ocean depths, by H.H. Haynes, R.S. Highberg, and B.A. Nordby. Port Hueneme, Calif., Apr 1976. (AD A026192)
27. _____. Technical Note N-1603: Compressive strength of freshly mixed concrete placed, cured, and tested in the deep ocean, by H.H. Haynes and L.D. Underbakke. Port Hueneme, Calif., Feb 1981. (AD B058918L)
28. _____. Technical Memorandum M-44-80-6: Concrete spherical structures subjected to rapid loading by external pressure - an exploratory investigation, by H.H. Haynes. Port Hueneme, Calif., Mar 1980.
29. S. Stockl, "Strength of concrete under uniaxial sustained loading," Concrete for Nuclear Reactors, vol I, ACI Special Publication SP-34, pp 313-326.
30. H.H. Haynes and M.B. Balachandra, "Low-cycle fatigue of fiber reinforced concrete spheres under hydrostatic loading," ACI Special Publication SP-75, Fatigue of Concrete Structures, Sep 1982, pp 289-305.

31. S.S. Takhar, I.J. Jordaan, and B.R. Gamble, "Fatigue of concrete under lateral confining pressure," ACI Special Publication SP-41, Fatigue of Concrete, 1973, pp 59-69.
32. M.E. Awad, and H.K. Hilsdorf, "Strength and deformation characteristics of plain concrete subject to high repeated and sustained loads," ACI Special Publication SP-41, Fatigue of Concrete, 1973, pp 1-13.
33. Naval Civil Engineering Laboratory. Technical Report R-447, Dynamic properties of plain Portland cement concrete, by W.L. Cowell, Port Hueneme, Calif., Jun 1966.
34. U.S. National Bureau of Standards. Report 1523: The Effect of loading rate on the compressive strength and elastic properties of plain concrete by D. Watstein and A.P. Boresi. Washington D.C., Mar 1952.
35. U.S. Army Corps of Engineers. Engineering Manual EM-1110-345-414: Engineering and design: Design of structures to resist the effects of atomic weapons. Washington D.C., Mar 1957.
36. U.S. Air Force Special Weapons Center. Technical Document Report Number AFSWC-TDR-62-138: Air Force design manual: Principles and practices for design of hardened structures. Kirtland Air Force Base, N.M., Dec 1962.
37. Naval Civil Engineering Laboratory. Technical Note N-1364: Behavior of steel bar reinforced concrete spheres under hydrostatic loading, by N.D. Albertsen. Port Hueneme, Calif., Apr 1975. (AD A011810)
38. American Concrete Institute. ACI 318: Building code requirements for reinforced concrete, Detroit, Mi., 1983.

39. Naval Civil Engineering Laboratory. Technical Memorandum M-44-78-03: Test results from repeated hydrostatic loading of thick-walled concrete spheres, by P.C. Zubiate, Jr. and H.H. Haynes. Port Hueneme, Calif., Nov 1977.
40. _____. Technical Memorandum M-44-77-08: Data from hydrostatic test of concrete sphere AY-11, by H.H. Haynes and P.C. Zubiate, Jr. Port Hueneme, Calif., May 1977.
41. American Concrete Institute. ACI 503R: "Use of epoxy compounds with concrete," Detroit, Mi., 1980
42. Naval Civil Engineering Laboratory. Technical Note N-1173: Evaluation of eight epoxy adhesives for bonding concrete and micro-concrete structural components exposed to room and to hydrostatic pressure conditions, by T. Roe, A.F. Curry, and P.C. Zubiate. Port Hueneme, Calif., Jul 1971. (AD 888505L)
43. Federation Internationale de la Precontrainte (FIP), Recommendations for the design and construction of concrete sea structures, 3rd edition, London, England, 1977.
44. Naval Civil Engineering Laboratory. Technical Memorandum M-44-76-04: Results of concrete cylinder implosion test program, by H.H. Haynes and R.S. Highberg. Port Hueneme, Calif., Apr 1976.
45. R.S. Highberg and H.H. Haynes. "Ocean implosion test of concrete (SEACON) cylindrical structure," paper presented at Proceedings of the Offshore Technology Conference, Houston, Texas, May 1977. (OTC Paper No. 3011)
46. H. Kupfer, H.K. Hilsdorf, and H. Rusch. "Behavior of concrete under biaxial loading," ACI, vol 66, no. 8, Aug 1969, pp 656-666.

47. National Advisory Committee for Aeronautics, Langley Research Center. Report No. 874: A simplified method of elastic stability analysis for thin cylindrical shells, by S.B. Batdorf. Jun 1947, pp 285-309.
48. S.P. Timoshenko and J.M. Gere. Theory of elastic stability. 2nd ed., New York, N.Y., McGraw-Hill Book Company, Inc., 1961, p 293.
49. ACI Committee 363: State-of-the-art report on high strength concrete, Journal of ACI, Jul-Aug 1984, pp 364-411.
50. O. Olsen, "Implosion analysis of concrete cylinders under hydrostatic pressure," ACI, vol 75, no. 3, Mar 1973, pp 82-85.
51. K.P. Buchert. Buckling of shell and shell-like structures. K.P. Buchert and Associates, Columbia, Mo., 1973.

CHAPTER 8. NOMENCLATURE

D_i	Inside diameter (ft or in.)
D_o	Outside diameter (ft or in.)
e_D	Diameter deviation (ft or in.)
e_t	Wall thickness deviation (ft or in.)
E_c	Modulus of elasticity of concrete (psi)
f'_c	Uniaxial compressive strength of concrete (psi)
k_c	Strength increase factor in hoop direction for cylinders
k_s	Strength increase factor for spheres
L	Uninterrupted length of cylinder (ft or in.)
P	Hydrostatic pressure (psi)
P_{bi}	Pressure at initiation of crushing on inside wall of sphere (psi)
P_{im}	Implosion pressure (psi)
P_{op}	Operational pressure (psi)
P_{pl}	Initiation of in-plane cracking pressure (psi)
P_s	Sustained pressure (psi)
R	Mean radius (ft or in.)
R_i	Inside radius of cylinder (ft or in.)
R_o	Outside radius of cylinder (ft or in.)
F.S.	Factor of Safety
t	Wall thickness (ft or in.)
Z	Curvature parameter
β	End condition factor
λ	Long-term loading factor

γ_f Partial load factor

γ_{mc} Partial material factor for concrete

η Plasticity reduction factor

θ Length-to-diameter factor

ν Poisson's ratio

σ_{im} Average stress in hoop direction of cylinder or sphere wall at implosion (psi)

σ Stress in concrete (psi)